AD-A113 733 KOHL (RONALD H) AND ASSOCIATES TULLAHOMA TN F/G 4/1
PROCEEDINGS OF THE 1979 CHEMICAL SYSTEM LABORATORY SCIENTIFIC C--ETC(U)
DEC 80 R H KOHL DAAK11-80-M-0021

UNCLASSIFIED ARCSL-CR-81023 NL

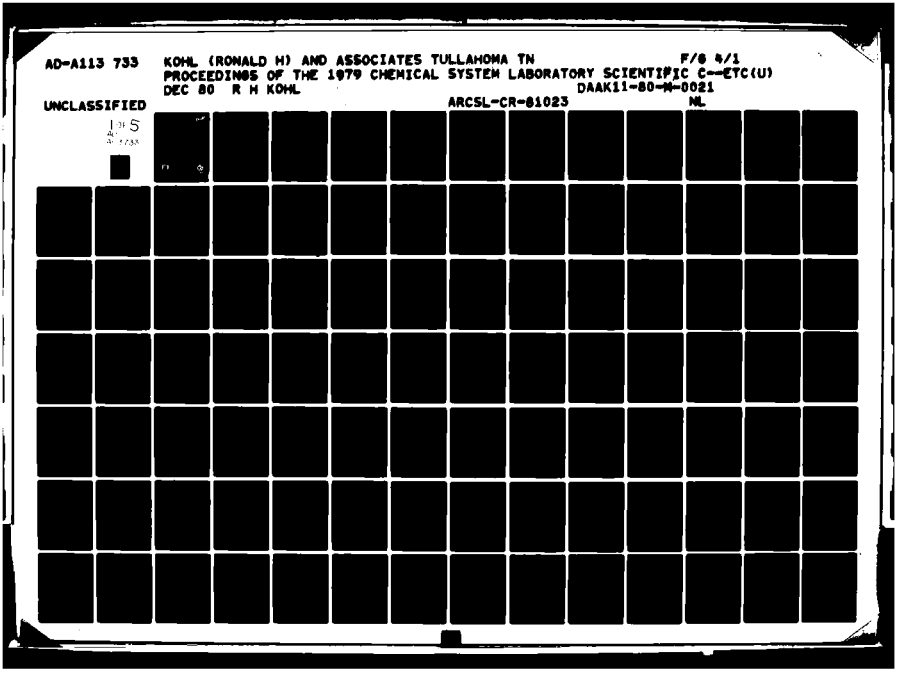

AD

CHEMICAL SYSTEMS LABORATORY CONTRACTOR REPORT

ARCSL-CR-81023

PROCEEDINGS
OF THE
1979
CHEMICAL SYSTEMS LABORATORY
SCIENTIFIC CONFERENCE
ON
OBSCURATION AND AEROSOL RESEARCH

Edited by

Ronald H. Kohl

December 1980

RONALD H. KOHL & ASSOCIATES
Tullahoma, Tennessee 37388

Contract No. DAAK11-80-M-0021

US ARMY ARMAMENT RESEARCH AND DEVELOPMENT COMMAND
Chemical Systems Laboratory
Aberdeen Proving Ground, Maryland 21010

Disclaimer

The views, opinions, and/or findings contained in this report are those of the authors and should not be construed as an official Department of the Army position, policy, or decision unless so designated by other documentation.

Disposition

Destroy this report when it is no longer needed. Do not return it to the originator.

UNCLASSIFIED

SECURITY CLASSIFICATION OF THIS PAGE *(When Data Entered)*

REPORT DOCUMENTATION PAGE

READ INSTRUCTIONS BEFORE COMPLETING FORM

1. REPORT NUMBER: ARCSL-CR-81023	2. GOVT ACCESSION NO.: AD A [illegible]
3. RECIPIENT'S CATALOG NUMBER:	
4. TITLE *(and Subtitle)*: PROCEEDINGS OF THE 1979 CHEMICAL SYSTEM LABORATORY SCIENTIFIC CONFERENCE ON OBSCURATION AND AEROSOL RESEARCH	5. TYPE OF REPORT & PERIOD COVERED: Proceedings 1979 Conference
	6. PERFORMING ORG. REPORT NUMBER:
7. AUTHOR(s): Edited by Ronald H. Kohl	8. CONTRACT OR GRANT NUMBER(s): DAAK 11-80-M-0021
9. PERFORMING ORGANIZATION NAME AND ADDRESS: Ronald H. Kohl & Associates, Route 2, Box 283B, Tullahoma, TN 37388	10. PROGRAM ELEMENT, PROJECT, TASK AREA & WORK UNIT NUMBERS:
11. CONTROLLING OFFICE NAME AND ADDRESS: Commander/Director, Chemical Systems Laboratory, Attn: DRDAR-CLJ-R, Aberdeen Proving Ground, Maryland 21010	12. REPORT DATE: December 1980
	13. NUMBER OF PAGES: 446
14. MONITORING AGENCY NAME & ADDRESS *(if different from Controlling Office)*: Commander/Director, Chemical Systems Laboratory, Attn: DRDAR-CLB-PS/Stuebing (301) 671-2326, Aberdeen Proving Ground, Maryland 21010	15. SECURITY CLASS. *(of this report)*: UNCLASSIFIED
	15a. DECLASSIFICATION/DOWNGRADING SCHEDULE: NA

16. DISTRIBUTION STATEMENT *(of this Report)*

Approved for public release; distribution unlimited

17. DISTRIBUTION STATEMENT *(of the abstract entered in Block 20, if different from Report)*

18. SUPPLEMENTARY NOTES

19. KEY WORDS *(Continue on reverse side if necessary and identify by block number)*

Obscurants	Scattering	Raman Scattering
Obscuration	Electromagnetic Waves	Fluorescence
Aerosol	Spherical Particles	Inhomogeneous Particles
Absorption	Mie Scattering	Aerosol Clusters
Extinction	Rayleigh Scattering	Variational Methods (Continued)

20. ABSTRACT *(Continue on reverse side if necessary and identify by block number)*

Thirty papers on current or recent research are included under the headings of Optical Properties of Aerosols, Physical and Chemical Properties of Aerosols, Aerosol Characterization Methods and Obscurant Materials.

DD FORM 1 JAN 73 1473 EDITION OF 1 NOV 65 IS OBSOLETE

UNCLASSIFIED

SECURITY CLASSIFICATION OF THIS PAGE *(When Data Entered)*

19.
Scattering by Spheres
Scattering by Cylinders
Scattering by Rough Particles
Scattering by Irregular Particles
Scattering by Non-spherical Particles
Scattering by Active Particles
Infrared Emission by Aerosols
Cooperative Scatter
Multiple Scattering
Radiative Transfer
Smoke
Brush Fires
Drop Growth
HC Smoke
Fog Oil Smoke
Particle Mechanics
Plume Mechanics
Atmospheric Optics
Atmospheric Dispersion
Cloud Dynamics
Aerosol Collectors
Aerosol Characterization
Particle Sizing
Hydroscopic Smokes
Asbestos Fibers
Gravimetric Measurements
Interferometry
Particle Size Distribution
Diffusion Battery
Optical Constants
Infrared
Infrared Absorption
Infrared Scattering
Tri-n-Butyl Phosphate
Reflection Spectroscopy
Far-Infrared
Refractive Index
Index of Refraction
Refractive Indices of Materials
Carbon
Low Dimensional Materials
Diffraction Studies
Organic Compounds
Infrared Extinction
Polymers

PREFACE

The 1979 Chemical Systems Laboratory Scientific Conference on Obscuration and Aerosol Research was held 17-21 September, 1979 at the Edgewood Area of Aberdeen Proving Ground, Maryland. It was organized by and under the direction of Dr. Edward W. Stuebing, Scientific Area Coordinator, Aerosol/Obscuration Science.

The Conference is an informal forum for scientific exchange and stimulation amongst investigators in the wide variety of disciplines required for a total description of an obscuring aerosol.

The participants develop some familiarity with the Army Aerosol/ Obscuration Science research program and also become personally acquainted with the other investigators and their research interests and capabilities. Each attendee is invited to talk on any aspect of a topic of interest and may make last minute changes or alterations in his talk as the flow of ideas in the Conference develops.

While all participants in the Conference are invited to submit written papers for the Proceedings of the Conference, each investigator who is funded by the Army Smoke Research Program is requested to provide one or more written papers which document the progress made in his funded effort in the previous year and which indicate future directions.

Therefore, while the papers in these Proceedings tend to closely correspond to what was presented at the Conference, there is not an exact correspondence. The reader will find the items relating to the Conference itself, the list of attendees, the agenda and the contents of the Conference sessions, in the appendixes following the papers collected for these Proceedings and the indexes pertaining to them.

The use of trade names in these Proceedings does not constitute an official endorsement or approval of the use of such commerical hardware or software. These Proceedings may not be cited for purposes of advertisement.

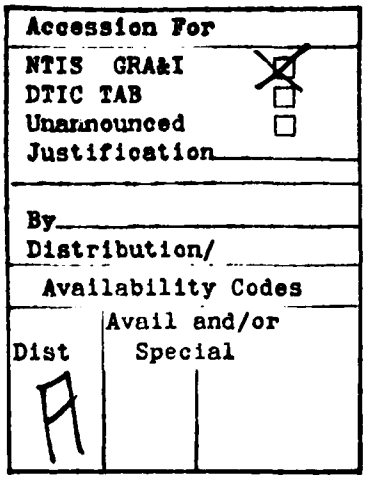

CONTENTS*

* See also the indices of the authors and organizations with papers in these Proceedings on page 413.

I. OPTICAL PROPERTIES OF AEROSOLS

ACTIVE PARTICLES

Milton Kerker
Clarkson College of Technology
Potsdam, New York 13676

PUBLICATIONS

M. Kerker, Appl. Opt. 17, 3337 (1978).
M. Kerker, Appl. Opt. 18, 1180 (1979).

In a highly perceptive paper, Alexopoulos and Uzunoglu[1] have observed that Lorenz-Mie scattering theory predicts some rather remarkable effects when the particles are assumed to have negative absorption. In the usual case, the medium of which the particle is comprised absorbs radiation. For media with negative absorption, corresponding to a population inversion, the medium may be conceived as being stimulated to emit radiation at the exciting frequency.

What had been a particle absorption cross section in the latter case is now designated an amplification cross section.[2] Except for this single change in nomenclature, each relevant cross section is defined precisely the same as for an absorbing medium. Now, as shown in Table 1, the amplification cross section is negative, the scattering cross section remains positive, and the extinction cross section may assume negative, zero, or positive values.

The authors[1] have commented that for zero extinction the particle is electromagnetically invisible in the rather restricted sense that a distant observer in the forward direction would not detect attenuation of the incident beam. The distance of the observer must be sufficiently great so that forward scattered light and multiply scattered light, which is returned to the forward direction, be reduced below detection limits by virtue of their propagation as spherical waves.

Actually, as we have noted,[3] such a particle is highly visible in the conventional sense, because at the condition for zero extinction, i.e.,

$$Q_{ext} = Q_{sca} + Q_{amp} = 0, \qquad (1)$$

the equal values of Q_{sca} and $|Q_{amp}|$ are each quite large. Q_{ext}, Q_{sca}, and Q_{amp} denote the efficiencies for extinction, scattering, and amplification, respectively, i.e., these are the cross sections that have been normalized relative to the cross-sectional area of the particle.

Whenever $|Q_{amp}| > Q_{sca}$, so that the extinction cross section is negative, the incident beam, which is taken to be a plane wave, is amplified. Accordingly, a portion of the emitted radiation, not included as part of Q_{sca}, propagates as a parallel

beam in the direction of the transmitted wave in addition to the remainder of the radiation arising within the particle, which propagates variously in all directions as spherical or cylindrical waves.

The implications of the above features for applications raise the question of the conditions under which the Lorenz-Mie formalism might be valid for so-called active particles comprised of materials with a negative absorption index. A Lorenz-Mie scatterer may be viewed as an assembly of dipoles undergoing forced oscillation in phase with the internal electric field. The internal field, which satisfies the boundary conditions at the particle surface, may vary considerably throughout the particle. In the present instance one might consider that the particle has been raised to saturation at the pumping frequencies so that the population inversion and hence the amplification index are uniform throughout the particle, and also that stimulation of emission is proportional to the square of the magnitude of the local field at each position within the particle at the stimulating frequency. Then the Lorenz-Mie solution at the stimulating frequency will describe the scattered field for such active particles. Of course, these equations will apply only at the onset of stimulation or as long as the pumping proceeds rapidly enough to maintain the population inversion corresponding to the particular value of the amplification index.

Quite a different formalism must be used if the medium has not attained saturation. Consider, for example, that the particle has been pumped so that the population inversion at each position is proportional to the square of the magnitude of the local internal field at a pumping frequency. If now the entire inverted population at each location within the particle were stimulated to drop to the ground state emitting at some new shifted frequency, the formalism recently developed by us for fluorescence and Raman scattering would apply.[4] That formalism can be extended to include other mechanisms of pumping and stimulation.

Even though the Lorenz-Mie formalism can be applied to stimulated emission only under the conditions specified above, it may still be useful as a guide to predicting the qualitative behavior of active particles. With this in mind, we have carried out a number of computations. Circular cylinders have been selected for these computations rather than spheres because of the greater ease of manipulating single submicron and micron-sized cylinders compared with single similar-sized spheres. Accordingly, cylinders are more likely candidates for investigations described.

The respective contributions of Q_{sca} and Q_{amp} can be seen Fig. 1 where Q_{2amp} and $-Q_{2sca}$ are plotted against the size parameter $\alpha = 2\pi a/\lambda$. Here the subscripts 1 or 2 designate polarization with the electric vector vibrating parallel or perpendicular to the cylinder axis, respectively, for radiation propagating perpendicular to that axis. The major oscillation of

Q_{2sca} is similar to that for the nonabsorbing case except for the slow increase from the average value of 2. This increase reflects the contribution to the scattering by the sources within the particle as evidenced by the rising values of $-Q_{2amp}$ with increasing size.

At higher negative absorption or for similar negative absorption at higher values of α extraordinarily sharp resonances occur. This is illustrated in Fig. 2. Indeed such resonances may occur without limit. These resonances may be attributed to resonances in a single expansion coefficient in the scattering functions. In order to increase without limit, both the real and the imaginary parts of the denominator of such a coefficient must become zero for the same values of the parameters (i.e., α and the complex refractive index). Such a condition is illustrated in Fig. 3. The curves with small negative slopes are plots of the real part of the denominator of expansion coefficient b_0 vs α at constant nk; the curves with steep positive slopes are for the corresponding imaginary parts of the denominator of b_0. The condition for resonance is that both the real and imaginary parts of the denominator change signs simultaneously, i.e., traverse zero simultaneously.

The intersections of these curves correspond to equal values of the real and imaginary parts of the denominator of b_0. The locus of these intersections near the transition is plotted in the inset to Fig. 3. Three values of the real and imaginary parts of the denominator of b_0 are indicated on this locus showing how the denominator does pass through zero, thereby causing b_0 to increase without limit.

The effect only occurs for particles that exhibit negative absorption. For nonabsorbing spheres and cylinders the loci of a_n and b_n can be represented as a circle in the complex domain with a center at 0 and 0.5 and a radius at 0.5. The coefficients trace clockwise circles with increasing α. For absorbing particles, the loci spiral inward from the circle. Thus, in no case may the coefficient of a passive particle exceed a value prescribed by the circular locus. However, for active particles the loci spiral outward from the unit circle executing extended outward loops in the neighborhood of resonances.

An example of zero and negative extinction is shown in Fig. 4. The resonance $\alpha = 94.1$ and $n\kappa = 0.0051$ is expanded in the inset showing a negative extinction in the region of this resonance. Such negative extinctions may occur over quite broad ranges of the physical parameters.

Although resonances in Q_{1sca} and Q_{2sca} do not generally coincide, there are exceptions to this in some instances. Such a resonance is explored in Fig. 5 where $Q_{1sca} = 8.7\times10^{11}$ at $\alpha = 16.24756$ and $n\kappa = 0.0493585$. In this case Q_{2sca} is precisely half

of Q_{1sca}. This behavior is an exception and corresponds to a simultaneous resonance in two expansion coefficients, b_1 and a_0. The a_n coefficients determine the component Q_2 while the b_n coefficients determine the component Q_1. This coincidence in the resonance of Q_1 and Q_2 follows from the fact that for these two coefficients a_0 and b_1, the relation $a_1 = b_0$ holds.

REFERENCES

1. N.C. Alexopoulos and N.K. Uzunoglu, Appl. Opt. 17, 235 (1978).
2. We assume in this report that the reader is familiar with the usual nomenclature and notation such as can be found in M. Kerker, The Scattering of Light and other Electromagnetic Radiation, Academic Press, New York, 1969.
3. M. Kerker, Appl. Opt. 17, 3337 (1978).
4. H. Chew, P.J. McNulty and M. Kerker, Phys. Rev. A13, 386-404 (1976).
5. M. Kerker, Appl. Opt. 18, 1180 (1979).

Table 1. Cross sections for particles with positive and negative absorption.

Absorbing media	Emitting media
$Q_{sca} > 0$	$Q_{sca} > 0$
$Q_{abs} \geq 0$	$Q_{amp} \leq 0$
$Q_{ext} = Q_{sca} + Q_{abs} > 0$	$Q_{ext} = Q_{sca} + Q_{amp} \gtrless 0$

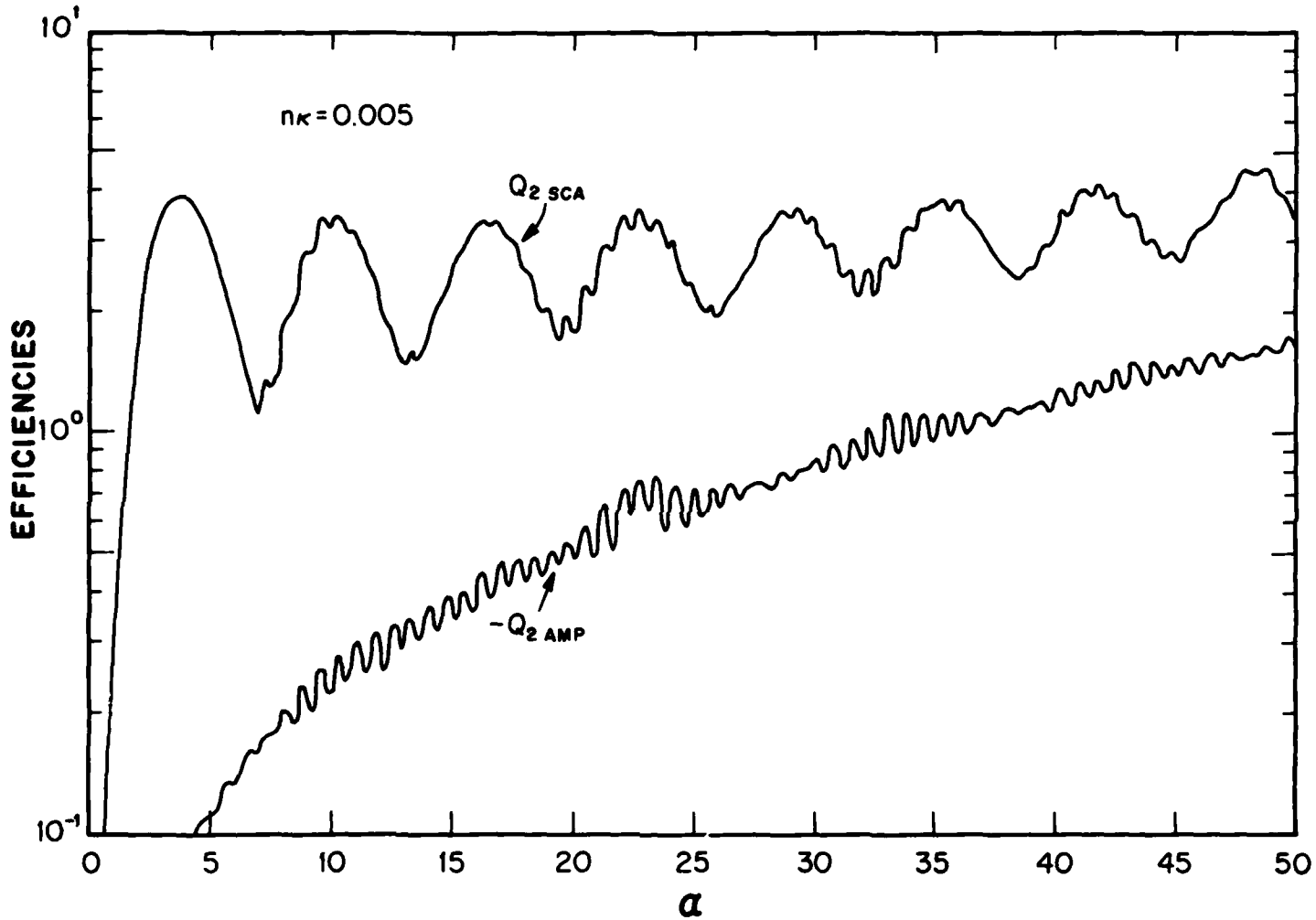

Figure 1. Efficiencies for scattering Q_{2sca} and for amplification $-Q_{2amp}$ vs size parameter α for m = 1.5+0.005i.

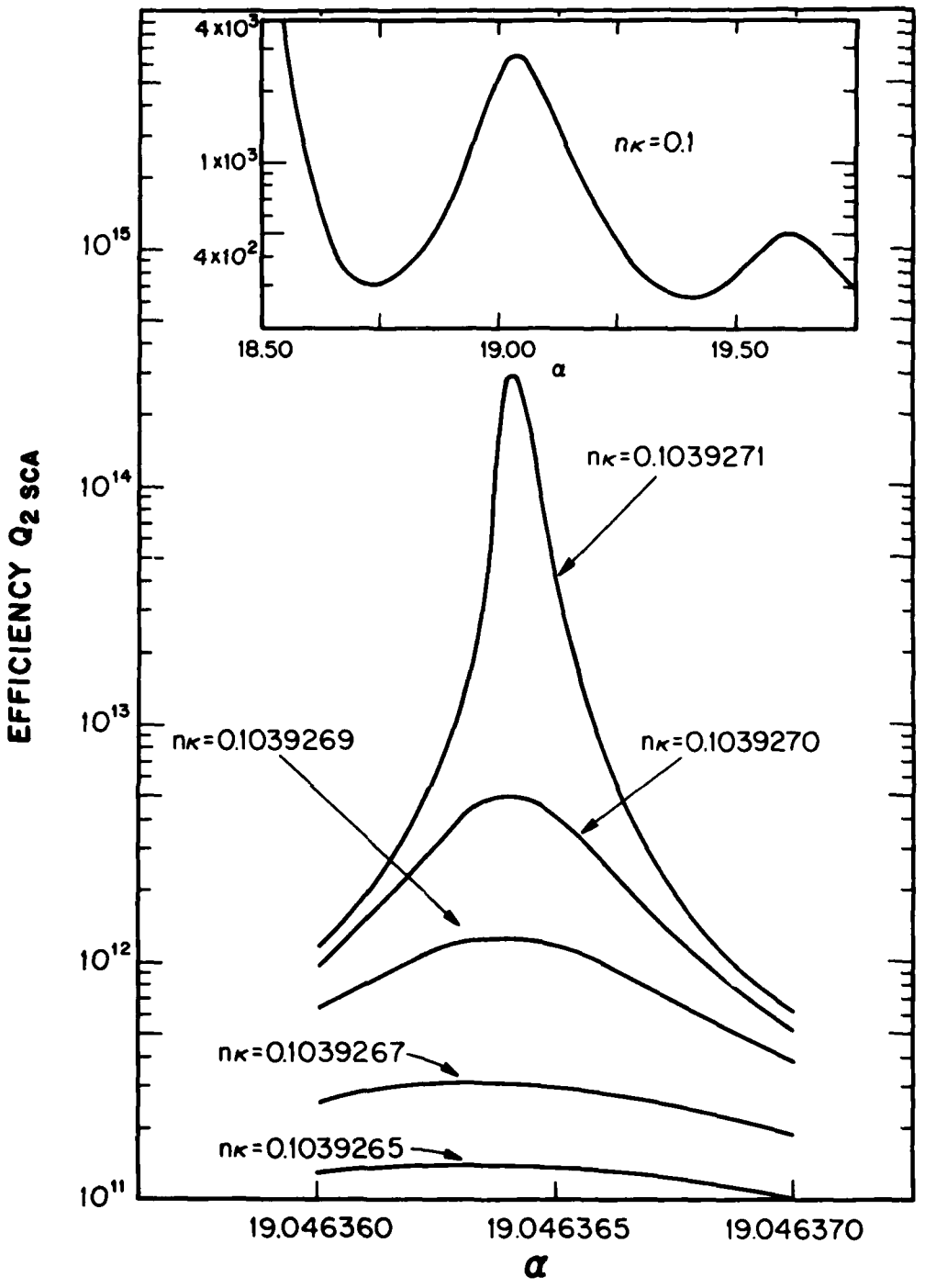

Figure 2. Efficiencies for scattering Q_{2sca} vs α for n = 1.5 at various values of $n\kappa$ showing the sensitivity of the resonance to $n\kappa$.

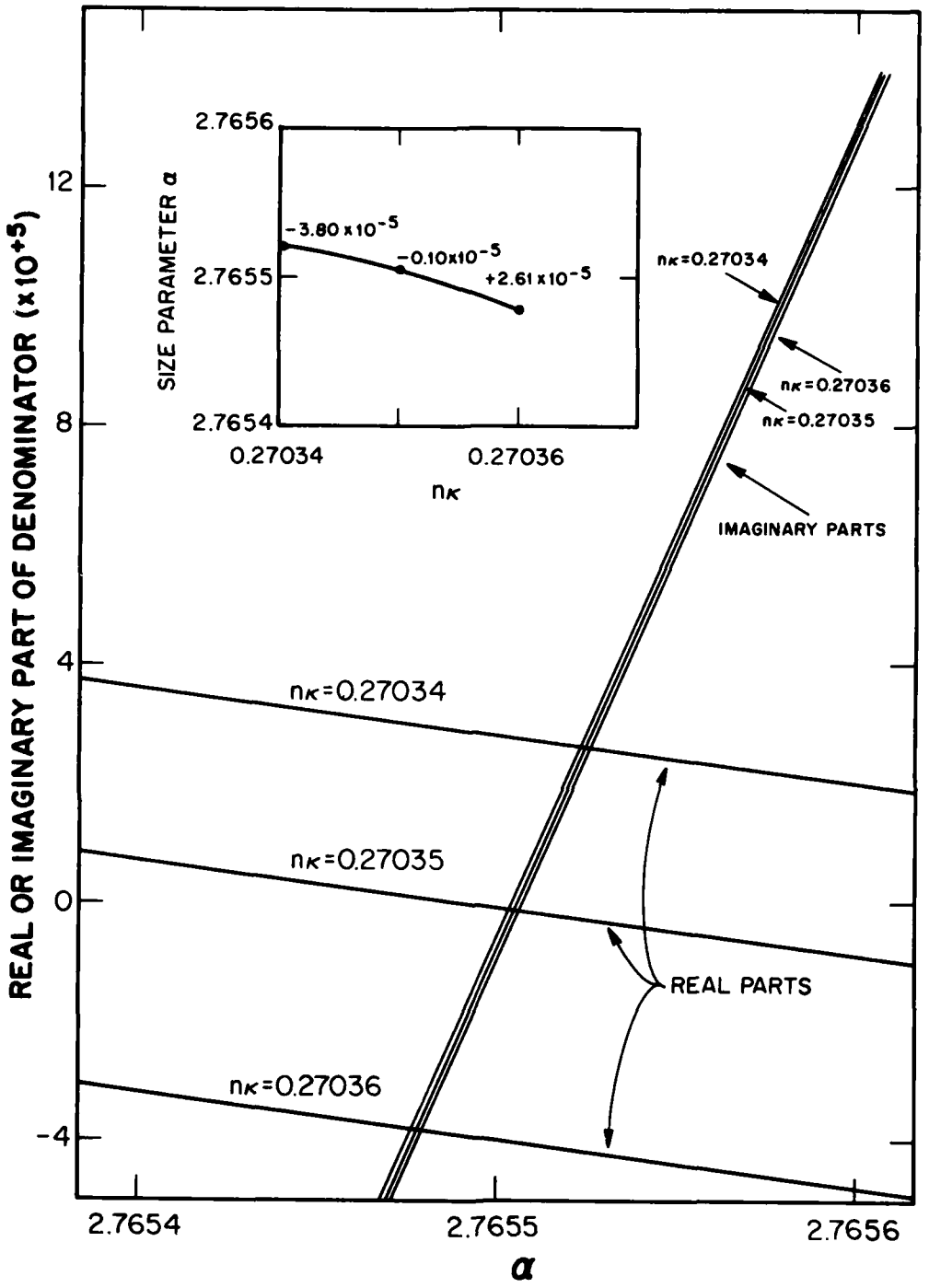

Figure 3. Real (lines with small negative slope) and imaginary (lines with steep positive slope) parts of the denominator of the coefficient b_0 vs α for m = 1.5 + 0.27035i, and 1.5+0.27036i. Inset plots the locus for equal values of the real and imaginary parts of the denominator of b_0. Values at three points on the locus show how b_0 goes through zero as the sign changes.

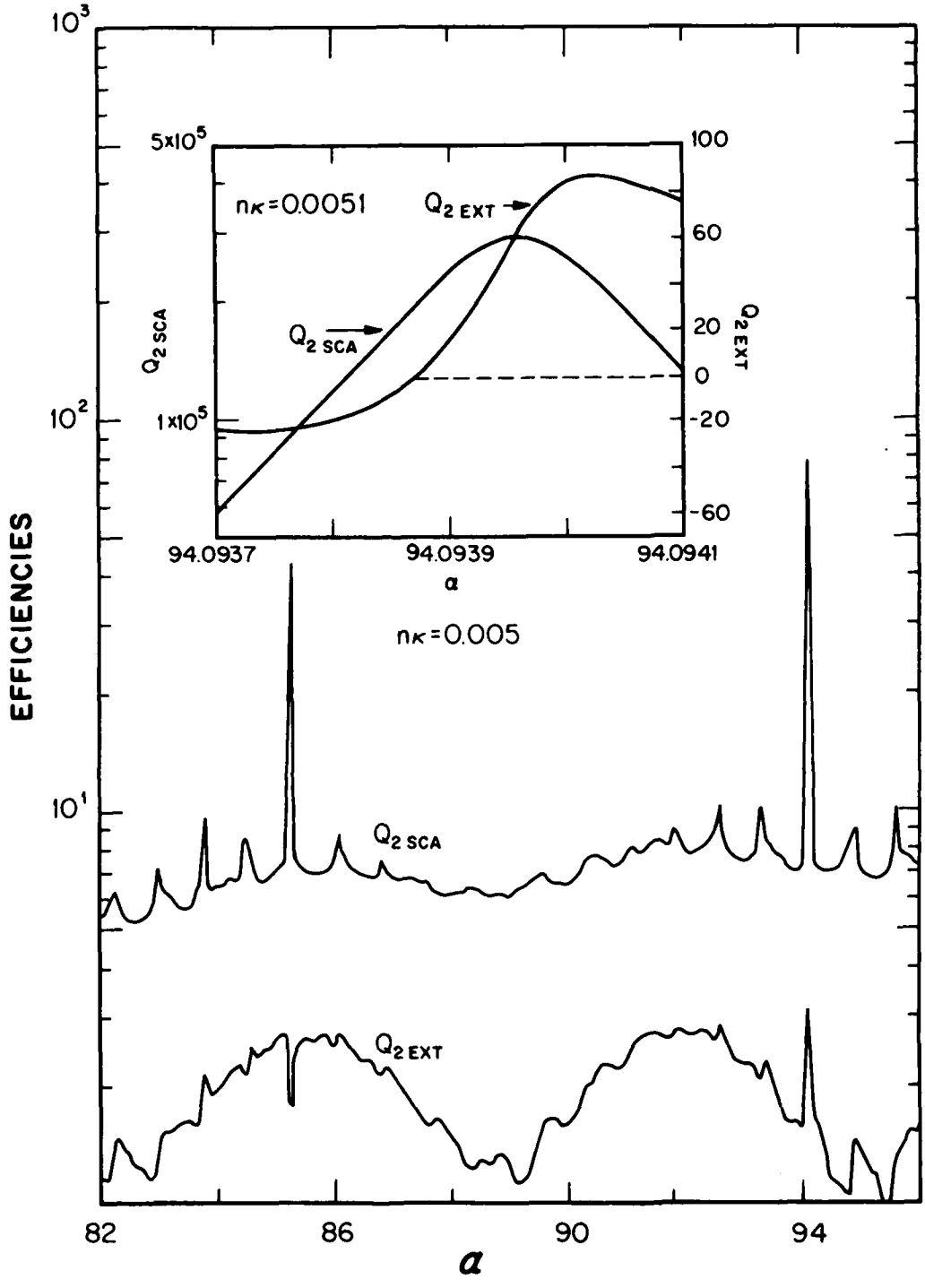

Figure 4. Efficiencies for scattering Q_{2sca} and for extinction Q_{2ext} vs size parameter α for m = 1.5 + 0.005i. Inset shows resonance at α = 94.09395 and nκ = 0.0051 illustrating negative values of Q_{2xt}.

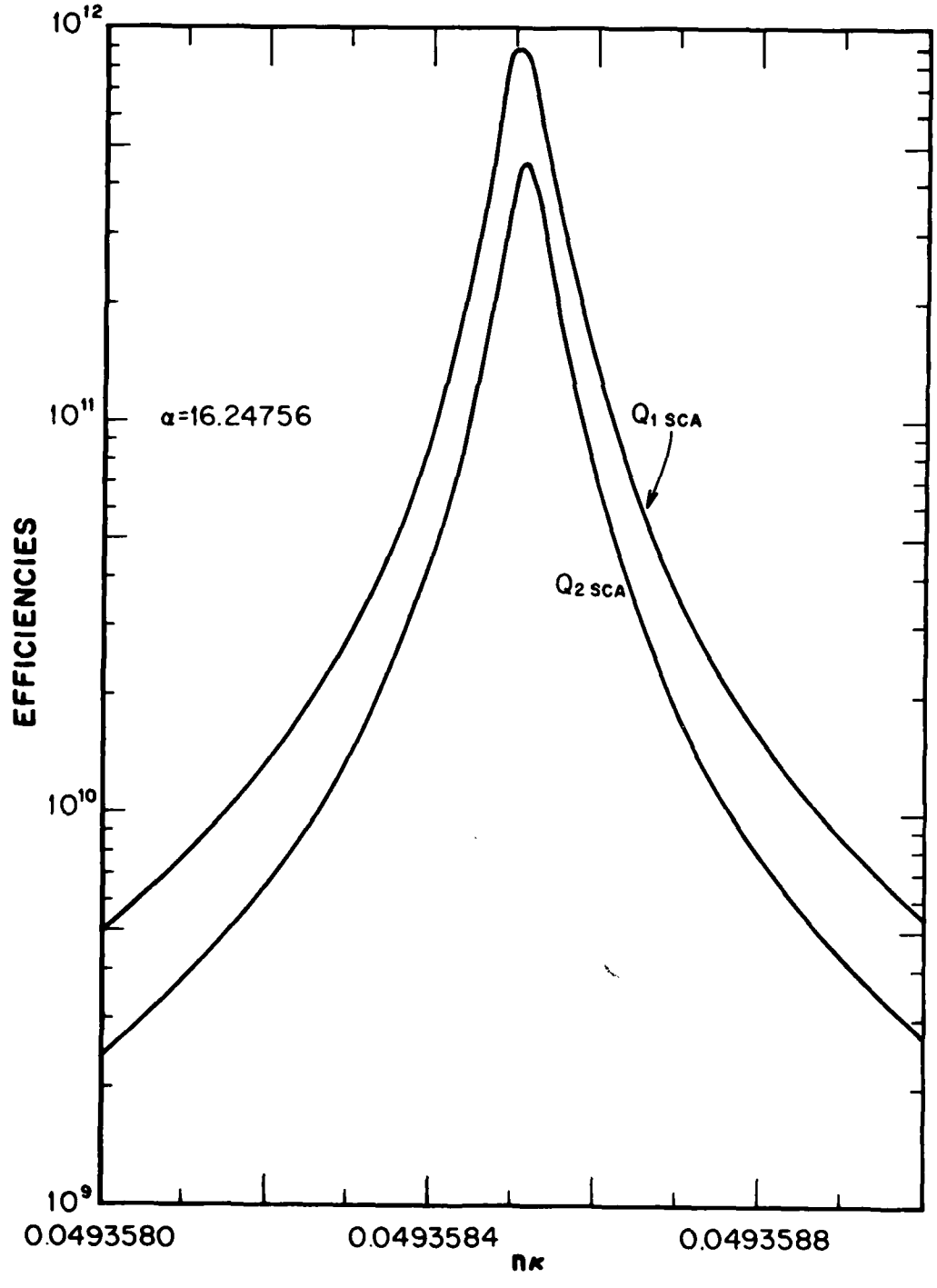

Figure 5. Efficiencies for scattering Q_{1sca} and Q_{2sca} vs negative absorption $n\kappa$ for n = 1.5 and α = 16.24756. At this resonance $Q_{1sca} = 2Q_{2sca}$.

VARIATIONAL METHODS FOR ELECTROMAGNETIC WAVE SCATTERING FROM AEROSOL CLUSTERS*

R. H. Andreo**, J. A. Krill, and R. A. Farrell
Applied Physics Laboratory, The Johns Hopkins University

PUBLICATIONS

Andreo, R. H., "Variational Methods for Wave Scattering from Random Systems," Proceedings of the Conference on Mathematical Methods and Applications of Scattering Theory, Catholic University, Washington, D.C., May 21-25, 1979. To be published by Springer-Verlag.

Andreo, R. H. and J. A. Krill, "Stochastic Variational Formulations of Electromagnetic Wave Scattering," Proceedings of the Conference on Recent Developments in Classical Wave Scattering: Focus on the T-Matrix Approach, The Ohio State University, Columbus, Ohio, June 25-27, 1979. To be published by Pergamon Press.

Krill, J. A. and R. H. Andreo, "Vector Stochastic Variational Principles for Electromagnetic Wave Scattering," to be submitted to IEEE Trans. Ant. Prop. (1979).

SUMMARY

The investigation of cooperative phenomena in electromagnetic wave scattering from randomly clustered aerosol particles is of considerable interest in such areas as environmental pollutants, obscurants, and radar chaff. As a first step towards assessing the importance of cooperative effects in light scattering from an aerosol, we have extended the stochastic variational method developed by Hart and Farrell[1] for scalar waves and homogeneous boundary conditions to include vector waves and inhomogeneous boundary conditions.[2]

BACKGROUND

The stochastic variational methods extend to random scattering problems the computational advantages which have been found to be useful for determinstic scattering.[3] The main advantage is variational invariance, i.e., cancellation of first-order errors introduced by approximating the (unknown) fields. This important property allows a variational calculation to improve upon existing approximations. However, the application of variational methods to scattering from stochastic systems has been extremely limited. The reason is as follows: the variational form of the scattering amplitude T is $4\pi T = N_1 N_2 / D$, where N_1 is

---

* This work was supported by the Department of the Navy (Naval Sea Systems Command) and by the Department of the Army (Armament Research and Development Command) under Contract N00024-78-C-5384.

**Speaker.

the familiar noninvariant integral representation of $4\pi AT$ (with A the amplitude of the incident wave) and the quotient of integrals, N_1/D, is the variational correction factor. The average of this expression for a random system requires the formidable average $4\pi\langle T\rangle = \langle N_1 N_2/D\rangle$. This calculation has proven intractable.

In 1977 Hart and Farrell[1] showed that this difficulty could be overcome. For the case of scalar wave scattering with homogeneous Neumann boundary conditions, they demonstrated for arbitrary scatterer statistics that the average of T could be re-expressed exactly as $4\pi\langle T\rangle = \langle N_1\rangle\langle N_2\rangle/\langle D\rangle$, and, more importantly, that this expression is variationally invariant. Because this simpler variational method allows the possibility of tractable variational approximations for the statistical moments and probability density functions of T, it has been labeled a stochastic variational principle.

The first application of the scalar stochastic variational principle was by Gray, Hart, and Farrell.[4] They calculated the differential cross section for the scattering of a normally incident TM (transverse-magnetic) plane wave from a model random rough surface consisting of many parallel, nonoverlapping perfectly conducting hemicylinders randomly distributed over an infinite conducting plane (Figure 1). They computed the Born approximation to $\langle|T|^2\rangle$ and compared it to the stochastic variational approximation using the same plane wave function. In the low frequency (Rayleigh) limit, both approximations were found to be of the form

$$\langle|T|^2\rangle = C(1-\nu\alpha) \tag{1}$$

to first order in ν, the area fraction of the plane occupied by the hemicylinders. In both cases, the constant C in this expression is twice the absolute square of the scattering amplitude for an isolated hemicylinder; however, the parameter α is equal to 2 for the Born approximation and 4.08 for the variational result.

In order to investigate the discrepancy between these two results, Krill and Farrell[5] considered a special case of this surface with only two hemicylinders present. They were able to obtain the *exact* solution as well as the Born approximation and its variational improvement, again finding the result (1), where now the constant $\alpha = 1.89$ for the exact solution, $\alpha = 2.04$ for the variational approximation, and $\alpha = 1$ for the Born approximation. The variational result is thus the more accurate of the two approximations. A careful examination of these solutions revealed that the variational approximation accounts for multiple scattering, but the Born approximation, which it clearly improves upon, does not.

ELECTROMAGNETIC WAVE SCATTERING

The variational treatment of the scattering of electromagnetic radiation from an aerosol, whose particles generally have finite conductivity and are of arbitrary shape, requires the development of stochastic variational methods for vector waves and inhomogeneous boundary conditions. To this end Krill and Andreo[2] have developed a vector stochastic variational principle for the scattering of a plane electromagnetic wave $\left(\text{with electric field } \vec{E}_i = A\,\hat{e}_i\, e^{i\vec{k}_i\cdot\vec{x}}\right)$ from a localized inhomogeneous and anisotropic conducting dielectric (Figure 2).

The electric field $\vec{E}$ satisfies an equation of the form

$$\vec{\nabla}\times\vec{\nabla}\times\vec{E}(\vec{x}) - k^2\vec{E}(\vec{x}) = \overline{\overline{U}}(\vec{x})\cdot\vec{E}(\vec{x}), \tag{2}$$

where k is the wave number. The dyadic operator is defined as $\overline{\overline{U}}(\vec{x}) \equiv k^2[\overline{\overline{\varepsilon}}(\vec{x}) + (4\pi i/\omega)\overline{\overline{\sigma}}(\vec{x}) - \overline{\overline{I}}]$, where $\overline{\overline{\sigma}}(\vec{x})$ is the conductivity, $\overline{\overline{\varepsilon}}(\vec{x})$ is the permittivity, $\overline{\overline{I}}$ is the unit dyadic, and ω is the angular frequency. We use Green's Theorem[6] with the free-space dyadic Green function $\overline{\overline{G}}_0(\vec{x},\vec{x}') = (\overline{\overline{I}}+\vec{\nabla}\vec{\nabla}/k^2)\exp(ik|\vec{x}-\vec{x}'|) \div 4\pi|\vec{x}-\vec{x}'|$ to rewrite (2) as the integral equation

$$\vec{E}(\vec{x}) = \vec{E}_i(\vec{x}) + \int d^3x'\ \overline{\overline{G}}_0(\vec{x},\vec{x}')\cdot\overline{\overline{U}}(\vec{x}')\cdot\vec{E}(\vec{x}'). \tag{3}$$

The asymptotic form of this equation,

$$\vec{E}(\vec{x}) \xrightarrow[|\vec{x}|>>|\vec{x}'|]{} \vec{E}_i(\vec{x}) + A\,\vec{T}\,\frac{e^{ikr}}{r},$$

allows identification of the vector scattering amplitude

$$\vec{T} = \frac{1}{4\pi A}\,\vec{N}_1, \tag{4}$$

where

$$\vec{N}_1 = \int d^3x' \left(\overline{\overline{I}}_{\hat{k}_s}\, e^{-i\vec{k}_s\cdot\vec{x}'}\right)\cdot\overline{\overline{U}}(\vec{x}')\cdot\vec{E}(\vec{x}') \tag{5}$$

is the usual noninvariant integral representation of $4\pi A\vec{T}$. The presence of the projection operator $\left(\overline{\overline{I}}_{\hat{k}_s} \equiv \overline{\overline{I}} - \hat{k}_s\hat{k}_s\right)$ onto the plane orthogonal to the direction of propagation ($\hat{k}_s \equiv \vec{x}/|\vec{x}|$) of the scattered radiation guarantees the asymptotic transversality of the scattered field, in the sense that $\hat{k}_s\cdot\vec{T} = 0$.

The expression (4) for $\vec{T}$ can be recast into an invariant form by introducing an "adjoint" field $\tilde{\vec{E}}$, together with the associated operator $\tilde{\overline{\overline{U}}}$, and using (3) to write the amplitude A as $A = D/N_2$, in terms of the integrals

$$N_2 = \int d^3x\ \tilde{\vec{E}}(\vec{x})\cdot\tilde{\overline{\overline{U}}}^{Tr}(\vec{x})\cdot\left(\hat{e}_i\, e^{i\vec{k}_i\cdot\vec{x}}\right) \tag{6}$$

and

$$D = \int d^3x\, \tilde{\vec{E}}(\vec{x})\cdot\tilde{\bar{\bar{U}}}^{Tr}(\vec{x})\cdot\vec{E}(\vec{x}) - \int d^3x \int d^3x'\, \tilde{\vec{E}}(\vec{x})\cdot\tilde{\bar{\bar{U}}}^{Tr}(\vec{x})\cdot\bar{\bar{G}}_0(\vec{x},\vec{x}')\cdot\bar{\bar{U}}(\vec{x}')\cdot\vec{E}(\vec{x}'), \tag{7}$$

where the superscript Tr denotes matrix transposition. Elimination of A in (4) then yields the *deterministic* variational result

$$T = \frac{1}{4\pi}\frac{N_1 N_2}{D}\ . \tag{8}$$

Here we have defined $T \equiv \hat{e}_s\cdot\vec{T}$ as the component of the scattering amplitude along an arbitrary polarization direction $\hat{e}_s$, and $N_1 \equiv \hat{e}_s\cdot\vec{N}_1$.

The requirement that (8) be stationary about the exact fields $\vec{E}$ and $\tilde{\vec{E}}$, i.e.,

$$\frac{\delta T}{T} = \frac{\delta N_1}{N_1} + \frac{\delta N_2}{N_2} - \frac{\delta D}{D} = 0,$$

determines an equation for the (as yet unknown) field $\tilde{\vec{E}}$ and suggests the natural choice $\tilde{\bar{\bar{U}}} = \bar{\bar{U}}^{Tr}$ for the operator $\tilde{\bar{\bar{U}}}$. As a consequence $\tilde{\vec{E}}$ satisfies an integral wave equation of the form (3) with the parameters $\hat{e}_i$, $\vec{k}_i$, and $\bar{\bar{U}}$ replaced by $\bar{\bar{I}}_{\hat{k}_s}\cdot\hat{e}_s$, $-\vec{k}_s$, and $\tilde{\bar{\bar{U}}}$. This solution thus describes a plane wave incident along $-\vec{k}_s$ and scattering from an obstacle characterized by $\bar{\bar{U}}^{Tr}$ in the direction $-\vec{k}_i$ (i.e., the "adjoint" problem). Eqs. (4)-(8) can then be used to show that $\hat{e}_s\cdot\vec{T}(\vec{k}_s,\vec{k}_i,\hat{e}_i;\bar{\bar{U}}) = \hat{e}_i\cdot\vec{T}(-\vec{k}_i,-\vec{k}_s,\bar{\bar{I}}_{\hat{k}_s}\cdot\hat{e}_s;\bar{\bar{U}}^{Tr})$, which is a reciprocity relation.

RANDOM SCATTERERS

Assume now that the scatterer is characterized by some randomness, e.g., in position, orientation, size, shape, or material parameters. The quantity of experimental interest is then a statistical moment, for instance, the mean $\langle T\rangle$. The prohibitive calculation $\langle N_1N_2/D\rangle$ which results from a direct average of (8) can be simplified by the observation that the amplitude A of the incident plane wave is independent of the scatterer and is therefore nonstochastic. This readily yields

$$4\pi\langle T\rangle = \frac{1}{A}\langle N_1\rangle$$

and

$$A\langle N_2\rangle = \langle D\rangle,$$

from which we conclude the *exact* result

$$4\pi\langle T\rangle = \frac{\langle N_1\rangle\langle N_2\rangle}{\langle D\rangle}\ , \tag{9}$$

when the exact fields are used in evaluating the integrals N_1, N_2, and D. In addition, the nonstochastic nature of the incoming plane wave for the "adjoint" problem described by $\tilde{\vec{E}}$ can be used to show that the variation of (9) about the exact solutions for $\vec{E}$ and $\tilde{\vec{E}}$ vanishes by virtue of the deterministic variational principle, i.e.,

$$\delta\langle T\rangle/\langle T\rangle = \langle D(\delta N_1/N_1 + \delta N_2/N_2 - \delta D/D)\rangle/\langle D\rangle = 0.$$

Thus, the expression (9) for $\langle T\rangle$ is indeed a *stochastic* variational principle.

Similarly, we can show that

$$(4\pi)^n\langle T^n\rangle = \frac{\langle N_1{}^n\rangle\langle N_2{}^n\rangle}{\langle D^n\rangle} \tag{10}$$

and

$$(4\pi)^{2n}\langle|T|^{2n}\rangle = \frac{\langle|N_1|^{2n}\rangle\langle|N_2|^{2n}\rangle}{\langle|D|^{2n}\rangle} \tag{11}$$

are stochastic variational expressions for the statistical moments of the scattering amplitude T and of the differential scattering cross section $d\sigma/d\Omega = |T|^2$. These relations can be used to derive expressions for the Fourier transforms of the probability density functions of T and $|T|^2$, e.g.,

$$F\{f(|T|^2)\} = \sum_{n=0}^{\infty} [(i\nu)^n/n!]\langle|T|^{2n}\rangle, \tag{12}$$

where F indicates the Fourier transform over parameter ν.[7]

DISCUSSION

We have developed an important and practical theoretical tool, the vector stochastic variational principle, which promises to allow tractable variational calculation of cooperative effects, e.g., interference and multiple scattering, in electromagnetic wave scattering from random systems such as aerosols. These expressions are derived from corresponding deterministic variational principles and extend the applicability of stochastic variational methods from scalar waves and homogeneous boundary conditions to the more general case of vector waves and inhomogeneous boundary conditions. They provide a means for the variational

evaluation of the statistical moments and probability density functions of T and $|T|^2$, and allow the variational improvement of the accuracy of existing approximations.

REFERENCES

[1] R. W. Hart and R. A. Farrell, "A Variational Principle for Scattering from Rough Surfaces," IEEE Trans. Ant. Prop. AP-25, 708-710 (1977).

[2] J. A. Krill and R. H. Andreo, "Vector Stochastic Variational Principles for Electromagnetic Wave Scattering," to be submitted to IEEE Trans. Ant. Prop. (1979).

[3] L. Cairo and T. Kahan, *Variational Techniques in Electromagnetism*, Gordon and Breach, Science Publishers, Inc., New York (1965).

[4] E. P. Gray, R. W. Hart, and R. A. Farrell, "An Application of a Variational Principle for Scattering by Random Rough Surfaces," Radio Science 13, 333-348 (1978).

[5] J. A. Krill and R. A. Farrell, "Comparison between Variational, Perturbational, and Exact Solutions for Scattering from a Random Rough Surface Model," J. Opt. Soc. Am. 68, 768-774 (1978).

[6] C-T. Tai, *Dyadic Green's Functions in Electromagnetic Theory*, Intext, San Francisco (1971).

[7] A. Papoulis, *Probability, Random Variables, and Stochastic Processes*, McGraw-Hill, New York (1965).

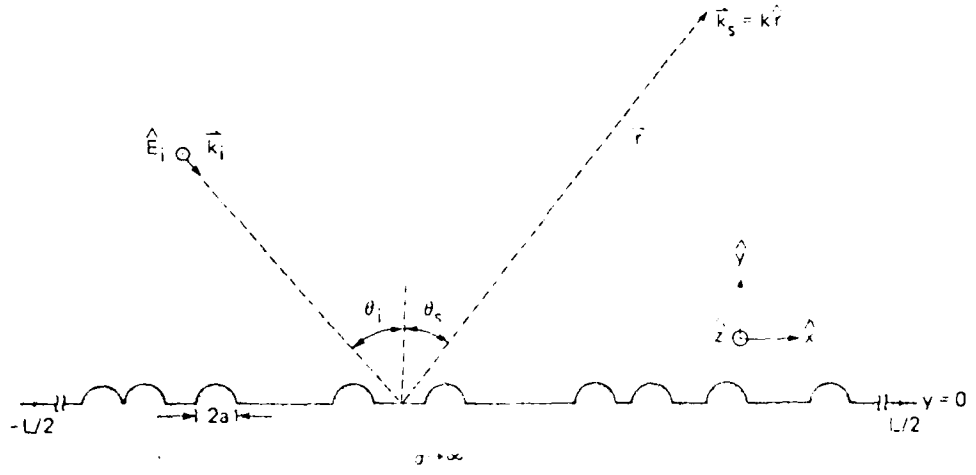

Figure 1. Scattering from a model rough surface consisting of parallel, perfectly conducting hemicylindrical bosses randomly distributed on a conducting plane.

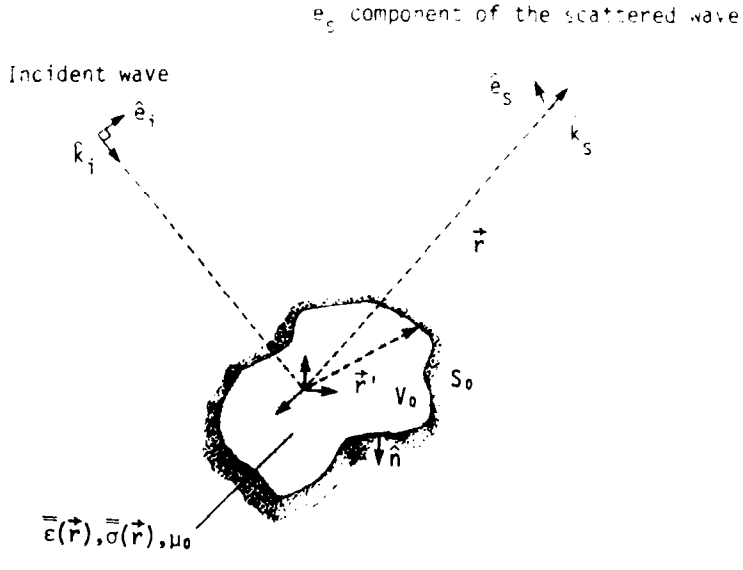

Figure 2. Scattering of a plane electromagnetic wave from an arbitrary inhomogeneous and anisotropic conducting dielectric.

VARIATIONAL TREATMENT OF SCATTERING BY A SPHERE*

M. Feinstein** and R. A. Farrell
Applied Physics Laboratory, The Johns Hopkins University

SUMMARY

We report preliminary results of an investigation into what constitute good trial functions for variational scattering calculations. Analyses of scattering of a scalar wave by a dielectric sphere show that a "spherical lens" trial function is superior to "plane wave" trial functions.

INTRODUCTION

An important phase in the development of the stochastic variational methods for scattering problems discussed in the previous paper[1] is the detailed analysis of specific test cases, such as scattering from spheres or cylinders. Analyses of such test cases can give considerable insight into the potential scope and tractability of the proposed variational techniques and are of intrinsic interest as new variational analyses of classical problems. The study of test cases is, in addition, of particular importance in the development of variational techniques because of the well-known sensitivity of these techniques to the choice of trial solution.

Our aim in this study is to pinpoint the critical variables in trial solutions to a test case, and thus obtain insight into what constitutes a "good" trial solution.

To achieve this goal, we have emphasized the use of relatively simple analytic functions for the trial solutions, known to be valid in limited regimes of wavelength and refractive index, and have examined the degree to which the variational formulation extends the validity of these approximate solutions. The use of simple analytic trial solutions enables us to compare the analytic behavior of different approximations with the known analytic properties of the exact solution, and facilitates the extension of the variational methods to other scattering problems.

Our test case has been scattering of a scalar plane wave by a single light dielectric sphere, that is, we assume a scatterer defined by

$$U(\underset{\sim}{r}) = (n^2-1) \qquad |\underset{\sim}{r}| \leq a$$

$$= 0 \qquad |\underset{\sim}{r}| > a$$

---

* This work was supported by the Department of the Navy (Naval Sea Systems Command) under Contract N00024-78-C-5384.

**Speaker

where n, the refractive index, is near unity, generally between 1.0 and 1.5. We examine this so-called "anomalous diffraction"[2] regime by trying to extend approximations valid for long wavelengths into shorter wavelength regimes. Our analysis complements previous studies of the application of variational techniques to perfectly conducting spheres[3] and is a problem for which the exact solution and its limiting cases are very well known,[4] thus facilitating our own studies.

GENERAL THEORY

Given some approximation $\psi(\underset{\sim}{r})$ for the values of a scalar wave inside a sphere, we calculate a variationally invariant approximation[5] for the scattering amplitude

$$f^{(v)}(\underset{\sim}{k}_i,\underset{\sim}{k}_s) = \frac{k^2}{4\pi} N_1 N_2 / D$$

where

$$N_1 = \int e^{-i\underset{\sim}{k}_s\cdot\underset{\sim}{r}} U(\underset{\sim}{r})\psi(\underset{\sim}{r})d^3\underset{\sim}{r}$$

$$N_2 = \int e^{i\underset{\sim}{k}_i\cdot\underset{\sim}{r}} U(\underset{\sim}{r})\psi^+(\underset{\sim}{r})d^3\underset{\sim}{r}$$

$$D = \int \psi^+(\underset{\sim}{r})U(\underset{\sim}{r})\psi(\underset{\sim}{r})d^3r - \frac{k^2}{4\pi}\iint \psi^+(\underset{\sim}{r})U(\underset{\sim}{r})G(\underset{\sim}{r},\underset{\sim}{r}')U(\underset{\sim}{r}')\psi^+(\underset{\sim}{r}')d^3\underset{\sim}{r}d^3\underset{\sim}{r}'.$$

The vectors $\underset{\sim}{k}_i$ and $\underset{\sim}{k}_s$ are the incident and scattering wave vectors as shown in Figure 1, $\psi^+(\underset{\sim}{r})$ is the adjoint to $\psi(\underset{\sim}{r})$, and $G(\underset{\sim}{r},\underset{\sim}{r}')$ is the free space Green function

$$G(\underset{\sim}{r},\underset{\sim}{r}') = \frac{e^{ik|\underset{\sim}{r}-\underset{\sim}{r}'|}}{|\underset{\sim}{r}-\underset{\sim}{r}'|}.$$

The adjoint solution is obtained from $\psi(\underset{\sim}{r})$ by replacing $\underset{\sim}{k}_s$ by $-\underset{\sim}{k}_i$ and $\underset{\sim}{k}_i$ by $-\underset{\sim}{k}_s$.

We can then gauge the effect of the variational correction by comparing $f^{(v)}$ to the usual non-variational approximation $f^{(0)}$:

$$f^{(0)}(\underset{\sim}{k}_i,\underset{\sim}{k}_s) = \frac{k^2}{4\pi B} N_1 \qquad (1)$$

where B is the incident amplitude.

To gauge the properties of our approximations for $\psi(\underset{\sim}{r})$, we use the optical theorem[6] to calculate a variationally invariant approximation for the total cross section from the approximate scattering amplitude

$$\sigma_{TOT}^{(v)}(k) = \frac{4\pi}{k} \, \mathrm{Im}\left[f^{(v)}\left(\underset{\sim}{k}_i = \underset{\sim}{k}_s\right)\right]$$

and compare $\sigma_{TOT}^{(v)}(k)$ to the exact cross section.

Use of the optical theorem to calculate the total cross section provides a criterion which is useful because it is sensitive to both the amplitude and phase of the scattering amplitude, and is generally more tractable than the usual definition

$$\sigma_{TOT}(k) = \int |f(\underset{\sim}{k}_i, \underset{\sim}{k}_s)|^2 \, d\Omega_{SCATT} \qquad (2)$$

which depends on scattering at non-forward angles.

PLANE WAVE TRIAL FUNCTIONS

The first family of trial solutions we tested were plane waves, and linear combinations of plane waves. This was motivated by the Rayleigh-Gans or Born Approximation (RGBA)[7] in which the field inside the sphere is assigned the value it would have in the absence of the scatterer, i.e.,

$$\psi(\underset{\sim}{r}) \simeq e^{i\underset{\sim}{k}_i \cdot \underset{\sim}{r}}.$$

If we calculate the cross section by inserting this approximate field into Equations (1) and (2) we obtain a long wavelength approximation for $\sigma_{TOT}(k)$. On the other hand, if we apply the optical theorem to the non-variational RGBA scattering amplitude we obtain $\sigma_{TOT}(k) \equiv 0$. In contrast, the approximate values of $\sigma_{TOT}(k)$ obtained by applying the optical theorem to the variational RGBA scattering amplitude are close to the true values of $\sigma_{TOT}(k)$ for $ka(n-1) \lesssim 1$. Thus we find that the variational method provides a substantial improvement out to $ka(n-1) \sim 1$, but, as discussed below, not much beyond.

For example, Figures 2a and 2b show $\sigma_{TOT}^{(v)}(k)$ for the trial solution

$$\psi_1(\underset{\sim}{r}) = e^{i\underset{\sim}{k}_i \cdot \underset{\sim}{r}}$$

for n = 1.1 and 1.2, while Figures 2c and 3a give $\sigma_{TOT}^{(v)}(k)$ for

$$\psi_1(\underset{\sim}{r}) = e^{ink_{\sim i}\cdot\underset{\sim}{r}}$$

for the same n's. The rationale for using $\psi_2(\underset{\sim}{r})$ was that the magnitude of the wave vector inside the sphere is nk. For comparison, Figures 3b and 3c give the exact cross section for n = 1.1 and 1.2. Although both ψ_1 and ψ_2 give satisfactory results for small k, they diverge from the exact solution by more than 10 per cent for $ka(n-1) \gtrsim 0.8$ and $ka(n-1) \gtrsim 1.2$, respectively. This criterion of 10 per cent divergence is marked on the figures by a vertical dotted line. We note that the wave number dependence of the exact cross section scales approximately with $[(n-1)a]^{-1}$ when n is near one,[8] so that ka(n-1) is an appropriate reduced wavenumber.

Since the inner surface of the sphere will reflect some of the energy incident on it, we have also tested plane wave trial solutions which include a reflected plane wave within the sphere:

$$\psi_3(\underset{\sim}{r}) = \psi_1(\underset{\sim}{r}) + A\, e^{-ik_{\sim i}\cdot\underset{\sim}{r}}$$

$$\psi_4(\underset{\sim}{r}) = \psi_2(\underset{\sim}{r}) + A'\, e^{-ink_{\sim i}\cdot\underset{\sim}{r}}$$

where A and A' are determined variationally. In the particular case of a "two-part" trial function

$$\psi(\underset{\sim}{r}) = \psi_1(\underset{\sim}{r}) + C\,\psi_2(\underset{\sim}{r})$$

the variational condition $\partial f^{(v)}/\partial C = 0$ allows one to eliminate C <u>algebraically</u> from the variational expression for the scattering amplitude, leaving a rather simple expression for $f^{(v)}$ as a rational function of integrals of trial functions. It turned out, perhaps surprisingly, that adding this reflected wave has almost no effect on $\sigma_{TOT}^{(v)}(k)$.

Another plane wave trial function we tested was

$$\psi_5(\underset{\sim}{r}) = e^{in_v k_{\sim i}\cdot\underset{\sim}{r}}$$

where n_v is determined variationally. In this case, the variational condition $\partial f/\partial n_v = 0$ generated a transcendental equation for n_v in terms of k and n which

had to be solved numerically. As shown in Figure 4a this trial function gave satisfactory results for $ka(n-1) \lesssim 1.7$ but failed catastrophically for larger k.

SPHERICAL WAVE TRIAL FUNCTION

According to van de Hulst,[9] the region in wavelengths $ka(n-1) \sim 1$ is where interference between diffracted and transmitted portions of the wave first becomes significant. We therefore felt it was probable that a trial function whose phase agreed with the phase of the exact solution more closely than do plane wave trial functions would give superior results.

A first attempt to represent the phase of the wave in the sphere more accurately was suggested by considerations from geometrical optics. As illustrated in Figure 5, the rays inside a sphere converge towards a point a distance $R = a/(n-1)$ from the center of the sphere in the forward direction. This suggests a trial function

$$\psi_6(\underset{\sim}{r}) = \frac{e^{-ink|\underset{\sim}{R}-\underset{\sim}{r}|}}{|\underset{\sim}{R}-\underset{\sim}{r}|}$$

where $\underset{\sim}{R} = R\,\underset{\sim}{k}_i/k$. In order to avoid a singularity at $|\underset{\sim}{R}-\underset{\sim}{r}| = 0$, corresponding to having the rays intersect inside the sphere, we assume $n < 2.0$. The cross section calculated from this trial function is shown in Figures 4b and 4c. The spherical wave trial function gives good results up to $ka(n-1) \sim 4.0$, which is a considerable improvement over any of the plane wave trial functions.

CONCLUSIONS

Although the spherical wave trial function is a considerable improvement over the plane wave trial function, it nonetheless fails for large k. This indicates that some critical aspect of the trial solution is not adequately represented by either the plane wave or the spherical wave.

Further research into this question is clearly needed, involving trial functions whose phase, amplitude, or direction mimic the exact solution more closely than either the plane wave or the spherical wave.

REFERENCES

[1] R. H. Andreo, J. A. Krill, and R. A. Farrell, "Variational Methods for Electromagnetic Scattering from Aerosol Clusters", these proceedings.

[2] H. C. van de Hulst, *Light Scattering by Small Particles*, Wiley, New York (1957), Chapter 11; R. G. Newton, *Scattering Theory of Waves and Particles*, McGraw-Hill, New York (1966), §3.4.1.

[3] R. D. Kodis, "Variational Principles in High-Frequency Scattering", Proc. Camb. Phil. Soc. 54, 512 (1958).

[4] H. C. van de Hulst, *op. cit.*; R. G. Newton, *op. cit.*, Chapters 2 and 3.

[5] P. M. Morse and H. Feshback, *Methods of Theoretical Physics*, McGraw-Hill, New York (1953), p. 1131.

[6] H. C. van de Hulst, *op. cit.*, p. 30.

[7] *Ibid.*, Chapter 7.

[8] See, e.g., H. C. van de Hulst, *op. cit.*, Figure 32, or M. Kerker, *The Scattering of Light*, Academic Press, New York (1969), Figure 4.8

[9] *Ibid.*, §11.22.

SCATTERING FROM A DIELECTRIC SPHERE

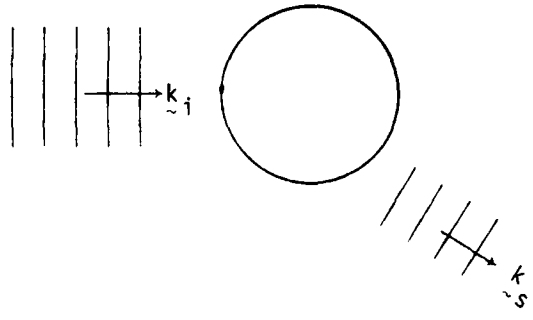

$k = \frac{2\pi}{\lambda}$

n = REFRACTIVE INDEX

a = RADIUS OF SPHERE

- GENERALLY WE TREAT $(n-1) < 1$

Figure 1

Basic geometry and parameters

Figure 2a.

Trial function (1), n = 1.1

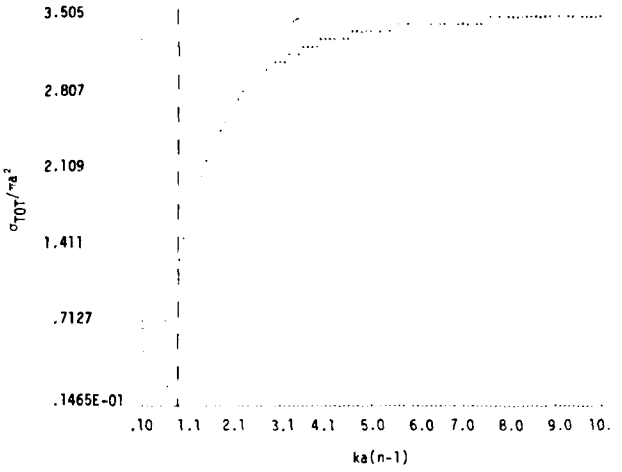

Figure 2b.

Trial function (1), n = 1.2

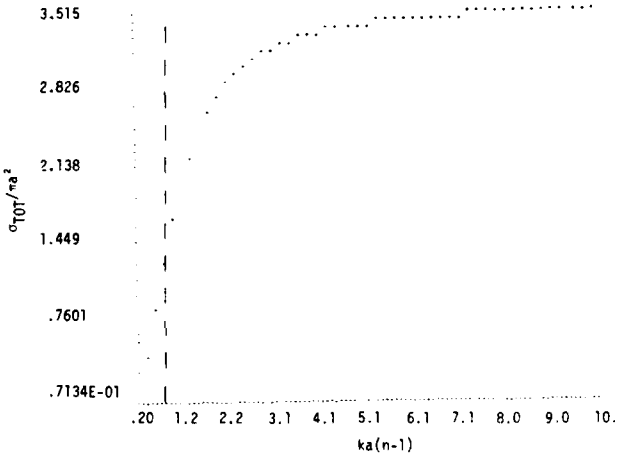

Figure 2c.

Trial function (2), n = 1.1.

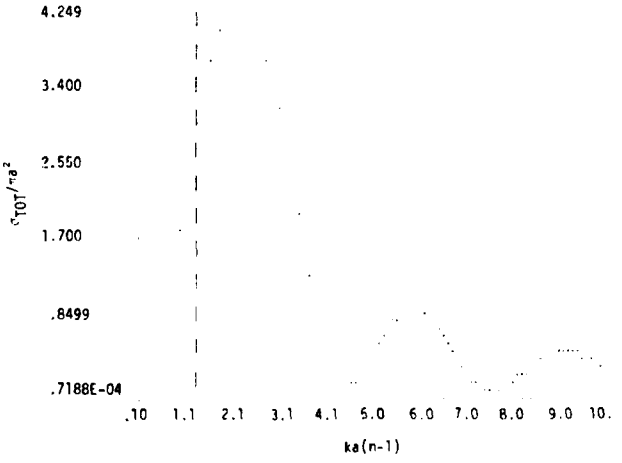

Significance of vertical dotted lines in these figures explained in text.

Figure 3a.

Trial function (2), n = 1.2

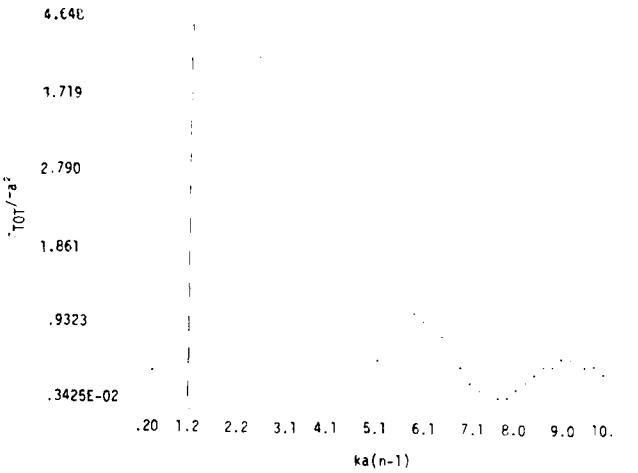

Figure 3b.

Exact solution, n = 1.1.

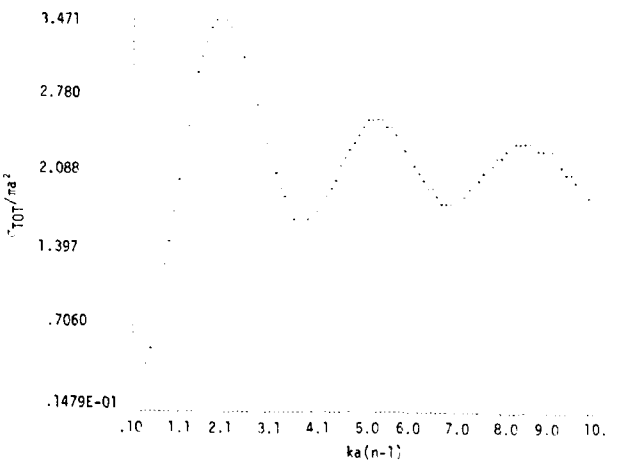

Figure 3c.

Exact solution, n = 1.2.

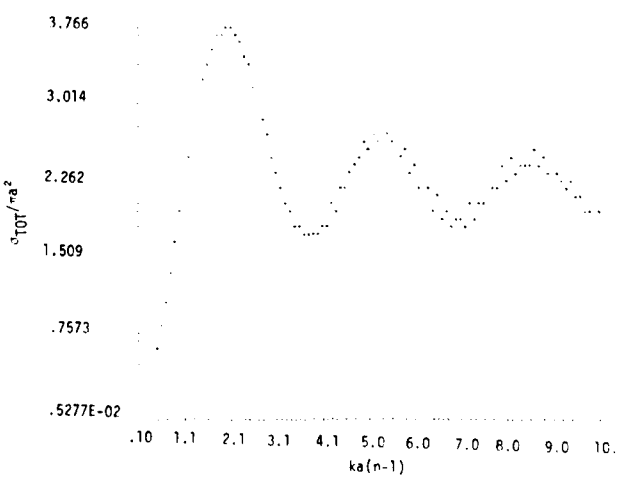

Figure 4a.

Trial function (3), n = 1.3.

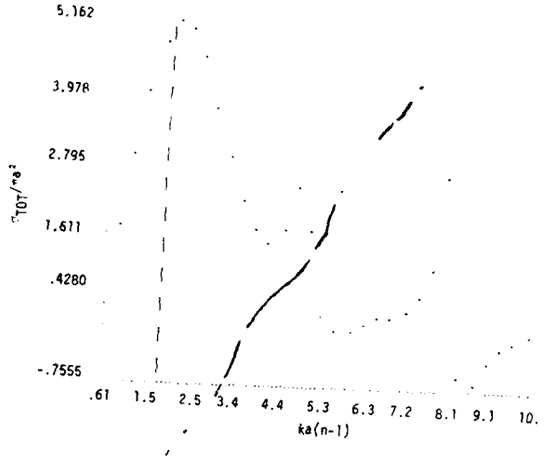

Figure 4b.

Trial function (4), n = 1.2.

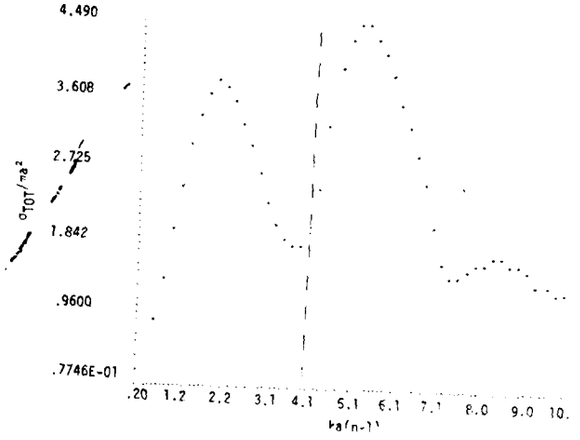

Figure 4c.

Trial function (4), n = 1.3.

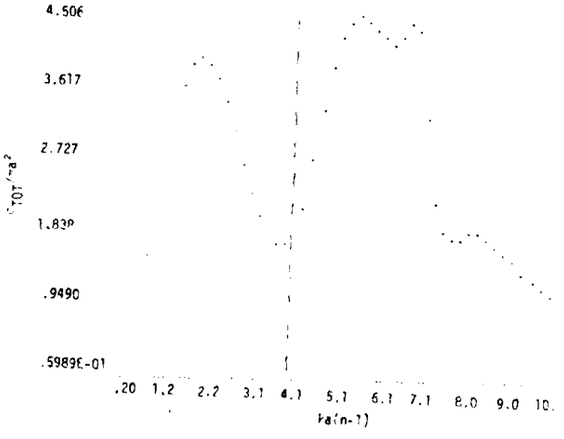

SPHERICAL WAVES

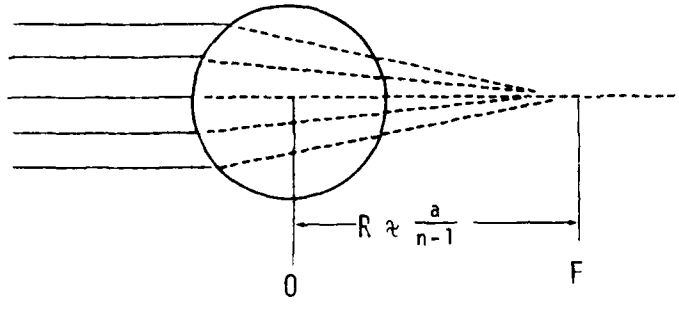

TRY

$$\psi(r) = \frac{e^{-ink|R-r|}}{|R-r|}$$

WHERE

$$R = \frac{a}{n-1}\,\hat{n}_{k_i}$$

Figure 5.

Spherical wave geometry and parameters.

RAMAN AND FLUORESCENT SCATTERING BY MOLECULES EMBEDDED IN DIELECTRIC CYLINDERS

H. Chew, D.D. Cooke and M. Kerker
Clarkson College of Technology
Potsdam, New York 13676

PUBLICATIONS

H. Chew, D.D. Cooke and M. Kerker, Appl. Opt. 19 (1980) [To appear in the January 1980 issue].

This report is a continuation of a program of study of the effects upon Raman and fluorescent scattering when the active molecules are embedded in dielectric particles. Earlier work has dealt with spheres[1] and concentric spheres[2] for which numerical results have been obtained when the emissions are either incoherent[3,4] or coherent.[5] Experiments have been carried out and compared with theory.[6,7] Also, the effect of illuminating the particle by an evanescent wave has been considered. Work currently underway is treating spheroidal particles and also the effect of active molecules adsorbed at or near the outer surface of a particle.

When inelastically scattered molecules such as those which give rise to Raman and fluorescent light scattering are distributed within a small dielectric particle, the scattered signals are affected by the morphology and optical properties of the particle and by the distribution of active molecules within it. These signals may be strikingly different from those obtained when the molecules are distributed within the same material in bulk and this must be considered in practical applications such as Raman microprobe analysis of particles or identification of biological particles in fluorescence activated flow cytometers. The effects we consider are due to the influence of the particle upon the electromagnetic fields.

Inelastic scattering by molecules embedded in small particles can be viewed in two steps. In the first step a molecule located at a particular position is excited by absorption of a photon at the incident frequency. The probability that active molecules will be raised to the excited state is assumed to be proportional to the square of the magnitude of the local electric field at the incident frequency and also to the number density of active molecules at this location, just as in the bulk material. But the local field, which varies in a complicated way within a small particle, is a sensitive function of particle geometry and optical properties as well as of the incident frequency. Accordingly, the rate of excitation will vary with location due to variation both of the field and the concentration of molecules.

The second step is the emission of radiation at the shifted frequency by the active molecules. This differs from the emission produced in the corresponding bulk medium because, in addition to the dipole field normally associated with the emission process, a

secondary induced field is needed to satisfy the boundary conditions at the surface of the particle. The inelastically scattered fields at the shifted frequency outside of the particle due to a single radiating dipole at any location within the particle can be obtained by solving the appropriate boundary value problem. For fluorescence and spontaneous Raman emission, the radiation from the sources within the particle adds incoherently so that it is necessary to sum the time average power over the particular distribution of dipoles within the particle to obtain the total emitted power. For coherent processes, the electric fields at the point of observation must be added prior to calculation of the power.

The formalism is extended here to the case when the scattering molecules are embedded in an infinite dielectric cylinder. The analysis has been presented elsewhere.[8] Formulas are given for the scattered fields due to an arbitrarily positioned dipole source for arbitrary angles of incidence. The general results, which involve an integral and a sum, are rather lengthy. Accordingly, the saddle point method has been used to carry out the integration approximately. Only a few illustrative numerical results will be presented here for single dipoles and for cylinders uniformly filled with incoherently emitting dipoles. These results are for perpendicular incidence on cylinders with radii comparable to the wavelength and for observation in a plane perpendicular to the cylinder axis. They demonstrate the sensitivity of the signals to cylinder size and refractive index as well as the different angular distribution and polarization of these signals from those emanating from bulk material.

We assume that the molecules are fixed in space and are isotropically polarizable, i.e., the polarizability is a scalar, so that the induced dipole is directed along the local field at each site within the cylinder. More realistic polarizabilities can be treated but isotropic polarizability has the advantage that comparison of the scattered irradiances with comparable results from bulk media is simple. For the latter, the scattered irradiances polarized perpendicular to the scattering plane do not vary with scattering angle, θ_{sc}; scattered irradiances polarized parallel to the scattering plane vary as $\cos^2\theta_{sc}$. These polarized irradiances will be designated I_1 and I_2, respectively. Accordingly any deviations from these simple angular patterns can be ascribed to the effect of the cylinder.

The numerical results presented here are further restricted to the case when the scattering plane is the x-y plane ($\theta=\frac{\pi}{2}$) and the cylinder axis is along the z-axis as shown in Fig. 1.

It is instructive to examine the scattering patterns of a single dipole with changing position in the cylinder since those from a distribution of dipoles, whether uniformly distributed or organized in some structured array, are obtained by superposition of the constituent dipoles. Figures 2-5 illustrate single dipole scattered irradiances versus scattering angle for relative refractive index m = 1.5 and for size parameter $\alpha = 2\pi a/\lambda = 5$ where

a is the cylinder radius and λ is the shifted wavelength in the medium outside the cylinder. Figures 2 and 4 are for I_1; Figures 3 and 5 are for I_2. In each case the various curves correspond to dipole positions at the center and one quarter, one half and three quarters the radial distance along a coordinate axis; i.e., along the positive y, positive x, negative x, and negative y axes for Figs. 2-5, respectively.

There are a number of interesting features. Immediately obvious is the quite different angular pattern from that of a dipole embedded in bulk media except for the case when the dipole is at the cylinder axis for which there is the typical dipolar angular dependence; I_1 remains constant with scattering angle, I_2 is proportional to $\cos^2\theta_{sc}$. This follows from symmetrical considerations. However, unlike the bulk situation, I_1 and I_2 are not equal to $\theta_{sc} = 0°$ and 180°. This is because even though the internal fields at the axis are not depolarized (they point in the same directions as the incident fields), the field strengths for the perpendicular and parallel components do differ.

The patterns are quite structured, some exhibiting various maxima and minima as well as considerable dynamic range in the values of the scattered irradiances. Except for Figure 2, the patterns are asymmetrical about the 90° scattering direction. In some cases the backscatter is greater than that in the forward direction, a feature not usually encountered for inelastic scattering.

The symmetry about 90° for the curves in Figure 2 follows from two considerations. For incident radiation polarized parallel to the cylinder axis, the internal field throughout the cylinder is also polarized in this direction so that both the dipole field and the induced field are in this direction. Accordingly, any dipole oscillating along the y-axis will be viewed similarly by observers in the x-y plane located symmetrically about the 90° scattering direction. This is not the case for other locations or even for locations along the y-axis for incident radiation polarized perpendicular to the cylinder axis. In that case the incident field is depolarized. Although it continues to be polarized within the x-y plane, it no longer necessarily points along the y-axis as does the incident field. This destroys the symmetry for observers about 90° as is indicated by the curves in Figure 5.

The remaining figures (Figures 6-9) illustrate scattering for cylinders of various sizes and refractive indexes uniformly filled with inelastically, incoherently scattering dipoles. As noted above, for perpendicular incidence and observation in the x-y plane it is only necessary to make calculations for a circular array of dipoles in that plane. The dipoles were distributed uniformly. For these calculations 2025 dipoles were sufficient to provide convergence. The final results were normalized to a single dipole so these results correspond to a fixed amount of active molecules distributed within cylinders of various sizes

rather than to a fixed concentration. Accordingly, any differences in the values of the scattered irradiances from size to size or from refractive index to refractive index indicate the effect of the cylinder upon the scattered emissions. Since the polarizability is the same in each of these calculations, such variations are not due to molecular effects but classical effects of the electromagnetic fields.

Figures 6 and 7 depict the scattered irradiances I_1 and I_2 versus θ_{sc} for m = 1.5 and for various size parameters from α = 1 to 30. As might be expected, the highly structured patterns for single dipoles are no longer obtained. The averaging process washes out the main structural features. Even so there is significant angular variation and polarization which varies somewhat with particle size and refractive index. The most marked effect occurs for I_2 for which the very deep minimum at the smallest sizes, characteristic of the bulk dipolar scattering, becomes shallower with increasing size parameter. A similar effect was found for spherical particles.

There is significantly greater back scattering for most of the cases illustrated here. This differs from elastic scattering for which the predominance of forward scattering is due to the diffracted and surface reflected rays, which, of course, are absent in inelastic scattering. This too is similar to the results obtained with spheres.

Finally we consider the variation of the magnitudes of the irradiances themselves with increasing particle size. This is illustrated in Figures 8 and 9 for m = 1.5 and for I_1 and I_2, respectively. Here too the general trends resemble those obtained earlier for spheres.[8] I_2 exhibits a broad maximum for $\alpha > 3$. I_1 tneds to decrease with increasing size parameter, particularly beyond α = 10. These curves oscillate irregularly. For I_1 the forward-backward dissymmetry is sufficiently close to unity on the plotted scale so that only curves for 0°, 45° and 90° are shown. However, for I_2 there is sufficient dissymmetry at intermediate values of the size parameters (α=1 to 15) so that curves for θ_{sc} = 135° and 180° are also shown.

The variation of the scattered irradiances, not only with scattering angle but especially with size parameter is a noteworthy result. Since these calculations are for a constant total amount of inelastically scattered material distributed within each cylinder, it means that analytical techniques for estimating the amounts of embedded inelastically scattering molecules must consider the effects of polarization, of scattering angle and of particle size.

The general trends are not completely unlike those for elastic scattering. In that case the internal field pumps an array of dipoles which emit coherently at the same wavelengh. The scattering cross sections of the particle per dipole (or per

unit volume of the particle) increases to a maximum value and then decreases with increasing size. In one sense this decreasing trend at larger sizes can be thought of as due to the increase of radiant energy within the particle being proportional to the cross sectional areas of the particle while the number of dipoles comprising the particles increases with volume.

For the incoherent case the decreasing trend for the larger sizes originates in a similar fashion. The relative constancy of I_1 in the small particle regime is due to the fact that the field strength at the pumping frequency is independent of particle size so that the secondary emission at the shifted frequency per dipole will also be independent of particle size.

REFERENCES

1. H. Chew, P.J. McNulty and M. Kerker, Phys. Rev. A13, 396 (1976).
2. H. Chew, M. Kerker, P.J. McNulty, J. Opt. Soc. Am. 66, 440 (1976).
3. M. Kerker, P.J. McNulty, M. Sculley, H. Chew and D.D. Cooke, J. Opt. Soc. Am. 68, 1676 (1978).
4. M. Kerker and S.D. Druger, Appl. Opt. 18, 1172 (1979).
5. H. Chew, M. Sculley, M. Kerker, P.J. McNulty and D.D. Cooke, J. Opt. Soc. Am. 68, 1686 (1978).
6. J.P. Kratohvil, M.-P. Lee and M. Kerker, Appl. Opt. 17, 3030 (1978).
7. P.J. McNulty, S.D. Druger, M. Kerker and H.W. Chew, Appl. Opt. 18, 1484 (1979).
8. H. Chew, D.D. Cooke and M. Kerker, Appl. Opt. 19 (1980) (In press).

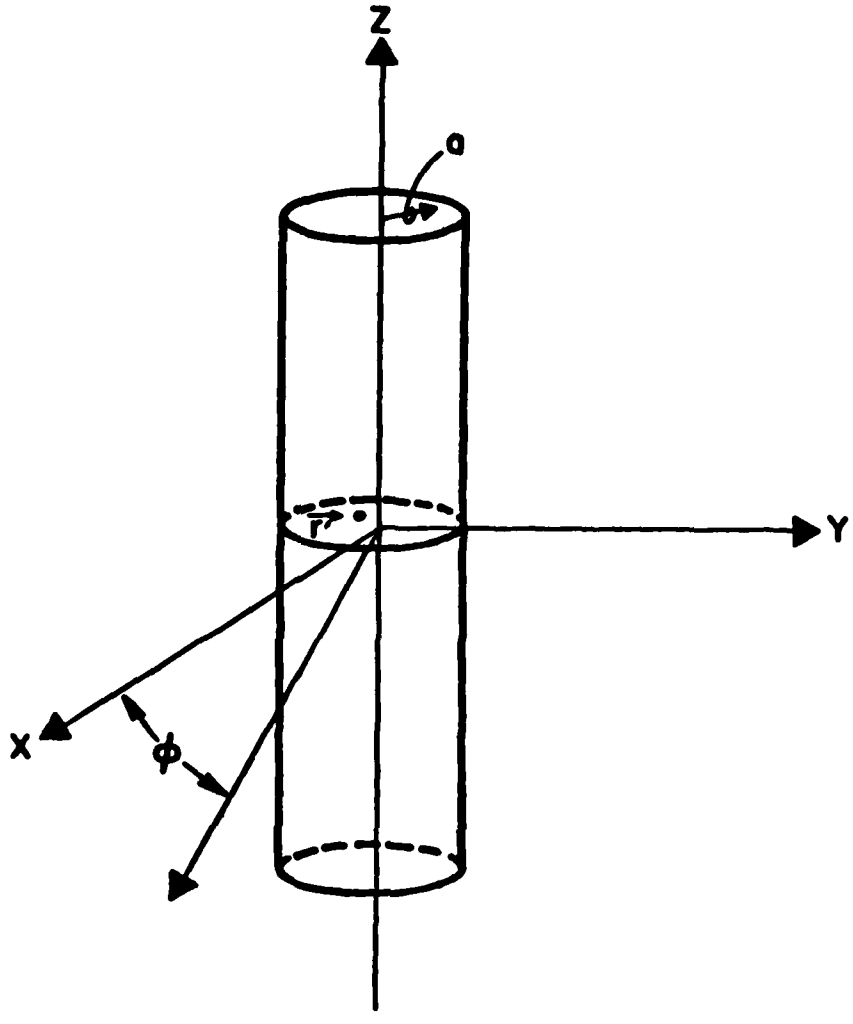

Figure 1. The scattering geometry. The cylinder axis passes through the origin and is along the z-axis. The incident plane wave is along the x-axis, and the scattering plane is the x-y plane. The fluorescing molecule is located at a point $\vec{r}'$ inside the cylinder, whose radius is a. The scattering angle, designated as θ_{sc} in the text and as theta on the following figure coordinates, corresponds to ϕ on this figure.

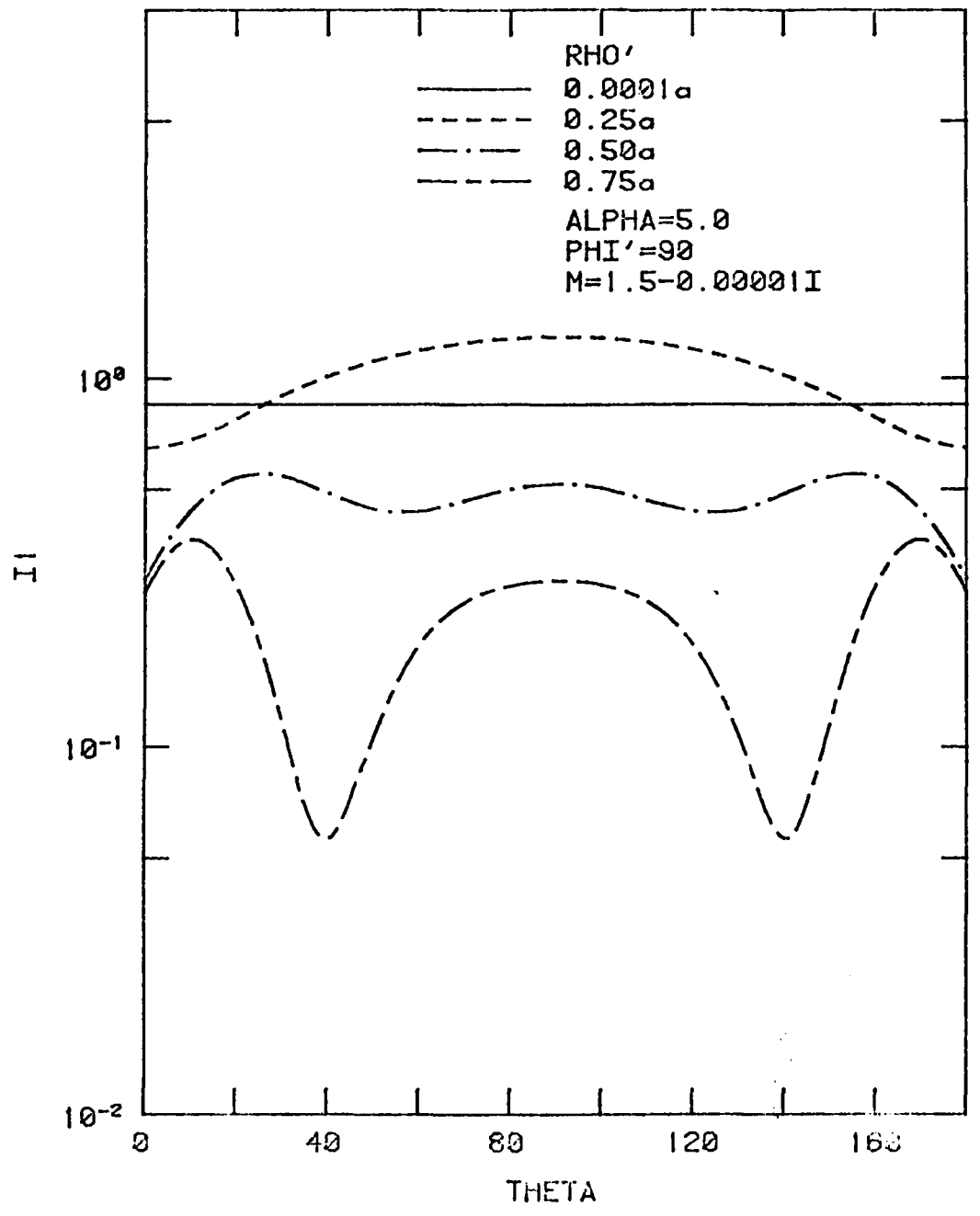

Figure 2. I_1 vs. θ_{sc} for α = 5.0, m = 1.5 for a single dipole located at radial distances along the positive y-axis 0.0001 a, 0.25 a, 0.50 a and 0.75 a.

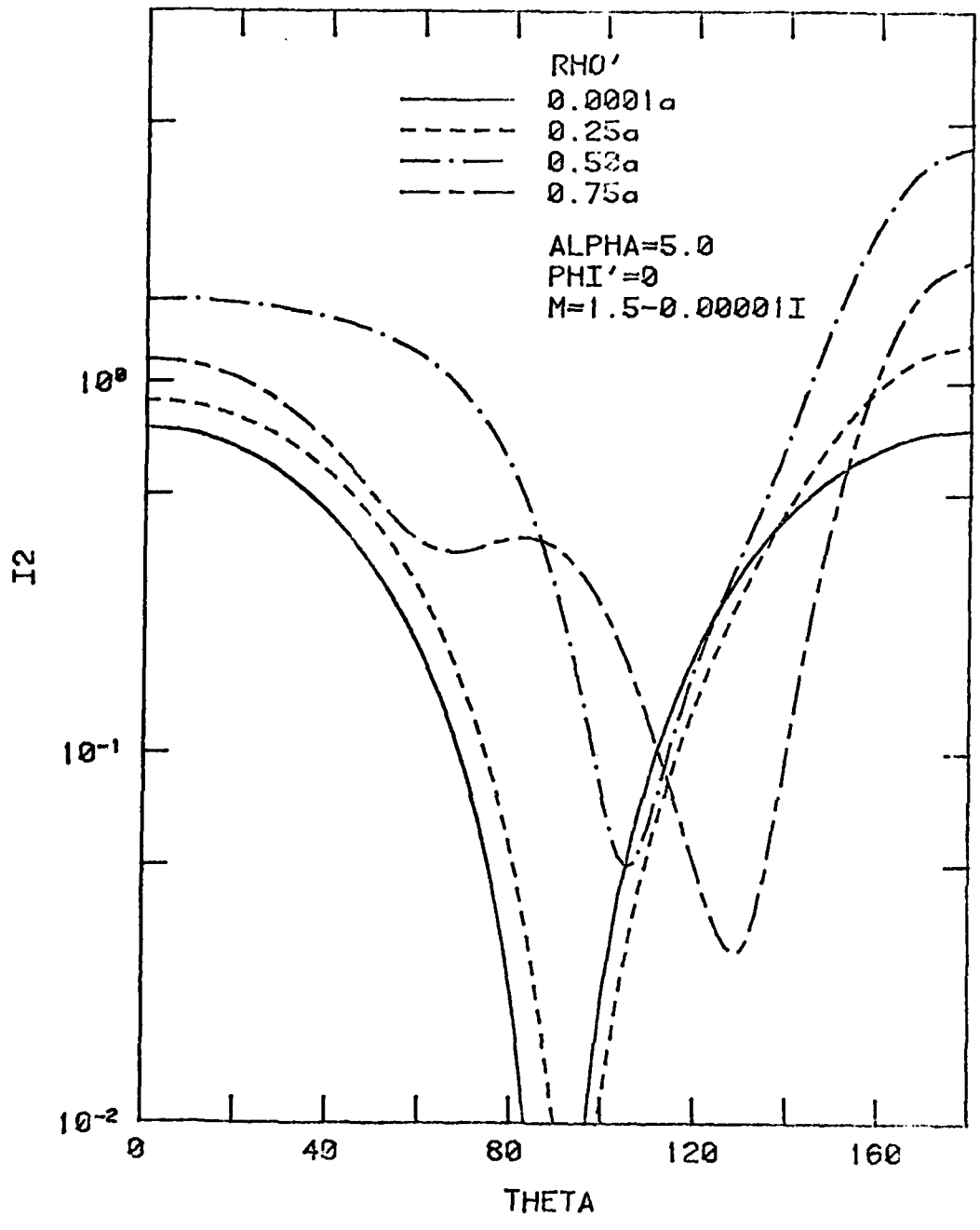

Figure 3. Same as Figure 2 for I_2 and locations along the positive x axis.

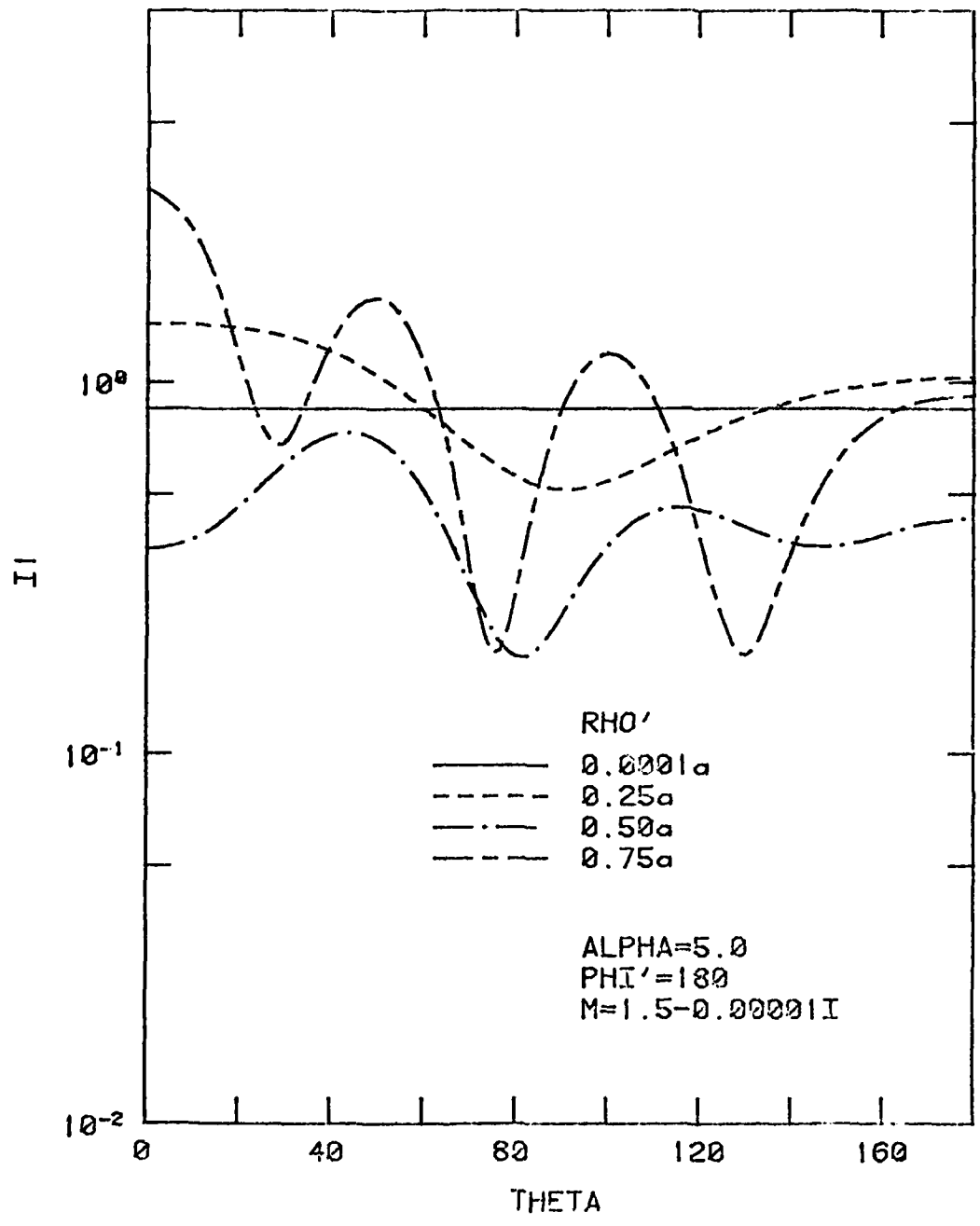

Figure 4. Same as Figure 2 for I_1 and locations along the negative x-axis.

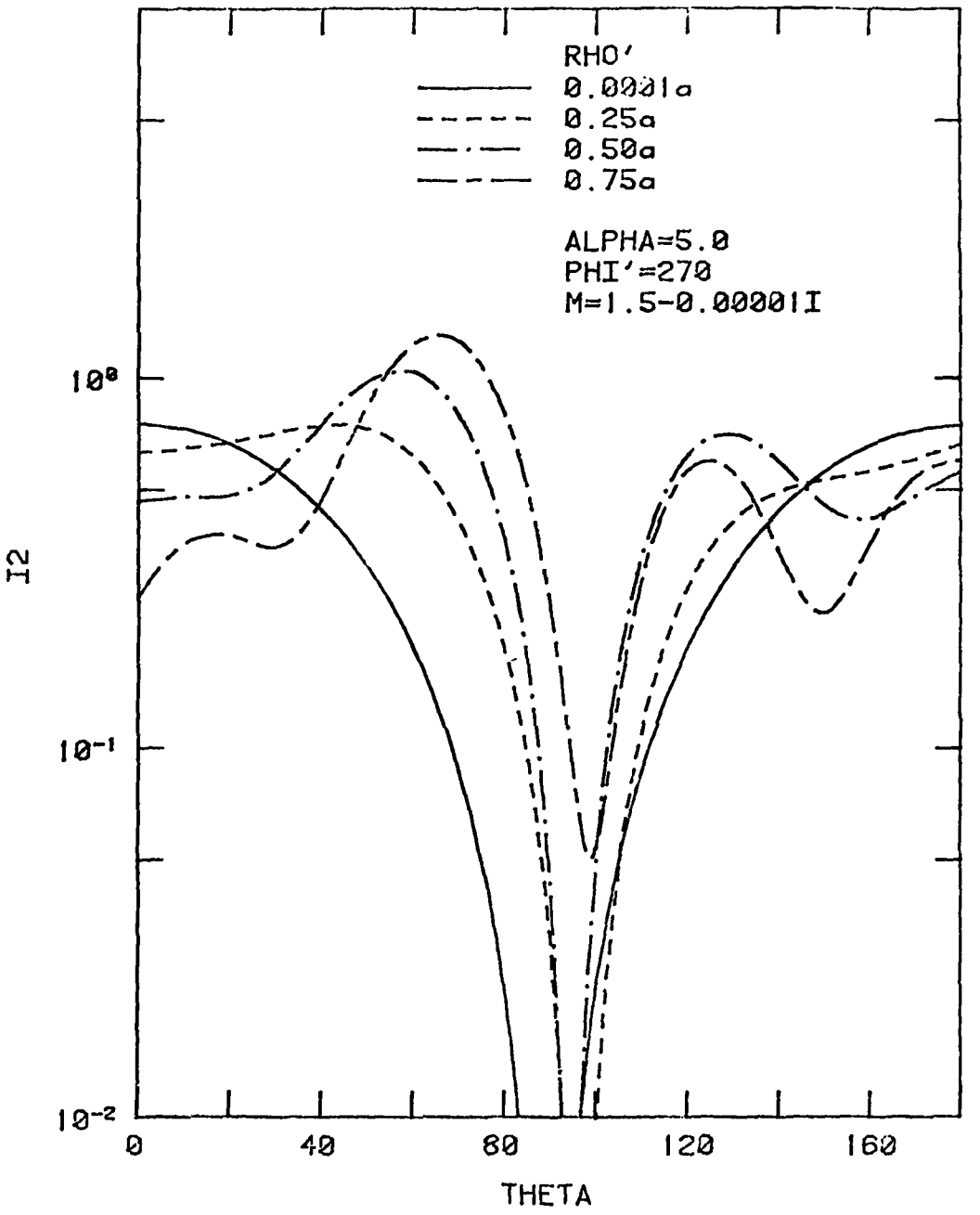

Figure 5. Same as Figure 2 for I_2 and locations along the negative y-axis.

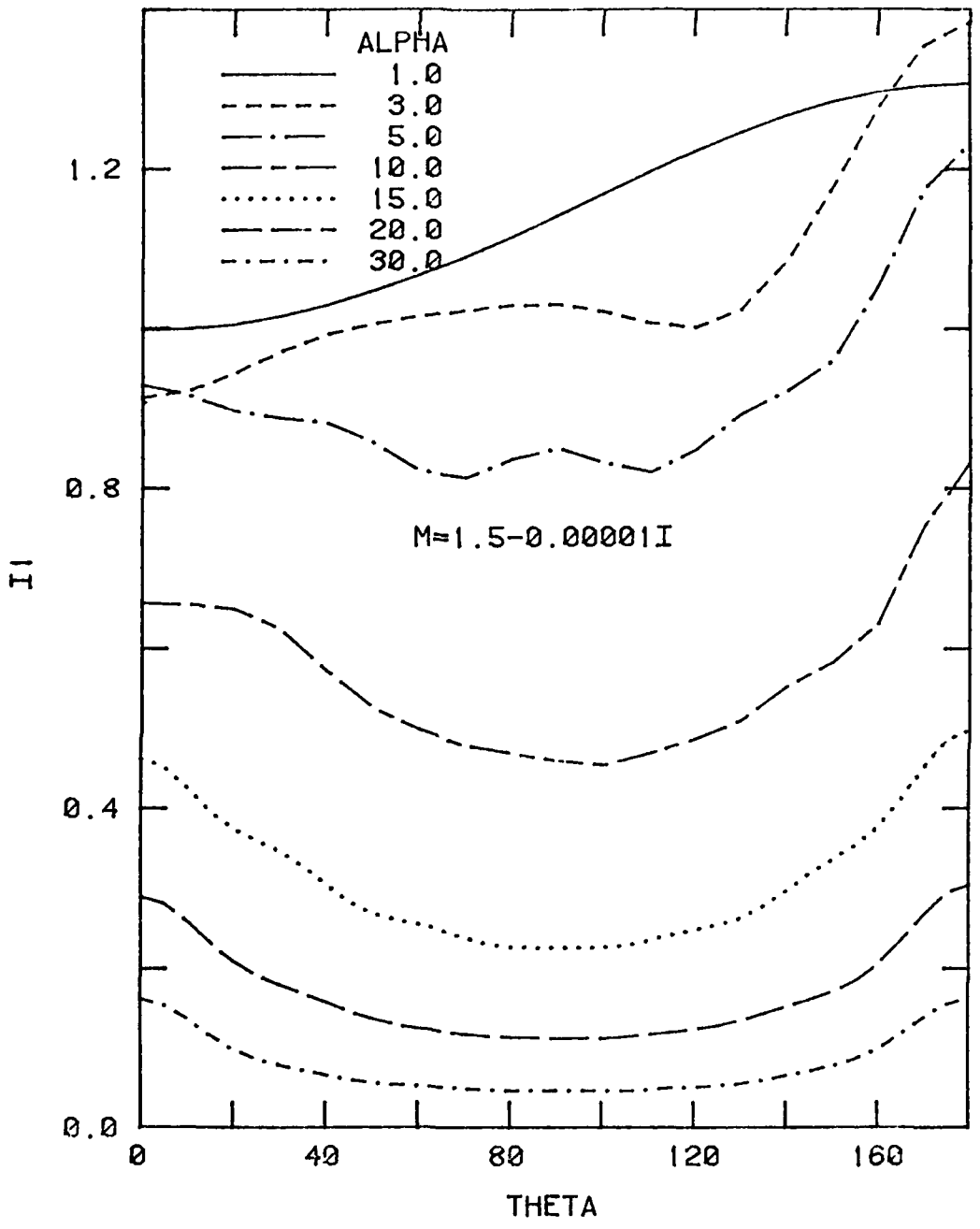

Figure 6. I_1 vs. θ_{sc} for cylinder uniformly filled with dipoles and various values of α as indicated, m = 1.5.

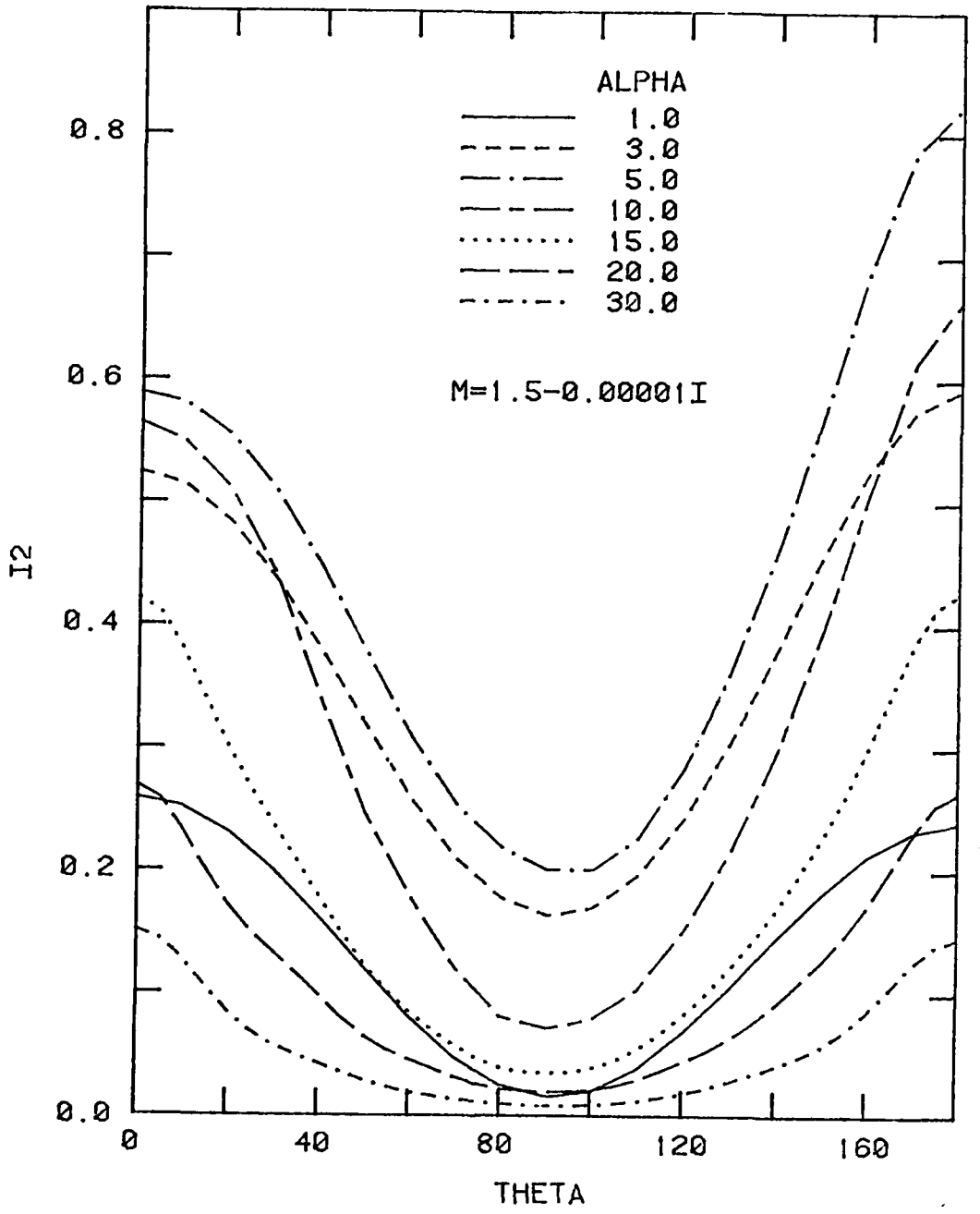

Figure 7. Same as Figure 6 for I_2.

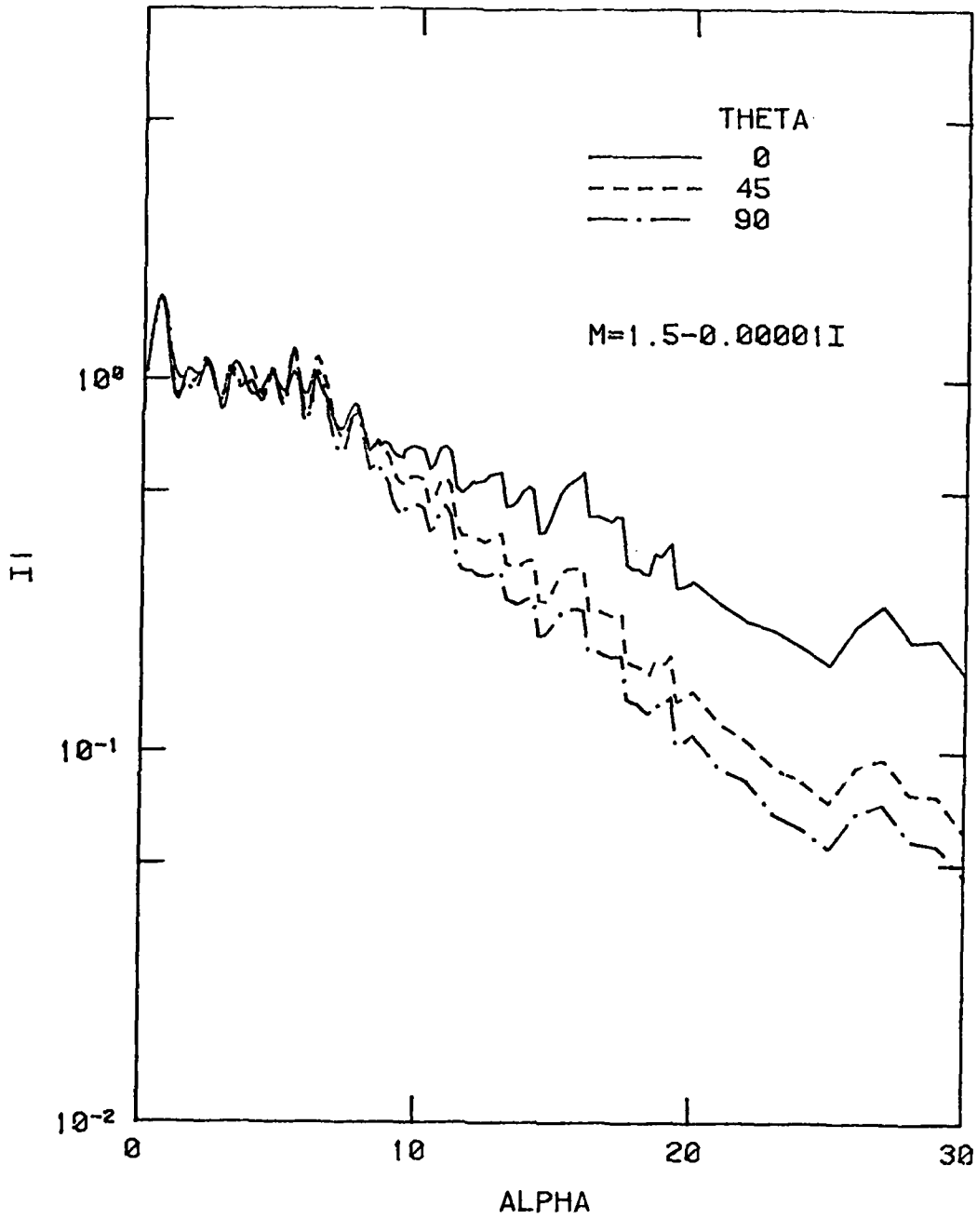

Figure 8. I_1 vs. α for cylinder uniformly filled with dipoles and $m = 1.5$, θ_{sc} as indicated.

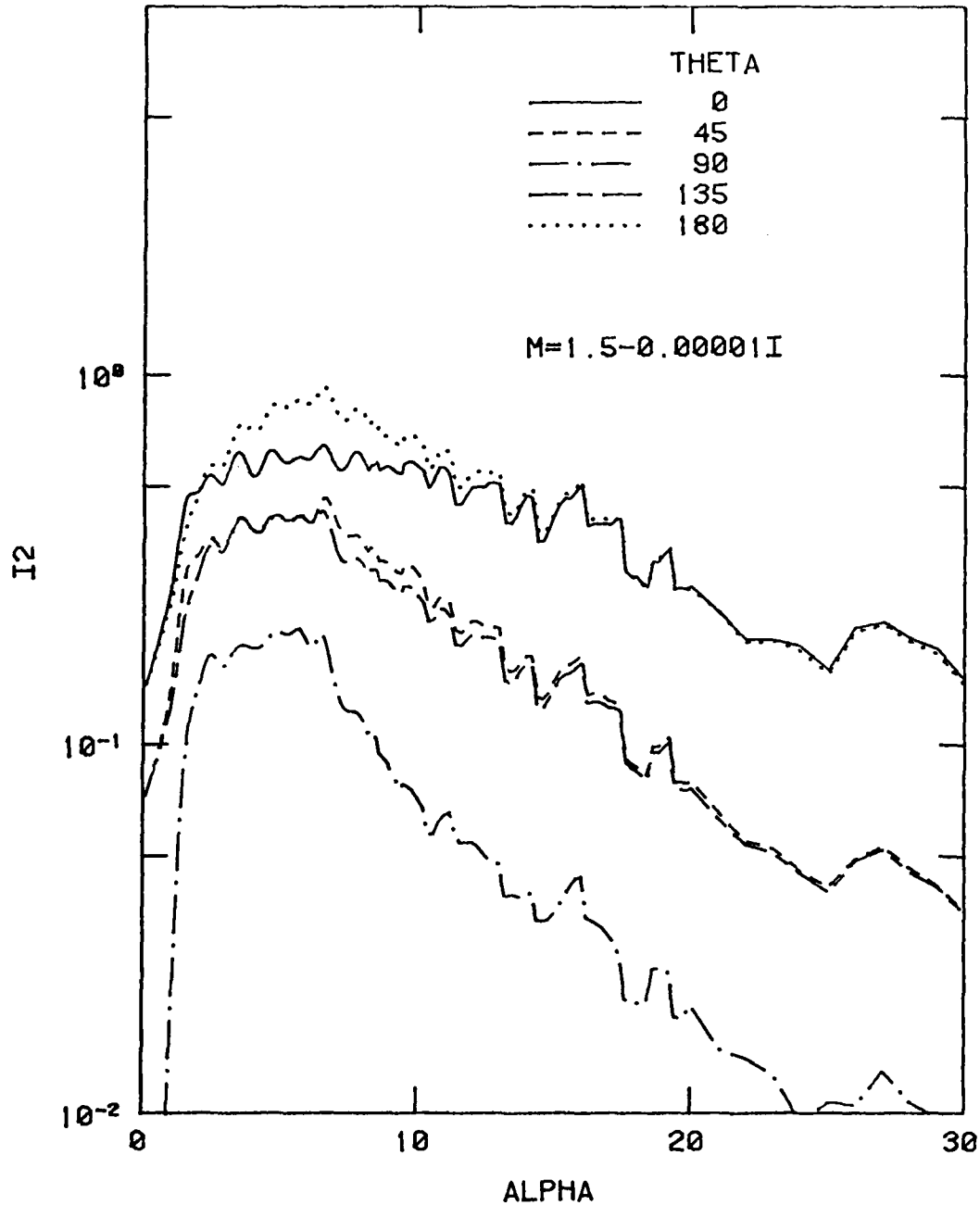

Figure 9. Same as Figure 8 for I_2.

LIGHT SCATTERING BY INHOMOGENEOUS PARTICLES

S.D. Druger, M. Kerker, D.-S. Wang and D.D. Cooke
Clarkson College of Technology
Potsdam, New York 13676

PUBLICATIONS

M. Kerker, D.D. Cooke, H. Chew and P.J. McNulty, J. Opt. Soc. Am. 68, 592 (1978).
M. Kerker, S.D. Druger, M. Kerker, D.-S. Wang and D.D. Cooke, Appl. Opt. 18, (1979).

Purcell and Pennypacker[1] have described an approximate method for calculating light scattering and absorption cross sections from homogeneous particles of arbitrary shape in which the particle is replaced by a cubic array of N polarizable dipoles. The purpose of this report is to present calculations which demonstrate the usefulness of this method for inhomogeneous particles. Ultimately, we would anticipate application to biological particles (viruses, bacteria, eukaryotic cells) for which the distribution of refractive index may become arbitrarily complex. However, the present calculations designed to test the accuracy of the method are done for a simpler configuration in which one sphere is embedded within another (without the two being necessarily concentric). This has the advantage that the present algorithm can be tested against the extended boundary condition method (EBCM)[2] and against the field average method (FA).[3] Also, it may serve as a simple model of a biological cell in which the nucleus is off center.

In the method of Purcell and Pennypacker (PP), the effective complex polarizability α' of each point dipole is determined from the complex dielectric constant ε using the Clausius-Mosotti relation

$$\frac{4\pi}{3}\rho\alpha' = \frac{\varepsilon-1}{\varepsilon+2} \tag{1}$$

where ρ is the number of dipoles per unit volume. The assumed relation between the local field $\vec{E}_i$ evaluated at the position $\vec{r}_i$ and the corresponding dipole moment $\vec{P}_i$

$$\vec{P}_i = \alpha'\vec{E}_i \tag{2}$$

then leads to the following set of N inhomogeneous linear equations for the local fields in terms of the incident (field $\vec{E}_o$ (assumed polarized in the z-direction)

$$\vec{E}_i = E_o\vec{l}_z\exp(ikx_i) + \sum_{j\neq 1}\frac{\exp(ikr_{ij})}{r_{ij}^3}\times[k^2(\vec{r}_{ij}\times\vec{P}_j)\times\vec{r}_{ij} + \frac{(1-ikr_{ij})}{r_{ij}^2}(3\vec{P}_j\cdot\vec{r}_{ij}\vec{r}_{ij}-r_{ij}^2\vec{P}_j)] \ . \tag{3}$$

Standard methods may be employed to solve eq. (3) numerically. Using an iterative method for a system of 137 dipoles, PP have obtained close agreement with the results of Lorenz-Mie calculations for a sphere having a size parameter $\alpha = 2\pi a/\lambda$ of about 1.5 where a is the equivalent radius and λ the wavelength in the medium. The agreement should depend upon the number of dipoles used; i.e., upon how closely this grainy array approximates the homogeneous sphere. Accordingly, there is a requirement that N becomes larger with increasing size. Because convergence is slower for larger values of α and ε, and especially because the computing time per iteration is proportional to N^2, the calculating time increases rapidly with size.

From the formal viewpoint, extension of PP to inhomogeneous structures involves replacing the single α' in eq. (2) by α'_i the polarizability at position $\vec{r}_i$. For the layered structure considered here the value depends on whether $\vec{r}_i$ lies in the inner sphere or in the region between the inner and outer spheres. In either region, the appropriate polarizability can be obtained from the corresponding dielectric constant using the Clausius-Mosotti relation.

We have employed essentially the same iterative method as that used by PP to solve the system of equations. Our results for a homogeneous sphere with size parameter $\alpha = 1.5$ and refractive index $m = 1.33$ were very close to those reported by these authors. Our new results for the layered spheres are presented in Figs. 1 and 2 and compared with those calculated for the same parameters using EBCM and FA.

EBCM is an exact method for scattering by nonspherical bodies based upon an equivalence principle in which the scattering object is replaced by a set of surface currents.[4] It has been shown to give accurate results when compared with the boundary value solution for concentric spheres.[2,5]

In FA the internal field for an inhomogeneous sphere is approximated by that of a homogeneous particle whose dielectric constant is obtained from the volume weighted average of the polarizability.[3] The scattered field is then calculated from an integral involving the internal field. FA provides accurate results for concentric spheres provided the particle is not too large and the dielectric constants in the two regions are not too different.

Comparison of PP, EBCM and FA is shown in Fig. 1 where the differential scattering cross sections are plotted versus scattering angle (0° is forward scattering) for concentric spheres. The upper curves are for the linear polarization with the electric vector vibrating perpendicular to the scattering plane; the lower curves are for the parallel component. The inner sphere has size parameter $\alpha_1 = 0.75$, $m_1 = 1.33$; the outer region has size parameter $\alpha_2 = 1.1$, $m_2 = 1.5$. The curves are normalized in the forward direction. EBCM and FA give nearly identical results. The PP

calculation was carried out both for 297 dipoles and for 389 dipoles. Although the agreement is not as good as for a homogeneous sphere, it is reasonably good considering the graininess of the model. The calculation with 389 dipoles is considerably closer to the EBCM calculation than that with 297 dipoles so that increasing the number of dipoles would presumably continue to improve the accuracy.

In Fig. 2 the inner sphere is displaced in the direction of the incident beam with its center halfway toward the outer surface. As noted in earlier work[2,3] this has little effect upon the forward scattering (indeed this is why normalization was effected at zero scattering angle) but there is about a 20% displacement of the differential back scattering signal. Here again EBCM and FA are in close agreement. PP differs somewhat as expected from the graininess of the model. As already noted, the agreement should become better with a larger number of dipoles but this would require considerably greater computing time.

We find generally in our calculations that the simple iterative method of solving eqs. (3) (used also by PP) tends to have poor convergence for size parameters greater than about 1.5. Furthermore, our results indicate that a far larger number of dipoles is needed to calculate accurately the scattering cross sections for structured spheres. Presumably, other numerical methods, such as the extremum principle of Yung[6] might be employed to reduce the time required to solve eq. (3) for these cases.

Despite these limitations, PP provides a highly general method for calculating scattering cross sections for particles of arbitrary shape and internal structure. Indeed as noted in the original paper[1] it is also applicable to particles comprised of anisotropic media. The further extension of our algorithm to irregularly-shaped particles or to dipoles with anisotropic polarizability appears to require only obvious minor changes in evaluating the coefficients in eq. (3) without any changes in the method of solution. By taking the view that the polarizability per unit volume is an inherent point property of the material comprising the particle, it is possible to argue that the polarizability to be assigned to the dipole at $\vec{r}_i$ is that computed using the Clausius-Mosotti relation for the dielectric constant at $\vec{r}_i$, as if, for each $\vec{r}_i$, the particle were regarded as uniform for purposes of calculating the corresponding α'_i. Using α'_i values calculated in this way, it should be possible to extend the method to the general case of continuously inhomogeneous particles.

REFERENCES

1. E.M. Purcell and C.R. Pennypacker, Astrophys. J. 186, 705 (1973).
2. D.-S. Wang and P.W. Barber, Appl. Opt. 18, 1190 (1979).
3. M. Kerker, D.D. Cooke, H. Chew and P.J. McNulty, J. Opt. Soc. Am. 68, 592 (1978).
4. P. Barber and C. Yeh, Appl. Opt. 14, 2864 (1975).

5. A.L. Aden and M. Kerker, J. Appl. Phys. 22, 1242 (1951).
6. Y.L. Yung, Appl. Opt. 17, 3707 (1978).

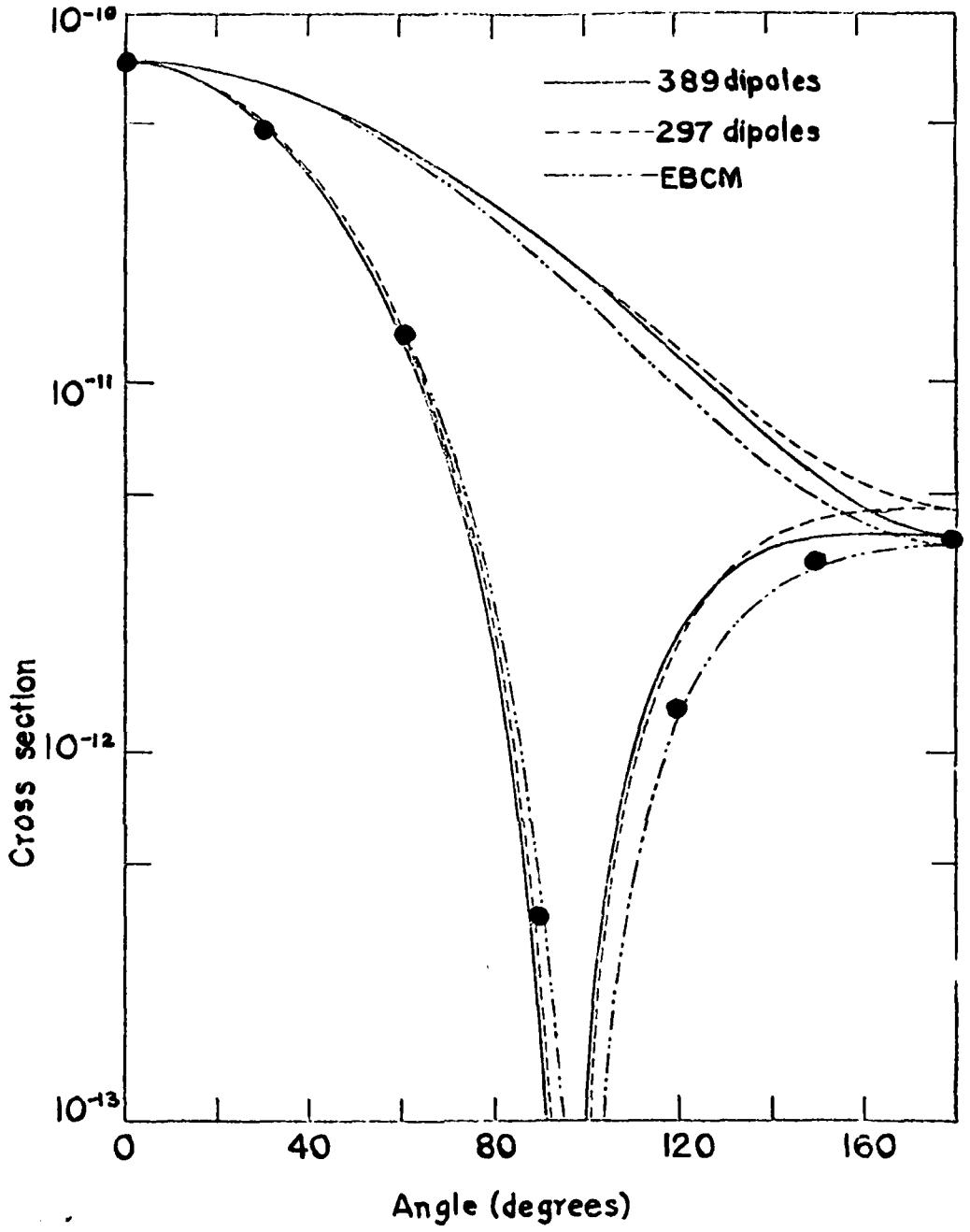

Figure 1. Calculated differential scattering cross sections versus scattering angle for concentric spheres. Upper curves are for component with electric vector vibrating perpendicular to scattering plane; lower curves are for parallel component. Refractive indexes and size parameters of inner and outer regions are $\alpha_1 = 0.75$, $m_1 = 1.33$; $\alpha_2 = 1.10$, $m_2 = 1.5$. Large dots are for FA.

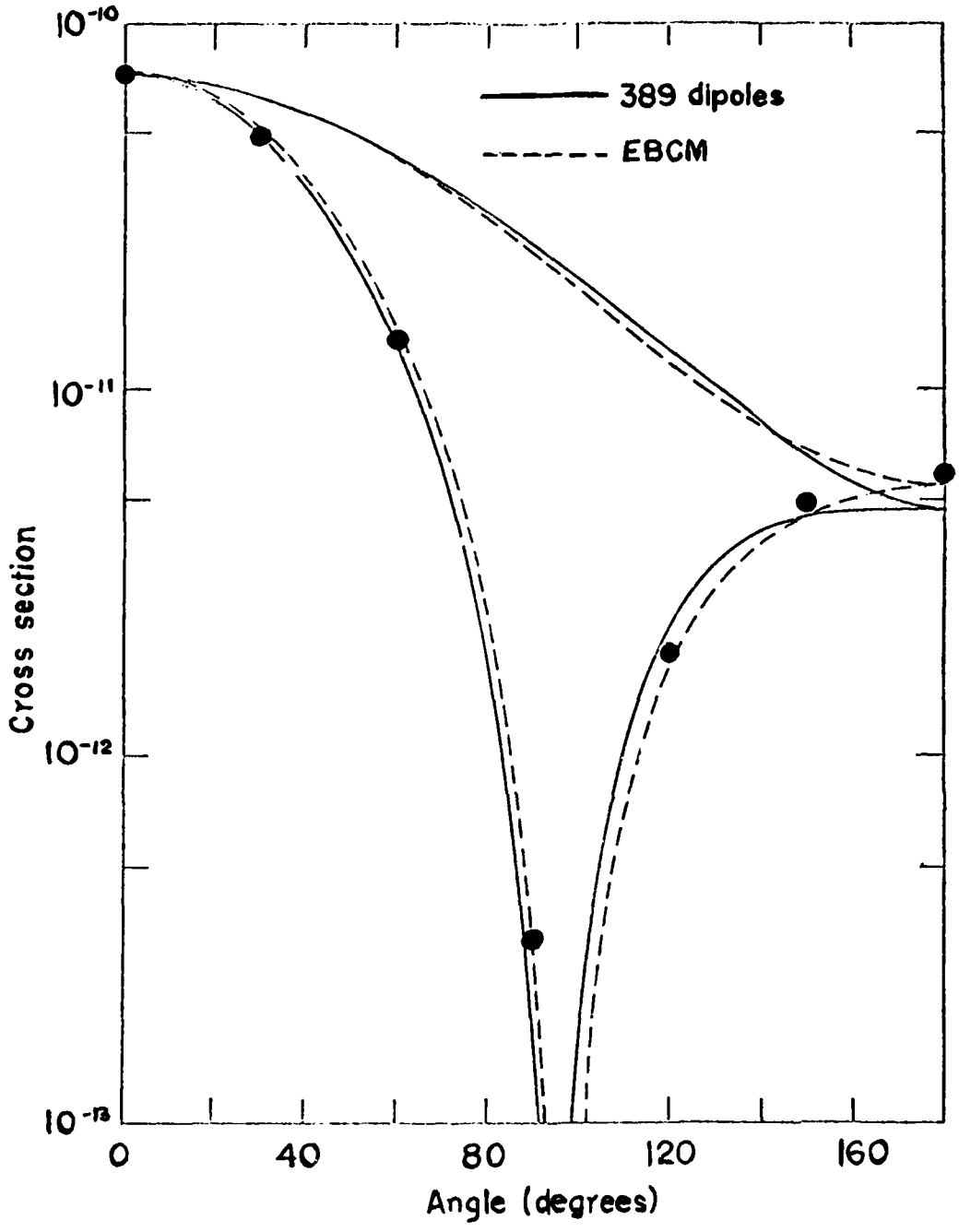

Figure 2. Same as Fig. 1 with center for inner sphere displaced in the direction of the incident beam with its center halfway toward the outer surface.

ELECTROMAGNETIC THEORY OF SCATTERING AND ABSORPTION FROM FINITE ELONGATED OBJECTS

Jeanne Pedersen and Norman Pedersen, Panametrics, Inc.

BACKGROUND AND INTRODUCTION

The purpose of this paper is to present a summary of work which we have done and which is presently underway with the Chemical Systems Laboratory in the area of electromagnetic cross sections of highly elongated conductive particles. A more expanded paper will be submitted to C. S. L. in the near future.

In 1965, a new technique was originated and later developed for the purpose of providing various modes of radar target obscuration and concealment.[1,2] Since the 1960's, considerable work has been done by a number of Government laboratories for the purpose of implementation of the technique. Although extensive experimental programs[2] had quite thoroughly verified the theoretical predictions, implementation posed significant practical difficulties. Recent work by a number of Government laboratories, including C. S. L., have removed certain of these difficulties, and have also extended the practical wavelength range into the infrared and visible regions.

In this paper, we will present and compare some of the results of the early theory and a more advanced theory which we developed in order to extend the range of validity. Finally, we will present a summary of our most recent work, which involves the inclusion of a more complex trial function for the current flow in the cylinder.

All of the numerical work to be presented in this paper involves integration over the full range of cylinder orientation with respect to the (polarized) incident plane wave. The scattering cross sections are the result of integration of differential scattering cross section over 4π steradians for each set of orientation coordinates of the cylinder.

PREDICTIONS AND LIMITATIONS OF THE 1965 THEORY

This early work[1,2] was based on a quazistatic approximation which involved the solution of Laplace's equation, the calculation of the depolarizing factors, and subsequent calculation of the various cross sections appropriately averaged over aspect angle and orientation. Although a number of shapes, such as oblate spheroids and spherical shells were investigated, the long slender conducting cylinder (prolate spheroid approximation) turned out to be

optimum for obtaining maximum extinction and absorption per unit volume of particle mass over a substantial wavelength range. The strict Rayleigh region criteria ($mk_o\ell << 1$, $mk_oa << 1$; m = refractive index) were extended to the limits of $k_o\ell \leqq 1$ and $k_oa \leqq 0.1$. In the case of $k_o\ell > 1$, the approximation $\ell \longrightarrow k_o^{-1}$ was used for the calculation of absorption cross section, but was inadequate for scattering calculations which were strictly limited to the region $k_o\ell \leqq 1$.

The absorption and scattering cross sections (averaged over orientation) resulting from this early work are given below:

$$\overline{\sigma}_{abs} = \frac{1}{3} \frac{V_p \sigma_c \sqrt{\mu_o/\epsilon_o}}{1 + (L\epsilon'')^2}, \tag{1}$$

$$\overline{\sigma}_{sca} = \left(\frac{1}{5}\right)\left(\frac{k_o^2}{4\pi}\right) \frac{V_p^2 \sigma_c^2 \left(\frac{\mu_o}{\epsilon_o}\right)}{1 + (L\epsilon'')^2} \tag{2}$$

where V_p = particle volume, σ_c = electrical conductivity, L = devolarizing factor, and ϵ'' = imaginary part of the dielectric constant (metallic conductor).

The quality $L\epsilon''$ in the above equations obviously plays an important role in determining the volume efficiency for absorption ($\overline{\sigma}_{abs}/V_p$) and scattering ($\overline{\sigma}_{sca}/V_p$). This quantity is explicitly given by

$$L\epsilon'' = 4\left(\frac{a}{\ell}\right)^2 \left[\ell n\left(\frac{\ell}{a}\right) - 1\right] \frac{\sigma_c}{\omega \epsilon_o}, \tag{3}$$

where a = radius, ℓ = total length, ω = angular frequency.

As mentioned above, when $k_o\ell > 1$, we can let $\ell \longrightarrow k_o^{-1}$, and substantially increase the range of computation for absorption cross section, which terminates at or before the limit $k_oa = 0.1$.

It should be noted here that Dr. P. C. Waterman has recently done an exact calculation of the depolarizing factor for a right circular cylinder[3], which replaces [ ] in equation 3 by $\left[\ell n\left(\frac{2\ell}{a}\right) - 7/3\right] = \left[\ell n\left(\frac{\ell}{a}\right) - 1.64\right]$. This represents the only difference between his value for orientation averaged scattering cross section and that given by Eq. 2. The difference, of course, is due to the fact that Eq. 3 is derived for a prolate spheroid. This difference would only be consequential for low aspect ratios or large k_oa values ($k_oa \simeq 0.1$) and at worst results in a factor of 2 discrepancy at $k_oa = 0.1$.

The above results proved to be extremely useful and adequately covered the range of parameters encountered during the 1960's. However, new ranges of operating and material parameters now exist, and it has become necessary to provide a more sophisticated theory for the primary purpose of extending the useful $k_o \ell$ region for scattering and absorption cross section calculations. An outline of this "intermediate" theory developed several years ago and more recently programmed, are given in the next section.

PRESENT THEORY

The present theory is based upon a variational procedure first set forth by Tai for perfectly conducting wires,[4] and later extended to the case of finite conductivity by Cassedy and Fainberg, who, however, considered only broadside incidence.[5] In the present theory, scattering, absorption, extinction, and radar cross sections are calculated for arbitrary angles of incidence. The results can then be averaged over all angles of incidence to obtain results for a cloud of randomly oriented particles.

Consider a plane electromagnetic wave incident upon a cylindrical wire of finite conductivity at arbitrary angle of incidence, θ_i, and arbitrary polarization angle, ψ, as shown in Fig. 1.

Assuming the wire is sufficiently thin for the current to be uniform around the axis at any position along the wire, one may consider the current as a current filament I(z) along the axis. As the wire is assumed to be thin, only the component of the electric field parallel to the axis will stimulate a response, and the integral equation for the boundary condition at the cylinder surface may be written

$$E_o \sin\theta_i \cos\psi \, e^{jkz\cos\theta_i} = I(z)Z$$

$$+ \frac{1}{2\pi} \int_0^{2\pi} \frac{j\eta k}{4\pi} \int_{-\ell}^{\ell} I(z') \left(1 + \frac{\partial^2}{k^2 \partial z'^2}\right) \frac{e^{-jkR}}{R} \, dz' \, d\phi' \qquad (4)$$

Here, Z is the skin impedance per unit length of the cylinder and is given by[6]

$$Z = \frac{j}{a} \sqrt{\frac{\nu\mu}{2\pi\sigma}} \left[\frac{\mathrm{Ber}\,(p) + j\mathrm{Bei}\,(p)}{\mathrm{Ber}'\,(p) + j\mathrm{Bei}'\,(p)}\right] \qquad (5)$$

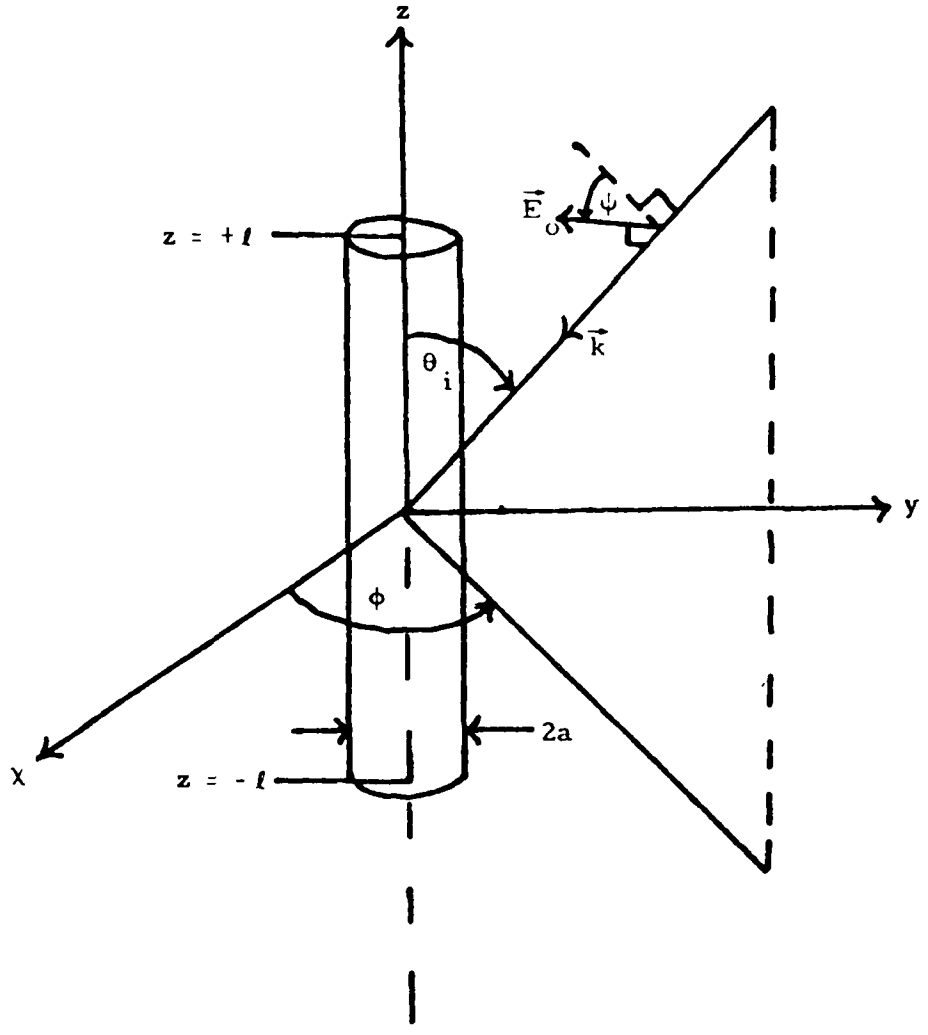

Fig. 1. Geometry of the cylindrical wire with respect to the propagation vector, $\vec{k}$, and the electric field vector, $\vec{E}$. θ_i is the angle between k and the z axis; ψ is the angle $\vec{E}$ makes with the k-z plane.

with

$$p = a\sqrt{\omega \mu \sigma}$$

$$\eta = \sqrt{\mu_o/\epsilon_o} \quad \text{is the characteristic impedance of free space, and}$$

$$R = \sqrt{(z-z')^2 + 4a^2 \sin^2\left(\frac{\phi - \phi'}{2}\right)}$$

The Ber and Bei functions are the real and imaginary parts of the Bessel function of complex argument.

A stationary homogeneous functional expression can now be constructed for the current in terms of the backscattered amplitude S, giving

$$\frac{1}{S} = \frac{\frac{k}{2\pi}\int_0^{2\pi} d\phi \int_{-\ell}^{\ell}\int_{-\ell}^{\ell} I(z)I(z')\left(1 + \frac{\partial^2}{k^2 \partial z'^2}\right)\frac{e^{-jkR}}{R}dz'dz - \frac{4\pi jZ}{\eta}\int_{-\ell}^{\ell} I^2(z)dz}{\left[k \sin\theta_i \int_{-\ell}^{\ell} I(z)\ e^{jkz\cos\theta_i}\ dz\right]^2} \qquad (6)$$

The current trial function chosen is that of Tai,

$$\begin{aligned} I(z) &= I_o \left\{\left[\cos kz \cos qk\ell - \cos k\ell \cos qkz\right]\right. \\ &\quad \left. + A \left[\sin kz \sin qk\ell - \sin k\ell \sin qkz\right]\right\} \qquad (7) \\ &= I_o \left\{f_c(z) + A f_s(z)\right\}, \end{aligned}$$

where I_o and A are arbitrary constants and $q = \cos\theta_i$. Thus, the "boundary condition" $I(\pm\ell) = 0$, has been imposed on the solution.

Defining the quantities

$$\gamma_c = \frac{k}{2\pi}\int_0^{2\pi} d\phi \int_{-\ell}^{\ell}\int_{-\ell}^{\ell} f_c(z) f_c(z') \left(1 + \frac{1}{k^2}\frac{\partial^2}{\partial z'^2}\right) \frac{e^{-jkR}}{R}\, dz'\, dz \tag{8}$$

$$\gamma_s = \frac{k}{2\pi}\int_0^{2\pi} d\phi \int_{-\ell}^{\ell}\int_{-\ell}^{\ell} f_s(z) f_s(z') \left(1 + \frac{1}{k^2}\frac{\partial^2}{\partial z'^2}\right) \frac{e^{-jkR}}{R}\, dz'\, dz \tag{9}$$

$$\lambda_c = \frac{4\pi jZ}{\eta}\int_{-\ell}^{\ell} f_c^2(z)\, dz \tag{10}$$

$$\lambda_s = \frac{4\pi jZ}{\eta}\int_{-\ell}^{\ell} f_s^2(z)\, dz \tag{11}$$

$$g_c = k \sin\theta_i \int_{-\ell}^{\ell} f_c(z)\, e^{jkz\cos\theta_i}\, dz \tag{12}$$

$$g_s = k \sin\theta_i \int_{-\ell}^{\ell} f_s(z)\, e^{jkz\cos\theta_i}\, dz \tag{13}$$

Equation 6 reduces to the simpler form

$$\frac{1}{S} = \frac{(\gamma_c - \lambda_c) + A^2(\gamma_s - \lambda_s)}{\left[g_c + A\, g_s\right]^2} \tag{14}$$

The integrals containing cross product terms such as $f_c(z)f_s(z)$ can be shown to vanish. The integrals for $\gamma_c, \gamma_s, \lambda_c, \lambda_s$, g_c and g_s can all be evaluated in closed form, although the details are somewhat tedious and we omit them here.

By the variational technique, the constant A may now be evaluated by setting

$$\frac{\partial}{\partial A}\left(\frac{1}{S}\right) = 0, \tag{15}$$

yielding

$$A = \frac{g_s(\gamma_c - \lambda_c)}{g_c(\gamma_s - \lambda_s)} . \tag{16}$$

Thus from Eq. 14 the backscattered amplitude is given by

$$S = \frac{g_c^2}{\gamma_c - \lambda_c} + \frac{g_s^2}{\gamma_s - \lambda_s} . \tag{17}$$

From the definition of backscattered amplitude one has

$$4\pi E_o S \cos\psi = j\eta k^2 \sin\theta_i \int_{-\ell}^{+\ell} I(z) e^{jkz\cos\theta_i}\, dz \tag{18}$$

and it now follows that

$$\frac{I_o}{E_o} = \frac{4\pi \cos\psi}{jk\eta}\left(\frac{g_c}{\gamma_c - \lambda_c}\right). \tag{19}$$

The general far-field scattering amplitude $S(\theta, \theta_i)$ is defined by the equations

$$\frac{E_{S\theta}(\theta, \theta_i)}{E_o \cos\psi} = \frac{e^{-jkR}}{kR} \qquad S(\theta, \theta_i) \tag{20}$$

$$S(\theta, \theta_i) = \frac{jk^2\eta \sin\theta}{4\pi E_o \cos\psi} \int_{-\ell}^{\ell} I(z)\ e^{jkz\cos\theta}\ dz \tag{21}$$

where $E_{S\theta}$ is the component of the scattered E field polarized in the θ direction. Upon substitution of the previous results the scattered amplitude becomes, after integration,

$$S(\theta, \theta_i) = 2\sqrt{1 - p^2}\left\{\left(\frac{g_c}{\gamma_c - \lambda_c}\right)\left[\frac{\cos qk\ell}{(1 - p^2)}\right.\right.$$

$$\cdot\ (\sin k\ell\ \cos pk\ell\ - p \cos k\ell\ \sin pk\ell\ ) - \frac{\cos k\ell}{(q^2 - p^2)}$$

$$\left.\cdot\ (q \sin qk\ell\ \cos pk\ell\ - p \cos qk\ell\ \sin pk\ell\ )\right]$$

$$+ j\left(\frac{g_s}{\gamma_s - \lambda_s}\right)\left[\frac{\sin qk\ell}{(1 - p^2)}\ (p \sin k\ell\ \cos pk\ell\ - \cos k\ell\ \sin pk\ell\ )\right.$$

$$\left.\left. - \frac{\sin k\ell}{q^2 - p^2}\ (p \sin qk\ell\ \cos pk\ell\ - q \cos qk\ell\ \sin pk\ell\ )\right]\right\} \qquad (22)$$

where

$$q = \cos\theta_i$$

$$p = \cos\theta.$$

This is the basic equation from which the various cross sections are computed.

By definition, the differential scattering cross section is given as

$$\sigma(\theta, \theta_i) = R_o^2 \left|\frac{E_{S\theta}}{E_o}\right|^2$$

$$= \frac{\cos^2\psi}{k^2}\left|S(\theta, \theta_i)\right|^2 \qquad (23)$$

The total scattering cross section is then

$$\sigma_S = \frac{2\pi \cos^2\psi}{k^2}\int_0^{\pi}\left|S(\theta, \theta_i)\right|^2 \sin\theta\, d\theta. \qquad (24)$$

The extinction cross section is defined by the well-known forward amplitude theorem as

$$\sigma_e = \frac{4\pi}{k^2} \cos^2\psi \ \mathrm{Im}\ S(\pi - \theta_i, \theta_i)$$

$$= \frac{4\pi}{k^2} \cos^2\psi \ \mathrm{Im} \left\{ \frac{g_c^2}{\gamma_c - \lambda_c} - \frac{g_s^2}{\gamma_s - \lambda_s} \right\}. \qquad (25)$$

The absorption cross section is just the rms power absorbed in the scatterer divided by the rms intensity of the incident beam. The rms power absorbed in the wire is given by

$$P_a = \mathrm{Re}(Z) \int_{-\ell}^{\ell} \left| I(z) \right|^2 dz$$

and the rms intensity of the θ component of the incident beam is

$$I_\theta = \frac{E_o^2}{2\eta} \cos^2\psi$$

so that the absorption cross section, after substitution of the expression for current, becomes

$$\sigma_a = \frac{4\pi}{k^2} \frac{\mathrm{Re}(Z)}{|Z|} \cos^2\psi \left\{ \left| \frac{g_c}{\gamma_c - \lambda_c} \right|^2 |\lambda_c| + \left| \frac{g_s}{\gamma_s - \lambda_s} \right|^2 |\lambda_s| \right\} \qquad (26)$$

Finally, the radar cross section is defined to be

$$\sigma_{RCS} = 4\pi\, \sigma(\theta_i, \theta_i)$$

$$= \frac{4\pi}{k^2} \cos^4\psi \left| S(\theta_i, \theta_i) \right|^2$$

$$= \frac{4}{k^2} \cos^4\psi \left| \frac{g_c^2}{(\gamma_c - \lambda_c)} + \frac{g_s^2}{(\gamma_s - \lambda_s)} \right|^2. \qquad (27)$$

The results of the present theory have been compared with experimental measurements made by Webb in the microwave region,[7] and comparison with the theory is shown in Figure 2. The experiments were carried out at 9.3 GHz on 1 mil tungsten wire, having a conductivity of 1.81×10^7 mho/m, and the figures show these results, versus aspect angle, for wire lengths to wavelength the ratios of $2\ell/\lambda = 0.46$. As can be seen, there is excellent agreement between the theory and the experiment.

There are also theoretical checks upon the theory which can be made. The first is reciprocity which is satisfied. The second check is provided by energy conservation requirements, namely, that

$$\sigma_e = \sigma_a + \sigma_s. \tag{28}$$

Because each of the three cross sections is independently calculated, Eq. 28 provides an internal consistency check on the validity of the results. This criterion is satisfied for $2\ell/\lambda$ ratios up to at least 1 or 2.

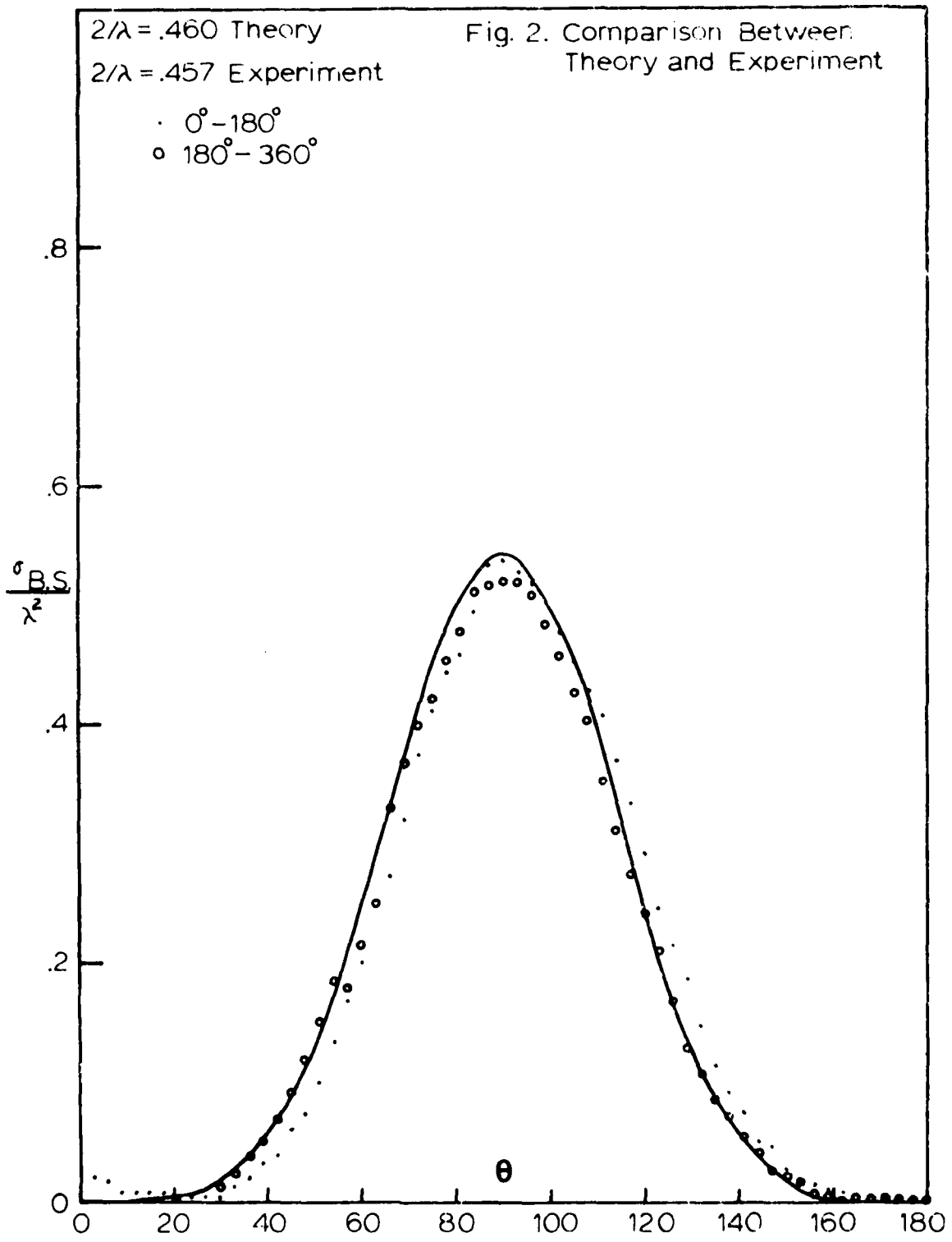
2/λ = .460 Theory
2/λ = .457 Experiment
· 0°–180°
o 180°–360°
Fig. 2. Comparison Between Theory and Experiment
.8
.6
.4
.2
0
σ B.S. / λ²
θ
0
20
40
60
80
100
120
140
160
180

COMPARISON AND DISCUSSION OF PRESENT THEORETICAL RESULTS

The authors have programmed the results of the 1965 theory and that given in the preceeding section for the Hewlett Packard 9825A computer and 9872A plotter. The averaged cross sections are computed as a function of wavelength. Computations are presently made for twenty (equally spaced on a log scale) wavelengths. The computation time is approximately three minutes per wavelength. The angular increment used for numerical integration is 5 degrees, which is somewhat coarse for the larger $k\ell$ values. To date, 112 sets of computations have been made and the results are stored on magnetic tape for plotting. We will attempt here to present a few such plots to indicate ranges of validity and obvious limitations of the two earlier theories.

In Figure 3, we have plotted (via machine) orientation and polarization averaged absorption, scattering, extinction, and backscatter (RCS) cross sections, normalized to the particle volume, as a function of wavelength from 0.1 micron to 100 microns. Computation of the averaged cross section values for a given wavelength involves a total of 798 individual cross section computations. The results of the theory of the last section and the 1965 theory (for absorption and scattering) are plotted. Note that the values of wavelength for which $ka = 1$ and $k\ell = 1$ are labeled, as is the value of wavelength for which $L\epsilon'' = 1$, where $L\epsilon''$ is given by equation 3. The 1965 theory plot is purposely limited in the scattering computations to $k\ell < 1$, and in the absorption computations to $ka < 0.1$. Note that the data explicitly depend upon only four parameters: radius, length, conductivity, and wavelength.* Although magnetic losses could have been included, it was determined[2] that these are negligible as compared with electrical losses when the particle parameters are such that the electrical loss is optimized. The wavelength range for this optimization for the particle parameters of Figure 3 is below 10 microns. The set of Figures 3, 4, 5, and 6 were plotted to demonstrate only one of a number of functional characteristics. In this set, the radius and conductivity are fixed at 10^{-8}m and 10^{5}mho/m, respectively. The length takes on values from 3×10^{-7}m (Fig. 3) through 10^{-5}m (Fig. 6).

We first note in Figure 3 that the two theories agree quite well within the valid range of comparison. Also note that, for the more recent theory, the extinction and absorption cross sections are coincident over almost the entire wavelength range. This should be expected since the extinction cross section is the sum of the scattering and absorption cross

*The computations made thus far span the range of radius from 33 Angstroms to 0.1 micron, of length from 0.3 micron to 10 microns, and of conductivity from 10^{4} to 10^{7} mho/m.

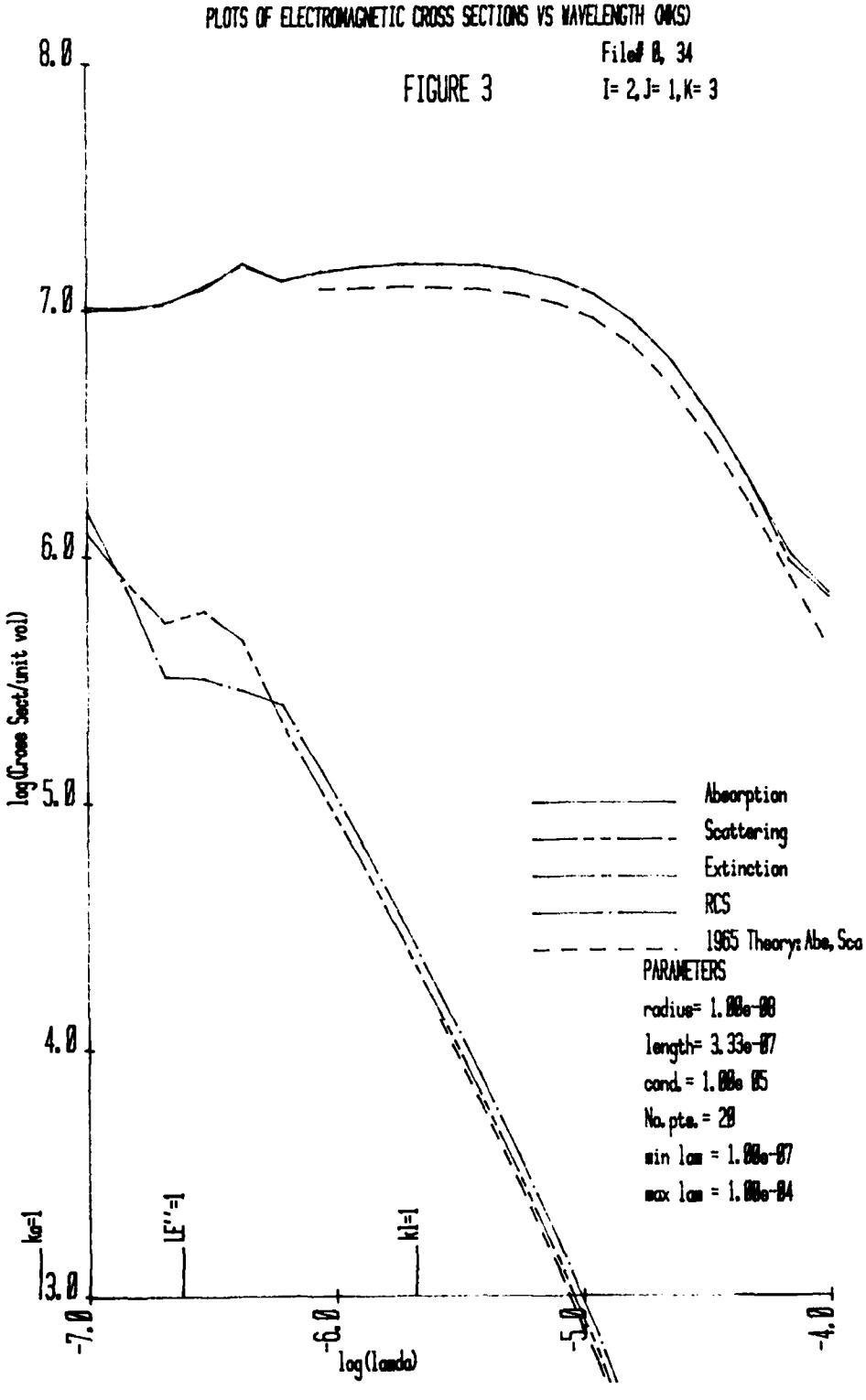
PLOTS OF ELECTROMAGNETIC CROSS SECTIONS VS WAVELENGTH (MKS)
File# 0, 34
FIGURE 3
I= 2, J= 1, K= 3
8.0
7.0
6.0
5.0
4.0
3.0
log(Cross Sect/unit vol)
ka=1
LE''=1
k1=1
-7.0
-6.0
-5.0
-4.0
log(lamda)
Absorption
Scattering
Extinction
RCS
1965 Theory: Abs, Sca
PARAMETERS
radius= 1.00e-08
length= 3.33e-07
cond.= 1.00e 05
No. pts.= 20
min lam = 1.00e-07
max lam = 1.00e-04

sections, and the scattering cross section is an order of magnitude or more below the absorption cross section.

Going to Figure 4, we see that the length has increased by a factor of 3. Since the scattering cross section per unit volume of the particle is proportional to particle volume in the Rayleigh region, the scattering cross section/vol. should be greater than that of Figure 3 by 3x in the $k\ell<1$ region, which it is. Also note in Figure 4 that the absorption cross section vs wavelength remains large at the longer wavelengths. This is because of the behavior of $L\epsilon''$ (Equation 3) in the regime $k\ell < 1$. In this regime, $L\epsilon''\sim(\lambda/\ell^2)$. We have increased ℓ by a factor of 3. Therefore, λ must increase in Figure 4 by $\sim$10x in order to obtain the same value of $L\epsilon''$, and thus the same value of absorption cross section per unit volume, in the two figures.

Proceeding to Figure 5, in which the length is increased to 3.3 microns, we see that the extinction and absorption curves are reasonably well behaved, but that the scattering and backscatter curves now display a regular (on the log λ scale) oscillation. This effect is more pronounced for the scattering than for the backscatter cross section. Note that the first perturbation (going towards the shorter wavelengths) occurs at $(\ell/\lambda)\simeq 0.5$, which obtains for all four figures. Although this behavior would appear to be representing the natural longitudinal resonances of the cylinder, we believe that the overall oscillatory behavior may not be correct, since, on a log λ scale, we would expect the rate of oscillation to increase towards the left, which it does not. We would also expect that the averaged backscatter cross section vs λ would exhibit oscillations at least as large as those of the scattering cross section vs λ, but this is not the case.

Note that in Figure 5 the course wavelength dependence of scattering and RCS are correct $(1/\lambda^2)$. The conductivity of 10^5 mho/m is not sufficiently high for this particle geometry to give rise to the usual $(1/\lambda^4)$ dependence for infinitely conducting wires. *

Figure 6 shows the same general characteristics as Figure 5, except that the average values of scattering and RCS per unit volume are increased by the three-fold increase in particle length, which is to be expected. When Figures 6 and 5 are overlayed, and the $k\ell = 1$ tick marks made to coincide, it is found that λ-axis locations and the amplitudes of the scattering oscillations agree very closely over nearly all the wavelength range

*The $(1/\lambda^4)$ dependence on RCS and scattering cross section does obtain in our results for sufficiently high conductivity values, e.g., for $\sigma_c = 3\text{x}10^6$ mho/m, $a = 3\text{x}10^{-8}$m, $\ell = 3\text{x}10^{-7}$m, the $(1/\lambda^4)$ dependence occurs at wavelengths greater than one micron.

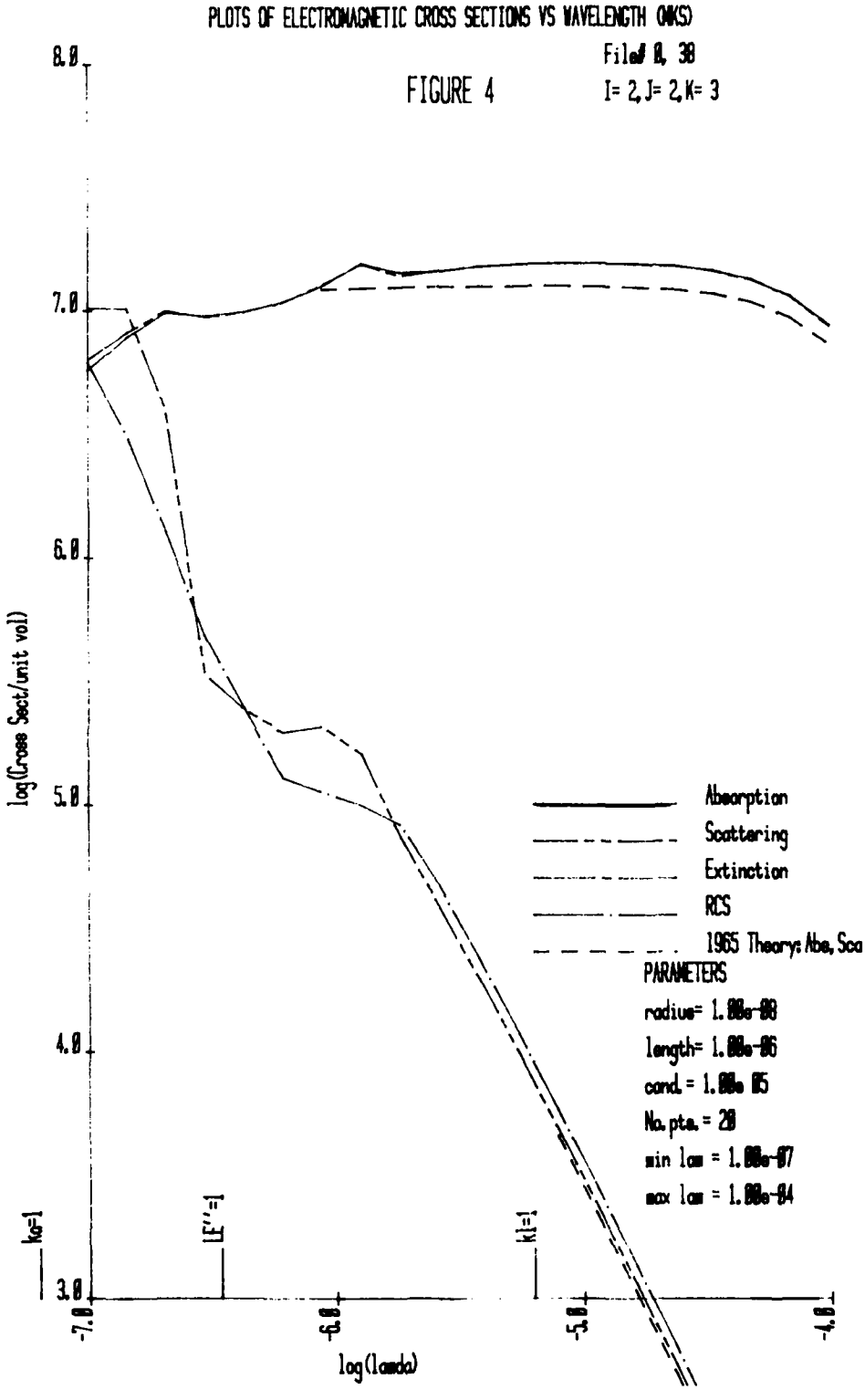
PLOTS OF ELECTROMAGNETIC CROSS SECTIONS VS WAVELENGTH (MKS)
File# 0, 38
I= 2, J= 2, K= 3
8.0
7.0
6.0
5.0
4.0
3.0
log(Cross Sect/unit vol)
-7.0
-6.0
-5.0
-4.0
log(lamda)
ka=1
|E''|=1
k1=1
Absorption
Scattering
Extinction
RCS
1965 Theory: Abs, Sca
PARAMETERS
radius= 1.00e-00
length= 1.00e-00
cond.= 1.00e 05
No. pts.= 20
min lam = 1.00e-07
max lam = 1.00e-04

FIGURE 4

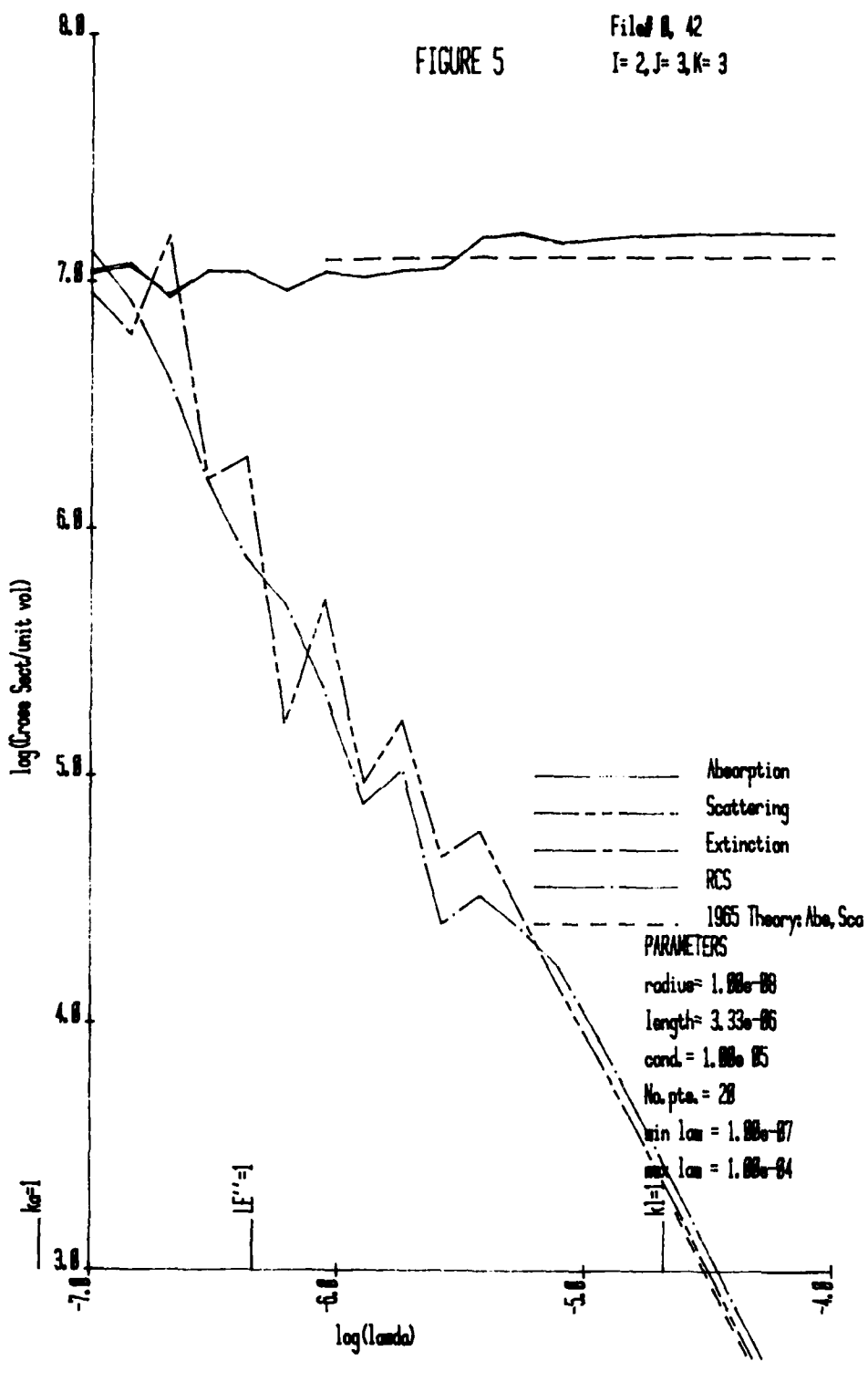
PLOTS OF ELECTROMAGNETIC CROSS SECTIONS VS WAVELENGTH (MKS)
File# 11, 42
FIGURE 5
I= 2, J= 3, K= 3
8.0
7.0
6.0
5.0
4.0
3.0
log(Cross Sect/unit vol)
ka=1
LE''=1
kl=1
-7.0
-6.0
-5.0
-4.0
log(lamda)
Absorption
Scattering
Extinction
RCS
1965 Theory: Abs, Sca
PARAMETERS
radius= 1.00e-08
length= 3.33e-06
cond.= 1.00e 05
No. pts.= 20
min lam = 1.00e-07
max lam = 1.00e-04

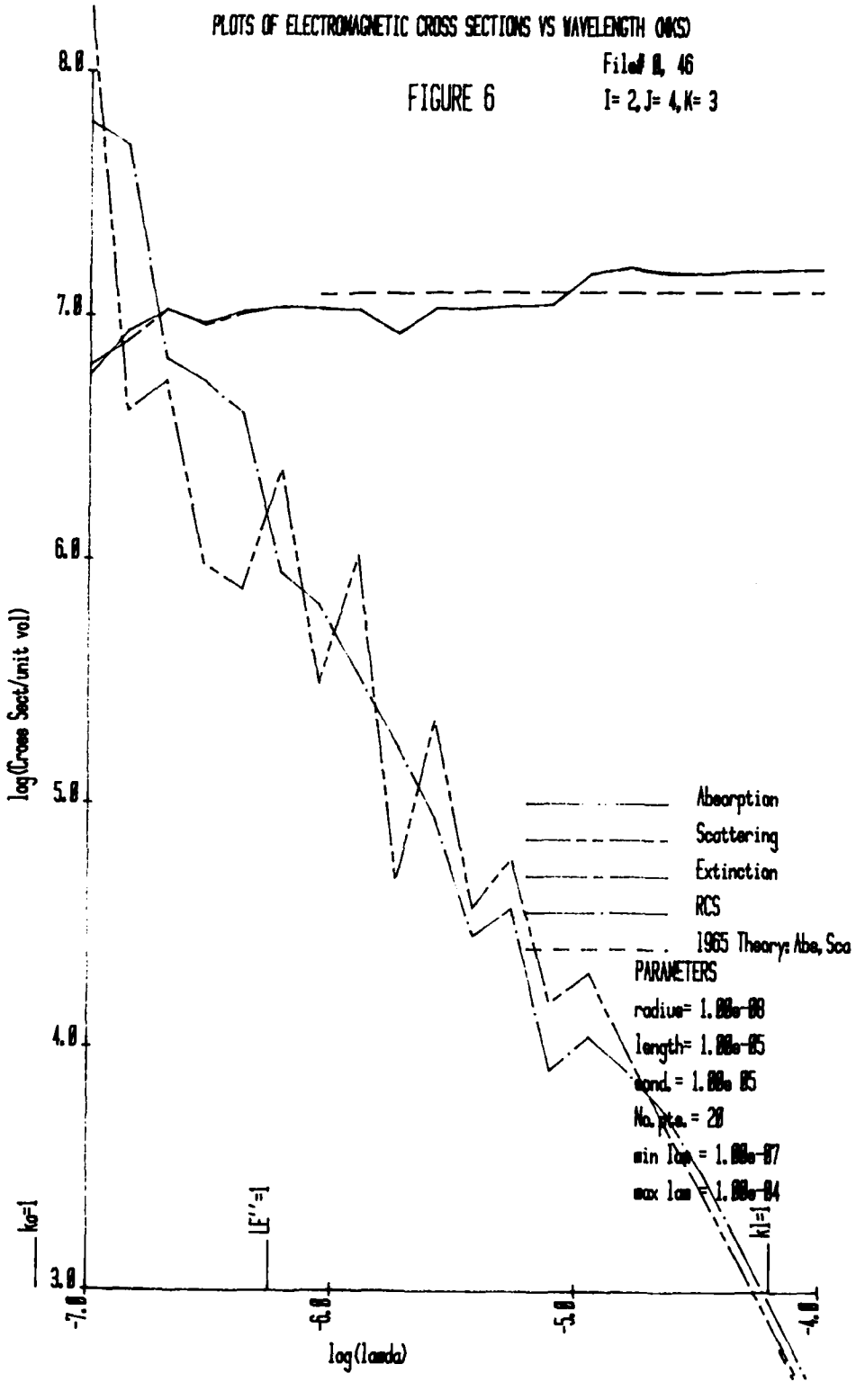
PLOTS OF ELECTROMAGNETIC CROSS SECTIONS VS WAVELENGTH (MKS)
File# 8, 46
FIGURE 6
I= 2, J= 4, K= 3
8.0
7.0
6.0
5.0
4.0
3.0
log(Cross Sect/unit vol)
Absorption
Scattering
Extinction
RCS
1965 Theory: Abs, Sca
PARAMETERS
radius= 1.00e-08
length= 1.00e-05
cond.= 1.00e 05
No. pts.= 20
min Iam = 1.00e-07
max Iam = 1.00e-04
ka=1
LE''=1
k1=1
-7.0
-6.0
-5.0
-4.0
log(lamda)

over which the curves can be compared. As a further comment regarding Figure 6, it should be noted that, at wavelengths shorter than 0.2 microns, the scattering cross section and/or the absorption cross section is higher than the extinction cross section. Thus, the theory is obviously inconsistent at these very short wavelengths.

Generally speaking, from the thirty or so sets of data which we have examined, it appears as though the theory presented in the preceeding section is applicable for ℓ/λ ratios as large as about 2, but the apparent limit depends upon ka and conductivity. The smaller the values of these latter two parameters, the greater apparent valid range of ℓ/λ. Within the useful range of the 1965 theory, the agreement is generally quite good.

The particle angular orientation increments are 5^{o}, as are the computations of differential cross section. This 5^{o} increment is rather too coarse for the larger (ℓ/λ) values. Similarly, the selection of only 20 wavelengths over a three order of magnitude wavelength range is too coarse at the shorter wavelengths. We intend to reduce both the wavelength increments and angular increments to see what effect this will have on the wavelength dependent cross section results. (This will presnt some problems due to computer memory limitations.)

In spite of the above, our present conclusion regarding the theory of the preceeding section is that the trial function, made up of a sin and cos, is too simple to provide accurate results for large values of (ℓ/λ). However, it should be borne in mind that the theory presented thus far in this paper and reduced to production software is capable of accurately predicting scattering and absorption efficiencies over a very wide range of particle parameters.

The work presented in the next section describes our present efforts to improve the trial function but to maintain the basic framework of the theory.

EXTENDED THEORY

In order to extend the theory to higher ratios of $2\ell/\lambda$, we are presently considering a current function which is a summation of terms which are harmonics of the original trial function. Thus,

$$I(z) = I_o\left[\sum_{n=1}^{\infty}\right]B_n\left[f_{cn}(z) + A_n f_{sn}(z)\right] \tag{29}$$

will replace the simpler trial function of Eq. 7. Here

$$f_{cn}(z) = \cos nkz \cos nqx - \cos nx \cos nqkz \tag{30}$$

and

$$f_{sn}(z) = \sin nkz \sin nqx - \sin nx \sin nqkz \tag{31}$$

where $q = \cos\theta_i$ and $x = k\ell$.

The variation equation, Eq. 6, for 1/S then becomes

$$\frac{1}{S} = \frac{I_1 - I_2}{I_3} \tag{32}$$

where

$$I_1 = \frac{k}{2\pi I_o^2}\int^{2\pi} d\phi \int_{-\ell}^{\ell}\int_{-\ell}^{\ell} I(z)\, I(z')\left(1 + \frac{1}{k^2}\frac{\partial^2}{\partial z'^2}\right)\frac{e^{-jkR}}{R}\, dz\, dz', \tag{33}$$

$$I_2 = \frac{4\pi j Z}{\eta I_o^{\,2}}\int_{-\ell}^{\ell} I(z)^2\, dz \tag{34}$$

and

$$I_3 = \frac{k \sin\theta i}{I_o}\int_{-\ell}^{\ell} e^{jkz\cos\theta_i}\, I(z)\, dz\,. \tag{35}$$

Substituting Eq. (29) for the current trial function I(z) into Eq. (35), one obtains

$$I_3 = k \sin\theta_i \sum_{n=1}^{\infty} B_n \left[\int_{-\ell}^{\ell} f_{cn}(z)\, e^{jkz\cos\theta_i}\, dz \right.$$

$$\left. + A_n \int_{-\ell}^{\ell} f_{sn}(z)\, e^{jkz\cos\theta_i}\, dz \right].$$

It can be seen that I_3 contains no cross product terms and has been directly integrated. The integrals are similar to those of equation (12) and (13) of the present theory and can be represented as g_{cn} and g_{sn} respectively. Thus,

$$I_3 = \sum_{n=1}^{\infty} \left[g_{cn} + A_n g_{sn} \right] \tag{36}$$

Upon substitution of Eq. 29 for I(z) into equation (34) for I_2, one obtains

$$I_2 = \frac{4\pi j Z}{\eta} \int_{-\ell}^{\ell} \left[\sum_{n=1}^{\infty} B_n \left(f_{cn}(z) + A_n f_{sn}(z) \right) \right]^2 dz$$

$$= \frac{4\pi j Z}{\eta} \sum_{n=1}^{\infty} \sum_{m=1}^{\infty} \int_{-\ell}^{\ell} \left\{ B_n B_m \left[f_{cn}(z) f_{cn}(z) \right.\right.$$

$$\left.\left. + A_n f_{cm}(z) f_{sn}(z) + A_m f_{cn}(z) f_{sm}(z) + A_n A_m f_{sn}(z) f_{sm}(z) \right] \right\} dz.$$

From symmetry (odd-even) considerations, it can be shown that the integrals involving $f_{cn}(z) f_{sm}(z)$ and $f_{cm}(z) f_{sn}(z)$ vanish. The remaining integrals have been evaluated for $n = m$ and for the cross-product terms when $n \neq m$. Using a terminology similar to the simpler theory,

$$I_2 = \sum_{n=1}^{\infty} B_n^2 \left[\lambda_{cn} + A_n^2 \lambda_{sn} \right] + \sum_{n=1}^{\infty} \sum_{m=1}^{\infty} B_n B_m \left[\lambda_{cnm} + A_n A_m \lambda_{snm} \right] \tag{37}$$

Finally, substitution of Eq. 29 for I(z) into Eq. 33 yields

$$I_1 = \frac{k}{2\pi}\int_0^{2\pi} d\phi \int_{-\ell}^{\ell}\int_{-\ell}^{\ell}\left\{\sum_{n=1}^{\infty}\sum_{m=1}^{\infty} B_n B_m\left[f_{cn}(z) f_{cm}(z')\right.\right.$$

$$+ A_n f_{cm}(z') f_{sn}(z) + A_m f_{cn}(z) f_{sm}(z')$$

$$\left.\left. + A_n A_m f_{sn}(z) f_{sm}(z')\right]\left(1 + \frac{1}{k^2}\frac{\partial}{\partial z'^2}\right)\frac{e^{-jkR}}{R}\right\} dz\, dz'$$

The terms involving $f_{cn}(z) f_{sm}(z')$ and $f_{cm}(z') f_{sn}(z)$ vanish for $n = m$ but do not vanish for $n \neq m$. Again, using the notation of the simple theory

$$I_1 = \sum_{n=1}^{\infty} B_n^2\left[\gamma_{cn} + A_n^2 \gamma_{sn}\right] + \sum_{n=1}^{\infty}\sum_{m=1}^{\infty} B_n B_m\left[\gamma_{cnm}\right. \tag{38}$$

$$\left. + A_n A_m \gamma_{snm} + A_n \gamma_{sncm} + A_m \gamma_{cnsm}\right]$$

At present, the integrals represented by the g's, λ's, and γ's in Equations 36, 37, and 38 have been analytically evaluated.

If equations 36 - 38 are now substituted into the equation 32,

$$\frac{1}{S} = \frac{I_1 - I_2}{I_3}$$

and using the variational technique of setting

$$\frac{\partial}{\partial B_n}\left(\frac{1}{S}\right) = 0 \qquad \text{and} \qquad \frac{\partial}{\partial A_n}\left(\frac{1}{S}\right) = 0,$$

2n simultaneous equations will result for the A_n's and B_n's. These can be solved by matrix inversion, and the A_n's and B_n's will be determined as a function of the previously evaluated g's, λ's, and γ's. This part of the theoretical work remains to be done.

Once the A_n's and B_n's have been determined, the formulation of the scattering, extinction, absorption, and radar cross sections will follow as presented in equations 22 through 27.

DISCUSSION AND CONCLUSIONS

Our 1965 work and the "Present" theory compliment each other in the sense that in the regions of mutual validity the former provides a quick analytical tool for explaining the behavior of the latter, which is far too complex to easily evaluate. Although certain overflow and underflow conditions in the program itself have recently been overcome, we are not yet sure as to the valid upper limit on ℓ/λ, but feel reasonably confident out to $(\ell/\lambda) \leq 2$. Further analysis involving finer increments in numerical integration and in wavelength will help clarify this. Notwithstanding, an extremely wide range of wavelengths (including radar frequencies and lower) and particle parameters can be handled with the present programs.

The "Extended" theory should provide accurate results for wavelengths well beyond $(\ell/\lambda)=2$. The new trial function, which is described as purely longitudinal, can probably be further improved by the inclusion of an exponential decay factor for the radial distribution of the longitudinal current. This should allow for a wider range of (ka) than would otherwise be possible.

ACKNOWLEDGEMENTS

We gratefully acknowledge many helpful discussions with Dr. P. C. Waterman, consultant to Panametrics, Dr. Galen Daum of the Army Ballistics Research Laboratory, and Professor Alan Glasser, also a Panametrics consultant.

REFERENCES

1. Pedersen, N. E., Pedersen, J. C., Theoretical, Experimental, and Systems Studies on a New Technique for Radar Cross Section Reduction, (Secret), Avco RADTN-65-67, 8 December 1965.

2. Pedersen, N. E., Pedersen, J. C., Bethe, H. A., "A New Method of Radar Target Concealment", Proc. Tri-Service Radar Symposium, San Diego, 1969 (Secret).

3. Waterman, P. C., Matrix Methods in Potential Theory and Electromagnetic Scattering, J. A. P. Vol. 50, pp. 4550-4566, 1979.

4. Tai, C. T., Electromagnetic Backscattering from Cylindrical Wires, J. Appl. Phys., Vol. 23, pp. 909-916, (August 1952).

5. Cassedy, E. S. and Fainberg, J., Electromagnetic Cross Sections of Cylinders of Finite Conductivity, The Hohns Hopkins Laboratory Technical Report No. AF-81, August 1960.

6. Rano, S. and Whinnery, J. R., Fields and Waves in Modern Radio, John Wiley and Sons, Inc., New York, NY, 1949.

7. Weber, J. R., Radar Backscatter Measurements for Tungstn and Copper Dipoles, Lockheed-Georgia Company Report No. ER-6948, June 1964.

Long Thin Cylinders at Arbitrary Incidence and Polarization

Gaelen R. Daum
USAARRADCOM Ballistic Research Laboratory

The problem of scattering and absorption by an infinite cylinder at an arbitrary angle of incidence was solved by Wait.[1] The solutions are rather complicated, being expressed as an infinite series of terms involving logarithmic derivatives of Bessel functions. In many uses of interest however, the full solution is not necessary, and the expressions may be simplified by passing to the appropriate limits. Here we consider a long (with respect to wavelength) cylinder whose diameter is much less than the wavelength. Since the cylinder is long, we use the expressions for the cross section per unit length of an infinite cylinder, and, since the cylinder is thin, the arguments of the Bessel functions are small and may be replaced by their limiting forms. The notation is that of Kerker[2] with which we assume the reader is familiar.

The coefficients as given by Kerker may be written

$$a_{nI} = C \times \begin{vmatrix} inh/\alpha & inh/\alpha & inh/\alpha & jn^1(ja) \\ \ell^2 & j^2 & \ell^2 & 0 \\ \ell n^1(\ell a) & m^2 jn^1(ja) & \ell n^3(\ell a) & -inh/\alpha \\ 0 & 0 & 0 & j^2 \end{vmatrix}$$

$$b_{nI} = -C \times \begin{vmatrix} \ell n^3(\ell a) & inh/\alpha & inh/\alpha & jn^1(ja) \\ 0 & j^2 & \ell^2 & 0 \\ -inh/\alpha & m^2 jn^1(ja) & \ell n^1(\ell a) & -inh/\alpha \\ \ell^2 & 0 & 0 & j^2 \end{vmatrix} \qquad (1)$$

$$a_{nII} = C \times \begin{vmatrix} -\ell n^1(\ell a) & inh/\alpha & inh/\alpha & jn^1(ja) \\ 0 & j^2 & \ell^2 & 0 \\ inh/\alpha & m^2 jn^1(ja) & \ell n^3(\ell a) & -inh/\alpha \\ -\ell^2 & 0 & 0 & j^2 \end{vmatrix}$$

$$b_{nII} - C \times \begin{vmatrix} \ell n^3(\ell) & inh/\alpha & \ell n^1(\ell a) & jn^1(ja) \\ 0 & j^2 & 0 & 0 \\ inh/\alpha & -m^2 jn^1(ja) & inh/\alpha & inh/\alpha \\ \ell^2 & 0 & \ell^2 & j^2 \end{vmatrix}$$

where η^1 and η^3 are the logarithmic deviatives of the Bessel functions and the Hankel functions of the second kind, respectively. In Eq. 1

$$C = (mk_o)^{-1} J_n(\ell a) H_n(\ell a) J_n^2 (ja) \Delta^{-1}$$

$$\Delta = J_n^2(\ell a) H_n^2 (\ell a) (mk_o)^{-1} \begin{vmatrix} \ell\eta^3(\ell a) & inh/\alpha & inh/\alpha & -j\eta^1(ja) \\ 0 & j^2 & \ell^2 & 0 \\ -inh/\alpha & m^2 j\eta^1(ja) & \ell\eta^3(\ell a) & inh/\alpha \\ \ell^2 & 0 & 0 & -j^2 \end{vmatrix}$$

For small arguments, the Bessel and Hankel functions may be replaced by *their limiting forms:*

$$J_n(z) = \frac{(z/2)^n}{\Gamma(n+1)} ; \; H_o(z) = (2/i\pi) \ell nz; \; H_n = -(i\pi)^{-1}\Gamma(n)(z/2)^{-n} \qquad (2)$$

Equation 1 then becomes

$$a_{nI} = \frac{-\pi\alpha^{2n}}{2^{2n} n!(n-1)!} \frac{m^2-1}{m^2+1} \cos^{2n-2}\phi \sin\phi$$

$$b_{nI} = \frac{i\pi\alpha^{2n}}{2^{2n} n!(n-1)!} \frac{m^2-1}{m^2+1} \cos^{2n-2}\phi \sin\phi \qquad (3)$$

$$a_{nII} = \frac{i\pi\alpha^{2n}}{2^{2n} n!(n-1)!} \frac{m^2-1}{m^2+1} \cos^{2n-2}\phi$$

$$b_{nII} = \frac{-\pi\alpha^{2n}}{2^{2n} n!(n-1)!} \frac{m^2-1}{m^2+1} \cos^{2n-2}\phi \sin\phi$$

for $n \geq 1$. The n=0 terms are:

$$a_{oI} = b_{oII} = a_{oII} = 0$$

$$b_{oI} = \frac{i\pi}{4} \alpha^2 (m^2-1) \cos^2\phi \qquad (4)$$

Since α is small, we keep only terms of order less than α^4. Equations 3 and 4 yield

$$
\begin{aligned}
a_{oI} &= 0 \\
a_{1I} &= -(\pi\alpha^2/4)\left(\frac{m^2-1}{m^2+1}\right)\sin\phi \\
b_{oI} &= (i\pi\alpha^2/4)(m^2-1)\cos^2\phi \\
b_{1I} &= (i\pi\alpha^2/4)\left(\frac{m^2-1}{m^2+1}\right)\sin\phi \\
a_{oII} &= 0 \\
a_{1II} &= (i\pi\alpha^2/4)\left(\frac{m^2-1}{m^2+1}\right) \\
b_{oII} &= 0 \\
b_{1II} &= -(\pi\alpha^2/4)\left(\frac{m^2-1}{m^2+1}\right)\sin\phi
\end{aligned}
\tag{5}
$$

The extinction cross sections are proportional to the real part of these coefficients, and the scattering cross sections are proportional to the square of the modulus. For a transverse magnetic (TM) incidence wave, we have

$$
\begin{aligned}
C_{1ex} &= -\frac{\pi\alpha^2}{k_o}\left[\cos^2\phi\ \mathrm{Im}\,(m^2-1) + 2\sin^2\phi\ \mathrm{Im}\left(\frac{m^2-1}{m^2+1}\right) + 2\sin\phi\ \mathrm{Re}\left(\frac{m^2-1}{m^2+1}\right)\right] \\
C_{1sc} &= \frac{\pi\alpha^2}{k_o}\left[|m^2-1|^2\cos^4\phi + 2\sin^4\phi\ \left|\frac{m^2-1}{m^2+1}\right|^2 + 2\sin^2\phi\ \left|\frac{m^2-1}{m^2+1}\right|^2\right]
\end{aligned}
\tag{6}
$$

and for a transverse electric (TE) incident wave

$$
\begin{aligned}
C_{2ex} &= -\frac{\pi\alpha^2}{k_o}\left[\sin\phi\,\mathrm{Re}\left(\frac{m^2-1}{m^2+1}\right) + 2\ \mathrm{Im}\left(\frac{m^2-1}{m^2+1}\right)\right] \\
C_{2sc} &= (8/k_o)\ (\pi\alpha^2/4)^2\left|\frac{m^2-1}{m^2+1}\right|^2(1+\sin^2\phi)
\end{aligned}
\tag{7}
$$

We note that Eqs. 6 and 7 agree with Kerker[2] for perpendicular incidence ($\phi = 0$). Averaging the cross section over the angle of incidence, we obtain

$$C_{1ex} = -(\pi\alpha^2/k_o)\left[\tfrac{1}{2}\,\mathrm{Im}\,(m^2-1) + \mathrm{Im}\left(\frac{m^2-1}{m^2+1}\right)\right]$$

$$C_{1sc} = (\pi^2\alpha^4/4k_o)\left[\frac{3}{8}\left|m^2-1\right|^2 + \frac{14}{8}\left|\frac{m^2-1}{m^2+1}\right|^2\right]$$

$$C_{2ex} = -(\pi\alpha^2/k_o)\left[2\,\mathrm{Im}\,\frac{m^2-1}{m^2+1}\right] \qquad (8)$$

$$C_{2sc} = (\pi^2\alpha^4/2k_o)\left[\frac{3}{2}\left|\frac{m^2-1}{m^2+1}\right|^2\right]$$

To average over the polarization, we decompose the incident wave into TE and TM waves, each of which will scatter according to Eq. 8. Writing $E = E_{TM}\cos\theta + E_{TE}\sin\theta$ and a similar expression for H, the cross sections are seen to go as $\cos^2\theta$ and $\sin^2\theta$ since the cross section is proportional to $|E|^2$ from the Poynting vector. The average value of $\sin^2\theta$ and $\cos^2\theta$ is ½, so

$$C_{ex} = -(\pi\alpha^2/2k_o)\left[\tfrac{1}{2}\,\mathrm{Im}\,(m^2-1) + 3\,\mathrm{Im}\left(\frac{m^2-1}{m^2+1}\right)\right]$$

$$C_{sc} = (\pi^2\alpha^4/64\,k_o)\left[3\left|m^2-1\right|^2 + 38\left|\frac{m^2-1}{m^2+1}\right|^2\right] \qquad (9)$$

For a long, finite, cylinder these expressions are multiplied by the length L.

This work was done at the request of Jay Embury of CSL, who needed the results for a study of scattering by different geometrical shapes.

REFERENCES

1. J. R. Wait, Can, J Phys. 33, 189 (1955).
2. M. Kerker, The Scattering of Light and Other Electromagnetic Radiation, Academic Press, NY (1969), p.255ff.

Scattering From Axially Symmetric Bodies

Melvin Lax
CCNY

Gaelen R. Daum
USAARRADCOM Ballistic Research Laboratory

INTRODUCTION

This paper describes work that is far from complete, the feasibility and practicality of which has not yet been demonstrated. Rather than presenting any results then, we will content ourselves with describing what it is we hope to accomplish, what has been done to date, and what problems we are currently facing.

The basic integral equation for the electric field is

$$E(r) = E_{inc}(r) + (k^2\bar{\bar{1}} + \bar{\nabla}\bar{\nabla}) \int G_o(r-r')(n^2-1)E(r')dr' \qquad (1)$$

where $G_o(r,r') = 4\pi|r-r'|^{-1} \exp(ik|r-r'|)$, n is the refractive index, and k is the wave number. This equation is exact, being derivable directly from Maxwell's equations and the usual constitutive relations. Like most exact equations, it is also too complicated to solve. The numerous researchers who take Eq. 1 for their starting point usually go directly to various limiting cases and seek approximate solutions. What we are investigating is whether or not the imposition of an axis of symmetry is, by itself, sufficient to make Eq. 1 tractable. If it is, then we intend to apply the technique to long fibers with a symmetrically varying radius. If imposition of a symmetry axis is not sufficient to make Eq. 1 tractable, then it is hoped that this investigation will provide insight into what further minimum requirements are necessary.

EXPANSION OF THE EQUATION

The existence of a symmetry axis suggests that cylindrical coordinates are the preferred system. This isn't the case however, because the cylindrical unit vectors are not constant, and this is inconvenient in doing the integral. A better choice of coordinates consts of E_z, $E_+ = E_x+iE_y$ and $E_- = E_x-iE_y$. These behave simply under a rotation about $\hat{z}$ and are related to the cylindrical components through

$$\begin{aligned} E_z &= E_z \\ E_\rho &= (\tfrac{1}{2}) [\exp(i\phi)E_- + \exp(-i\phi) E_+] \\ E_\phi &= (\tfrac{i}{2}) [\exp(i\phi)E_- - \exp(-i\phi) E_+] . \end{aligned} \qquad (2)$$

If we define F(r) to be the integral in Eq. 1, we can expand both E and F in cylindrical harmonics.

$$E_z = \Sigma Z_m(z,\rho)\exp(im\phi) \qquad F_z = \Sigma Y_m(z,\rho)\exp(im\phi)$$

$$E_\rho = \Sigma R_m(z,\rho)\exp(im\phi) \qquad F_\rho = \Sigma S_m(z,\rho)\exp(im\phi) \tag{3}$$

$$E_\phi = \Sigma \Phi_m(z,\rho)\exp(im\phi) \qquad F_\phi = \Sigma \Psi_m(z,\rho)\exp(im\phi)$$

The expansion coefficients for F can be related to those of E by Eq. 3 and the definition of F. The result is

$$Y_m(\tau) = \int K_m(\tau,\tau')\, d\tau' \,[n^2(\tau') - 1]\, Z_m(\tau')$$

$$S_m(\tau) = \int L_m(\tau,\tau')\, d\tau' \,[n^2(\tau') - 1]\, R_m(\tau')$$

$$+ \int N_m(\tau,\tau')\, d\tau' \,[n^2(\tau') - 1]\, \Phi_m(\tau') \tag{4}$$

$$\Psi_m(\tau) = \int L_m(\tau,\tau')\, d\tau' \,[n^2(\tau') - 1]\, \Phi_m(\tau')$$

$$- \int N_m(\tau,\tau')\, d\tau') \,[n^2(\tau') - 1]\, R_m(\tau') \quad ,$$

where τ stands for the combination (z,ρ), and the kernels are given by

$$K_m(\tau,\tau') = \int G_o(r-r') \exp\,[im(\phi-\phi')]\, d\phi'$$

$$L_m(\tau,\tau') = (\tfrac{1}{2})\,[K_{m+1}(\tau,\tau') + K_{m-1}(\tau,\tau')] \tag{5}$$

$$N_m(\tau,\tau') = (\tfrac{i}{2})\,[K_{m+1}(\tau,\tau') - K_{m-1}(\tau,\tau')] \quad .$$

INCIDENT WAVE

The remaining term in Eq. 1 to be treated is the incident wave which we write

$$E^{inc} = \exp(ikz\cos\alpha)\exp(ik\rho\sin\alpha\cos\phi)\,\hat{e},$$

where $e = a\,e_E + b\,e_H$. The TE mode corresponds to a=1, b=0, and the TM mode to a=0, b=1. The cylindrical components are then

$$\begin{aligned}
E_z^{inc} &= a\exp(ikz\cos\alpha)\,\Sigma\, i^m \exp(im\phi)\,J_m(k\rho\sin\alpha)\\
E_\rho^{inc} &= \Sigma i^m \exp(im\phi)\,[-bm(k\rho\sin\alpha)^{-1}J_m(k\rho\sin\alpha)\\
&\qquad + ia\cos\alpha\,J_m'(k\rho\sin\alpha)]\\
E_\phi^{inc} &= \Sigma\, i^m \exp(im\phi)\,[-ib\,J_m'(k\rho\sin\alpha)\\
&\quad - am\cos\alpha\,(k\rho\sin\alpha)^{-1}J_m(k\rho\sin\alpha)]\ .
\end{aligned} \tag{6}$$

We also have

$$\begin{aligned}
E_z^{inc} &= a\,\Phi\sin\alpha\\
E_+^{inc} &= (-a\cos\alpha + ib)\,\Phi\\
E_-^{inc} &= (-a\cos\alpha - ib)\,\Phi\ ,
\end{aligned} \tag{7}$$

where

$$\Phi = kz\cos\alpha\,\Sigma\, i^m J_m(k\rho\sin\alpha)\exp(im\phi).$$

WORKING EQUATIONS

Taking Eq. 3 and 7 and substituting into Eq. 1 leads to the final integral equations for the Forier coefficients:

$$Z_m = a \sin\alpha \exp(ikz\cos\alpha)\, i^m J_m(k\rho\sin\alpha) + [k^2 + (\partial^2/\partial z^2)]\, Y_m$$

$$+ (1/\rho)(\partial/\partial\rho)[\rho(\partial S_m/\partial z)] + (im/\rho)(\partial\psi_m/\partial z)\ ;$$

$$R_m = \exp(ikz\cos\alpha)\, i^m [-bm(k\rho\sin\alpha)^{-1} J_m(k\rho\sin\alpha)$$

$$+ ia\cos\alpha\, J_m'(k\rho\sin\alpha)] + k^2 S_m + (\partial^2 Y_m/\partial\rho\partial z) \qquad (8)$$

$$+ (\partial/\partial\rho)[(1/\rho)(\partial/\partial\rho)(\rho S_m)] + im(\partial/\partial\rho)(\partial\psi_m/\partial\rho);$$

$$\Phi_m = \exp(ikz\cos\alpha)\, i^m [-ib\, j_m'(k\rho\sin\alpha) - \cos\alpha\,(k\rho\sin\alpha)^{-1} J_m(k\rho\sin\alpha)]$$

$$+ k^2\psi_m + (im/\rho)[(\partial Y_m/\partial z) + (1/\rho)(\partial/\partial\rho)(\rho S_m) + (im/\rho)\psi_m]\ ,$$

where Y_m, S_m and ψ_m on the right hand side of Eq. 8 are expressed in terms of Z_m, R_m and Φ_m by means of Eq. 3. Study of Eq. 8 and 3 shows that terms of different m are not coupled together. This indicates that we have properly exploited the cylindrical symmetry.

THE GREEN'S FUNCTIONS

From the integral representation

$$(z^2 + \rho^2)^{-1/2} \exp[ik(z^2+\rho^2)^{1/2}] = \int_0^\infty (\lambda^2 - k^2)^{1/2} J_0(\lambda\rho) \qquad (9)$$

$$x \exp[-|z|(\lambda^2 - k^2)^{1/2}]\, \lambda d\lambda\ ,$$

and the addition theorem

$$J_o\left(\lambda[\rho^2 + \rho'^2 - 2\rho\rho' \cos\phi]^{\frac{1}{2}}\right) = \Sigma\, J_m(\lambda\rho)\, J_m(\lambda\rho') \exp(im\phi)\ , \quad (10)$$

the Green's function of Eq. 5 becomes

$$K_m(z,\rho;z',\rho') = \int \frac{\exp[ik[(z-z')^2 + (\rho^2+\rho'^2 - 2\rho\rho'\cos\phi)^{\frac{1}{2}}]}{4\pi[(z-z')^2 + (\rho^2+\rho'^2 - 2\rho\rho'\cos\phi)]^{\frac{1}{2}}} \exp(im\phi)\, d\phi$$

$$= (\tfrac{1}{2})\, G_m(z, \rho; z', \rho') = (\tfrac{1}{2}) < R^{-1} \exp(ikR) \exp(im\phi) > \quad (11)$$

$$= (\tfrac{1}{2})\, G_m(z-z'; \rho,\rho')\ ,$$

where $< > = (2\pi)^{-1}\int d\phi$ is seen to be an even function of m. From Eq. 9 and 10 we also have

$$G_m(z; \rho, \rho') = \int (\lambda^2-k^2)^{-\frac{1}{2}} \exp\left[-|z|(\lambda^2+k^2)^{\frac{1}{2}}\right] \lambda d\lambda\, J_m(\lambda\rho)\, J_m(\lambda\rho'). \quad (12)$$

If we put $q = z^2 + \rho^2 + \rho'^2$, $p = \rho\rho'$; Eq. 12 becomes

$$G_m(z;\rho, \rho') = (2\pi)^{-1} \int [q-2\rho\cos\phi]^{-\frac{1}{2}} \exp\left[ik(q-2\rho\cos\phi)^{\frac{1}{2}}\right] \cos m\phi\, d\phi\ . \quad (13)$$

It can be shown that for $ka \ll 1$, Eq. 13 yields

$$G_o = \exp(ikq^{\frac{1}{2}}) \quad (2\pi)^{-1} \int_0^{2\pi} [q-2\rho\cos\phi]^{-\frac{1}{2}} (1-ikq^{\frac{1}{2}})\, d\phi - ik + \ldots$$

$$G_1 = \exp(ikq^{\frac{1}{2}}) \quad (2\pi)^{-1} \int_0^{2\pi} [q-2\rho\cos\phi]^{-\frac{1}{2}} (1-ikq^{\frac{1}{2}})\, d\phi - 0 + \ldots \quad . \quad (14)$$

Equations 14 are identical to those derived by Brillouin[2] for the antenna problem. They can be readily evaluated for small k by reducing Eq. 14 to elliptic integral form and expanding the elliptic integrals as power series in k.

As a further check on what has been done so far, it was decided to compare with Uzonoglu et al.[3] To compare with them we must specialize to the TE case (b=0), normal incidence, and take the limit ka << 1. For b=0, E_ϕ is not excited at all, and therefore Φ_o=0. If we let ka << 1 but temporarily retain non-normal incidence, we find

$$Z_o(z,\rho) = \sin\alpha \exp(ikz\cos\alpha) + [k^2 + (\partial^2 Y/\partial z^2)] + (1/\rho)(\partial/\partial\rho)[\rho(\partial S_o/\partial z)]; \quad (15)$$

$$R_o(z,\rho) = i\cos\alpha \exp(ikz\cos\alpha)\, k\rho\sin\alpha + (\partial^2 Y_o/\partial\rho\partial z) + k^2 S_o + (\partial/\partial\rho)[(1/\rho)(\partial/\partial\rho)(\rho S_o)] \quad .$$

Equation 15 suggest that for a thin enough scatterer, the variation of E_z or z_o over the radius of the scatterer can be neglected, and that the radial component R_o varies as $k\rho\, r_o(z)$. The technique of Ref. 3 is to omit R_o and assume that E_z is independent of ρ. It is then possible to obtain a one dimensional equation for $z_o(z) = Z_o(z,o)$. Instead, UAF choose to write

$$\overline{Z}_o(z) = 2a^{-2}\int Z_o(z,\rho)\,\rho\, d\rho \quad , \quad (16)$$

an average over the cross section. In principle, precisely the same equations should result if the initial assumption that $Z_o(z,\rho) = Z_o(z,o)$ is valid. Nonetheless, two different equations with different kernels result, and it remains to be seen whether or not we can establish equivalence. In what follows, a bar over the variable refers to the averaging process of Eq. 16 while no bar refers to evaluation on the axis.

Both equations take the same form

$$z_o(z) = \sin\alpha \exp(ikz\cos\alpha) + [k^2 + (\partial^2/\partial z^2)]y_o(z) + c(z), \quad (17)$$

where $y_o(z) = (\tfrac{1}{2})(n^2-1)\int G_o\ (z-z')\ dz'\ z_o\ (z')$.

For evaluation at $\rho=o$

$$G_o(z-z') = \int G_o\ (z-z';\ \rho=0,\ \rho')\ \rho'\ d\rho'. \tag{18}$$

and for the averaging process

$$\overline{G}_o(z-z') = 2a^{-2}\iint \rho d\rho\ G_o\ (z-z';\ \rho,\ \rho')\ \rho'\ d\rho'. \tag{19}$$

Similarly

$$C(z) = (1/\rho)\ (\partial/\partial\rho)\ [\rho(\partial S_o\ (z,\rho)/\partial\rho)\big|_{\rho=o}\ , \tag{20}$$

and

$$\overline{C}(z) = (2a^{-2})\quad \rho d\rho\ [\rho^{-1}\ (\partial/\partial\rho)[\rho(\rho S_o\ (z,\rho)/\partial z)].$$

In either case

$$S_o(z,\rho) = (\tfrac{1}{2})(n^2-1)\ \int G_1\ (z-z';\ \rho,\ \rho')\ \rho'\ d\rho'\ k\rho'\ r_o\ (z'). \tag{21}$$

It appears likely, though we have not yet been able to demonstrate it, that the differences in these two procedures are of higher order in ka. In order to compare with UAF, we return to Eq. 17 and use the same assumptions as UAF. We find that

$$k_o(z,z') = 2a^{-2}\iint K_o\ (z,\rho;\ z',\ \rho')\ \rho d\rho\ \rho'\ d\rho' \tag{22}$$

$$= a^2 \int [(\lambda a)^{-1}\ J_1\ (\lambda a)]^2(\lambda^2-k^2)^{-\frac{1}{2}}\lambda\ \exp\ [-|z-z'|(\lambda^2-k^2)^{\frac{1}{2}}]\ d\lambda.$$

A solution of $[(d^2/dz^2) + k^2]\ g\ (z,z') = -\delta(z-z')$

is

$$g(z,z') = i(2k)^{-1}\ \exp\ (ik|z-z'|)\quad . \tag{23}$$

Using Eq. 22 and 23, the second term of Eq. 17 becomes

$$[k^2 + (d^2/dz^2)]\, y_o(z) = (n^2-1) \int [J_1\ (\lambda a)]^2\ (\lambda^2-k^2)^{\frac{1}{2}}$$

$$x \exp\ [-(\lambda^2-k^2)^{\frac{1}{2}}\ ]\ \lambda d\lambda\ z_o\ (z') \qquad (24)$$

$$+ 2(n^2-1) \int - [(\lambda a)^{-1}\ J_1\ (\lambda a)]^2\ \lambda d\lambda\ z_o\ (z')\ ,$$

and we find

$$n^2\ Z_o(z) = \sin\alpha \exp\ (ikz\ \cos\alpha) + (n^2-1) \iint (\lambda^2-k^2)^{\frac{1}{2}}\ [J_1\ (\lambda a)]^2 \qquad (25)$$

$$x \exp\ [-\ |z-z'|\ (\lambda^2-k^2)^{\frac{1}{2}}]\ \lambda d\lambda\ z_o\ (z')\ dz' + c\ (z)\ .$$

Equation 25 with $\alpha = \pi/2$ is the same as Eq. 8 of Ref. 3, provided that we omit the correction term c(z).

CONCLUSION

While the research presented here is very preliminary and any or all of it is subject to change, the results so far are encouraging. We have a procedure that reproduces both Brillouin's equations for a cylindrical antenna[2] and the equations of Uzonoglu, Alexopoulis and Fikiaris[3] for dielectric fibers. Several important theoretical questions remain to be answered; among them, the equivalence of the averaging process and evaluation on the axis has yet to be shown. Even when these points are resolved, and the procedure is on a sound theoretical foundation, the numerical solution of the equations will be a non-trivial task. There is still a great deal to be done before the practicality of this scheme can be demonstrated.

This research is being performed primarily by M. Lax; this paper however, was prepared by G. Daum. Any errors or omissions are those of G. Daum and not M. Lax.

REFERENCES

1. J. A. Stratton, Electromagnetic Theory, Mc Graw-Hill, NY, (1941). pg. 576.

2. L. Brillouin, Quarterly Applied Math. 1, 201 (1943).

3. N. K. Uzonoglu, N. G. Alexopoulis, J. G. Fikiaris, Jour. Opt. Soc. Am. 68, 194 (1978).

SUMMARY OF THE PROCEEDINGS OF THE "INTERNATIONAL WORKSHOP ON LIGHT SCATTERING BY IRREGULARLY SHAPED PARTICLES"

Donald W. Schuerman

State Univ. of N.Y. at Albany, Space Astronomy Lab

Albany, New York 12203

ABSTRACT

An "International Workshop on Light Scattering by Irregularly Shaped Particles" was held on June 5-7, 1979, at the State University of New York at Albany (SUNYA). The proceedings of this U.S. Army sponsored workshop (hosted by the Space Astronomy Laboratory, SUNYA) are summarized.

1. INTRODUCTION

Observational, experimental, theoretical, and computing techniques involving resonant light scattering have all recently improved to the point where the effects of particle shape must be addressed. Recognizing this fact, particularly in view of its current research needs, the U.S. Army Research Office (ARO) agreed to sponsor the first workshop dedicated to exploring the role of particle shape. The Workshop was held at SUNYA where ARO is sponsoring an on-going microwave analog investigation of scattering by irregular particles. Attendance at the workshop was originally envisioned to number about thirty-five people, ten of whom would discuss the interests of various sponsoring agencies. However, the concept of a meeting devoted to such a topic generated a larger than anticipated response from investigators in widely varying disciplines. Invitations were finally sent to over sixty people selected by the Scientific Organizing Committee (P. Chýlek, SUNYA/NCAR; R. Fenn, AFGL; J. M. Greenberg, Univ. Leiden; R. Pinnick, Army ASL; J. Reagan, NASA/Univ. of Arizona; D. Schuerman, SUNYA; R. Zerull, Ruhr Univ., FRG). Thus, the meeting grew to a hybrid workshop-conference. Question and answer periods and a panel-floor discussion were used to maintain a high level of

technical interaction. Plenum Publishing Corporation will publish, advertise, and distribute the Workshop Proceedings at a cost of about $40 per hard-cover volume. The titles of those papers that will be included in the volume are preceded by an asterisk in the program summarized below.

2. THE PROGRAM

Review Paper: D. Deirmendjian (Rand Corp., Santa Monica, CA)
*SOME REMARKS ON SCIENCE, SCIENTISTS, AND THE REMOTE SENSING OF PARTICULATES

Review Paper: J. Mayo Greenberg (Univ. of Leiden, Netherlands)
*FOCUSING IN ON PARTICLE SHAPE

LIDAR MEDLEY

J. Bunting (AFGL, Hanscom AFB, MA)
*SENSING ICE CLOUDS FROM SATELLITES

The meteorology Division of the Air Force Geophysics Laboratory seeks improved techniques to detect cloud properties from satellites. Radiative transfer models for clouds are important tools for technique development; however, their applications to ice clouds are highly tentative due to limited knowledge of light scattering in ice clouds. The problem exists for terrestrial radiation in the IR, as well as scattered sunlight in the visible and near-IR.

E. Moroz (AFGL, Hanscom AFB, MA)
*LIDAR VISIBILITY MEASUREMENTS

The Air Force requires information on light scattering by atmospheric particles in order to determine visibility for aircraft operations at airfields. The multiple scattering process is one facet that comes into strong play in the measurement of visibility in Category II and III conditions. An experimental lidar slant visual range measuring system will be described.

E. Shettle (AFGL, Hanscom AFB, MA)
*NON-SPHERICAL PARTICLE SCATTERING: AIR FORCE APPLICATIONS

Particles of primary interest are natural aerosols and cloud constituents, the latter being more well-defined. Cloud problem areas include: distinguishing between ice and water clouds, determining their ice or water content, and understanding these differences in terms of visual and infrared measurements. The effect of particle shape in aerosol detection methods (*e.g.*, lidar or optical particle counters) is also of great interest.

R. Pinnick (U.S. Army ASL, White Sands, NM)
SOME IRREGULAR AEROSOL PARTICLES OF ARMY INTEREST

Aerosols of natural and anthropogenic origin affect the

operation of military electro-optical systems and high energy lasers. In this paper characteristics of some irregular particles that are of interest to the U.S. Army are given: their shape and range of sizes, their refractive indexes, their multi-component character, and the radiation wavelengths that are particularly interesting.

J. Embury (U.S. Army CSL, Aberdeen, MD)
*PARTICLES PRODUCING STRONG EXTINCTION IN THE INFRARED

A summary of particle shapes, sizes and compositions which produce strong extinction per unit mass is presented. Their corresponding albedo and phase function are discussed in a single scatter and multiple scatter context. These particles are of considerable interest to the Army Smoke Program at Chemical Systems Laboratory.

SPECIFIC PARTICLE DESCRIPTIONS

V. Ramaswamy and P. Chylek (ASRC SUNYA, NY/NCAR, Boulder, CO)
*SHAPE OF RAINDROPS

Water drops found in natural rains acquire the simple, spherical forms at only the smallest sizes. Both laboratory and field research reveal that the larger sized raindrops undergo considerable deviation from a spherical shape. We review the evidence for deformed drops and show a technique for parameterizing the drop surface in accordance with the forces acting on falling raindrops.

R. Cheng (ASRC SUNYA, Albany, NY)
*PHYSICAL PROPERTIES OF ATMOSPHERIC PARTICULATES

Microscopic investigations of atmospheric particulates reveal a complex variation with respect to size and shape. Emission from combustion processes contributes more than 70% of the fine particle burden in the atmosphere. Flyash from coal-fired boilers have a relatively smooth surface in contrast to flyash from oil-fired boilers which have a rough, honeycomb-like surface. Particles from automobile exhaust and smoke are extremely small, spherical, and fairly uniform in size. In addition they always exhibit a chain-like aggregation. Classification of fine structure of ice crystals is based on environmental conditions such as temperature and degree of supersaturation. However, recent evidences have shown that it is also dependent on the origin of their freezing nuclei. Selected micrographs and classification, based on major sources, size, and major chemical components, from the "ASRC Atmospheric Particulates Atlas" are presented.

B. Vonnegut (ASRC SUNYA, Albany, NY)
*ATMOSPHERIC ICE CRYSTALS

Photographs of naturally occurring atmospheric ice crystals will be presented and their formation and occurrence will be discussed.

D. Woods (NASA Langley, VA)
*EXAMPLES OF REALISTIC AEROSOL PARTICLES COLLECTED IN A CASCADE IMPACTOR

In this paper some scanning electron microscope photomicrographs showing examples of a variety of particulate aerosol shapes are presented. Compositions of particles also are presented. These particles represent samples from a number of different sources and locations including: solid propellant rocket motor plumes, active volcano plumes, the lower stratosphere over Sondrestrom, Greenland, and the upper troposphere over northern Texas. The particles were collected from aboard an aircraft with a cascade impactor which classified them according to aerodynamic size into 10 size intervals ranging from submicron to greater than 25 micrometers in diameter. The cascade impactor also served to measure the mass concentration as a function of particle size. The variety of shapes and compositions found among these particles suggest difficulties in obtaining reliable size distribution data from light scattering measurements.

A.W. Hogan (ASRC SUNYA, Albany, NY)
*SOME CHARACTERISTICS OF THE ANTARCTIC AEROSOL

Aerosol concentrations have been systematically measured at the South Pole for five years. These climatological measurements have been supported by vertical and horizontal profiles obtained in summer with aircraft flights. Aerosol size data has been obtained with diffusion batteries, electrostatic precipitators, and cascade impactors. There is a strong (5 to 1) seasonal variation in surface aerosol concentrations, with the maximum aerosol concentration generally occurring with the beginning of summer mixing in November. Vertical profiles consistently show the greatest aerosol concentrations to occur in the moist layer, a few hundred meters above the surface, and then diminishing quite steadily with altitude. Examination of collected particles by light and electron microscopy shows them to be soluble, with refractive index of 1.54 and often with the appearance of flattened drops. The maximum particle radius found was 3 μm and the peak volume concentration occurred at 2 μm radius. The size distributions are of similar slope to those measured over the Weddell Sea by Meszaros and in Tasmania by Bigg. We interpret this as evidence that the Southern Ocean and especially the Weddell Sea as the source of these particles. The particles arriving at the station are then quite probably the residue of evaporated clouds, and the aerosol is representative of that occurring at the end point of many of nature's particle removal mechanisms.

THEORETICAL METHODS

J. Embury (U.S. Army CSL, Aberdeen, MD)
*ABSORPTION BY SMALL REGULAR NON-SPHERICAL PARTICLES IN THE RAYLEIGH REGION

Smaller particles characterized by a complex refractive index generally absorb more radiation per unit mass than larger particles.

AD-A113 733 KOHL (RONALD H) AND ASSOCIATES TULLAHOMA TN F/G 4/1
PROCEEDINGS OF THE 1979 CHEMICAL SYSTEM LABORATORY SCIENTIFIC C--ETC(U)
DEC 80 R H KOHL DAAK11-80-M-0021

UNCLASSIFIED ARCSL-CR-81023 NL

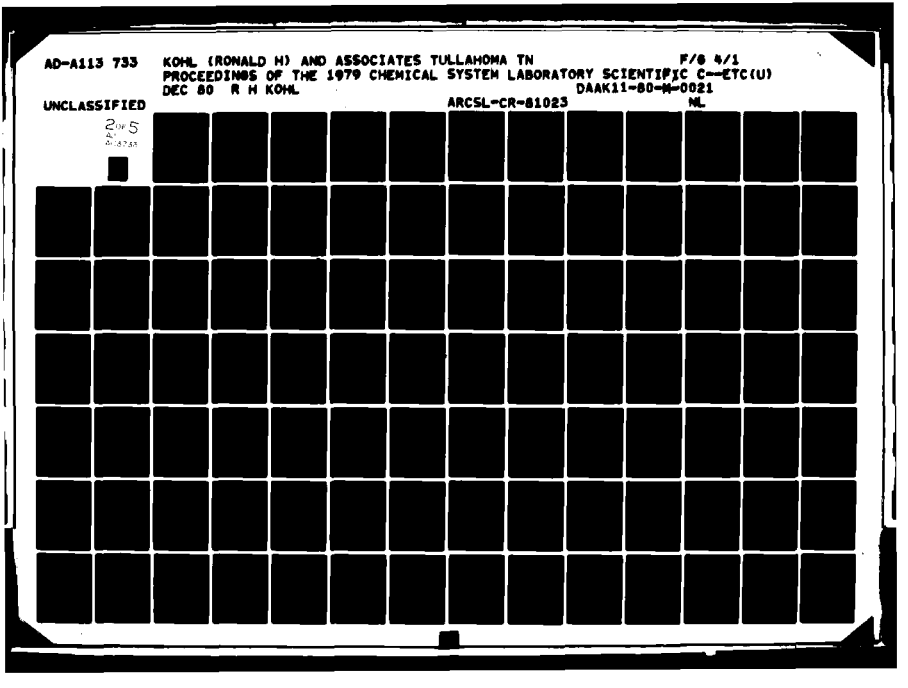

This absorption reaches a maximum in the Rayleigh region where it becomes size independent. We explore the dependence of dipolar resonant absorption on both shape and refractive index in the Rayleigh region. We suggest mechanisms prohibiting asymptotic approach to infinite resonant absorption poles.

P. Chýlek (ASRC SUNYA, Albany, NY/NCAR, Boulder, CO), J.T. Kiehl (SUNYA, Albany, NY/NCAR, Boulder, CO), M.K. Ko (Atmos. & Environ. Res. Inc., Cambridge, MA) and A. Ashkin (Bell Labs, Holmdel, NJ)
*SURFACE WAVES IN LIGHT SCATTERING BY SPHERICAL AND NON-SPHERICAL PARTICLES

Resonances in partial wave scattering amplitudes a_n and b_n are responsible for the ripple structure of the extinction curve and for sharp peaks in the backscattering (glory). A connection between the resonances and surface waves is suggested.

R. Welch (Colorado St. Univ., Fort Collins, CO)
NON-SPHERICAL EXTINCTION AND ABSORPTION EFFICIENCIES

Predictions concerning the scattering and absorption characteristics of electromagnetic radiation interacting with non-spherical particles are obtained by suppression of particle resonances (surface waves) in classical Mie scattering theory. The importance of the particle resonance phenomenon and thus the non-spherical corrections is related to the three classical variables n_i, n_r, and x, the imaginary and real components of the index of refraction and the size parameter, respectively.

P. Chýlek (ASRC SUNYA, Albany, NY/NCAR, Boulder, CO) and R. Pinnick (U.S. Army ASL, White Sands, NM)
OPTICAL THEOREM AND APPROXIMATIONS FOR THE LIGHT SCATTERING BY NON-SPHERICAL PARTICLES

Many of the approximations for the light scattering by spherical and non-spherical particles are nonunitary approximations. In these cases the optical theorem cannot be used to calculate the extinction cross sections. The extinction cross section can be obtained only by calculating the scattering and absorption cross sections and summing them together. If the optical theorem is used, obviously incorrect results are obtained.

C. Aquista (Drexel Univ., Phila., PA) and H.A. Holland (NASA Wallops, VA)
*ENERGY CONSERVATION: A TEST FOR SCATTERING APPROXIMATIONS

We explore the roles of the extinction theorem and energy conservation in obtaining the scattering and absorption cross section for several light scattering approximations. We show that the Rayleigh, Rayleigh-Gans, Anomalous Diffraction, Geometrical Optics, and Shifrin approximations all lead to reasonable values of the cross sections, while the Modified Mie approximation does not. Further examination of the Modified Mie approximation for the ensembles of non-spherical particles reveals additional problems with that method.

C. Yeh and K.K. Mei (UCLA and EMtec, Los Angeles, CA)
*ON THE SCATTERING FROM ARBITRARILY SHAPED INHOMOGENEOUS PARTICLES - EXACT SOLUTION

Discussion will be given on an exact approach to the problem of resonant scattering by arbitrarily shaped inhomogeneous particles. This exact approach is based on the Global-Local Finite Element which combines the contemporary finite element method with a hybrid-Ritz approach. Examples will be shown.

J. Pollack and J. Cuzzi (NASA Ames, CA)
*SCATTERING BY NON-SPHERICAL PARTICLES OF SIZE COMPARABLE TO A WAVELENGTH: A NEW SIMIEMPIRICAL THEORY

We propose an approximate method for evaluating the interaction of randomly oriented, non-spherical particles with the total intensity component of electromagnetic radiation. When the particle size parameter, x, the ratio of particle circumference to wavelength, is less than some upper bound x_o ($\sim$5), Mie theory is used. For $x > x_o$, the interaction is divided into three components: diffraction, external reflection, and transmission. Physical optics theory is used to obtain the first of these components; geometrical optics theory is applied to the second; and a simple parameterization is employed for the third. The predictions of this theory are found to be in very good agreement with laboratory measurements for a wide variety of particle shapes, sizes, and refractive indices. Limitations of the theory are also noted.

J.T. Kiehl (SUNYA, Albany, NY/NCAR, Boulder, CO), M.W. Ko (Atmos. & Environ. Res. Inc., Cambridge, MA), A. Mugnai (NCAR, Boulder, CO/ Elettrofisica Atmosferica, Frascati, Italy) and P. Chýlek (ASRC SUNYA, Albany, NY/NCAR, Boulder, CO)
*PERTURBATION APPROACH TO THE LIGHT SCATTERING BY NON-SPHERICAL PARTICLES

Applying the perturbation theory we have derived the first order perturbation corrections to the scattering characteristics for the case of light scattering by slightly deformed spheres. Numerical results are compared with those obtained using the extended boundary conditions method. The range of applicability of the first order perturbation corrections are discussed.

J.T. Kiehl (SUNYA, Albany, NY/NCAR, Boulder, CO), A. Mugnai (NCAR, Boulder, CO/Elettrofisica Atmosferica, Frascati, Italy) and P. Chýlek (ASRC SUNYA, Albany, NY/NCAR, Boulder, CO)
LIGHT SCATTERING BY A PAIR OF CONJUGATE NON-SPHERICAL PARTICLES

Using the first order perturbation theory a theorem is derived which shows that under specific conditions a sum of the scattering matrices of two non-spherical particles can be replaced by a scattering matrix of a sphere. The implications for the inverse scattering problem are discussed.

K.N. Liou and R. Coleman (Univ. Utah, Salt Lake City)
*LIGHT SCATTERING BY HEXAGONAL COLUMNS AND PLATES

Computations of light scattering by hexagonal columns and plates randomly oriented in two- and three-dimensional space are carried out by means of the geometrical ray tracing technique. Analyses are made for a number of crystal sizes and for a visible wavelength of 0.5 μm and an infrared wavelength of 10 μm at which absorption plays a significant role. Scattering phase functions and degree of linear polarization computed from the ray tracing program are compared with those derived from experimental nephelometer measurements performed in the laboratory. Effects of the crystal size and shape on the scattering parameter will be described. We will also present the theoretical and experimental programs concerning light scattering by ice clouds to be carried out in the future.

D. Huffman and C. Bohren (Univ. Arizona, Tucson)
*INFRARED ABSORPTION SPECTRA OF NON-SPHERICAL PARTICLES TREATED IN THE RAYLEIGH-ELLIPSOID APPROXIMATION

A comparison of small particle extinction spectra calculated for spheres with extinction measurements shows the inadequacy of the spherical approximation in treating strong infrared absorption bands. A simple expression for absorption cross sections of non-spherical particles is derived by integrating over a distribution of shape parameters in the Rayleigh-ellipsoid approximation. For comparison with the theoretical results infrared extinction measurements were made of sub-micron quartz particles dispersed in a KBr matrix. The favorable comparison of theory and experiment suggests that the treatment of shape effects in infrared absorption spectra by means of a distribution of ellipsoids constitutes a major improvement.

S. Asano (NASA Goddard, NY/Tohoku Univ, Sendai, Japan)
LIGHT SCATTERING PROPERTIES OF SPHEROIDAL PARTICLES

The extinction and scattering cross sections, asymmetry factor, and scattering matrix elements have been calculated, based on our solution of the scattering by a homogeneous spheroid, for spheroids in arbitrary orientations and random orientations. The scattering characteristics of an assembly of randomly oriented, identical spheroidal particles will be discussed in comparison with scattering measurements.

C. Acquista (Drexel Univ., Phila., PA)
*SHIFRIN'S METHOD APPLIED TO SCATTERING BY TENUOUS NON-SPHERICAL PARTICLES

Shifrin constructed an integrodifferential equation to describe the scattering characteristics of an irregular particle and developed an iterative procedure for solving the equation. This procedure is fast enough to handle many physical problems where we have scattering by a cloud of particles with different sizes, shapes and orientations. In particular, the case of tenuous particles (small size or weakly refracting) will be considered, and Shifrin's procedure will be shown

to be a generalization of the Rayleigh-Gans approximation.

M. Kerker (Clarkson Coll. Tech., Potsdam, NY)
SCATTERING BY PARTICLES WITH INTERNAL STRUCTURE

Our interest has been in developing algorithms which permit calculations of scattering patterns for particles having internal structure. One such approach has been to utilize an integral to represent the scattered field in terms of the internal field, which itself must be approximated. Another has been to utilize a self-consistent method developed by Purcell and Pennypacker for application to non-spherical problems.

W. Wiscombe (NCAR, Boulder, CO) and A. Mugnai (NCAR, Boulder, CO/ Elettrofisica Atmosferica, Frascati, Italy)
*EXACT CALCULATIONS OF SCATTERING FROM MODERATELY NON-SPHERICAL T_n - PARTICLES: COMPARISONS WITH EQUIVALENT SPHERES

We study extinction efficiency, absorption efficiency, and forward and backscatter efficiency for rotationally symmetric particles of the form $r(\theta) = r_o[1 + \varepsilon T_n(\cos\theta)]$. Using the Extended Boundary Condition Method, as embodied in a computer code from Dr. Peter Barber, we have compared the various efficiencies, for T_2- and T_4-particles and $0 < \varepsilon \leq 0.2$, with the corresponding results for equal-volume and equal-projected-area spheres. A range of 0 to 10 in equivalent Mie size parameter x was considered, and results are given for nose-on incidence, for random orientation, and for random orientation plus a running mean over a size interval $\Delta x = 1$.

H. Weil and C.M. Chu (Univ. Michigan, Ann Arbor, MI)
*SCATTERING AND ABSORPTION BY WAVELENGTH SIZE DISCS

An integral equation for the current density induced in flat lossy dielectric discs by incident polarized waves is solved by a partly analytic, partly numerical method designed specifically to be efficient for the disc shape with thickness small and radius comparable to the incident wavelength. The computed currents are then used to compute, for arbitrary direction and polarization of the incident wave, the bistatic scattering matrix elements, total scattering and absorption cross sections. The extinction cross section is found both by summing the latter two cross sections and by using the optical theorem relating forward scatter and extinction.

J. Aronson and A. Emslie (Arthur D. Little Co., Cambridge, MA)
*ABSORPTION BY PARTICLE EDGES AND ASPERITIES

Measurements of infrared reflectance from powders indicate that edges and other asperities on the particles cause enhanced absorption. A theory of the particle phase function, in which the asperities are represented by a surface distribution of induced dipoles, was able to fit the experimental results and to predict the outcome of further experiments correctly.

S. Mukai (Kanazawa Inst. Tech., Ishikawa, Japan) and R.H. Giese (Ruhr Univ., Bochum, FGR)
*SCATTERING OF RADIATION BY A LARGE PARTICLE WITH A ROUGH SURFACE

The scattering of radiation by a large particle bounded by a rough surface is treated. The irregularity of a particle is defined by surface roughness represented by the slope distribution function. Since surface roughness causes multiple reflection of incident light, the multiple scattering theory is applied to get the reflected intensity from a particle with a rough surface. It is shown that experimental results are well explained by this model.

G. Kattawar and T.J. Humphreys (Texas A&M, College Station)
*ELECTROMAGNETIC SCATTERING FROM TWO IDENTICAL PSEUDOSPHERES

In an attempt to gain some insight into the problem of how close particles have to be on the average before phase effects become important, we calculated the cross section and phase matrices for two identical particles as a function of the distance between their centers for both broadside and end-on illumination. We employed the point dipole approximation to build two pseudospherical particles each consisting of 32 dipoles with an effective size parameters of 0.9283 and refractive index of 1.54-0.0i. In regard to cross sections we found that in certain cases several percent deviation from the converged value, which is twice the single particle cross section, could be found up to distances of separation of 25 single particle diameters. The maxima and minima in the cross section curves can be explained in terms of simple interference effects. Also the element P_{11} of the phase matrix showed a great deal of structure and the position of maxima and minima could be explained by phase shift analysis.

P. Barber and H. Chen (Univ. Utah, Salt Lake City)
APPROXIMATING THE SCATTERING FROM RANDOMLY ORIENTED NON-SPHERICAL PARTICLES BY A DISTRIBUTION OF SPHERES

There is great interest in finding "equivalent" spheres to characterize the scattering by irregular particles. Rather than searching for a single "equivalent" sphere as is usually done, this study utilizes the radial mass distribution of non-spherical particles to define an "equivalent" distribution of spheres. Calculations using Mie Theory and the Extended Boundary Condition Method show that the angular scattering by a randomly oriented distribution of spheroids can be predicted quite accurately by a spherical polydispersion which has been selected *a priori*.

EXPERIMENTAL METHODS

D.W. Schuerman (SAL SUNYA, Albany, NY)
*THE MICROWAVE ANALOG FACILITY AT SUNYA: CAPABILITIES AND CURRENT PROGRAMS

This newly renovated facility at the Space Astronomy Laboratory (SUNYA) is a powerful experimental tool for investigating scattering

by non-spherical particles. Single particle extinction data, averages of the scattering function over random particle orientation, precise knowledge of the size, shape, index of refraction, and particle-shape versus incident-beam geometry are advantages not realized by other experimental methods. Three on-going programs at the facility are also briefly described.

A. Ashkin and J. Dziedzic (Bell Labs, Holmdel, NJ)
*OBSERVATION OF LIGHT SCATTERING FROM ORIENTED NON-SPHERICAL PARTICLES USING OPTICAL LEVITATION

The optical levitation technique has been used to assemble spheroids and other non-spherical particles of simple shape. These particles are held at fixed orientation in laser beams where their light scattering properties can be studied.

M. Saunders (Bell Labs, Norcross, GA)
*THE EFFECT OF AN ELECTRIC FIELD ON THE BACKSCATTERED RADIANCE OF A SINGLE WATER DROPLET

Microscopic droplets formed by the condensation of water vapor on sodium chloride crystals are supported on spider threads and subjected to a horizontal electric field. The shape of the droplet and the near field surface wave radiance are dependent upon the intensity of the field. The spider thread method of support should permit the angular scattering pattern of an isolated irregularly shaped particle to be obtained.

G. Grams (Georgia Inst. Tech., Atlanta)
*IN-SITU LIGHT SCATTERING TECHNIQUES FOR DETERMINING AEROSOL SIZE DISTRIBUTIONS & OPTICAL CONSTANTS

Our Atmospheric Optics Group at Georgia Tech is developing a research program to improve existing instrumentation and data analysis techniques for obtaining in-situ observations of size distributions and optical properties of airborne particles. This work emphasizes the use of laser polar nephelometers to measure scattering phase functions for aerosols of known size, shape, and composition for use as input data for testing the validity of proposed techniques for calculating scattering by non-spherical particles.

A. Holland (NASA Wallops, VA)
*PROBLEMS IN CALIBRATING A POLAR NEPHELOMETER AND IN CHARACTERIZING THE SCATTERING MEDIUM

A calibration method based on Pritchards original work is outlined. Results for an existing nephelometer system are discussed. In addition the problems of characterizing the scattering medium used in the nephelometer system are outlined, and several methods of calibrating the jet are demonstrated.

R. Detenbeck (Univ. Vermont, Burlington)
LIGHT SCATTERING FROM ORIENTED FIBERS IN A FIBROUS-AEROSOL PARTICLE COUNTER

Asbestos fibers in an aerosol are completely aligned by a combination of an airflow-velocity gradient of 33000 sec^{-1} and an electric field of 3000 V cm^{-1}. Light-scattering signatures then serve to count individual fibers. The technique can be applied to any mono/polydisperse, dielectric/conducting, rodlike aerosol.

EXPERIMENTAL RESULTS

R. Wang (SAL SUNYA, Albany, NY)
*EXTINCTION SIGNATURES OF NON-SPHERICAL/NON-ISOTROPIC PARTICLES

Microwave analog measurements of $\theta=0°$ scattering by particles of various shape and refractive indexes are presented. The scattering targets are non-isotropic spheres, aggregates of 2^n (n=1,2,3) identical spheres, and stacked 7-cylinder rough particles. Both the orientation and the physical properties of the target produce signatures in the extinction and polarization curves. Theoretical explanations are presented wherever possible.

R. Zerull, R.H. Giese, S. Schwill and K. Weiss (Ruhr Univ., Bochum, FRG)
*SCATTERING BY PARTICLES OF NON-SPHERICAL SHAPE

The scattering of particles deviating more or less from spherical shape is discussed based on microwave scattering measurements. To point out the differences between spheres and extremely irregular particles, fluffy structures will be of primary interest in this paper.

W. Bickel and M.E. Stafford (Univ. Arizona, Tucson)
*BIOLOGICAL PARTICLES AS IRREGULARLY SHAPED SCATTERERS

Light scattering techniques used in biology provide a fast, nondestructive probe that is very sensitive to small but significant biological changes that are *not seen by any other optical technique.* The S_{34} component of the scattering matrix is particularly sensitive to temporal changes in the biosystem as depicted in several examples.

J. Bottiger, E. Fry, and R. Thompson (Texas A&M, College Station)
*PHASE MATRIX MEASUREMENTS FOR ELECTROMAGNETIC SCATTERING BY SPHERE AGGREGATES

An instrument which permits accurate measurement of all elements of the phase matrix simultaneously has been constructed. Aggregates consisting of attached polystyrene spheres are suspended in an electric field and the phase matrix is measured.

M. Srivastava (SUNY at Stony Brook, NY) and D.E. Brownlee (Univ. Washington, Seattle)
*REFLECTIVITY OF SINGLE MICRON SIZE IRREGULARLY SHAPED DUST GRAINS

We have developed a microscopic technique to measure the optical albedo of *single*, micron size (5 to 7 μm in diameter) irregularly shaped dust grains in the wavelength range of $\lambda \sim .35$ μm to 0.6μm. The experimental setup consists of a microscope, photometer,

polarization analyzer and light sources. The illuminating spot size is limited to 5 μm in diameter. Dust grains are mounted on the tip of a thin (1 μm) glass fiber in order to reduce the background illumination. Our results on single, micron size carbonaceous chrondite type meteorites with application to the optical properties of interplanetary dust grains and stratospheric particles are presented. Our results indicate that single grains of carbonaceous chrondite material have an aptical albedo of 5% at $\lambda \sim .35$ μm which decreases to 2% at $\lambda \sim 0.55$ μm. Scattered light from single grains is strongly polarized, and it also exhibits an angular dependence.

INVERSION AND INFORMATION CONTENT

G. Grams (Georgia Inst. Tech., Atlanta) and P. Chýlek (ASRC SUNYA, Albany, NY/NCAR, Boulder, CO)
OPTICAL CHARACTERISTICS OF NON-SPHERICAL MARTIAN DUST PARTICLES

The surface wave correction method is applied to the Mariner 9 ultraviolet spectral reflectance measurements to obtain the size distribution and the complex index of refraction of non-spherical Martian dust particles.

W. Pearce (EG & G, Riverdale, MD)
*INFERENCE OF SCATTER SIZE DISTRIBUTION FROM SINGLE SCATTERING MATRIX DATA

We have studied procedures for inferring the scatterer size distribution from the scattered radiation. The information content of specific matrix element measurements is evaluated with assessments of the impact of the assumption of sphericity and other modeling errors as well as random measurement errors on the computed size distribution.

J. Reagan (NASA Langley, VA/Univ. Arizona, Tucson) and B. Herman (Univ. Arizona, Tucson)
*LIGHT SCATTERING BY IRREGULARLY SHAPED PARTICLES VERSUS SPHERES: WHAT ARE SOME OF THE PROBLEMS PRESENTED IN REMOTE SENSING OF ATMOSPHERIC AEROSOLS?

Effects of light scattering by irregularly shaped particles versus spheres are discussed in the context of defining how they influence aerosol properties inferred from optical remote sensing measurements. Particular attention is given to identifying effects on aerosol properties inferred from data acquired by monostatic and bistatic lidar and spectral solar radiometer measurements.

3. PANEL-FLOOR DISCUSSION

The workshop closed with a panel and floor discussion summarizing the current state of the art of irregular particle scattering as described in the individual presentations and highlighting areas of emphasis for future research. The panel consisted of the two

review speakers, the seven topical session leaders (E. Stuebing, R. Pinnick, M. Kerker, P. Chýlek, R. Zerull, A. Holland and J. Reagan) and the Workshop Chairman, Don Schuerman. R. Fenn and E. Shettle kindly recorded the discussion and provided the summary paraphrased below.

E. Stuebing expressed the users' elation over both the depth and the wide range of theoretical and experimental research being applied to the problem. A large number of research groups are conducting studies which are applicable to atmospheric aerosol problems (both natural and man-made) including the special cases of ice crystal clouds and extraterrestrial dust. He felt that the characterization of the scattering matrix was not adequately discussed. This concern about the lack of adequate characterization of irregularly shaped particles and their optical characteristics led to some discussion between panel members and the floor. As was pointed out by G. Kattawar, only 7 of the 16 intensity matrix elements are independent for a single particle; the 9 remaining relationships should be developed and exploited for consistency checks. W. Bickel felt that all 16 components should be measured experimentally whenever possible. A general discussion on whether there was a "best" set of independent elements led to naught. Further investigation of the behavior of the matrix elements will be required before all 9 general relations can be derived.

P. Chýlek emphasized that there is still much to be learned by comparing the scattering from irregular shapes to that from spheres. He also emphasized the powerful experimental tools which have recently been developed (*e.g.* the paper by Ashkin and Dziedzic) and pointed to the inspiration of crossfertilization resulting from the interdisciplinary mix of irregular particle research as demonstrated in this Workshop. Several panel members felt that in the experimental field great progress has been achieved by the biologists. M. Kerker stated that single particle scattering measurements have led the progress historically. Present techniques allow many particles to be viewed consecutively in very short times so that a statistical evaluation of all matrix elements can be made. M. Greenberg's contention was that we have to look at large numbers of particles, their shape, their roughness, etc., and develop an encyclopedia of scattering properties.

Several participants felt that the single particle measurement approach was certainly successful in laboratory studies for well defined particles, but that it could not work in the case of atmospheric aerosols because of their almost unlimited varieties and lack of particle definition. It was agreed (Jayaweera and Reagan) that for atmospheric aerosols a statistical approach offers the best solution. G. Kattawar emphasized the sensitivity of field polarization measurements as an indicator of nonsphericity, and R. Pinnick mentioned the possible effects of birefringence on scattering properties.

M. Greenberg summarized the conferences by pointing to the impressive range of capabilities for studying non-spherical particle scattering in theory and experiment. His impression from the three day meeting was that the interdisciplinary character of the Workshop will stimulate new ideas and approaches for future research in the various scientific fields.

Acknowledgements The author thanks the Scientific Organizing Committee for their generous investment of time and ideas. Sue Darbyshire handled the administrative aspects of the Workshop in her usual competent and cheerful manner. Partial funding was provided by the U.S. Army Research Office under grant number DAAG29-79-G-0016.

EXTINCTION SIGNATURES OF NON-SPHERICAL/NON-ISOTROPIC PARTICLES

R. T. Wang

State Univ. of N. Y. at Albany, Space Astronomy Laboratory

Albany, New York 12203

ABSTRACT

Microwave analog measurements of $\theta=0°$ scattering by particles of various shape and refractive indexes are presented. The scattering targets are non-isotropic spheres, aggregates of 2^n (n=1,2,3) identical spheres, and stacked 7-cylinder rough particles. Both the orientation and the physical properties of the target produce signatures in the extinction and polarization curves. Theoretical explanations are presented wherever possible.

1. INTRODUCTION

A small particle obscures (or dims) the incident light through a subtle interference phenomenon between its forward-scattered ($\theta=0°$) wave and the incident wave. This interpretation of extinction leads to the well-known Optical Theorem (Feenberg, 1932; van de Hulst, 1946, 1949, 1957; Montroll and Greenberg, 1954),

$$C_{EXT} = \frac{4\pi}{k^2}|S(0)|\sin\phi(0) = \frac{4\pi}{k^2}\,\mathrm{Re}\{S(0)\} \quad , \qquad (1)$$

which relates the extinction cross section C_{EXT} to the real part of the dimensionless complex amplitude $S(\theta)$ along the incident direction ($\theta=0°$) and polarization, or equivalently, to the absolute magnitude $|S(0)|$ and the phase shift $\phi(0)$ of the forward scattered wave.

Each P,Q plot presented in this paper is a cartesian representation of S(0) as a function of particle orientation angle χ; *i.e.*, in the complex plane the dimensionless P and Q components are:

$$P = \frac{4\pi}{k^2 G} \text{Im}\{S(0)\} \quad ; \quad Q = \frac{4\pi}{k^2 G} \text{Re}\{S(0)\} \qquad (2)$$

where G is the appropriate geometrical cross section of the particle (or ensemble of particles) and Q is the so called "extinction efficiency". As the orientation of the particle changes, a curve is generated in this plane. The vector from the origin to a specific point (particle orientation) on the curve represents S(0) while the angle between this vector and the P axis corresponds to $\phi(0)$. The absolute magnitude, $|S(0)|$ is calibrated against that of a standard sphere of known $|S(0)|$ in the same P,Q plot. The projection of S(0) into the Q axis gives the extinction efficiency. For a particle of rotational symmetry, the totality of the extinction information is obtained by rotating the symmetry axis through 90° in two mutually orthogonal planes, the k-E and the k-H plane of the incident wave. For example, if the particle axis makes an arbitrary angle χ from the incident direction $\vec{k}$, S(0) is the simple linear composition of those values of S(0) obtained when the symmetry axis is in these two planes (k-E and k-H), tilted by χ from $\vec{k}$. Furthermore, if one keeps χ fixed and sweeps the axis on a cone around $\vec{k}$, the tip of the S(0) vector draws a straight line in the P,Q plot. These remarkable. scattering properties at $\theta=0°$, which are the result of mathematical symmetry and independent of target material, considerably reduce the number of required measurements. It has been our experience that this property of simple linear composition is nearly true even for particles of less rotational symmetry like helixes (Wang, 1970). More details on information necessary to interpret the experimental plots are contained in the rather lengthy figure captions and earlier publications (Lind *et al.*, 1965; Lind, 1966; Greenberg *et al.*, 1967; Wang, 1968; Wang *et al.*, 1977; Wang and Greenberg, 1978).

Extinction is perhaps the least sensitive scattering measurement for distinguishing among anisotropic particles, especially when they are randomly oriented. Nevertheless, there exist conspicuous, systematic differences in the $\theta=0°$ scattering which seem to provide a (unique?) particle signature. This is particularly true as a function of particle orientation as seen in the discussions to follow. Remember the following rules for interpreting each P,Q plot. *A vector drawn from the coordinate origin to each χ position along the curve yields the complex value of S(0) at χ. The phase shift $\phi(0)$ is given by the angle between this vector and the P axis. The extinction efficiency (C_{EXT}/G) is found at χ by projecting this vector on the calibrated Q axis. The length of the vector represents the absolute value $|S(0)|$, and its numerical value is obtained by comparing this length with that of the "standard" or calibration vector (obtained from a sphere) provided in each plot. The proper numerical value of $|S(0)|$ for the calibration sphere is given in the figure caption. The geometrical cross section G of an aggregate of spheres is taken to be the sum of those of the component spheres.*

2. EXPERIMENTAL RESULTS & COMPARISON WITH THEORETICAL PREDICTIONS

2.1 Non-isotropic Spheres

A medium composed of thin alternating layers of different electromagnetic properties has anisotropic refractive indexes with respect to the polarization of the propagating wave (Born and Wolf, 1965; Rytov, 1955). By inserting an absorbing (conducting) film into each interface of neighboring dielectric (expanded polystyrene) layers, spheres of various anisotropies have been constructed for extinction studies (Wang, 1968; Wang and Greenberg, 1976). P,Q plots resulting from two such spheres are shown in Figures 1A and 1B. These two spheres differ from each other only in their inserted films. One has the absorbing film called "teledelto" while the other has aluminum foil. In both cases the axis of symmetry passes through the center, perpendicularly to the layer planes. These spheres are characterized by three indexes of refraction, each measured along one of three principal directions. Based on reasons similar to those used in the Eikonal approximations (van de Hulst, 1957; Greenberg, 1960; Wang and Greenberg, 1976), one can construct an effective index m_χ for each particle orientation angle. By applying the rigorous Mie solution for isotropic spheres with this adjusted m_χ, one obtains a fairly close theoretical prediction for the χ-dependence of S(0).

For the anisotropic sphere represented in Figure 1A, m_χ was computed according to the Fresnel formula of crystal optics (Born and Wolf, 1965):

$$\frac{1}{m_\chi^2} = \frac{\cos^2\chi}{m_k^2} + \frac{\sin^2\chi}{m_E^2} \qquad \text{(particle-axis in the k-E plane)}$$

$$\frac{1}{m_\chi^2} = \frac{\cos^2\chi}{m_k^2} + \frac{\sin^2\chi}{m_H^2} \qquad \text{(particle-axis in the k-H plane)} \qquad (3)$$

The ensuing Eikonal-Mie prediction is shown in the P,Q plot as a dotted curve. It agrees closely with the experimental S(0) vs χ curve, expecially in the E orientation where the particle axis is parallel to the incident $\vec{E}$ vector and where the most precise refractive-index measurement of the medium is possible. The same technique has been used in Figure 2 to display the degree of polarization by extinction as a function of χ for 3 spheres of the same type of anisotropy. A comparison with non-spherical particles such as spheroids in the same size range (Wang and Greenberg, 1978) demonstrates that the anisotropic sphere is a more efficient polarizer in its orientation dependence.

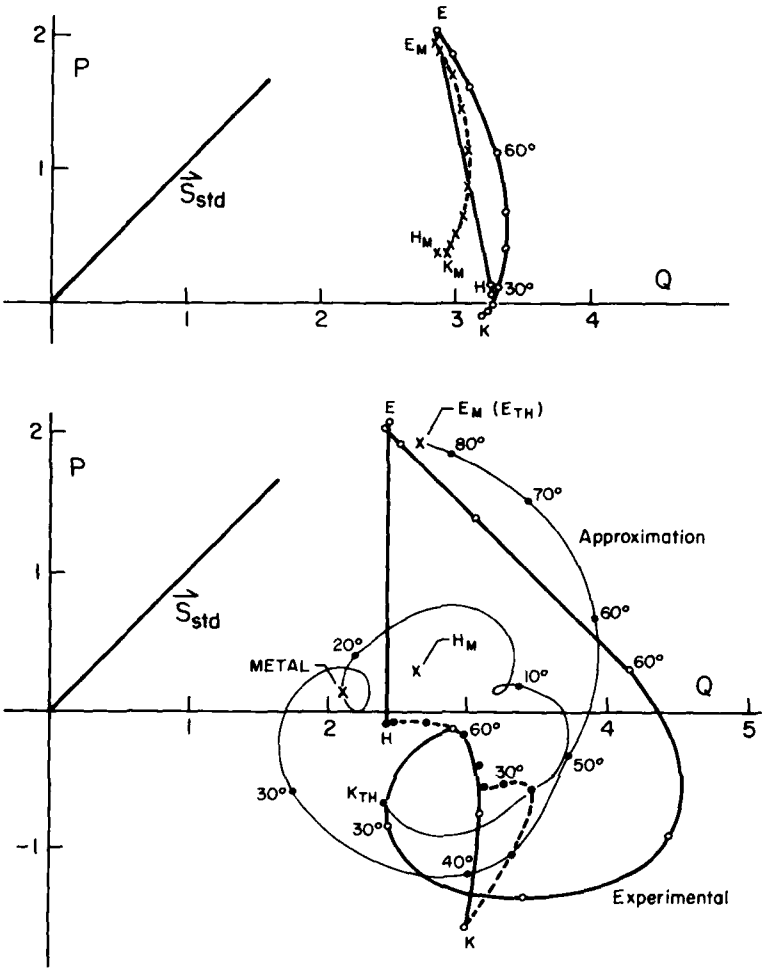

FIG. 1A(top) and 1B(bottom). Two P,Q plots showing the target orientation dependence (χ given in deg) of S(0) for two layered-spheres. Fig. 1A refers to the teledelto-layered sphere (x=4.86); the bottom figure corresponds to a similar (x=4.83) sphere but layered with aluminum foil. The refractive indexes as measured along the three principal target media directions are (Fig. 1A) $m_k = 1.39-i0.14$, $m_E = 1.28-i0.005$, $m_H = 1.38-i0.15$; (Fig. 1B) m_k = metallic, $m_E = 1.27-i0.009$, $m_H = 1.62-i5.44$. At the orientation marked k, the particle symmetry axis is parallel to the incident direction, $\vec{k}$. It is then continuously swept through 90° in the k-E and k-H planes of the incident wave to display two (thick) experimental curves. The Eikonal-Mie theory predictions are shown either by a dotted or by a thin curve. In particular, k_M, $E_M(E_{TH})$, H_M and Metal are Mie theory results using m_k, m_E, m_H and $m=\infty$, respectively. For the standard sphere, $|S(0)| = 13.57$; see the last paragraph of section 1.

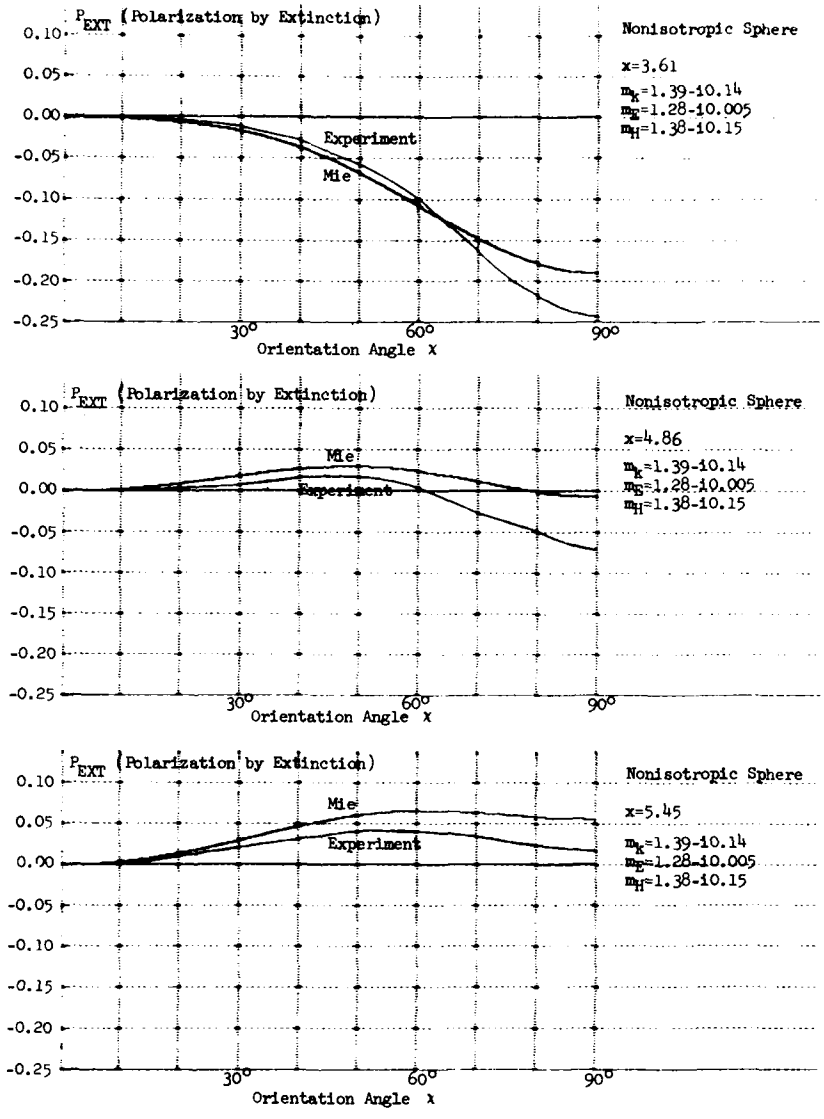

FIG. 2. Target-orientation (χ) dependence of $P_{EXT}=\left(Q_E(\chi)-Q_H(\chi)\right)/\left(Q_E(\chi)+Q_H(\chi)\right)$, the polarization by extinction, for three spheres of non-isotropic refractive indexes. $Q_E(\chi)$ and $Q_H(\chi)$ are extinction efficiencies when the symmetry axis is in the k-E and in the k-H planes, respectively, tilted by an angle χ from the incident direction $\hat{k}$. The results of Eikonal-Mie theory prediction are also shown.

The Eikonal-Mie approximation is applicable only for the k-E rotation in a sphere of enhanced anisotropy as in Figure 1B. The first empirical finding (Wang, 1968) showed the amazing fact that at E orientation the incident wave almost did not see the aluminum foils that separated the dielectric layers! The penetrating wavelets are guided along each dielectric layer independently of each other. As the particle-axis is tilted by $\pi/2-\chi$ from the $\vec{E}$ direction toward $\vec{k}$, each ray of length L in the particle has to traverse an additional distance of $L(1-\sin\chi)$ in free space to cover the same distance in the $\vec{k}$ direction as that in the E orientation. This consideration gives the effective m_χ as

$$m_\chi = m_E + 1 - \sin\chi. \tag{4}$$

Application of the Mie theory prediction with this m_χ is shown as a thin curve, E_{TH} to k_{TH} in Figure 1B. The agreement with observation is not as good as in Figure 1A, but qualitatively predicts the changes in magnitude and phase of S(0) as the particle rotates. For rotation in the k-H plane, the layer structure exhibits a waveguide cutoff phenomenon, and the Eikonal picture loses its meaning. No progress has been made in the explanation of this phenomenon.

2.2 2^n Identical Spheres; n=1, 2, 3

A number of polystyrene spheres have been made from three different sized metallic molds. For each size, spheres of nearly the same measured $|S(0)|$ and $\phi(0)$ were selected for this dependent scattering study. The refractive index of these particles resembles that of water or ice in the optical region. For each size group the phase-shift parameter $\rho = 2x(m'-1)$ and extinction efficiency of a single sphere are, respectively, $\rho_1 = 2.278$, $Q_1 = 2.278$; $\rho_2 = 2.746$, $Q_2 = 2.985$ and $\rho_3 = 3.396$, $Q_3 = 3.753$. 2, 4 or 8 of these identical spheres were assembled on nylon strings to form an array of simple geometry, and the array was rotated in the incident-wave k-H plane to display a P,Q plot.

A quick glance at Figures 3A-3I for a 2-sphere array at various center-to-center separations (s) reveals several interesting features: a) The tip of the S(0) vector draws a clockwise spiral as the array axis rotates from the $\vec{k}$ to the $\vec{H}$ direction of the incident wave, with an overall decreasing trend in $\phi(0)$. Prolate spheroids of similar target-parameters have the same trend (Wang and Greenberg, 1978) except that the S(0)-tip tends to go counterclockwise. b) In the H orientation, the S(0) vector is nearly equal to the vector sum of those of 2 spheres, *i.e.*, dependent scattering is at a minimum. c) As s increases, the size of the spiral shrinks, perhaps nonmonotonically. This is accompanied by the faster convergence of the

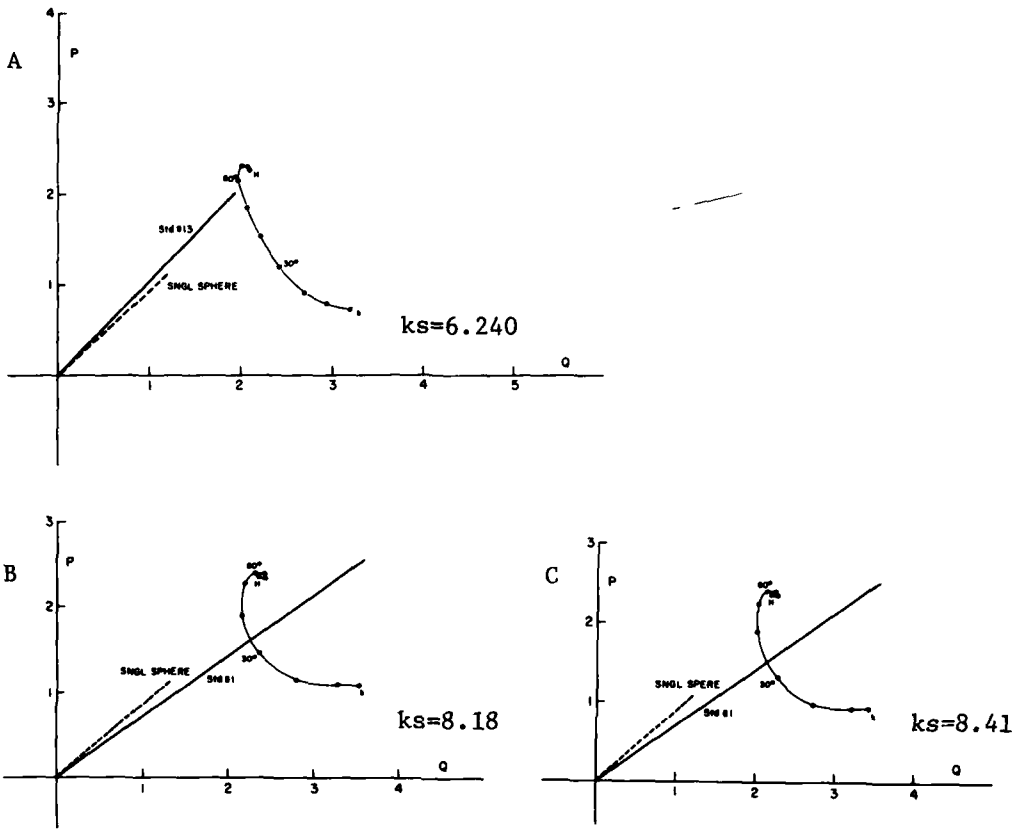

FIGS. 3A-3C. Experimental P,Q plots of the target-orientation (χ) dependence of S(0) of an ensemble of two identical spheres ($x_1=x_2=3.120$, $m_1=m_2=1.365$) at various separations $ks=2\pi s/\lambda$. s is the center to center distance between two spheres. At the orientation position marked k, the symmetry axis of the array is parallel to the incident direction $\vec{k}$. This axis is then continuously swept through 90° in the k-H plane of the incident wave to display the experimental curve. A dotted straight line marked SNGL SPHERE is the S(0) vector of an isolated sphere from the ensemble, as measured during the same experimental run. *The calibration vectors have* $|S(0)|=21.38$ (std #1) and $|S(0)|=13.57$ (std #13); see the last paragraph of section 1.

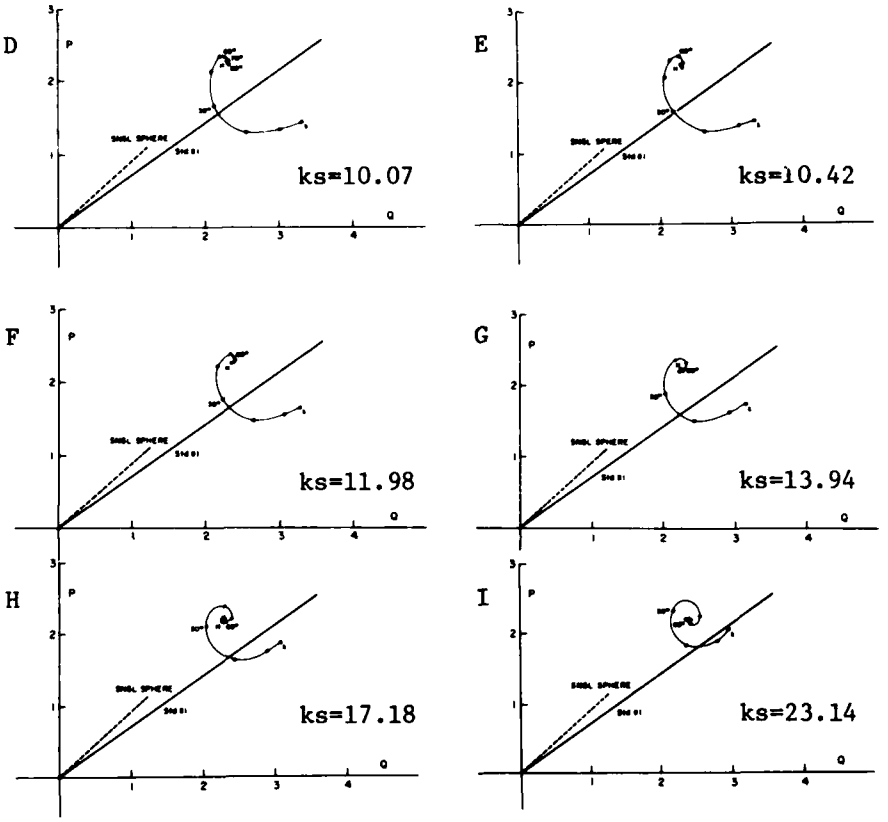

FIGS. 3D-3I. Same as Figs. 3A-3C.

S(0)-tip toward the H orientation with respect to the χ variation. Figures 3A-3I thus render a vivid picture of how dependent scattering diminishes with increasing s.

A combination of ray optics and Mie theory is proposed here to explain the above subtle χ dependence of S(0). In this approximation the total S(0) from a 2-sphere array (spheres A & B) having a separation s and an orientation χ takes the form:

$$S(0) = S_{1A}(0)+S_{1B}(0) + \frac{S_{1A}(\chi)S_{1B}(\chi)}{ik s} e^{-ik s(1-\cos\chi)} + \frac{S_{1A}(\pi-\chi)S_{1B}(\pi-\chi)}{ik s} e^{-ik s(1+\cos\chi)} \quad . \tag{5}$$

$S_{1A}(\chi)$ is the perpendicular scattering amplitude component at scattering angle χ from sphere A, and so on for other expressions, as evaluated from Mie theory, all in van de Hulst's (1957) notations. The 1st and 2nd terms represent the summation of independent scattering by spheres A & B. The 3rd term takes account of a multiple-scatter correction to S(0) due to the scattering by sphere B of radiation from sphere A. In going from sphere A to B the near field is approximated by a wave of plane phase front perpendicular to the ray path but with an inverse s dependence in its amplitude. Similarly, the 4th term is that due to the scattering by sphere A of radiation from sphere B. This approximation is shown in Figures 4A-4C for 3 sets of s, and it can also be shown to give the same expression as derived from a rigorous solution using the relocation technique of vector spherical functions (Liang and Lo, 1967; Bruning and Lo, 1971) for large values of s. For $s < 8a$, the approximation overestimates $|S(0)|$ and underestimates $\phi(0)$ for this particular ensemble, especially near the k orientation.

Figures 5A-5C and Figures 6A-6C show the $\theta=0°$ scattering signatures resulting from 4 and 8 spheres forming contacting square and cubic ensembles, respectively. Despite their simple appearance, no detailed theoretical explanation is presently available. Nevertheless, there exist similarities between ensembles made up of the same size spheres. First, note the comparisons between Figures 5A and 6A, 5B and 6B, and 5C and 6C. The signatures are similar except that $|S(0)|$ for the 8-sphere ensemble is about twice the value as that of the 4-sphere ensemble. This implies no appreciable interference between the two arrays of the 8-sphere ensemble that are parallel to the k-H plane. Second, the experimental Q's of each of the 8-sphere ensembles shown in Figures 6A-6C (multiplied by a factor 2 for equivalent normalization) can be compared with the Q's calculated by Mie theory for a sphere equal in volume to each ensemble. For the 3 sets of 8-sphere ensembles used in Figures 6A-6C, the observed minimum

Fig. 4A

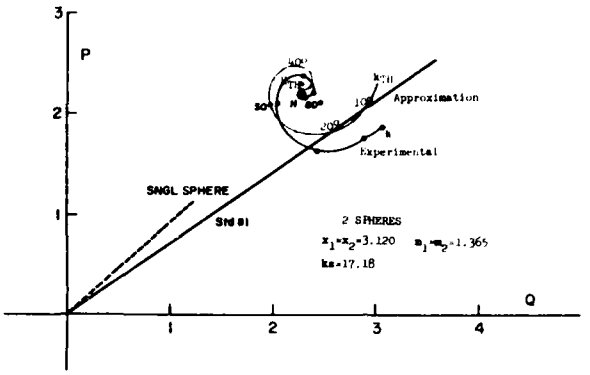

Fig. 4B

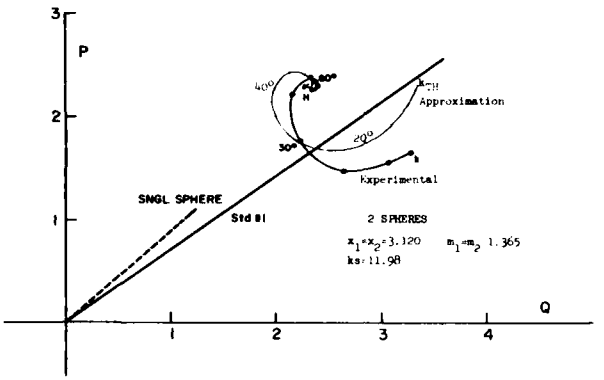

Fig. 4C

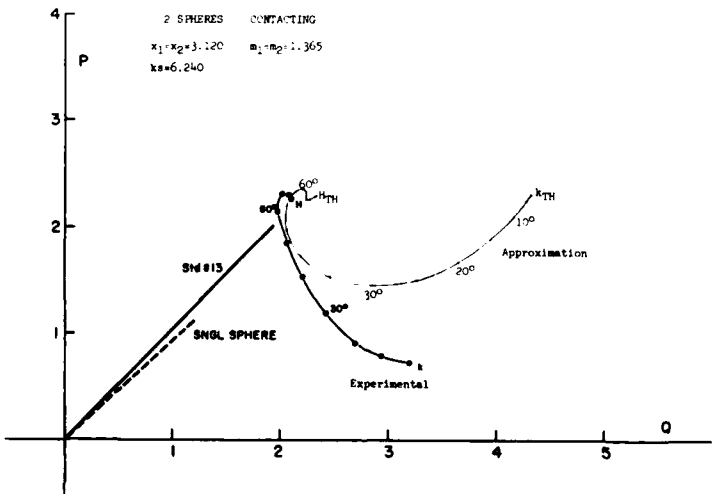

FIGS. 4A-4C. Same as in Figs. 3A-3I. Here, the Geometrical Optics + Mie Theory prediction is added as a thin curve (k_{TH} to H_{TH}) on each P,Q plot for 3 sets of mutual separation ks.

Fig. 5A

$x_1=x_2=x_3=x_4=3.120$

$m_1=m_2=m_3=m_4=1.365$

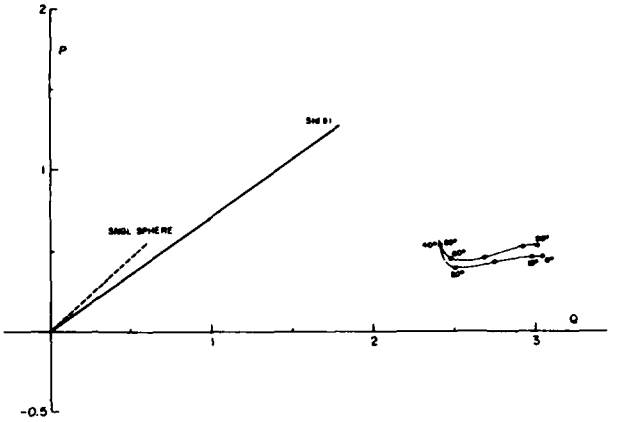

Fig. 5B

$x_1=x_2=x_3=x_4=3.752$

$m_1=m_2=m_3=m_4=1.366$

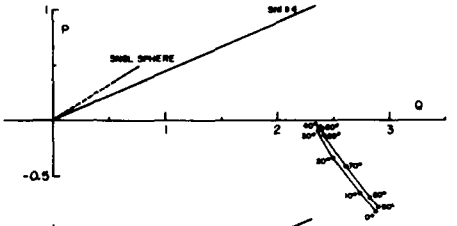

Fig. 5C

$x_1=x_2=x_3=x_4=4.678$

$m_1=m_2=m_3=m_4=1.363$

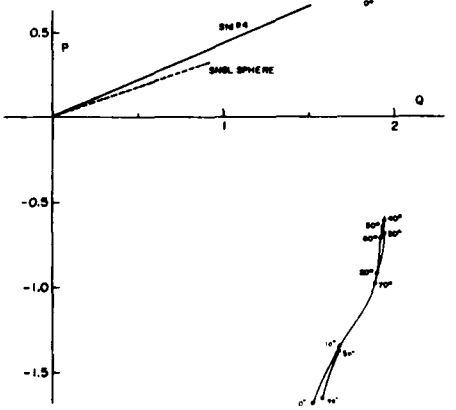

FIGS. 5A-5C. Three experimental P,Q plots, each of which shows the target-orientation (χ) dependence of S(0) for an ensemble of 4 identical spheres forming a contacting square array. Each plot differs from the others on the size parameter of composite spheres. At $\chi=0°$ (or 90°) one side of the square is parallel to the incident $\vec{k}$ vector, and the square is then continuously rotated in the k-H plane through 90° to display the experimental curve. The dotted straight line marked SINGL SPHERE is the S(0) vector of an isolated sphere from the ensemble, as measured during the same run. $|S(0)|=21.38$ (std #1) and $|S(0)|=36.06$ (std #4); see the last paragraph of section 1.

Fig. 6A

$x_1=x_2...=x_8=3.120$

$m_1=m_2...=m_8=1.365$

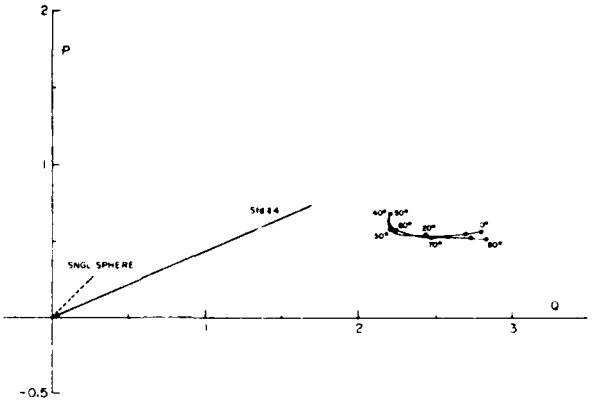

Fig. 6B

$x_1=x_2...=x_8=3.752$

$m_1=m_2...=m_8=1.366$

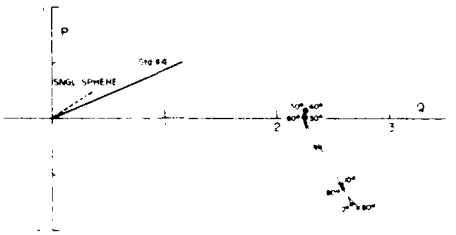

Fig. 6C

$x_1=x_2...=x_8=4.678$

$m_1=m_2...=m_8=1.363$

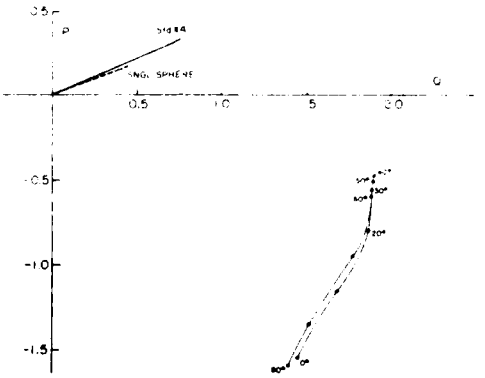

FIGS. 6A-6C. Three experimental P,Q plots, each of which shows the target-orientation (χ) dependence of S(0) for an ensemble of 8 identical spheres forming a contacting cubic array. Each plot differs from others on the size parameter of composite spheres. At χ=0° (or 90°) one face of the cube is parallel to the incident $\vec{k}$ vector but is perpendicular to $\vec{H}$. The array is then continuously rotated through 90° in the k-H plane to display the experimental curve. The dotted straight line marked SNGL SPHERE is the S(0) vector of an isolated sphere from the ensemble, as measured during the same run. Std. #4 has $|S(0)|$=36.06; see the last paragraph of section 1.

and maximum Q's, the phase-shift parameters, and Q's for the equivalent spheres are, respectively, $Q_{MIN} = 4.41$, $Q_{MAX} = 5.66$, $\rho_v = 4.555$, $Q_{MIE} = 3.938$; $Q_{MIN} = 4.49$, $Q_{MAX} = 5.44$, $\rho_v = 5.493$, $Q_{MIE} = 3.131$; $Q_{MIN} = 2.77$, $Q_{MAX} = 3.79$, $\rho_v = 6.792$, $Q_{MIE} = 1.920$. This gives an interesting similarity with the extinction exhibited by the 7-cylinder rough particles discussed next.

2.3 7-Cylinder Rough Particles

A dielectric rough particle of this type is made by stacking 7 polystyrene (or polysterene admixed with carbon dust) cylinders of the same diameter, six of which have a common length/diameter ratio of 2:1 and symmetrically surround a longer one which has a ratio of 3:1. By coating such a particle with aluminum foil or by stacking copper cylinders in the same manner, a totally reflecting particle without interstices is prepared. Because the maximum longitudinal and lateral dimensions of such a particle are the same, it resembles a roughened sphere. The size parameter x_v (or the phase-shift parameter $\rho = 2x_v(m'-1)$) is taken to be that of an equal-volume smooth sphere. The ρ or x_v dependencies of extinction efficiency Q for low-absorbing/reflecting particles at some principal particle-orientations were published earlier (Greenberg et al., 1971), and a more detailed account of some of the P,Q plots has also been reported (Wang and Greenberg, 1978). Attention is focused here on the ρ or x_v dependence of Q_{RAV}, the estimated extinction efficiency averaged over random particle orientations, and of $\delta Q = Q_{MAX} - Q_{MIN}$, the range of variation in the observed Q as the particle is rotated. A few absorbing particles are also included here for a more complete picture despite some uncertainties in their refractive index which may amount to an error of ≈ 0.6 in the ρ scale. Detailed target parameters and their resulting Q's are listed in Tables 1A and 1B.

The Q's as a function of ρ for 23 such rough particles are plotted in Figure 7A. Also shown in the same figure are Mie results for smooth spheres with $m = 1.360 - i0.0$ and $m = 1.360 - i0.05$. For each rough particle, δQ is represented by a vertical bar, and Q_{RAV} is shown by a horizontal mark. Some striking contrasts between rough and smooth particles in this extinction signature are:

a) Up to $\rho \approx 2.8$, low-absorbing rough particles extinguish the incident light as if they were absorbing equal-volume spheres. If $\rho \lesssim 2.2$ this can be qualitatively expected from theoretical considerations of the statistical variation of ray-paths passing through the particle (Greenberg and Stoeckly, 1970).
b) δQ tends to increase with ρ and is smaller for an absorbing rough particle than for one of the same size with low-absorption.
c) Near the first major resonance in extinction, $3 \lesssim \rho \lesssim 4.5$, the Q_{RAV}'s of rough particles are near those of smooth spheres.
d) Beyond $\rho \gtrsim 4.5$, Q_{RAV} is consistently larger than Mie results for smooth spheres.

TABLE 1A

TARGET PARAMETERS AND EXTINCTION EFFICIENCIES
FOR 7-CYLINDER DIELECTRIC ROUGH PARTICLES

x_v is the size parameter of the equal-volume sphere; m = complex refractive index = $m'-im''$; $\rho = 2x_v(m'-1)$; and Q_{MIN}, Q_{MAX} and Q_{RAV} are the minimum, maximum, and the estimated random average (over particle orientation) of the extinction efficiencies.

Target ID #	Carbon Inclusion	x_v	m'	-m"	ρ	Q_{MIN}	Q_{MAX}	Q_{RAV}
022003	0	4.33	1.100	~0	0.87	0.39	0.48	0.47
021005	0	2.83	1.184	~0.003	1.04	0.48	0.56	0.52
023003	0.5%	4.33	1.141	~0.005	1.22	0.85	0.92	0.88
022002	0	6.17	1.101	~0	1.25	0.67	0.75	0.71
022001	0	7.72	1.100	~0	1.54	1.03	1.10	1.08
021003	0	4.33	1.208	~0.003	1.80	1.28	1.54	1.42
023002	0.5%	6.17	1.158	~0.005	1.95	1.58	1.67	1.64
021004	0	3.52	1.277	~0.003	1.95	1.55	1.94	1.73
020005	0	2.81	1.368	~0.005	2.07	1.48	2.01	1.76
021002	0	6.17	1.192	~0.003	2.37	2.06	2.29	2.15
020004	0	3.55	1.333	~0.005	2.37	2.16	2.55	2.25
025003	0.1%	4.33	1.297	~0.005	2.57	2.46	2.74	2.62
021001	0	7.72	1.178	~0.003	2.75	2.64	2.85	2.76
020003	0	4.31	1.354	~0.005	3.05	3.11	3.33	3.25
025002	0.1%	6.17	1.306	~0.005	3.78	4.03	4.34	4.20
020002	0	6.11	1.362	~0.005	4.42	3.63	4.24	3.95
025001	0.1%	7.72	1.321	~0.005	4.95	3.48	4.30	4.01
020001	0	7.72	1.356	~0.005	5.49	3.18	4.17	3.65
020+02	0	9.36	1.369	~0.005	6.91	2.46	4.12	3.18
028002	1%	6.15	~1.37	~0.02	~4.6	3.27	4.08	3.72
028003	1%	4.24	~1.37	~0.02	~3.1	3.37	3.71	3.55
029002	5%	6.08	~1.6	~0.4(?)	~6.8	3.34	4.28	3.78
029003	5%	4.26	~1.6	~0.5(?)	~5.0	3.12	3.52	3.35

TABLE 1B

TARGET PARAMETERS AND EXTINCTION EFFICIENCIES
FOR 7-CYLINDER TOTALLY-REFLECTING ROUGH PARTICLES

Notation is the same as in Table 1A.

Target ID #	x_v	Q_{MIN}	Q_{MAX}	Q_{RAV}
030001	7.86	2.64	3.34	2.96
030002	6.19	2.26	3.21	2.93
030003	4.39	3.02	3.71	3.45
030004	3.62	3.17	3.65	3.44
030005	2.86	2.62	3.54	3.30
030007	1.86	3.44	4.24	3.83
030009	1.50	3.10	4.46	3.89

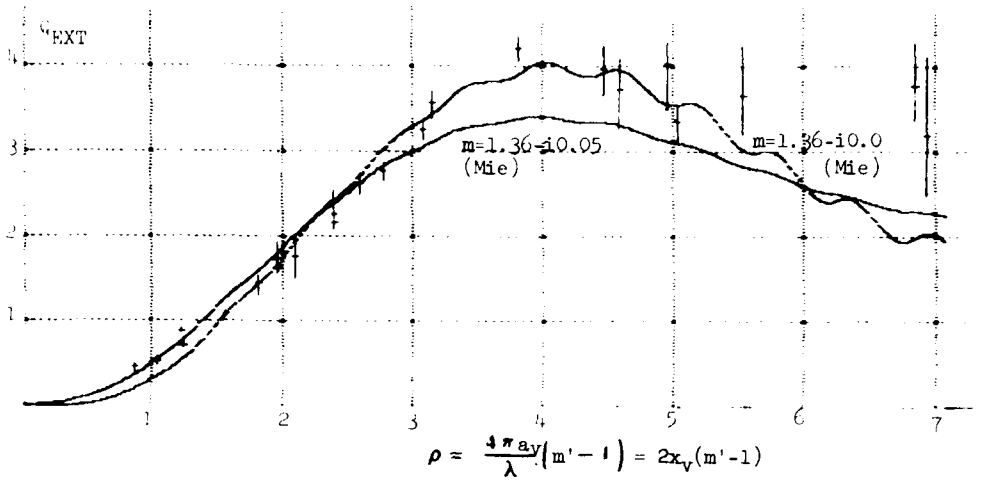

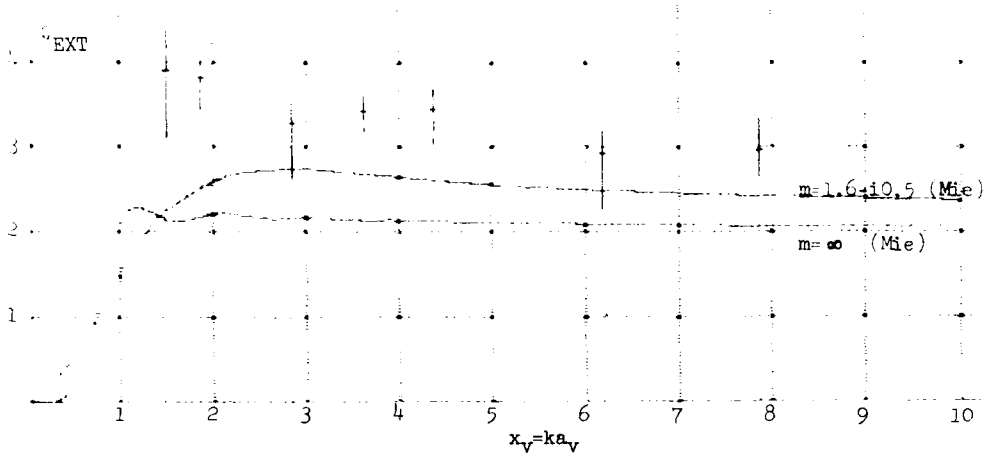

FIGS. 7A (top) and 7B (bottom). Dependence of Q_{EXT} on ρ or x_v for 7-cylinier rough particles. Fig. 7A is for dielectric (penetrable) rough particles while Fig. 7B is for totally reflecting rough particles. ρ is the phase shift parameter = $2x_v(m'-1)$, and x_v is the size parameter of a smooth sphere having the same volume as a rough particle. The range of Q_{EXT} variation as each particle is rotated is shown by a vertical bar, and a horizontal mark on each gives the estimated Q_{EXT} averaged over random orientations. In both figures, the Mie theory results for smooth spheres using appropriate refractive indexes are also shown by continuous curves.

The Q vs ρ oscillation, which is characteristic of smooth particles, is here greatly damped, and the extinction efficiency becomes almost target-parameter independent. Direct optical turbidity measurements on irregular quartz and diamond particles in liquid suspension (Hodkinson, 1963; Proctor and Harris, 1974) show similar rise in Q for small particle sizes. However, while their extinction curve also shows the damping of (the smooth sphere) oscillations, their Q values are consistently lower than ours (even after accounting for their use of a G based on projected area), and the onset of maximum Q (~2) occurs at considerably larger values of ρ (~6.5) compared to our value of ρ~4.

A theoretical attempt to model d) by replacing the actual rough particle with an aggregate of independently scattering spheres (a sphere of the same mean radius plus spheres representing the protuberances) could not explain the higher observed Q in this size range. However, the extinction signature by rough particles presented in this report combined with some angular distribution data (Wang and Greenberg, 1978) and θ=180° empirical findings (Wang *et al.*, 1977) leads to the tentative conclusion that an irregular particle, near and above the first major resonance in size, casts more scattered light in the forward direction and less in the backward direction than an equivalently-sized smooth sphere.

The behavior of totally reflecting rough particles, as shown in the Q_{RAV} vs x_v plot of Figure 7B, is also curious. Here too Q_{RAV} is considerably higher than the corresponding smooth sphere as shown by the Mie curve for m=∞ in the same figure. The extinction peak for reflecting rough particles is shifted to a value of x_v that is smaller than that found for equivalent dielectric rough particles. (The same is true, of course, for smooth spheres). Furthermore, there seems to be no correlation between δQ and x_v.

3. CONCLUSION

The findings of this extinction study can be summarized as follows:

a) Judicious use of combined ray optics and Mie theory for spheres is capable of predicting the θ=0° scattering signatures for a variety of non-spherical/non-isotropic particles. This is particularly true for scatterers having fewer inhomogeneities and/or interstices so that multiple reflections within the targets are insignificant.

b) For an aggregated particle, describing the scattering due to an individual component is by no means trivial. The effect of dependent scattering might be assessed if one replaces the complex near field by a simpler wave field consistent with physical reasoning. The most difficult case seems to be when the particle components are aligned along the incident direction.

Even for this case, a simple summation of independent scattering is not in serious error in the evaluation of extinction if the component separation exceeds about four times the dimension of the largest component.

c) The fact that rough particles produce an extinction which is larger than that due to equivalent-volume spheres remains to be explained. But this empirical fact, along with the evidence that rough particles do not exhibit sphere-like oscillations in the extinction curve, is useful for estimating the extinction due to irregular particles.

Acknowledgements. The author would like to express his sincere appreciation to Prof. J. M. Greenberg and Dr. D. W. Schuerman for helpful discussions and for critically reviewing this manuscript. The analysis of these data is supported by the U. S. Army Research Office under contract No. DAAG29-79-C-0055.

REFERENCES

Born, M. and Wolf, E., 1965, "Principles of Optics," Pergamon, N.Y.

Bruning, J. H. and Lo, Y. T., 1971, *IEEE Trans. Ant. Prop. AP-19*, 378.

Feenberg, E., 1932, *Phys. Rev. 40*, 40.

Greenberg, J. M., 1960, *J. Appl. Phys. 31*, 82.

Greenberg, J. M., Lind, A. C., Wang, R. T., and Libelo, L. F., 1967, *in* "Electromagnetic Scattering," L. Rowell & R. Stein, Eds., Gordon & Breach, N.Y., p. 3.

Greenberg, J. M. and Stoeckly, R., 1970, *in* IAU Symposium No. 36, L. Houziaux & H. E. Butler, Eds., D. Reidel, Dordrecht-Holland, p. 36.

Greenberg, J. M., Wang, R. T., and Bangs, L., 1971, *Nature, Phys. Sci. 230*, 110.

Hodkinson, J. R., 1963, *in* "Electromagnetic Scattering," M. Kerker, Ed., Pergamon Press, p. 87.

Liang, C. and Lo, Y. T., 1967, *Radio Science 2*, 1481.

Lind, A. C., Wang, R. T., and Greenberg, J. M., 1965, *Appl. Opt. 4*, 1555.

Lind, A. C., 1966, Ph.D. thesis, Rensselaer Polytechnic Inst., Troy, N.Y.

Montroll, E. W. and Greenberg, J. M., 1954, *in* "Proc. of Symposia on Appl. Math., Wave Motion and Vibration, Pittsburgh, Pa.," 5, McGraw Hill, N.Y., p. 103.

Proctor, T. D. and Harris, G. W., 1974, *Aerosol Science (GB) 5*, 81.

Rytov, S. M., 1955, *J. Eksp. Theor. Fiz. 29*, 605, (*Sov. Phys. JETP 2*, 466, 1956).

van de Hulst, H. C., 1946 "Thesis Utrecht," *Recherches Astron. Obs. d'Utrecht 11*, part 1.

van de Hulst, H. C., 1949, *Physica 15*, 740.

ven de Hulst, H. C., 1957, "Light Scattering by Small Particles," Wiley, N.Y.

Wang, R. T., 1968, Ph.D. thesis, Rensselaer Polytechnic Inst., Troy, N.Y.
Wang, R. T., 1970, unpublished experimental results.
Wang, R. T. and Greenberg, J. M., 1976, *Appl. Opt.* 15, 1212.
Wang, R. T., Detenbeck, R. W., Giovane, F., and Greenberg, J. M., 1977, Final report, NSF ATM75-15663 (June).
Wang, R. T. and Greenberg, J. M., 1978, Final report, NASA NSG 7353 (August).

INFRARED EMISSION BY AN AEROSOL CLOUD

Raymond A. Mackay
Department of Chemistry
Drexel University

INTRODUCTION

Infrared radiation in the atmosphere above normal background levels can be produced in a variety of ways. For example, combustion gases can produce significant amounts of radiation in the infrared region (2-20 μm). However, the total mass of material, and thus the radiant emittance, is small. In addition, the gas cloud rapidly cools and disperses. In order to significantly increase the amount of airborne material, an aerosol must be employed.

The objective of this work is to investigate the feasibility of producing an aerosol which will emit infrared radiation above normal background levels. Specifically, we are investigating the use of gas-aerosol reactions for this purpose. This first stage of this study involves the search for a model reaction suitable for examining the parameters involved, such as reaction rate, heat of reaction, rate of cooling and emission, etc. We report here some of our initial results on the gas-aerosol reaction systems screened to date.

RESULTS AND DISCUSSION

General Considerations: The rate of the gas-aerosol reaction will be liquid phase controlled; i.e., controlled either by the rate of diffusion in the liquid drop or by the bulk reaction rate. Typically, this will involve reaction rates V_s of 3×10^{-7} - 3×10^{-8} moles $cm^{-2} s^{-1}$ for 1μ drops, although faster rates are possible. The aerosol will cool rapidly by conduction to the surrounding air such that a steady-state between the rate of heat generation by reaction ($\dot{q}_s$) and heat loss by conduction ($\dot{q}_c$) should be rapidly (∿30μs) achieved. Thus, the temperature of the aerosol drops (T_d) and surrounding air in the aerosol cloud (T_c) should be given by eqn (i),

$$T_d = T_c + rV_s \Delta H_s/\kappa_g \qquad (i)$$

where r, ΔH_s and κ_g are the drop radius, heat of reaction, and thermal conductivity of the air, respectively. For the above conditions and a ΔH_s of 100 kcal $mole^{-1}$, $\Delta T = T_d - T_c$ should only be a few hundreths of a degree. Further, if we take an idealized model of the aerosol cloud as a sphere of radius R (e.g., 10 m), then the cloud as a whole should lose heat principally by radiation (neglecting convection and treating the cloud as a blackbody). Under these conditions, the rate at which the cloud heats up is given by the rate of heat generation by the drops less the radiation loss ($\dot{Q}_r$), as given by equation (ii)

$$NV_c \dot{q}_s = M_c C_c \frac{dTc}{dt} + \dot{Q}_r \qquad (ii)$$

Here, N, V_c, M_c, C_c and t are aerosol number density, cloud volume, cloud air mass, air heat capacity, and time, respectively. For a blackbody, $\dot{Q}_r = 16\ \pi R^2\ \sigma T_o^3\ (T_c - T_o)$, where σ and T_o are Stefan's constant and the ambient air temperature, respectively. For a constant reaction rate, $\dot{q}_s = 4\pi r^2 V_s \Delta H_s$. Solving the differential equation, we obtain

$$T_c = T_o + \frac{NV_c r^2 V_s \Delta H_s}{4\sigma R^2 T_o^3} \left[1 - \exp\left(\frac{-16\pi R^2 \sigma T_o^3\ t}{M_c\ C_c}\right)\right] \qquad (iii)$$

Equation (iii) is valid for $0 \leq t \leq t_r$, where t_r is the amount of time required for complete reaction of the aerosol. For an aerosol of number density 10^6 cm^{-3} and bulk liquid control, $t_r \sim 10$ sec. The entire mass of aerosol can be consumed if the reactive gas constitutes $\lesssim$ 0.3 % by weight of the entire air mass of the cloud. The maximum temperature rise is about 12° C, which is equal to that calculated by assuming that all of the heat of reaction is deposited in the cloud with no loss. This is so because the radiative loss by the cloud has a lifetime τ of about 10 minutes and is thus small compared with t_r. A sketch of this expected (idealized) behavior is shown in figure 1.

Screening Studies. A number of candidate gas-aerosol reaction systems were examined for possible use as radiation models. A schematic of the flow system

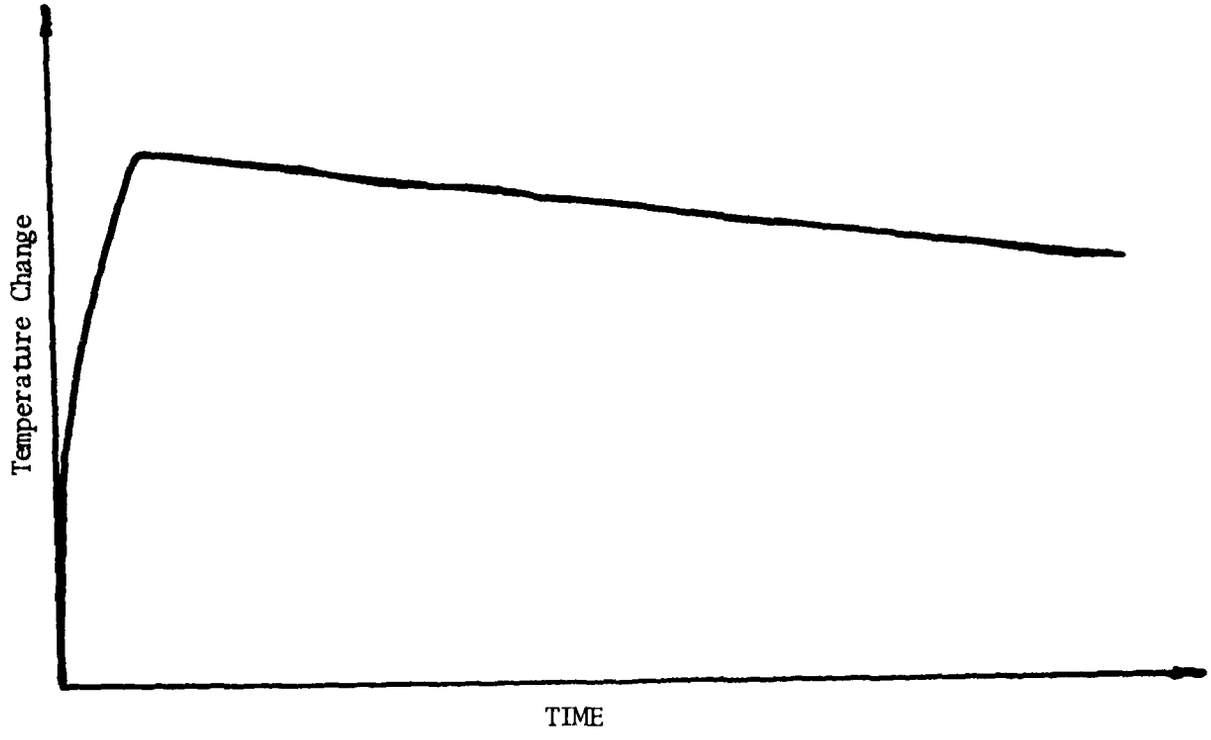

Figure 1. Dependence of cloud temperature change on time according to equation (iii).

is given in Figure 2. The gas and aerosol are combined in a reaction vessel, the temperature measured with a thermistor and the emitted radiation with a molectron pyroelectric radiometer. For the screening studies, the radiometer is fitted with a KRS-5 window which has a cutoff at about 50 μ. Thus essentially all of the emitted radiation is collected. The extent of reaction and/or concentrations of gas and aerosol are determined by collection in an impinger. The pH in the impinger can be monitored continuously via a glass combination electrode, and samples withdrawn periodically for titration. Molecular sieve is employed when necessary to remove the reactant gas from the aerosol stream prior to analysis. The aerosol may be monitored continuously using a Sinclair-Phoenix light scattering photometer. The two principal reaction vessels employed to date are shown in Figure 3. Vessel A is most useful for screening since the field of view of the radiometer (0.1 Sr) encompasses the entire volume, resulting in maximum readings. However, there is some turbulence as well as a large degree of heterogenity in both the reaction and temperature profiles from the top to the bottom of the vessel. The reaction tube in Figure 3 (Vessel B) provides a more uniform but much smaller, reaction volume. In addition, a sheath of flushing air may be employed which serves to prevent accumulation of material on the window and both material and conductive heat transfer to the walls.

We have been able to generate relatively monodisperse aerosols of all of the liquids employed to date using a condensation-type generator. However, a compressed air nebulizer (DeVilbis) was used for most of the screening. This generator produces a polydisperse aerosol, but is more convenient to use.

Reaction Systems. A number of systems involving acid-base reactions were employed for the initial screening runs since these reactions are normally rapid and reasonably exothermic. The systems are listed in Table 1. Only the chlorosulfonic aerosol produced detectable infrared emission.

It should be noted that even the $ClSO_3H/H_2O$ system produced emission, while apparently more exothermic H_2SO_4/NH_3 and H_2SO_4/NH_3-H_2O systems did not. The expected reactions and experimental conditions for the chlorosulfonic acid system are given in Table 2. The aerosol particle is underlined, and complete reaction is assumed. The reactions with water and ammonia are written sequentially, although they do not necessarily occur in this manner. The gas-gas reaction between HCl and NH_3 produces solid ammonium chloride which both forms an aerosol and deposits on the walls of the reaction vessel and connecting tubing. This difficulty is avoided if only water is used as the reactant gas, but a considerably lower (four to five fold) emission is observed. It is thus desireable to find another system to use for detailed model studies.

Analysis of the extent of reaction at a point downstream from the reaction vessel which is equivalent to 2-3 residence times in Vessel A indicates that the reaction is essentially complete.

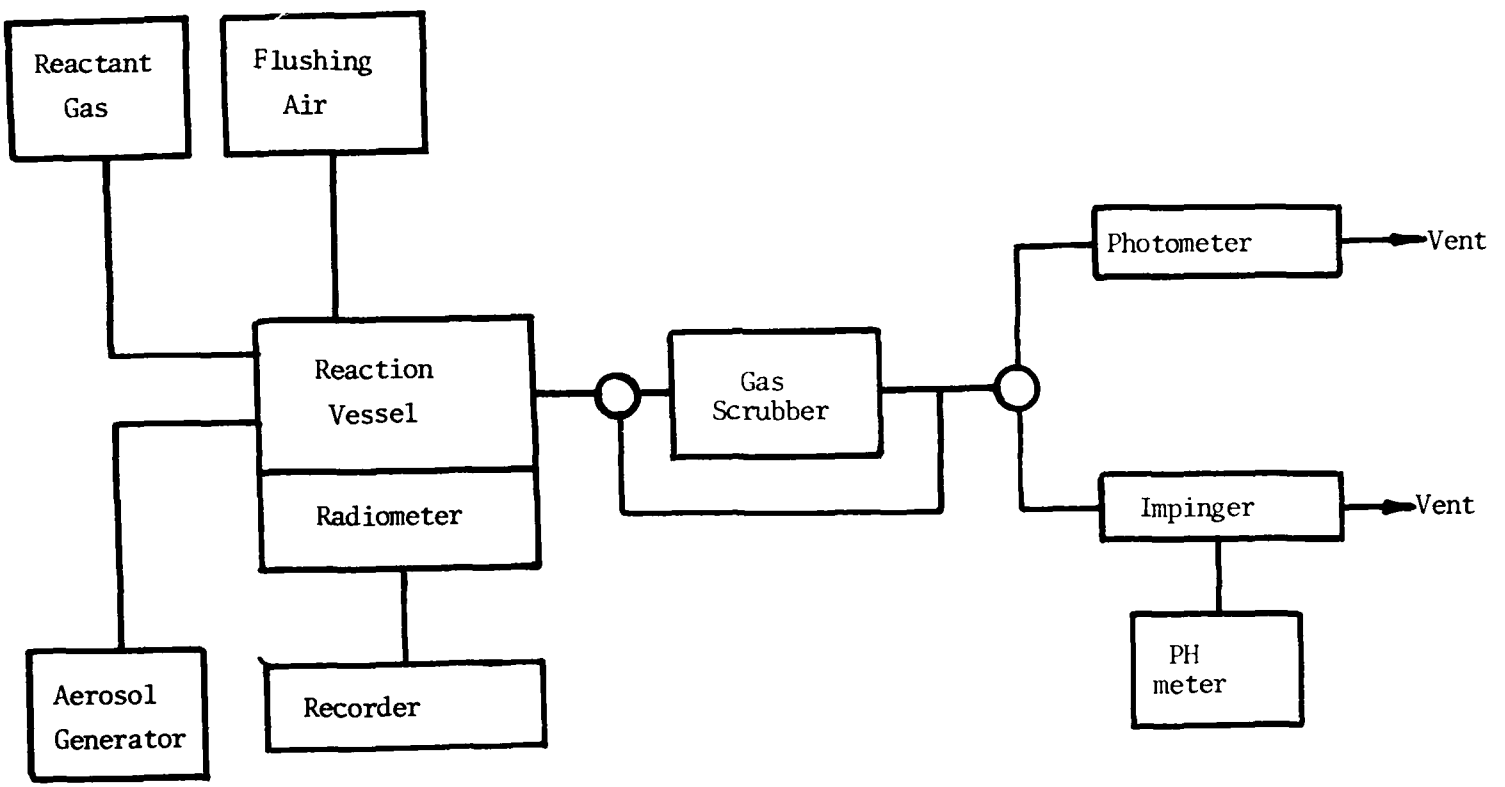

Figure 2. Aerosol flow system. Approximate flow rates are; gas (0.5 - 1 l min^{-1}), aerosol (2-3 l min^{-1}) and flushing air (1 l min^{-1}).

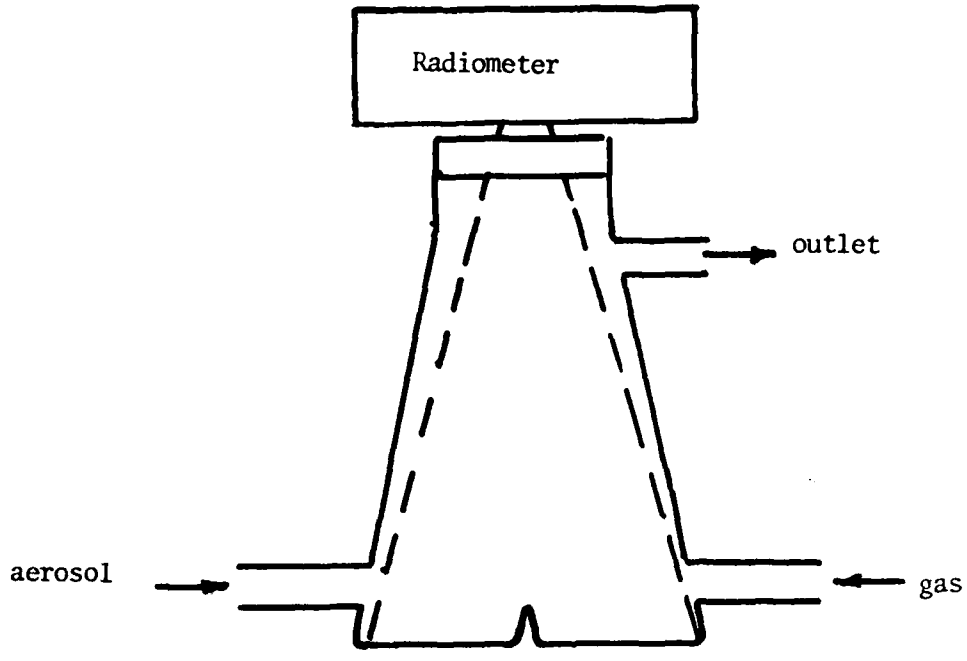

Vessel A

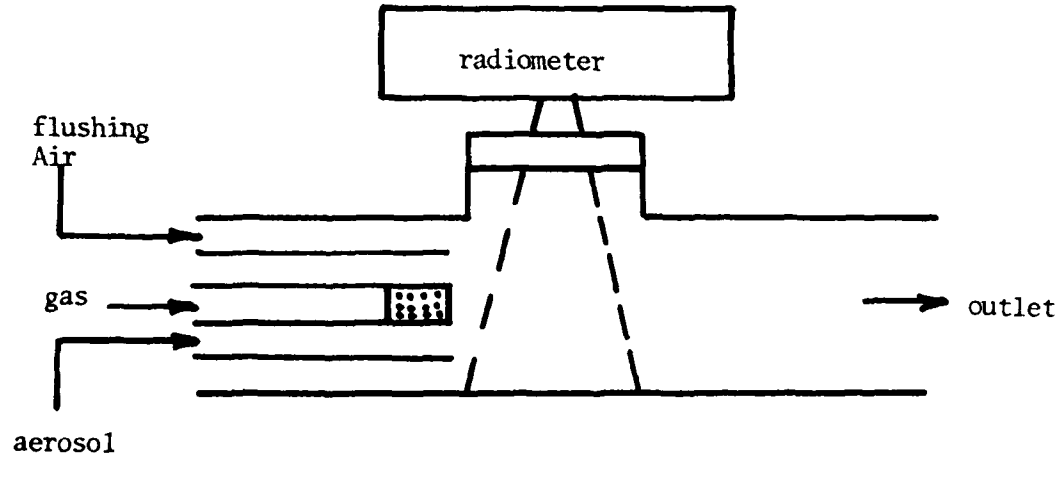

Vessel B

Figure 3. Reaction vessels. The dashed lines represent the radiometer field of view.

Table 1 Gas - Aerosol Reaction Systems

Aerosol	Gas	ΔH^a	IR[b]
Decanoic Acid	NH_3	21	No
Octyl Amine	H Cl	--	No
H_2SO_4	NH_3	65	No
	NH_3/H_2O	64	No
$ClSO_3H$	H_2O	0-40[c]	Yes
	NH_3/H_2O	96-114[c]	Yes

a. Estimated heats of reaction in kcal per mole of aerosol.

b. Indicates detectable infrared emission.

c. Upper figure includes heat of hydration of reaction products.

Table 2: Chlorosulfonic Acid System: Reactions and Conditions

I. Reactions

$$\underline{ClSO_3H} + H_2O_{(g)} \rightarrow \underline{H_2SO_4} + HCl_{(g)}$$

$$\underline{H_2SO_4} + 2NH_3(g) \rightarrow \underline{(NH_4)_2\ SO_4}$$

$$HCl_{(g)} + NH_3(g) \rightarrow NH_4Cl(s)$$

II. Conditions

A. Total flow rates 2.5-5 l/min

B. $ClSO_3H$ aerosol

mass concentration 1-3 g/m^3

mass median diameter 2-4 μm

number concentration $\sim 10^6$ cm^{-3}

C. Reactive gas

Ammonia 10 - 30 g/m^3

Water ~ 25 g/m^3

A further indication that complete reaction occurs in the larger vessel (A) comes from a study in which the $ClSO_3H$ aerosol and gas (NH_3/H_2O) were mixed in a long 2 cm diameter tube. The temperature was measured by a thermistor at various distances along the tube. From the known flowrate, a temperature vs. residence time profile was obtained. The temperature (rise) was about 1^oC up to about 1 sec, increased to 2^oC at 1.5 sec, and may have started to decrease slightly at 2 sec. This may be compared with residence times of 3-6 seconds in Vessel A.

Infrared Emission. Employing the general conditions listed in Table 2, a number of runs were carried out in which the radiometer reading was displayed continuously on a strip chart recorder. A typical result using Vessel A is shown in figure 4. The radiometer response time is about 1.3 min. for a reading of 20 $\mu W\ cm^{-2}$ full scale. These results may be compared with those obtained using Vessel B, shown in figure 5. The radiometer readings are of course lower. However, it is interesting to note that in this case, both H_2O and NH_3/H_2O yield almost the same results. In this reaction vessel, the reaction is not complete and it may be that the reaction rate is controlling the results. With the flushing air on, a somewhat higher reading is obtained. This may be due to a decrease in transfer to the wall (vide supra).

As a basis for comparison of the measured power per unit area (R), equation (iv) may be employed.

$$R = 4\ \varepsilon\sigma T^3\ \Delta T\ \Omega/\Pi \qquad \text{(iv)}.$$

Here ε is the emissivity and Ω is the radiometer field of view (solid angle) which is occupied by the object. Assuming a blackbody (ε=1) with T = 298^oK and Ω=0.1 Sr, R should increase by about 20 $\mu W\ cm^{-2}$ for each 1^oK rise in temperature. In Vessel A, for the $ClSO_3H/NH_3$-H_2O reaction system, a maximum temperature increase of $\sim 2^oC$ was observed. The maximum observed increase in R was $\sim 28 \mu W\ cm^{-2}$. For water as the reaction gas, the maximum increase was $\sim 7 \mu W\ cm^{-2}$. If there are no contributing artifacts, these relatively high emissions are somewhat surprising in view of the rather low emissivity of air.

Summary Detectable levels of infrared emission have been observed from the reaction of chlorosulfonic acid aerosol with both water vapor and gaseous mixtures of water and ammonia. It appears that both the rate and heat of reaction are important in determining the emission-time profile, and that the emitted power is greater than expected. The chlorosulfonic acid system does not possess all the attributes of an ideal model system, and others should be sought.

Acknowledgement This work was supported by the U.S. Army Research Office under grant DAAG 29-78-G-0117.

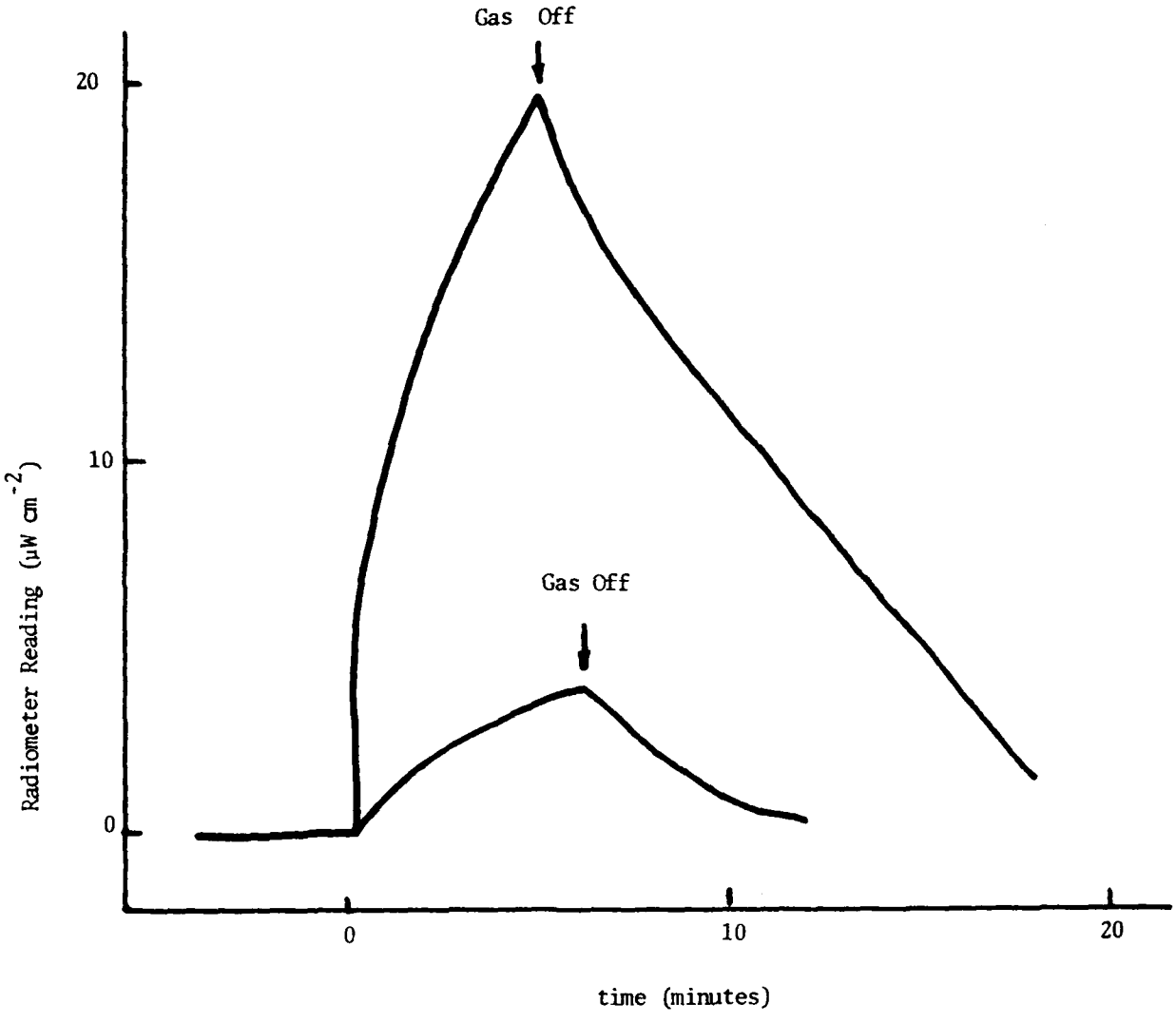

Figure 4. Reaction of $ClSO_3H$ with NH_3/H_2O (upper curve) and H_2O (lower curve) in vessel A. The reactant gas was turned on at time zero.

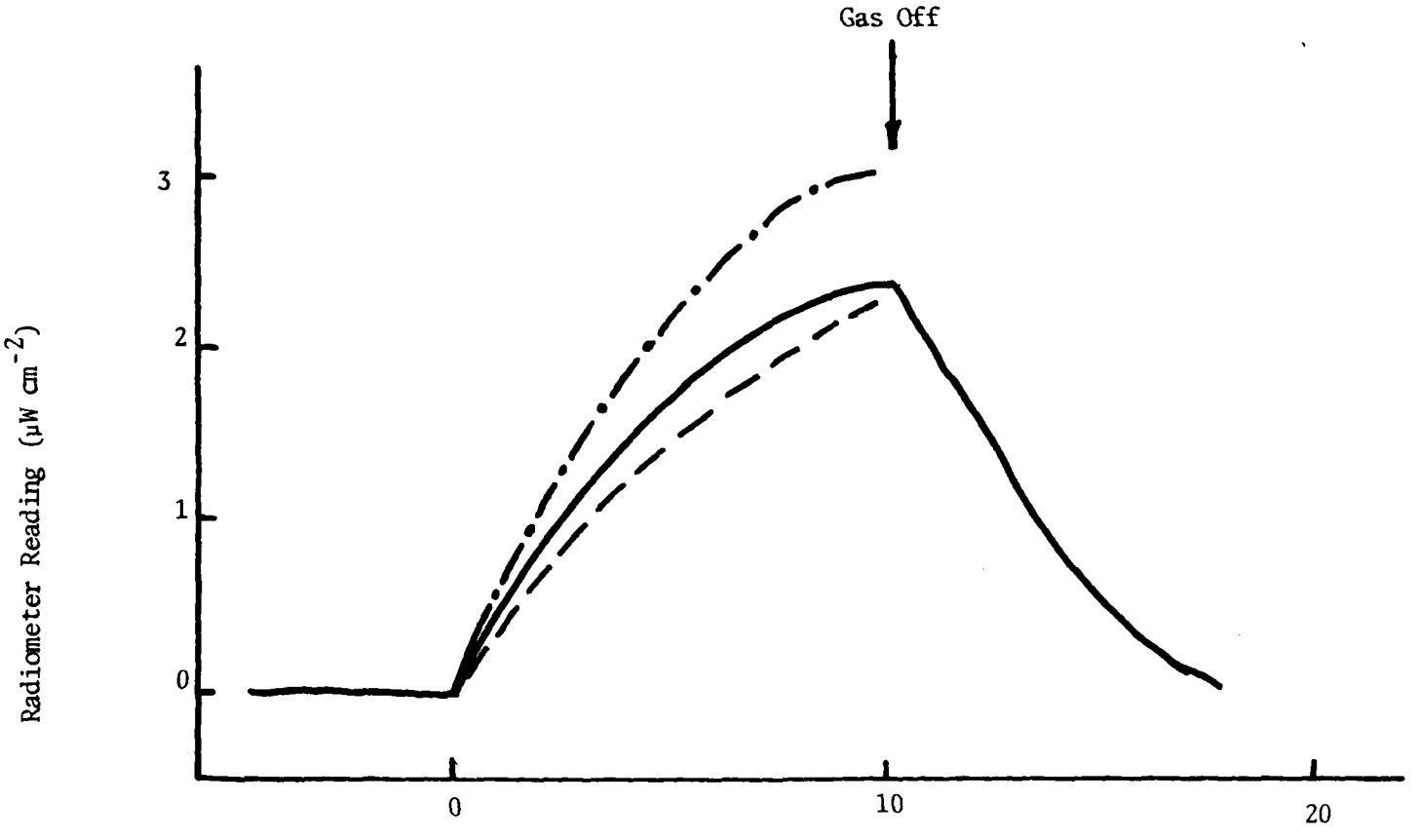

Figure 5. Reaction of $ClSO_3H$ with NH_3/H_2O (solid line) and H_2O (dased line) in vessel B with no flushing air. The dot-dash line is for NH_3/H_2O with flushing air. The reactant gas was turned on at time zero.

ENGINEERING FORMULAS FOR RADIATIVE TRANSFER

Peter C. Waterman, Panametrics, Inc.

INTRODUCTION

In order to find the attenuation occurring when incoherent radiation propagates through a region containing absorbing/scattering particles, it is necessary to consider the radiative transfer problem. The basic concepts involved in radiative transfer are discussed by Chandrasekkar.[1] A useful introduction to the subject has also been given by Wing, in the equivalent context of neutron transport theory.[2] Several modern techniques appear promising for numerical computations, including the j_N method which involves Fourier transformation of the integral form of the transport equation, followed by expansion of the resulting kernel in spherical Bessel functions.[3] The C_N method involves expansion of the flux function in powers of the cosine of the scattering angle,[4] as does the F_N method.[5] Both of these latter techniques are based on the Placzek lemma, which relates solutions of the problem in an unbounded region to those in a bounded region with surface source distributions prescribed in a special way.[6]

The purpose of the present work is to provide approximate engineering formulas that can be used in the context of a larger computer program to obtain the transmission coefficient for a layer of material, given the scattering and absorption cross sections and orientation-averaged phase functions of individual particles. The particles in question are thin conducting filaments, with both geometry and physical properties tailored so as to yield high absorption per unit mass in either the infrared, visible, or microwave region.

The following section summarizes the basic concepts of radiative transfer needed to develop our approximations. We will then obtain a simple analytical expression describing the results of numerical computations for the slab geometry with isotropic scattering, and show how to rescale this expression to include the case of anisotropic scattering.

BASIC THEORY

Consider the slab geometry as shown in Fig. 1. In the desired application, the slab region is filled by a uniform random distribution of this filaments with number density n per unit volume. For the moment, we suppose each filament to scatter isotropically, with scattering and absorption cross sections given by σ_s, σ_a respectively. The slab has optical depth

$$\tau = n(\sigma_a + \sigma_s)s_0 \tag{1}$$

in terms of its thickness s_0.

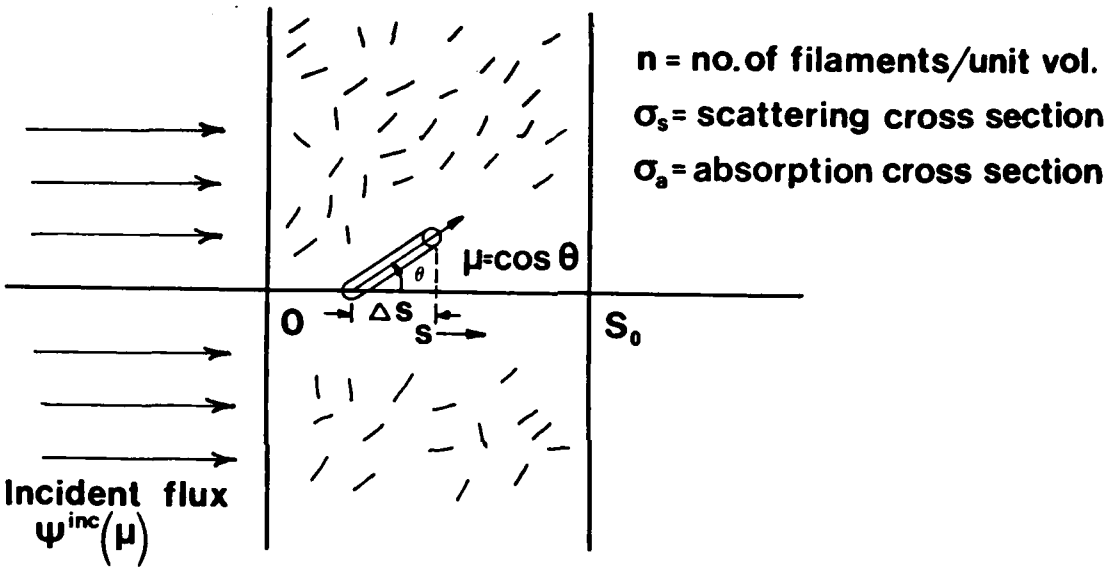

Figure 1. Geometry of the slab of thin conducting filaments is shown.

One begins by introducing the intensity $\psi(s,\mu)$ which gives the flux of photons per steradian at any depth s in the slab, in the direction specified by $\mu = \cos\theta$. The basic radiative transfer equation is then obtained by simple balance relations applied to the small cylindrical volume shown in Fig. 1 to get

$$\Delta\psi = [-n(\sigma_a + \sigma_s)\psi + (n\sigma_s/2)\int_{-1}^{+1} d\mu\,\psi(s,\mu)]\Delta s/\mu. \tag{2}$$

That is, the change in ψ while traversing the cylinder is a consequence of losses due to scattering and absorption, which are then partially offset by scattering within the cylinder of the flux entering from all directions (the integral term in Eq. 2).

This equation can be simplified somewhat by measuring distance

$$x = n(\sigma_a + \sigma_s)s$$

in optical units, and defining the albedo

$$a = \sigma_s/(\sigma_a + \sigma_s)$$

as the fraction of absorbed power which is then reradiated. In terms of these quantities, Eq. 2 becomes

$$\mu\,\partial\psi/\partial x = -\psi + (a/2)\int_{-1}^{+1} d\mu\,\psi(x,\mu). \tag{3}$$

To this equation must be appended boundary conditions

$$\psi(0,\mu) = \psi^{inc}(\mu),\ 0 \le \mu \le 1 \text{ (given)}$$

$$\psi(\tau,\mu) = 0,\ -1 \le \mu \le 0, \tag{4}$$

which state that ψ must reduce to the known incident intensity ψ^{inc} $(\mu \ge 0)$ at the entrance face $x = 0$, and at the same time no flux shall enter the slab through the exit face $x = \tau$. We note that for the case of pure absorption ($\sigma_s = 0$), the solution of Eqs. 3 and 4 is trivial, and one obtains

$$\psi(x,\mu) = \psi^{inc}(\mu)\,e^{-x/\mu}. \tag{5}$$

For this case the incident intensity is replicated throughout the slab, with an attenuation corresponding to the path length traversed.

It is also convenient to define the total intensity

$$\Psi_0(x) = \int_{-1}^{+1} d\mu\, \psi(x, \mu), \tag{6}$$

and the photon flux vector (x component)

$$f(x) = \int_{-1}^{+1} d\mu\, \mu\, \psi(x, \mu). \tag{7}$$

Conservation of flux now manifests itself as follows. From Eq. 3 we have

$$\mu\, \partial\psi/\partial x = -\psi + (a/2)\psi_0. \tag{8}$$

Integrating over allowed values of μ then gives

$$df/dx = (a - 1)\psi_0, \tag{9}$$

and we see that for an albedo of unity (no absorption) the divergence of the photon flux vanishes, as it must.

The radiative transfer Eq. 8 can be converted to an integral equation for the total intensity ψ_0, effectively eliminating dependence on the angle μ during the course of the main computation. To do this, one multiplies Eq. 8 by an integrating factor $\exp(x/\mu)$ and integrates over the slab thickness to get

$$\psi(x, \mu) = \begin{cases} \psi^{inc}(\mu)e^{-x/\mu} + (a/2\mu)\int_0^x dx'\, e^{\frac{x'-x}{\mu}}\psi_0(x'), & \mu > 0 \\ -(a/2\mu)\int_x^\tau dx'\, e^{\frac{x'-x}{\mu}}\psi_0(x'), & \mu < 0. \end{cases}$$

Integrating again over all angles μ then gives

$$\psi_0(x) = \int_0^1 d\mu\, \psi^{inc}(\mu)\, e^{-x/\mu} + (a/2)\int_0^\tau dx'\, E_1(|x - x'|)\psi_0(x'), \tag{10a}$$

which is an integral equation for ψ_0. The inhomogeneous driving term is simply the known total intensity that would be present if only absorption were involved, and the kernel consists of the exponential integral, defined by

$$E_1(x) = \int_x^\infty dt(1/t)e^{-t} \tag{10b}$$

After solving Eq. 10, which in general must be done numerically, the angular dependence of the intensity is readily recovered from the preceding equation. In particular, the emergent intensity at the slab faces is given by

$$\psi(\tau, \mu) = \psi^{inc}(\mu)e^{-\tau/\mu} + (a/2\mu)\int_0^\tau dx\, e^{\frac{x-\tau}{\mu}}\psi_0(x),\ \mu > 0$$
$$\psi(0, \mu) = -(a/2\mu)\int_0^\tau dx\, e^{x/\mu}\psi_0(x),\ \mu < 0. \tag{11}$$

Finally, transmission and reflection coefficients T, R are defined respectively by

$$T(\tau, a) = \int_0^1 d\mu\ \mu\ \psi(\tau, \mu), \tag{12}$$

$$R(\tau, a) = \int_{-1}^0 d\mu\ \mu\ \psi(0, \mu). \tag{13}$$

NUMERICAL AND ANALYTICAL RESULTS

With the above discussion as background, we turn our attention to numerical results available from the literature, in order to develop analytical approximating formulas.

Feix and Valentin[7] have carried out detailed numerical computations for the slab problem for the case of a collimated beam normally incident, i. e.

$$\psi^{inc}(\mu) = \delta(1 - \mu).$$

Their results for the transmission coefficient, which is the quantity of primary interest to us, are shown by the solid curves in Fig. 2 for slabs up to six optical units thick, and albedos ranging from pure scattering to pure absorption. The curve for the lossless case has also been obtained independently by Hinchey and co-workers.[8] After some trial and error, we find that T can be described approximately by the formula

$$T(\tau, a) = e^{-(1-a^2)^{(2/3)\tau}}\left[(1-a^2) + a^2(1 + 3\tau/4)^{-1}\right], \tag{14}$$

values of which are shown by the dashed curves in Fig. 2. In the region of highest loss $0 \le a \le 0.6$, additional comparisons (not shown for clarity) indicate excellent agreement. The fit is seen to deteriorate somewhat as one approaches

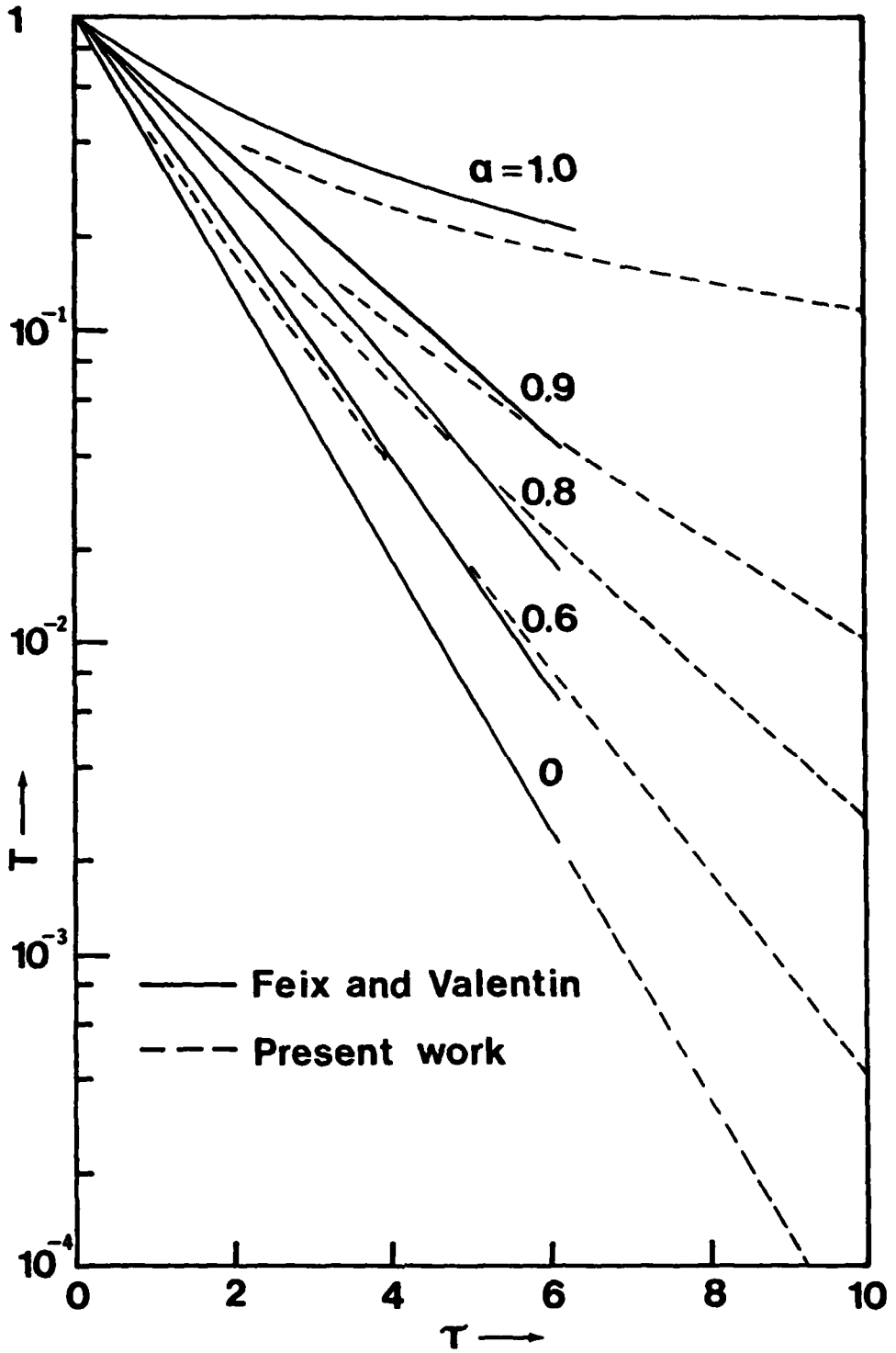

Figure 2. The slab transmission coefficient is compared for numerical calculations (solid curves) and the engineering formula Eq. 14 (dashed curves.

the pure scattering case $a \longrightarrow 1$, but nevertheless should be quite acceptable for engineering purposes.

Equation 14 was constructed to meet certain analytical constraints. In addition to reducing correctly to $T(0, a) = 1$ at zero slab thickness, note that

$$T(\tau, 0) = e^{-\tau} \tag{15}$$

$$T(\tau, 1) = (1 + 3\tau/4)^{-1}.$$

The first of these equations is of course the exact exponential result for pure absorbers, while the second gives the correct asymptotic behavior of T for pure scattering in the thick slab limit $\tau >> 1$.

So far we have considered only isotropic scatterers, as would be appropriate in the acoustic case (or the neutron transport problem). For anisotropic scatterers, the radiative transfer equation becomes

$$\hat{n}.\nabla \psi(\underline{r}, \hat{n}) = -n(\sigma_a + \sigma_s)\psi(\underline{r}, \hat{n}) + (n\sigma_s/4\pi)\int d\hat{n}' p(\hat{n}', \hat{n})\psi(\underline{r}, \hat{n}'), \tag{16}$$

where the phase function $p(\hat{n}', \hat{n})$ gives the scattered intensity in the direction $\hat{n}$ for incident flux in the direction $\hat{n}'$, as shown in Fig. 3. The phase function satisfies the normalization condition

$$(1/4\pi)\int d\hat{n}' p(\hat{n}', \hat{n}) = 1. \tag{17}$$

If scatterers are not embedded in the medium with preferred fixed orientation, then

$$p(\hat{n}', \hat{n}) = p(\hat{n} - \hat{n}'). \tag{18}$$

If further the scattered intensity is symmetric about the incoming $\hat{n}'$ direction, then

$$p(\hat{n}', \hat{n}) = p(\hat{n}'.\hat{n}) = p(\mu),$$

where $\mu = \cos\theta = \hat{n}'.\hat{n}$ (see Fig. 3). This is the case we want to consider.

Evans et al. have carried out numerical computations employing a phase function expressed in Legendre polynomials,

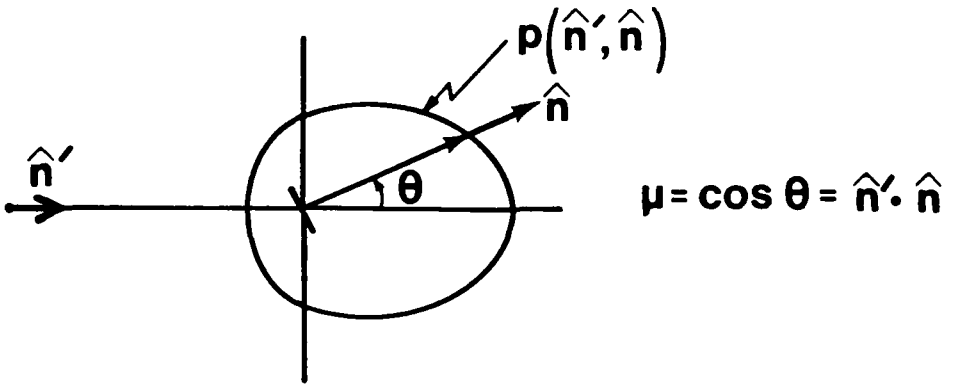

Figure 3. Geometry of the phase function is shown.

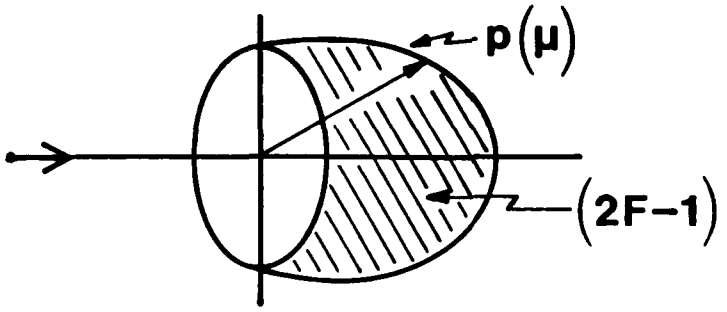

Figure 4. The excess part of the phase function due to forwardness (shaded region) may be discarded, leaving a function with front-back symmetry.

$$p(\mu) = a_o + a_1 P_1(\mu) + a_2 P_2(\mu), \tag{18a}$$

for various values of the expansion coefficients.[9] In particular they considered the two cases

$$p = 1 \tag{18b}$$

$$p = \frac{3}{4}(1+\mu^2). \tag{18c}$$

The first of these of course describes isotropic scattering, while the second holds for Rayleigh scattering by small spheres in the electromagnetic case. Numerical results for the transmission coefficients in the two cases were found to be identical for all practical purposes (although intermediate results may have differed).

Now for the thin filament case of interest to us, in the low frequency limit filament length/wavelength << 1 pure dipole scattering will result at any fixed orientation. If $\hat{a}$ is a unit vector along the filament axis, and $\hat{e}$ represents the incident electric field polarization, then the scattered field amplitude in the $\hat{n}$ direction will be proportional to

$$\hat{e}\cdot\hat{a}\,|\hat{a}\times\hat{n}|. \tag{19a}$$

Averaging over all orientations and incident field polarizations, the appropriate phase function has the form

$$p \sim \frac{1}{2\pi}\int d\hat{e}\,\frac{1}{4\pi}\int d\hat{a}\,[\hat{e}\cdot\hat{a}\,|\hat{a}\times\hat{n}|\,]^2, \tag{19b}$$

which finally gives

$$p = \frac{9}{10}\left(1+\frac{1}{3}\mu^2\right). \tag{19c}$$

This falls right between the two phase functions noted above, and in fact is very nearly isotropic. Because the transmission coefficients for isotropic and Rayleigh scattering were indistinguishable, we conclude that all of the preceding results, and in particular the analytical expression Eq. 14 for T, apply also to the thin filament case at low frequencies.

At higher frequencies the phase function for the thin filament will no longer have front-back symmetry. Instead, radiated power will tend to be concentrated in the forward hemisphere, and at the same time more sharply peaked in the forward direction. In order to investigate this effect, Evans et al.[9] define the quantities

$$F = \frac{1}{2}\int_0^1 d\mu\, p(\mu) \qquad \text{forwardness,} \tag{20a}$$

$$P = \int_0^1 d\mu\, \mu^2 p(\mu) \Big/ \int_0^1 d\mu\, p(\mu) \qquad \text{peakedness.} \tag{20b}$$

The corresponding phase function is sketched in Fig. 4. If we were to define B as the analogous integral to F over the back hemisphere, then F + B = 1 and the excess power in the forward hemisphere over that in the back is given by 1 - 2B = 2F - 1, as indicated by the shaded region in the figure.

Numerical studies that were carried out[9] for various choices of the phase function Eq. 18a indicate that, whereas the transmission coefficient increases with increasing F, it is practically independent of P, the peakedness. This suggests that a simple rescaling approximation may be useful. Returning for a moment to the general radiative transfer Eq. 16, note that if p contained any fraction of the radiated power in the form of a δ-function peak in the forward direction, then the integration could be performed to give a term which cancels out a corresponding fraction of σ_s in the first term on the right hand side of the equation. In short, the equation can be rigorously rescaled, reducing σ_s and dropping the δ-function term from p.

Because T is insensitive to the peakedness, the same rescaling can be carried out, if only approximately, whenever F exceeds B. From Fig. 4, upon discarding the shaded portion of p, the scattering cross section is replaced by $2B\sigma_s = 2(1 - F)\sigma_s$. The remaining (unshaded) portion of p falls in the class of functions of Eq. 18b, c having front-back symmetry, for which the isotropic results may be used. The net effect of all this, after carrying out some arithmetic, is to employ the analytical Eq. 14 for $T(\tau', a')$, where the scaled variables are given by

$$\tau' = (1 + a - 2Fa)\tau, \tag{21a}$$

$$a' = \frac{2(1 - F)a}{1 + a - 2Fa} \tag{21b}$$

Figure 5 shows a comparison of Eqs. 21 with numerical computations. Results of Evans et al.[9] are shown by the solid curve for values of F ranging from 0.5 (which corresponds to the isotropic case) to 0.933. Numerical values shown explicitly in the figure are different values of the peakedness for which the numerical result for T was effectively unchanged. These results are for a slab having true thickness of one optical depth, and an albedo of 0.9. Using the scaled variables of Eqs. 21 in Eq. 14 yields the dashed curve shown. Although the agreement is perhaps not as good as in the earlier Fig. 2, the trend to increasing T at higher forwardness is clearly shown. More extensive

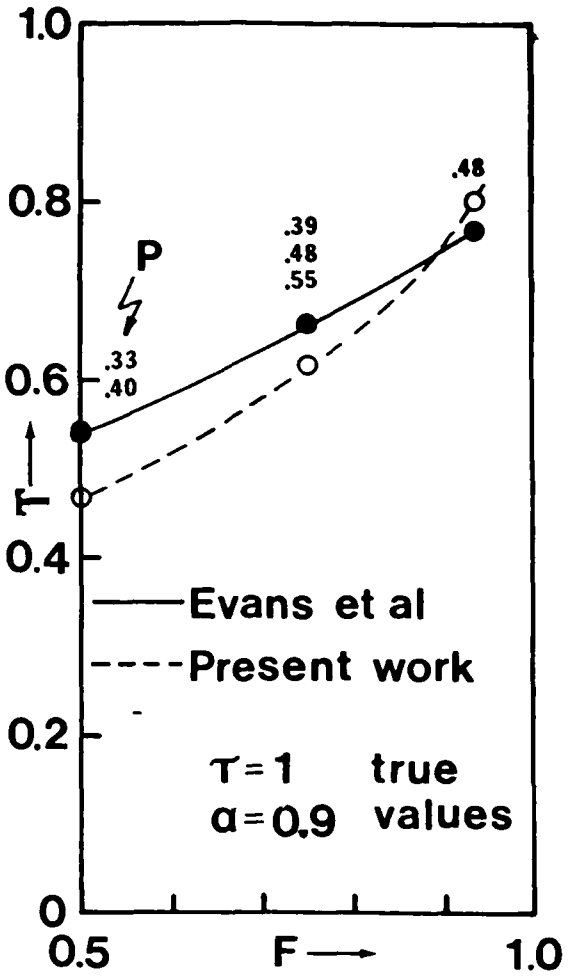

Figure 5. Dependence of the transmission coefficient on forwardness is shown: solid curve gives numerical results, dashed curve computed from scaled analytical formula (see text).

comparison with numerical data is of course required, however, in order to establish full confidence in the scaling approximation of Eqs. 21.

DISCUSSION

In the above we have established that a fairly simple analytical expression will describe, to good engineering accuracy, the incoherent transmission of light through a cloud of thin conducting filaments, provided they are assumed to be randomly oriented, and the wavelength is sufficiently long that only electric dipole behavior occurs. A scaling procedure was also given that enables the method to be extended to shorter wavelengths, but further comparisons with numerical computations are necessary if one is to have full confidence in this extension.

As a separate part of the program, Drs. N. Pedersen and J. Pedersen are developing computer programs to evaluate the scattering and absorption cross sections of the filaments for a variety of physical and geometrical parameters for those shorter wavelengths which cannot be described by an electric dipole response. This work will be integrated with the radiative transfer results to yield a program capable of specifying all parameters required to achieve desired obscuration properties when dealing with transmission in the infrared, visible, and microwave regions.

The major remaining theoretical task that must be carried out to complete the present phase of the program involves particle aggregates. There are two problems here. First, methods must be developed to determine, under various climatic conditions, the rate and extent to which aggregates are formed. Knowing this, the second problem is to determine the electromagnetic scattering and absorbing properties of such aggregates. It seems clear that approximation methods will have to be employed here; the precise way in which this will be carried out remains to be established.

REFERENCES

1. S. Chandrasekhar, Radiative Transfer (Dover Publications, Inc., New York, 1960).

2. G. M. Wing, Introduction to Transport Theory (John Wiley and Sons, Inc., New York, 1962).

3. H. Kschwendt, Nucl. Sci. Eng. 36, 447-453 (1969).

4. A. Kavenoky, Nucl. Sci. Eng. 65, 209-225 (1978); 65, 514-531 (1978).

5. C. E. Siewert and P. Benoist, Nucl. Sci. Eng. 69, 156-160 (1979); 69, 161-168 (1979).

6. K. M. Case, F. de Hoffmann and G. Placzek, Introduction to the Theory of Neutron Diffusion (U. S. Gov't. Printing Office, Washington, D. C., (1953).

7. M. Feix and S. Valentin, Compt. rend. 242, 617-620 (1956).

8. F. A. Hinchey, E. A. Dean and J. B. Pearce, Nucl. Sci. Eng. 20, 88-92 (1964).

9. L. B. Evans, C. M. Chu and S. W. Churchill, J. Heat Trasf. (Trans. ASME) 87, 381-387 (1965).

The Transfer of 11.5 μm Radiation Through Smoke Produced by Brush Fires

J.A. Weinman[1,2] Harshvardan[2] R. Davies[3]

(1) Department of Meteorology, University of Wisconsin, Madison, WI 53706

(2) Goddard Laboratory for Atmospheric Science, Greenbelt, MD 20771

(3) Space Science & Engineering Center, University of Wisconsin, Madison, WI 53706

1. Introduction:

A clear, cloud free atmosphere is normally transparent to 11.5 μm radiation. However if smoke is produced by brush fires , the smoke laden atmosphere will become opaque to such radiation. This note presents some characteristics of the radiative transport properties of such smoke.

2. Microphysics of Brush Fire Smoke

2.1 Composition and Sizes

Three major constituents of smokes are water, carbon and silicates.

It will be assumed that water droplets are polydispersions characterized by model size distributions designated as either Haze M or Cloud C-1 by Deirmendjian (1969). The result of the application of Mie theory to such size distributions is presented in Deirmendjian's book. The results of these computations will be used in the next section.

Table 1 shows the characteristics of Australian brush fires measured by Vines et al. (1971). It is evident that various carbonaceous products comprise more than half of the mass of smoke from such fires, Conner and Hodkinson (1967) showed that carbon from power station plumes was distributed in size as $\sim r^{-5}$. Twitty and Weinman (1971) computed the radiative properties of carbonaceous aerosols with a similar size distribution. The refractive index for carbonaceous substances reported in the literature varies considerably, however $m = 1.8 - i\ 0.5$ is a characteristic value.

The smoke model parameters are summarized in Table 2.

2.2 Radiative Characteristics of Smoke Particles

The Mie theory describes the interaction of radiation with homogeneous spherical particles, see Deirmendjian (1969). This theory was applied to the ensemble of particles presented in Table 2.

CHARACTERISTICS OF AUSTRALIAN BUSH FIRES: FROM VINES ET AL. (1971)

DATE	LOCATION OF SAMPLE	PARTICLE CONCENTRATION (MG/M^3)	SCATTERING COEF $K(KM^{-1})$	$\frac{K}{e}$	TAR%	SOOT%	ASH%*
10/31/70	10 N.M. FROM FIRE	0.37	1.44	3.89	59	39	2
	24 N.M. FROM FIRE	0.32	1.46	4.56	60	34	5
11/09/70	9 N.M. FROM FIRE	0.55	1.46	2.65	29	55	17
12/07/70	8 N.M. FROM FIRE	0.78	2.22	2.85	51	11	38
	31 N.M. FROM FIRE	0.20	1.17	5.85	54	2	44
12/09/70	NEAR FIRE	0.60	3.06	5.10	58	5	36
	LATER, SAME LOCATION	1.09	4.80	4.40	60	5	36
12/11/70	3 N.M. FROM FIRE	0.47	1.80	3.83	56	5	39
12/15/70	NEAR FIRE	0.88	4.11	4.67	56	34	10

*CARPENTER ET AL. (1977) FOUND THAT ~90% OF THE MASS OF ASH IS SILICATE.

Table 1

SMOKE MODEL PARAMETERS

SIZE DISTRIBUTIONS, dn/dr		REFRACTIVE INDICES, $\lambda = 11.5\mu m$
CARBON: TWITTY + WEINMAN (1971)		
10^7	$r \leq .006\ \mu m$	$1.8 - i\ 0.5$
$400r^{-2}$	$.006 < r < .05\ \mu m$	$1.95 - i\ 0.66$ ($\lambda = .55\mu m$)
r^{-4}	$.05 < r \leq 2\ \mu m$	FAXVOG & ROESSLER
WATER HAZE M: DEIRMENDJIAN (1969)		
$5.33 \times 10^4\ r\ \exp(-8.94\ r^{1/2})$		$1.111 - i\ 0.183$
WATER CLOUD C-1 : DEIRMENDJIAN (1969)		
$2.37\ r^6\ \exp(-1.5\ r)$		$1.111 - i\ 0.183$

Table 2.

Table 3

RADIATIVE PROPERTIES OF MODEL SMOKES AT $\lambda = 11.5 \mu m$

a	Carbon	Water Haze M	Water Cloud 1
ALBEDO FOR SINGLE SCATTER	.075	.044	.289
K/ρ (M^2/GM) EXTINCTION PER UNIT MASS	.285	.197	.161
PHASE FUNCTION PARAMETERIZATION (SEE BELOW)			
b	1	.887	1
G_1	.175	.412	.842
G_2	--	-.449	--

DOUBLE HENYEY GREENSTEIN APPROXIMATION

$$P(\theta) = bP_{H.G.}(G_1) + (1 - b)P_{H.G.}(G_2)$$

$$P_{H.G.}(G) = (1 - G^2)/(1 + G^2 - 2G\cos\theta)^{3/2}$$

The albedo for single scattering, a, is the ratio of the scattering coefficient to the total extinction coefficient k. Note in Table 3 that the scattering is less important than absorption if the particles are small compared to the wavelength, but that scattering becomes more significant as the particles become larger. The difference between a for Water Haze M and Water Cloud C-1 demonstrates this effect.

The extinction coefficient is nearly independent of the size distribution if the wavelength is large compared to the particle size, see Pilipowskyj (1968) but it is proportional to the mass loading of the smoke. Thus the ratio k/ρ is characteristic of the smoke substance, where ρ is the mass density of the aerosol. The ratio k/ρ is inversely proportional to the wavelength of radiation, and it is gratifying to note that the values measured for Australian brush fire smoke at $\lambda = 0.5$ μm shown in Table 1 are about 23 times larger than those computed for $\lambda = 11.5$ μm which are shown in Table 3.

The phase functions which describe the scattering distribution as a function of scattering angle were obtained at numerous angles. However, it is convenient to parameterize these results with three empirical constants b, g_1, and g_2 which can be obtained from a least squares fit to the results of the Mie theory computations by means of a double Henyey-Greenstein function depicted in Table 3, see Irvine (1965).

3. Radiative Transfer Calculations

3.1 Horizontally Homogeneous Smoke Clouds

Fig. 1 illustrates the geometry that is used to represent the model for horizontally homogeneous smoke covering a smoldering ground. The smoke is assumed to be isothermal. Downwelling infrared radiation incident on the upper boundary of the smoke is neglected. The upwelling infrared radiation

Table 4

NADIR VIEWED BRUSH FIRE BRIGHTNESS TEMPERATURE ($\mu = 0.974$)

$T_0 = 36.8^{\circ}C$ $T_1 = 46.8^{\circ}C$

	Carbon	Haze M	Cloud C-1
a	.075	.044	.289
$\rho_{N_2}^{*}$ (gm/m^2)	($^{\circ}$C)	($^{\circ}$C)	($^{\circ}$C)
.316	37.5	37.4	37.1
1	38.9	38.5	37.8
3.16	42.1	41.2	39.8
10	45.5	45.1	43.6
31.6	46.1	46.4	46.2

Table 5

GRAZING VIEWED BRUSH FIRE BRIGHTNESS TEMPERATURE ($\mu = 0.149$)

$T_0 = 36.8^{\circ}C$ $T_1 = 46.8^{\circ}C$

	Carbon	Haze M	Cloud C-1
a	.075	.044	.289
$\rho_{N_2}^{*}$ (gm/m^2)	($^{\circ}$C)	($^{\circ}$C)	($^{\circ}$C)
.316	40.0	39.7	37.5
1	43.2	43.1	39.1
3.16	44.6	45.4	41.5
10	44.7	45.6	42.2
31.6	44.7	45.7	42.3

incident on the lower cloud surface is characterized by a Planck function for temperature T_o .

Fig. 1

$\lambda = 11.5\mu m$ RADIATIVE TRANSFER MODEL

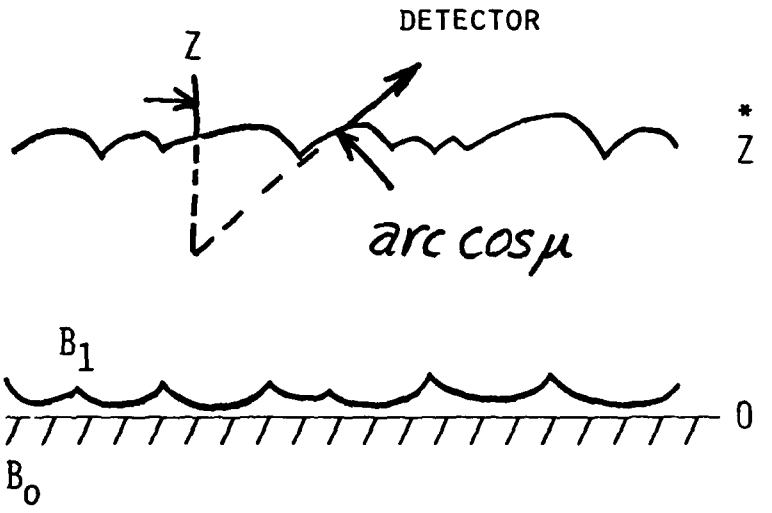

B_o = PLANCK FUNCTION @ $11.5\mu m$ FOR GROUND TEMPERATURE T_o

B_1 = PLANCK FUNCTION @ $11.5\mu m$ FOR SMOKE TEMPERATURE T_1

BOUNDARY CONDITIONS:

$$I(Z^*, \mu<0) = 0$$
$$I(0, \mu>0) = B_o$$

The spectral radiance emerging from the smoke, I, at an angle, arc cos μ , with respect to zenith satisfies the equation of radiative transfer

$$\mu \frac{dI}{dz} = - kI + \frac{ka}{4\pi} \int_{4\pi} P(\Omega' \rightarrow \Omega)\ I\ (\Omega')d\Omega' + (1-a)k\ B_1$$

where B_o and B_1 are Planck functions evaluated at 11.5 μm for the ground temperature T_o and smoke temperature T_1 respectively.

The radiative transfer equation is solved in terms of a Neumann solution which keeps track of the various orders of scattering, see Irvine (1965). The spectral intensities, I, are presented in terms of equivalent brightness temperatures in Tables 4 and 5. Note that the smokes viewed from above (μ = .974) have a brightness temperature closer to that of the underlying ground (36.8°C) than they exhibit when they are viewed at a grazing angle (μ = .149). It is also evident that the brightness temperatures approach those of a black body at the smoke temperature for thick smokes at 31.6 gm/m^2. However the C-1 cloud, which produces more scattering approaches this limit more slowly.

We intend to extend this analysis to include calculations of the radiative effects of ash as well as carbonaceous and water aerosols.

3.2 Finite Cuboidal Smoke Clouds

The influence of the finite horizontal extent on the transport of infrared radiation through smoke clouds can also be computed. Because smoke clouds can assume many shapes, a simple analytical radiative transfer model has been developed. While Weinman and Davies (1978) employed three dimensional Eddington approximation to derive microwave radiances emerging from finite clouds of precipitation, it was noted that the Eddington approximation could yield emissivities slightly greater than unity in plane parallel clouds. Because the two stream approximation did not produce this artifact, we adapted it to the transfer of radiation in cuboidal smoke clouds. The equation of transfer in three dimensions is transformed into an inhomogeneous Helmholtz

equation with prescribed boundary conditions. The solutions are in the form of double Fourier series.

Some illustrative results are shown in Figures 2 and 3. They show, respectively, cuboidal clouds having optical dimensions of 1 x 1 x 1 and 1 x 1 x 5 at $\lambda = 10$ μm. Water clouds are represented by scattering properties, $a = 0.638$, $b =$ and $g_1 = 0.865$. Emission refers to the hemispheric flux exiting from each face of an isolated cloud whereas transmission refers to the flux exiting the faces of a non-participating cloud over a surface. The total flux exiting the cloud faces may be obtained by a superposition of the two patterns weighted by the Planck function at their respective temperatures. The cloud is assumed to be isothermal, although in principle a temperature lapse rate within the cloud is permissible. H and L on the figures refer to regions of relatively high and low flux values. Thus, in emission, the center of the cloud is brighter than the edges, whereas in transmission, the edges are brighter due to leakage. It may be noted that there is a lack of any feature on the reflected face for the 1 x 1 x 5 case.

It is possible to model the infrared radiance viewed by a sensor directed at an isolated cuboidal cloud. The viewing geometry is shown in Figure 4 in plan and elevation. Restricting ourselves to the average intensity over the projected area of the cloud viewed side-on ($\phi = 0°$), it is possible to compute this radiance as a function of zenith angle. For comparison with observations, it is assumed here that the arbitrary shape of a real smoke cloud will eliminate any azimuthal preference and the single case of $\phi = 0°$ will suffice. Figures 5 and 6 give the average radiances as a function of zenith angle for clouds of optical depth, Z* equal to 1 and 5 respectively. The various curves on each figure correspond to the horizontal dimension, again in optical depth units. The anisotropic nature of the radiance pattern is clearly visible. The above

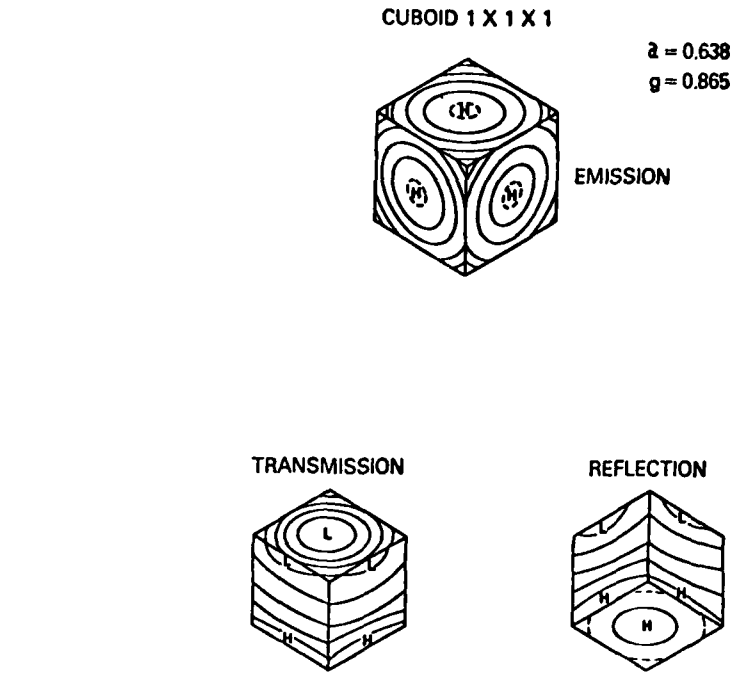
CUBOID 1 X 1 X 1
a = 0.638
g = 0.865
EMISSION
TRANSMISSION
REFLECTION

Fig. 2

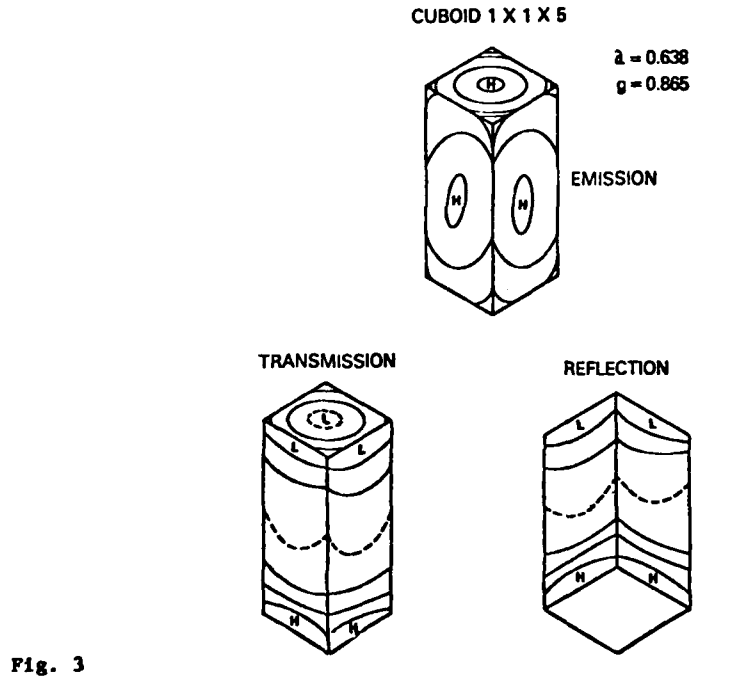
CUBOID 1 X 1 X 5
a = 0.638
g = 0.865
EMISSION
TRANSMISSION
REFLECTION

Fig. 3

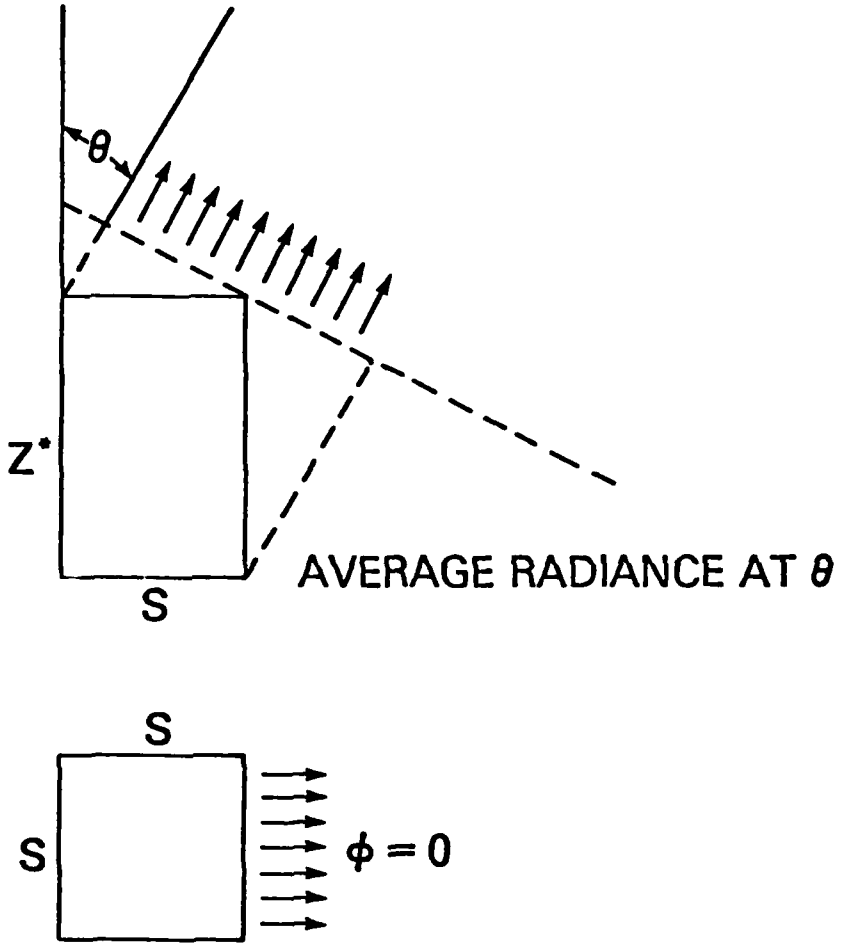

Fig. 4

Fig. 5

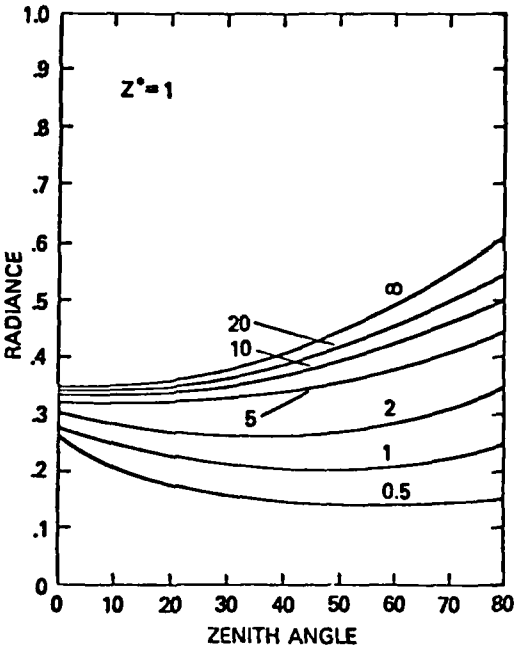
Z°= 1
RADIANCE
ZENITH ANGLE
∞
20
10
5
2
1
0.5
0
.1
.2
.3
.4
.5
.6
.7
.8
.9
1.0
0 10 20 30 40 50 60 70 80

Fig. 6

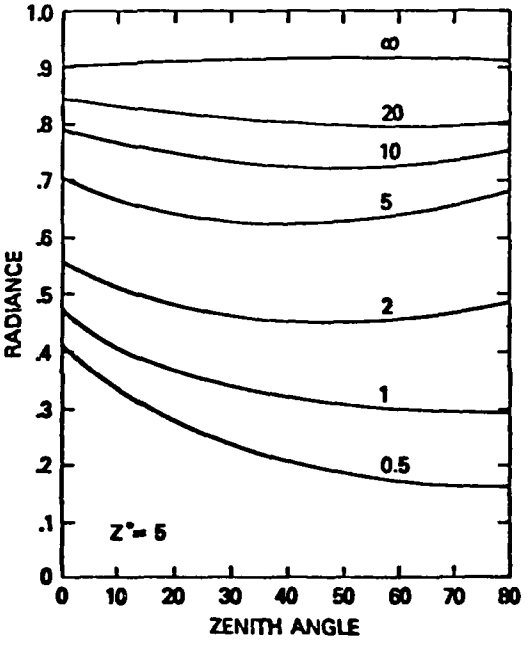
Z°= 5
RADIANCE
ZENITH ANGLE
∞
20
10
5
2
1
0.5
0
.1
.2
.3
.4
.5
.6
.7
.8
.9
1.0
0 10 20 30 40 50 60 70 80

cases were for isolated clouds. The combined radiance pattern of a cloud at 250°K overlying a surface at 300°K is shown in Figure 7 for optical dimensions 10 x 10 x 2 compared to the infinite cloud situation. The contribution of the side faces to the radiance at large zenith angles is a prominent feature of the results. The local maximum is a function of the geometry of the cloud. The results obtained by this analytical method must be compared with Monte Carlo simulations to give some measure of confidence. These simulations are in the process of development. Once it is established that the analytical method provides answers within prescribed errors for a range of geometries and cloud properties, then computations of radiances may be considered meaningful. However the last three figures clearly demonstrate the importance of the extent of a smoke cloud on the infrared radiances emerging from such clouds.

In summary, we have been able to construct simple analytical models to treat infrared radiative transfer in clouds of infinite and finite horizontal extent. It is still necessary to model clouds embedded in a participating atmosphere. For infinite clouds this is a simple problem but for finite clouds some approximating assumptions will be required.

4. Acknowledgments:

This research was mainly supported by funding provided by ARO-D grant DAAG 29-76-G-0109. Some facilities used in this research were also provided by the NASA Goddard Laboratory for Atmospheric Science as part of NASA grant NSG5209. We thank these agencies for their support.

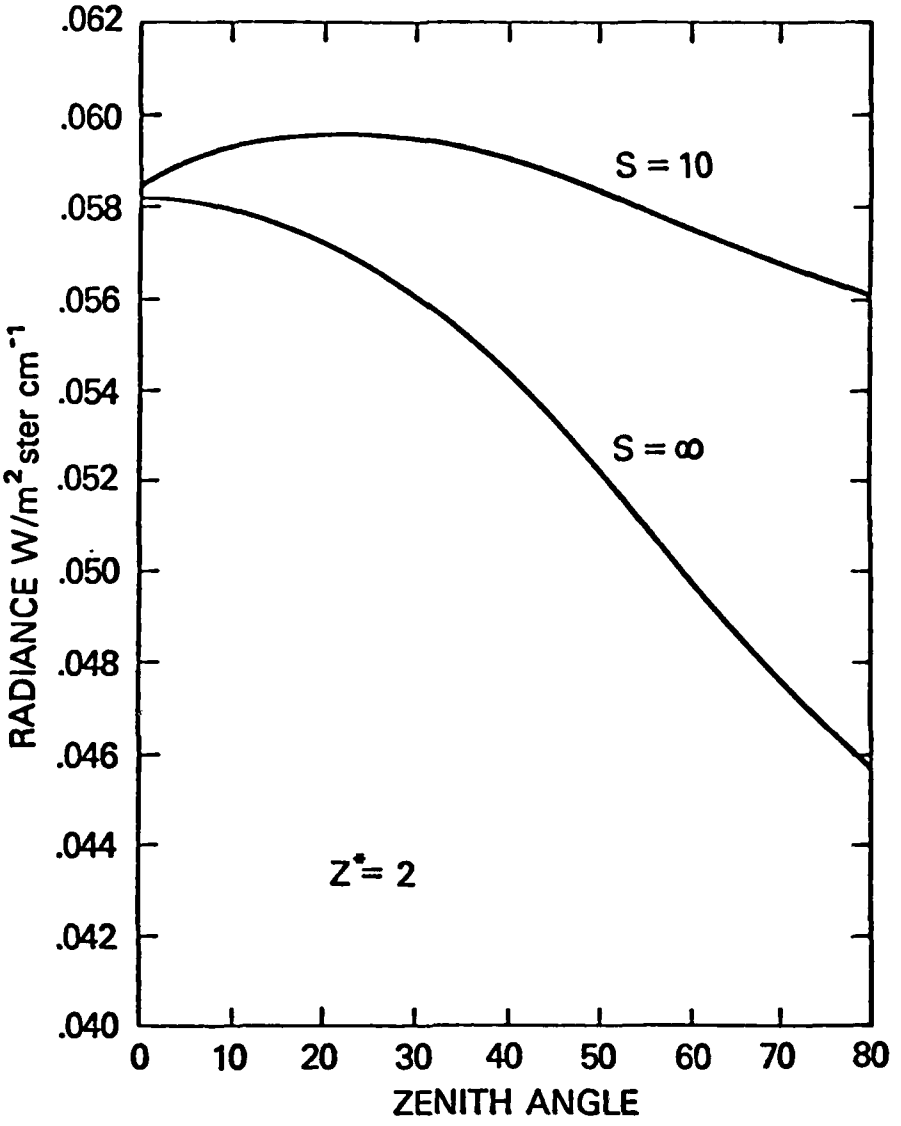
.062
.060
.058
.056
.054
.052
.050
.048
.046
.044
.042
.040
RADIANCE W/m² ster cm⁻¹
S = 10
S = ∞
Z* = 2
0
10
20
30
40
50
60
70
80
ZENITH ANGLE

Fig. 7

References

Carpenter, A.B., True, D.K., Stanek, E.J. (1977): Leaf Burning as a Significant Source of Urban Air Pollution, J. Air Pollution Cont. Assoc., 27, 574-6.

Connor, W.D., Hodkinson, J.R. (1967): Optical Properties and Visual Effects of Smoke Stack Plumes, U.S. Dept. of H.E.W. Doc AP30 pp 89, Cincinnati, Ohio.

Deirmendjian, D. (1969): Electromagnetic Scattering on Spherical Polydispersions, Am. Elsevier Pub. Co., NY pp 292.

Irvine, W.M. (1965): Multiple Scattering by Large Particles. Astrophys. J., 142, 1563-1575.

Pilipowskyj, S., Weinman, J.A., Clemesha, B.R., Kent, G.S., Wright, R.W. (1968): Investigator of the Stratospheric Aerosol by Infrared and Lidar Techniques, J.G.R., 73, 7553-7560.

Twitty, J.T., Weinman, J.A. (1971): Radiative Properties of Carbonaceous Aerosols, J. App. Met., 10, 725-731.

Vines, R.G., Gibson, L., Hatch, A.B., King, N.K., Mac Arthur, D.A., Packham, D.R., Taylor, R.J. (1971): On the Nature, Properties and Behavior of Bush-fire Smoke. C.S.I.R.O., Melbourne, Australia. Div. of App. Chem. paper #1, pp 32.

Weinman, J.A., Davies, R. (1978): Thermal Microwave Radiances from Horizontally Finite Clouds of Hydrometeors, J. Geophys. Res., 83, 3099-3107.

Figure Captions

Figure 1. Schematic view of radiative transfer in a plane parallel model cloud.

Figure 2. Flux patterns on faces of a cloud of optical dimensions 1 x 1 x 1.

Figure 3. Flux patterns on faces of a cloud of optical dimensions 1 x 1 x 5.

Figure 4. Viewing geometry for sensing average radiance from cubic cloud.

Figure 5. Average radiance as a function of zenith angle for isolated cloud of optical depth, $Z^* = 1$.

Figure 6. Same as above but with $Z^* = 5$.

Figure 7. Average radiance as a function of zenith angle for a cloud of optical dimensions 10 x 10 x 2 and infinite cloud of optical depth 2 at 250°K over surface at 300°K.

II. PHYSICAL AND CHEMICAL PROPERTIES OF AEROSOLS

EXPERIMENTAL AND THEORETICAL INVESTIGATIONS OF THE FORMATION AND GROWTH OF SCREENING SMOKES

S.H. Baek and J.R. Brock
Department of Chemical Engineering
University of Texas at Austin
Austin, Texas 78712

PUBLICATIONS

J.R. Brock, "The Kinetics of Ultra-Fine Particles", in W. Marlow, Ed. Aerosol Microphysics, vol. 1, Springer Verlag, Heidelberg, 1979.

S.H. Suck and J.R. Brock, "Evolution of Atmospheric Aerosol Particle Size Distributions: A Simulation of Brownian Coagulation Dynamics", J. Aerosol Science (1979).

S.H. Baek, J.E. Harris and J.R. Brock, "The Evaporation Rate of Complex Hydrocarbon Oils with Low Ambient Vapor Pressures: Experiment", Submitted for Publication.

K.S. Yom, S.H. Baek and J.R. Brock, "The Evaporation Rate of Complex Hydrocarbon Oils with Low Ambient Vapor Pressures: Theory", Submitted for Publication.

S.H. Baek, K.S. Yom and J.R. Brock, "Lower Bound Estimates of Fog Oil Droplet Lifetimes", Submitted as CSL Note.

INTRODUCTION

The effectiveness of a given obscurant material depends importantly[1] on the particle size, shape and composition in the dispersed state. These properties are determined by particle growth and dispersion processes. Our experimental and theoretical program is concerned with the investigation of these processes.

In general, screening smoke formation involves several steps: particle formation, growth, and dispersion. The first step involves the various nucleation processes involved in particle formation from molecules in a smoke generating system. Subsequent to particle formation, the growth of particles take place by coagulation and condensation processes[2] which lead to particle size distributions which may be largely independent of the details of the nucleation process.

At the same time, turbulent dispersion of the smoke plume modifies the particle size distribution and will tend to decrease smoke particle number density and thereby to suppress the growth processes. Also, the particles themselves may alter the dispersion of the plume.

In the case of a smoke generated by cooling of hot vapor, the nucleation process is governed by the local supersaturation of condensable vapor whose concentration is given by the stochastic conservation equations;

$$\partial C_A/\partial t + \overline{V}\cdot\nabla C_A = \nabla D\nabla C_A + \sigma A \qquad (1)$$

$$\rho C_p \frac{\partial T}{\partial t} + \rho C_p \overline{V} \nabla T = \nabla K\cdot\nabla T + \sigma_h \qquad (2)$$

Together with the equation of motion and appropriate boundary and initial conditions. C_A is the concentration of condensable vapor A, σ_A and σ_h are sources or sinks of vapor and heat, and the other symbols have their usual definitions.

It is assumed that cooling of the vapor emitted from an orifice of diameter L, occurs by mixing and heat transfer between the vapor jet and external air. As cooling proceeds, supersaturation of A increases to the point where homogeneous and/or heterogeneous nucleation may occur. At some axial downstream distance x_o, such that $x_o/L<<1$, homogeneous nucleation has terminated[2] and subsequent particle growth entails condensation of vapor on existing nuclei and coagulation.

In the case of smokes generated by chemical reactions, including combustion, the nucleation step occurs in the combustion zone and particle growth occurs subsequently by condensation and coagulation.[2] In the case of hygroscopic smokes this would include condensation of water vapor.

At a sufficiently large distance downstream, the particle size distribution is governed almost entirely by the dispersion of the plume. Particle growth processes are suppressed in this region owing to the decrease in particle and vapor concentrations.

We have undertaken first an experimental and theoretical investigation of the formation of oil fogs. The more complex problem of smoke formation by combustion and chemical reaction will be studied subsequently.

This paper begins with a description of our work towards understanding the formation of oil fogs. This includes a detailed investigation of some of the important properties of the complex oils used as obscurant materials. We close with a description of the experimental facility developed for the study of the formation of oil fogs in a hot, turbulent jet.

THE VAPOR PRESSURE OF COMPLEX OILS

A number of complex oils are in common use as obscurant materials. These include the fog oils, SGF-1 and SGF-2, diesel oils, and others. These materials are extremely complex and consist of many thousands or hundreds of thousands of different chemical species. Any investigation of the formation and growth of these oil fogs must first consider the meaning of the vapor pressure of such complex mixtures and the role of this complexity in the resultant particle size distribution.

The piezoelectric microbalance technique

A new experimental technique has been used[3] to study the evaporation rates of complex hydrocarbon oils with low ambient vapor pressure. The technique follows the evaporation of an oil film on a piezoelectric quartz crystal in a vacuum.

The piezoelectric quartz crystal microbalance represents a very useful method for the study of the evaporation rates of complex mixtures. A schematic diagram of the system is shown in Fig. 1. The system is extremely sensitive to mass changes of films deposited on the quartz crystal with ultimate resolution of the order of tenths of nanograms. The papers presenting our results[3,4] may be consulted for details of our measurement procedures.

The validity of our procedures was examined experimentally by the measurement of the vapor pressure of a pure substance, dioctylphthalate (DOP), which has been studied previously by other methods.[5,6,7] According to exact free molecular theory, the time derivative of fraction evaporated, E, at a given temperature, T, is given by:

$$\frac{dE}{dt} = \alpha m \bar{v} P_v A / 4 M_o k T \qquad (1)$$

where α is the evaporation coefficient (we assume $\alpha = 1$). m is the molecular mass of an oil molecule, $\bar{v}$ the mean molecular speed, k Boltzmann's constant, and A is the total surface area of the evaporating film (assumed to be constant).

Application of the relevant equations to the data for DOP yields a vapor pressure of 0.96×10^{-4} dyne/cm^2 at 24°C. Vapor pressure determinations at such low pressures have been difficult in the past. Values reported in the literature for DOP at 25°C are: 3.07×10^{-4}[5], 1.89×10^{-4}[6], 1.89×10^{-4} [8], and 0.93×10^{-4} [7] dyne/cm^2. The first three values we believe to be not as reliable as the fourth as, among other deficiencies, they are all obtained by extrapolation to 25°C of experimental values at higher temperatures. We believe that the value[7] 0.93×10^{-4} dyne/cm^2 is more reliable (estimated by the authors[7] to be accurate to ~ 30%) in that it is based upon free molecular theory and dew point determination under high vacuum ($\lesssim 10^{-7}$ mmHg) at 31°C so that extrapolation of experimental data to 25°C was over only a small temperature range (~6°C). Consequently, our reported value for dioctylphthalate appears to be satisfactory and our experimental system is capable of providing reliable information on the evaporation rates of complex oil mixtures at very low vapor pressures.

Figs. 2 and 3 present the experimental results for the four complex oil mixtures whose evaporation rates were studied. Initial evaporation of the oils is most easily assessed by inspection of Fig. 2. The asymptotic behavior for large times is illustrated in Fig. 3.

It is obvious from Fig. 2, that for undistilled #2 diesel oil, E varies vearly linearly with time up to E ~ 0.8. This is consistent with a rather narrow distribution of hydrocarbon molecular weights of the lighter components so that the initial evaporation resembles a single component system. Above E ~ 0.8, E exhibits non-linearity indicative of the pressure of a relatively broad distribution of mole-

cular weight and vapor pressure. Such behavior is more pronounced for the other less volatile oil in our experiments; #2 diesel oil is a relatively narrow boiling fraction in oil refinery runs.

The complex oil mixtures examined consist of many thousands of various hydrocarbon species; evan now, only a few of these chemical species have been identified.[9] In our analysis we have not sought complete chemical identifications, but instead use empirically determined relationships between molecular weight, vapor pressure, and other parameters.

The effect of thermal cracking of high molecular weight hydrocarbon species on the evaporation rate is shown in Figs. 2 and 3 for undistilled and distilled (at 1 atm. pressure) fog oil SGF-2. The distillation termperatures ranged from 340°C to over 500°C; at higher temperatures a residual tarry fraction of about 5% of the initial oil sample was found. As is evident from a comparison of the undistilled and distilled, recombined oil, the vapor pressure has been increased for the latter by thermal cracking.

By inspection of Fig. 2, it can be inferred that the two crude oils consist of a broad range of high molecular weight species; the curves are non-linear even for very small times.

The asymptotic behavior of these oils is indicated in Fig. 3, where E is given as a function of 1/t. A notable feature of this plot is the linearity of E vs 1/t for smaller values of 1/t. There is a relatively large region of 1/t where linearity is observed for #2 diesel oil and the distilled SGF-2 at 50°C and 23°C, but this is not evident for the undistilled SGF-2 or the two crude oils.

Complex hydrocarbon oils such as those we have studied (#2 diesel oil, SGF-2, and two crude oils) consist of many thousands of different chemical species. It is of course not exact to characterize the evaporation rates of these mixtures in terms of concepts such as "average molecular weight" or "average vapor pressure", although similar approximations may be sufficient in special cases.

It is possible, however, to develop a more satisfactory, though still approximate, analysis of the evaporation rates of these mixtures in the experimental system used here. This analysis rests on the following assumptions:

(1) The liquid oil is a mixture with vapor pressure given by Raoult's law. Since most components consisting of oil mixtures are hydrocarbons, obviously, this assumption can be relaxed by introducing activity coefficients for non-ideal mixtures, but this additional complication will not be considered.

(2) Evaporation takes place in the free molecular regime and the liquid phase is always at or very near equilibrium, with regard to thermal and diffusive flows. Evaporation in the piezoelectric microbalance is carried out at pressures $\lesssim 10^{-4}$ torr with a constant leak to purge the system of evaporated oil vapor. The crystal has a diameter of 1.4 cm. and the mean free path in the gases $\lesssim$ 50 cm; therefore the conditions are free molecular since $K_n \gtrsim 30$. The oils studied have very low vapor pressures and the piezoelectric crystal is in contact with a thermostatic bath in the system; these conditions en-

sure thermal equilibrium. The deposited oil films have thicknesses ~ 0.1 - 1.0μm which indicates diffusional relaxation times, even for very low diffusion coefficients ~ 10^{-8}cm^2/sec., of $\lesssim$ 1 sec. which is small in comparison with the rate of evaporation; consequently, diffusive equilibrium is approximated closely.

(3) The various chemical species in the oil are so numerous that the molecular weight or mass, m, may be regarded as a continuous parameter. n(m,t) dm, therefore, gives the number of chemical species in a liquid oil having molecular masses in the range m, dm at time, t. From n(m,t) one defines the total number, N(t), of chemical species in the oil sample:

$$N(t) = \frac{b}{a} \; n(m,t) \; dm \qquad (2)$$

and total mass, M(t):

$$M(t) = \frac{b}{a} \; m \; n(m,t) \; dm \qquad (3)$$

with little error for high molecular weight oils: a=0, b=∞.

(4) The vapor pressure of the oil is given as a unique function of the molecular weight or molecular mass, m. This assumption is implicitly made in the petroleum industry where, for an oil of given characterization factor,[10] molecular weight is specified as a function of boiling point. More explicitly, for various classes of substances such as polyesters, dibasic esters, mineral oils, etc. at a given temperature, empirical relations have been found between vapor pressure, P_v, and m:

$$P_v = \alpha e^{-\beta m} \qquad (4)$$

where α and β are constants (4).

These various assumptions permit the development of a theory for the evaporation of complex oil mixtures in our piezoelectric microbalance.

If the experimental system consists of the piezoelectric microbalance and an oil film of some pure substance, the appropriate expression for the mass fraction of this substance evaporated, E, as a function of time would be:

$$E = 1-M(t)/M(o) = (mP_v\bar{V}A/4M(o)kT)t \qquad (5)$$

where M(o) and M(t) are respectively the total initial mass of oil on the crystal with total oil surface area A and the total mass at time t. $\bar{V}$ is the mean molecular speed and kT is the thermal energy. As is obvious from this equation, E for evaporation of a pure substance in our system is a linear function of time, t. In this case t increases until E=1 where the sample is completely evaporated. This is, of course, not the case for the complex oils we have studied. With the assumptions listed above, however, the evaporation rate of complex oils in the piezoelectric microbalance system may be described. From

free-molecular theory, with the introduction of the density function $n(m,t)$, we obtain for the time rate of change of $n(m,t)$:

$$\frac{dn(m,t)}{dt} = - \frac{(A/\sqrt{2\pi mkT}\ P_v(m)\ n(m,t)}{n(m,t)dm} \qquad (6)$$

Equation (6) is a non-linear integro-differential equation whose solution for realistic $n(m,o)$ and $P_v(m)$ must be obtained numerically.

Equation (6) can be solved formally for $n(m,t)$:

$$n(m,t) = n(m,o)\exp\left[\frac{- AP_v(m)}{\sqrt{2\ \pi\ mKT}} \int_o^t \frac{d\zeta}{N(\zeta)} \right] \qquad (7)$$

From this, the experimentally observed quantity, E, is:

$$E = 1 - \frac{1}{N(o)} \int_o^\infty n(m,o)\ m\ \exp\left[\frac{- AP_v(m)}{\sqrt{2\pi\ mKT}} \int_o^t \frac{d\zeta}{N(\zeta)} \right] dm \qquad (8)$$

This equation reduces properly to equation (5) for a single component.

Equation (8) is, of course, merely a formal solution. The explicit solution of (8), discussed subsequently, can only be obtained numerically for realistic $n(m,o)$ and $P_v(m)$ for complex oils. In a number of special, but possibly unrealistic cases, an explicit solution of equation (8) is possible. For example, when $P_v(m)m^{-1/2} \sim m^{-1}$, E is a linear function of t.

A very approximate idea of the form of $n(m,o)$ can be obtained from batch distillation data. For distilled "100 pale oil" $n(m,o)$ was estimated roughly from batch distillation data (at 1 atm.) and the empirical relation between characterization factor, normal boiling point and molecular weight. Figure 4 shows the form of $n(m,o)$ deduced in this way. The bimodal form displayed indicates that this sample is a blend of two oils of separate boiling ranges; such blending is common in the formulation of lubricating oils.[11]

We have carried out a numerical analysis of equation (8) and have found that theoretical curves for E vs t can be generated which agree well with the experimental curves. This leads to the determination of the parameters α and β of equation (4) for these complex oil mixtures. Our paper on this subject be consulted for details.

Lower bound estimates of fog oil droplet lifetimes

For fog oil SGF-2 and #2 diesel oil, the lifetime of an isolated oil droplet particle size (down to lower bound of validity calculations of $R_i \simeq 10^{-5}$cm.) has been calculated using the experimental evaporation data and non-continuous droplet evaporation theory. The results are given in Fig. 5, where the ordinate is the lower bound

estimate of the lifetime of an oil droplet in hours and the abscissa is the radius of the oil droplet at the start of evaporation. For example, an isolated droplet of #2 diesel oil with an initial radius of 3×10^{-5}cm. reaches 10^{-5} radius in around 0.3 hours (18 min.). As pointed out earlier, however, in a plume the lifetime will be longer than this because of the presence of neighboring oil droplets which act to maintain a partial pressure of oil vapor (taken to be zero for the isolated droplet). The actual time for a droplet to evaporate to 10^{-5}cm radius will be longer therefore, and will depend on ambient conditions. For highly unstable atmospheric conditions (high wind speed, strong surface heating), the lifetime will approach the lower bound estimate.

In any event, diesel oil appears to be rather volatile for a screening substance in spite of its convenience.

By way of contrast, a fog oil SGF-2 droplet lifetime calculation has been carried out using vapor pressure estimates supplied by CSL based on extrapolations of high temperature distillation data for SGF-2. This extrapolation is inaccurate but conservative as it underestimates droplet lifetimes.

MODELLING NUCLEATION AND GROWTH OF COMPLEX OIL FOGS

A first question which we thought should be examined in our investigation of oil fog formation and growth was the role of the complexity of these oils in the particle growth processes. Do these complex oils yield particle size distributions which differ from what might be expected for oil fogs formed from a pure vapor or vapors of mixtures of relatively small numbers of chemical species?

We are now examining this question both theoretically and experimentally.

Theoretical approach

In our theoretical approach we start with a kinetic aerosol model which has been worked out sometime previously.[12] This general model is used in conjunction with our model for the vapor pressure of a complex oil as outlined above and discussed in detail in our recent papers.[3,4] These results will be presented in a forthcoming publication.[13]

In the next section, our experimental approach in simulation of oil fog generation is presented. The experimental system will be used in tests of our theoretical model.

Experimental approach

Our experimental approach is designed to simulate the salient features of oil fog growth. These include, in the most realistic

case, nucleation and particle growth in a hot, turbulent circular jet. These features are present in fog oil generator technology. A description of our system and preliminary test results of the system are given in the final section of this paper.

The study of formation and growth of an oil fog in a hot, turbulent jet is a difficult undertaking. In fact, the system contains the two remaining unresolved problems of classical physics--nucleation and turbulence. Consequently, useful progress will require some innovations in experimental techniques. We are investigating several innovative approaches, but these will not be discussed here. Instead, our current approach is described which utilizes more traditional methods for experimental analysis and observation.

An experimental system has been constructed to permit the in situ observation and measurement of oil fog growth. A dense oil fog represents a highly unstable state. As a consequence, sampling as a means for measuring particle size distribution cannot be considered to be reliable. Of course, the introduction of a sampling probe into a jet will also result in substantial perturbations of the various growth and dispersion processes.

Fig. 6 shows the complete experimental system. It is divided into five major parts: clean air supply, vapor generator, air supply, aerosol growth chamber, and optical and data acquisition system. Details of important elements are shown in Figs. 7,8,9,10, and 11.

a. Clean air supply

Air is supplied to the system from either the building air supply (150 psi), or a rotary pump. Air passes through a fiberglass prefilter (a-3), liquid nitrogen cold trap, silica gel dehumidifier (a-4), absolute filter of 0.22 micron pore size (a-5), a linear pressure regulator (a-6), and finally to the surge tank (a-7) for distribution to the system. The air temperature and humidity are monitored at the jet inlet. Maximum air cleaning capability of this system is about 70 l/s.

b. Humidity control

The temperature and humidity of air supplied to the generator are controlled to simulate different environmental situations. A desired humidity is achieved by mixing in proper proportions of saturated air with dried air. The temperature and humidity are monitored in the mixing chamber.

c. Aerosol generator

In the study of fog oils, vapor is generated in a boiler as shown in Fig. 7. This is made of 3" O.D. X 10 1/2" long No. 306 stainless steel tubing. A 3 Kw electric heater and several layers of coarse copper mesh vaporize smoke oil which is sprayed into the chamber by a small nozzle. Smoke oil is heated to lower the viscosity at preheater section (b-2). Volumetric flow rate of oil is measured by a rotameter. An inert carrier gas (N_2) is used for carrier gas for the oil vapor. An iron-constantan thermocouple is inserted in the boiler and a safety pressure release valve is installed to protect from over pressure should an explosion occur.

d. Aerosol growth and detection chamber

The central part of the system is the glass chamber for the study

aerosol formation and growth. An optical quality pyrex glass chamber of 4" O.D. X 24" long has four pairs of optical windows, two ports for sensors, two gas inlets and one gas outlet. Figure 8 shows this chamber. It is designed to achieve three different states of flow: laminar jet, transition jet and turbulent jet. Two honey-comb flow collimators are mounted at both ends of the chamber. One side of each optical window can be mounted with either Rayleigh horns or optically flat laser windows.

The specifications of temperature sensors and humidity sensors at the sensing ports are as follows:

Sensor	Sensing Element	Specification
temperature	thermistor, 0.095" dia.	maximum operating range 0-150°C, 0.2°C accuracy, 1 sec response time for 63% temperature change
electrohumidity sensor	chemically treated styrene copolymer	0-100% relative humidity, 2.5% RH accuracy, -5°C-75°C operating temperature, 30 sec to 63% RH change
strain gage relative humidity sensor	inert cellulose crystallite, conditioned Xeric element, piezoresistive and thermally matched strain gage	0-100% RH, 4% RH accuracy, up to 100°C, 1 min. response time to 63% RH change

By translational movement of these sensors, temperature and humidity profiles can be measured inside the glass chamber.

d. Optical and data acquisition systems

The principal aerosol measurement technique adopted for this research is the in situ optical method. Two laser systems; Ar-ion laser and tunable dye laser, are used for this purpose.

High power C.W. Ar-ion laser

maximum power:	all lines	5 watts C.W.
	514.5 nm	2 watts
single line	488.0 nm	1.5 watts
	476.5 nm	0.75 watts
polarization:	vertical	
beam divergence:	0.5 milliradians	
beam diameter:	0.5 cm	
long term stability:	0.5% over 10 hours	
frequency noise:	0.2% rms	

Tunable C.W. dye laser

dye option: Rhodamin-590, 560, 610, Coumarin 450, Disodium fluorescein, Cresyl violet, nile blue

Tunability: from 435 nm to 790 nm, less than 10 Å resolution

maximum power: 1 watt with Rhodamin 590

polarization: vertical
beam divergence: 1.5 milliradians
long term stability: 0.5% over 10 hours
frequency noise: 1% rms

Other optical components are as follows: laser beam expander, broadband polarization rotator (98%-T), optical spectrum analyzer with scanning interferometer, Ar lines and visible range narrow band pass filters, C.W. and pulsed laser power meter, extended spectral S-20 photomultipliers, 50/50 and 2/98 laser beam splitters, visible range nuetral density filters, high power laser beam reflectors, and additional equipment.

Microprocessor and magnetic tape recorder systems are planned for addition in the future.

An electrostatic mobility analyzer has been constructed as shown in figure 9. It will be used for calibration of the optical system and for addition of foreign nuclei to the oil vapor.

Experimental procedures

Smoke agents to be used in our experiments are as follows:

Non-hygroscopic smoke		
	a. single component	glycerol, DOP
	b. multicomponent	binary or ternary mixtures of pure high hydrocarbon substances, fog oil
Hygroscopic smoke		phosphoric acid

In situ aerosol measurement methods:

a. higher order Tyndall spectra to determine the narrowness of the particle size distribution.

b. laser transmission rate for different laser frequencies. This method will give the average particle size and number density if the particle system is reasonably monodisperse. If the particle system is not monodisperse, it will give the average surface-volume dia-

meter--that is, the ratio of second to third moments of particle size distribution.[14]

c. angular laser scattering methods for different frequencies This method will give the parameters of particle size distribution by using either Rayleigh-Gans-Debye theory,[15] or exact Mie theory inversion method.[16]

d. laser induced particle chemiluminescene and chemiluminescent reactions of aerosol particles are being evaluated as supplements to these conventional optical methods.

Sampling methods

a. Climet optical particle counters are available.

b. A cascade impactor of new design is available capable of giving complete particle size distribution with time ersolution of 0.5 sec.

Experimental results

Several preliminary experiments have been carried out of formation of a glycerol aerosol in a smooth laminar flow. Flow was observed up to downstream distances of around 160 nozzle diameters. It is found that the velocities of fog at nozzle and surrounding air must be matched to maintain laminar flow in the system. A velocity mismatch was found to change the flow pattern from laminar to turbulent. By simple visual observation, a transparent aerosol formation region can be confirmed at the edge of the nozzle. This indicates that a supersaturation region exists somewhere between the tip of the nozzle and the region of the fog formation.

The first measurements of laser transmission rates in these preliminary experiments have been carried out. Conditions and results of these experiments are as follows:

nozzle diameter	0.159 cm
volumetric air flow rate	2.27 liters/min
air temperature	24.5°C
relative humidity of air	70%
aerosol generating method	vaporization/condensation of glycerol
aerosol generator temperature	149°C
diagnostic laser	Ar-ion at 488.0 nm, 200mW

length from the nozzle	ratio to diameter of nozzle	transmittance T(%)
3.3 cm	20.75	97.7
15.0	94.33	95.6
25.5	160.37	95.3

These data indicate the feasibility of the use of laser light transmission in the array of in situ optical methods which will be applied in our experimental program.

CONCLUSION

First steps in an experimental and theoretical program for the investigation of the formation and growth of screening smokes have been described. We wish to ensure that the fundamental processes involved in screening smoke generation are, at least in principal, known; their exact descriptions will require considerable time and effort.

Our future plans call for the completion of studies on oil fog generation. After completion of this simpler program, we plan to examine the process of screening smoke generation by combustion as in phosphorous smokes.

REFERENCES

1. Green, H.L. and Lane, W.R., "Particlate Clouds: Dusts, Smokes and Mists", spon ltd., London (1964)

2. Hidy, G.M. and Brock, J.R., "The Dynamics of Aerocolloidal System", Pergamon Press, Oxford (1970)

3. Baek, S.H., Harris, J.E., and Brock, J.R., "The Evaporation Rate of Complex Hydrocarbon Oils with Low Ambient Vapor Pressure I", Submitted for publication.

4. Yom, K.S., Baek, S.H., and Brock, J.R., "The Evaporation Rate of Complex Hydrocarbon Oils with Low Ambient Vapor Pressure II", Submitted for publication.

5. Hickman, K.C.D., Hecker, J.C., and Embree, N.D., I.E.C. 9 264 (1937).

6. Small, K.W. and Cowley, P., "Trans Farad. Soc. 44, 810 (1948).

7. Kopff, S.F. and Jacobs, R.R., Rev. Sci. Instr. 18, 581 (1947).

8. Chang, R. and Davis, E.J. J. Colloid and Int. Sci. 54, 352 (1976).

9. Altgelt, K.H. and Gouw, T.H. in Giddings J. et al Eds., "Advances in Chromatography", Vol 13, Chapter 3, Marcel Dekhez, NY, 1975.

10. API databook, Vol I, tabe 2B2-1.

11. Coburn, J.F. ASME Transaction 12, 129 (1969).

12. Middleton, P. and Brock, J.R., J. Colloid and Int. Sci., 54, 249 (1976).

13. Baek, S.H., Yom, K.S., and Brock, J.R., "Lower Bound Estimates of Fog Oil Droplet Lifetimes", Submitted as CSL Note.

14. Zinn, B.T., Powell, R.A., Cassanova, R.A., and Bankston, C.P., Fire Research 1, 23 (1977).

15. Box, M.A., Lo, S.Y., McKellar, B.H., and Rich, M., Quart. J. R. Met. Soc., 104, 959 (1978).

16. Kerker, M. "The Scattering of Light", Academic Press, New York (1969).

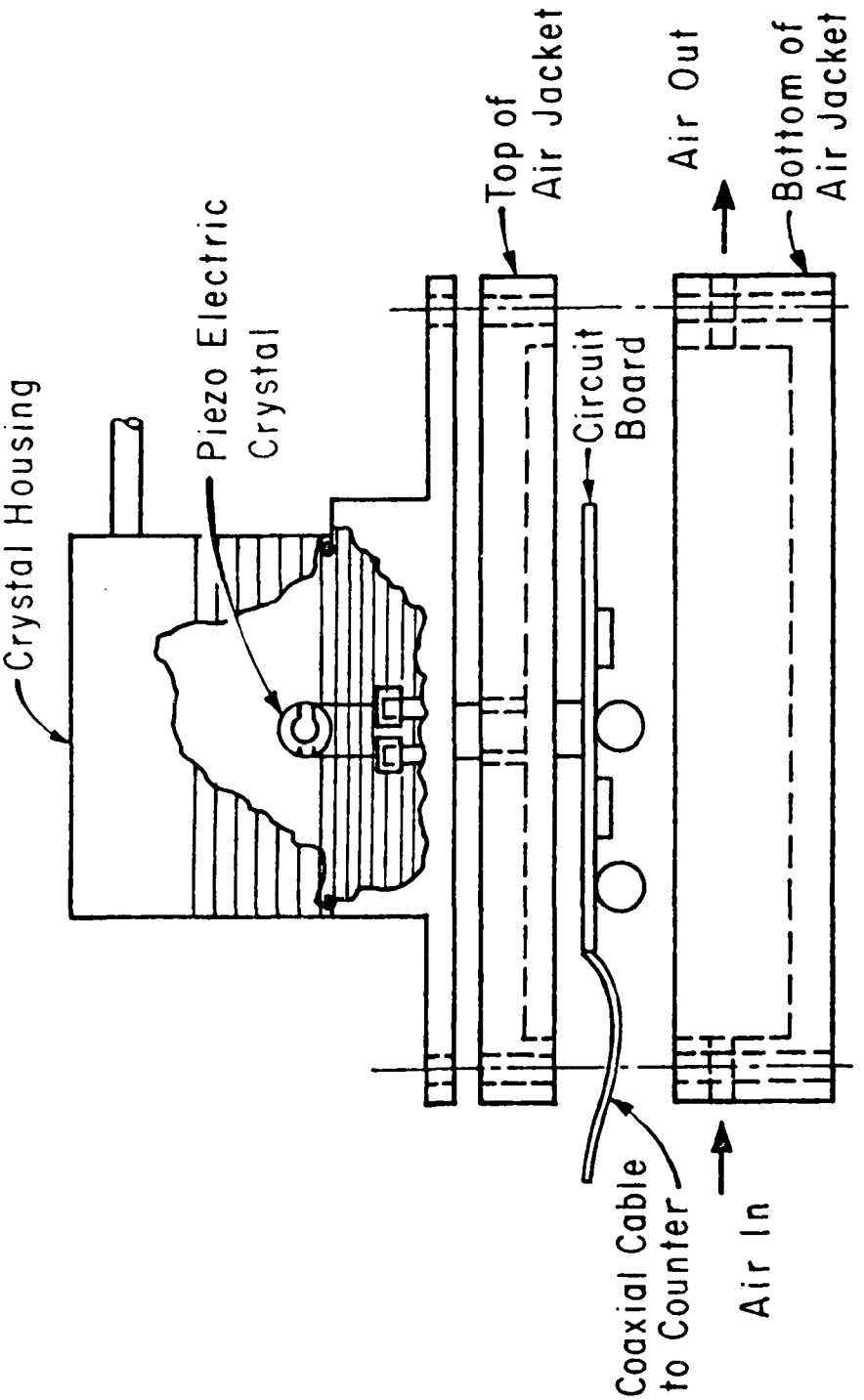

Figure 1 Schematic diagram of quartz microbalance.

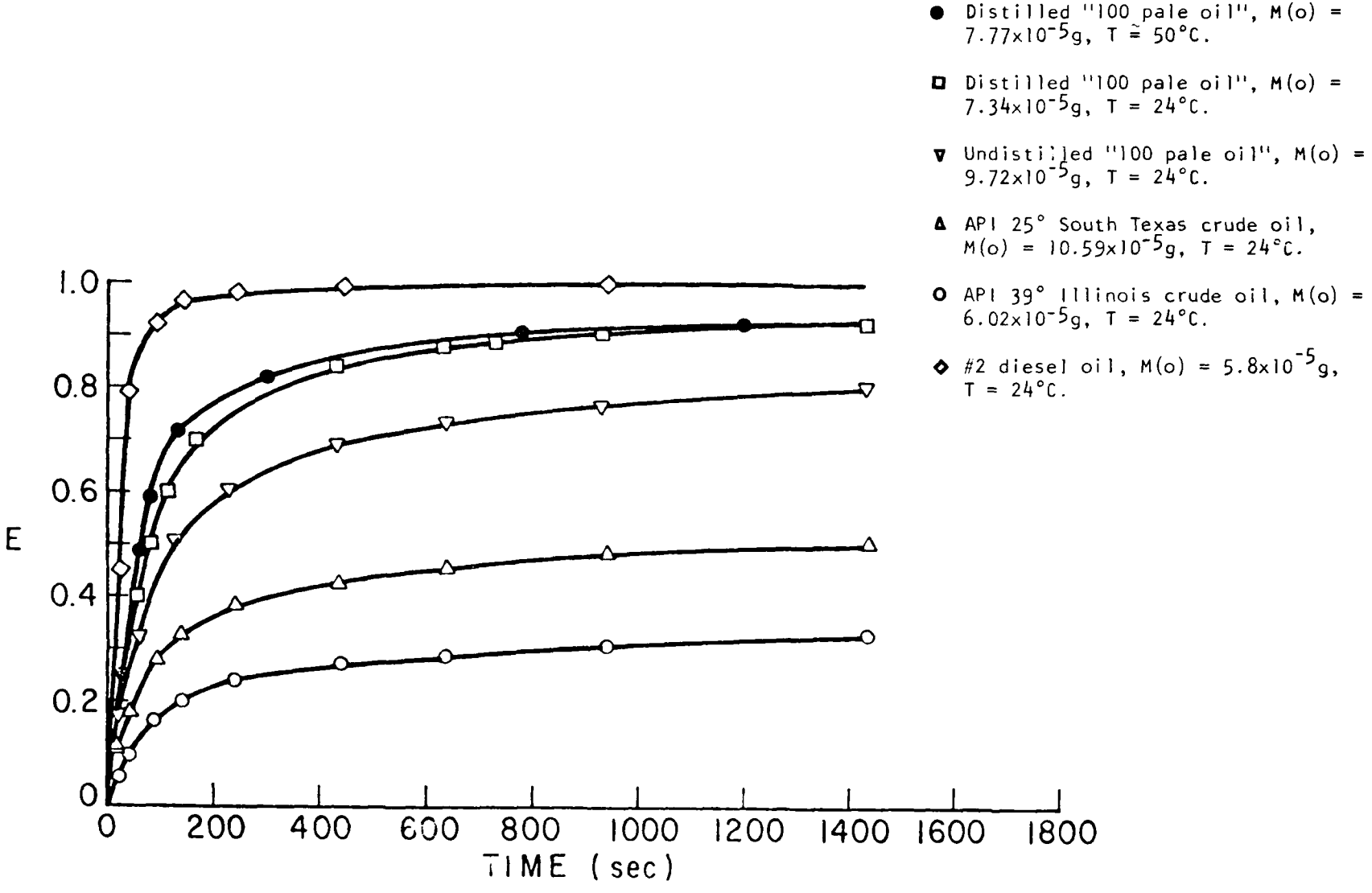

Figure 2. Experimental results for evaporated mass fraction, E, as a function of time t.

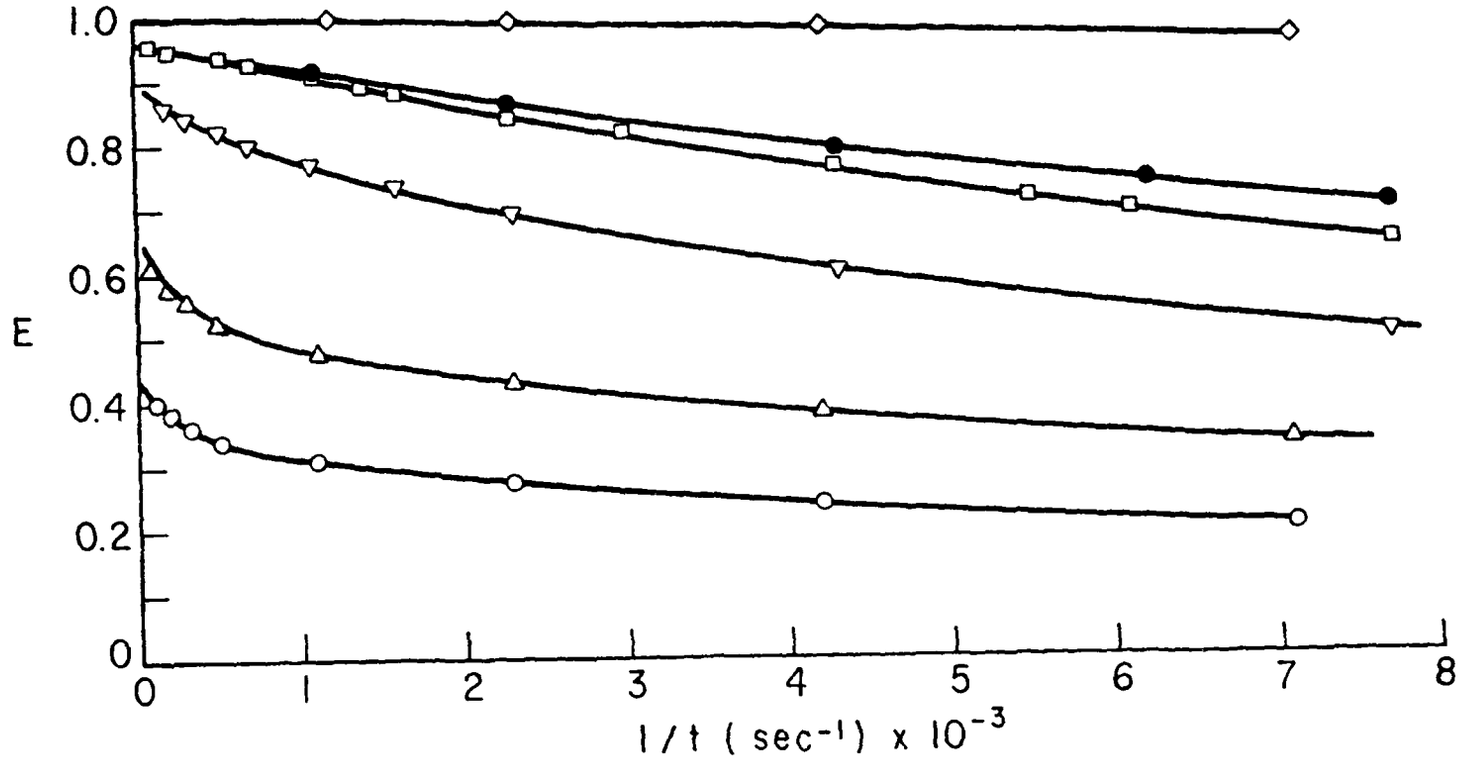

Figure 3. Experimental results for evaporated mass fraction, E, as a function of reciprocal time, 1/t (See legend of Figure 2).

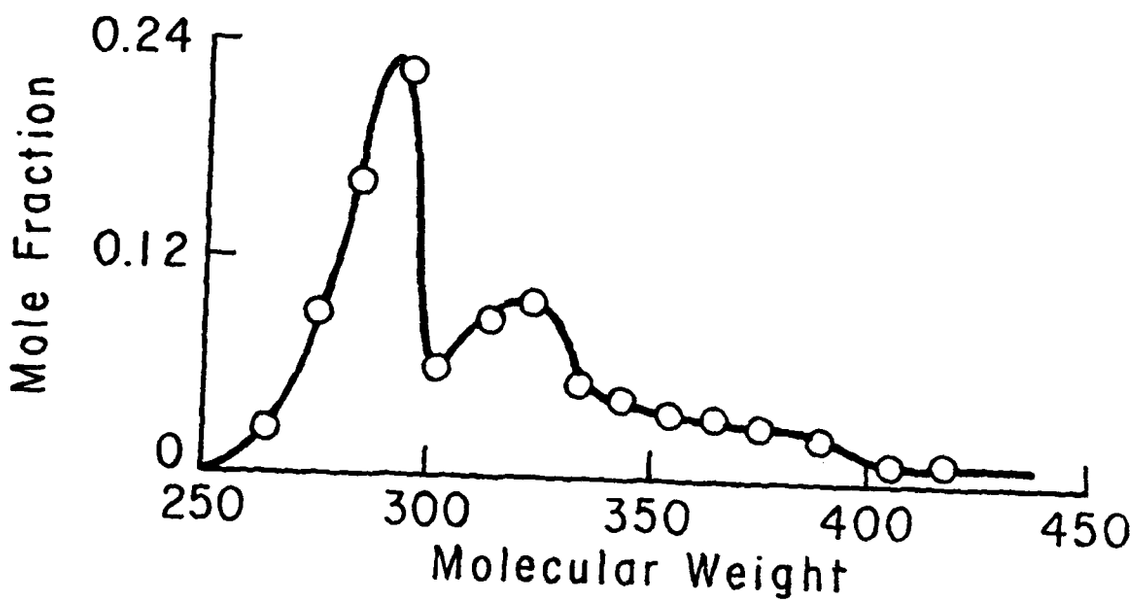

Figure 4. Mole fraction as a function of molecular weight for distilled "100 pale oil" based on estimates from batch distilled data (1 atm.) and empirical relations between characterization factor, normal boiling point, and molecular weight.

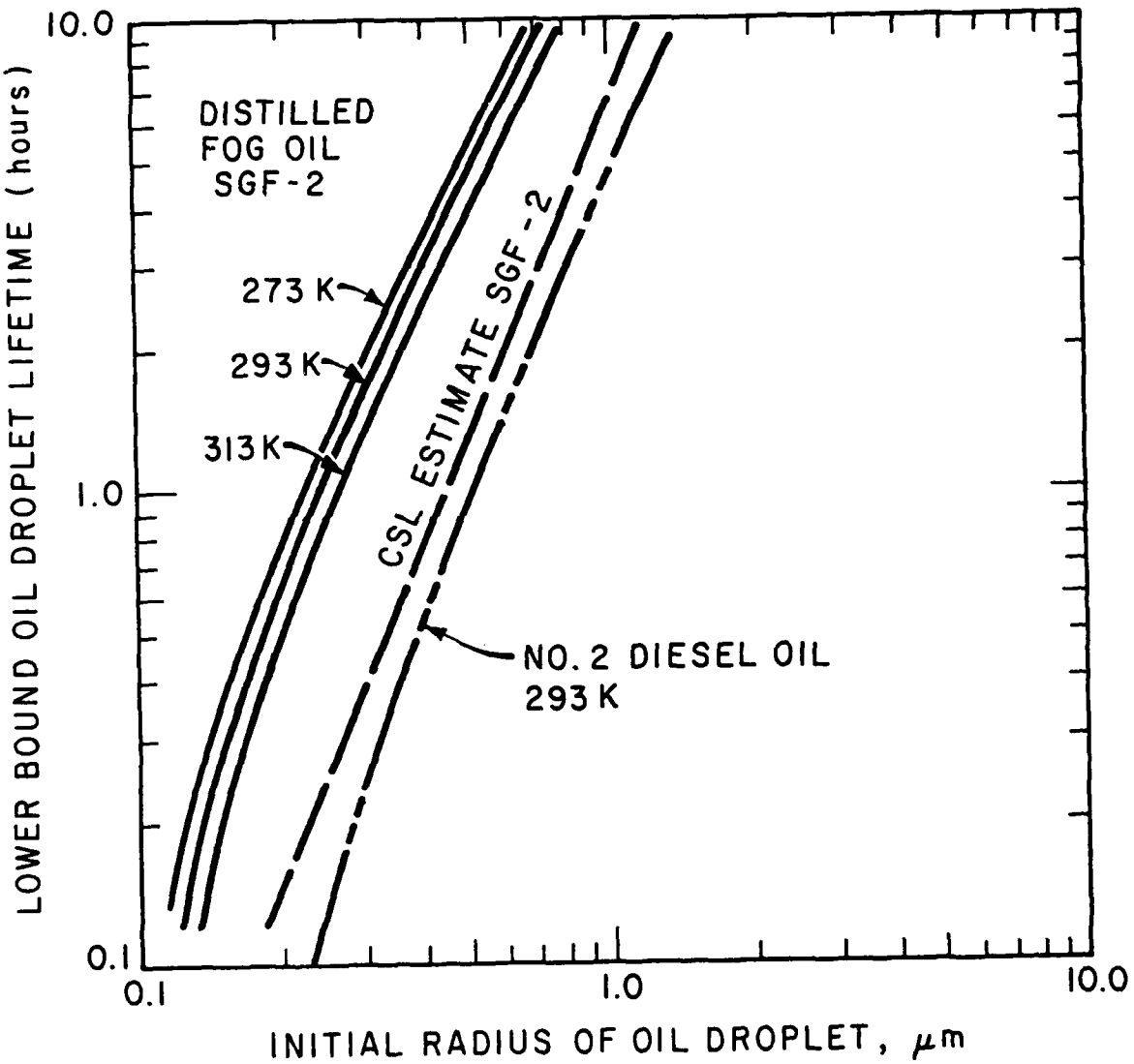

Figure 5. Estimated lower bound oil droplet lifetime.

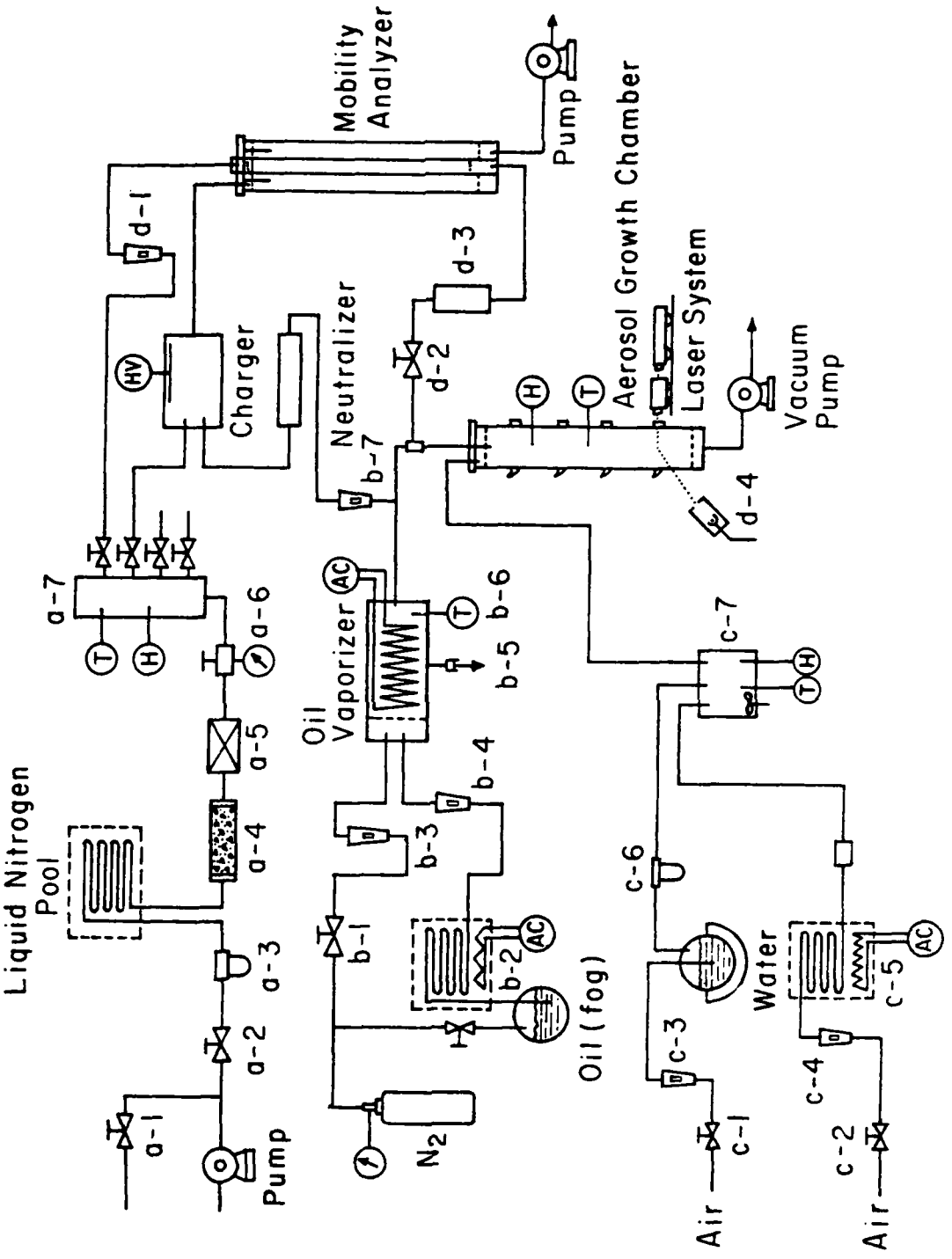

Figure 6. Experimental system for studies of aerosol growth. See legend on next page.

Legend

clean air supply

a-1	control valve
a-2	control valve
a-3	glass wool rough filter
a-4	silica gel dehumidifier
a-5	0.2 micron pore size absolute filter
a-6	linear pressure regulator
a-7	distributing ports

hot oil vapor generator

b-1	control valve
b-2	hot oil bath for heating fog oil
b-3	nitrogen gas flow meter
b-4	fog oil flow meter
b-5	pressure set safety valve
b-6	thermal sensor
b-7	flow meter

humid air supply

c-1	control valve
c-2	control valve
c-3,c-4	flow meters
c-5	hot oil bath to heat clean air
c-6	glass wool rough filter
c-7	humid-dry air mixing chamber

electrostatic mobility analyzer and aerosol growth chamber

d-1	flow meter
d-2	control valve
d-3	radia active aerosol neutralizer
d-4	photo-multiplier assembly

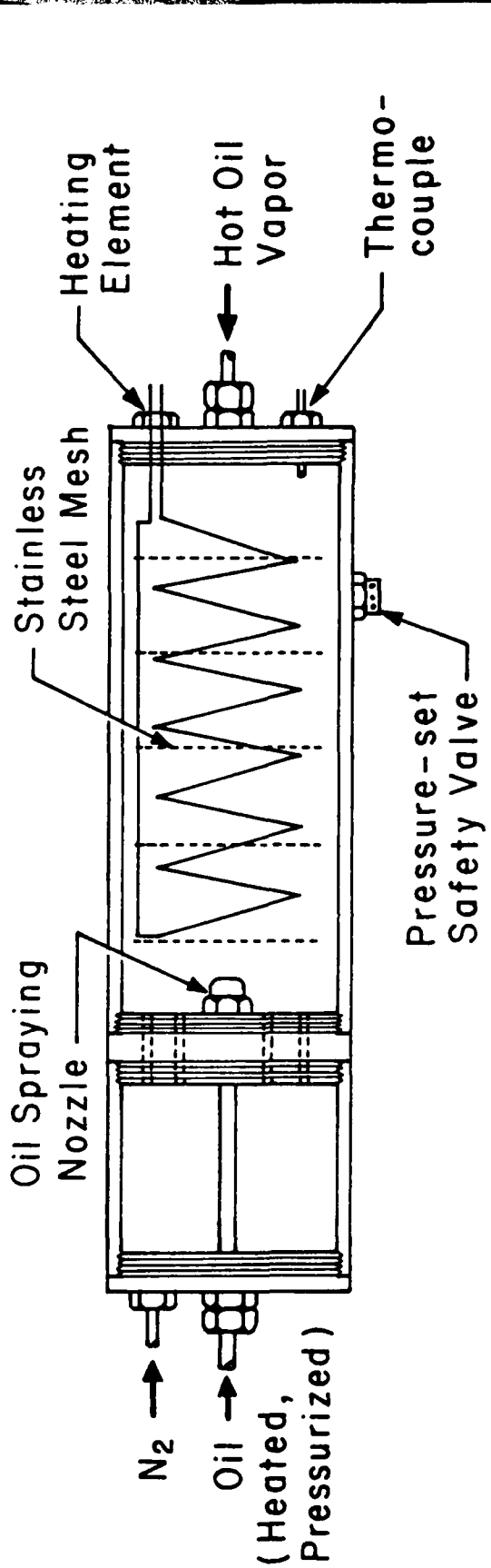

Figure 7. Oil boiler.

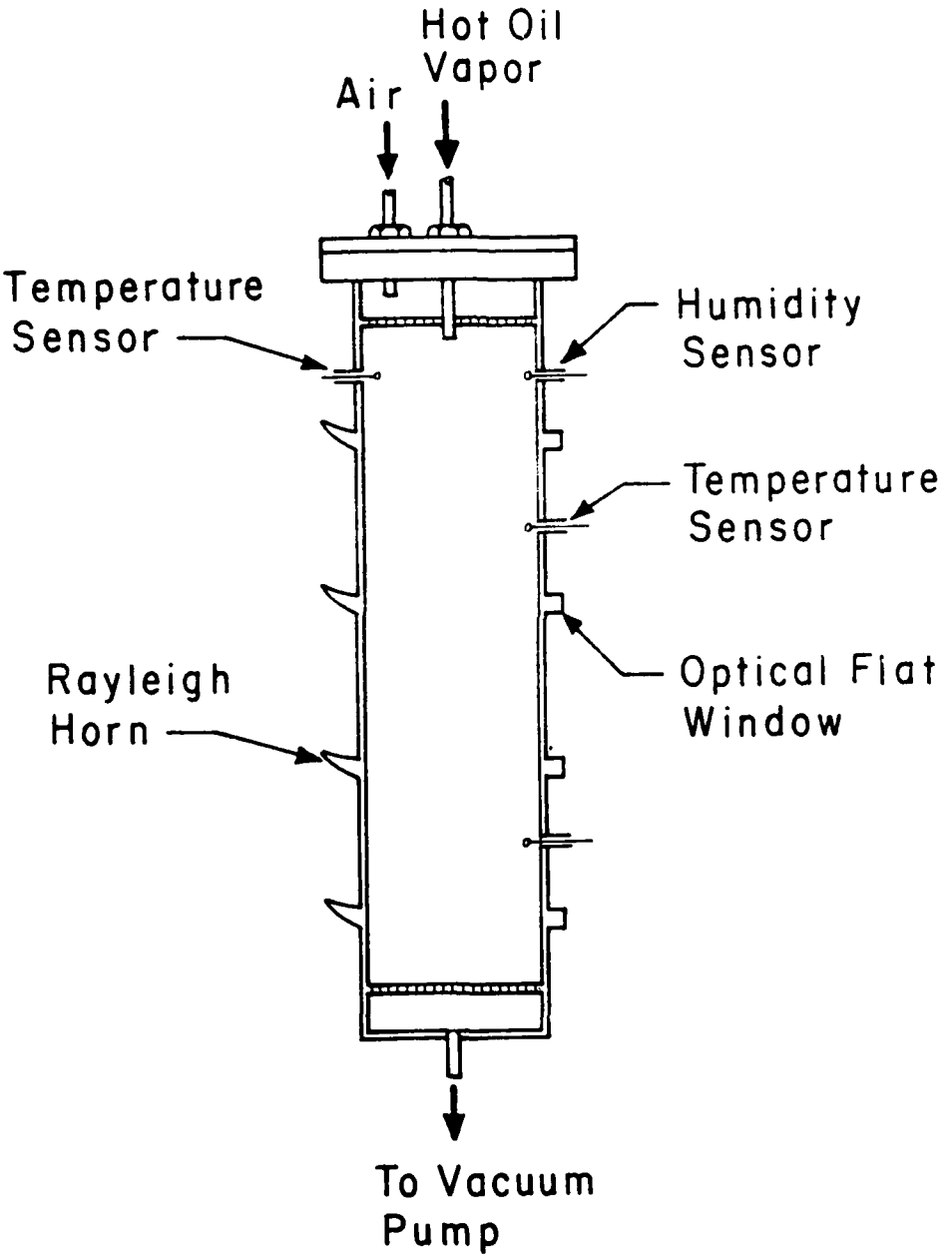

Figure 8. Aerosol growth chamber.

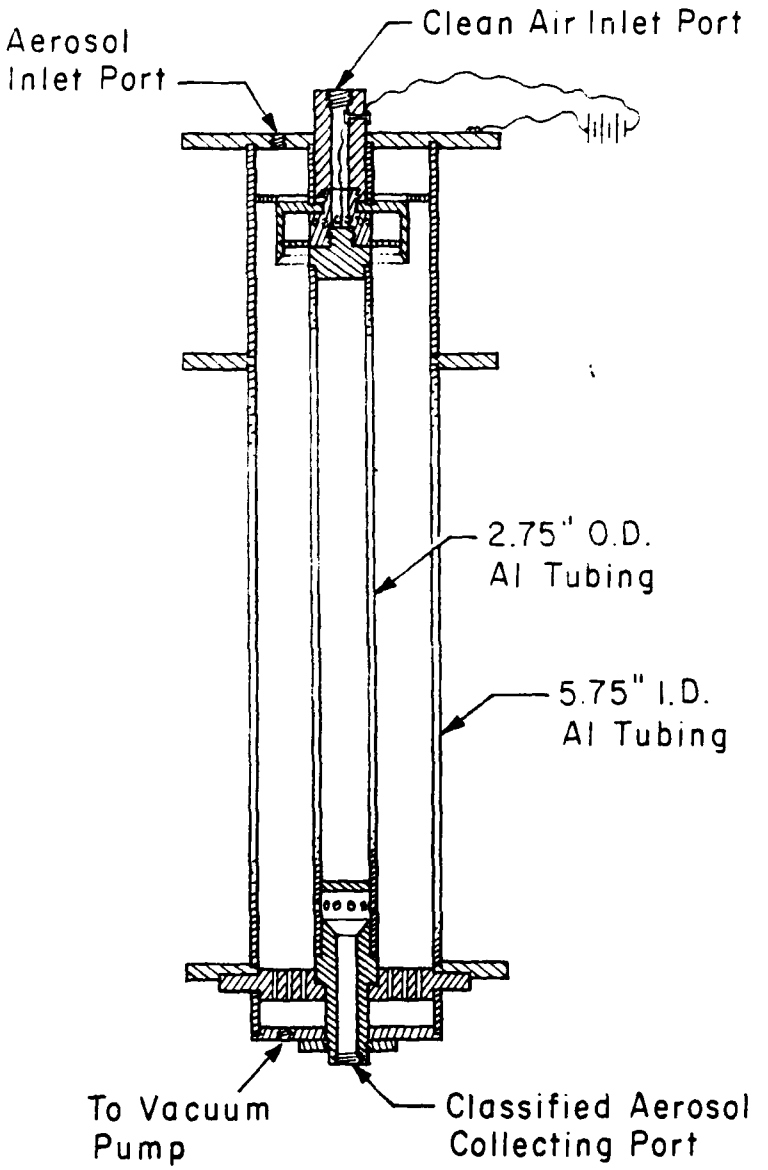

Figure 9. Electrostatic mobility analyzer.

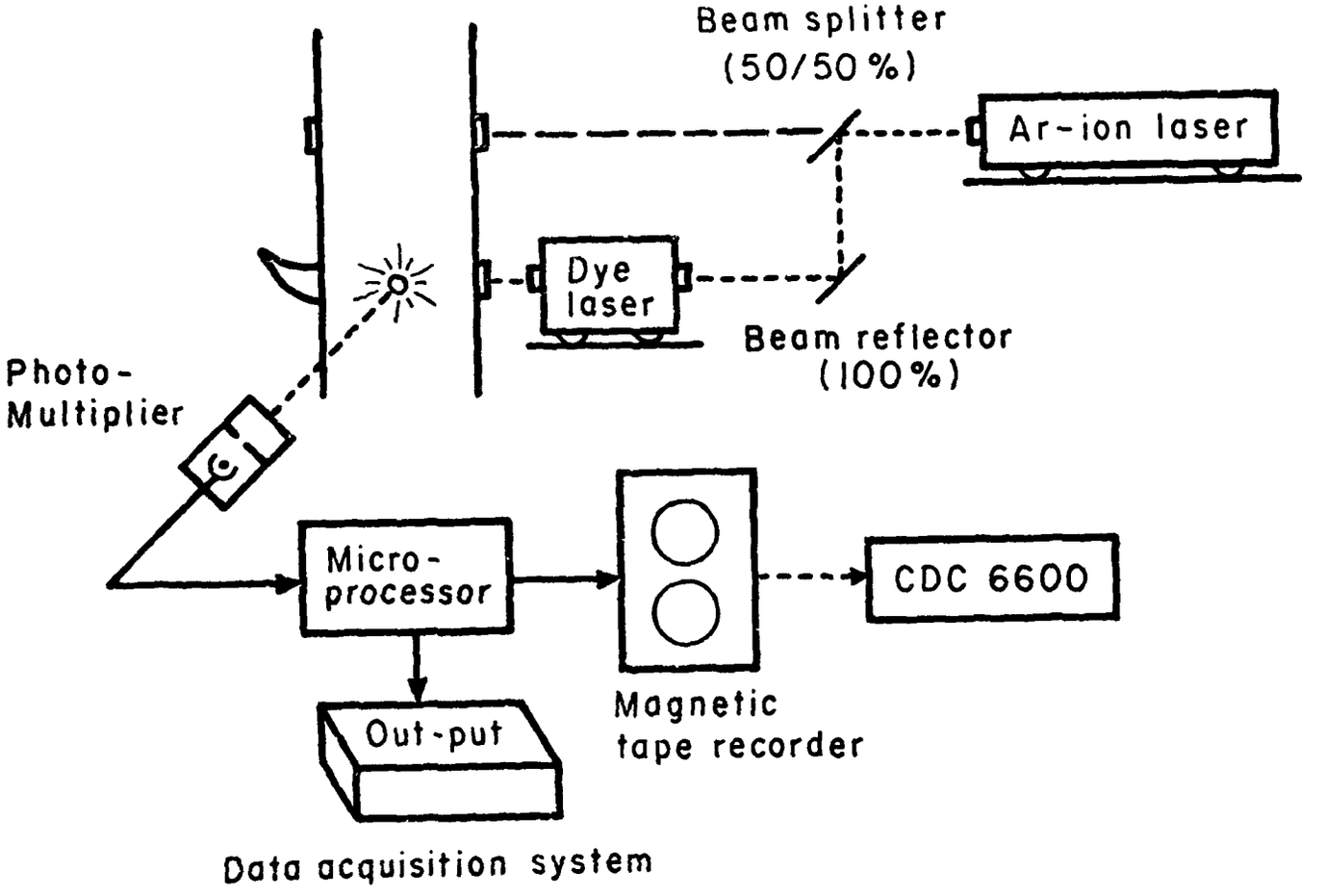

Figure 10. Optical and data acquisition systems.

LOWER BOUND ESTIMATES OF FOG OIL DROPLET LIFETIMES

by

S.H. Baek, K.S. Yom, and J.R. Brock
Department of Chemical Engineering
University of Texas
Austin, Texas 78712

ABSTRACT

Experimental data for evaporation of samples of #2 diesel oil and SGF-2 fog oil are used to make lower bound estimates of oil droplet lifetimes over possible ranges of ambient temperature. These calculations suggest that the lifetime of a SGF-2 fog oil droplet is up to 10 times that of a #2 diesel oil droplet. As a specific example, a 0.5μm radius #2 diesel oil droplet has a lower bound lifetime of around 1 hour and a 0.2μm droplet has a lifetime of 0.1 hour.

INTRODUCTION

This paper gives details of calculations necessary to estimate lower bounds for the lifetime of oil droplets of SGF-2 (fog oil), and #2 diesel oil. Reference is made to companion papers,[1,2] in which experimental evaporation rate data are obtained for SGF-2 and #2 diesel oil as well as several other complex hydrocarbon mixtures.

ASSUMPTIONS AND CALCULATIONS

The crucial assumption from the standpoint of the Chemical Systems Laboratory (CSL) in the calculations presented here is that the samples of SGF-2 and #2 diesel oil are representative of all SGF-2 and #2 diesel oils in terms of their vapor pressures. This is not generally correct since the specifications for SGF-2 and #2 diesel oil are based on other factors than vapor pressure, such as viscosity, pour point, etc. This assumption can be examined in detail and such a study is now underway. The present calculations should serve as rough indications of expected lower bound oil droplet lifetimes.

In addition, the following assumptions are made in the lower bound estimate:

(1) Evaporation of a single fog oil droplet takes place in an infinite expanse of air at atmospheric pressure. This assumption of an isolated droplet gives rise to the lower bound estimate. In a cloud of oil droplets, a given droplet is not isolated and its evaporation rate is

diminished by the oil vapor pressure of adjacent droplets.

In the center of a dense cloud of oil droplets, the gaseous phase will usually be near saturation for oil vapor; and very little evaporation will occur. Therefore assumption (1) establishes that the evaporation time of a cloud of oil droplets will always be longer than that given by this estimate.

(2) The evaporation of oil droplets in the atmosphere may be considered to be an isothermal process because of the very low vapor pressure of liquid oils at ambient conditions. In this case, droplet temperature in the atmosphere is determined by the ambient conditions. The droplet will be heated by solar radiation, but this serves only to raise the droplet temperature to some average temperature above the ambient atmospheric temperature; the amount of this rise will depend on the absorptive charcteristics of the droplet and meteorological conditions. In this analysis, oil lifetimes are estimated for droplet temperatures ranging from 273°K to 313°K. Droplet lifetime varies only slightly over this range, so that a detailed analysis of droplet temperature as a function of solar radiation is not necessary. Such an analysis, however, is easily performed.[3]

(3) The vapor pressure of bulk liquid fog oil can be approximated in two regions: (a) for evaporation of 0-40% of the mass of a fog oil droplet (previously completely vaporized at high temperature and recondensed), the vapor pressure of a planar liquid surface of simulated fog oil, SGF-2, is

$$P_v^\circ = (1.2 \times 10^{-3}) \cdot 10^{-81.6/T} \qquad (1)$$

in dynes/cm^2 where T is in degrees Kelvin. The average molecular weight is 300. For evaporation of 40-83% of a fog oil droplet of SGF-2,

$$P_v^\infty = (9.4 \times 10^{-4}) \cdot 10^{-288/T} \qquad (2)$$

with same definitions as above. The average molecular weight is 317.

(b) For evaporation of #2 diesel oil, the vapor pressure of a planar liquid surface of simulated diesel is:

$$P_v = 9.4341 \times 10^{-5} \cdot \sqrt{T} \qquad (3)$$

in dynes/cm^2 where T is in degrees Kelvin. Average molecular weight is 220, based on characterization factor of 11.8. Equations (1), (2), and (3) were obtained using the Clausius-Clapeyron equation and approximations to the experimental data of Reference (1).

Fog oil SGF-2 and #2 diesel oil are very complex hydrocarbon mixtures consisting of thousands of different chemical species. The assignment of a single vapor pressure is therefore a gross approximation which results in a conservative lower bound calculation of fog oil lifetimes.

(4) The evaporation rate of a single, isolated spherical oil droplet is given approximately by the equation:

$$\Phi_i = \frac{-4\pi R_i D_{ig} [n_i^\circ - n_i(\infty)]}{1 + c_{di}\lambda_g/R_i} \qquad (4)$$

in which it is assumed that the evaporation involves a single chemical species having the properties (3a) and (3b) above. Equation (4) is approximately valid over the range $0 \leq \lambda_g/R_i \lesssim 0.7$. In Equation (4):

Φ_i = evaporation rate (molecules/sec.) of fog oil liquid droplet.

R_i = droplet radius (cm)

D_{ig} = mutual gaseous diffusion coefficient for droplet substance, i, in inert suspending gas, g, (cm^2/sec.), to be determined from dates of Birks and Bradley[4] for dibutylphthalate (MW = 278).

n_i° = vapor number density (number/cc) of substance i at droplet surface.

$n_i(\infty)$ = number density (number/cc) of substance i at large distance distance from droplet surface.

C_{di} = dimensionless slip coefficient taken from data of Birks and Bradley.[5]

λ_g = molecular mean free path of suspending gas molecules (air in calculation). (6.6×10^{-6} cm for air at 1 atm, 25°C).

Equation (4) provides a description of the evaporation rate for the range of droplet sizes of interest in screening smokes -- that is, down to radii of $\sim 10^{-5}$ cm.

(5) Assumptions in the assignment of numerical values in evaporation rate, Equation (4), are:

(a) D_{ig}: Values are used for dibutylphthalate in air: 0.031 cm^2/sec @ 20°C, 0.064 cm^2/sec @ 135°C. $D_{ig}(T) \simeq 6.6 \times 10^{-6} T^{3/2}$.

(b) $$n_i^\circ = \frac{P_{vi}^\infty}{kT} \exp(2\sigma_i v_i / R_i kT) \qquad (5)$$

P_{vi}^∞ is given by Equations (1), (2), and (3). The term $\exp(2\sigma_i v_i/R_i kT)$ is the Kelvin correction for the effect of curvature on the vapor pressure. σ_i is the vapor-liquid surface tension (dynes/cm) of fog and diesel oil -- in air it is assumed to be 34 dynes/cm @ 25°C from Ref. 3. v_i is the molecular volume (cm^3/molecule) with density of liquid = 0.91 g/cc @ 25°C.

For these calculations, $\exp(2\sigma_i v_i/R_i kT) \simeq \exp(2.5 \times 10^{-4}/R_i kT)$ since σ_i and v_i (for SGF-2 and diesel oil which have large pseudo-critical temperatures) are not strongly dependent on temperature compared with $P_{vi}^\infty(T)$. Over the range of interest in temperature and particle size -- that is $R_i \sim 10^{-5}$ cm, $253 \leq T \leq 313$ $\exp(2.5 \times 10^{-4}/R_i T) \simeq 1 + 2.5 \times 10^{-4}/R_i T$.

All these assumptions are reasonable over conditions of interest in this lower bound calculation. Their aggregate effect is believed to be less than a few per cent of error.

DEVELOPMENT OF EQUATION FOR FOG OIL RADIUS AS A FUNCTION OF TIME

In Equation (4), ϕ_i can be expressed in terms of droplet radius and mass density, ρ_i

$$\phi_i = \frac{d}{dt}\left(\frac{4}{3}\pi R^3{}_i \rho_i\right) \cdot \left(\frac{6\times10^{23}}{M_i}\right) \qquad (6)$$

where M_i is the molecular weight of chemical species in evaporation. Therefore:

$$\phi_i = 4\pi R_i^2 \rho_i \left(\frac{6\times10^{23}}{M_i}\right) \frac{dR_i}{dt} \qquad (7)$$

according to assumptions introduced above.

Equating (4) and (7):

$$\frac{dR_i}{dt} = \frac{-D_{ig} P_{vi}^{\infty}(T)\,(1+2\sigma_i \upsilon_i / R_i kT)}{kT\left(\frac{6\times10^{23}}{M_i}\right) R_i \rho_i\,(1 + C_{di}\lambda g/R_i)} \qquad (8)$$

which is approximately valid over the range $0 \leq \lambda g/R_i \leq 0.7$ according to experimental data of Birks and Bradley.[5] Putting in all numerical values:

$$\frac{dR_i}{dt} = \frac{2.45\times10^{-11}\, T^{1/2}\, P_{vi}^{\infty}(T)\{1+2.5\times10^{-4}/R_i T\}}{R_i\,(1 + 8\times10^{-6}/R_i)} \qquad (9)$$

This is readily integrated to give:

$$\frac{1}{2}\left(R_i + \frac{2.5\times10^{-4}}{T}\right)^2 + \left(8\times10^{-6} - \frac{5\times10^{-4}}{T}\right)\cdot\left(R_i + \frac{2.5\times10^{-4}}{T}\right) +$$

$$\left(\frac{6.2\times10^{-8}}{T^2} - \frac{2\times10^{-9}}{T}\right)\cdot\left(\ln\left|R_i + \frac{2.5\times10^{-4}}{T}\right|\right) - \frac{1}{2}\left(R_{io} + \frac{2.5\times10^{-4}}{T}\right)^2$$

$$- \left(8\times10^{-6} - \frac{5\times10^{-4}}{T}\right)\cdot\left(R_{io} + \frac{2.5\times10^{-4}}{T}\right) - \left(\frac{6.2\times10^{-8}}{T^2} - \frac{2\times10^{-9}}{T}\right)$$

AD-A113 733 KOHL (RONALD H) AND ASSOCIATES TULLAHOMA TN F/G 9/1
PROCEEDINGS OF THE 1979 CHEMICAL SYSTEM LABORATORY SCIENTIFIC C--ETC(U)
DEC 80 R H KOHL DAAK11-80-M-0021

UNCLASSIFIED ARCSL-CR-81023 NL

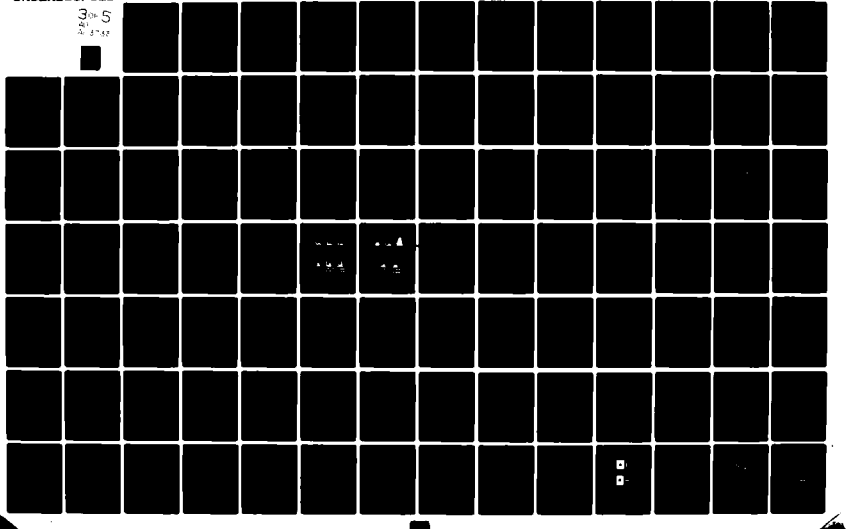

$$\left(\ln \left| R_{io} + \frac{2.5 \times 10^{-4}}{T} \right|\right) \approx -2.45 \times 10^{-11} T^{1/2} P_{vi}^{\infty}(T) (t-t_o) \quad (10)$$

where R_{io} is the initial radius at the start of evaporation at time, $t=t_o$.

RESULTS

For fog oil SGF-2 and #2 diesel oil, lifetime as a function of initial particle size (down to lower bound of validity of calculations of $R_i \approx 10^{-5}$cm) has been calculated using eq. (10). The results are given in Fig. 1, where the ordinate is the lower bound estimate of the lifetime of an oil droplet in hours and the abscissa is the radius of the oil droplet at the start of evaporation. For example, an isolated droplet of #2 diesel oil with an initial radius of 3×10^{-5}cm reaches 10^{-5}cm radius in around 0.3 hours (18 min.). As pointed out earlier, however, in a plume the lifetime will be longer than this because of the presence of neighboring oil droplets which act to maintain a partial pressure of oil vapor (taken to be zero for the isolated droplet). The actual time for a droplet to evaporate to 10^{-5}cm radius will be longer therefore and will depend on ambient conditions. For highly unstable atmospheric conditions (high wind speed, strong surface heating) the lifetime will approach the lower bound estimate.

In any event, diesel oil appears to be rather volatile for screening substance in spite of its convenience.

By way of contrast, a fog oil SGF-2 droplet lifetime calculation has been carried out using vapor pressure estimates supplied by CSL based on extrapolations of high temperature distillation data for SGF-2. This extrapolation is inaccurate but conservative since it underestimates droplet lifetimes.

ACKNOWLEDGEMENT

The authors wish to acknowledge support of this work by the Chemical Systems Laboratory through research grants DAAG29-78-G-0123 and DAAG29-78-G-0131.

REFERENCES

1. Baek, S.H., Harris, J.E., and Brock, J.R., "A Study of the Evaporation of Complex Hydrocarbon Mixtures. I." (In preparation).

2. Yom, K.S., Baek, S.H., and Brock, J.R., "A Study of the Evaporation of Complex Hydrocarbon Mixtures. II." (In preparation).

3. Hidy, G.M. and Brock, J.R., J. Geophys. Research 72 455 (1967).

4. Hidy, G.M. and Brock, J.R., The dynamics of Aerocolloidal Systems, (Pergmon Press, Oxford, 1970).

5. Birks, J. and Bradley, R.S., Proc. Rog. Soc. 198A 226 (1949).

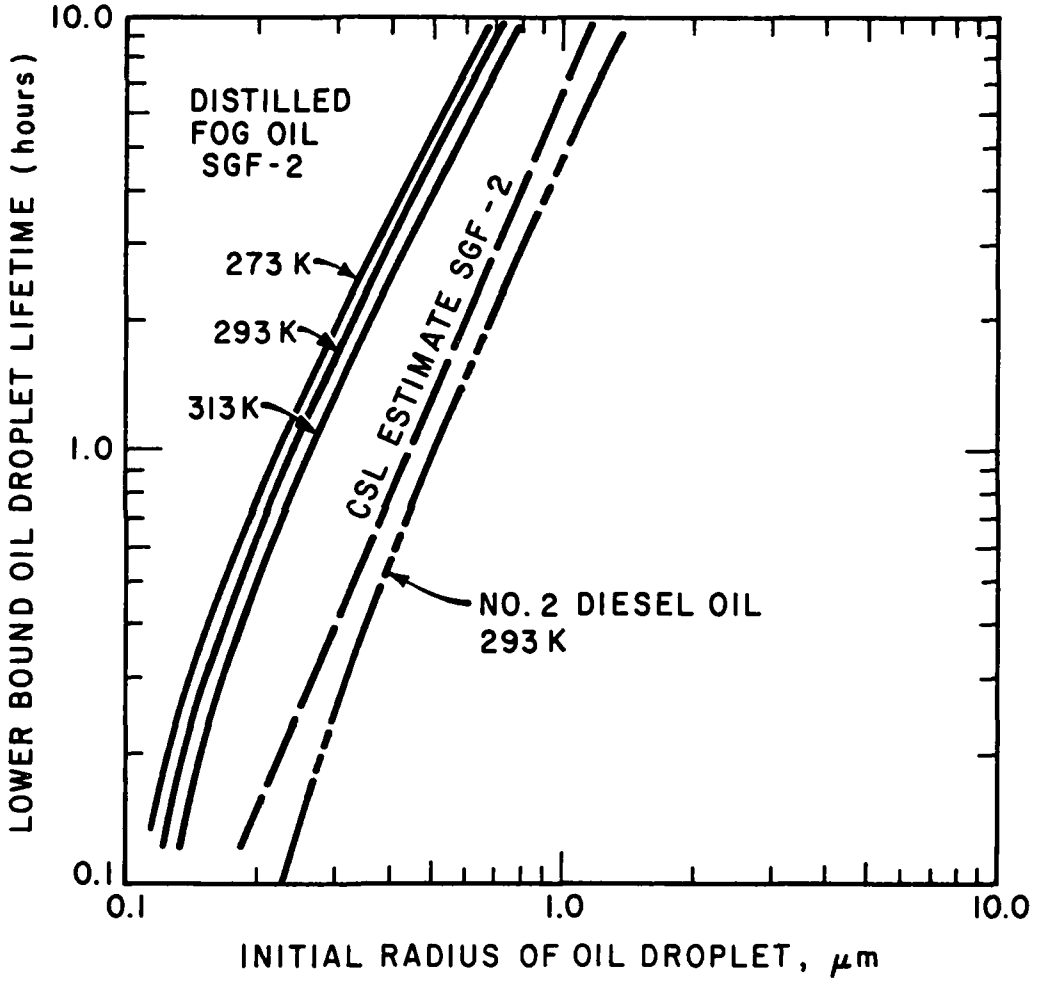

Figure 1. Lower bound estimate of oil droplet lifetime for fog oil SGF-2 and #2 diesel oil.

CHEMICAL COMPOSITION OF DROPLETS OF HC AND FOG OIL SMOKE MATERIALS

A. Snelson

IIT Research Institute
Chicago, Illinois

INTRODUCTION

In this study, HC and fog oil smokes are generated and characterized both physically and chemically. In the present context physical characterization relates specifically to the smoke aerosol particle size distribution under conditions of normal use and the possible effects on the particle size distribution of humidity, aging, concentration and amount of smoke mix burned. Chemical characterization relates to the determination of the gaseous and particulate products of the smoke generation. In particular, a qualitative and quantitative analysis of the gaseous products with relation to the amount of smoke mix burned and aerosol compositions only for particles below about 10 μm, i.e., those in the respirable region were required. A primary object of the investigation was to obtain the above data to enable realistic HC aerosol smokes to be generated for animal health effect studies.

At the present time, the HC study has been completed and a final report has been prepared which will shortly be available for distribution. For this reason, only a brief summary of the experimental findings will be presented here. Studies are currently in progress on the fog oil smokes. Some preliminary findings are presented.

HC SMOKES

Five different lots of M5-30lb HC smoke pots (manufactured at different times) were provided. The smoke pots were disarmed and opened. The pyrotechnic mixture was composed of two layers, the upper of which was colored pink due to the addition of <0.2% toluidine red to the mix.[1] The upper and lower layers of the smoke mixes were analyzed with the results shown in Table 1.

Table 1. Composition of HC Smoke Reagent

COMPONENT	WEIGHT %	
	Upper Layer	Lower Layer
Hexachloroethane	44.4	46.5
Zinc Oxide	47.5	48.3
Aluminum	7.0	5.2

The higher aluminum content of the upper layer facilitates ignition of the mixture.

The principal inorganic impurities present in the mix were found to be cadmium [15-1500 ppm(w)] and lead [30-990 ppm(w)]. Trace quantities of arsenic [<5 ppm(w)] and mercury [<1 ppm(w)] were also found.

A series of "scaled down" smoke generation canisters were designed for laboratory experiments using HC reagent charges ranging in size from 12-700 g. These pots were ignited in an 18 ft diameter steel sphere for chemical analyses and particle size measurements. The gaseous products shown in Table 2 were identified. The amounts of the various combustion species formed were quite variable. The values shown in Table 2 are the average of some twelve measurements.

Table 2. Trace Gas Species formed on Combustion of the HC Smoke Mix

GASEOUS COMPONENT	AMOUNT FORMED, mg/g REAGENT
CO	23
HCl	22
$COCl_2$	3
CCl_4	18
C_2Cl_4	72
C_2Cl_6	12
C_6Cl_6	5
Cl_2	8

Chemical analyses of the HC smoke aerosol showed it to be predominantly $ZnCl_2$ together with 1-4% $AlCl_3$.

Particle size analyses on the HC aerosols were made under a variety of particle loadings and humidities. Under conditions of low agglomeration rates the mean particle diameter was determined at ≈0.3 μm and was found to be independent of humidity over the range 10-80% relative humidity.

FOG OIL SMOKES

Three different lots of fog oils were obtained and subjected to chemical analyses by HPLC. The results are presented in Table 3. The polar fraction listed in Table 3 consists of esters, alcohols, and acids. The various oil fractions from the HPLC have been subjected to glass capillary column gas chromatography and compositional profiles obtained. As expected, even using these high resolution techniques chromatograms were obtained which although resolving numerous peaks also showed considerable evidence of an unresolved continuum of species. Combined GC-mass spectrographic analyses have been made on the aliphatic and aromatic fractions and specific compounds identified.

Oil fogs from these oils have been generated using five different M3A3 fog oil generators. Aerosol particles for physical and chemical analyses were collected after the generators' operational characteristics had stabilized. The excess oil fog was incinerated. Preliminary particle size analyses indicates a trimodal particle size distribution. The largest number of particles

Table 3. HPLC Class Fractionation of Fog Oils

	Fog Oil Lot No.		
	1	2	3
Character	lt. yellow	brown	amber
Density	0.89	0.93	0.91
Mol. Wt. Range*	100-400	90-350	90-350
Mol. Wt. Max.*	160	150	150
254 nm O.D. / Refractive Index	1.97×10^4	3.93×10^4	2.56×10^4
% Paraffins	57	53	54
% Aromatic	41	42	44
% Polars	2	5	2

* Determined by gel permeation chromatography on μ Styragel; calibration with saturated standard hydrocarbons and alcohols.

have a median diameter of ≃0.2 μm, with the largest particles all lying below 2 μm in diameter. Preliminary chemical analyses of the oil fogs indicates a small increase in the aromatic fraction at the expense of the cyclic alkanes and an increase in the polar acid fraction.

It is anticipated that the chemical and physical characterization of the oil fogs will be completed by December 31, 1979 with a final report available by Summer, 1980.

ACKNOWLEDGMENTS

This work is supported by the U.S. Army Medical Bioengineering Research and Development Laboratory, Jesse J. Barkley, Jr., Contract Officer's Technical Representative.

REFERENCES

1. Field Manual, Military Chemistry and Chemical Compounds, Army FM3-9/Air Force AFR 355-7, October 1975.

AEROSOL CLOUD DYNAMICS

Lee Parker, Panametrics, Inc.

A cloud of infrared-absorptive submicron particles in sunlight will absorb heat and rise, perhaps into the upper atmosphere. There is concern regarding the rate of increase of cloud size, the altitude the cloud would attain, its transport to distant points, and its residence time in the atmosphere, since sufficient numbers of these particles could cause a significant imbalance in solar energy transfer.

The cloud rises initially owing to its buoyance and original vertical momentum, while being carried along the horizontal direction by the wind. The cloud's upward velocity relative to the ambient air produces a velocity shear at the external surfaces, causing ambient air to be entrained. Entrainment or mixing also occurs due to turbulence in the air. Its buoyancy changes because of the changing relative density of the entrained air. Also, the cloud's shape will change because of wind-shear.

Under stable conditions the cloud will attain its limiting height when its buoyance decays to zero. This normally occurs at a temperature inversion; hence the cloud may reach the tropopause altitude. Under unstable conditions, however, the cloud could continue to rise indefinitely.

The aerosol particles within the cloud tend to settle gravitationally, but this rate of settling is so slow for submicron particles that the particles essentially remain suspended in and move with the air. They undergo Brownian motion, however, and would tend to diffuse outward, thereby essentially increasing the diameter of the cloud. The dynamical behavior of the aerosol particles is similar to that of droplets in clouds.

The particles absorb energy from the sun and subsequently deliver thermal energy to the air of the cloud by radiation, conductivity, and convection. They constitute a heat source which remains active as long as they are sunlit, continuously driving the cloud as it rises and is moved vertically and horizontally by winds.

Ultimately, the particles may agglomerate to form large aggregates and settle out. Or, they may be scavenged by rain or snow. The latter can occur because a water cloud can be formed.

In the previous paragraphs we were discussing a dry cloud of aerosol particles. However, a wet cloud can arise as follows. The buoyancy causes an updraft to occur, and, depending on the humidity and temperature

of the air, water vapor will condense at a sufficiently great altitude. The small aerisik oartuckes can, by their presence, enhance this condensation by acting as cloud condensation nuclei. They can then accrete water and grow by condensation, and fall as rain, collecting water droplets after they have grown to precipitation size. The aerosol can also diffuse toward and be captured by water droplets and rain.

In the following we present a computational model for wet cloud (aerosol plus water) dynamics. In the absence of humidity the problem reduces to that of a dry aerosol cloud.

The dynamic equations are those of cloud dynamics, plus the advective diffusion (conservation) equation for the aerosol particles. The acceleration equations and the equation of state for a mixture of dry air and water vapor may be written:

$$\frac{\partial u}{\partial t} = -\vec{v} \cdot \nabla u - \frac{1}{\rho} \frac{\partial p}{\partial x} + F_x \tag{1}$$

$$\frac{\partial w}{\partial t} = -\vec{v} \cdot \nabla w - \frac{1}{\rho} \frac{\partial p}{\partial t} - g - gm + F_z \tag{2}$$

$$\nabla \cdot \vec{v} = 0 \tag{3}$$

and

$$p = \rho RT \frac{(1 + rM_A/M_W)}{(1 + r)} \tag{4}$$

where

$\vec{v}$ = air velocity vector
u = x-component of $\vec{v}$.
w = z-component of $\vec{v}$.
ρ = density
p = pressure
g = acceleration of gravity.
F_x, F_z = frictional accelerations
m = mixing ratio of <u>both</u> liquid water <u>and</u> aerosol (mass per unit mass of air).
r = mixing ratio of water vapor
R = gas constant, dry air
T = temperature
M_W/M_A = ratio of molecular weights of water and dry air.

The above equations are based on those of Orville (1965), but are modified here to include aerosol particles. Equation (3) implies incom-

Orville, H. D., J. Armos. Sci. 22, 684 (1965).

pressibility, so that the description is not strictly applicable to deep convection problems. It may suffice for our purposes, however.

The geometry implied by the above equations is 2-D slab geometry. The corresponding equations for cylindrically-simmetric 2-D geometry are straightforward (e.g., Ogura, 1963). It is common practice to reformulate the equations in terms of the stream function and vorticity function (e.g., Ogura, 1963; Orville, 1965). Orville follows Ogura (1963) in approximating F_x and F_z using an eddy diffusion to represent turbulent transport, namely,

$$F_x = K\nabla^2 u$$
$$F_z = K\nabla^2 w \tag{5}$$

where K denotes the (constant) eddy coefficient. In addition, an equation for T is needed, i.e., an energy transport equation, plus transport equations for the aerosol particles and for the water.

The thermodynamic energy equation may be written as

$$\frac{\partial \phi}{\partial t} = -\vec{v}\cdot\nabla\phi + K\nabla^2\phi + \text{sources} - \text{sinks} \tag{6}$$

for entropy ϕ which is related to the temperature T.

The conservation of water and aerosol particles may be expressed as:

$$\frac{\partial q}{\partial t} = -\vec{v}\cdot\nabla q + K\nabla^2 q \tag{7}$$

and

$$\frac{\partial A}{\partial t} = -\vec{v}\cdot\nabla A + K\nabla^2 A - \text{sinks} \tag{8}$$

where

q = mixing ratio of water (both liquid and vapor) to dry air
A = mixing ratio of aerosol material to dry air.

The terms involving K in all of the above equations represent the effects of turbulent transport. Turbulent mixing (entrainment) is modeled implicitly by these terms. In other types of models the entrainment is modeled explicitly.

Ogura, Y., J. Atmos. Sci. 20, 407 (1963).

We now discuss the "sources" and "sinks" terms in Eqs. (6), (8). There is no source/sink term in (7). In (6) the source terms includes the effect of insolation of the aerosol particles as a source of heat driving the cloud. The other principal source/sink of heat is through condensation/evaporation of water. In (8), the source term which would be due to the creation of aerosol particles is not present. We will assume an initial distribution of aerosol and no additional sources as time goes on. The two principal sinks of aerosol are (a) diffusion, and (b) scavenging by cloud water and raindrops.

The sin in (8) due to scavenging by cloud water can be represented by diffusion to the surfaces of cloud droplets and raindrops, plus precipitation scavenging (washout). Other depletion mechanisms exist for aerosol particles, including phoretic and agglomeration effects. These are all affected to some extent by electric fields and charges. These mechanisms can be included in the equation.

The aerosol heat source in (6) will be modified by the insolation attenuation due to the "cloudy air" above the air parcel of interest.

The Fickian diffusion terms are zero-order approximations. Spatially-varying nonlinear and anisotropic formulations have been studied and are available from the literature.

During the next phase of the work, attempts will be made to obtain solutions to the above equations by analytical or numerical means. The sink and source terms, and cloud and aerosol microphysics including agglomeration, will be discussed in a later report.

FREE FALL OF NON-SPHERICAL COLLECTORS OF AEROSOL PARTICLES

J. Podzimek and P. C. Yue
Dept. of Mechanical & Aerospace Engineering and
Graduate Center for Cloud Physics Research
University of Missouri-Rolla
Rolla, MO 65401

INTRODUCTION

The main purpose of this contribution to the conference is to report on the course of the research work of the scavenging of smoke particles by non-spherical collectors and to indicate several lines of the future investigation.

The program started in our laboratory half a year ago and was motivated by the idea that an improvement of visibility can be reached by cleaning the smoke cloud by a large number of collectors - particles with high scavenging efficiency - and by depositing the particles with the collectors on the ground. There is solid evidence that ice crystals can bind on their surface micron size droplets and aerosol particles and that the solid precipitation elements usually show high content of chemical substances in atmospheric aerosol (e.g., Podzimek[1]; Magono et al.[2]; Macku et al.[3]). Therefore, our effort will focus on finding sizes, shapes and surface properties of artificially generated scavengers which will ensure the highest scavenging efficiency for a specific type of smoke particulates.

THEORY OF PARTICLE DEPOSITION ON ICE CRYSTALS

There are four characteristic regimes for the collection of aerosol particles by non-spherical bodies. The first corresponds to $Re < 1$ and is featured by the arbitrary and steady position of the falling tiny collector. For our practical application the three remaining regimes are the most important. The regime of steady fall ($1 < Re < 150$ for a disk) with the plate collector maintaining the position of its largest cross section perpendicular to the direction of fall, the transitional regime with oscillation and slip fall ($150 < Re < 5{,}000$ for a disk) and the regime of tumbling fall ($Re > 5{,}000$ for a disk). The regime of steady fall was described theoretically by several authors (e.g., Pitter and Pruppacher[4], Parker[5]).

For a polydisperse aerosol one can define the "scavenging coefficient" in the known way

$$S = \int_{r_o}^{r_1} \pi(R+r)^2 \, E(R,r) \, [U(R) - u(r)] \, N(r) dr$$

where R, r, U(R), u(r) are the radii and velocities of the collector and of the aerosol particle. N(r) is the particle size distribution function and E(R,r) is the collection efficiency of scavengers. E(R,r) is defined in the simplest way by combining Langmuir's relationship $E_L = (\pi y^2)/[\pi(R+r)^2]$ with a suitable coalescence efficiency E_c i.e., $E = E_L \cdot E_c$. y is the initial offset of the aerosol particle center of the collector's center path. The

fraction F of the aerosol removed after the collector has been falling for t seconds through the polluted space can be calculated according to the formula $F=\exp(-S.t)$.

In the case of collector oscillation, sliding or tumbling, no analytical solution exists and only an attempt has been made to describe the accelerated motion of a spherical particle (Basset's equation) in a straight line by a numerical model. Therefore, an experimental investigation of the collector motion in the transition and tumbling regime, where the most intensive catching of aerosol is expected, seems to be expedient. This will enable one to establish a stochastic model based on the mean time and space where the collector in a specific position (with a mean collection efficiency) will scavenge particles during its fall. Finally, we will investigate the scavenging effect of a large population of non-spherical collectors released at the same time and the effect of horizontal wind or turbulence on the clearing of smoke cloud by scavenging.

INVESTIGATION OF FREE FALL REGIMES OF SCAVENGERS

We tried to exploit our previous experience with the investigation of the fall of plate type and columnar models (Podzimek[6,7]) in a large tank filled with different glycerol - water mixtures and to complete them by new pilot experiments in air. We deduced the dynamic parameters of falling models from time lapse camera pictures and from stroboscopic pictures. The former were taken in previous experiments using two cameras oriented perpendicularly towards the experimental tank containing the mixture (Figs. 2 and 3). The latter were taken from experiments recently performed in air.

Simple dimensional analysis was made (under the assumption that a model falls steadily or oscillates) for the following parameters (Fig. 1): fall velocity - V_x, V_z, medium density - ρ_f, medium dynamic viscosity - μ, collector major axis (diameter) - d, collector minor axis (thickness) - c, driving force - F, collector surface area - S, collector density ρ_p, frequency of oscillatory motion - n, amplitude of the oscillatory motion - A. The surface roughness and other surface or body properties of the collector were neglected in the first approximation. Because some of the parameters can be expressed by the others and some can be combined, we find the following similarity parameters important for our experiments:

$$\frac{V_z \rho_f d}{\mu} = Re \; ; \; \frac{\rho_p}{\rho_f} \; ; \; \frac{c}{d} \; ; \; \frac{F}{V_z^2 \rho_f d^2} = C_D \; ; \; \frac{d \cdot n}{V_z} = f;$$

$$\frac{S}{d^2} \; ; \; \frac{A}{d} \; ; \; \frac{V_z}{V_z} \; .$$

Combination of $(\rho_p \cdot c)/(\rho_f \cdot d)$ leads to Wilmarth's stability number I (for disks $I = (\pi \rho_p c)/(64\ \rho_f\ d)$ and $C_D\ R_e^2 = Be$ (Best number). The ratios V_z/V_x and A/d can be expressed by the other parameters, so that the shape factor

$(S/d^2, c/\sqrt{ab})$ and the frequency number $f = (d \cdot n)/V_z$ remain with the Reynolds and the Best number and Wilmarth's parameter as the most important factors in featuring the behavior of free falling collectors. This simplified picture assumed the oscillation of models in one plane which must not be necessarily true e.g., for a hexagonal plate the plane of oscillation regularly changes with the time (Figs. 2 and 3).

Fig. 4 shows the dependence of drag coefficient of the disk on the Re covering the whole range from $0.25 < Re_z < 5{,}000$ ($17{,}000\ Re_x$). Also, included are our data from this year for the most important transitional regime. The data obtained for disks at $Re < 700$ were obtained in liquids, the data this year, denoted by triangles, correspond to the fall in clean air. There is an apparent consistency of drag coefficients measured by different authors ten years ago (Stringham et al.[8], Shemenauer[9], and Podzimek[6,7,10]) up to $Re_z = 100$. At larger Re_z, there is an agreement between Shemenauer's and Podzimek's data (up to $Re_z = 300$) and disagreement with Stringham. The data taken this year with paper and foam models falling in air further show the importance of Wilmarth's and other parameters on the mode of motion. The groups of points, corresponding to the same stability parameter I, are characterized by a typical position in the $C_D = f(Re)$ diagram. The amplitudes of oscillatory motion are smaller in air than in liquids (where the driving force was also much higher) and the models falling in air had a tendency to slide around $Re = 1{,}000$ and to tumble at $Re > 2{,}000$). This statement requires, however, confirmation based on many more experiments which are currently undertaking. These measurements, performed with differently shaped collectors such as squares, hexagonal plates, triangles and ellipses (Figs. 5, 6, 7 and 8) show that all "symmetrical bodies" behave like disks (Fig. 9) while a large spread of data for triangles and ellipses (Fig. 10) exists. In total, 45 model falls were analyzed. Large scattering of C_D in the case of "unsymmetrical" bodies is clearly related to the oscillatory-slip regime and the transition to tumble which will be investigated in the future together with the tumble of L-shaped collectors at a high rotational speed.

DETECTION OF PARTICLES DEPOSITED ON COLLECTORS

Knowing the mode of collector motion from the experiments in clean air we intend to apply the results for the fall of collectors in a model smoke cloud. We anticipate that the smoke cloud will consist of chloride particulates (NaCl or $TiCl_4$) at concentrations and size distribution similar to that of military smokes. The first question we ask is how far the experiments with collector motion in the clean air are applicable for particulate cloud. Cloud physicists usually assume that no correction is necessary. We plan to use a simple model based on generalized equation for the motion of bodies with variable mass and experiments in a settling tube.

The second question is related to the evaluation of the size distribution and deposition pattern of particles on individual models which will be performed with an optical microscope. A slightly modified Liesegang circle technique described elsewhere (i.e., Podzimek[11], Preining et al[12]) will be used for chloride particle detection. Its main feature is simplicity, despite the time consuming evaluation process. However, from our previous calibration of this technique with an aerosol centrifuge

(Preining et al.[12], Yue and Podzimek[13]) we found a considerable dependence of the "magnification factor", which relates the aerodynamic particle (drop) diameter, D_{ae}, to the spot size D_{sp} in the gelatine, on humidity (Fig. 11). For this reason, the humidity control must be considered in designing the modification of the existing environmental chamber which should enable us to monitor the fall of non-spherical collectors in a controlled environment of smoke cloud and in storing the samples for evaluation. This modification of the chamber will also enable us to observe the scavenging effect in low speed horizontal air flow.

CONCLUSION

The brief summary of half a year's work on the program related to the clearing of smoke clouds focused on the study of collector motion and finding the peculiarities of different models falling in a specific fall regime. Some additional measurements will be necessary in the oscillation - slip and tumble regime which seems to be promising to produce a higher collection efficiency of smoke particles.

The future of the program is undoubtedly in making experiments with a large population of suitably dispersed collectors. We would like to perform such experiments in a small scale at the end of the two year program.

ACKNOWLEDGEMENT

The authors are indebted to Mr. Mark A. Jones who performed most of the falling model experiments, and to Mrs. Vickie Maples and Miss Donna C. Tubbesing, who helped with the techninal preparation of this contribution.

The financial support of the Army Research Office under the grant DAAG-29-79-C-0073 is appreciated.

REFERENCES

1. Podzimek, J., 1970: Contribution to the problem of the collection efficiency of the falling ice crystals, Preprints of Papers, Conf. on Cloud Physics, Ft. Collins, Colo., Aug., AMS, 13.

2. Magono, Ch., T. Endoh, T. Harimaya and S. Kubota, 1974: A measurement of scavenging effect of falling snow crystals on the aerosol concentration, J. Met. Soc. Japan, 52, 407-416.

3. Macku, M., J. Podzimek, and L. Sramek, 1959: Distribution of chemical compositions in atmospheric precipitations over Czechoslovakia, Geof. Pura e Applic. 42, 1.

4. Pitter, R. L., and H. R. Pruppacher, 1973: A numerical study of viscous flow past a thin oblate spheroid at low and intermediate Reynolds numbers, J. Atmos. Sci., 30, 125-134.

5. Parker, L. W., 1973: Computer method for calculation of aerosol scavenging by snow, Proposal submitted to AEC, Div. of Biomed. and Envir. Research, Washington, D. C., April, pp. 40.

6. Podzimek, J., 1965: Movement of ice particles in the atmosphere, Proc. Int. Conf. on Cloud Physics, Tokyo-Sapporo, 224-230.

7. Podzimek, J., 1968: Aerodynamic conditions for ice crystal aggregation, Proc. Int. Conf. on Cloud Physics, Toronto, Univ. of Toronto, 295-299.

8. Stringham, G. E., D. B. Simons, and H. P. Guy, 1969: The behavior of large particles falling in quiescent liquids, Geolog. Survey Prof. Paper 562-C. U. S. Gov. Print Office, Washington, D. C. pp. 36.

9. Shemenauer, R. S., 1969: Measurements of the drag coefficients and characteristic motions of snow crystal, graupel and small hail models, M.S. Thesis, Univ. of Toronto, Nov. pp. 108.

10. Podzimek, J., 1969: Contribution to the explanation of the motion of a falling column-like ice crystal. Studia geoph. et geod. 13, 199-206.

11. Podzimek, J., 1959: Measurement of the concentration of large and giant chloride condensation nuclei during flight, Studia geoph. et geod. 3, 256-296.

12. Preining, O., J. Podzimek, and P. Yue, 1976: The magnification factor for sodium chloride Liesegang circles established with an aerosol centrifuge, J. Aerosol Sci. 7, 351-358.

13. Yue, P. C., and J. Podzimek, 1976: A laboratory method for the study of droplet deposition pattern on simple ice crystal models, Tech. Rep. AG-6, GCCPR, Univ. of Missouri-Rolla, Sep. pp. 43.

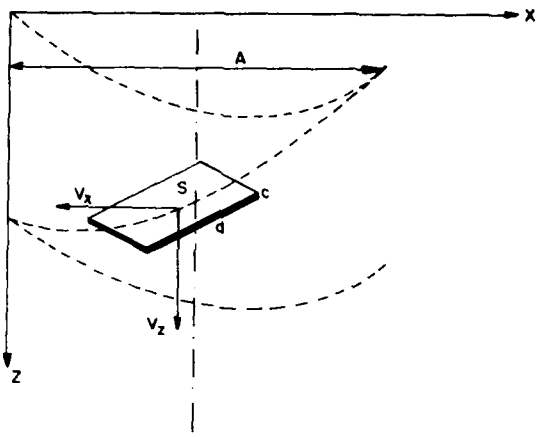

Fig. 1. Main parameters featuring an oscillatory motion of a falling model.

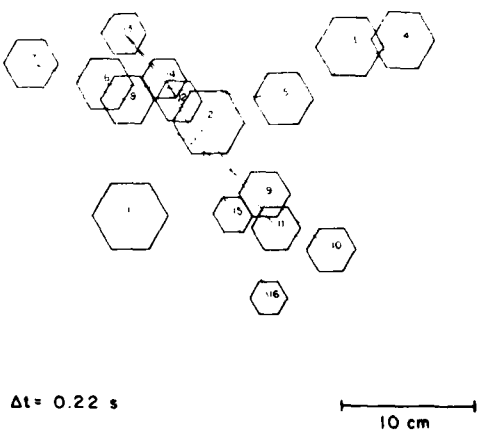

Fig. 2. Top view of a hexagonal plate model falling in water at Re_Z = 6120; Re_X = 16300. Model 5.0 cm in diameter and 0.15 cm in thickness was made of aluminum. Time intervals between model positions (not corrected for perspective distortion) are Δt = 0.22 s.

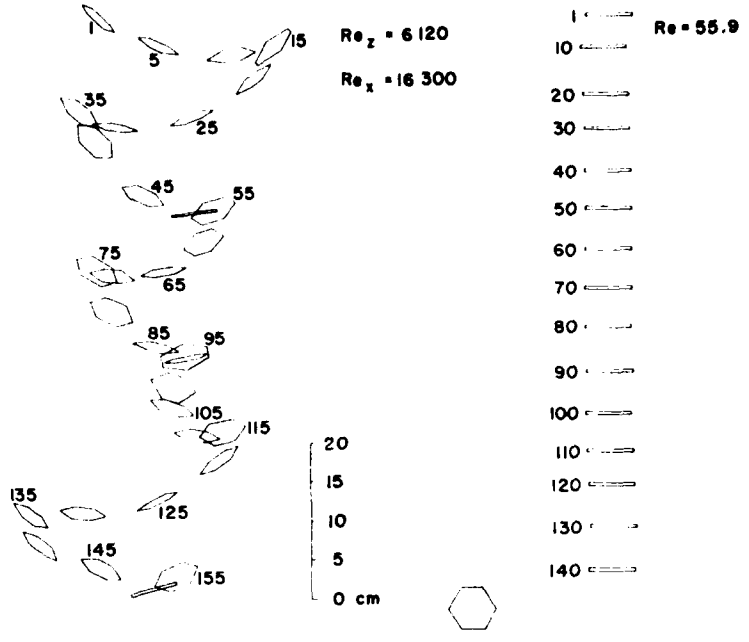

Fig. 3. Side view of a falling hexagonal plate (the same as in Fig. 2) in water at Re_z = 6120; Re_x = 16300. The numbers indicate the time in 1/24 seconds. On the right hand side is the same model falling steadily in glycerol-water mixture (85% of glycerol by weight) at Re = 55.9.

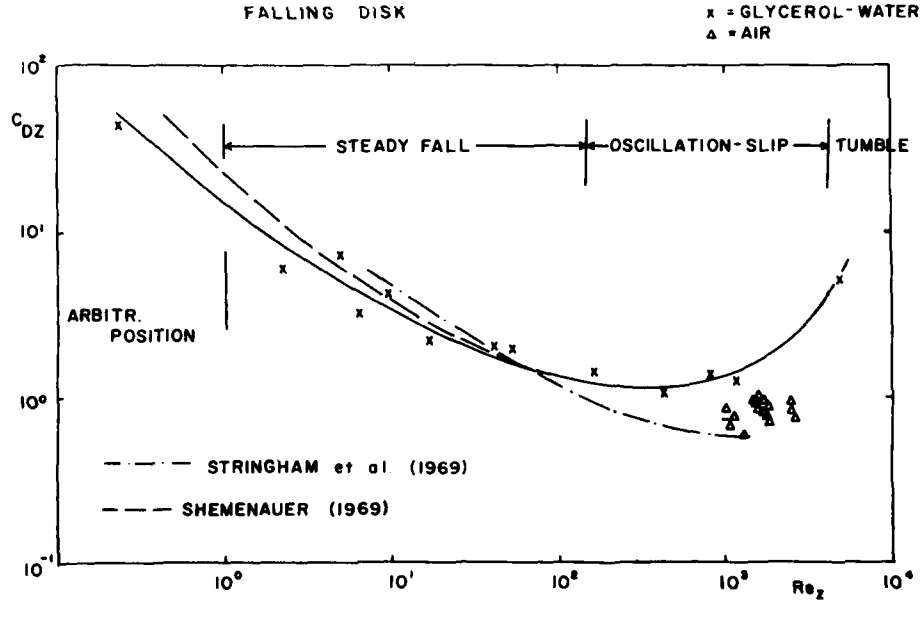

Fig. 4. Drag coefficient (C_{DZ}) dependence on the Reynolds number (Re_z) for a falling disk.

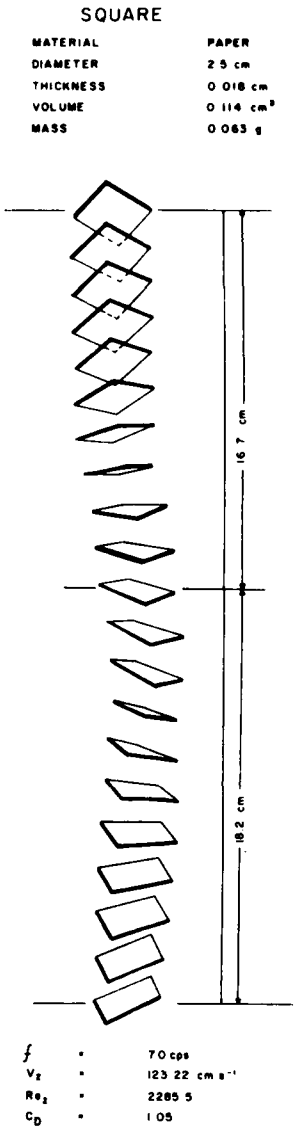

Fig. 5. Model with square cross section falling in air (Re_z = 2285.5). Redrawn from the stroboscopic picture.

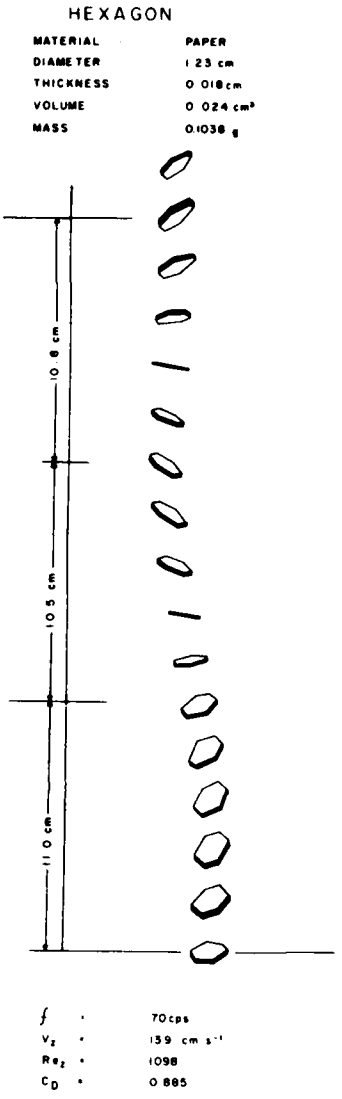

Fig. 6. Model with hexagonal cross section falling in air at Re_z = 1098. Redrawn from the stroboscopic picture.

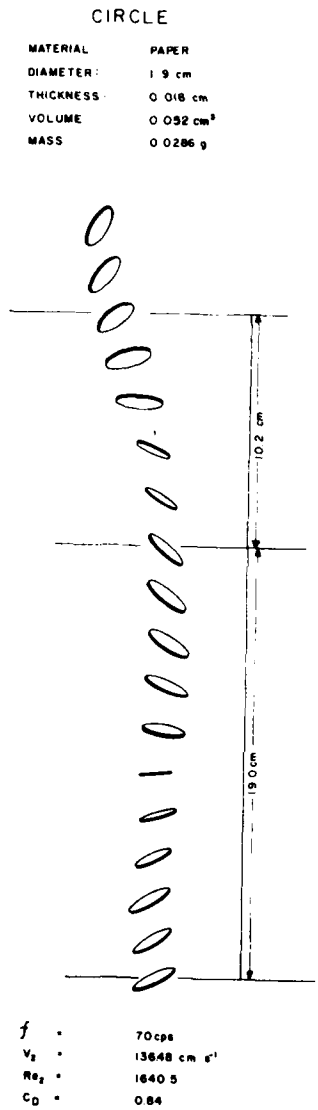

Fig. 7. Disk falling in air at Re_z = 1640.5. Redrawn from the stroboscopic picture.

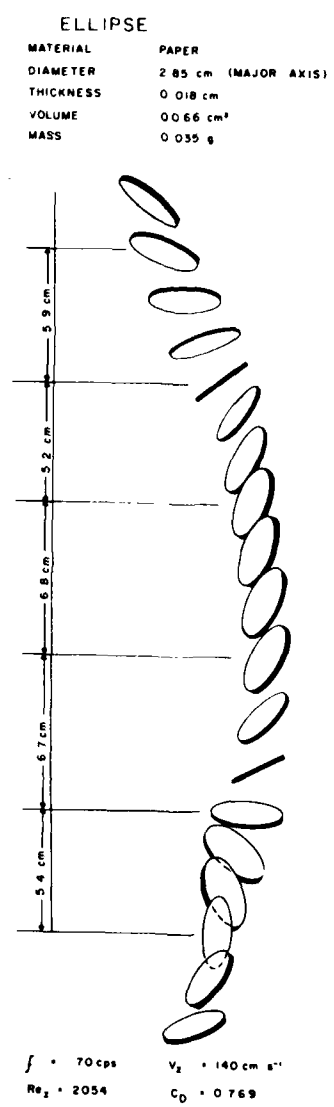

Fig. 8. Model with ellipsoidal cross section falling in fully developed slip regime at Re_z = 2054. Redrawn from the stroboscopic picture.

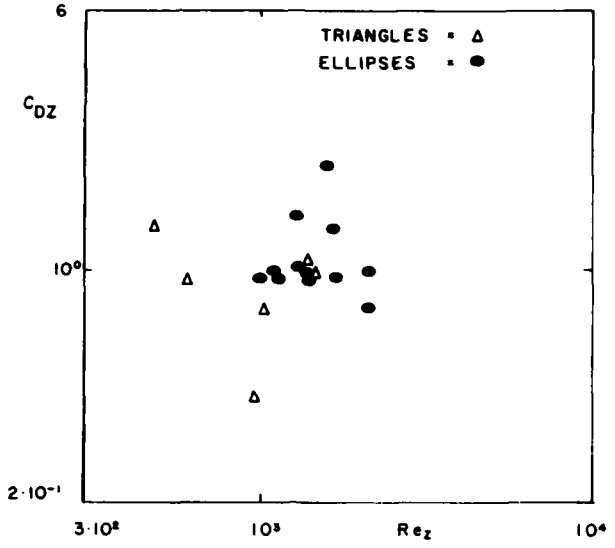

Fig. 9. Drag coefficient (C_{Dz}) plotted as a function of the Reynolds number (Re_z) for disks and models with hexagonal and square cross section.

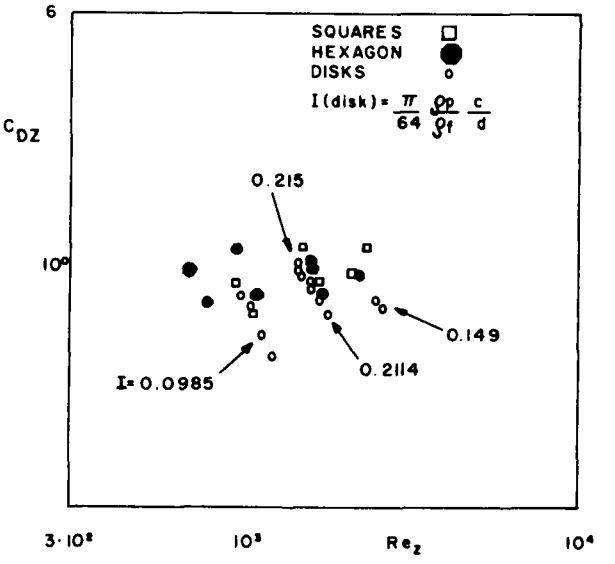

Fig. 10. Drag coefficient (C_{Dz}) plotted as a function of the Reynolds number (Re_z) for models with triangular and ellipsoidal cross section.

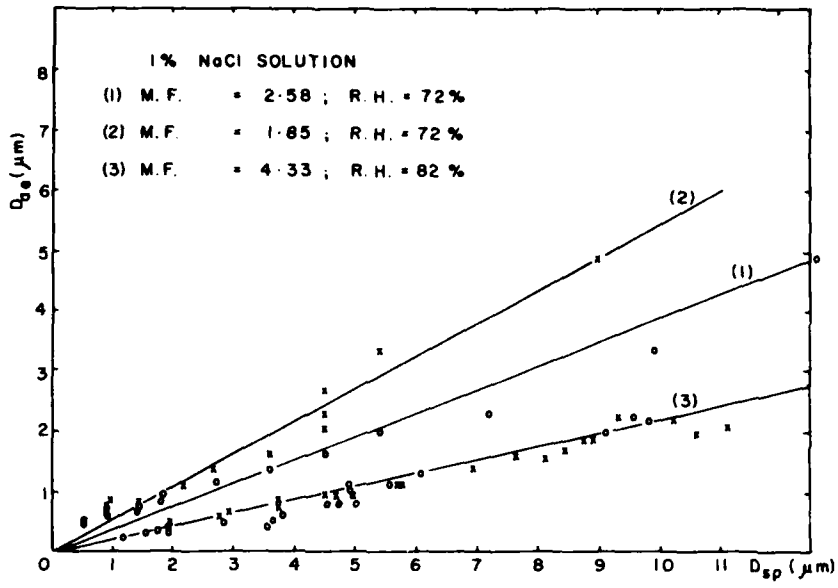

Fig. 11. Relationship between salt particle aerodynamic diameter (D_{ae}) formed in the sensitized gelatin sheet as a function of relative humidity (R.H.) during aerosol sampling. Mean magnification factors (M.F.) are calculated for each case. X - the sample was stored in a container above distilled water. 0 - the sample was stored in clean dry atmosphere.

III. AEROSOL CHARACTERIZATION METHODS

PARTICLE SIZING INTERFEROMETER MEASUREMENTS OF HYDROSCOPIC SMOKES IN LABORATORY AND FIELD ENVIRONMENTS

W. M. Farmer, R. D. Morris, F. A. Schwartz
Gas Diagnostics Research Division
The University of Tennessee Space Institute
Tullahoma, Tennessee

and

R. H. Doherty
Chemical Systems Laboratory
Aberdeen Proving Ground, MD

INTRODUCTION

A High Humidity Hydroscopic Smoke (H^3S) test was conducted at the Edgewood area of Aberdeen Proving Grounds during July 1979. The objective of the test was to examine the optical performance of hydroscopic smokes as a function of humidity in a field environment. The detailed results of that test will be available in a report to be published through the Smoke Project Manager's office at Aberdeen Proving Grounds. Data obtained in these tests included transmissivity for wavelengths ranging from the visible to 10 micrometers, dosage along the transmission path, and particle size distributions obtained with commercially available optical counters (Climet) and the particle sizing interferometer (PSI). Results obtained using these particle size analyzers during Smoke Week II showed significant differences in the particle size distribution. The PSI system consistently obtained larger geometric mean particle sizes than the commercial instrument. A primary reason why this may have been the case was the differences in the size ranges covered by the two instruments. The PSI covered a size range of roughly 0.5 - 8 micrometers while the commercial counter ranged between 0.2 and 6 micrometers. Other possibilities have been advanced to explain the differences, however, none have conclusively demonstrated why the differences existed. In an attempt to obtain data which might aid in an explanation of these differences, it was decided to use both instruments along with a third commercially available instrument (a PMS CSASP-100-HC) in laboratory controlled experiments at the Chemical Systems Laboratory Research Division prior to using the same instruments in the H^3S test. It was expected that the laboratory and field comparison would not only show direct variations in instrument performance under controlled conditions but would also indicate how well laboratory simulations compared with field data. The Climet optical counter did not arrive in time for the laboratory comparison. However, it was used in field tests. In the laboratory test the PSI and the PMS instruments were compared for size distribution

estimates. Mass concentration estimates were obtained using mechanical impactors and filter samples. Transmissometer measurements for wavelengths of 633 and 1150 nm were also made. Additional rests were conducted using a monodisperse generator and latex spheres. In this paper we will discuss the results of the various laboratory comparisons and the PSI measurement results obtained during H^3S. Results from the measurements obtained with the Climet instrument in the field tests are not available at this time.

LABORATORY TESTS

Particle size analyzers - The optical geometry for the PSI is shown in Fig. 1. The system was arranged to measure a particle size range of 0.3 - 6.0 micrometers. The smallest particle size detectable with the system was estimated to be approximately 0.2 micrometers for water droplets. This PSI used a 5 milliwatt HeNe laser, and F/2.2 receiving lens. An EMI 9781R photomultiplier tube was used as the photodetector. A description of the theory and operation of the PSI system is given in Appendix I. Data obtained with the PSI signal processor and data acquisition system were recorded on magnetic disk for hard copy presentation and data storage. The PSI measured particle velocity, signal magnitude, the PSI size parameter, visibility, and a particle number density parameter. The particle size histogram was divided into 21 bins corresponding to 0.3 micrometer size increments ranging from all particles less than 0.3 micrometers to all greater than 6.0.

The PMS CSASP-100-HC uses an exponential horn to shape the air flow drawn through the instrument with a small fan. The device uses a 5 milliwatt laser and measures the scattered signal magnitude observed with a lens in the forward scatter direction. The signal magnitudes (corresponding to equivalent latex sphere diameters) are sorted into histogram bins beginning at 0.3 micrometers and increasing in 0.04 micrometer increments to 1.0 micrometer where the bin width increases to 0.1 micrometer. The last two histogram bins cover 1.8 - 2.1 and 2.1 - 2.4 micrometers. For this experiment the histogram bin counts were recorded manually as read from a panel display on the PMS data acquisition and signal processing system.

Test chamber - The laboratory measurements were conducted in a sealed box with atmosphere initially at ambient temperature and humidity conditions. Figure 2 schematically illustrates the experimental arrangement for the measurements. The PSI system was placed directly inside the chamber. Filter samples and samples obtained with an Andersen Cascade Impactor were obtained via samples drawn from wall ports. Since the PMS particle analyzer measurements become uncertain due to the probability of multiple particle signals when particle number density is high, it was necessary to first dilute the smoke by allowing it to enter a dilution chamber through a small hole (diameter

approximately 3 mm) in the side of the main chamber.

Experimental procedure - Phosphorus and HC smokes were generated by igniting small samples at one end of the chamber. Fog oil was generated using a small commercially available fog oil generator. After initial smoke generation, the smoke was given time to become evenly dispersed in the chamber. During this time the operating parameters for the PSI were set and the other instruments tested for operational readiness. A common clock was used to synchronize time for all instrument samples. Transmissometer recordings were made continuously on strip charts. As soon as filter samples were obtained they were weighed to minimize any evaporation losses. The PSI was instructed to obtain chronological histograms of 10^3 counts each and to record all data on magnetic disks. The PMS system was manually interrogated at approximately 10 minute intervals. A typical test might run 30 to 60 minutes, after which the chamber was exhausted in preparation for the next test.

Data reduction and presentation - Transmissometer measurements were used to compute an optical depth as a function of time after smoke initiation. Mass concentration as a function of time was obtained using filter samples which trapped a portion of the smoke withdrawn from the chamber at a fixed flow rate. The PMS CSASP data were plotted on log-probability paper to obtain the geometric mean diameter and logarithmic geometric standard deviation. PSI data were used to compute the probability density, geometric mean diameter, standard deviation and particle number density. The method of estimating particle number density is new and described in a recent UTSI report.[1] By using the PSI measured distribution functions a mean particle volume was computed which together with the particle number density estimates provided an estimate of the mass concentration.

Experimental results - Table I shows a comparison of typical data for the three smokes examined, HC, red phosphorus, and fog oil. Geometric mean diameter, geometric standard deviation and third moments are compared for the particle size distributions determined by the PSI and the PMS CSASP. It should be borne in mind when comparing these data that the PSI measured particles less than 0.3 micrometers in diameter while the PMS system began at 0.3 micrometers and the smoke entered a dilution chamber through a relatively small hole prior to measurement. There is surprisingly good agreement between the two measurements when the geometric means are compared. The agreement is deceptive however. This becomes apparent when the logarithmic geometric standard deviations are compared. The PSI values are typically 1.6 to 2.4 times greater than that measured by the PMS system. This results from the fact that the PMS system measured virtually no particles greater than 1.0 micrometer in diameter. The PSI on the other hand typically found 3 - 4% of the distribution was greater than 1.0 micrometer. This difference is significant when the third moments of the distributions are computed in order to estimate mass concentration. A number density estimate

could not be obtained from the PMS system since the smokes were diluted before measurement. The number density column in Table I is the estimate obtained with the PSI. In order to indicate the fraction of particles less than 0.3 micrometers measured by the PSI, a column labelled % < 0.3 μm provides the probability density amplitudes for this size fraction. The last column compares the mass concentration as determined by the PSI estimates of third moment and number density with weight measurements of the filter extractions. A major uncertainty in the comparison is the material density of the smokes measured. Zinc chloride (density = 2.2 gm/cc) is assumed for HC Orthophosphoric acid (density = 1.82 gm/cc) assumed for red phorphorus and a density of 0.9 gm/cc is assumed for the fog oil. Agreement between the filter and the PSI estimates is remarkably good for the red phosphorus and fog oil when the large differences in the two methods to arrive at the concentrations are considered. The PSI technique is purely optical and subject to any localized variations in number density which may exist in the test chamber. The filter method of determining the concentration is purely mechanical—the smoke is pulled to the filter at a fixed flow rate for a fixed time interval and weighed. A significant difference exists in the HC comparison. It is not clear why this should be so. A possible explanation can be found in the fact that the HC is difficult to measure with the PSI— it scatters very poorly—and there may be relatively large concentrations of carbon. Hence, it takes a much longer time to measure the HC distribution than for the phosphorus or fog oil smokes. It should also be noted that the HC concentration was low for the measurements due to poor combustion. This may have led to a chemical composition different than zinc chloride and possible large inhomogenities in the spatial distribution of the particles in the test chamber.

Figures 3 through 5 plot the particle size distributions obtained with the PMS system. The deviations from the straight line fits to the data occur where the particle counts are relatively small and potential uncertainties large. As the figures show, the PMS size distributions are represented reasonably well by log normal distributions with mean diameters and logarithmic standard deviations indicated in the figures.

Figure 6 shows representative probability density functions as measured by the PSI for the smokes and for the background aerosol present in the laboratory where the measurements were made. The histograms for the smokes have been computed by suppressing all measurements involving particle sizes less than 0.3 micrometers. The data clearly show the contribution of the smokes to the small particle background. The strong multimodal characteristic of the fog oil smoke is a result consistently seen in a large number of different tests. These figures are somewhat deceptive in that with those sizes less than 0.3 micrometers suppressed the histograms represent only about 5 to 10% of the total numeric distribution measured. Nevertheless, they do show the source of most of the mass present in the smoke.

HIGH HUMIDITY HYDROSCOPIC SMOKE FIELD TEST

Test conditions and arrangement - The PSI used in the laboratory measurements was moved to a field test site and was used to obtain data under relative humidity conditions ranging from approximately 64 to 97%. The PSI measurements were part of a set of measurements that included UV through IR transmissometry, cloud shape measurements, aerosol photometry and chemical sampling along the transmission line-of-sight, particle size analysis, and meterological conditions.

Three types of hydroscopic smokes were measured 1) red phosphorus, 2) white phosphorus, and 3) HC. Standard phosphorus grenades were used to disperse the red phosphorus. White phosphorus was dispersed either as wicks or wedges from standard munition sources. HC was also dispersed using standard sources.

During the field trials the PSI was mounted at the center of the test grid approximately 80 cm above ground level. Within 2 m of the PSI position there were other particle sizing systems (Climet) and chemical impingers. The immediate ground surface surrounding the PSI was mowed grass. Plowed circular increments approximately 3 m wide on radii increasing in 10 m increments was used to minimize and prevent grass fires which could produce carbon smokes and damage instrumentation signal lines. The van housing the UTSI signal processing electronics was parked near the end of the test grid. Signals from the PSI optical system were transmitted down 150 m of coaxial cable. During a test PSI data were transferred to magnetic disk after 10^3 measurements were acquired in the microprocessor memory. The transfer process was identical to that used in the laboratory tests. In transferring data from memory to disk it was necessary for the system operator to instruct the data acquisition memory that no system constants were changed and no messages needed to be added to the next data file. Thus a 20 to 30 second time interval existed between the end of a data set and the initiation of the next set.

Test results - PSI data for 21 out of 28 test trials is presented here. Of the trials for which data is not presented either wind conditions changed after smoke initiation causing most of the smoke to miss the PSI or resulting in insufficient sample size for reliable data or there were uncontrollable system malfunctions resulting from, for example, burning phosphorus landing on signal transmission lines.

Table II summarizes the PSI measurements from the various trials. The data is grouped by type of obscurant and listed in terms of decreasing humidity. The average geometric mean particle diameter and the standard deviation for all data sets obtained during a trial is listed as is the average logarithmic geometric standard deviation. The range of particle number densities for the data sets in a given trial is listed in terms of 10^6 cc^{-1}. The average probability density amplitude and standard deviation for particle sizes less than 0.3 micrometers is listed to

indicate the most predominant mode in the size distribution. The typical mass concentration was computed using the most frequently occurring number density found in the data sets. As with the laboratory data a density of 1.82 gm/cc (orthphosphoric acid) was assumed for the phosphorus smokes. Insufficient particle counts for the HC smokes did not provide reliable data for mass concentration estimates.

It is of interest to compare the laboratory results for red phosphorus with those obtained in the field. Trial 3 in Table II is nearest in humidity conditions for the laboratory data shown in Table I. The data shows that the geometric mean diameters agree within 10% (mean field diameter being larger) and that the field variation is sufficient to cover that measured in the laboratory. The logarithmic geometric standard deviations agree within an 8% difference. The typical number density used for the laboratory measurements was 50% greater than that of the field trial. The greatest apparent difference in the two sets of data apparently occurs in the amplitude of the probability density for particle diameters less than 0.3 micrometers. The data shows that there are approximately 10% fewer particles in the field test small size mode than that found in the laboratory tests.

Figure 7 plots the measured geometric mean diameter as a function of humidity for all smokes for which reliable data exists (i.e. when more than a single set of measurements is obtained in a given trial). The variation in the mean values is typically the size of the symbol used to distinguish the various smokes. Figure 6 shows little if any dependence on humidity. This result arises from the fact that most of the size distribution occurs for particle sizes less than or equal to 0.3 micrometers. Hence, the figure reflects the fact that most of the particle diameters are less than the smallest size resolvable by the PSI.

When only the resolvable particle diameters are considered the geometric means show significant variations with humidity. Figure 8 plots the geometric mean diameter for all sizes greater than 0.3 micrometers. The general trend is for the mean size to increase with humidity. The large variations between the methods of dispersion may be due to the fact that only about 10% of the total numeric distribution is represented by these values.

The volumetric mean particle diameter has been predicted to be a function of humidity for hydroscopic smokes. Figure 9 plots the volumetric mean diameter as a function of humidity. The volumetric mean diameter was computed by raising the third moment of the entire distribution to the one-third power. The results shown in Fig. 9 are striking. They show a decrease in mean volumetric diameter with humidity until the humidity is about 80% at which point the diameter begins to increase. An interesting effect revealed in Fig. 9 is the apparent difference in mean diameter resulting from the method of dispersal. The white phosphorus wicks and wedges yield volumetric mean diameters

about 30% greater than the red phosphorus grenades when the humidity is less than about 80%. At about 80% the volumetric mean diameters are about the same. As the humidity increases the differences are again about the same.

Since the volumetric mean diameter is most sensitive to the particle mass distribution, these data suggest that at humidities greater than about 90% the white phosphorus wedges yield greater smoke mass than either the RP grenades or the white phosphorus wicks. The wicks and grenades have about the same yield above 90% humidity. At about 80% humidity, the mass yields for all phosphorus smokes is about the same. At humidities below 80%, the wicks and wedges have about the same yield as a function of humidity and it is greater than the RP grenades.

One feature of Fig. 9 which clearly stands out is the apparent decrease in particle diameter with increasing humidity until approximately 80% RH is reached when the trend is reversed and the particle size increases. This effect is consistent with PSI observations made during Smoke Week II. During Smoke Week II, no measurements were made for humidities greater than 80%. The smallest particle size detectable with the PSI used in Smoke Week II was approximately 0.4 to 0.5 micrometers. Hence, mean particle diameters determined by the PSI during Smoke Week II PSI data are plotted in Fig. 8. These points were chosen because they conveniently fit on the scale chosen for the H^3S test data. Data for humidities as low as 40% show the same trend.

Trials 9 and 13 obtained for 80% humidity show the remarkable result that the volumetric mean diameters are identical. This data is for white phosphorus wicks and was taken on two successive trial days. Trial 9 was obtained at 1635 hours while trial 13 was obtained at 0832 hours on the following day.

Trials 4 and 27 were obtained for 73% humidity with approximately 48 hours separating the tests. The quantity of munitions used in trial 27 was approximately twice that used in trial 4. This is the only apparent external difference in the two tests. This suggests that for a given humidity, the mass yield of the smoke depends on the quantity of munitions used. It should be emphasized that this is a size distritution effect. The number density at the PSI for trial 27 was estimated to be less than that for trial 4 (wind conditions dispersed the smoke differently in the two trials).

In order to illustrate the distribution functions which yielded the data shown is Figs. 8 and 9, representative distributions have been selected for the various trials listed in Table II. The probability density distributions have been computed for all particle sizes greater than 0.3 micrometers. These data are presented in Figs. 10 through 12. Figure 10 shows the distributions for red phosphorus grenades. The multimodal character of the distributions is evident. Note the apparent shift of the peak of the large particle mode toward larger particle

sizes as the humidity decreases. Data shown in Fig. 11 strongly resembles that in Fig. 12 with the exception of trial 8 where the magnitude of the probability density for the particle size increment 0.3 to 0.6 micrometers is roughly 50% that of the other distributions. Data for trials 27 and 4 in Fig. 11 shows a distinct shift toward a larger particle size in the large particle modes for trial 27 which used twice the munition source of trial 4. The histograms shown in Fig. 12 are strikingly different than those shown in Figs. 10 and 11. The primary difference between the probability densities is the significantly smaller probability density amplitudes for the particle sizes less than about 1.2 micrometers for the white phosphorus wicks.

There is a marked difference in the probability density distributions for laboratory tested red phosphorus (Fig. 6) and red phosphorus grenades at about the same humidity (trial 3, Fig. 10). The field test reveals a distinctly bimodal distribution while that measured in the laboratory tests does not reveal a distinct peak in the particle size range greater than 1.5 micrometers but rather a relatively smooth roll off in probability density amplitude with increasing size. The volumetric mean diameter of that found in the laboratory is roughly 20% smaller than that found in the field tests.

SUMMARY AND CONCLUSIONS

A comparison between a PSI and a commercially available optical particle sizer has been obtained. Both instruments were used to measure phosphorus, fog oil, and HC smokes under laboratory conditions while simultaneous transmission and filter sample measurements were made. The PSI determined geometric mean size agreed reasonably well with that determined by the commercially available instrument. There was a significant difference when the third moments of the size distributions were compared. The third moments determined by PSI measurements were significantly larger than those determined by the commercially available device. Mass concentrations were determined with the PSI data and found to be in reasonable agreement with that obtained with a filter sampler.

The same PSI system examined in the laboratory tests was next used in the H^3S field tests to examine particle size distribution as a function of humidity. Relative humidity for the tests varied between 67 and 97%. The PSI data show the following results:

1. Geometric mean particle diameter for all smokes measured is essentially independent of humidity.

2. Volumetric mean diameter measurements indicate a decrease in diameter with increasing humidity to values of about 80% at which point the diameter begins to increase with increasing humidity.

3. The data for white phosphorus wedges show a potential for increasing the volumetric mean particle diameter by increasing the amount of munitions used to generate the smoke.

4. The volumetric mean diameter for phosphorus smokes appears to depend on the method used for dispersal.

These results appear to be at variance with generally well-known theoretical predictions which predict a monotonic diameter increase with increasing humidity. However, the results presented here appear to be consistent with PSI results found during Smoke Week II for lower humidity values and appear to be reasonably consistent with extinction coefficients measured as a function of humidity during H^3S for the 8 to 12 micrometer transmissometer system. The variance of this data with theoretical results indicates that additional detailed experimental effort is called for in testing these smokes under high humidity conditions in a field environment.

APPENDIX I

PSI MEASUREMENT PRINCIPLES

For completeness, a brief review is given of the basic principles underlying the determination of particle size from a measurement of the signal visibility of a particle passing through interference fringes produced by two laser beams. A more complete description of the measurement technique is given in Ref. 1.

As shown in Fig. 1, consider two equal intensity, well-collimated coherent light beams which intersect as a common origin (geometric center) with an included angle α. A Huygen's diagram of the wave fronts shows that planar interference fringes are formed which are perpendicular to the plane defined by the beam centerlines and are parallel to the bisector between the beams. The distance δ between the periodic fringes is given by

$$\delta = \lambda/[2\sin(\alpha/2)] \tag{1}$$

where λ is the wavelength of the coherent light. When a particle (assumed spherical) much less than δ in diameter crosses the fringe pattern, it can be assumed to be uniformly illuminated at all points along its path through the fringe pattern, and the light which is scattered by the particle is proportional to the observable flux illuminating it. Thus, measurement of the time period, τ, of the scattered light is related to the velocity, v, of the particle through the relationship

$$V = \delta/\tau \tag{2}$$

As the size of the scattering particle increases relative to δ, the illumination of the particle is no longer uniform and must be averaged over the cross-sectional area of the particle. The non-uniform illumination of the particle results in a reduction of the contrast or visibility of the scattered light signal. Let I_{max} be the maximum value in intensity in a period of the scattered light from a particle and I_{min} the next successive minimum. The visibility, V, can then be defined as:

$$V = \frac{I_{max} - I_{min}}{I_{max} + I_{min}} \tag{3}$$

It is straightforward to show that V is fully equivalent to the ratio of AC amplitude divided by the DC amplitude of the scattered light signal. The high frequency "Doppler" portion of the signal is defined as the "AC," it usually has many cycles of information relative to that of the DC component (the DC component refers to the Gaussian shaped low frequency term describing the signal). Analytically the visibility may be written as:

$$V \simeq \frac{\int_{A_p} I_o \cos(2\pi y/\delta) dA_p}{\int_{A_p} I_o \, dA_p} \tag{4}$$

where A_p is the cross-sectional area of the particle, I_o is intensity distribution across one of the illuminating beams, and y is the coordinate normal to the fringe planes. When I_o is a Gaussian function (TEM_{ooq} laser beam) it can be shown that Equation 4 is an accurate approximation over a depth of field, ℓ, given by:

$$\ell \simeq 0.8 \, b/\alpha \tag{5}$$

where b is the radius of the e^{-2} intensity point in the illumination beam. For depths of field greater than ℓ, the signal visibility is function of particle size and position in the illumination. In order to simplify Equation 4 for Gaussian beams and still maintain accuracy, it is required that the particle diameter, D, satisfy the relationship:

$$D \lesssim 0.2b \tag{6}$$

and for δ to satisfy:

$$\delta \lesssim 0.2b \tag{7}$$

Under these conditions V for a sphere can be written as

$$V \simeq 2J_1(\pi D/\delta)/(\pi D/\delta) \tag{8}$$

where J_1 is a Bessel function of the first kind. For a cylinder V can be written as

$$V = \sin(\pi L/\delta)/(\pi L/\delta) \qquad (9)$$

Equations 8 and 9 are plotted in Fig. 2 to illustrate the salient features of the visibility in particle size measurement.

Figure 2 shows that for spherical particles, the visibility function is not monotonic for sizes greater than about 1.05 δ. This value fixes the upper limit of the PSI size range. The lower limit results from the acceptable error in the particle size measurements. Since particle size is a non-linear function of visibility, a 1% uncertainty in visibility gives a 1% uncertainty in D when D/δ is about 1, but ±30% when D/δ is about 0.1. Acceptable sizing uncertainty and signal processor accuracy thus limit the low end of the PSI size range to about 0.05 D/δ. Hence, the PSI can cover about a 20:1 size range for a given δ. By scaling δ through a variation of the angle between the beams, particle sizes from submicron to greater than millimeter can be measured.

The PSI can also be used to obtain estimates of particle number density. As Reference 7 will show, the PSI signal processing electronics subjects the signal to certain logic tests to determine if the signal results from more than one particle. Multiple particle signals are not accepted for size measurement, but are counted as being detected. Also counted, but not measured are those single particles which pass near the edge of the sample space which are detected but generate signals with insufficient information for a size measurement. A random walk analysis can be used to relate particle number density to the ratio of number of measurements accepted for measurement to those detected. The random walk analysis yields the relationship

$$A = 1 - 2 \exp\left(-\frac{\gamma}{2}(1 + K^2)\right) \left| \sinh(\gamma) \sinh(K^2\gamma) \right|^{1/2} \qquad (10)$$

where

A = Number of particles accepted for measurement/number of particles detected.

$\gamma = a \rho_N^{1/3}$

a,K = Optical System Constants

ρ_N = Particle Number Density

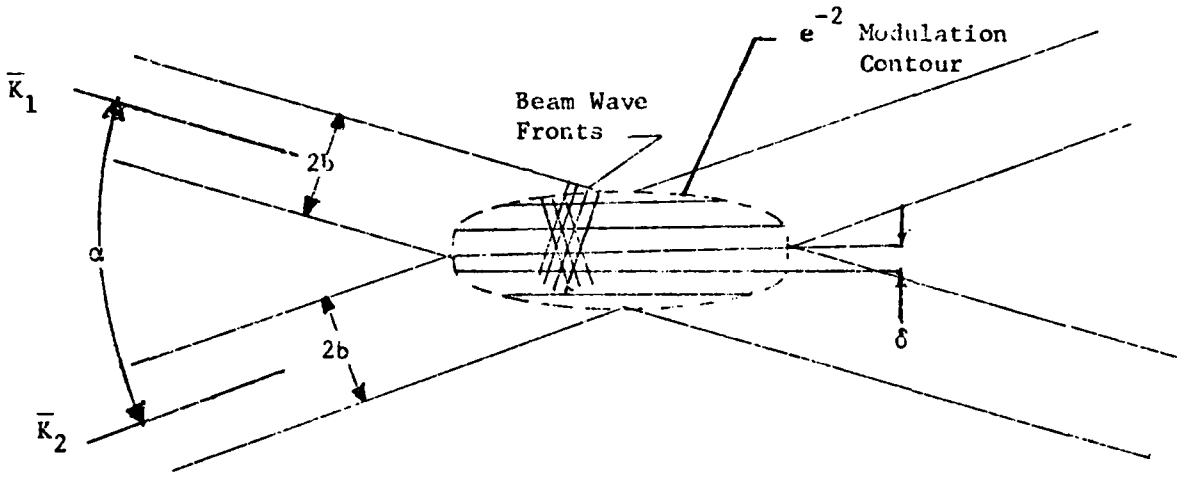

Figure I.1. Huygen's diagram of interference fringe generation in probe volume.

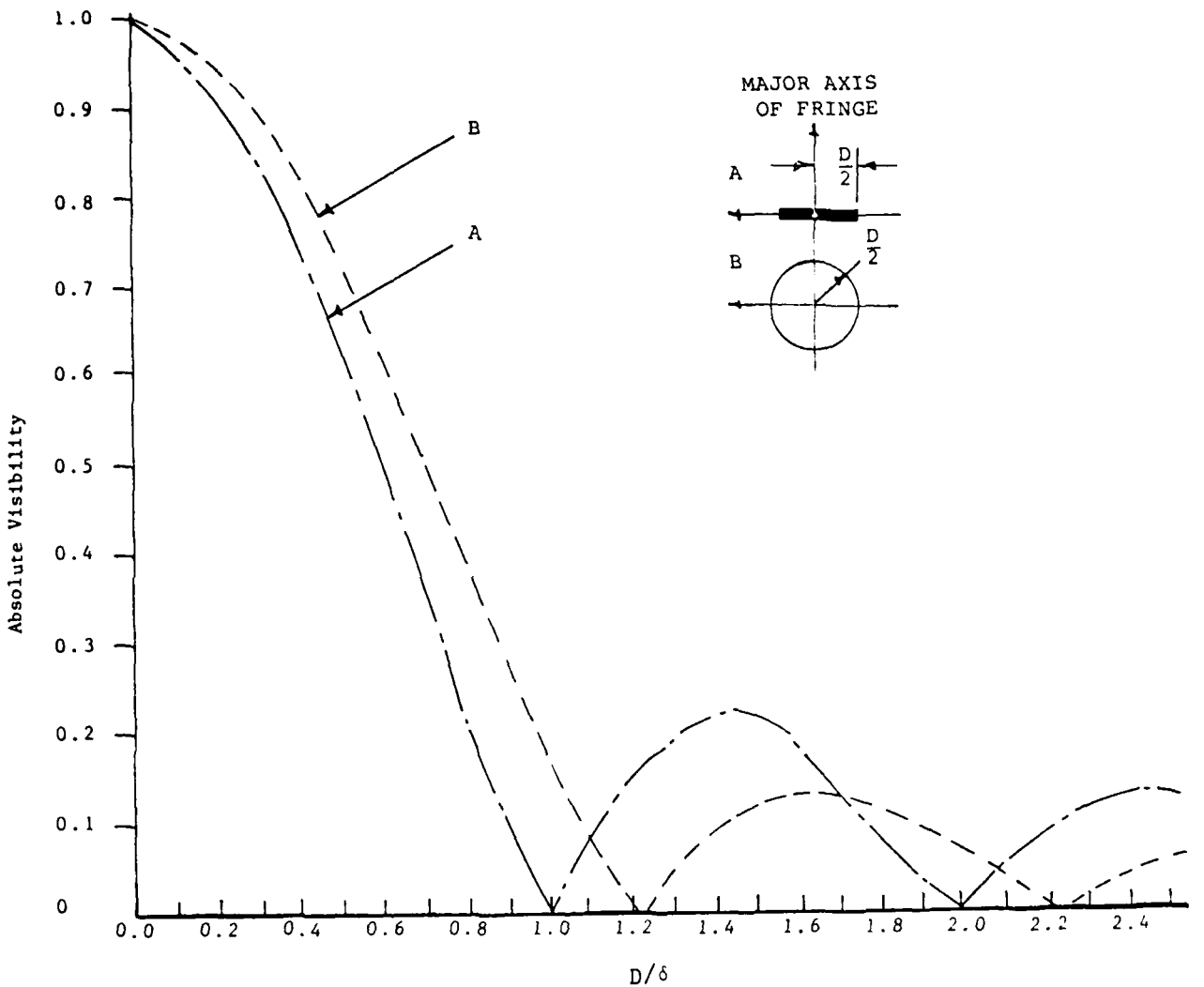

Figure I.2. Visibility as a function of D/δ for two particle shapes.

TABLE 1

COMPARISON OF TYPICAL LABORATORY CALIBRATION DATA FOR 81-83% RH

	GEOMETRIC MEAN DIAMETER (μm)		LOGARITHMIC GEOMETRIC STANDARD DEVIATION		THIRD MOMENT (μm^3)		NUMBER DENSITY	% < 0.3 μm	MASS CONCENTRATION (gm/m^3)	
	PSI	PMS CSASP	PSI	PMS CSASP	PSI	PMS CSASP	($cc^{-1} \cdot 10^{-6}$)		PSI	FILTER SAMPLE, IMPACTOR
HC	0.334	0.34	0.421	0.175	0.72	0.01	0.576	93	0.44	0.17
RED PHOSPHORUS	0.328	0.415	0.431	0.262	0.97	0.0865	1.62	94.8 $\pm$ 0.8	1.50	1.4
FOG OIL	0.326	0.42	0.432	0.26	0.969	$9.5 \cdot 10^{-4}$	1.07	95.2 $\pm$ 0.9	0.49	0.34

TABLE 2

COMPARISON OF H^3S TRIAL RESULTS
(PSI DATA ONLY)

TRIAL	TYPE OBSCURANT	RELATIVE HUMIDITY	GEOMETRIC MEAN DIAMETER (μm)	LOGARITHMIC GEOMETRIC STANDARD DEVIATION	NUMBER DENSITY RANGE ($CC^{-1} \cdot 10^{-6}$)	$\% \leq 0.3\ \mu m$	TYPICAL MASS CONC. (gm/m^3)
	RP GRENADES						
10	4.8 lbs.	97%	0.362 ± 0.02	0.468	0.33 - 1.53	90 ± 3.1	1.23
15	3.2 lbs.	89%	0.357 ± 0.02	0.455	0.238 - 0.6	90 ± 2.5	0.40
3	3.2 lbs.	79%	0.359 ± 0.03	0.465	0.381	86.5 ± 2.3	0.74
7	6.4 lbs.	73%	0.370 ± 0.01	0.474	0.59 - 0.97	88.6 ± 2.6	0.79
18	6.4 lbs.		0.459 ± 0.11	0.570	0.464	86.4	
19	3.2 lbs.	67%	0.428 ± 0	0.539	0.275	81.5	0.71
	WP WEDGES						
17	13.7 lbs.	92%	0.365 ± 0.02	0.461	0.411 - 0.681	88.4 ± 2.4	1.1
12	13.7 lbs.	89%	0.358 ± 0.02	0.471	0.465 - 6.4	90.7 ± 1.7	1.59
8	13.7 lbs.	79%	0.362 ± 0	0.463	0.245 - 0.325	89.7 ± 1.9	0.53
4	13.7 lbs.	73%	0.381 ± 0.03	0.492	0.325 - 0.938	87.4 ± 5.2	1.26
27	27.4 lbs.	73%	0.430 ± 0.068	0.530	0.275 - 0.638	81.8 ± 8.08	1.13
	WP WICKS						
16	2.1 lbs.	94%	0.347 ± 0.01	0.45	0.317 - 0.725	92.2 + 2.0	0.49
2	6.3 lbs.	82%	0.358 ± 0.02	0.466	1.03 - 3.49	91.9 ± 1.1	0.98
9	4 2 lbs.	80%	0.363 ± 0.01	0.463	0.238 - 0.653	89.4 ± 1.7	0.35
13	4.2 lbs.	80%	0.363 ± 0.01	0.468	0.343 - 1.17	90 ± 2.0	1.82
28	4.2 lbs.	75%	0.447 ± 0.01	0.536	0.454 - 0.89	78.9 ± 0.9	1.69
25	4.2 lbs.	71%	0.409 ± 0.03	0.501	0.237 - 0.652	82.0 ± 4.5	0.56
	HC						
11	10.8 lbs.	97%	0.341 ± 0.01	0.448	0.32 - 4.95	93.1 ± 0.3	
23	10.8 lbs.	87%	0.367 ± 0	0.466			
14	5.4 lbs.	84%	0.402	0.470	0.411		
6R	10.8 lbs.	72%	0.407 ± 0	0.540			

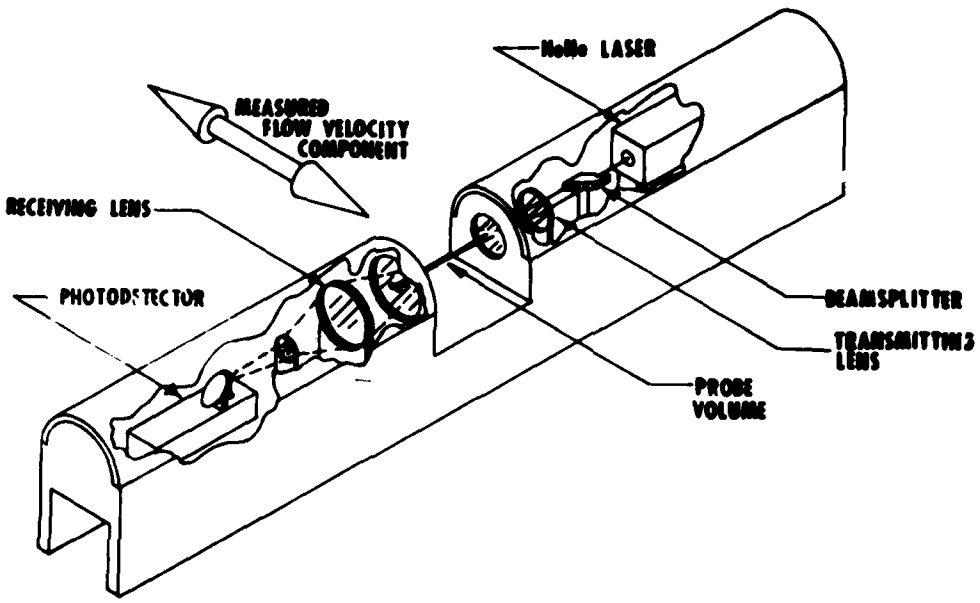

Figure 1. Schematic of the PSI optical system used in the laborator and field measurements.

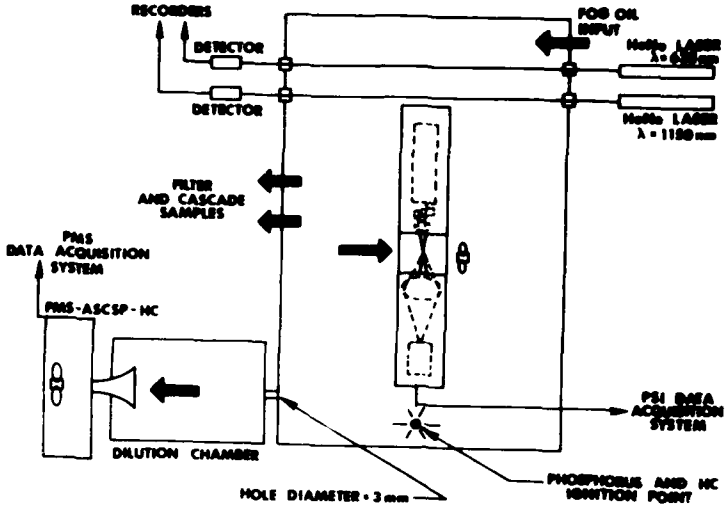

Figure 2. Schematic of the smoke chamber for laboratory comparisons.

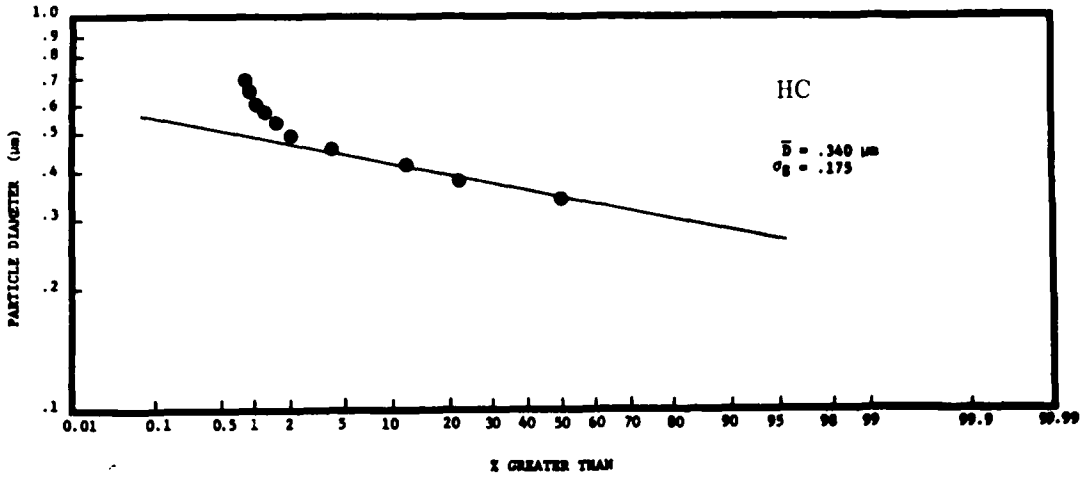

Figure 3. PMS measured size distribution for HC.

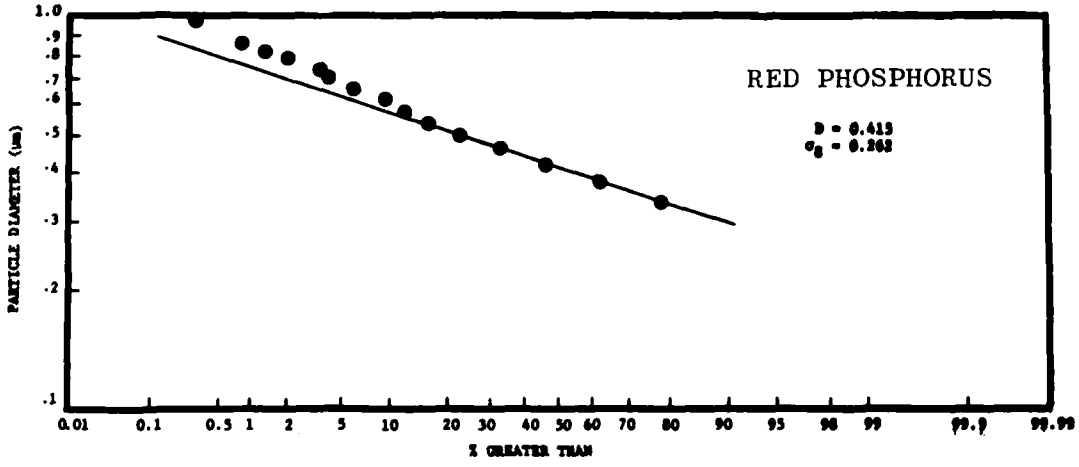

Figure 4. PMS measured size distribution for red phosphorus.

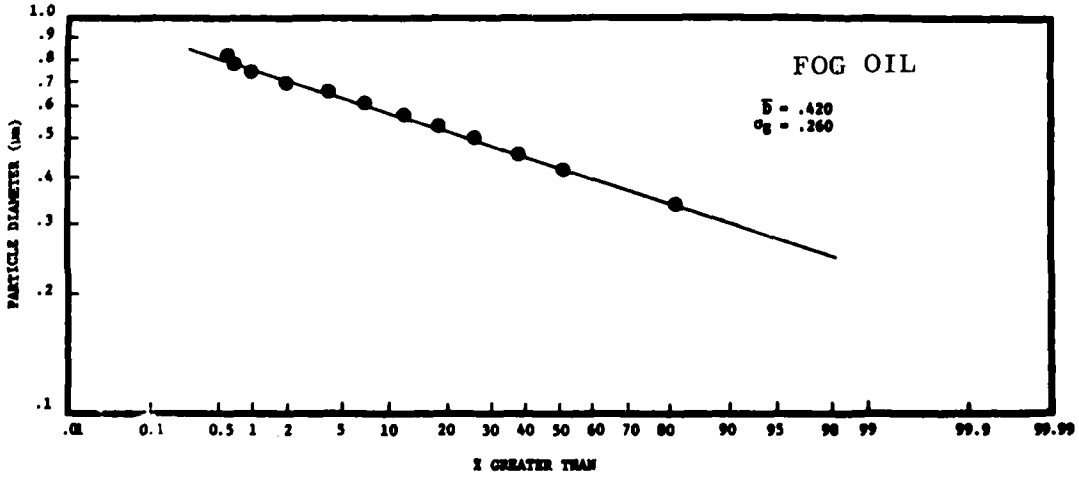

Figure 5. PMS measured size distribution for fog oil.

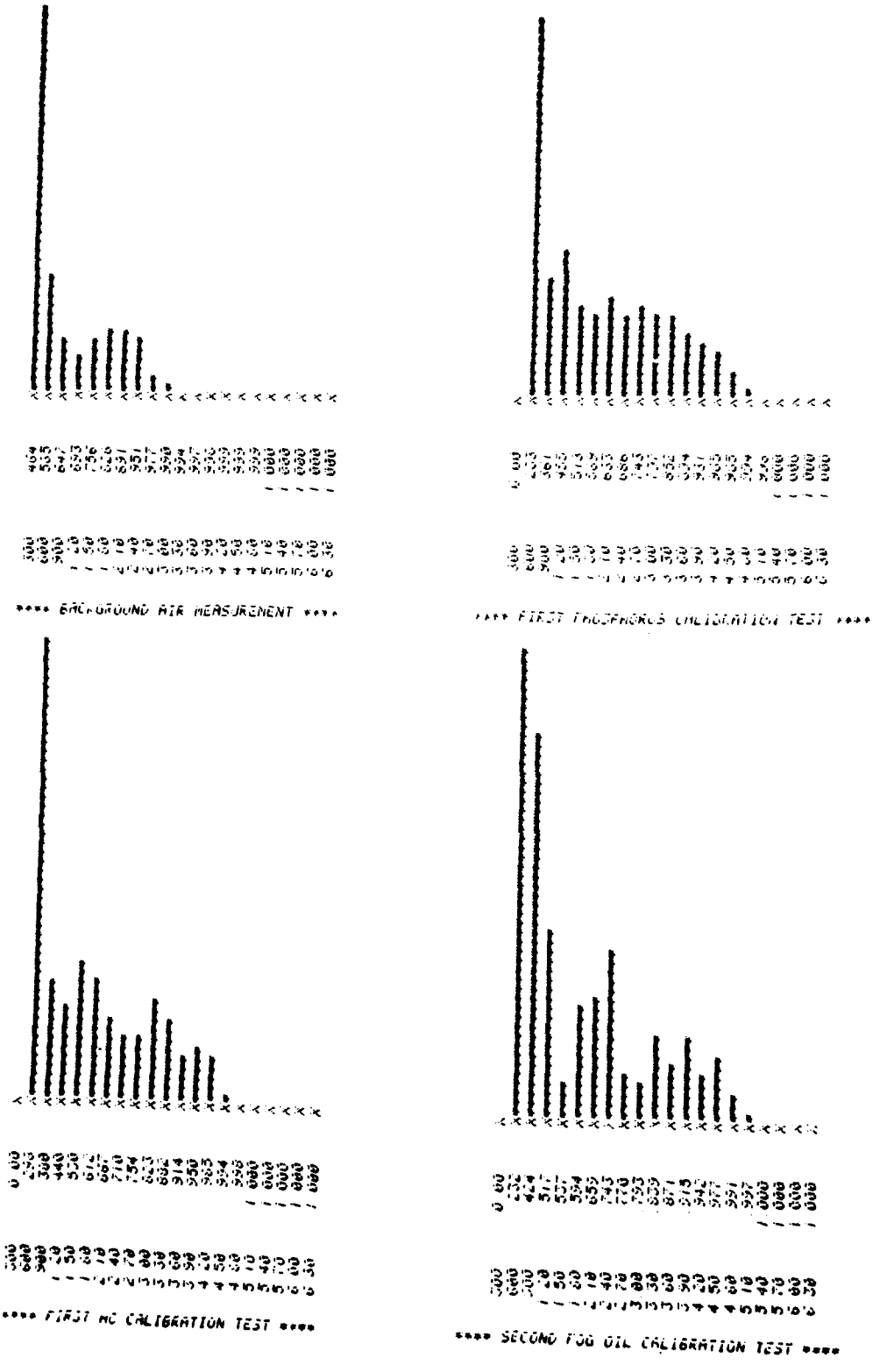

gure 6. Examples of the probability density distributions obtained in laboratory measurements.

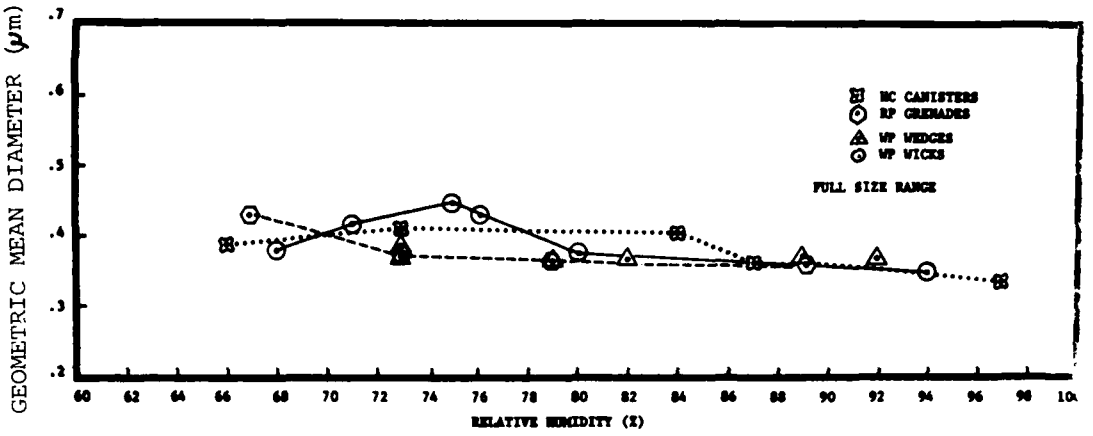

Figure 7. PSI determined geometric mean diameters as a function relative humidity for smokes measured during H^3S.

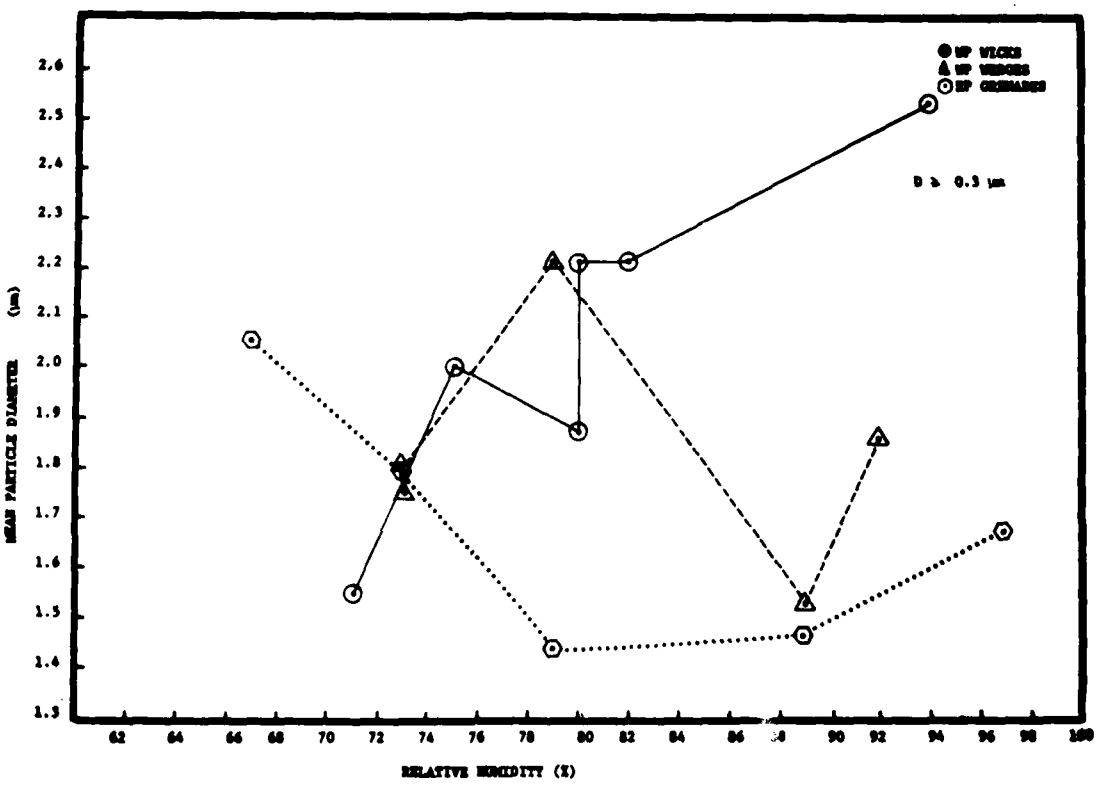

Figure 8. Geometric mean diameters as a function of relative humidity with all particle sizes less than 0.3 micrometers suppressed for phosphorus smokes in H^3S.

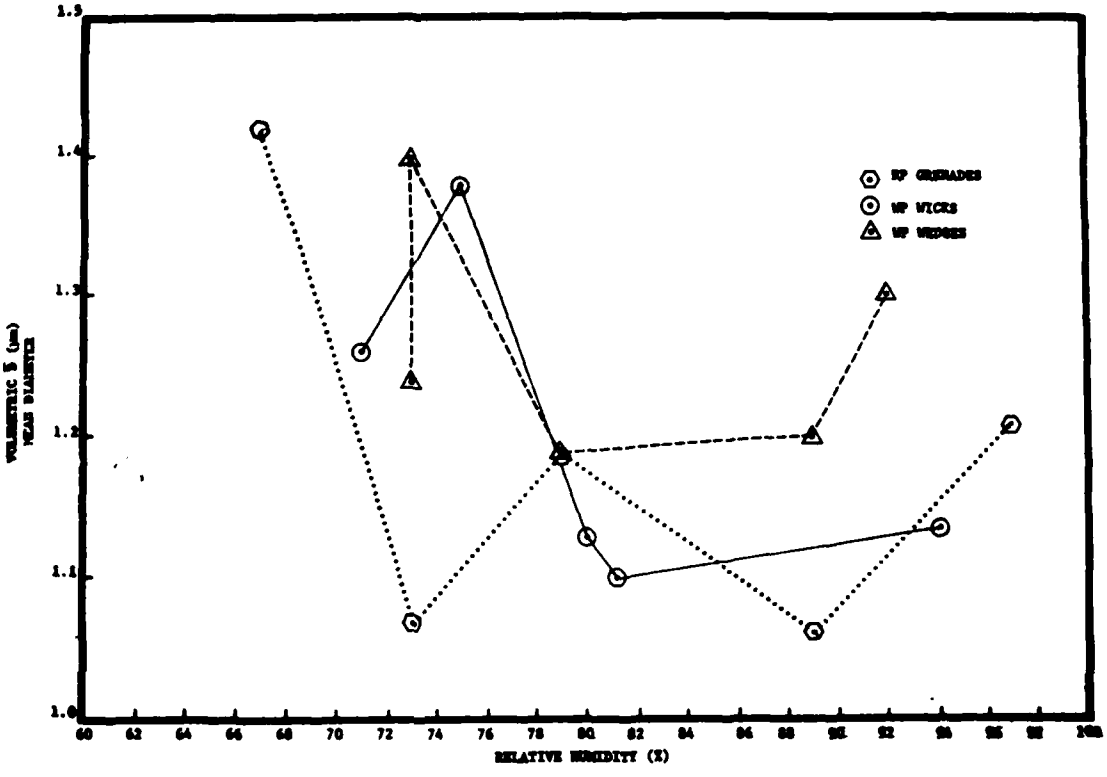

Figure 9. Volumetric mean diameters as a function of relative humidity for phosphorus smokes measured during H^3S.

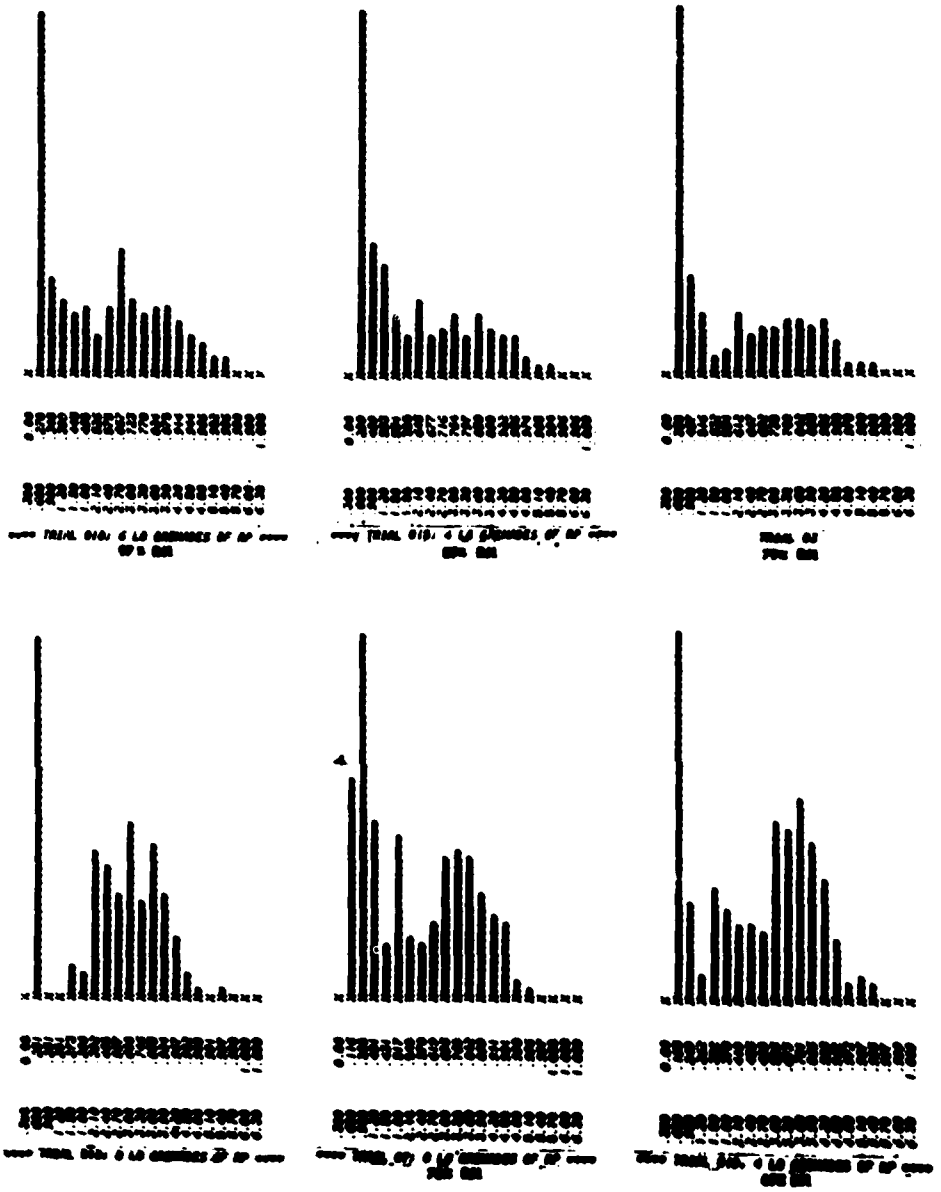

ure 10. Examples of probability density distributions for L8 Granades of RP with relative humidities ranging between 97 and 67%.

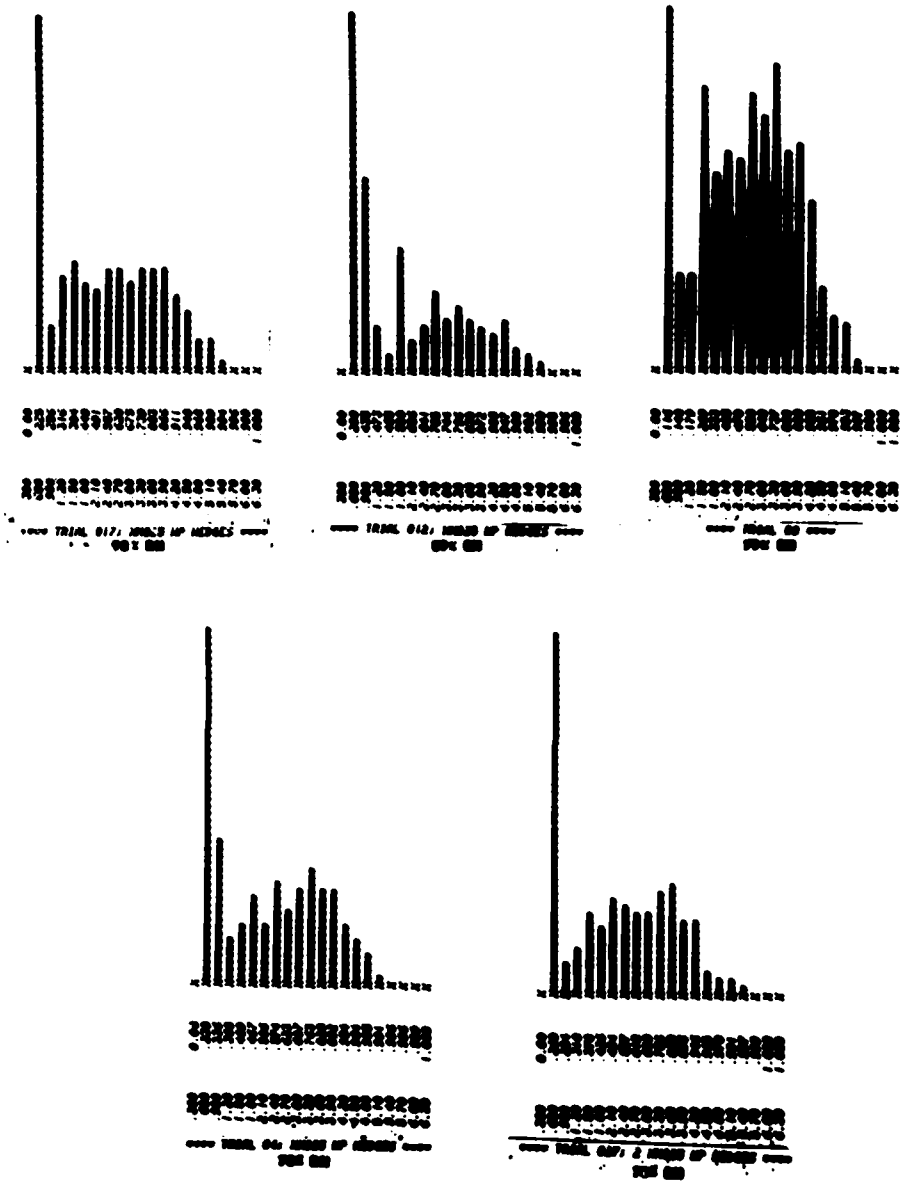

Figure 11. Examples of probability density distributions for white phosphorus wedges with relative humidities ranging between 92 and 73%.

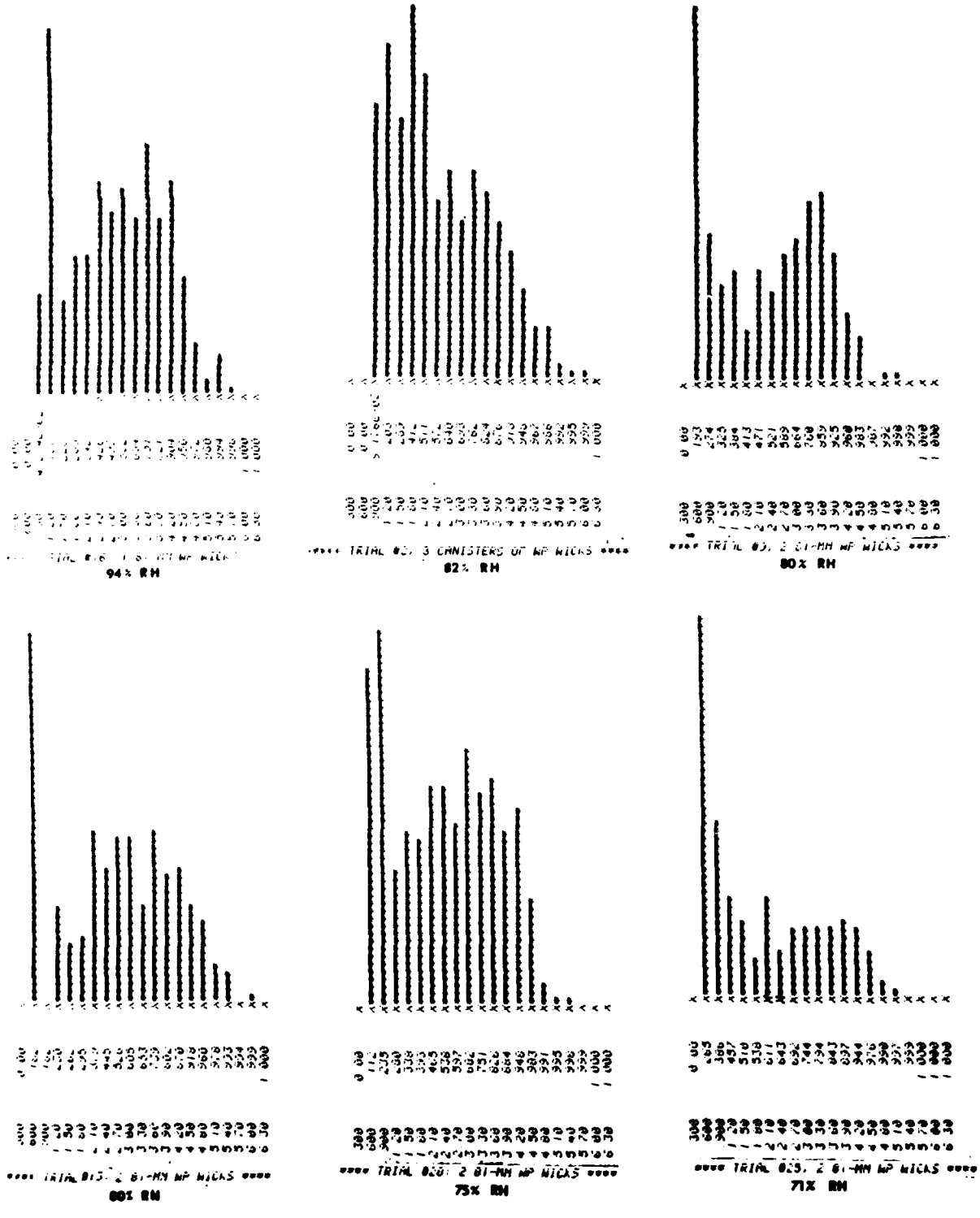

Figure 12. Examples of probability density distributions for white phosphorus wicks with relative humidities ranging between 94 and 71%.

RESPONSE OF LIQUID DROPS TO OSCILLATING ELECTROMAGNETIC FIELDS AS A MECHANISM FOR PARTICLE SIZE DETERMINATION

Dr. N. Karayianis, Dr. R. P. Leavitt, Dr. C. A. Morrison
and Dr. D. E. Wortman, Harry Diamond Laboratories

PUBLISHED RESULTS:

The Extended Rayleigh Theory of the Oscillation of Liquid Droplets. Submitted for publication in J. Fluid Mech. (Sept. 1979).

The Oscillation of Liquid Droplets Driven by an Electric Field. HDL-TR (in press Aug. 1979).

Possible use of two Laser Beams to Determine Particle Size Distribution. HDL-TR-1878 (Jan. 1979).

Increased Transmission of Electromagnetic Radiation through a Fog by Amplitude Modulation at the Resonant Frequency of the Average Droplet. HDL-Report-R-RCB-77-1 (Jan. 1977).

Quasistatic Approximation to the Electric Field in a Liquid Drop. HDL-Report-R-RCB-77-3 (Feb. 1977).

Theory of Vibrating Drops and Coupling to the Electric Field. HDL-Report-R-RCB-77-4 (Feb 1977).

Scattering Caused by Oscillating Drops. HDL-Report-R-RCB-77-5 (Feb. 1977).

Rayleigh's Method Applied to a Conducting Liquid Drop in the Presence of a Point Charge. HDL-Report-R-R-CM-AP-79-4 (June 1979).

The Extended Rayleigh Theory of the Oscillation of Liquid Droplets. HDL-Report-R-R-CM-AP-79-9 (Aug. 1979).

PRESENTATIONS:

Particle Response to Amplitude Modulated Electric Fields as a Mechanism for Particle Size Determination. First CSL Scientific Conference on Obscuration and Aerosol Research, June 1978.

Light Scattering from Oscillating Dielectric Spheres. First CSL Scientific Conference on Obscuration and Aerosol Research, June 1978.

Extended Rayleigh Theory of the Oscillation of Liquid Droplets. Second CSL Scientific Conference on Obscuration and Aerosol Research, September 1979.

An experimental and theoretical study has been made to determine whether particle size distributions for small diameter aerosols (radius $\leq$ 20 μm) such as fog can be determined by a new, novel technique[1] based on resonantly distorting the liquid drops by an oscillating electric field. This technique utilizes the fact that a liquid drop elongates along the axis parallel to an applied electric field.[2,3] It can be shown that the elongation is independent of the sign of the field; hence the force acting on the drop is proportional to the square of the electric field. This phenomenon suggests the following two cases where a drop can be resonantly driven[4] at its natural vibrational frequency by an alternating electric field.

For case 1, suppose that a linearly polarized beam of electromagnetic radiation is modulated so that the amplitude of the electric field varies as $E = E_o \cos\omega t\ (1 + m\cos\omega_m t)$, where E_o is a constant, $\omega/2\pi$ is the carrier frequency, $\omega_m/2\pi$ is the modulation frequency, and m is the index of modulation. The force on the drop, which is proportional to E^2, varies approximately as $E_o^2\ (1 + 2m\cos\omega_m t)/2$. The modulation frequency, ω_m, can be adjusted to match the mechanical vibrational frequency[5], ω_n, given by:

$$\omega_n = \sqrt{\frac{n(n-1)(n+2)\gamma}{\rho a^3}},$$

where n is the mode number, γ is the surface tension, ρ is the density, and a is the drop radius. As other workers have pointed out[6], the lowest order (n = 2) mode dominates; thus resonance occurs when the electromagnetic wave incident upon the liquid drop is amplitude modulated at $\omega_2 = (8\gamma/\rho a^3)^{\frac{1}{2}} = \omega_m$.

For case 2, suppose an alternating voltage is applied to two condenser plates which produce an electric field varying as $E = E_o \cos\omega_m t$. The force on a liquid drop situated between these plates varies as $E_o^2 \cos^2\omega_m t = E_o^2(1 + \cos 2\omega_m t)/2$. A resonance occurs for this case when $\omega_2 = 2\omega_m$. Hence the electric field driving the drops will be only $\frac{1}{2}\omega_2$, whereas $\omega_2 = \omega_m$ for case 1. Billings and Holland[7] have made measurements previously on mm size water drops under experimental conditions that correspond to this latter case.

In other earlier work, Brook and Latham[8] demonstrated that single vibrating mm-size drops can produce modulation of backscattered microwave signals and that the modulation frequency can be related to drop size. Also several earlier studies, for examples references 2-7 and 9-15, have shown that mm-size water drops can be caused to elongate in dc electric fields,

to vibrate in ac electric fields, and to elongate so much that they rupture in electric fields of the order 10^4 volts/cm. In addition, Billings and Holland[7] found that rupture for drops smaller than 3 mm occured at considerably lower field strengths when they varied the frequencies of the applied field near the drops' resonance frequencies than occured in the static case. Results of these earlier studies suggest that somewhat weaker amplitude modulated electric fields, as transmitted by a CO_2 laser, might suffice to cause mechanical oscillations of detectable magnitude for drops driven at their resonance frequencies.

Results of this study indicate that particle size distributions for liquid drops larger in size, $\geq$ 20 μm, than those that comprise most fogs, < 20 μm, might be determined by driving liquid drops resonantly with an oscillating electric field. In performing the experiments, this technique required our first, using a linearly-polarized, amplitude-modulated CO_2 laser beam to drive water drops of a given radius resonantly at their fundamental vibration frequency; second, determining that the drops are indeed oscillating by detecting an ac component at the modulation frequency in He-Ne laser light scattered from the drops; and third, varying the modulation frequency to correspond to the mechanical oscillation frequency of drops of another radius. The intensity of the ac signal would then vary with the concentration of drops of a particular radius.

In the measurements that were made with:

a) a linearly-polarized, amplitude-modulated 3-watt CO_2 laser focussed to give a power density of 100 watts/cm^2, and

b) a 2 milliwatt He-Ne laser and a sensitive detection system capable of measuring ac signals with intensities as low as about 10^{-17} watts,

no ac signals corresponding to oscillating water drops of radii in the range 1.19 to 21.2 μm were detected. This result is consistent with the results of theoretical calculations that were also made, first, to determine oscillation amplitudes for the drops driven resonantly at their fundamental vibration frequency and, second, to determine scattering intensities made from drops of different radii and shapes. In the first calculation, it was found that the amplitude of oscillation for 20 μm radius drops, for example, is 2.7×10^{-10} meters, and the oscillation amplitudes decrease for smaller drops as the 5/2 power of the radius. Since the calculated oscillation amplitudes scale directly with the power density, slightly higher powered lasers would produce detectable oscillations in 20 μm drops, for example, but to obtain observable oscillations in 1 μm radius drops, one would require power densities greater than 10^7 watts/cm^2, which would cause air breakdown and would vaporize the drops.[16] Estimates of the required oscillation amplitudes needed to produce measurable ac signals were obtained from intensity calculations[17-19] of the light scattered as a function of angle, drop size and, to some degree, drop shape. These intensity calculations are not presented in detail here since

calculations are presently underway to determine better estimates for the scattering of laser light from oscillating water drops. However, the preliminary results indicate that radius changes of 0.5% for drops of radii greater than about 20 μm should be detectable according to the calculations and according to experimental results of other workers.[20] The calculations indicate that the backscattered light intensity changes [18,19] more with the drop radius and shape for the values of ka used here than it does at more forward angles. In addition, the calculated results for mm-size water drops indicate that the drops driven resonantly may be distorted to the same b/a values in electric fields lower in amplitude than Billings and Holland[7] reported where b/a is the ratio of the maximum to minimum axis ratio for a prolate spheroidal water drop. Future studies of the light scattered from drops larger than 20 μm in radius between conducting plates will examine this point.

ACKNOWLEDGEMENT

The authors wish to thank Mr. Robert Doherty of ARRADCOM at the Aberdeen Proving Ground for his help in this experiment. He furnished some of the aerosol generation equipment, provided the particle size measuring device, and made the measurements to determine the particle size. Dr. Ed Stuebing of ARRADCOM is thanked for many interesting ideas and his encouragement to do this work. Professor P. Barber of the University of Utah is thanked for making several intensity calculations and for use of his computer program.

REFERENCES

1. Morrison, C. A., Karayianis, N., and Wortman, D. E., "Transmission of Electromagnetic Radiation Through a Fog", HDL internal report R-RCB-77-5.

2. Mack, W. A., Proc. Roy. Soc. London A 133, 565 (1933).

3. Taylor, Sir G., Proc. Roy. Soc. London A 280, 383 (1964).

4. O'Konski, C. T. and Thacher, H. C., J. Phys. Chem. 56, 955 (1953).

5. Lord Rayleigh (Strutt, J. W.), The Theory of Sound, (Dover, New York 1877, revised 1894, reprinted 1945).

6. Brazier-Smith, P. R., Brook, M., Latham, J., Saunders, C. P. R., and Smith, M. H., Proc. Roy. Soc. A 322, 523 (1971).

7. Billings, J. J. and Holland, D. F., J. Geophys. Res. 74, 6884 (1969).

8. Brook, M. and Latham, D. J., J. Geophys. Res. 73, 7137 (1968).

9. C.A. Morrison, R.P. Leavitt, and D.E. Wortman, "The Extended Theory of the Oscillation of Liquid Drops," Harry Diamond Laboratories, Report HDL-TR- (1979, in press).

10. Wortman, D. E., "Possible Use of Two Laser Beams to Determine Particle Size Distribution", Harry Diamond Laboratories, Report HDL-TR-1910 (1978).

11. Garton, C. G. and Krasucki, Z., Proc. Roy. Soc. A 280, 211 (1964).

12. Rosenkilde, C. E., Proc. Roy. Soc. A 312, 473 (1969).

13. Brazier-Smith, P. R., J. Fluid Mech. 50, 417 (1971).

14. Matthews, J. B., J. Geophys. Res. 72, 3007 (1967).

15. Ausman, E. L. and Brook, M., J. Geophys. Res. 72, 6131 (1967).

16. See for example Glicker, S. L., Appl. Optics 10, 644 (1971).

17. Barber, P. W., Dept. of Elect. Eng., Univ. of Utah, Salt Lake City, Utah.

18. Barber, P. W. and Wang, D-S, Applied Optics 17, 797 (1978).

19. Kerker, M., The Scattering of Light and Other Electromagnetic Radiation, (Academic Press, New York 1969).

20. Davis, E. J. and Ray, A. K., J. Chem. Phys. 67, 414 (1977).

Table 1. Mechanical oscillation frequency of the fundamental mode for a water drop and the calculated change in radius which the drop undergoes in an alternating electric field of amplitude 275 volts/cm. The dielectric constant, surface tension and viscosity coefficients for water used in the calculation are $\varepsilon = 1.39$, $\gamma = 75$ dyne/cm and $\mu = 0.1$ poise. This dielectric constant is obtained from the index of refraction at a wavelength of 10.6 μm and corresponds to case 1.

Drop Radius (μm)	Mechanical frequency (MHz)	Change of Drop Radius (μm)
1	3.90	2.2×10^{-9}
1.1	3.38	2.7×10^{-9}
1.2	2.97	3.4×10^{-9}
1.3	2.63	4.2×10^{-9}
1.4	2.35	5.0×10^{-9}
1.5	2.12	6.0×10^{-9}
1.6	1.93	7.0×10^{-9}
1.7	1.76	8.1×10^{-9}
1.8	1.61	9.4×10^{-9}
1.9	1.49	1.1×10^{-8}
2.0	1.38	1.2×10^{-8}

Table 2. Mechanical oscillation frequency of the fundamental mode for a water drop and the calculated change in radius which the drop undergoes in an alternating electric field of amplitude 275 volts/cm. The dielectric constant, surface tension, and viscosity coefficient for water used in the calculation are $\varepsilon = 78.2$, $\gamma = 75$ dynes/cm, and $\mu = 0.1$ poise. These values correspond to case 2, with the static dielectric constant.

Drop Radius (μm)	Mechanical Frequency (Hz)	Elongation of Drop Radius (μm)
1.0	3.90×10^{6}	1.5×10^{-7}
1.2	2.97×10^{6}	2.4×10^{-7}
1.4	2.35×10^{6}	3.5×10^{-7}
1.6	1.93×10^{6}	4.9×10^{-7}
1.8	1.61×10^{6}	6.6×10^{-7}
2.0	1.38×10^{6}	8.6×10^{-7}
3.0	7.50×10^{5}	2.4×10^{-6}
4.0	4.87×10^{5}	4.8×10^{-6}
5.0	3.49×10^{5}	8.5×10^{-6}
6.0	2.65×10^{5}	1.3×10^{-5}
7.0	2.10×10^{5}	2.0×10^{-5}
8.0	1.72×10^{5}	2.7×10^{-5}
9.0	1.44×10^{5}	3.7×10^{-5}
10.0	1.23×10^{5}	4.8×10^{-5}
20.0	4.36×10^{4}	2.7×10^{-4}
30.0	2.37×10^{4}	7.5×10^{-4}
40.0	1.54×10^{4}	1.5×10^{-3}
50.0	1.10×10^{4}	2.7×10^{-3}
100.0	3.90×10^{3}	1.5×10^{-2}

Table 3. Mechanical oscillation frequency of the fundamental mode for a water drop and the calculated change in radius which the drop undergoes in an alternating electric field of amplitude 275 volts/cm. The dielectric constant, surface tension, and viscosity coefficient for water used in the calculation are $\varepsilon = 78.2$, $\gamma = 75$ dynes/cm, and $\mu = 0.1$ poise, as for case 2.

Drop Radius mm	Mechanical Frequency (Hz)	Elongation of Drop Radius (μm)
0.25	986	0.15
0.50	349	0.85
0.75	190	2.33
1.0	123	4.78
1.2	93.8	7.55
1.4	74.4	11.10
1.6	60.9	15.49
1.8	51.0	20.80
2.0	43.6	27.07
2.2	37.8	34.35
2.4	33.2	42.70
2.6	29.4	52.16
2.8	26.3	62.77
3.0	23.7	74.59
3.2	21.5	87.65
3.4	19.7	102.0
3.6	17.3	126.0
3.8	16.6	134.7
4.0	15.4	153.1

Table 4. Calculated electric field strength required to distort prolate spheroidal water drop so that the ratio of the maximum to minimum axis ratio b/a = 2 for the static and near static cases. The static case corresponds to an external dc electric field applied to the drop and the near static case corresponds to an alternating field applied at the fundamental mechanical frequency of the drop where ϵ = 78.2 and ka >> 1 (case 2).

Drop Radius (mm)	Electric field for the Near Static Case (kV/cm)	Electric field for Static Case (kV/cm)
1	2.81	13.62
1.2	2.45	12.43
1.4	2.18	11.51
1.6	1.98	10.76
1.8	1.81	10.15
2.0	1.67	9.63
2.2	1.56	9.18
2.4	1.46	8.79
2.6	1.37	8.44
2.8	1.30	8.14
3.0	1.23	7.86
3.2	1.17	7.61
3.4	1.12	7.38
3.6	1.08	7.18
3.8	1.03	6.98
4.0	.99	6.81

OPTICAL AND GRAVIMETRIC MEASUREMENTS OF ASBESTOS FIBERS

J. W. Gentry
University of Maryland

K. R. Spurny
Fraunhofer-Institut für Toxikologie und Aerosolforschung

PUBLICATIONS

Gentry, J., Spurny, K.R., "Measurements of Collection Efficiency for Asbestos Fibers", J. Colloid and Interface Science, Vol. 65, No. 1, 174-180 (1978).

Gentry, J., Spurny, K., Weiss, G., Opiela, H., "Measurement of Collection Efficiency of Amosite Fibers", Atmospheric Pollution 1978, Proceedings of the 13th International Colloquium, Paris, 107-110, April 25-28 (1978).

Gentry, J., Spurny, K.R., "The Effect of Orientation on the Optical and Collection Properties of Fibers", Aerosole in Naturwissenschaft Medizin und Technik, Proc. 4th Tagung der Gesellschaft für Aerosolforschung, 38-42 (1977).

Gentry, J.W., Spurny, K., Opiela, H., Weiss, G., "Comparisons of Measurement Techniques for Penetration of Amosite Fibers Through Nuclepore Filters", Aerosole in Naturwissenschaft, Medizin und Technik, Vol 6, 400-405 (1979).

Gentry, J. W., Spurny, K. R., Opiela, H., Weiss, G., "Measurement of Collection Efficiency of Amosite Fibers", Product Research and Development, December 1979.

INTRODUCTION

This paper presents a comparison between gravimetric and optical methods for measuring the fractional penetration of amosite fibers through nuclepore filters. The primary variables in the study were the pore diameter of the nuclepore filters (NPF) and the flow rate through the filters. Penetration measurements with fibers present additional difficulties in comparison to isometric or spherical particles as follows:

1. One does not have a test aerosol of monodisperse fibers; and, consequently, the particles must be generated by mechanical shear of mineral samples. The resulting aerosol contains a large fraction of agglomerates--up to 80% by weight.

2. The penetration of fibers through filters and impactors is

considerably greater than isometric particles of similar aerodynamic diameters. This is probably due to the property of the fibers aligning in order to penetrate the filters.

3. When optical instruments are used to determine the particle size, the signal is dependent on fiber orientation and the length to diameter ratio (aspect ratio) as well as particle diameter.

It is the objective of this research to develop procedures for correlating optical measurements (which require a relatively short measurement time and have the potential of providing information regarding the behavior of different particle sizes in polydisperse aerosols) with gravimetric measurements which can be unambiguously related to the geometry of the particle. We have investigated the following: 1) The effect of flow rate on the collection efficiency of fibers; 2) The relation between the collection efficiency based on particle mass obtained gravimetrically and that obtained optically; and 3) Changes in the fiber size distribution as measured by scanning electron microscopy (SEM).

GRAVIMETRIC METHODS

In gravimetric methods, we include all methods in which the measured variable is proportional to particle mass. Besides direct weighing of samples, methods based on elemental composition (i.e. neutron activation) or indicator materials (i.e. radioactive isotopes) are included among gravimetric methods. For the experiments used in our studies, irradiated amosite--a type of asbestos characterized by relatively high concentrations of Fe--was used as the source material for the aerosol.

The experimental procedure consists of the following steps:

1. The amosite sample is ground, dried, and then irradiated to prepare a suitable test aerosol.

2. The aerosol produced with a vibrating bed generator is passed through a glass impactor and a 8 μm NPF prefilter. The nuclepore prefilter is essential, for otherwise, the aerosol consists mostly of agglomerates. By passing the aerosol through the prefilter, an aerosol consisting of isolated fibers is obtained.

3. The filtered test aerosol is passed through a test stage consisting of two filters--the test NPF filter and a backing filter of a 0.2 μm millipore membrane filter. The radioactivity of the dust collected on the test filter and the backing filter was measured by a Frieske-Hoepfner methane-flow radiometer. The collection efficiency is the ratio of the counts on the test filter to the sum of the counts on the test filter and the backing filter.

4. For all the experiments, the control variables were 1 liter/min through the fluidized bed, a frequency of 55 Hz, and an amplitude of vibration of 241 μm. An effort was made to insure that the test aerosol was reproducible. Experimental measurements with non-radioactive amosite as measured with a Royco did not significantly change (<10%) for repetitive runs under the same conditions of aerosol generation.

5. The flow rates varied from 1 to 4 liters/minute and five pore sizes of nuclepore filters were used.

The experimental measurements, shown in TABLE 1, indicate that the collection efficiency is independent of flow rate. Based on the fiber size distribution measured by scanning electron microscopy (SEM), the mass mean diameter is 1.20 μm. (The fibers were assumed to be problate spheroids.) The efficiencies presented in TABLE 1, based on gravimetric measurements, are controlled by fibers greater than 1 μm in diameter.

TABLE 1

Collection Efficiency From Gravimetric Measurements (Radioactively Labeled Asbestos) as Function of Pore Size

Pore Diameter (μm)	Number of Measurements	Collection Efficiency	Standard Deviation
1.0	5	97.5	2.1
3.0	11	83.9	2.4
5.0	8	65.6	2.7
8.0	9	43.6	4.6
12.0	5	20.0	1.4

OPTICAL MEASUREMENTS

Whereas the gravimetric measurements measure a penetration related to particle mass, the optical measurements (based on measurements with a Model 208 Climet) provide a penetration measurement based on the number of fibers. Because the signal from the Climet is divided into different "optical diameters" (the diameter of a hypothetical latex particle having the same signal as the aerosol), this measurement provides information regarding the size distribution of the aerosol.

The experimental design differed slightly from that for the gravimetric measurements in that the amosite was not radioactive, the fibers were passed through a ^{85}Kr source in order to minimize electrostatic charges, and the penetration was determined by measuring the ratio of concentrations before and after the test filter. In this design, no backing filter was used. Three points

concerning the experiment should be stressed. Fine control of the flow rates (in our experiment, by Nu Pro S series needle valves), by maintaining a high flow rate (>4 l/min) through the optical instrument (it is our belief that the fibers acquire a preferential alignment in the flow field, simplifying the optical signal), and the use of a prefilter before the test section in order to remove agglomerates. Our experience indicates that the latter two steps are essential for reproducible experiments.

The first experimental results were to determine the mass mean diameter based on the size distribution of optical diameters. For our measurements, 68% of the counts were in the 0.3 µm channel, 25% in the 0.5 µm channels, 7% in the 1 µm channel, and fewer than 0.1% in channels corresponding to optical diameters greater than 1 µm. Fitting these data with a log-normal distribution indicates a mass mean "optical diameter" of 1.18 µm.

As in the case of the gravimetric measurements, the penetration through the NPF were measured as a function of flow rate. Four different pore diameters--3.0, 5.0, 8.0, and 12.0 µm NPF--were used. Typical results are shown in TABLE 2 where the "optical diameter" is presented as a function of NPF pore diameter and "optical diameter".

TABLE 2

Collection Efficiency as a Function of NPF Pore Diameter and "Optical Diameter"

NPF Pore Diameter	"Optical Diameter"	Collection Efficiency %
3.0	0.3	44
	0.5	69
	1.0	87
5.0	0.3	22
	0.5	40
	1.0	61
8.0	0.3	10
	0.5	21
	1.0	33
12.0	0.5	11
	1.0	22

As in the case for the gravimetric measurements, the collection efficiency did not vary with increasing flow rate. Considerable scatter was observed in the experiment for the larger pore size NPF. If the curves presenting the efficiency as a function of optical diameter were extrapolated to an optical diameter of 3 µm, for each NPF size, and if a symbol were placed on the curve with the same efficiency as measured gravimetrically, it was found that

the efficiency measured gravimetrically corresponded to an optical diameter of 1.20 μm.

SUMMARY

For both the gravimetric and optical measurements, the collection efficiency was found to be independent of flow rate. The variation in flow rate (~400%) was sufficient that inertial impaction could be discounted. Similarly, the fibers were sufficiently large that it is unlikely that diffusion played a significant role. Our conclusion is that interception is the principal mechanism of particle removal. Examination of the size distribution of fibers penetrating and collected on a 5 μm NPF suggest that the fiber diameter plays the dominant role in determining whether a fiber is collected and fiber length is relatively unimportant.

Secondly, the collection efficiency measured optically and gravimetrically appear to be correlated. The mass mean "optical diameter" of 1.18 μm is very close to the value 1.2 μm measured with a SEM. If the collection efficiency curves measured optically were extrapolated to 1.2 μm, the collection efficiency was the same as measured gravimetrically.

Additional work needs to be done to examine to test the generality of this result. Specifically, we hope to remove the thicker fibers and see if a similar result is obtained for distributions with mass mean diameters less than 1 μm.

ACKNOWLEDGEMENT

J. W. G. would like to acknowledge support by the Environmental Protection Agency grant # R8065180 10.

INTERFEROMETRIC PARTICLE LENGTH MEASUREMENTS OF ABSORBING FIBERS WITH LARGE ASPECT RATIOS

W. M. Farmer, F. A. Schwartz, L. Boyd
Gas Diagnostics Research Division
The University of Tennessee Space Institute
Tullahoma, Tennessee

INTRODUCTION

The theory of particle sizing interferometry has been well documented.[1-5] A brief description of the method is included in Appendix I. In principle, if the particle shape is known, a signal visibility function can be computed which relates the measured parameter, i.e. visibility, to particle size. Electron microscope observations of these particles showed that the simplest fundamental shape which could be assumed was that of a cylinder with a very high aspect ratio. Therefore, visibility functions for cylinders were used to analyze the data. Two such functions were computed. The first function assumed that the particle was oriented such that its major axis was perpendicular to the planes defined by the interference fringes. The second function was computed for an ensemble of randomly oriented particles. These functions are plotted in Fig. 1 as a function of particle length. The first function will be referred to as the visibility function for "perpendicular incidence," i.e. the major axis of the particle is assumed perpendicular to the incident interference fringe. The second function is referred to as the function of "random orientation."

In addition to different size ranges tested in these measurements two different incident polarizations were used. In the first case (see Fig. 2a) the polarization vector was made parallel to the interference fringes (referred to as "vertical polarization") while in the second case the polarization vector was perpendicular to the fringes (see Fig. 2b) and is referred to as "horizontal polarization." The reasons for obtaining measurements with these two polarization conditions are contained in the following hueristic arguments. The probability of obtaining an accurate measurement is a function of the signal-to-noise ratio. As the signal-to-noise ratio decreases, the possibility of obtaining an accurate measurement or a measurement at all decreases. For the PSI, the signal-to-noise ratio is directly proportional to scatter signal magnitude. Hence, particles which produce the greatest scatter magnitudes will be measured with greater accuracy and in fact will be preferentially measured over those particles which produce smaller signal magnitudes or equivalently produce signals with low signal-to-noise ratios. Van de Hulst[6] shows

that for cylindrical iron particles the extinction cross-section (which is proportional to the amount of light scattered by the particle) is significantly different for the cases where the polarization vector is parallel or perpendicular to the axis of the particle. Figure 3 is reproduced from Van de Hulst and shows the variation of extinction cross-section with a parameter X ($X = \pi D/\lambda$) for two cases of particle orientation relative to the incident polarization vector or electric field. For the wavelength used in the measurements reported here $D = 0.2X$. Where D is expressed in micrometers. Hence, when the particle diameter is less than 0.2 micrometers a stronger signal results when the particle axis is parallel to the polarization vector than when it is perpendicular to it. When D is greater than 0.2 micrometers the cases are reversed. Measurements made using other techniques suggested that the particle diameters were less than 0.1 micrometers. Hence, in the case of vertical polarization the scatter magnitude would be greater when the particle axis was parallel to the plane of the interference fringe than when oriented perpendicular to the fringe plane. The latter case of particle orientation relative to the fringe plane corresponds to a measurement of particle length, while the former corresponds to its diameter. When horizontal polarization is used these cases are reversed. Thus, size distribution measurements made using vertical polarization should produce a very strong mode for the sizes in the range of the particle diameters. On the other hand, measurements made using horizontal polarization should produce a strong mode for the length of the particle.

In addition to estimates of particle length for two different polarization directions, particle number density estimates were obtained from the statistics of the number of particles measured relative to those detected. A discussion of this method of estimating particle number density is contained in a recent UTSI report.[7]

The following structure has been used to report the test results. Section 2 describes the experimental procedures used in acquiring the data. Section 3 presents the experimental results and Section 4 provides:

1. a preliminary set of conclusions which may be drawn from the data and

2. suggestions for additional measurements which might be performed to further validate the results found in these experiments.

EXPERIMENTAL RESULTS

The experiments may be divided into two distinct sets:

1) Measurements of particle injected into a settling chamber and

2) Measurements made in a low pressure jet dispersal.

Fringe periods of 6 and 17.5 micrometers were used in both sets of experiments. Both vertical and horizontal polarization measurements were made in the settling chamber while only vertical polarization was used in the low pressure jet dispersal. The settling chamber consisted of a sealed plywood box of about 14 m^3 volume. Entrance and observation ports for the particle generator, and exhaust ports to exhaust the material during or after the experiments were available. The low pressure jet dispersal system injected the particles into a jet flow dumped into a reduced atmosphere.

For the settling chamber measurements the PSI optical system was mounted in a sealed box and placed inside the chamber. A 5 milliwatt HeNe laser (λ = 633 nm) provided the light source. The scattered light receiver consisted of an F/2, 10 cm diameter lens detecting scatter in the forward direction. An EMI Model 9781R photomultiplier tube was used as the photodetector. A small fan was used to draw the aerosol containing fiber through the sample space at a velocity of about 1 m/sec. Figure 4 schematically illustrates the optical arrangement of the PSI used in the settling chamber. The probe volume diameter for all measurements in the settling chamber was approximately 0.1 mm and depth-of-field was approximately 2 mm.

The PSI optical system used in the low pressure jet measurements is illustrated in Fig. 5. This optical system used a 25 milliwatt HeNe laser and was focused in the low pressure chamber where the jet was dumped. The probe volume diameter for the 17.5 micrometer fringe period was 316 micrometers. Depth-of-field was approximately 4 mm. For the 6 micrometer fringe period, the probe volume was 114 micrometers in diameter with a depth-of-field of approximately 3 mm. An F/6 aspheric telescope was used as the forward scatter receiver. This PSI optical system was mounted on an optical table which was shared with a HeNe transmissometer system.

The UTSI Mobile Laboratory Van housed the PSI signal processor and data acquisition system and was parked near the settling chamber and low pressure jet dispersal in order to transmit the PSI signals down co-axial cables with minimum signal distortion.

A block diagram of the electronics system used for measuring the scattered light signal current is shown in Fig. 6. In this configuration the signal is divided into two parts. One part enters

the visibility processor (lower portion of the diagram) while the second part enters the velocity processor. The velocity processor provides signal logic tests for multiple particle signals, signal-to-noise ratio and acceptable particle trajectories. These tests are used as the control logic for accepting or rejecting signals measured by the visibility processor.

As shown in the block labeled visibility processor, two signals from the photomultiplier preamplifier are processed separately to obtain the AC and DC portions of the scattered signal. One portion is integrated directly to yield the mean value (or the so-called DC) of the signal. The second portion is filtered to remove the low-frequency pedestal and then is full-wave rectified and integrated. This process yields a quantity which is proportional to the energy in the sinusoidal portion of the signal. In each parallel leg of the visibility processor, four multiplexed integrators are used to obtain a signal dynamic range of approximately $1:10^4$ with three digit accuracy.

After the integrations are complete, the value for the AC (sinusoidal) and the DC (mean value) components of the signal are sent to a microprocessor memory where they are recorded along with the signal time period measurement.

The velocity processor can be programmed to perform signal time period averages over a large and a small number of signal periods. The number can range between 2 and 256 for two simultaneous average time period measurements. One average is obtained over a preset time interval which is significantly longer than the second average. The acceptable aperiodicity in the signal is determined by the difference in the long time—short time averages. For brevity these are called long and short counts. The acceptable aperiodicity is programmable from 0.1 to 50%. The velocity processor has a so-called dropout detector which allows the processor to recycle the instrument immediately if the particle trajectories or noise are such that the signal has an insufficient number of cycles to meet the criteria imposed upon the signal processor logic.

After a sufficient data set has been obtained (the number of measurements which can be entered into memory is also programmable), the system stores the memory contents on a magnetic disk for permanent data storage. For each particle measurement the data recorded consists of 1) signal time period, 2) integrated signal magnitude, 3) signal visibility, 4) relative data acquisition time, and 5) sample size and population detected. A number of different data reduction programs can be used to analyze these data. Figure 7 illustrates some of the output options available with the system. For these measurements different particle size distributions were computed using the different visibility functions illustrated in Fig. 1. Reduced data from these measurements thus far has included (for a given visibility function) 1) the particle size distribution, 2) the probability density distri-

bution, 3) the geometric mean length, 4) the first moment of the size distribution assuming the distribution log-normal, 5) the particle number density parameter, 6) number of particles detected with signal amplitudes beyond the range of the signal processor, 7) mean particle velocity and, 8) turbulent intensity.

During system operation in the settling chamber the particle generator was used to generate a large initial particle input. The particles were then allowed to circulate in the settling chamber. Consecutive particle size histograms were then taken in order to determine any obvious particle growth patterns. This approach was repeated four times—once for each polarization state for a fringe period of 6 micrometers and once for each polarization state for a fringe period of 17.5 micrometers.

Measurements made during low pressure jet dispersal consisted of sets of data taken with either a 6 or 17.5 micrometer fringe period and a vertical polarization state only. Low, intermediate, and high volume (proportional to particle concentration) fractions were measured in each case.

Prior to a test effort the PSI system was used to obtain a background distribution of the aerosol particles present. These data were analyzed under the assumption that these particles were spherical.

SETTLING CHAMBER MEASUREMENTS

Data obtained from the settling chamber measurements is summarized in Tables II-IV. Table II lists the geometric mean and first moment (assuming a log-normal distribution) lengths of the particles for both fringe periods and polarization states. It should be borne in mind that the computations listed for perpendicular orientation and random orientation are from the same sets of data for a given fringe period and polarization state. The mean sizes in the columns are listed as they were acquired consecutively in time. This was done in order to detect any chronological changes in the particle length distribution. The mean sizes for the measured size distributions were computed by ignoring the size fraction greater than the size range defined by the fringe period. Hence, it should be expected that the mean size will increase somewhat when the larger fringe period is used. This result is clearly evident in Table II where it is found that the average of all geometric mean sizes is smaller for the 6 micrometer fringe period than for that at 17.5 micrometers. Table II reveals a number of interesting features about these particles which are listed below.

1. The time to acquire a set of measurements for the 6 micrometer fringe period is roughly three times shorter for horizontal polarization than for vertical polarization.

2. The same effect is indicated for the 17.5 micrometer fringe period though the time is only about 20% shorter.

3. The average geometric mean particle size is significantly smaller for the horizontal polarization than the vertical polarization for the 17.5 micrometer fringe period.

4. There is virtually no difference in the mean particle lengths for either state of polarization for the 6 micrometer fringe period measurements.

5. The histogram to histogram variation in geometric mean particle length is greater for the vertical polarization state than for the horizontal.

6. There is relatively little difference between the mean particle lengths obtained using the two different visibility functions.

7. A general trend is toward larger mean particle lengths as a function of time after particle injection is observed.

An examination of the probability distributions for the particle length measurements will reveal the multiple modes consistently exist in the distributions. It is also consistently observed that the largest mode size occurs in the smallest size increment in the particle size histogram. Table III lists a summary of the length distribution measurements obtained from the data. Two columns are listed for each optical setup and for random and perpendicular orientation size analysis. The first column in each section lists the percentage of particles which occur in the smallest particle size increment in the histogram. The second column lists the largest particle size and distribution amplitude in the next largest mode found in the histogram. For example, the first entry in the columns for vertical polarization, 6 micrometer fringe period and random orientation show 47.4% of the particles were less than 0.6 micrometers in length and that the next largest mode contained 10% of the particles and occurred for sizes greater than 13.8 micrometers. These data are listed in the same chronological order as those listed in Table II. From Table III it is observed that:

1. The small particle mode for horizontal polarization is typically 20% greater in amplitude than that for vertical polarization.

2. The second most frequently occurring mode is typically in the 6-8 micrometer range with an amplitude of 6-8%.

The PSI data acquisition system records the number of particles which generate signals that are so large in magnitude the amplifier electronics saturate and the signal is distorted. Such signals can pass the signal processing logic tests but will yield erroneous values

of signal amplitude and visibility. Hence, while they are counted they are not used in the computations of the particle size distributions. It is assumed that particles which generate such signals are much larger than those generally found in the distribution. The percentage of the total ensemble of particles accepted for measurement which saturated the signal amplifier or are equivalently very large particles is tabulated in Table IV. Generally Table IV shows that 3-6% of the ensemble consisted of large particles. Since such particles can be detected over a much larger optical volume than the smaller particles it should be understood that the number per unit volume relative to the small particles is probably quite small.

LOW PRESSURE JET DISPERSAL MEASUREMENTS

Data obtained during the low pressure jet dispersal measurements is summarized in Tables V-IX. It should be borne in mind that only one polarization state was employed in these measurements and a slightly different optical system was used with a more powerful laser.

Table V summarizes the particle length measurements obtained assuming random and perpendicular particle orientation and a fringe period of 17.5 micrometers.

Three different volume fractions, low, intermediate and high, representing increasing particle number density were measured. The data are presented in chronological order in the same fashion as that in Table II. Table V shows the following:

1. As the volume fraction increases, the data trend is toward smaller particle sizes.

2. The intermediate and high volume fraction mean particle lengths are nearly identical.

3. Random and perpendicular incidence assumptions yield particle lengths which are comparable.

4. When these data are compared with similar settling chamber data there is a significant difference in the mean particle lengths. The particles in the jet appear significantly smaller especially as the number density increases.

Table VI shows the mean particle lengths obtained using a 6 micrometer fringe period. With a few exceptions the histogram data yields surprisingly large particle size lengths. This result is not consistent with the settling chamber measurements. Examination of additional data may help to explain the variance and the discussion of these results will be continued later in this section after the

additional data are examined.

Table VII lists the predominent mode sizes and amplitudes in the probability density distribution for the 17.5 micrometer fringe period. As might be expected from the particle size lengths found in Table V, the smallest resolvable particle mode size is larger than that for comparable measurements in the settling chamber. When random orientation is assumed, the fraction of particles in the small mode size for the low volume fraction jet dispersal is 30% greater than that for the settling chamber and approximately 46% greater for the intermediate and high volume fractions. When these values are compared for the perpendicular orientation assumption these values increase to approximately 53% and 66% respectively. The "next largest mode" sizes are in good agreement with those found in the settling chamber although the mode amplitude are roughly 60% the magnitude found for the settling chamber.

Predominent mode sizes for data obtained with the 6 micrometer fringe period are listed in Table VIII. In light of the results listed in Table VI the results are not too surprising. Comparatively speaking, very few if any particles are found in the smallest resolvable particle size mode and the largest mode is found for sizes greater than the resolution obtainable for either particle orientation assumption.

The results shown in Table IX are consistent with the data shown in the previous tables. Table IX lists the absolute fraction of particles in the histograms which produced signals strong enough to saturate the amplifier electronics. As Table IX shows, very few particles produced overly large signals for the 17.5 micrometer fringe period while typically 9% were found for the 6 micrometer fringe period. This value is approximately 4 times greater than that found in the settling chamber for the 6 micrometer fringe period. It should be pointed out that when the results for the jet and settling chamber using the 17.5 micrometer fringe periods are compared, roughly 9 times more particles are found to saturate the signal amplifiers for the settling chamber than for the jet dispersal. In the jet dispersal measurements we also find that the trend is toward '0' particles saturating the signal amplifiers as the volume fraction increases. This result is consistent with the particle size distribution measurements tabulated in Table VII.

It is appropriate at this point to discuss the difference in the 6 micrometer fringe period measurements for the settling chamber and the jet dispersal. The following facts are pertinent to this discussion.

1. The settling chamber measurements were made at pressures of about 760 mm of H_g. The jet dispersal measurements were made at roughly 50-100 mm of H_g.

2. The probe volume power density in the jet dispersal measurements was approximately 8.5 times that in the settling chamber.

3. Oscilloscope observation of signals generated by the particles in the jet dispersal often revealed signal shapes which appeared to be badly distorted when compared to the shape of typical signals. Figure 8 sketches a typically distorted signal. Signal distortion did not begin until the particle was near the center of the probe volume.

4. Signal distortion was such that it could significantly reduce the measurable visibility of the signal.

5. Measurements made in the jet dispersal yielded particle size distributions which reflect a preponderance of signals with small visibilities.

6. Signals saturating the signal amplifiers occurred much more often for the jet measurements than for those of the settling chamber.

7. Velocities found using the 6 micrometer fringe period were significantly higher for all volume fractions than for those made using 17.5 micrometers.

8. Data acquisition times were much shorter for the 6 micrometer measurements than for the 17.5 micrometer measurements.

These facts strongly suggest either 1) that particle heating effects are being reflected in the jet dispersal measurements involving the 6 micrometer fringe period or 2) generator function was significantly different. The reduced visibilities observed in the middle of the signal could result in size distributions with apparently very large mean sizes. Physical changes in signal shapes result from:

1. Particles changing their apparent shape.

2. Particles becoming incandescent and adding an incoherent optical background to the signal.

3. Particles undergoing metallurgical surface changes and reactions with the nitrogen atmosphere surrounding the particle.

4. Some combination of the above.

Past experience indicates that the last alternative plus factors not yet guessed will ultimately explain potential effects due to particle heating. The alternative explanation of the generator simply producing larger particles is also a strong possibility and cannot be

discounted until comparison is made with transmissometry data taken at the same time.

EXAMPLES OF PROBABILITY DENSITY DISTRIBUTIONS

In this section representative histograms are presented in order to illustrate the general shapes of the probability density distributions obtained for both the settling chamber and jet dispersal measurements. Additional detailed data is available on request.

Figures 9-11 illustrate particle size distribution histograms obtained in the settling chamber. Figure 9 compares the shapes of the distributions for perpendicular orientation (left hand side) with corresponding random orientation (right hand side) and horizontal (top) versus vertical (bottom) polarization states. The data in Fig. 9 was obtained with a 6 micrometer fringe period. The ragged structure in the probability density results from the relatively few measurements used to obtain the data. Scales for the probability density amplitudes are relative. The first column under the probability density is the accumulative probability as a function of particle size. The second column lists the largest particle size in each histogram bin for the probability density. Figure 10 presents data similar to Fig. 9 except the fringe period used in the measurements was 17.5 micrometers and the number of particles used in the histogram was 10^3 instead of 200 as used in Fig. 9. Even so, there are too many bin increments for the random orientation histograms. Because the smallest particle size bin had the preponderance of measurements, the probability density plots show little of the distribution detail for the larger particle sizes. Figure 11 shows the particle size distributions for vertical (right side) and horizontal polarization (left hand side) with the smallest particle sizes removed from the distribution and the probability density recomputed. The difference between the two distributions are striking. Not only are the shapes of the distributions different, but the distributions for vertical polarization shows a periodic structure with a mode size that appears roughly for each 3.5 micrometer increase in apparent particle length.

Figures 12-14 illustrate histograms obtained in the jet dispersal measurements. Figure 12 shows the histograms obtained using the 17.5 micrometer fringe period with the smallest particle size bin suppressed as in Fig. 11. High to low volume fractions read top to bottom and perpendicular to random orientation left to right. The shape of the histograms suggests a shift toward smaller particles as the volume fraction increases. Note that the two strongest mode sizes in the low volume fraction histogram for random orientation are separated by an apparent size increment of roughly 3.5 micrometers in agreement with the results shown in Fig. 11. Figure 13 shows a comparison of

the size distributions for the different volume fractions assuming perpendicular orientation and fringe periods of 6 (left hand side) and 17.5 micrometers. The apparent effects due to particle heating or generator changes for the 6 micrometer fringe period data are clearly evident. Notice that for the 17.5 micrometer measurements that the particle sizes tend to cluster toward the smaller sizes as the volume fraction increases. For reference, probability densities assuming a random particle orientation for the 17.5 micrometer fringe period data shown in Fig. 13 are plotted in Fig. 14.

PARTICLE NUMBER DENSITY ESTIMATES

Particle number density estimates have been made using the data obtained from the settling chamber and jet dispersal measurements. These estimates were made using a statistical model that relates the ratio of single particles detected and multiple particles rejected to particle number density. Figure 15 plots particle number density observed in the settling chamber as a function of time. The initial rise in number density is due to the particle number density being dispersed throughout the chamber. After approximately 4 minutes the particle concentration begins to decrease due to apparent agglomeration and the particles being driven to the sides of the chamber. Figure 16 plots particle number density as a function of volume fraction for the low pressure jet dispersal measurements. The low volume fraction estimates were obtained near a time when the particle source for the generator ran out. Hence, the apparent large variation in number density for the low volume fraction. After the source was replenished the generator was started again and adjustments made for the change from low to intermediate volume fractions. During the final portion of the test, data were obtained for the high volume fraction concentration. These data indicate that roughly a factor of 10^2 variation in particle number density exists in the range between high and low volume fractions. Roughly a factor of 7 difference in number density can exist between successive volume fractions.

VELOCITY MEASUREMENTS IN THE LOW PRESSURE JET

Table X shows a listing of the velocity distribution measurement results for the data shown in Fig. 16. This data was obtained using a 17.5 micrometer fringe period. Table X lists the harmonic mean velocity and the standard deviation of the distribution in % (commonly called 'turbulent intensity'). These velocity measurements represent the component of velocity parallel to the center line of the dispersal chamber.

SUMMARY AND CONCLUSIONS

Interferometric measurements of particle length, number density and velocity have been obtained in a settling chamber and a low pressure jet. A summary of the results shows:

1. Multimodal size distributions with predominent mode sizes occurred at 6-8 micrometers and at less than 0.3-1.75 micrometers meters (depending on the assumption made for particle orientation).

2. Geometric mean particle lengths were found to lie between 1.5 and 3.0 micrometers.

3. Mean particle length measurements appeared to be independent of incident polarization. However, the shapes of the length distributions appeared to be radically different.

4. Peak number densities observed in the settling chamber were typically $5 \cdot 10^3 cc^{-1}$.

5. Number densities observed in the jet ranged between 10^3-$10^5 cc^{-1}$ for low to high volume fractions.

6. Mean particle velocities in the jet varied from 2-8 m/sec. with typical turbulent intensities of ± 30%.

7. Possible particle heating effects were observed in the jet measurements.

8. Mean particle sizes measured in the jet were measurably smaller than those observed in the settling chamber.

9. As the volume fraction in the jet increased the smallest particle size mode increased.

In addition to the quantitative observations listed above some qualitative observations and conclusions are in order.

1. It was somewhat surprising to observe signals as strong as those measured. The interferometer system could have detected signal magnitudes at least an order of magnitude smaller. This suggests that the particle diameters may be much greater than several hundred angstroms.

2. The relative insensitivity to polarization suggests, using Van de Hulst's calculations,[6] a diameter of about 0.2 micrometers.

3. If (a) a value of 10^{-7} is assumed for an intermediate volume fraction and (b) the particles are cylinders, then number density and particle length measurements yield a particle diameter of 0.19 micrometers which is in surprisingly good agreement with the conclusions drawn from the polarization measurements.

4. It was observed during data acquisition that the interferometer system was sensitive to relatively minor changes undergone by the generator during operation. This suggests that the interferometer would be a useful tool in defining the operating envelope of the particle generator.

5. If particle heating effects were indeed observed during the jet dispersal measurements, then the potential appears to exist for remote control of the particle's optical characteristics via high energy laser illuminators.

REFERENCES AND FOOTNOTES

1. Farmer, W. M., "Measurement of Particle Size, Number Density and Velocity Using a Laser Interferometer," Applied Optics, 11, 2603, (1972).

2. Robinson, D. M. and Chu, W. P., "Diffraction Analysis of Doppler Signal Characteristics for a Cross-Beam Laser Doppler Velocimeter," Applied Optics, 14, 2177 (1975).

3. Hong, N. S. and Jones, A. R., "A Light Scattering Technique for Particle Sizing Based on Laser Fringe Anemometry," J. Phys. D: Applied Physics, 9, 1976.

4. Farmer, W. M., Harwell, K. E., Hornkohl, J. O., and Schwartz, F. A., "Laser Particle Sizing Interferometer Measurements in Solid Propellant Plumes," Presented at the 11th JANNAF Plume Technology Meeting, Huntsville, Alabama, May 1978.

5. Farmer. W. M., Schwartz, F. A., Morris, R. D., Keefer, D., Hornkohl, J. O., and Harwell, K. E., "Interferometric Particle Size Measurements During Smoke Week II," Proceedings of Smoke Symposium III, Harry Diamond Laboratories, Adelphi, Maryland, March 1979.

6. Van de Hulst, H. C., Light Scattering by Small Particles," John Wiley and Sons, New York, 1957, p. 321.

7. Farmer, W. M., "Particle Number Density Estimates Using a Laser Velocimeter," Sept. 1979.

APPENDIX I

PSI MEASUREMENT PRINCIPLES

For completeness, a brief review is given of the basic principles underlying the determination of particle size from a measurement of the signal visibility of a particle passing through interference fringes produced by two laser beams. A more complete description of the measurement technique is given in Ref. 1.

As shown in Fig. 1, consider two equal intensity, well-collimated coherent light beams which intersect as a common origin (geometric center) with an included angle α. A Huygen's diagram of the wave fronts shows that planar interference fringes are formed which are perpendicular to the plane defined by the beam centerlines and are parallel to the bisector between the beams. The distance δ between the periodic fringes is given by

$$\delta = \lambda/[2\sin(\alpha/2)] \tag{1}$$

where λ is the wavelength of the coherent light. When a particle (assumed spherical) much less than δ in diameter crosses the fringe pattern, it can be assumed to be uniformly illuminated at all points along its path through the fringe pattern, and the light which is scattered by the particle is proportional to the observable flux illuminating it. Thus, measurement of the time period, τ , of the scattered light is related to the velocity, v, of the particle through the relationship

$$v = \delta/\tau \tag{2}$$

As the size of the scattering particle increases relative to δ, the illumination of the particle is no longer uniform and must be averaged over the cross-sectional area of the particle. The non-uniform illumination of the particle results in a reduction of the contrast or visibility of the scattered light signal. Let I_{max} be the maximum value in intensity in a period of the scattered light from a particle and I_{min} the next successive minimum. The visibility, V, can then be defined as:

$$V = \frac{I_{max} - I_{min}}{I_{max} + I_{min}} \tag{3}$$

It is straightforward to show that V is fully equivalent to the ratio of AC amplitude divided by the DC amplitude of the scattered light signal. The high frequency "Doppler" portion of the signal is defined as the "AC," it usually has many cycles of information relative to that of the DC component (the DC component refers to the Gaussian shaped low frequency term describing the signal). Analytically the visibility may be written as:

$$V \simeq \frac{\int_{A_p} I_o \cos(2\pi y/\delta) dA_p}{\int_{A_p} I_o \, dA_p} \tag{4}$$

where A_p is the cross-sectional area of the particle, I_o is intensity distribution across one of the illuminating beams, and y is the coordinate normal to the fringe planes. When I_o is a Gaussian function (TEM_{ooq} laser beam) it can be shown that Equation 4 is an accurate approximation over a depth of field, ℓ, given by:

$$\ell \simeq 0.8 \, b/a \tag{5}$$

where b is the radius of the e^{-2} intensity point in the illumination beam. For depths of field greater than ℓ, the signal visibility is function of particle size and position in the illumination. In order to simplify Equation 4 for Gaussian beams and still maintain accuracy, it is required that the particle diameter, D, satisfy the relationship:

$$D \lesssim 0.2b \tag{6}$$

and for δ to satisfy:

$$\delta \lesssim 0.2b \tag{7}$$

Under these conditions V for a sphere can be written as

$$V \simeq 2J_1(\pi D/\delta)/(\pi D/\delta) \tag{8}$$

where J_1 is a Bessel function of the first kind. For a cylinder V can be written as

$$V = \sin(\pi L/\delta)/(\pi L/\delta) \tag{9}$$

Equations 8 and 9 are plotted in Fig. 2 to illustrate the salient features of the visibility in particle size measurement.

Figure 2 shows that for spherical particles, the visibility function is not monotonic for sizes greater than about 1.05 δ. This value fixes the upper limit of the PSI size range. The lower limit results from the acceptable error in the particle size measurements. Since particle size is a non-linear function of visibility, a 1% uncertainty in visibility gives a 1% uncertainty in D when D/δ is about 1, but ±30% when D/δ is about 0.1. Acceptable sizing uncertainty and signal processor accuracy thus limit the low end of the PSI size range to about 0.05 D/δ. Hence, the PSI can cover about a 20:1 size range for a given δ. By scaling δ through a variation of the angle between the beams, particle sizes from submicron to greater than millimeter can be measured.

The PSI can also be used to obtain estimates of particle number density. As Reference 7 will show, the PSI signal processing electronics subjects the signal to certain logic tests to determine if the signal results from more than one particle. Multiple particle signals are not accepted for size measurement, but are counted as being detected. Also counted, but not measured are those single particles which pass near the edge of the sample space which are detected but generate signals with insufficient information for a size measurement. A random walk analysis can be used to relate particle number density to the ratio of number of measurements accepted for measurement to those detected. The random walk analysis yields the relationship

$$A = 1 - 2 \exp\left(-\frac{\gamma}{2}(1 + K^2)\right) \left| \sinh(\gamma) \sinh(K^2\gamma) \right|^{1/2} \tag{10}$$

where

A = Number of particles accepted for measurement/number of particles detected.

$\gamma = a \rho_N^{1/3}$

a,K = Optical System Constants

ρ_N = Particle Number Density

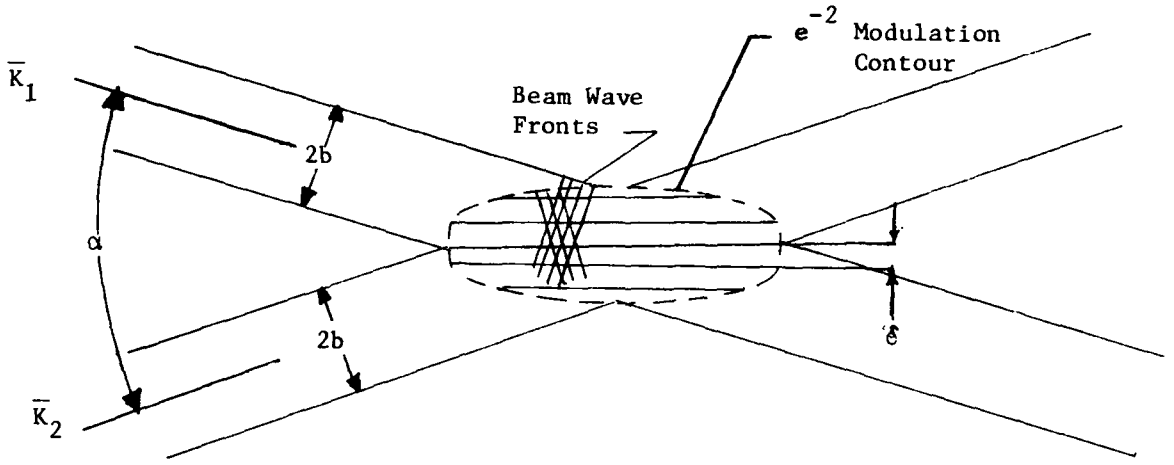

Figure I.1. Huygen's diagram of interference fringe generation in probe volume.

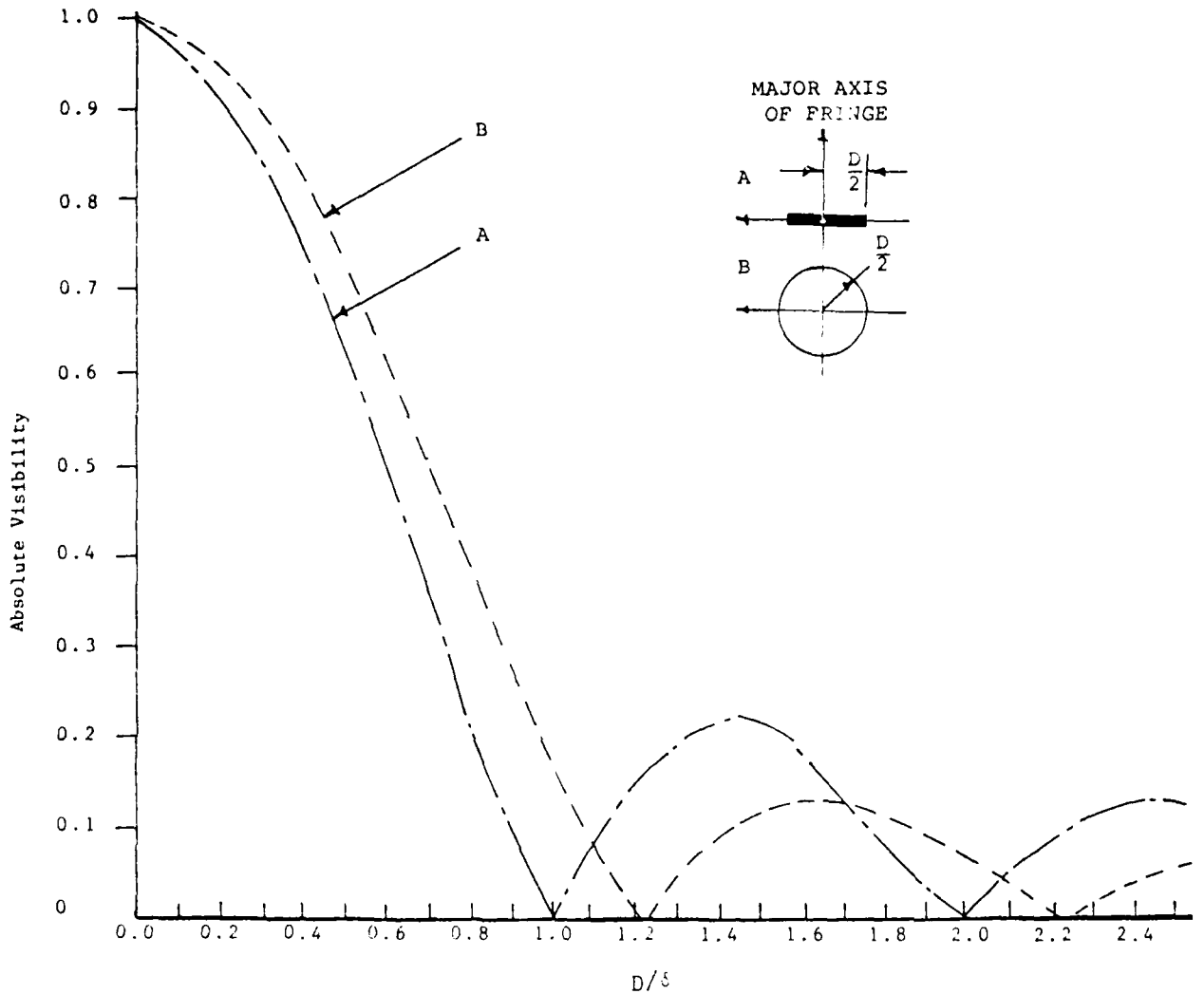

Figure I.2. Visibility as a function of D/δ for two particle shapes.

TABLE 1

PARTICLE SIZE RANGE
COVERED BY DIFFERENT
FRINGE PERIODS

6 μm FRINGE PERIOD		17.5 μm FRINGE PERIOD	
SIZE RANGE (μm)		SIZE RANGE (μm)	
PERPENDICULAR INCIDENCE	RANDOM ORIENTATION	PERPENDICULAR INCIDENCE	RANDOM ORIENTATION
0.3 - 6.0	0.6 - 13.8	0.875 - 17.5	1.75 - 40.2

TABLE 2

MEAN PARTICLE LENGTHS OBTAINED IN SETTLING CHAMBER MEASUREMENTS

VERTICAL POLARIZATION		HORIZONTAL POLARIZATION	
6 μm Fringe Period		6 μm Fringe Period	
RANDOM ORIENTATION	PERPENDICULAR ORIENTATION	RANDOM ORIENTATION	PERPENDICULAR ORIENTATION
1.26, 14.8	0.977, 2.05	1.89, 8.92	1.27, 6.93
3.72, 13.1	2.39, 4.02	1.50, 16.1	1.19, 5.58 3'20"
2.55, 8.18	1.70, 3.94 11'	1.38, 31.9	1.01, 1.93 Sample Time
1.82, 6.64	1.41, 17.7 Sample Time	3.04, 14.3	2.10, 4.40 200 Counts
1.19, 10.2	0.976, 2.25 200 Counts	9.26, 67.3	4.45, 8.49
0.812, 1.68	0.66, 0.936	1.62, 7.31	1.21, 5.57 1000
$\bar{D}$ = 1.89	$\bar{D}$ = 1.42	1.47, 14.5	1.13, 3.47 Counts
σ = ± 1.08	σ = 0.66	$\bar{D}$ = 1.95 (excluding 9.26)	$\bar{D}$ = 1.39
17.5 μm Fringe Period		σ = 0.76	σ = 0.484
		17.5 μm Fringe Period	
			1.80, 5.19 (BKG. COUNT)
3.3, 18.2	2.69, 19.1	2.17, 27.7	1.81, 5.39 Gen. Start 200/9.3sec.
2.6, 65.5	2.36	2.67, 32.1	2.23, 30.7
2.28, 129	2.15, 22.7	2.16, 26.0	1.84, 5.86 1'30" Sample Time
2.72, 34.2	2.40	2.29, 137 5'25"	2.02, 11.3 200 Counts
1.58, 64	2.19, 26.8	2.2, 56.7	2.04, 13.9
3.7, 22.9	3.07, 14.4 9'35"	2.12, 23.8	1.82, 6.04
3.09, 20.9	2.60, 33.3 Sample Time	1.93, 11.1	1.73, 5.22 3'24" Sample Time
2.80, 30.9	2.50, 85.5 1000 Counts	2.61, 48.2	2.22, 30.1 10^3 Counts
3.90, 22.3	3.18, 13.0	2.46, 401	2.14, 20.3
3.32, 19.9	2.74, 18.8	3.02, 20.2	2.52, 52.6
4.15, 28.2	3.47, 14.6		
5.65, 50.9	4.4, 18.4		
$\bar{D}$ = 3.34	$\bar{D}$ = 2.80	$\bar{D}$ = 2.38	$\bar{D}$ = 2.06
σ = ± 0.925	σ = ±0.642	σ = ±0.33	σ = ±0.247

NOTE: First number is geometric mean size.
Second number is first moment of distribution.
$\bar{D}$ = Average of geometric means.

TABLE 3

PREDOMINENT MODE SIZES IN THE PROBABILITY DENSITY DISTRIBUTIONS MEASURED IN THE SETTLING CHAMBER

VERTICAL POLARIZATION				HORIZONTAL POLARIZATION			
RANDOM ORIENTATION		PERPENDICULAR ORIENTATION		RANDOM ORIENTATION		PERPENDICULAR ORIENTATION	
	6 μm Fringe Period				6 μm Fringe Period		
% <0.6 μm	Next Largest Mode	% <0.3 μm	Next Largest Mode	% <0.6 μm	Next Largest Mode	% <0.3 μm	Next Largest Mode
47.4%	> 13.8 @ 10%	47.7%	0.6 m @ 6.8%	34.4%	1.5 @ 13.4%	33.6%	0.9 @ 11%
19.4%	> 13.8 @ 13%	17.0%	2.4, 2.7, 4.5 @ 12%	51.2%	> 13.8 @ 12%	47.4%	3.0 @ 7.5%
23%	1.5 @ 23%	21.3%	0.9 @ 21.3%	36.3%	1.2 @ 24.3%	36.1%	0.6,0.9 @ 12%
38.9%	2.1 @ 19.1%	39.4%	5.4 @ 11%	32.6%	> 13.8 @ 26.7%	27.9%	5.4 @ 15.4%
58.2%	> 13.8 @ 12%	55.4%	5.4 @ 7.8%	0.0	> 13.8 @ 36%	0	5.4 @ 19.2%
66.1%	7.5%	67.4%	Multiple Modes	41.9%	> 13.8 @ 10%	42.1%	5.4 @ 6.7%
	17.5 μm Fringe Period				17.5 μm Fringe Period		
% <1.75 μm	Next Largest Mode	% <0.875 μm	Next Largest Mode	% <1.76 μm	Next Largest Mode	% < 0.875 μm	Next Largest Mode
46.1%	6.12,9.6 @ 4.4%	44.6%	7.87 @ 7.3%	61.7%	7.0 @ 8.6%	62.1%	3.5 @ 5.8%
59.7%	7.87 @ 4.1%	55%	7.87 @ 6.1%	53.8%	5.25 @ 6.6%	63%	8.75 @ 6.6%
65.1%	7.87 @ 3.2%	60.4%	7-7.87 @ 4%	61.9%	8.75 @ 4.4%	53.2%	6.12 @ 8.5%
55.8%	4.37 @ 5.6%	51.5%	2.62 @ 6.1%	62.9%	7.0 @ 8.7%	61.9%	7.0 @ 8.3%
57.7%	6.12 @ 5.3%	57.2%	7.87 @ 6.4%	68%	8.75 @ 9%	61.3%	6.12 @ 5.4%
45.8%	7.0 @ 6.4%	43.5%	7-7.87 @ 7.4%	64.3%	7.0 @ 7.3%	64.5%	7.87 @ 5.1%
50.6%	7.0 @ 6.1%	49.4%	8.75 @ 7.6%	69.6%	7.0 @ 8.7%	65.1%	2.62 @ 5.3%
56.9%	6.12 @ 2.9%	51.6%	7.0 @ 5.2%	55.7%	7.0 @ 6.9%	69.6%	8.75 @ 3.9%
40.2%	6.12 @ 4.6%	38.6%	6.12 @ 7.1%	39.5%	6.12 @ 5.1%	55.1%	7.87 @ 5%
47.8%	7.87 @ 5%	45.6%	7.87 @ 5.7%	50.9%	9.62 @ 4.2%	58.9%	7.87 @ 4.4%
43.2%	6.12 @ 6.2%	39.6%	7.87 @ 7.3%			47.9%	7.0 @ 6.1%
27.8%	7.0 @ 9.8%	26.7%	8.75 @ 8.2%				

TABLE 4

FRACTION OF TOTAL PARTICLES MEASURED WITH SIGNAL AMPLITUDES GREATER THAN THE AMPLIFIER RANGE

VERTICAL POLARIZATION		HORIZONTAL POLARIZATION	
6.0 μm FRINGE PERIOD	17.5 μm FRINGE PERIOD	6.0 μm FRINGE PERIOD	17.5 μm FRINGE PERIOD
4.3 %	0.2 %	4 %	1.2% BKG COUNT
0.5 %	0.6 %	4.5 %	0% GEN. START
1.5 % 11' Sample Time	3.3 %	5.0 % 3'20" Sample Time	0%
3.5 %	5.6 %	6.5 %	0% 1'30" Sample Time
3 %	4.1 %	6.0 %	0.5%
1 %	4.8 % 9'35" Sample Time 1000 Counts	6.5 %	0.5
	5.8 %	1.0 %	4
	5.9 %		4.6 3'24" Sample Time - 10^3 Counts
	3.0 %		5.2
	3.8 %		4.7
	2.6 %		5.1
	4.2 %		

TABLE 5

MEAN PARTICLE LENGTHS OBTAINED IN THE LOW PRESSURE
JET DISPERSAL USING THE 17.5 MICROMETER FRINGE PERIOD

MEAN PARTICLE LENGTH (μm)

VERTICAL POLARIZATION

	RANDOM ORIENTATION			PERPENDICULAR ORIENTATION		
	17.5 μm FRINGE PERIOD					
	Geometric Mean Size	First Moment		Geometric Mean Size	First Moment	
LOW VOLUME FRACTION	1.87	8.54		1.42	2.56	
	1.74	6.31		1.37	2.39	
	1.71	5.79		1.35	2.29	
	2.00	13.9		1.64	4.38	
	2.06	16.6	4'56" sample time 1000 counts	1.52	3.19	4'56" sample time 1000 counts
	2.19	35.7		1.53	3.18	
	2.25	66.9		1.59	3.63	
INTERMEDIATE VOLUME FRACTION	1.65	5.23		1.66	4.25	
	1.94	11.6	7'54" sample time 1000 counts	1.36	2.39	7'54" sample time 1000 counts
	1.92	10.2		1.47	2.98	
	1.63	4.88		1.44	2.74	
	1.73	6.48		1.32	2.19	
HIGH VOLUME FRACTION	1.69	5.20		1.40	2.56	
	1.61	4.87	4'27" sample time 1000 counts	1.36	2.25	
	1.78	7.02		1.38	2.47	4'27" sample time 1000 counts
	3.52	20.7		1.42	2.60	
				2.27	60.2	

TABLE 6

MEAN PARTICLE LENGTHS OBTAINED IN THE LOW PRESSURE JET DISPERSAL USING THE 6.0 MICROMETER FRINGE PERIOD

MEAN PARTICLE LENGTH (μm)

VERTICAL POLARIZATION

	RANDOM ORIENTATION			PERPENDICULAR ORIENTATION	
	6 μm FRINGE PERIOD				
	Geometric Mean Size	First Moment		Geometric Mean Size	First Moment
LOW VOLUME FRACTION	2.71	11.5		1.30	29.00
	2.58	12.5		1.27	14.00
	12.0	159.0		5.40	12.90
	8.14	59.8		3.59	9.80
	11.0	119.0		5.14	11.60
	1.68	8.86		0.924	1.75
	11.5	139.0		5.22	12.1
	1.61	16.2		0.93	2.25
	10.0	88.7		4.87	10.6
INTERMEDIATE VOLUME FRACTION	13.3	221.0		5.56	13.8
	13.4	229.0	25" sample time-1000 cts.	5.53	13.6
	10.7	106.0		5.08	11.3
HIGH VOLUME FRACTION	2.86	15.7	27" sample time-1000 cts.	1.33	142.0
	11.8	152.0		5.17	12.0
	2.84	14.5	29" sample time-1000 cts	1.40	33.7
	5.67	129.0		2.61	7.47

TABLE 7

PREDOMINENT MODE SIZES IN THE PROBABILITY DENSITY DISTRIBUTIONS MEASURED IN THE LOW PRESSURE JET DISPERSAL WITH A 17.5 MICROMETER FRINGE PERIOD

LOW PRESSURE JET DISPERSAL
PREDOMINENT MODE SIZE

VERTICAL POLARIZATION

	RANDOM ORIENTATION		PERPENDICULAR ORIENTATION	
	% <1.75 μm	Next Largest Mode	% <0.875 μm	Next Largest Mode
	69.3%	7.87 @ 3.5%	75.3%	2.62 @ 4.4%
	73.1%	8.75 @ 2.5%	78.2%	2.62 @ 2.6%
	73.9%	9.62 @ 2.7%	78.8%	2.62 @ 2.6%
LOW VOLUME FRACTION	68.0%	7.87 @ 2.6%	73.2%	8.75 @ 3.1%
	67.3%	7.00 @ 4.0%	72.7%	2.62 @ 3.4%
	64.5%	4.37 @ 3.9%	71.3%	2.62 @ 5.7%
	65.1%	6.12 @ 5.2%	70.5%	3.50 @ 3.8%
	62.5%	7.87 @ 6.8%	71.7%	4.37 @ 3.6%
INTER-MEDIATE VOLUME FRACTION	61.6%	7.87 @ 4.3%	70.5%	7.87 @ 3.6%
	76.0%	6.12 @ 2.8%	79.4%	7.00 @ 2.3%
	70.1%	10.5 @ 3.1%	76.7%	6.12 @ 3.5%
	69.4%	5.25 @ 4.4%	77.1%	3.50 @ 3.2%
	76.2%	7.00 @ 6.1%	81.0%	2.62 @ 2.5%
	74.7%	4.37 @ 2.7%	78.3%	7.87 @ 3.4%
HIGH VOLUME FRACTION	71.2%	2.62 @ 5.3%	75.2%	1.75 @ 5.6%
	77.3%	3.50 @ 5.1%	78.6%	2.62 @ 5.3%
	72.7%	8.75 @ 5.8%	76.4%	2.62 @ 5.9%
	46.1%	6.12 @ 11.3%	58.0%	4.37 @ 8.1%

TABLE 8

PREDOMINENT MODE SIZES IN THE PROBABILITY DENSITY DISTRIBUTIONS MEASURED IN A LOW PRESSURE JET DISPERSAL WITH A 6.0 MICROMETER FRINGE PERIOD

LOW PRESSURE JET DISPERSAL
PREDOMINENT MODE SIZE

VERTICAL POLARIZATION

	RANDOM ORIENTATION		PERPENDICULAR ORIENTATION	
	% <0.6 μm	Next Largest Mode	% <0.3 μm	Next Largest Mode
LOW VOLUME FRACTION	33.9%	13.8 @ 31.2%	44.3%	5.70 @ 20.8%
	38.2%	13.8 @ 37.9%	46.2%	5.70 @ 26.1%
	0	13.8 @ 77.8%	0	5.70 @ 61.9%
	0	13.8 @ 57.4%	0	5.70 @ 39.8%
	0	13.8 @ 64.5%	0	5.70 @ 48.9%
	31.6%	9.0 @ 31.5%	34.7%	0.6 @ 34.8%
	0	13.8 @ 72.7%	0	5.70 @ 57.4%
	56.0%	13.8 @ 42.9%	61.4%	5.70 @ 30.0%
	0	13.8 @ 59.2%	0	5.70 @ 53.5%
	0	13.8 @ 89.9%	0	5.70 @ 74.9%
INTER-MEDIATE VOLUME FRACTION	0	13.8 @ 88.4%	0	5.70 @ 70.0%
	0	13.8 @ 57.4%	0	5.70 @ 54.4%
HIGH VOLUME FRACTION	37.5%	13.8 @ 40.2%	47.9%	5.70 @ 30.0%
	0	13.8 @ 74.9%	0	5.70 @ 56.5%
	35.7%	13.8 @ 40.8%	44.0%	5.70 @ 30.1%
	0	13.8 @ 43.9%	0	5.70 @ 30.0%

TABLE 9

FRACTION OF TOTAL PARTICLES MEASURED WITH SIGNAL AMPLITUDES GREATER THAN THE AMPLIFIED RANGE

PARTICLE FRACTION WITH SIGNAL MAGNITUDES GREATER THAN AMPLIFIER RANGE

VERTICAL POLARIZATION

6.0 μm Fringe Period		17.5 μm Fringe Period	
	9.9%		0.4%
	9.6%		0
	9.0%		0.2%
	10.2%		1.31%
LOW VOLUME FRACTION	6.9%		
	7.7%		2.94%
	7.0%		0.3%
	10.7%	LOW VOLUME FRACTION	0.3%
	9.9%		0.1%
	12.4%		0.6%
INTERMEDIATE VOLUME FRACTION	8.0%		0.3%
	8.6%		0.25%
HIGH VOLUME FRACTION	8.0%	INTERMEDIATE VOLUME FRACTION	0
	4.9%		0.2%
	7.8%		0
	6.4%		0
			0
		HIGH VOLUME FRACTION	0
			0
			0
			0.2%

TABLE 10

PARTICLE VELOCITY MEASUREMENTS
IN THE LOW PRESSURE JET
DISPERSAL

LOW VOLUME FRACTION		INTERMEDIATE VOLUME FRACTION		HIGH VOLUME FRACTION	
VELOCITY (m/sec.)	TURBULENT INTENSITY (%)	VELOCITY (m/sec.)	TURBULENT INTENSITY (%)	VELOCITY (m/sec.)	TURBULENT INTENSITY (%)
2.55	$\pm_{39}$	1.82	$\pm_{29}$	1.89	$\pm_{44}$
2.40	$\pm_{39}$	1.805	$\pm_{33}$	3.58	$\pm_{91}$
2.60	$\pm_{38}$	1.79	$\pm_{25}$	5.92	$\pm_{51}$
2.72	$\pm_{39}$	1.85	$\pm_{29}$	5.39	$\pm_{66}$
2.68	$\pm_{40}$	1.96	$\pm_{44}$		

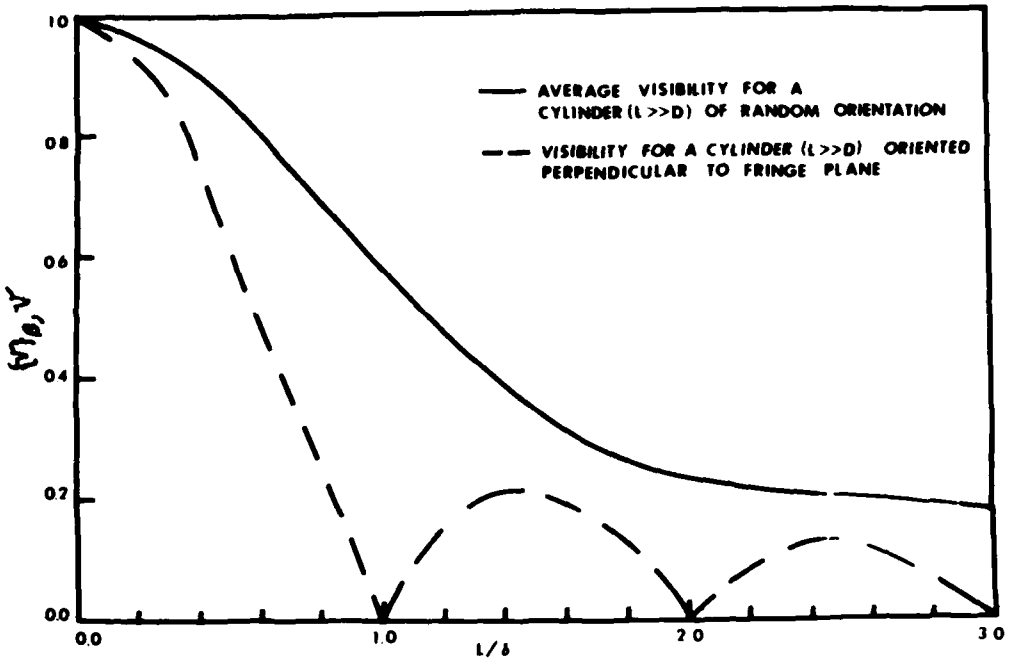

Figure 1. Visibility functions for a) cylinders at perpendicular incidence to the fringe planes, b) an ensemble of cylinders at random orientation.

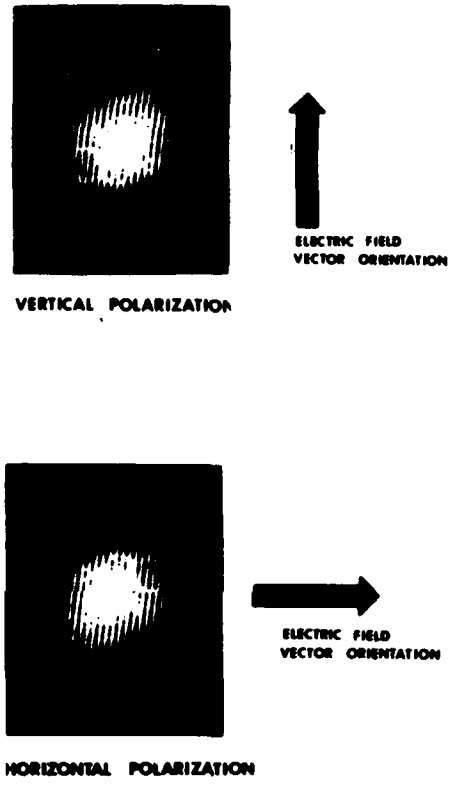

Figure 2. Orientation of the electric field vectors with respect to the fringe planes for the vertical and horizontal polarization states.

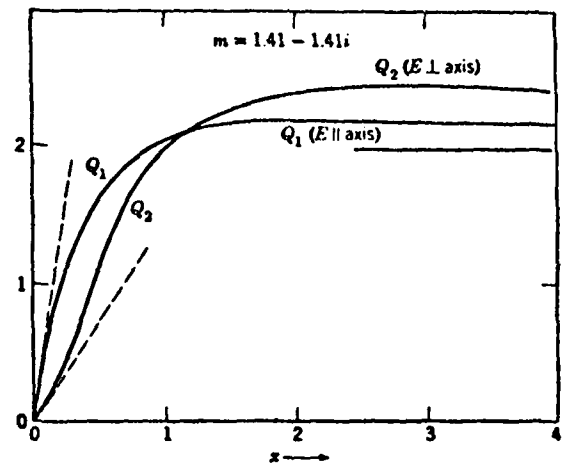

Figure 3. Extinction coefficient as a function of $X(\pi D/\lambda)$ for the electric vector parallel and perpendicular to the axis of an iron cyclinder (taken from reference 6).

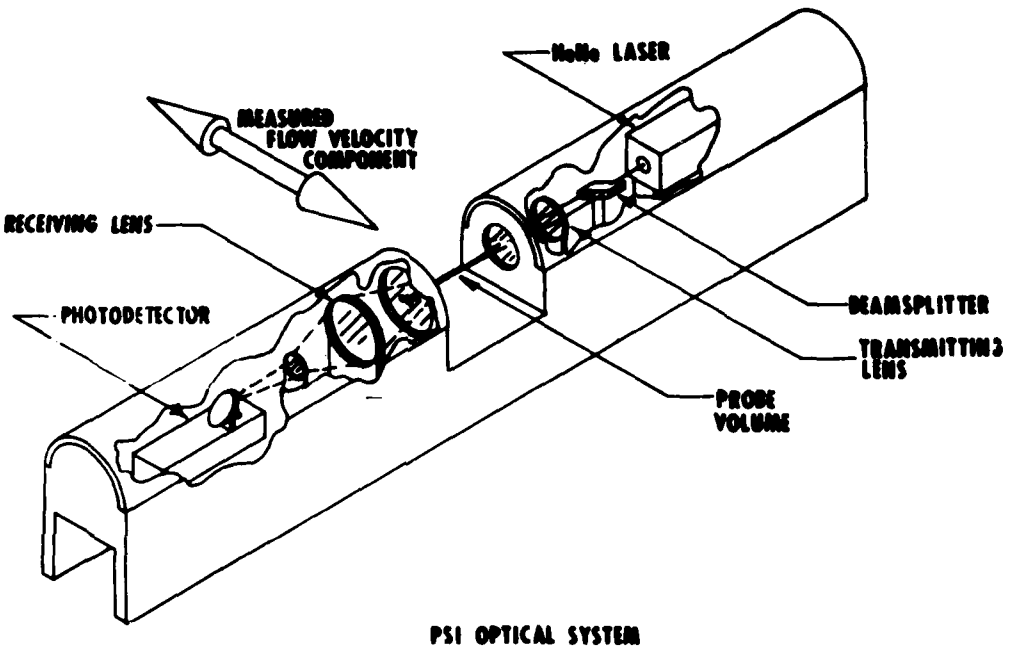

Figure 4. Schematic of the PSI optical system used in the settling chamber measurements.

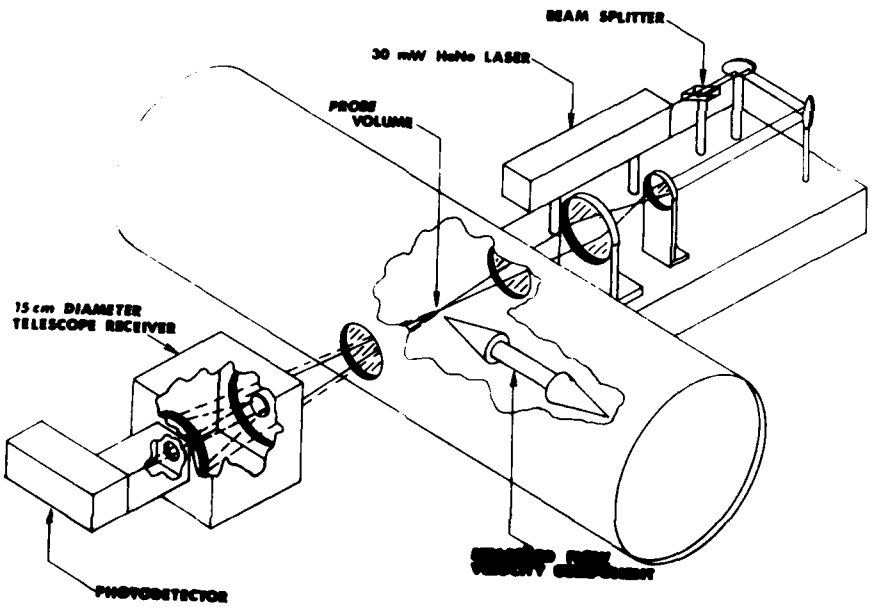

Figure 5. Schematic of the PSI optical system used in the low pressure jet dispersal measurements.

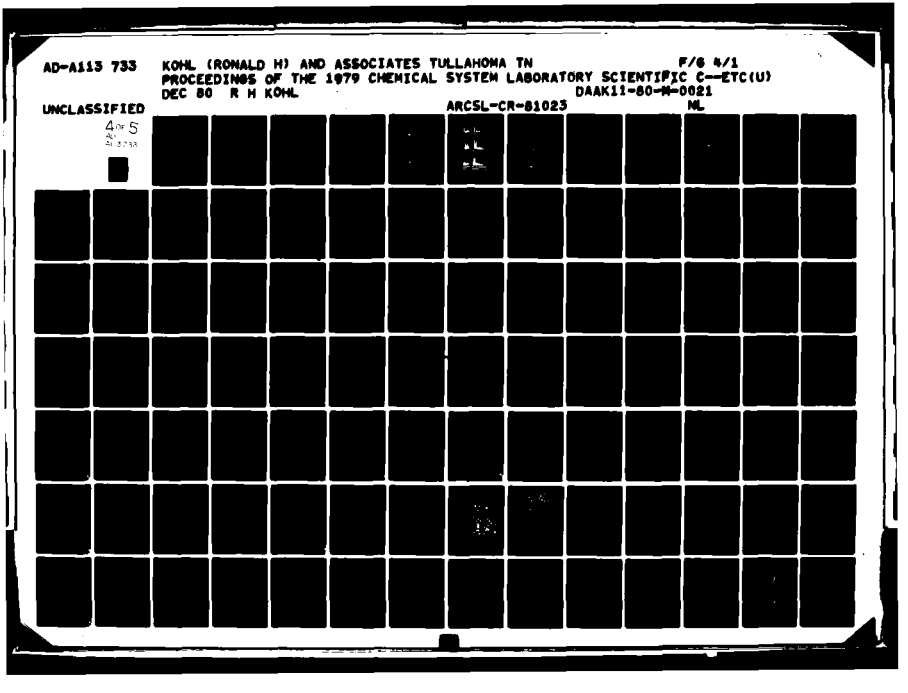
AD-A113 733
KOHL (RONALD H) AND ASSOCIATES TULLAHOMA TN
F/G 4/1
PROCEEDINGS OF THE 1979 CHEMICAL SYSTEM LABORATORY SCIENTIFIC C--ETC(U)
DEC 80 R H KOHL
DAAK11-80-M-0021
UNCLASSIFIED
ARCSL-CR-81023
NL
4 OF 5

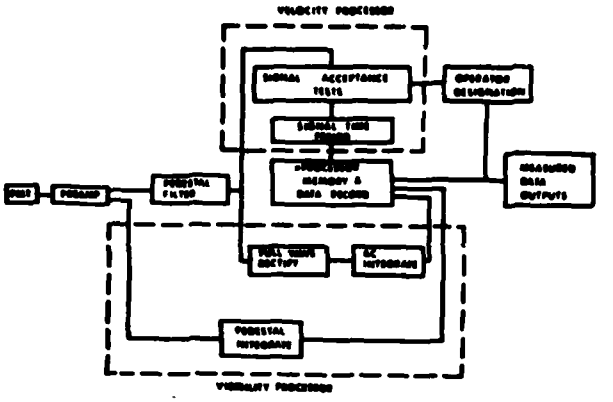

Figure 6. PSI Signal Processing and Data Acquisition System

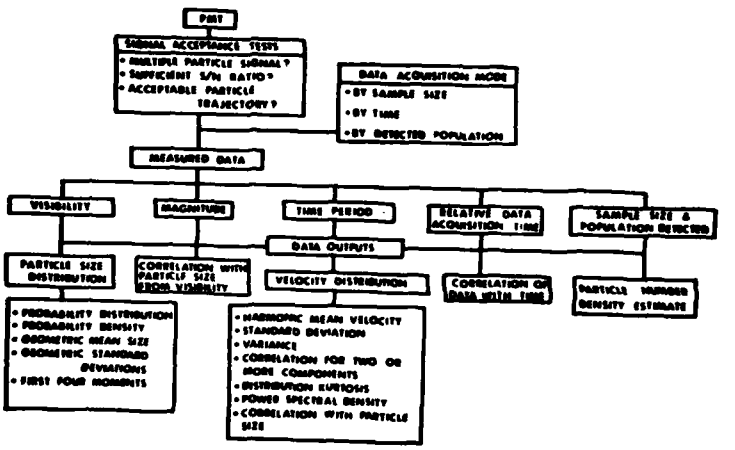

Figure 7. PSI measurement functions and data output options.

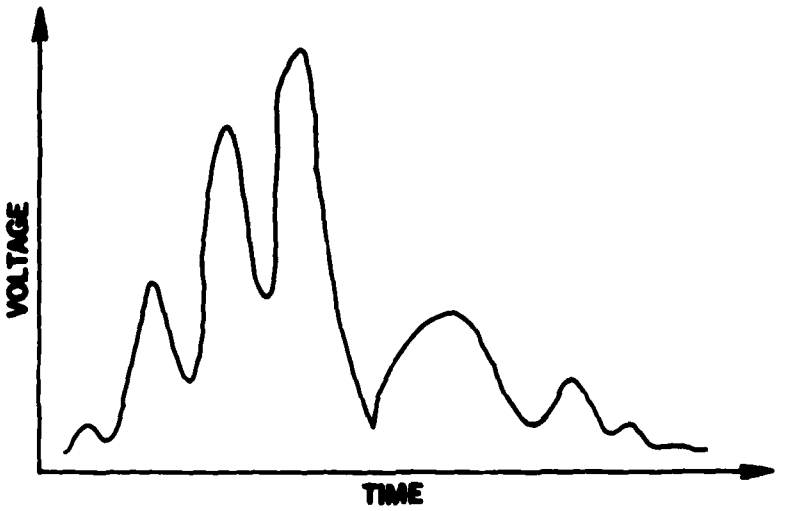

Figure 8. Schematic of distorted PSI signal believed to result from laser heating of the particle.

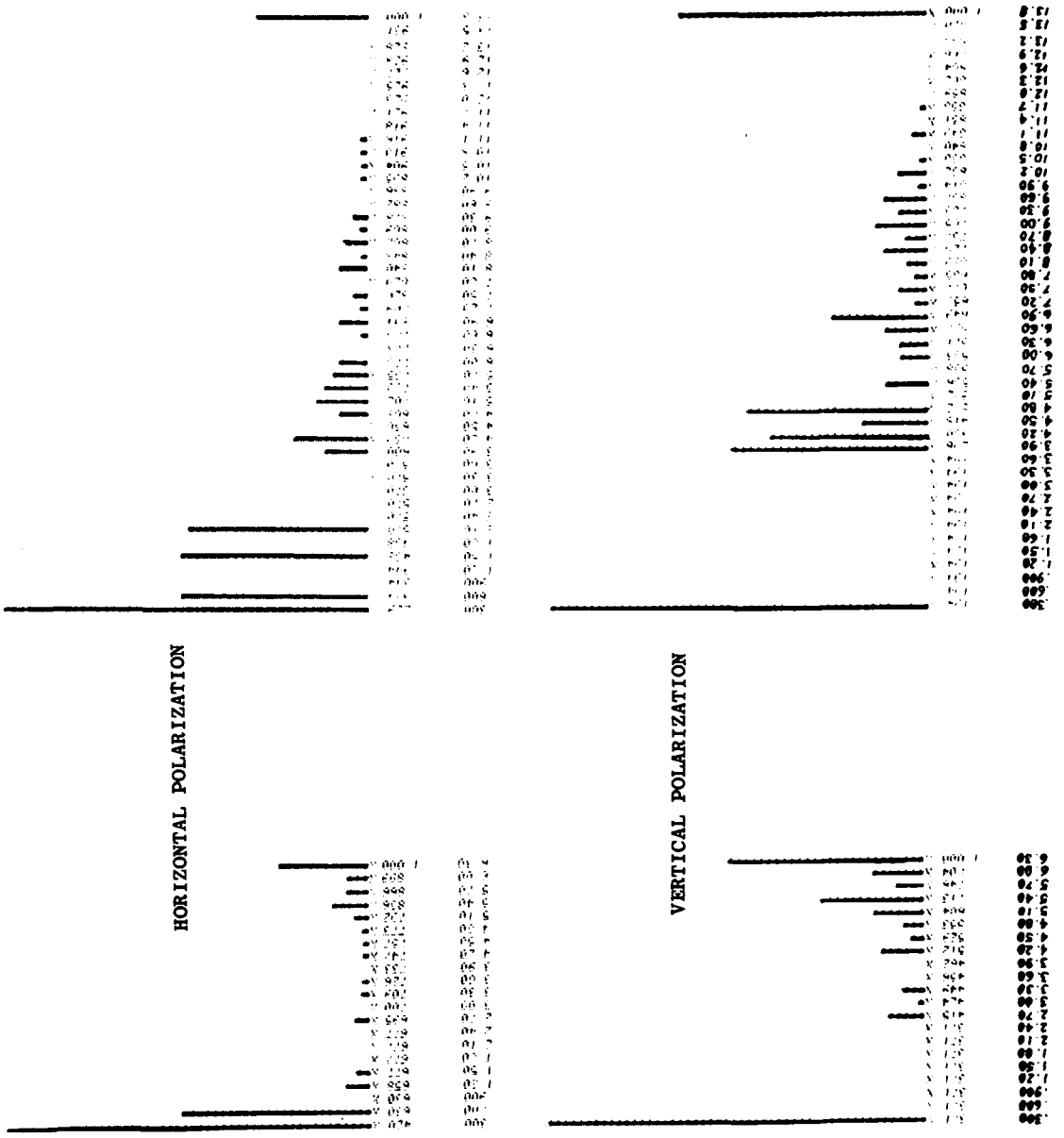

Figure 9. Probability density distributions for settling chamber measurements made with a 6 micrometer fringe period.

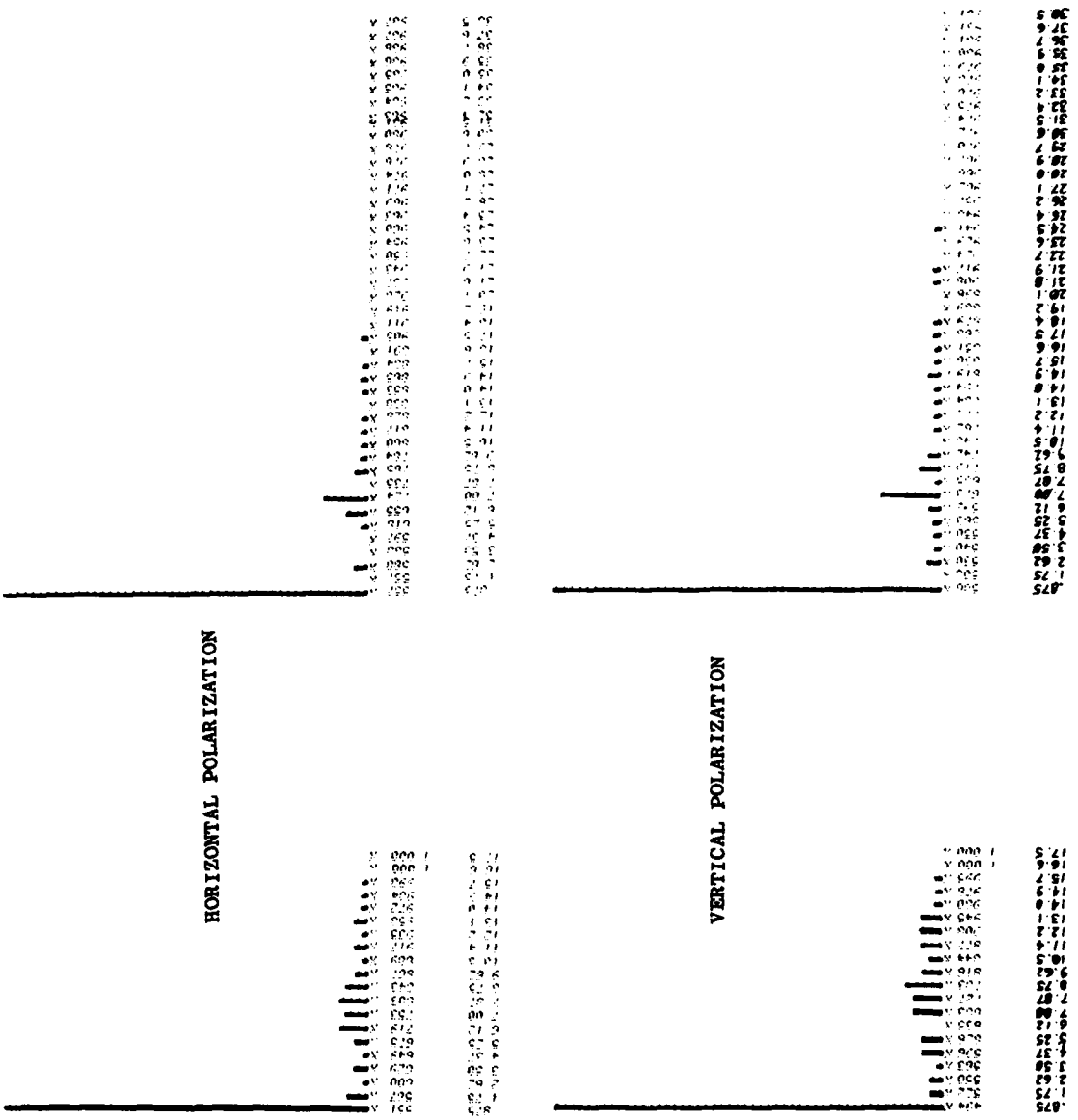

Figure 10. Probability density distributions for settling chamber measurements made with a 17.5 micrometer fringe period.

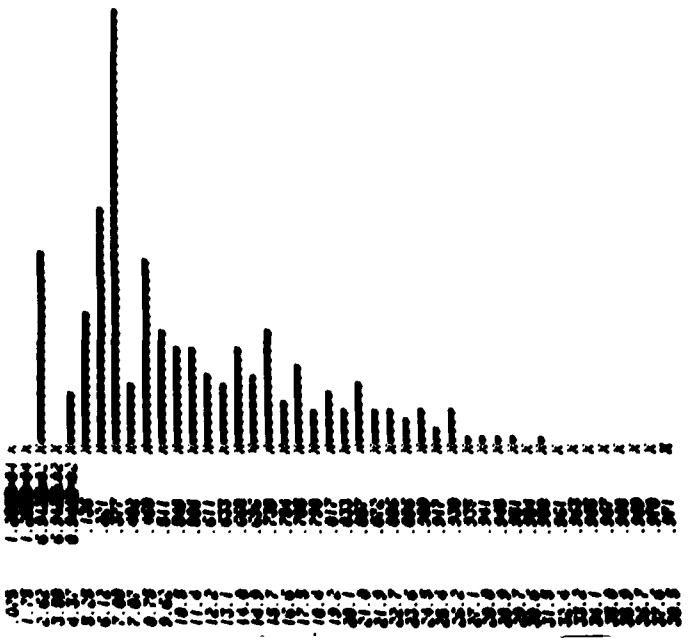

HORIZONTAL POLARIZATION

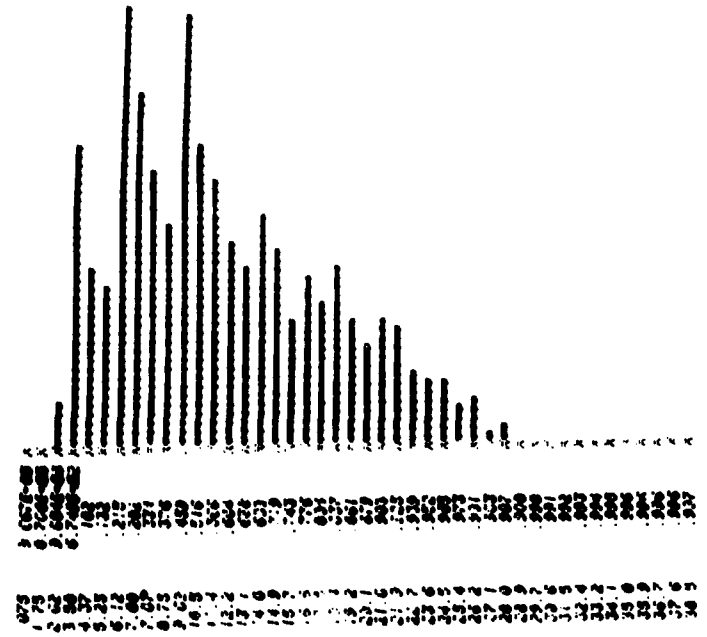

VERTICAL POLARIZATION

Figure 11. Examples of particle size distributions for vertical and horizontal polarization states with the smallest particl size increment removed.

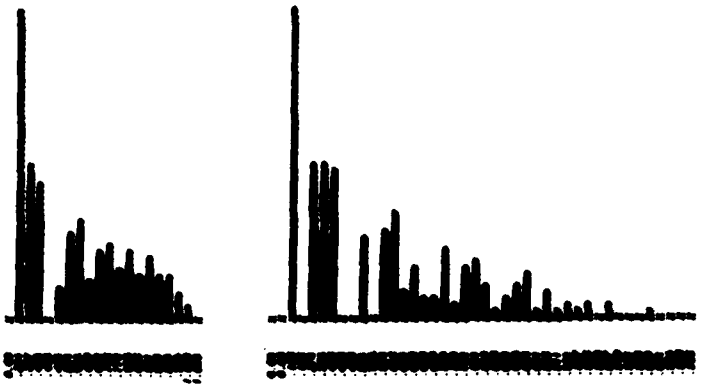

HIGH VOLUME FRACTION

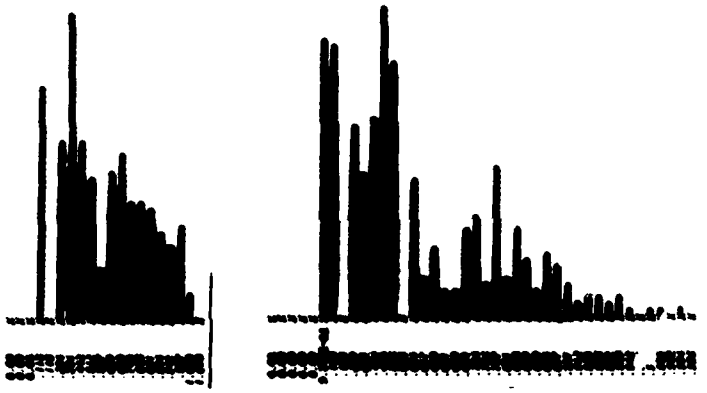

INTERMEDIATE VOLUME FRACTION

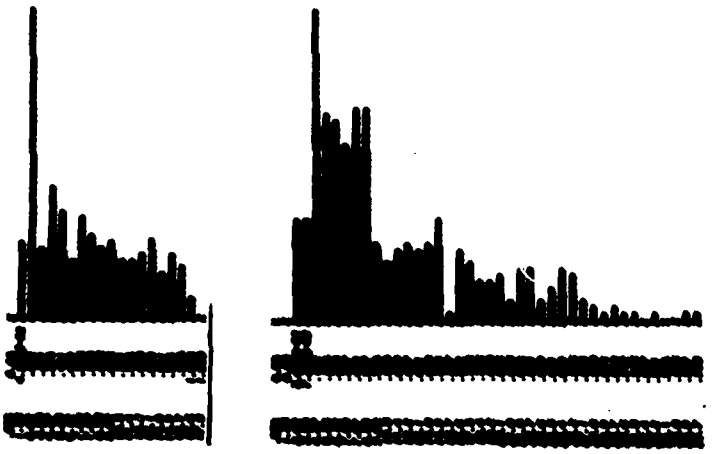

LOW VOLUME FRACTION

Figure 12. Examples of probability density distributions measured in the low pressure jet dispersal with a 17.5 micrometer fringe period with the smallest particle size increment suppressed.

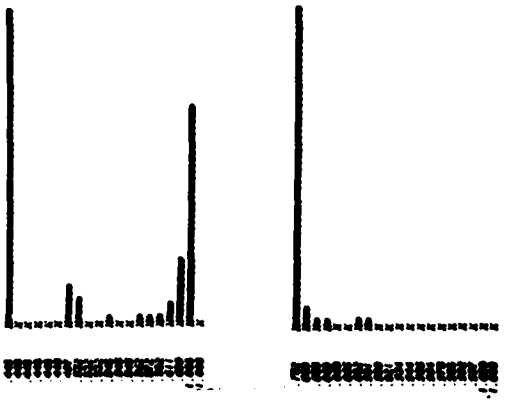

HIGH VOLUME FRACTION

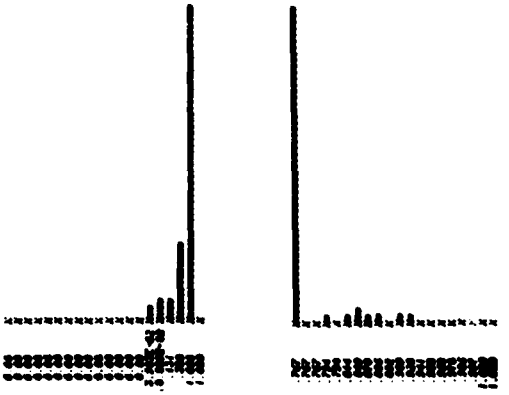

INTERMEDIATE VOLUME FRACTION

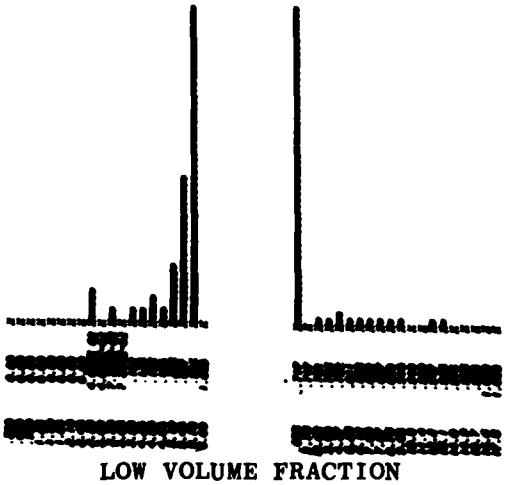

LOW VOLUME FRACTION

Figure 13. Comparison of the size distributions obtained for different volume fractions assuming perpendicular orientation and fringe periods of 6 and 17.5 micrometers.

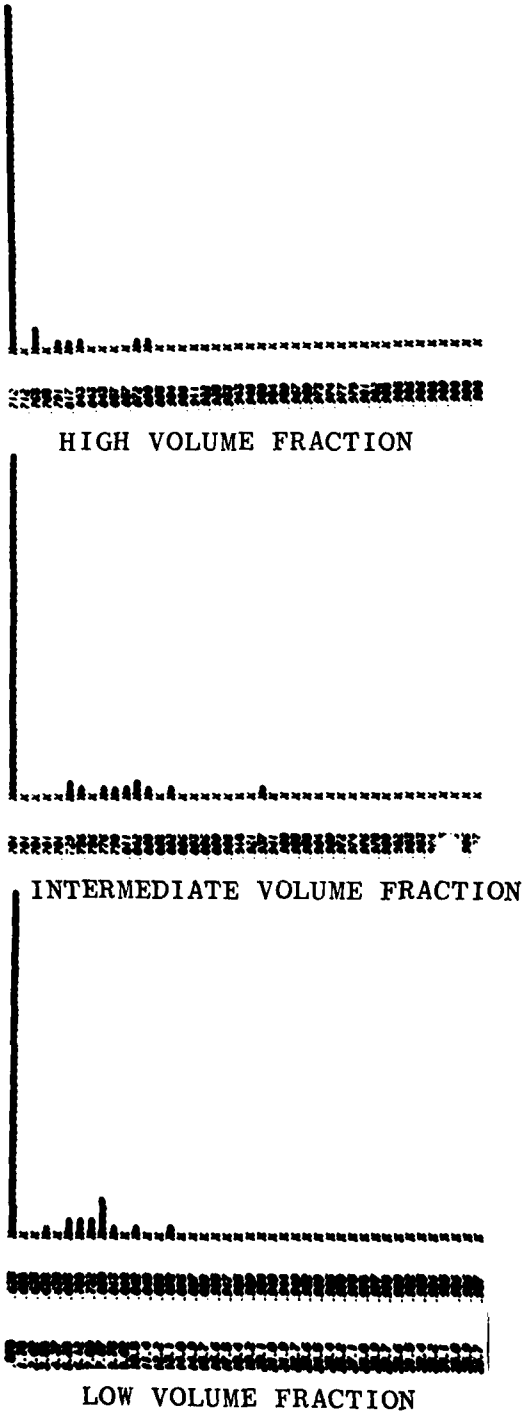

igure 14. Examples of probability density distributions assuming a random particle orientation for a 17.5 micrometer fringe period.

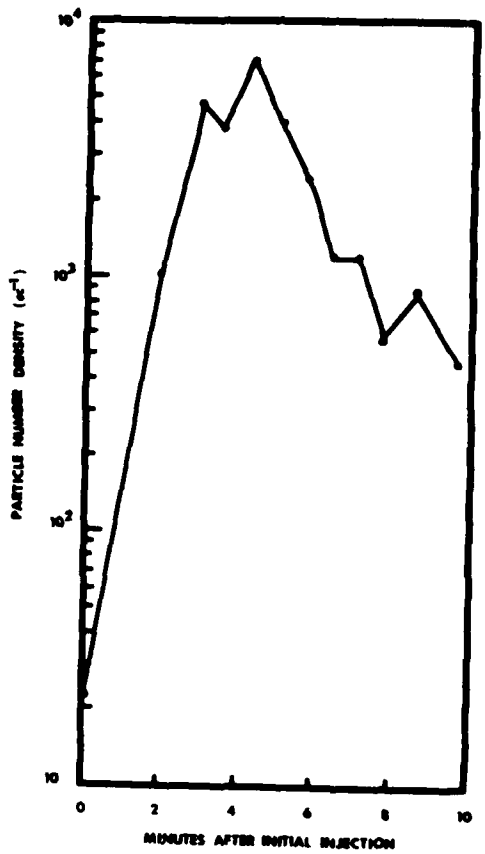

Figure 15. Particle number density as a function of time after injection into the settling chamber.

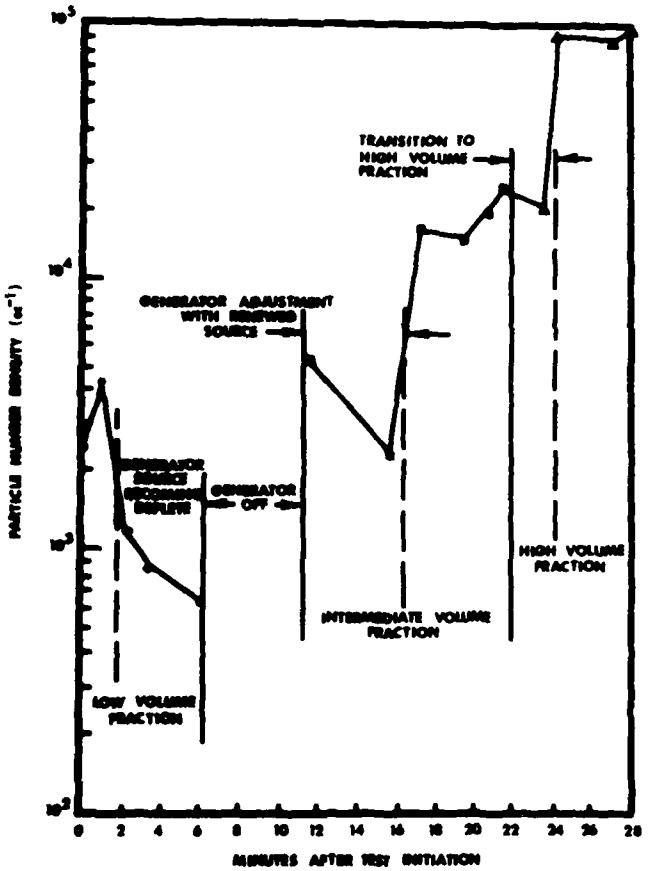

Figure 16. Particle number density as a function of volume fraction in the low pressure jet dispersal.

A New Method for Measuring the Particle Size Distribution of Aerosols

R.J. Tropp, P.J. Kuhn, and J.R. Brock
Department of Chemical Engineering, the University of Texas, Austin, Texas 78712

ABSTRACT

A new method (electronic cascade impaction) of measuring the particle size distribution of aerosols is presented, and an instrument we call an electronic cascade impactor (ECI) which uses the method is described. Aerosol particles are charged in a unipolar charger and enter a multistage cascade impactor. Each collection stage and the final filter is isolated electrically from other parts of the impactor and connected to an electrometer detector. Particles deposit on the collection stages according to their aerodynamic diameters, and from the associated electrical current the deposition rate onto each stage and the particle size distribution can be determined. Calibration data for the ECI are presented. The ECI has been used to study atmospheric aerosol dynamics in real time, and typical data are given. The ECI has proven to be reliable in several hundred hours of laboratory and field use and other versions employing the same general method should prove useful in a wide variety of measurement situations.

A New Method for Measuring the Particle Size Distribution of Aerosols

INTRODUCTION

Six years ago, in the course of investigations of the dynamics of the atmospheric aerosol, it became apparent that the instruments available for measuring particle size distributions were inadequate for our purposes. A new measurement method was sought with the following characteristics: (1) a response time of one second or less for the entire size spectrum; (2) capability to be calibrated absolutely; (3) capability to measure very dense (without a dilution step) as well as very dilute aerosols; (4) ability to classify (in time sequence, if desired) aerosol particles for subsequent chemical or physical analysis; (5) a large volumetric sampling rate to minimize errors introduced when sampling a spatially heterogeneous aerosol; (6) measurement of the aerodynamic particle diameter rather than such quantities as optical diameter, electrical mobility diameter, etc; (7) low cost in comparison with available instruments; (8) real time output of data that is easily interfaced to recording or data acquisition equipment.

We found a method which we believe has these characteristics. It is embodied in an instrument which we have termed an electronic cascade impactor (ECI). Aerosol particles acquire a unipolar electric charge before entering a cascade impactor (either real or virtual) in which each collection stage is isolated electrically from other parts of the impactor and connected to an electrometer detector. Particles are collected on a collection surface according to their aerodynamic diameter as in an ordinary impactor, but the current arising from the deposited charge can be measured, amplified, and recorded in real time. Moreover, the instrument is capable of absolute calibration since each collection surface may be removed and weighed and the result compared with the integrated signal over the length of time of sample collection.

The ECI has now been used in the study of ambient atmospheric aerosol dry deposition rates and in the investigation of the relation-

ship between aerosol particle size distribution and atmospheric electricity parameters.

The first section describes the design and performance of the ECI system. Next, an experiment for studying ambient atmospheric aerosol using the ECI along with other monitoring instruments is discussed. In the final section a brief discussion is given of the performance characteristics of the ECI, and suggestions are given for its modification.

I. THE ELECTRONIC CASCADE IMPACTOR

The electronic cascade impactor (ECI) system consists of three major components: the aerosol charger and associated high voltage power supplies, the cascade impactor and associated flow train components, and the elctrometer detector with associated power supply and output module. The system is shown schematically in Fig. 1.

The aerosol charger is a corona charger of unique design which includes a number of features described by others.[1-4] The operating parmeters of the charger have been adjusted to yield maximum signal strength consistent with high transmission efficiency of aerosol particles and stable operation at high volumetric flow rates. Under normal operating conditions at a flow rate of 1.5 l/s, the transmission efficiency, f, through the charger is 0.94 ± 0.02 for particles with diameter $D_p \leq 2\mu m$ with the corona current on; without charging f = 0.98 ± 0.01. The number of charges per aerosol particle as a function of particle diameter for polystyrene latex spheres used in calibration is shown in Fig. 2. The dominant charging mechanism under present operating conditions is diffusion charging by positive ions. The curve in Fig. 2 is that for diffusional charging with $Nt = 5 \times 10^{11}$ s/m^3 as determined from operating parameters, where N is the small ion concentration and t is the residence time in the charging region.

The cascade impactor consists of five impactor stages (with a sixth stage available) plus a final filter. Each impactor stage consists of four rectangular jets arranged in a symmetrical radial pattern. A removable, specially treated foil collection surface is located below the jets and rests on a teflon insulator. The inlet to

the next stage is located 45° from the previous stage. The design allows for a large flow rate with low wall losses and short travel time through the impactor. Dimensional scaling for the various impactor stages is based on the work of Marple.[6,7]

The collection efficiency of each impaction stage was determined under normal operating conditions using polystyrene latex spheres.[8] The 50% cutoff diameters for stages 1 through 5 are > 3, 2, 0.8, 0.6, and 0.26μm, respectively. These values represent departures from those to be expected from theory [6,7] and are caused by non-ideal flow characteristics in a cascade impactor.[9,10] The final filter is isolated electrically and consists of densely packed ultra-fine metal fibers. As shown in Fig. 3, the total residence time from stage 1 to the final filter is 0.2 s; the time delay between adjacent stages is 0.04 s. All parts of the impactor may be disassembled, including the impaction jets, for analysis, cleaning, and modification.

Each collection stage, including the final filter, is connected to an electrometer detector circuit similar to a previous design[11] with the circuits housed in an aluminum box that mounts directly onto the assembled impactor to reduce vibration and noise. Each detector features selectable sensitivity (from 10^{-12} to 10^{-9} A in for 10 V out at full scale), bipolar response, and fine and coarse zero adjustment. The detector time constant is approximately 0.6 s and was chosen to yield rapid response time with optimum noise characteristics.[12] All input and output connections to the electrometers are made through a multiconductor shielded cable and pass through a readout and meter module where the output signals can be monitored and connected to recording or other measuring instruments. Figure 4 shows a strip chart recording of the ECI for polystyrene latex sphere (PSL) calibration aerosols. Figure 4a is for spheres 1.09μm in diameter, and Figure 4b is for spheres 0.62μm in diameter. About 90% of the large signal on the final filter is due to solvent and other residues.

In addition to the major components of the ECI, the flow train includes a mass flow meter, flow control valve, and a carbon-vane rotary pump. The normal flow rate is 1.5 l/s with a long term stability of about 2%. The system has been operated reliably in the field for

10 hours per day for several days and for periods of over 30 continuous hours in laboratory sampling of outside ambient air. Including calibration and test runs, the total cumulative operating time with the ECI exceeds several hundred hours.

II. EXPERIMENTAL RESULTS

The ECI system has been used to monitor ambient atmospheric aerosols and look for short term correlations with atmospheric electrical parameters. Figure 5 shows a schematic diagram of the system used in these particular experiments. The arrangement permits a side-by-side comparison of the ECI with a Climet Model 208 optical particle counter (OPC) and an Environment One Rich 100 condensation nuclei counter (CNC). The results obtained from the OPC, CNC or ECI can be compared with the measurements of positive polar conductivity obtained by a Gerdien tube apparatus of standard design.[13]

In the experimental results to be discussed, outside ambient air is drawn through a duct 40 cm in diameter and approximately 3 meters long by means of a blower at the rate of 61 l/s. A small fraction of the air is drawn into two sampling lines, one to the CNC and another to the ECI and OPC. The output from the CNC is amplified and then fed to one channel of an eight track strip chart recorder (SCR) and a channel of a Sangamo 3500 14 channel FM tape recorder. The air in the ECI sampling line passes through a TSI Model 3054 Kr85 aerosol charge neutralizer used only for calibration with PSL particles and left in place for convenience. Approximately 0.04 l/s of air in the ECI line is drawn continuously through an isokinetic sampling line into the OPC. Every 45 minutes the output pulses obtained from the OPC during a one minute interval are fed to a Nuclear Data ND812 computer programmed to operate as a multichannel pulse height analyzer (MCA). The resulting particle size distribution is printed out by a teletype printer and photographed from the screen of a display oscilloscope (CRO).

The remainder of the air (1.5 l/s) passes through the charger of the ECI and then through the impactor wherein the entrained charged particles are deposited onto the various impactor stages and the final filter. An electrometer amplifier for each stage and final filter

amplifies the resulting current. The output of each electrometer detector is fed through the readout module to both a channel of the SCR and FM recorder. The air flow through the ECI system is measured by a Datametrics Model 800-VTP Mass Flowmeter with a sensor giving 2.36 l/s full scale. A carbon vane rotary pump moves the air through the ECI system.

Another duct also of 10 cm diameter but about 1.5 meters long brings air at the rate of 61 l/s through a Gerdien tube apparatus set up to measure positive polar conductivity. The voltage across a 10^{11} ohm resistor is measured by a Keithley Model 616 digital electrometer, the analog output of which is fed to both a channel of the SCR and the FM recorder.

With this arrangement a continuous record of positive polar conductivity, condensation nuclei concentration, and output of each stage of the ECI impactor is obtained. All of the data shown here are for 0730-0740 LST, 29 July 1979, at Austin, Texas. Particle size distributions from the OPC are obtained every 45 minutes. Periodic records of zero are obtained every 2 hours. Figure 6 shows a typical trace obtained by using the above mentioned arrangement during part of a 24 hour run. The excellent agreement between the output of the impactor's final filter, I-FF, and CNC is notable. Toward the beginning of the trace, discrete slips can be observed in the CNC recording due to the longer response time of the instrument and also the discrete nature of its sampling. Portions of the SCR record were subjected to time analysis.[14] Early morning, late morning, and late evening portions of the record were used. Two hour periods were sampled at one minute intervals, and a shorter period within each of the previous portions was examined at four second intervals. The following quantities were computed for the time series analysis: mean, variance, autocovariance and autocorrelation, power spectrum, and cross-covariance and cross-correlation.[15] The results indicate a positive correlation between the CNC and impactor final filter signals of 0.95 ± 0.02. Moreover, both are negatively correlated with positive polar conductivity having correlation coefficients of - 0.72 ± 0.09 for the fast analysis and -0.82 ± 0.02 for the longer time interval analy-

sis. Finally, the results of the impactor stage signals agree qualitatively with those of the OPC. Quantitative agreement is difficult to obtain between the OPC and ECI since they determine different moments of the particle size distribution and differ in particle size sensitivity.

Two power spectra for the ECI are shown in Figures 7 and 8. Figure 7 is the power spectrum for the final filter while Figure 8 is for stage 5. The time interval covered overlaps the recorder trace shown in Fig. 6. Note the agreement for many of the peaks. The power spectrum for the CNC (not shown) is virtually identical to that of the final filter, as one would expect from the close correlation between the two. An analysis of the higher frequency correlations and spectra from the FM record will be given in another publication.

III. DISCUSSION

The version of the ECI described above was optimized for rapid response and measurement of the portion of the atmospheric aerosol size spectrum having aerodynamic particle diameters less than 2μm. It has proven to be reliable and indispensable in our continuing studies of atmospheric aerosol dynamics. Already, the present ECI system has been operated under adverse field conditions for around a hundred hours with no apparent difficulties. It has been operated for over a year in the laboratory in various calibration tests also with no apparent problems.

The basic principles of operation of the ECI can be used in a wide variety of instrument designs to meet particular sampling requirements.[16] For example, one design would be appropriate for particle size distribution measurement of very high aerosol concentrations, another for very low aerosol concentrations. Similarly, changes could be effected for particle size range, response time, volumetric flow rate, detection method (current, accumulated charge, etc.), and impaction mode (e.g. virtual or real).

ACKNOWLEDGEMENTS

The authors wish to thank A.L. Mitchell and H. Lehnick for their helpful discussions and their assistance in the design and construction of various components of the ECI. This work has been supported in part by a research grant from the Aerosol Research Branch of the U.S. Environmental Protection Agency.

References

1. E. O. Knutson, "The distribution of electric charge among the particles of an artificially charged aerosol." Ph.D. Thesis, University of Minnesota, Minneapolis, Minnesota (1971).
2. G. W. Hewitt, Trans. AIEE 76, 300 (1957).
3. G. W. Penney and R. D. Lynch, Trans. AIEE 76, 294 (1957).
4. W. B. Smith, L. G. Felix, D. H. Hussey, D. H. Pontius, and L. E. Sparks, J. Aerosol Sci. 9, 101 (1978).
5. D. H. Pontius, L. G. Felix, J. R. McDonald, and W. B. Smith, "Fine Particle Charging Development," Environmental Protection Agency Report EPA-600/2-77-173 (1977).
6. V. A. Marple, "A Fundamental Study of Inertial Impactors," Ph.D. Thesis, University of Minnesota, Minneapolis, Minnesota (1970).
7. V. A. Marple and K. Willeke, Atmospheric Environment 10, 891 (1976).
8. Available from Dow Chemical U.S.A., P.O. Box 68511, Indianapolis, Indiana 46268.
9. N. A. Fuchs, in Fundamentals of Aerosol Science, edited by D. T. Shaw (Wiley, New York, 1978).
10. A. K. Rao and K. T. Whitby, J. Aerosol Sci. 9, 87 (1978).
11. J. P. Oliver, Rev. Sci. Instrum. 47, 581 (1976).
12. Keithley Instruments, Electrometer Measurements (Keithley Instruments, Cleveland, 1972).
13. W. E. Cobb and B. B. Phillips, Technical Paper No. 46, Weather Bureau, U.S. Department of Commerce, Washington, D.C. (1962).
14. G. M. Jenkins and D. G. Watts, Spectral Analysis and Its Applications, (Holden-Day, San Francisco, 1968).
15. W. J. Dixon, editor, BMD; Biomedical Computer Programs, (University of California, Berkeley, 1974).
16. AERA, Austin Environmental Research Associates, P.O. Box 5164, Austin, Texas 78763.

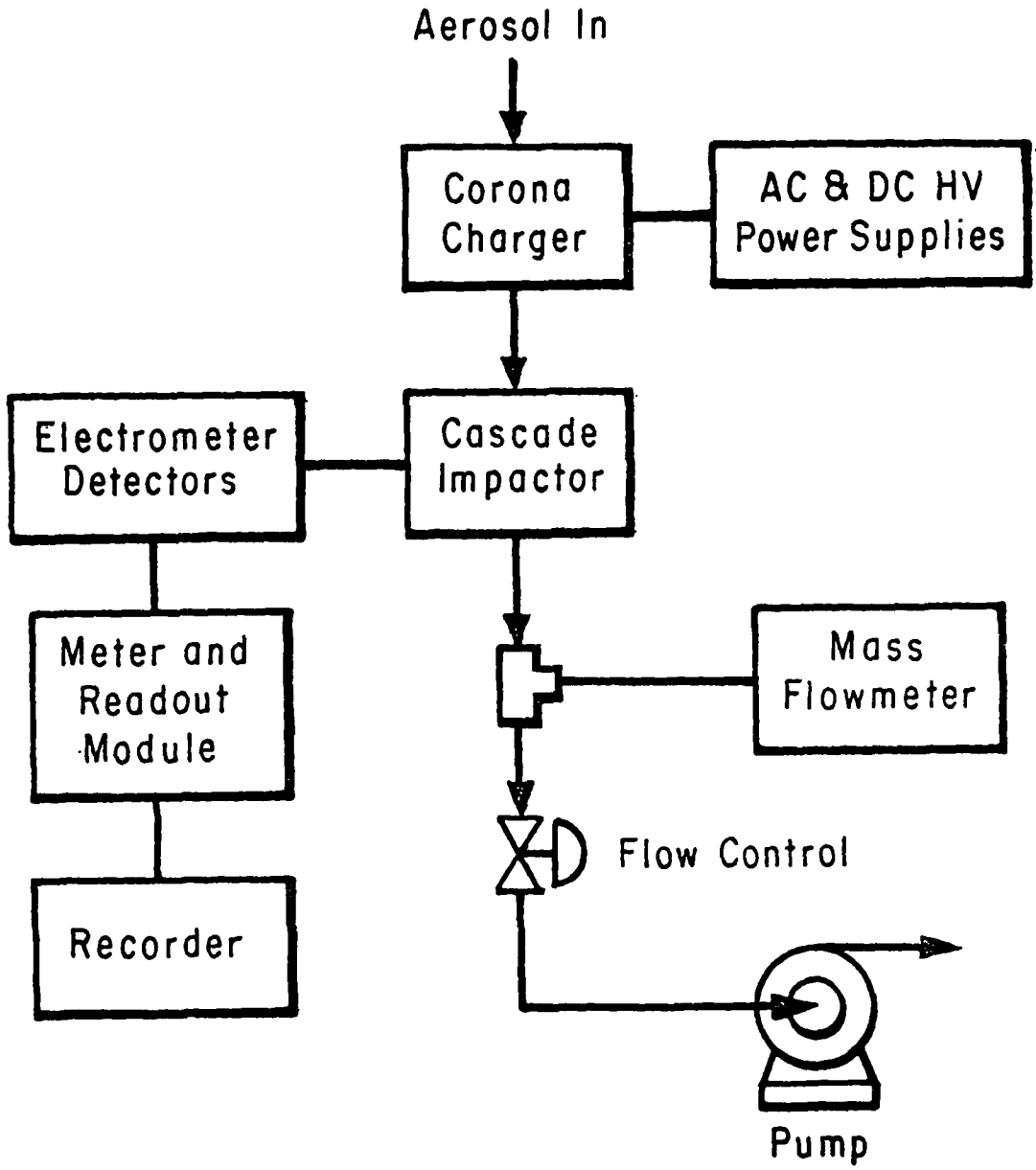

Fig. 1. Schematic diagram of the ECI system.

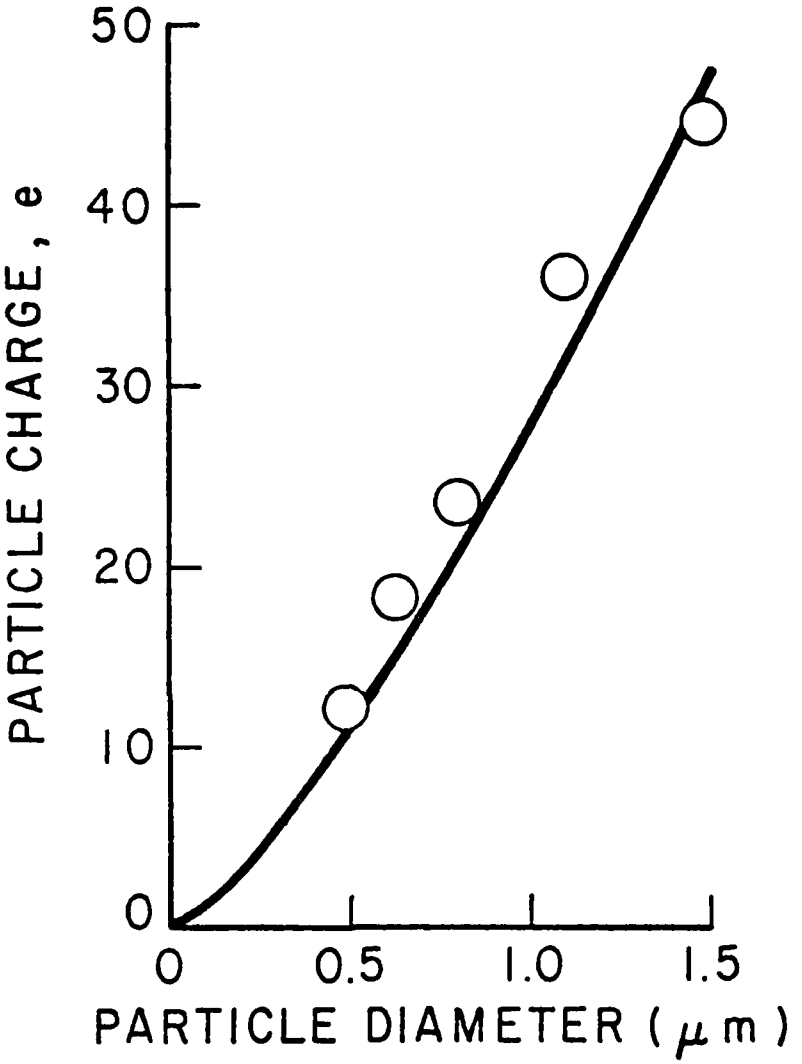

Fig. 2. Number of elementary charges per aerosol particle as a function of particle diameter. Aerosol particles are polystyrene latex spheres. The solid curve is obtained from diffusional charging theory with $Nt = 5 \times 10^{11}$ s/m^3 where N is the small ion concentration and t is the residense time in the charging region. The value of Nt is obtained from the normal operating parameters of the ECI charger for charging by small positive ions (see Ref. 5).

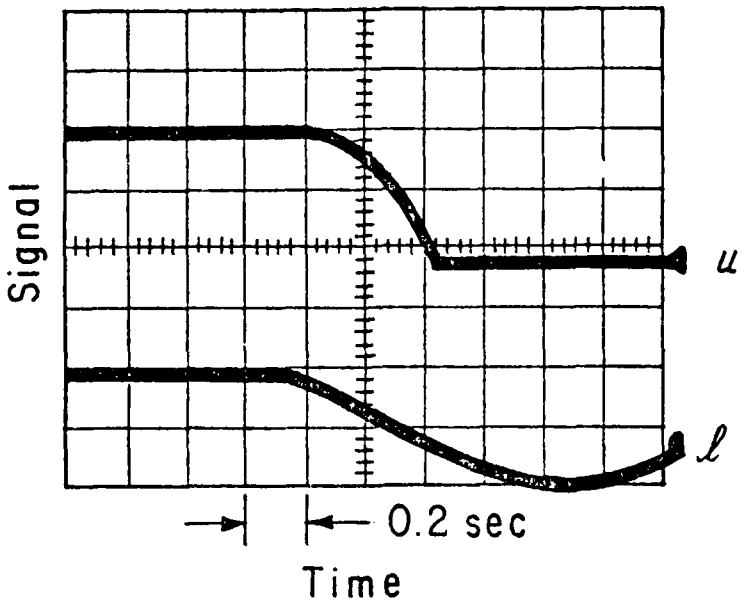

Fig. 3. Storage oscilloscope picture of the output from two channels of the ECI after injection of a pulse of smoke. Upper trace, u, is the output of the impactor final filter, (I-FF), while lower trace, l, is the output of impactor stage 1 (I-1). The horizontal scale is 0.2 s/div. The length of time between the response of I-1 and I-FF is $\simeq$ 0.2 s.

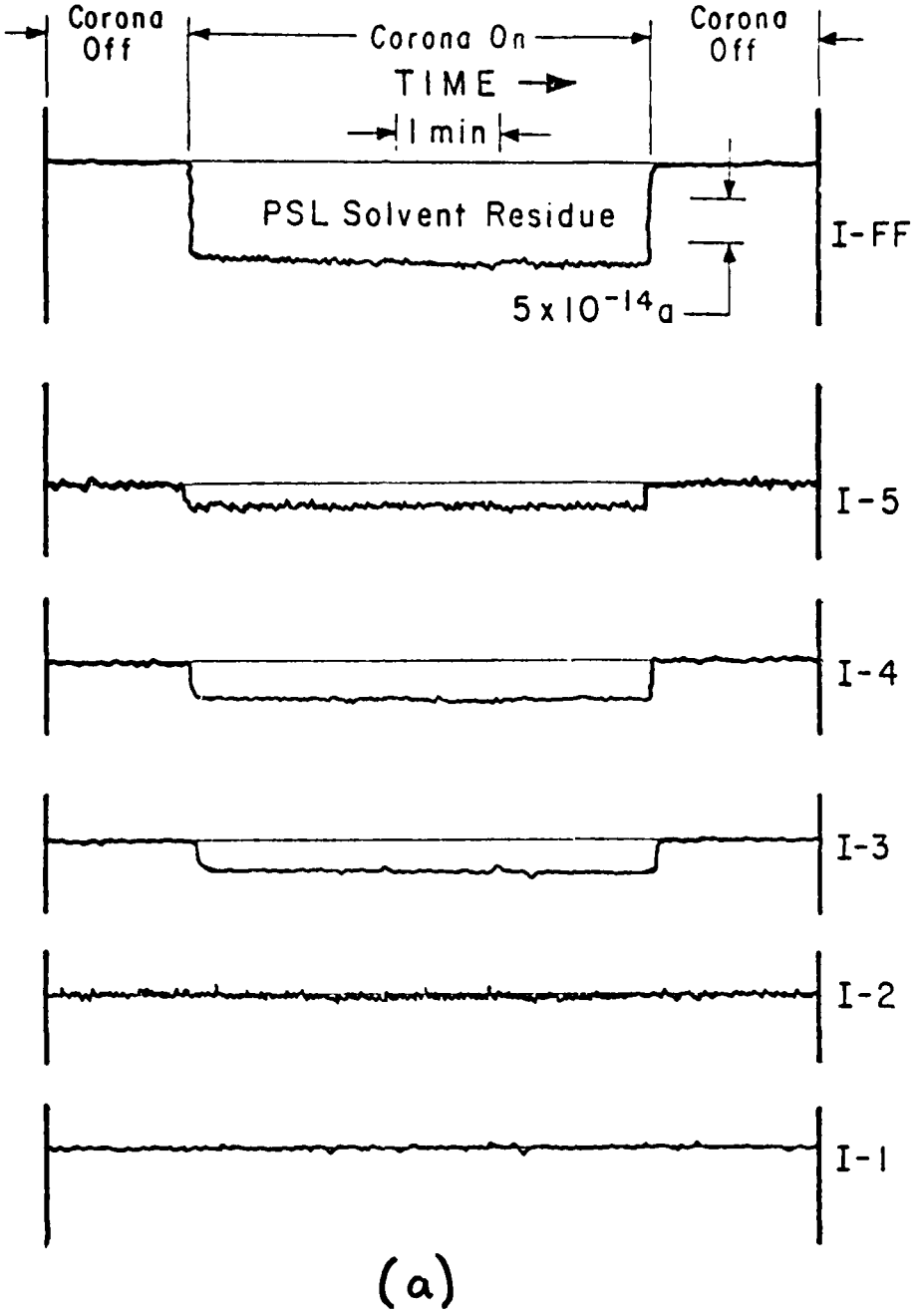

Fig. 4. Typical strip chart records of the output from the ECI with the corona charging current on and off. I-1 through I-5 are impactor stages 1 through 5 respectively and I-FF is the impactor final filter. (a) is for PSL calibration spheres with D=1.09μm and (b) is for PSL particles with D=0.62μm.

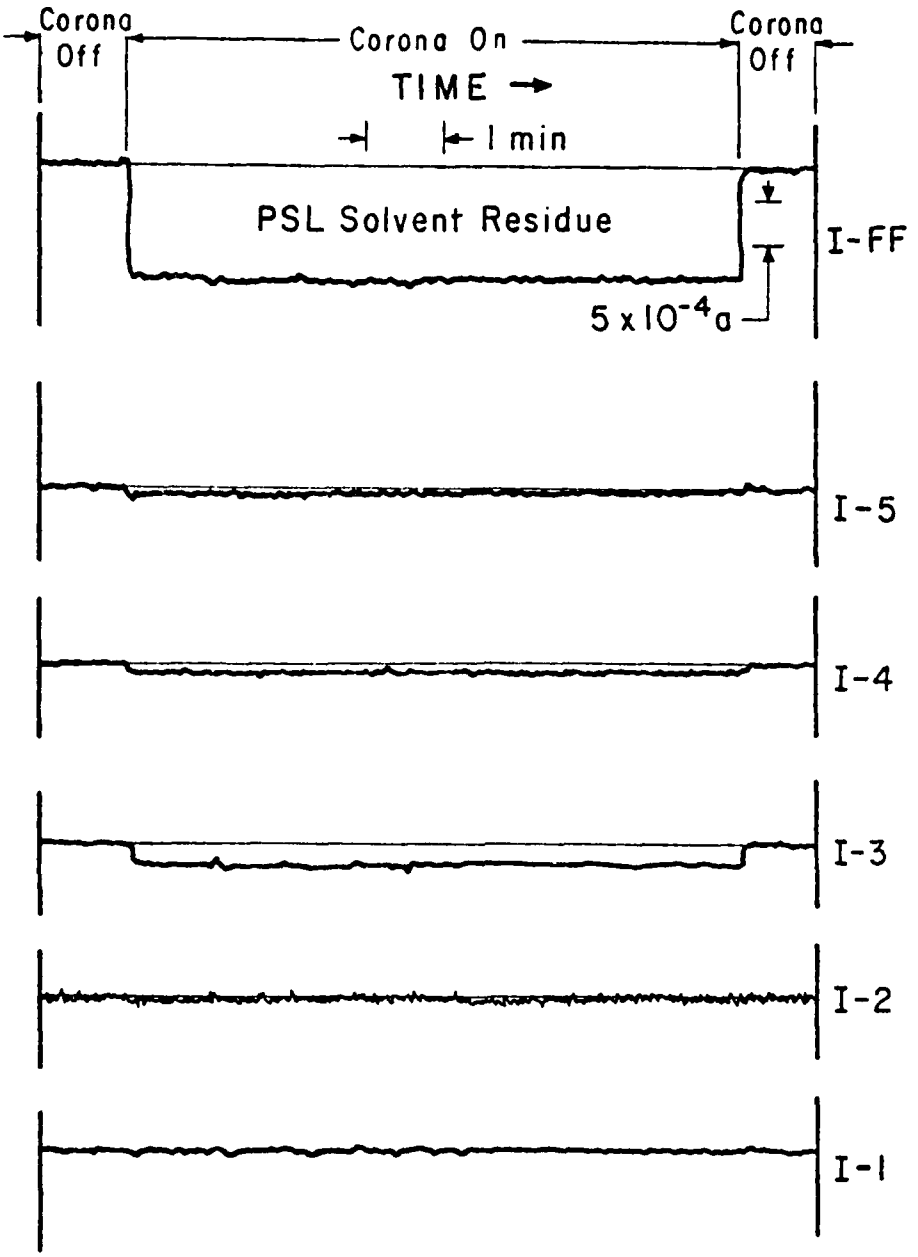

Fig. 4 (Continued.)

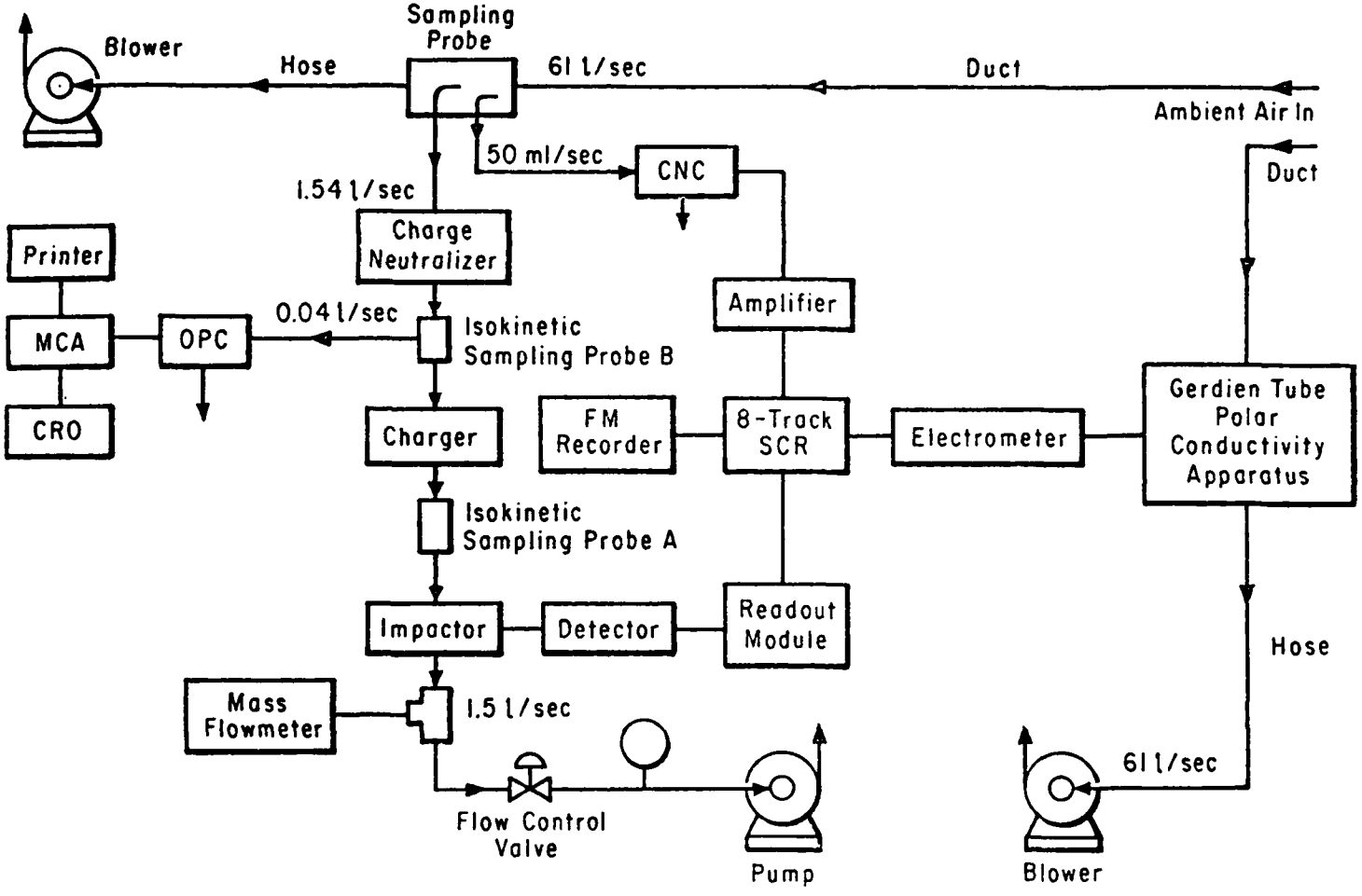

Fig. 5. Schematic diagram of experimental apparatus used to monitor ambient atmospheric aerosols and atmospheric electricity parameters.

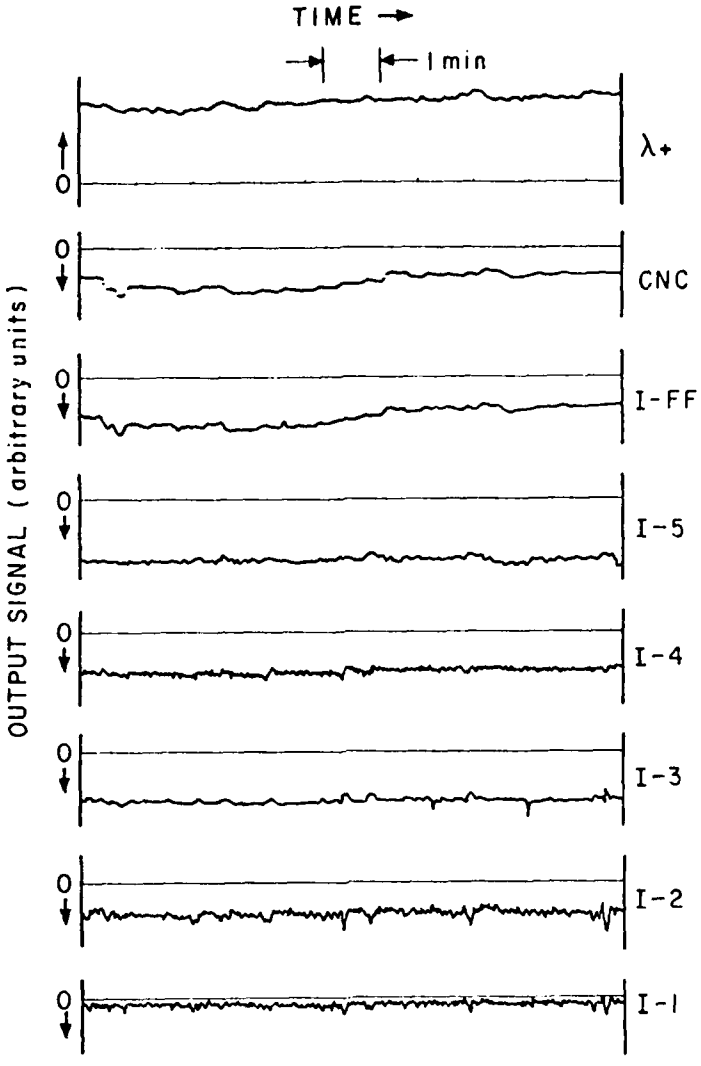

Fig. 6. Typical strip chart recording of ambient atmospheric data taken 0730-0740 LST, 29 July 1979, at Austin, Texas. $\lambda +$ is positive polar conductivity, CNC is condensation nuclei concentration, I-FF is ECI final filter, and I-1 through I-5 are ECI impactor stages 1 through 5, respectively. Note the excellent agreement between CNC and I-FF traces (correlation coefficient is 0.95 ± 0.02). The slips at the beginning of the CNC trace are due to its longer response time and the discrete nature of its sampling.

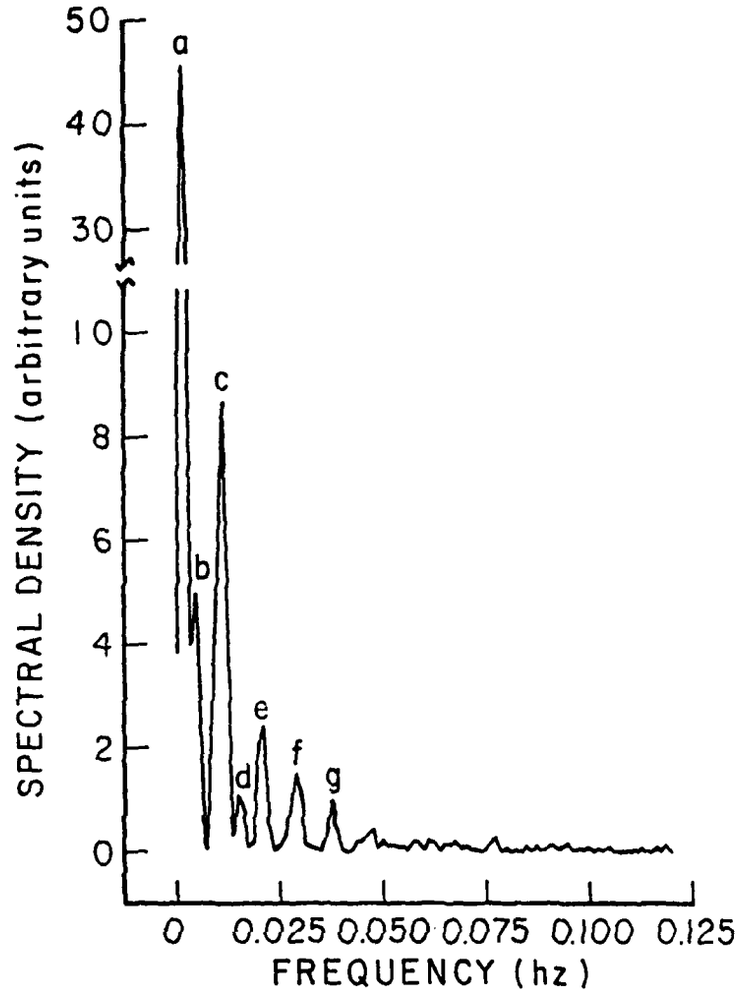

Fig. 7. Typical power spectrum for ECI final filter. Peaks a through g correspond to the following periods: (a) 9.5 ± 2 min., (b) 3.5 ± 0.7 min., (c) 1.6 ± 0.1 min., (d) 1.2 ± 0.2 min., (e) 51.5 ± 1.5 sec., (f) 34.5 ± 0.5 sec., and (g) 26.7 ± 0.3 sec.

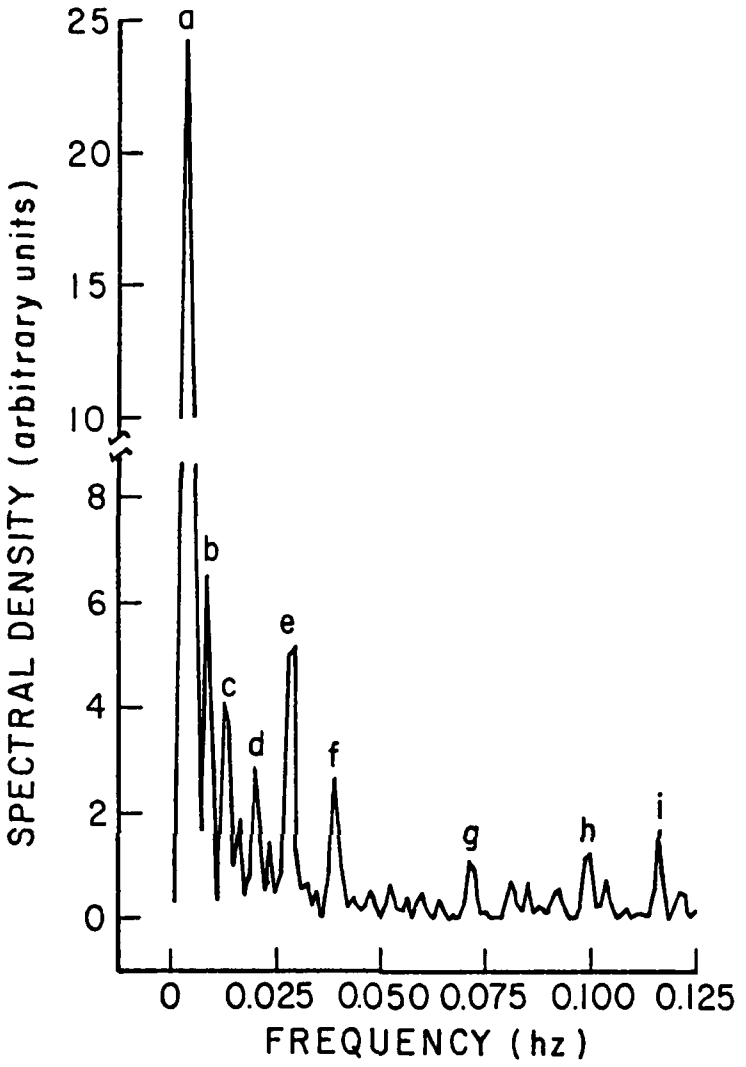

Fig. 8. Typical power spectrum for ECI stage 5, obtained for the same time as that of the final filter shown in Fig. 7. Note the fairly close correspondence of many of the peaks a through i correspond to the following periods: (a) 3.9 ± 0.5 min., (b) 1.8 ± 0.1 min., (c) 1.3 ± 0.1 min., (d) 49.5 ± 1.0 sec., (e) 35.1 ± 0.6 sec., (f) 25.6 ± 0.4 sec., (g) 14.0 ± 0.1 sec., (h) 10.1 ± 0.1 sec., and (i) 8.60 ± 0.03 sec.

INVERSION OF DIFFUSION BATTERY MEASUREMENTS

J. W. Gentry
Y. O. Park
University of Maryland

PUBLICATIONS

King, W.E., Gentry, J.W., Park, Y.O., "Determination of Distribution Functions from the Inversion of Fredholm Integral Equations", in "Multi-Phase Flow and Heat Transfer--Fundamentals, Reactor Safety Applications", edited by Dr. T. Nejat Veziroglu, Clean Energy Research Institute, University of Miami, P. O. Box 238294, Coral Gables, Florida 33124, published by Pergammon Press, 1979.

Park, Y.O., King, W.E., Jr., Gentry, J.W., "On the Inversion of Penetration Measurements to Determine Size Distributions", submitted to I&EC Product Research and Development, September, 1979.

King, W.E., Gentry, J.W., Park, Y.O., "Determination of Distribution Functions from the Inversion of Fredholm Integral Equations", April 16-18, 2nd Multi-Phase Flow and Heat Transfer Symposium Workshop, Miami, Florida (1979).

King, W.E., Jr., Gentry, J.W., Park, Y.O., "On the Inversion of Penetration Measurements to Determine Size or Charge Distributions", Colloid Symposium, June 11-13, Rolla, Missouri (1979).

INTRODUCTION

The objective of this paper is to incorporate the asymptotic behavior of the apparent diffusion coefficient in order to obtain the particle size distribution from diffusion battery measurements and to indicate suitable algorithms for the determination of multimodal distributions. The principal problem is to determine the particle size distribution F(D*) (expressed here in terms of the diffusion coefficient D* rather than the particle diameter D) by inversion of the Fredholm integral equation

$$\overline{Pt}(Q) = \int_0^\infty F(D^*)\ Pt(D^*,Q)\ dD^* \qquad (1)$$

where $\overline{Pt}$ is the experimentally measured penetration as a function of flow rate Q and Pt is the theoretical function for penetration. For simple geometries (flow through rectangular channels and cylindrical tubes) and laminar flow, the expressions for Pt are known.

The difficulties with equation (1) are that the solution is not

unique--at least for a finite number of flow rates, that penetration measurements have a scatter of 2-5%, and the penetration Pt is a very broad function of the diffusion coefficient.

The ideas developed in this paper are based on the use of the limiting behavior of the apparent diffusion coefficient $\bar{D}^*$ defined by the condition that the theoretical penetration is equal to the experimental penetration. That is

$$Pt(\bar{D}^*, Q) = \overline{Pt}(Q) \tag{2}$$

DESCRIPTION OF ALGORITHM

The principal ideas or assumptions in the algorithm can be summarized as:

1. The distribution function F(D*) can be approximated by one or more log normal distributions each characterized by a mean diffusion coefficient D_j^*, a standard deviation σ_j, and a weight C_j. That is

$$F(D^*) = \sum \frac{C_j}{\sigma_j} \exp \frac{\left[-\mathrm{Ln}^2 (D^*/D_j^*)\right]}{\sigma_j^2} \left(\frac{1}{\sqrt{\Pi}} \frac{d\mathrm{Ln}D^*}{dD^*}\right) \tag{3a}$$

$$= \frac{1}{\sqrt{\Pi}\sigma_1} \mathrm{Exp} - \mathrm{Ln}^2 \frac{(D^*/D_1^*)}{\sigma_1^2} \left(\frac{d\mathrm{Ln}D^*}{dD^*}\right) \tag{3b}$$

The idea of developing algorithms for finding σ_1 and D_1^* assuming a log normal distribution is due to Fuchs[1], and the idea of using the diffusion coefficient rather than the diameter as the independent variable is due to Mercer.[2]

2. The mean value of the diffusion coefficient is given by

$$\int_o^\infty \mathrm{Ln}D^* \, F(D^*) \, dD^* \approx \int_o^1 \mathrm{Ln}\bar{D}^* \, d\overline{Pt} \tag{4}$$

where the terms on the righthand side of the equation (the apparent diffusion coefficient $\bar{D}^*$ and the experimental penetration $\overline{Pt}$) are experimentally determined variables. If the distribution function were described by equations (3), one has

$$\int_o^1 \mathrm{Ln}\bar{D}^* \, d\overline{Pt} = \sum C_j \, \mathrm{Ln}D_j^* \tag{5a}$$

or

$$\int_o^1 \mathrm{Ln}\bar{D}^* d\overline{Pt} = \mathrm{Ln}D_j^* \tag{5b}$$

3. The limiting value of the apparent diffusion coefficient as the penetration approaches one is used to find the standard deviation σ. Specifically, one has

$$\underset{\overline{Pt}\to 1}{\text{limit}}\ \bar{D}^* = \left[\Sigma C_j D^{*2/3}\ \text{Exp}\left[+\frac{\sigma_j^2}{9}\right]\right]^{3/2} \tag{6a}$$

$$= D_1^*\ \text{Exp}\ \frac{\sigma_1^2}{6} \tag{6b}$$

The approach taken here was derived from an algorithm developed by Pollak.[3] [This algorithm, however, assumed a distribution function consisting of a series of monodisperse distributions and considered the limiting condition as the flow rate approaches zero ($\overline{Pt}\to 0$)].

In summary, for the case where one has a single log normal distribution, the parameters D_1^* and σ_1 are determined from

$$D_1^* = \text{Exp}\left[\int_0^1 \text{Ln}\bar{D}^*\, d\overline{Pt}\right] \tag{5b}$$

and

$$\sigma_1^2 = 6\ \text{Ln}\ \underset{\overline{Pt}\to 1}{\text{Limit}}\left[\frac{\bar{D}^*}{D_1^*}\right] \tag{6b}$$

DISCUSSION OF ALGORITHM (UNIMODAL FUNCTIONS)

In investigating the method, we considered several questions:

1. How did the conjecture, equation (4), perform when tested with simulated trial distributions consisting of multiple log normal distributions?

2. How did the algorithm perform in regenerating the parameters of a trial distribution consisting of a log normal distribution?

3. How sensitive is the algorithm to experimental error?

Extensive numerical calculations have been carried out to test the first two statements. The distributions included very broad distributions $\sigma\sim 2.25$, very narrow distributions $\sigma\sim 0.1$, and multiple distributions. In all cases, the conjecture, equation (4), was found valid. It seems probable that one can prove that equation (4) is an identity for a series of log normal distributions although we have not been able to do so yet. [Tests of equation (5) using 5 point Gaussian quadrature were within 1% even for very broad or multimodal distributions.] Similarly, we found that the value of σ was usually within 2% of the trial values. [Exceptions were found for very narrow distributions where a σ of 0.11 was found rather than $\sigma=0.1$.] Tables demonstrating these results are published elsewhere.[4,5]

The third point which we wished to examine was how sensitive the calculations are to random errors in the penetration measurements. When the apparent diffusion coefficient was plotted as a function of penetration, it was found that the curve was essentially linear for penetrations greater than 50%. The importance of this result is that the extrapolation of the apparent diffusion coefficient to limiting conditions, unlike the Pollak method, can be done with confidence. The critical problem is how sensitive equation (5) is to experimental error. This problem was examined by a numerical simulation (Table 1) in which assumed penetration errors of 2.0, 5.0, and 8.0% were assumed. Fifty numerical experiments were run with the 95% confidence limits for D_1^* (columns 4 and 5) presented in Table 1. The results presented here were for a fairly broad distribution $\sigma=1.0$ ($B_g=2.03$); but simulations with $\sigma=2.25$ ($B_g=4.91$) and $\sigma=0.4$ ($B_g=1.33$) gave essentially the same result. Although increasing the quadrature points (number of experiments) will result in a slightly narrower band of uncertainty, the values of D_1^* given by the algorithm are sensitive to experimental error.

In summary, the method is efficient, convenient, and non-ambiguous with simulated data. Uncertainties or errors in the experimental measurements will mean considerable scatter in the distribution parameter. The crux of the problem is that the distribution function determined from penetration measurements is sensitive to experimental error.

TABLE 1

Effect of Random Error in Penetration Measurements
Mean Diffusion Coefficient

Experimental Error (%)	Quadrature Points	D_1^* (Exact) ($\cdot 10^{-6}$)	90% Confidence Limits D_1^* (Lower) ($\cdot 10^{-6}$)	D_1^* (Upper) ($\cdot 10^{-6}$)
8.0	8	8.05	4.9	12.5
5.0	8	8.05	5.6	12.1
2.0	8	8.05	6.6	12.2
2.0	8	8.05	7.0	13.0
2.0	8	8.05	6.7	14.1

RECOMMENDATIONS AND CONCLUSIONS

The applications discussed in this paper are limited to unimodal distributions. A major limitation of the procedure is that the method does not readily lend itself to iteration. The parameters D_1^* and σ_1 are the parameters giving the best overall description of the data. We have investigated several other approaches. The primary problem is that for a distribution function consisting of

two log normal distributions, one has 5 parameters and only two equations. We have investigated the possibility of using equations (5a) and (6a) with an expression derived for the mass penetration. Generally, these procedures are successful when additional restrictions are imposed on the distribution function (i.e. $C_1=C_2=0.5$, $\sigma_1=\sigma_2$) or if the parameters of one of the log normal distribution functions are known. (This could be the case where the distribution function is determined by two different instruments.)

Of the work that we have finished, we can conclude:

1. The method accurately and unambiguously determines the parameters of unimodal test distributions in numerical simulations.

2. The method is subject to uncertainty in experimental measurements but this is likely to be a limitation in all data inversion algorithms.

3. The algorithm is efficient and versatile and can be incorporated into more complex inversion algorithms.

ACKNOWLEDGEMENT

J.W.G. wishes to acknowledgement support under the National Science Foundation Grant #78-00738-A01.

REFERENCES

1. Fuchs, N.A., Stechkina, I.B., Starosselskii, V.J., Br. J. Appl. Phys., 13, 280 (1962).

2. Mercer, T.T., Greene, T.D., J. Aerosol Sci., 5, 251 (1974).

3. Pollak, L.W., Metniecks, A.L., Geof. Purae Appl., 33, 183 (1957).

4. King, W.E., Park, Y.O., Gentry, J.W., 2nd Multiphase Flow and Heat Transfer Symposium, Miami, Florida (April 1979).

5. Park, Y.O., King, W.E., Jr., Gentry, J.W., "On the Inversion of Penetration Measurements to Determine Size Distributions", Interface Science and Colloid Symposium, Rolla, Missouri (1979).

IV. OBSCURANT MATERIALS

QUANTITATIVE INFRARED ABSORPTION MEASUREMENTS

ON TRI-n-BUTYL PHOSPHATE

Vincent P. Tomaselli
K. D. Moeller

Fairleigh Dickinson University
Physics Department

PUBLICATIONS

Progress Report, Contract No. DAAK10-77-C-0121, "Survey of Infrared Absorption Phenomena and Experimental Methods for Liquids and Solid Films", October 1977, U.S. Army Armament Research and Development Command, Dover, N. J. 07801

Submitted to Applied Spectroscopy

INTRODUCTION

Tri-n-butyl Phosphate $[(C_4H_9)_3PO_4]$, a liquid at room temperature, is of interest because of its strong absorption bands in the 2-5μm and 8-12μm region. That is, it is a candidate as a possible infrared obscuring compound. Accordingly, its effectiveness as an absorber must be measured quantitatively. We report measurements of the molar absorptivity of tri-n-butyl phosphate (TBP) and the associated concentration effects.

EXPERIMENTAL

Solutions of tri-n-butyl phosphate (TBP) were prepared by mixing purified-grade solute with spectral quality solvents (CCl_4 and CS_2). Various concentrations were produced by measuring known quantities of TBP, using Van Slyke pipets, into calibrated volumetric flasks and filling to level with solvent. Calibrated, sealed liquid cells were used for path lengths down to approximately 0.1 mm. At higher concentrations, demountable cells using various thinner spacers were required. Where possible, path lengths were determined by measuring cell fringe spacing. For very thin cells, for which the fringe method is not applicable, the spacer thickness was determined using a weak TBP absorption band, adjacent to the band of interest, as an "internal" calibration standard. This method has an advan-

tage in that both thickness of cell and absorbance of desired band are measured simultaneously and in a relatively short time interval. Thus, errors introduced by attempting to duplicate a pressure required to produce a given cell spacing, and cell distortion are minimized.

The quantity of interest is the molar absorptivity $\varepsilon(\bar{\nu})$ found in Beer's Law as

$$T(\bar{\nu}) = I(\bar{\nu})/I_o(\bar{\nu}) = e^{-\varepsilon(\bar{\nu})bc} \qquad (1)$$

Here T is the transmittance, $I_o(\bar{\nu})$ and $I(\bar{\nu})$ the incident and transmitted radiation intensities respectively, b the cell path length and c the solution concentration. Equation (1) will be taken as the defining relation for $\varepsilon(\bar{\nu})$ recognizing that all assumptions and conditions normally associated with its use are not satisfied here.

As recommended by Hawranek, et al,[1] no compensating solvent-containing cell was used in the reference beam. To account for cell reflection losses, a technique introduced by Draegert, et al[2] was used. Here the transmittance is taken to be $T = \rho I/\rho_o I_o$ where $\rho_o I_o$ and ρI are the actual incident and transmitted radiation intensities instead of I_o and I respectively. The coefficients ρ and ρ_o characterize the reflection properties. Beer's Law can now be written as

$$\ln\left[\frac{I(\bar{\nu})}{I_o(\bar{\nu})}\right] = \ln\left[\frac{\rho}{\rho_o}\right] - \varepsilon(\bar{\nu})bc \qquad (2)$$

where now the measured transmission of the cell containing solution, that is the chart pen deflection, is $T_M(\bar{\nu}) = I(\bar{\nu})/I_o(\bar{\nu})$. If one makes a series of measurements of $T_M(\bar{\nu})$ for various cell thicknesses b while holding the concentration c constant and plots $\ln T_M(\bar{\nu})$ against b, the resulting curve is a straight line with slope $-\varepsilon(\bar{\nu})c$. The molar absorptivity can then be extracted from the data, for example by a linear regression analysis. The ordinate intercept of this plot gives ρ/ρ_o, if this quantity is of interest. As a check of the method, we determined the molar absorptivity of pure spectral grade chloroform and from it, the extinction coefficient $k(\bar{\nu}) = (c/4\pi)\,\varepsilon(\bar{\nu})/\bar{\nu}$. Here $k(\bar{\nu})$ is the imaginary part of the complex index of refraction $n^*(\bar{\nu}) = n(\bar{\nu}) + i\,k(\bar{\nu})$. Our result at 3020 cm^{-1} is k = 0.011, which agrees very well with the value of k = 0.0115 reported by Hawranek and Jones[3] using a considerably more involved procedure.

RESULTS

Figure 1 shows the infrared spectrum of a capillary film of pure TBP. The absorption bands are, as expected, characteristic of the butyl [$(C_4H_9)^+$] and phosphate [$(PO_4)^{\equiv}$] groups. Consistent with our interest in strongly absorbing compounds, we have selected the three most intense bands in the 2-5 and 8-12μm regions for analysis. These are at 2950cm^{-1}, 1280cm^{-1} and 1030cm^{-1} and are assigned to the CH, P = O, and P - O groups respectively.

In studying the absorptivity of a possible obscuring agent, concentration effects are of major interest, both from a scientific and practical point of view. Accordingly, we have examined a range of concentrations from very dilute (.0073M) to pure liquid (3.65M).

For each solution of TBP, infrared spectra were recorded using at least three liquid cells with different path lengths. Multiple scans were obtained, and average measured transmittance values for each of the three bands of interest, were calculated. Equation (2) was used to obtain $\varepsilon(\bar{\nu})$ for each concentration, using a linear regression analysis of the $\ell n\ T_M(\bar{\nu})$ vs b data. The results are shown in Figure 2. Systematic errors were estimated from the uncertainties in transmittance, path length and concentration. Of these, the uncertainty in path length b was the dominant contribution. The fractional determinate error in $\varepsilon(\bar{\nu})$ was approximately 4-6% for the bands studied. For quantitative measurements, instrument error can be minimized by appropriate selection of scan settings, that is, wide slits, slow scan speed, minimum gain, etc.[4] In addition, it is known that photometric accuracy is optimum for transmittances between 20 and 60%.[5] In most cases, the range of concentrations used and variety of cell path length available, allowed for such optimizing.

The value of the molar absorptivity $\varepsilon(\bar{\nu})$ should, ideally, be independent of concentration. In real systems, however, one expects deviations from ideal behavior. Figure 2 suggests a behavior where the molar absorptivity is constant at low concentrations (normal Beer's law behavior), undergoes a transition to lower values as the concentration increases and "saturates" at high concentrations. Note that the transition regions for the 1030cm^{-1} and 1280cm^{-1}, obtained using the same solvent, are very similar in shape.

The onset of the transition region for the 2950cm^{-1} band, however, occurs at a considerably higher concentration. Note also that for this band the solvent used was CCl_4 while CS_2 was used for the two lower frequency bands. Both CCl_4 and CS_2 are considered to be non-polar solvents. If dipolar inter-

actions between solute and solvent are eliminated, we must then consider the other factors responsible for the observed behavior.

DISCUSSION

The concentration dependence of $\varepsilon(\bar{\nu})$ for a solute/non-polar system has been observed previously. In measurements of the OH stretching frequency of n-butanol dissolved in various solvents, Graja and Malecki[6] found the molar absorptivity to be characterized by two distinct regions. At low concentrations $\varepsilon(\bar{\nu}_{OH})$ was independent of concentration. Above some critical concentration, $\varepsilon(\bar{\nu}_{OH})$ decreased smoothly with increasing concentration. These investigators attributed the behavior to self-association of the solute molecules. In effect, at low concentration, self-association of the alcohol molecules is hindered. As the concentration increases, the n-BuOH molecules interact. The resulting perturbation of their electron distribution results in a decrease in $\varepsilon(\bar{\nu}_{OH})$. The data shown in Figure 2 appear to parallel the results from Graja and Malecki[6] although these authors were primarily interested in dilute solutions and, therefore, observed no saturation effects.

In Figure 2, we see the indication of two distinct constant absorptivity regions, at high and low concentrations, separated by a transition region. For example, the $2950cm^{-1}$ band has a molar absorptivity of approximately 1365 ℓ/mole-cm in dilute solution, and a value of ~950 ℓ/mole-cm as a pure liquid. Thus, the extinction of the CH stretching mode band in TBP decreases by approximately 30 percent over the range of concentrations studied. The similar shape of the $1030cm^{-1}$ and $1280cm^{-1}$ bands indicate that the phosphate ion modes in TBP are also effected by the concentration. The difference in the curves, other than the magnitudes of $\varepsilon(\bar{\nu})$, is the point at which the transition region begins. This point is indicated as c_o in Figure 2. For the $1030cm^{-1}$ and $1280cm^{-1}$ bands, the transition begins at a concentration of about $c_o = .03M$ while for the $2950cm^{-1}$ band the corresponding concentration is about $c_o = 0.4M$. To appreciate the significance of these values physically, we relate the molar concentration to the number of solvent molecules per solute (TBP) molecule. Using published data we get, approximately, $c_{CCl_4}(N) \simeq 10/N$ and $c_{CS_2}(N) \simeq 17/N$ where N is the number of solvent molecules complexed to a TBP molecule. For example, taking the value of $c_o \simeq 0.4M$ for the $2950cm^{-1}$ band from Figure 2, we get $N = 10/0.4 = 25$ molecules. This means that the molar absorptivity is independent of concentration up to

about 25 molecules of CCl_4 per molecule of TBP. At higher concentrations, that is smaller N, association effects cause $\epsilon(\bar{\nu})$ to change with concentration. For the 2950cm^{-1} band, concentrations above about 1.0M do not further change the absorption process. That is ϵ(2950cm^{-1}) saturates at about 1.0M.

The value of 25 molecules of CCl_4 per TBP molecule is a reasonable value. On the basis of elementary geometric considerations, approximately 20 CCl_4 molecules (assumed to be spheres) would be required to surround or shield each extended, uncoiled and planar, TBP molecule. If we now consider the 1030 and 1280cm^{-1} bands, the corresponding value of $c_o \simeq .03$M gives $N \simeq 17/.03 \simeq 567$ molecules of CS_2 per molecule of TBP to prevent TBP association. The fact that $N(CS_2) > N(CCl_4)$ implies that CS_2 molecules are not as effective in shielding TBP interactions as are CCl_4 molecules. Whether this effect is a geometric one or due to other factors cannot be determined from the present data. However, clearly there is a solvent effect exhibited. A similar solvent dependence of the molar absorptivity of n-BuOH was also observed by Graja and Malecki.[6] In earlier work on the dielectric polarization of alcohols in nondipolar solvents, Malecki and Jadzyn[7] found a strong solvent dependence to the end of the constant polarization region. However, in this earlier work, the effect of solvent molecule geometry, if any, was not clearly discernable.

REFERENCES

1. J. P. Hawranek, P. Neelakantan, R. P. Young and R. N. Jones, Spectrochim. Acta 32A, 75 (1976).
2. D. A. Draegert, N. W. B. Stone and D. Williams, J. Opt. Soc. Am. 56, 64 (1966).
3. J. P. Hawranek and R. N. Jones, Spectrochim. Acta 32A, 111 (1976).
4. W. J. Potts, Jr. and A. L. Smith, Appl. Optics 6, 257 (1967).
5. J. E. Stewart, Infrared Spectroscopy. Experimental Methods and Techniques. (Marcel Dekker, Inc., New York, 1970). Chap. 15, para. 5.
6. A. Graja and Malecki, Chem. Phys. Lett. 34, 373 (1975).
7. J. Malecki and J. Jadzyn, J. Phys. Chem. 78, 1203 (1974).

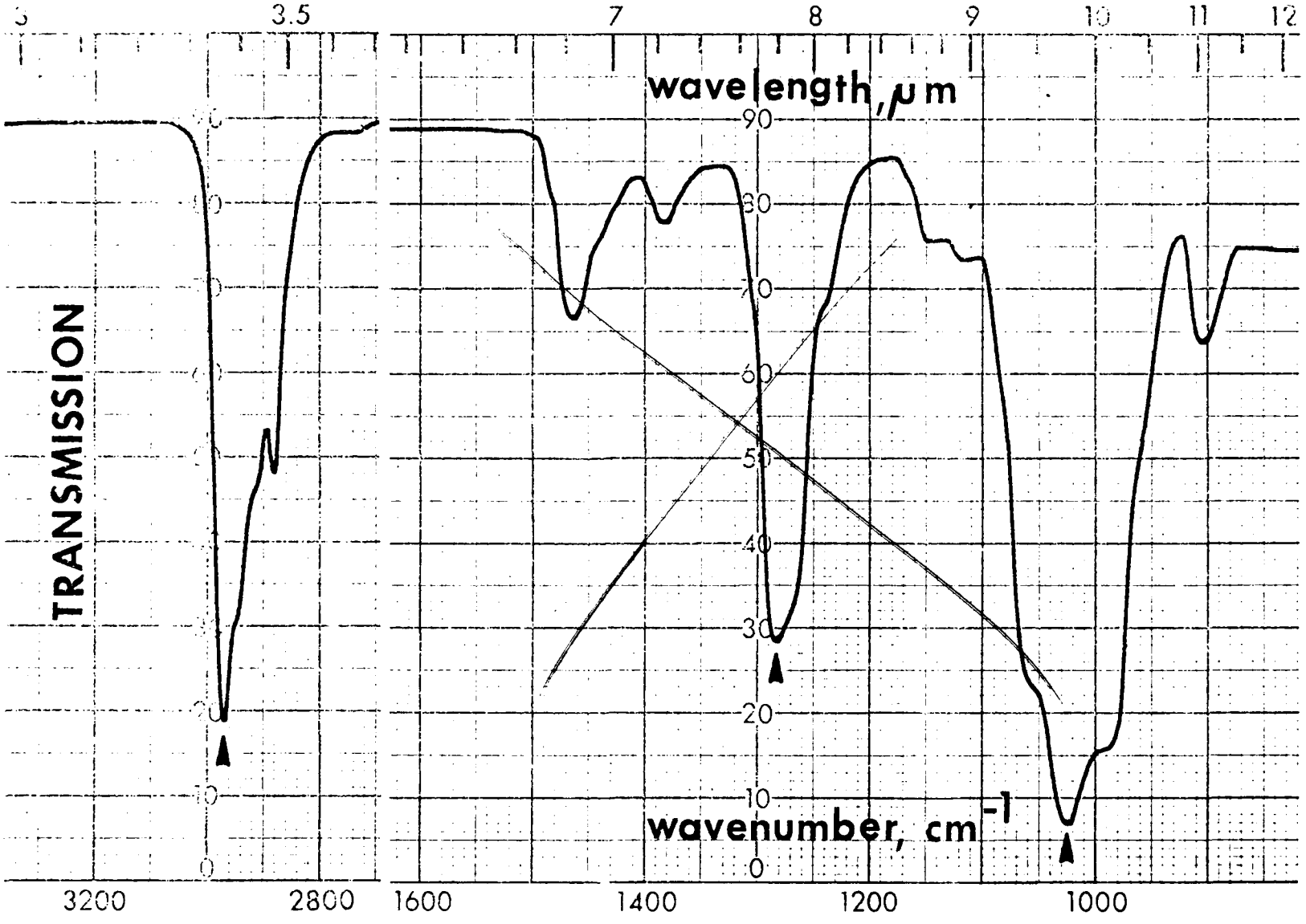

FIGURE 1. INFRARED SPECTRUM OF CAPILLARY FILM OF PURE TRI-N-BUTYL PHOSPHATE.

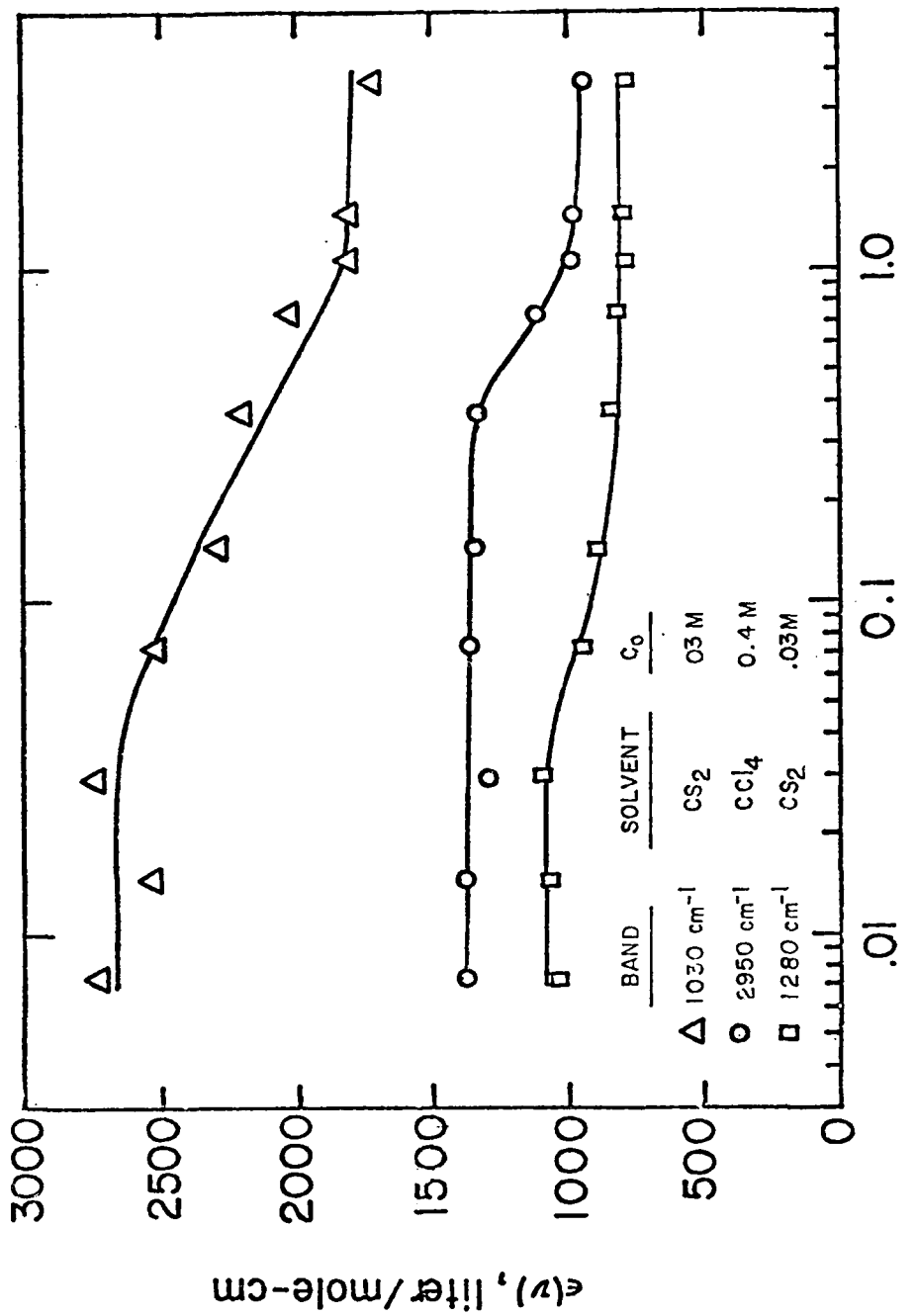

FIGURE 2. CONCENTRATION-DEPENDENCE OF THE MOLAR ABSORPTIVITY OF TRI-N-BUTYL PHOSPHATE.

REFLECTION SPECTROSCOPY

K. D. Moeller
Vincent P. Tomaselli

Fairleigh Dickinson University
Physics Department

INTRODUCTION

The description of the interaction of light with matter, as formulated from Maxwell's electromagnetic theory, uses macroscopic parameters to characterize the specific properties of a material involved in the process. These parameters (notably the dielectric constant) are related to the optical constants, the refractive index n and the absorption coefficient k of the material in question. In a simplified picture, the index n characterizes the refraction properties of the material, since it is the ratio of the velocity of the wave inside to that outside of the material, and the absorption coefficient k describes the attenuation of the wave as it penetrates the medium.

The optical constants can be obtained by an analysis of reflection and transmission data. One determines n and k using polarized light measurements, since the reflection and transmission properties of the material are, in general, different for light polarized parallel to or perpendicular to the plane of incidence. For crystals with optical axes, the optical constants depend upon the orientation of the surface relative to plane of incidence. This latter effect is lost in polycrystalline materials where only average optical constants can be obtained. Reducing the size of the domains of the polycrystalline sample results, eventually, in an amorphous material where long range order has disappeared and only short range order type prevails.

Powders have the non-oriented properties of the polycrystalline materials but, in addition, the powder particles are now embedded in a dielectric which might be air, KBr, other materials, or, in the limiting case, a vacuum. The discontinuity of the optical constants at the surface of the powder particles introduces alterations in the transmitted or reflected light. One effect is that light is scattered out of the direction of the

reflected or transmitted light beams. This scattered light is unavailable for analysis; its absence introduces an error in the determination of the optical constants. This effect is particularly troublesome if the absolute values of reflected and transmitted intensities are required. Nevertheless, using the pellet method, in which the powder is embedded in KBr and the optical constants are obtained from transmission and reflected data[1], surprisingly good results have been obtained. In this work, the "lost" light is simply disregarded in determining the optical constants. Observation of the transmitted and reflected light, from powder samples have also shown, in some instances, new spectral features when compared to the bulk materials. Careful investigation has shown that these features depend on the size, shape and nature of the dielectric in which the powder particles are embedded. The most interesting change occurs with the optically active transverse mode in, for example, alkali halide crystals. The frequency of this mode shifts to higher values if the size of the crystalling is reduced.[2]

Theoretically, one can account for these phenomena using the phonon concept. One considers finite atomic chains but omits the application of cyclic boundary condition used in large crystals. An alternate approach, the continuum theory first formulated by Frohlich[3], tests the polarizations in the mixed medium. The effect of particle shape was considered for spherical and cylindrical geometries. The latter can be extended to the case of fibers. The general approach to dielectric constant studies also provides the possibility of studying metal particles embedded, either in their own oxide layers, or in a dielectric matrix.

EVALUATION OF OPTICAL CONSTANTS OF HIGHLY ABSORBING MATERIALS. GRAPHICAL METHODS

The reflection coefficients, obtained from Fresnel's formulae, can be expressed as functions of the complex refractive index n* and the angle of incidence θ The squares of the absolute value of the reflection coefficients, are given by

$$|r_{E_\perp}|^2 = I_{E_\perp} = \frac{(a-\cos b)^2+b^2}{(a+\cos b)^2+b^2} \qquad (1)$$

and

$$|r_{E_{||}}|^2 = I_{E_{||}} = \frac{(a-\sin\theta\ \tan\theta)^2+b^2}{(a+\sin\theta\ \tan\theta)^2+b^2} \qquad (2)$$

where

$$a^2 = \frac{1}{2}\{[(n^2-k^2-\sin^2\theta)^2+4n^2k^2]^{\frac{1}{2}}+(n^2-k^2-\sin^2\theta)\}$$

$$b^2 = \frac{1}{2}\{[(n^2-k^2-\sin^2\theta)^2+4n^2k^2]^{\frac{1}{2}}-(n^2-k^2-\sin^2\theta)\}$$

These complicated formulae relate the intensity ratios of reflected light, for parallel and perpendicular components, to the angle of incidence θ and the optical constants. To determine the optical constants, one needs the inverse relationship, that is, n and k as a function of the ratios of the reflected light and the angle of incidence. Unfortunately, the above equations can not be inverted analytically. However, J. Vasicek has calculated "Tables of Determination of Optical Constants from the Intensities of Reflected Light", (Czechoslovakian Academy of Science, Prague, 1963.) In these tables, the following measurable quantities are tabulated as a function of θ, n and k: $I_{E_\perp}$, $I_{E_\parallel}$,

$$I = \frac{I_{E_\perp} + I_{E_\parallel}}{2}, \text{ and } I_\rho = \frac{I_{E_\parallel}}{I_{E_\perp}}$$

Numerical values are given for $0 \leq \theta \leq 80°$, in increments, of 5°. Values of n and k are given in increments of 0.2 for $0.2 \leq n \leq 7.0$ and $0.0 \leq k \leq 6.0$. A graphical analysis of the reflection data using Vasecek's tables can be used to obtain values of n and k as follows: For a given angle of incidence, one plots on an n-k curve, the locus of all points having the same measured reflected intensity $I_{E_\perp}$, $I_{E_\parallel}$, I or I_ρ.

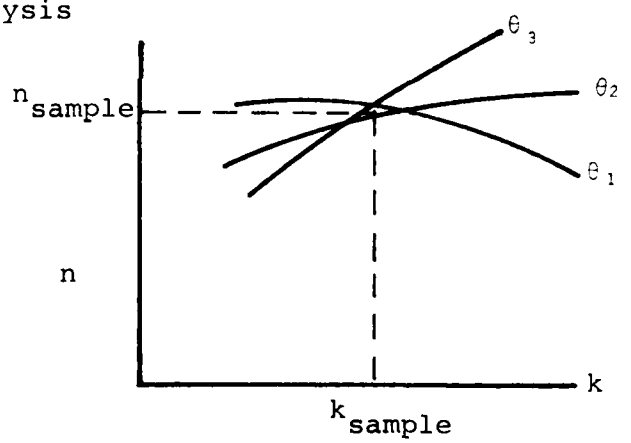

Fig. 1

This procedure is repeated for a second, and preferably a third, angle of incidence. The intersection of the three isoreflectance curves gives the optical constants of the material, see Fig. 1. Normally the curves do not intersect at a single point, but define a triangulary shaped region which, in effect, is an indication of the inherent error in the method. For such cases, the 'center of gravity' of the triangle is used to extract the values of n and k for the sample.

The behavior of the reflected intensities, as a function of angle of incidence, can be seen by plotting curves of $I_{E_\perp}$ and $I_{E_\parallel}$ as functions of θ. The parameters affecting the shapes of the curves are n and k. W. R. Hunter[4] has generated such plots for $0.2 \leq k \leq 3.3$ in increments of 0.1 and $0.3 \leq n \leq 2.3$ in increments of 0.5. A typical plot for $n = 1.3$ and $k = 2.3$ is shown in Fig. 2.

The difference between Fig. 2 and the corresponding plot for a lossless ($k = 0$) dielectric is that for the lossless case, $I_{E_\parallel} = 0$ at the Brewster angle. When $k > 0$, $I_{E_\parallel}$ never goes to zero. Also in Fig. 2 we see that $I_{E_\parallel}$ and $I_{E_\perp}$ differ most for large values of θ. Thus, experimentally, it is desirable to choose appropriately large values of θ to obtain the most accurate values of n and k.

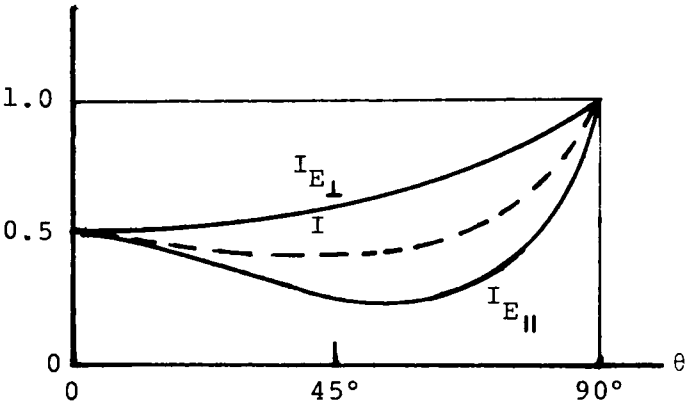

Fig. 2

THE EFFECT OF POLARIZATION PROPERTIES ON MEASURED REFLECTANCES

We assume that the experimental apparatus consists of a conventional double beam infrared spectrophotometer with an auxillary reflection unit mounted in the sample beam light path. Of interest here is the influence of the polarization properties of the instrument on the resulting measurements. Initially, we will consider only the use of a single reflection attachment.

Since both reflection coefficients are functions of θ, n, and k, in general, measurements at two angles of incidence will be required. That is since $r_{E_\perp} = f(\theta,n,k)$ and $r_{E_\parallel} = g(\theta,n,k)$, then $f(\theta_1,n,k)$, $f(\theta_2,n,k)$, $g(\theta_1,n,k)$ and $g(\theta_2,n,k)$ are required to extract n and k values from the measured data.

A schematic diagram of the essential features of the optical path of the instrument, as used for reflection measurements, is shown in Fig. 3.

Unpolarized light; two angles of incidence

Let us call the intensity of light emitted from the source, and polarized in directions perpendicular to and parallel to

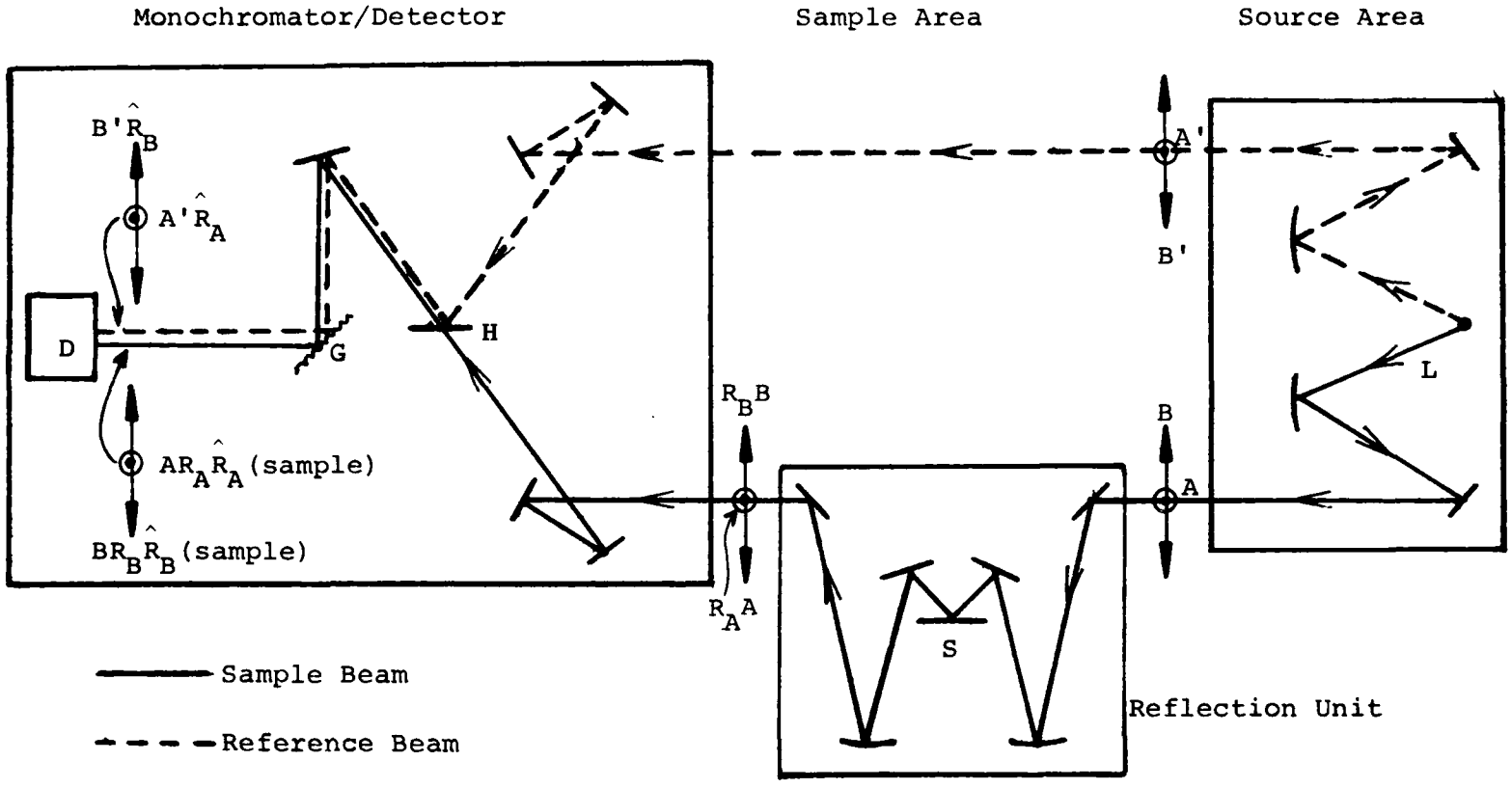

Fig. 3 Schematic diagram of optical path of spectrophotometer with reflection unit, showing polarization components. Legend: L = source, S = sample/standard, H = half mirror, G = diffraction grating, D = detector. A and B represent components of polarization perpendicular to and parallel to plane of incidence respectively, for sample beam. Sample and reference beam are shown as displaced from H to D for purposes of clarity only.

the plane of incidence, A and B respectively. Then A + B represents the intensity of the sample beam. We call A' + B' the corresponding light passing through the reference beam. Light reflected from the sample is attenuated by a factor of R_A for the perpendicular component and R_B for the parallel component. At the point of recombination of the two beams, the total intensity is $A R_A + B R_B$. This amount of light is instrumentally compared with the light passing through the reference beam , A' + B'. A comb attenuates the reference beam until both beams are of equal intensity, that is, until we have

$$A R_A + B R_A = (A' + B') T_1 \tag{3}$$

where T_1 presents the deflection of the pen on the chart paper. In order to obtain the attenuation of the two polarized beams, that is R_A and R_B, we make the same measurement with a standard replacing the sample. If it is assumed that the reflectivity of the standard is essentially unity, we obtain for that measurement

$$A + B = (A' + B') T_2 \tag{4}$$

where T_2 is the chart pen deflection when the standard is used. The desired result, that is the reflection properties of the sample, is obtained from the ratio.

$$\frac{T_1}{T_2} = \frac{AR_A + BR_B}{A + B} \tag{5}$$

The reflection coefficient, measured using unpolarized light, can only be extracted if we assume that A = B. Then Eqn.(5) gives

$$\frac{T_1}{T_2} = R_A + R_B \tag{6}$$

The assumption that A = B may be made in most cases since the source emits unpolarized radiation and, to a first approximation, it may be assumed that mirrors do not polarize infrared light.

We now must account for the polarization properties of the instrument between the beam recombination point and the detector. We know, for example, that the diffraction grating polarizes the incident parallel and perpendicular beams differently. Light from the sample beam which reaches the detector may be represented by $(AR_A\hat{R}_A + BR_B\hat{R}_B)$ where $\hat{R}_A$ and $\hat{R}_B$ are the attenuation factors, due to the instrument polarization for the perpendicular and parallel components, respectively. For the reference beam, the corresponding term is $(A'\hat{R}_A + B'\hat{R}_B)$. For the

measurement on the standard surface, we would get $(A\hat{R}_A + B\hat{R}_B)$ for the sample beam and $(A'\hat{R}_A + B'\hat{R}_B)$ for the reference beam. When the beams are combined, the equalization is given by

$$(AR_A\hat{R}_A + BR_B\hat{R}_B) = (A'\hat{R}_A + B'\hat{R}_B)\, T_1 \tag{7}$$

and

$$(A\hat{R}_A + B\hat{R}_B) = (A'\hat{R}_A + B'\hat{R}_B)\, T_2 \tag{8}$$

Dividing Eqn.(7) by (8) gives

$$\frac{T_1}{T_2} = \frac{AR_A\hat{R}_A + BR_B\hat{R}_B}{A\hat{R}_A + B\hat{R}_B} \tag{9}$$

To get the desired result, $T_1/T_2 = R_A + R_B$, we must not only assume that A = B, as before, but also that $\hat{R}_A = \hat{R}_B$. That is, the instrument polarization for each component must be assumed to be equal.

Notice that both Eqns. (6), and the above result from (9), contain two unknown quantities R_A and R_B. To extract either reflection component requires two measurements of (T_1/T_2) at different angles of incidence.

<u>One component of polarized light, two angles of incidence</u>

If a properly oriented polarizer is inserted into the optical beam before the detector, only one component of the total recombined beam will be sensed. If we retrace the analysis of the previous section, it is clear that this case can be treated by setting either A = 0 or B = 0. For example, if B = 0, Eqn.(9) gives

$$\frac{T_1}{T_2} = \frac{AR_A\hat{R}_A}{A\hat{R}_A} = R_A \tag{10}$$

Thus, we get the attenuation of one component of the light irrespective of the polarization properties of the instrument. Because the ratio T_1/T_2 is obtained by a manual division as opposed to the ratio recording done by the instrument, possible differences between A and A' are divided out and have no effect on the results. Such measurements at two angles of incidence will yield the information required to determine n and k.

<u>Both components of polarized light, one angle of incidence</u>

For each component of polarized light, the argument presented above is valid. Since two components of light are measured, only one angle of incidence is necessary.

Ratio of polarized light components; two angles of incidence, no standard

If measurements of the attenuation of reflected light from the sample are made for both components of polarized radiation, and no standard is used for comparison, the equalization of the beam intensity is represented by

$$AR_A\hat{R}_A = A'\hat{R}_A T_A \tag{11}$$

and

$$BR_B\hat{R}_B = B'\hat{R}_B T_B \tag{12}$$

Here T_A is the chart pen deflection for the sample with component A of polarized light and B that of component B. Note that these are two distinct measurements and that no standard is used for reference. The ratio T_A/T_B is given by

$$\frac{T_A}{T_B} = \frac{AR_AB'}{BR_BA'} \tag{13}$$

and only for $A = A'$ and $B = B'$ is the desired result $T_A/T_B = R_A/R_B$, obtained. If this measurement is made at two angles of incidence, n and k can be extracted from the data.

Since we are considering the use of a double beam instrument in which the ratio recording method senses the difference between the sample beam and reference beam, it seems reasonable to consider using a reflection unit in each beam. In the following, we consider arguments similar to those presented above, but now for the case where the instrument is operated with two reflection units.

Sample in sample beam, reference in reference beam; unpolarized light

For this case, the equalization of the beam intensity at the comb is given by

$$AR_A\hat{R}_A + BR_B\hat{R}_B = (A'\hat{R}_A + B'\hat{R}_B)\ T \tag{14}$$

The attenuation due to the sample, i.e. $T = R_A + R_B$, is given only if $A = A' = B = B'$ and $\hat{R}_A = \hat{R}_B$. In addition, it must be assumed that the light paths through both reflection units are identical

Sample in sample beam, reference in reference beam; one component of polarized light

With a polarizer mounted in the common beam before the detector, the attenuation of one component (e.g. $B = 0$) of re-

flected light is given by

$$AR_A\hat{R}_A = A'\hat{R}_A T \tag{15}$$

One only need require that $A = A'$ to get $T = R_A$. Thus assuming equivalent optical paths for each beam, we can directly get the reflection properties. Such measurements at two angles of incidence will allow for the calculation of n and k.

Samples in both beams, polarizers in both beams

Consider the possibility of using identical reflection units, polarizers and samples in each beam. Then if the polarizers are crossed, i.e. oriented perpendicularly, the condition for beam intensity equalization is given by

$$AR_A\hat{R}_A = B'R_B\hat{R}_B T \tag{16}$$

That is, the polarizer orientations produce $A' = B = 0$. The desired result, $T = R_A/R_B$, is only obtained if $A = B'$ and $\hat{R}_A = \hat{R}_B$. These restrictions are more severe than those previously discussed. While appearing to be an efficient technique, this method actually is the most difficult to apply.

From the above discussions one can see that using polarized light for measuring the reflected intensities from both sample and standard require the minimum number of assumptions on the instrument properties. For these cases, it is not necessary to assume equality of intensity of source components or grating polarization.

From a practical point of view, the most convenient method for isotropic samples, for example pressed powder disks, is to measure the reflected intensity from both sample and standard at one angle of incidence and one direction of polarization. The measurements are then repeated for the other direction of polarization.

ANISOTROPIC CRYSTALS

So far we have been concerned with the characteristics of isotropic materials. For anisotropic crystals, additional considerations are introduced. Recall that Fresnel's formulae are usually derived for isotropic materials where the optical properties are the same in all directions. For uniaxial crystals, the index of refraction has a different value along the optical axis than it has for the two directions perpendicular to the optic axis. To understand this, we might visualize a crystal with a structure having planar symmetry. That is, the crystal's molecular layers are shaped such that there is no asymmetry for the two perpendicular directions in the plane of the molecules (x,y planes). If the molecular layers are now

stacked up, as for example with pancakes, the molecular structure in the direction perpendicular to the planes (z axis) is different from that in the planes. If an electromagnetic wave propagates along the z axis, both electromagnetic field components oscillate in the plane of the molecule, and, since there is molecular symmetry, they "feel" the same polarization. Their propagation velocity is the same and so also is their dielectric constant or index of refraction. For a wave traveling along the x or y axis, the situation is different. The electric field component parallel to the Z axis will "feel" a different polarization of the molecules than the component in the plane of the molecules. Consequently the velocity of propagation will be different and the index of refraction will be different.

Measurements on anisotropic crystals

Uniaxial crystals are examined experimentally as follows. One prepares a sample having its optic axis in the plane of the sample. For the reflection measurements, one mounts the sample in such a way that the optic axis is oriented perpendicular to the plane of incidence. In order to measure the optical constants parallel to the crystal axis, one polarizes the incident light perpendicular to the plane of incidence. Then the sample is rotated by 90° and the measurements are repeated. For this second case, the incident light is polarized perpendicular to the optic axis. By using polarized light on an oriented crystal, one can study separately the optical properties of the crystal in directions parallel and perpendicular to the optic axis.

APPLICATIONS TO POWDER SPECTROSCOPY

From the above considerations, it is clear that measurement of the optical constants of anisotropic crystals must be made with care. The relationship between the optic axis and direction of incident light is critical. Consequently, the sample must be prepared appropriately if accurate material parameters are to be obtained. A similar situation is found for powders. The determination of the optical constants of powders requires careful sample preparation and controlled measurements. We first discuss powders made from isotropic materials. It is necessary to consider refraction and scattering effects. If transmission measurements are to be made, the initial problem in preparing a sample is to eliminate the voids between the powder particles. Such voids will cause the incident radiation to interact differently at particle-air interfaces. These different interactions will result in an optical characterization which can be significantly different from that of the bulk material. One can try to form a pressed disk sample by subjecting the powder to a high pressure, say in

a die. If the technique is successful and the sample's mechanical properties are accomodating, pressed disks having a density approaching that of the bulk can be prepared. In such cases, the measured optical properties should be quite close to the values determined from a solid.

An example of such an isotropic material is KBr. Pressed KBr pellets having the visual transparency of a polished crystal can be prepared, although probably not by everyone and not consistently.

Another isotropic material of interest is ZnS. Eastman Kodak manufactures optical quality disks obtained by pressing ZnS under high pressure and elevated temperatures. Irtran 2, as the product is known commercially, is transparent to about 14.5μm. Its refractive index at 1.5μm compares very well to that obtained from amorphous films and the bulk as the following table shows.

Table 1. Index of Refraction of ZnS at 1.5μm

Sample	n	Reference
Irtran 2	2.27	Kodak Publication U-72
amorphous ZnS film	2.26	J.F.Hall & W.F.C.Fergerson J.Opt.Soc.Am. 45, 714 (1955)
bulk ZnS	2.28	J.R.DeVore, J.Opt.Soc.Am. 41, 416 (1951)

Well characterized materials such as ZnS, which are available in various forms, are of use in studying the optical properties of powders. Principally, they serve as "optical standards" by which the accuracy and sensitivity of a given experimental method can be checked.

HIGHLY ABSORBING MATERIALS

For highly absorbing materials, of prime interest in this work, transmission measurements may not be feasible. The low concentrations and/or thin sample paths required for adequate energy throughput may introduce errors due to unabsorbed source radiation reaching the detector. In such cases, reflection measurements on solid samples must be considered. Here again, surface conditions are important. For sensitive specular reflection measurements, the reflecting surface should not introduce significant scattering effects. We have found that, for example, carbon and graphite powders can both be cold pressed at room temperature in a polished stainless steel die to yield acceptable reflecting surfaces. The graphite disks are quite stable mechanically while the carbon disks are fragile and must be handled with care. Providing the mechanical stability of these pressed disks can be adequately maintained, reflection measurements from good quality surfaces should be

realized and the optical constants calculated from procedures discussed above.

REFERENCES

1. F. E. Volz, Appl. Opt. 12, 564 (1973)
2. J. T. Luxon, D. J. Montgomery, and R. Summitt, Phys. Rev. 188, 1345 (1969)
3. H. Frohlich, Theory of Dielectrics, Oxford University Press, Oxford, 1948
4. W. R. Hunter, J. Opt. Soc. Am. 55, 1197 (1965)

FAR-INFRARED SPECTRAL INVESTIGATIONS

K. D. Moeller
Vincent P. Tomaselli

Fairleigh Dickinson University
Physics Department

INTRODUCTION

Spectroscopy in the far infrared and millimeter region (100 μm to 5 mm) is currently undertaken using two different methods. One utilizes monochromatic sources such as lasers or klystrons. This method, therefore, is restricted to investigations in a narrow spectral region if only one source is employed. It has the advantage that the high power available from the sources allows for the use of sensitive detection systems such as the superheterodyne detectors. The second method uses a mercury arc lamp as a source. The power output of this source is low but it is capable of producing radiation over the total spectral region under consideration. Liquid helium cooled detectors of low noise equivalent power, comparable to the best systems currently used in the optical region, are utilized.

For many applications, continuous spectra are desirable. In the past twenty years, a considerable improvement has been made in the sensitivity of detectors. Methods of recording and processing the spectral information leading to improved signal-to-noise ratios, have also been developed. These developments have improved the quality of continuous far-infrared and millimeter wave spectra.

FOURIER TRANSFORM SPECTROSCOPY

In Fourier transform spectroscopy one uses the idea that measuring the time interval over which a signal is recorded, results in a better signal-to-noise ratio. This is because the signal adds but the noise cancels out. This idea is used in the photographic recording of optical spectra. In the photographic process, all spectral lines are recorded during the total time of observation. In Fourier transform spectroscopy, one records an interferogram which consists of a superposition of all waves, each of which represents one spectral element. As an example, let us consider a conventional dispersion spectrometer which uses a diffraction grating. We scan the spectrum of 10 spectral elements, each observed for one minute, and represent the results, schematically, as follows

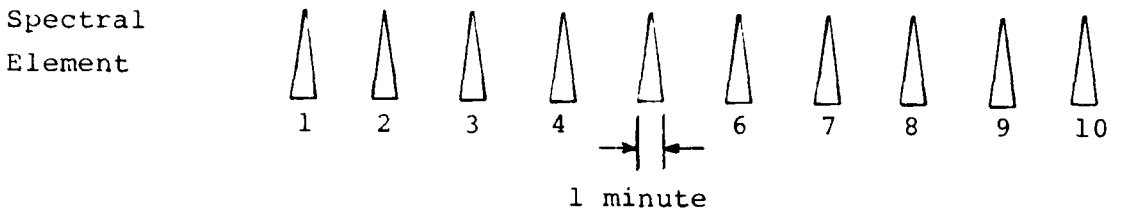

If we form an interferogram with these 10 spectral elements using an observation time of 10 minutes, then clearly we have

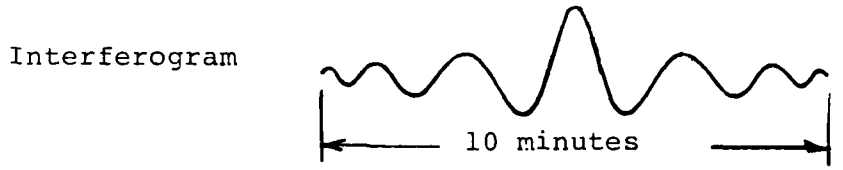

observed each spectral element for the full 10 minutes. The advantage of the increased observation time for each element is that a better signal-to-noise ratio is achieved for the same total observation time. The disadvantage is that the recorded interferogram does not give us the desired spectral distribution directly. A Fourier transformation of the interferogram will result in a conventionally displayed spectrum. If a dedicated minicomputer is available on site in the laboratory, the transformation is readily accomplished.

RADIATION SOURCE

The mercury lamp, mentioned above, has been the radiation source for far infrared spectroscopic investigations since the turn of the century. All attempts to replace it with improved sources have failed. An exception is the tunable electron laser developed by Schlesinger and Marshall at the Plasma Physics Laboratory at Columbia University. However, this is a plasma device and, as such, is not usable in a normal spectrometer. Recently, noise tubes for the millimeter region have been investigated as a source for this spectral region. These noise tubes consist of a ceramic housing filled with a gas mixture, at normal pressure, containing argon and a small quantity of Kr^{85}. The device is operated as a discharge tube. Its emission, in the millimeter region, is estimated to be the equivalent of a black body at 15,000 K. Using the Rayleigh-Jeans radiation law, one would expect to obtain roughly 10 times more radiation than that from a black body used as radiation source in the spectral region.

The noise tube, used for Fourier transform spectroscopy in the millimeter region, has been compared to a mercury lamp. In this comparison, which favored the noise tube, several inequalities were not addressed. First, the noise tube had a different

envelope than the mercury lamp. Second, the noise tube was mounted in a wave guide where an impedance matching problem may prevent the proper coupling of the emitted energy from the tube into the waveguide. Third, because of the geometry of the arrangement, no equivalent area times solid angle of both sources could be compared.

FOURIER TRANSFORM SPECTROMETER

A simplified Fourier transform spectrometer has been constructed. The instrument is designed so that emissions from both mercury arc lamps and noise tubes can be compared. A noise tube, with a fused quartz envelope and having dimensions similar to mercury lamp, has been ordered. Spherical mirrors have been used in the Michelson-type interferometer assembly and a conical light pipe directs the collected radiation to the detector. A schematic diagram of the spectrometer is shown in Fig. 1. The movable mirror M_1 is translated along its optic axis by a stepping motor. The signal at the detector D is amplified and recorded. Using a digital voltmeter, it is possible to store the digitized interferogram directly in a minicomputer. The interferogram is transformed, on site, and the spectrum is displayed on a CRT. Presently, the instrument is being operated with a

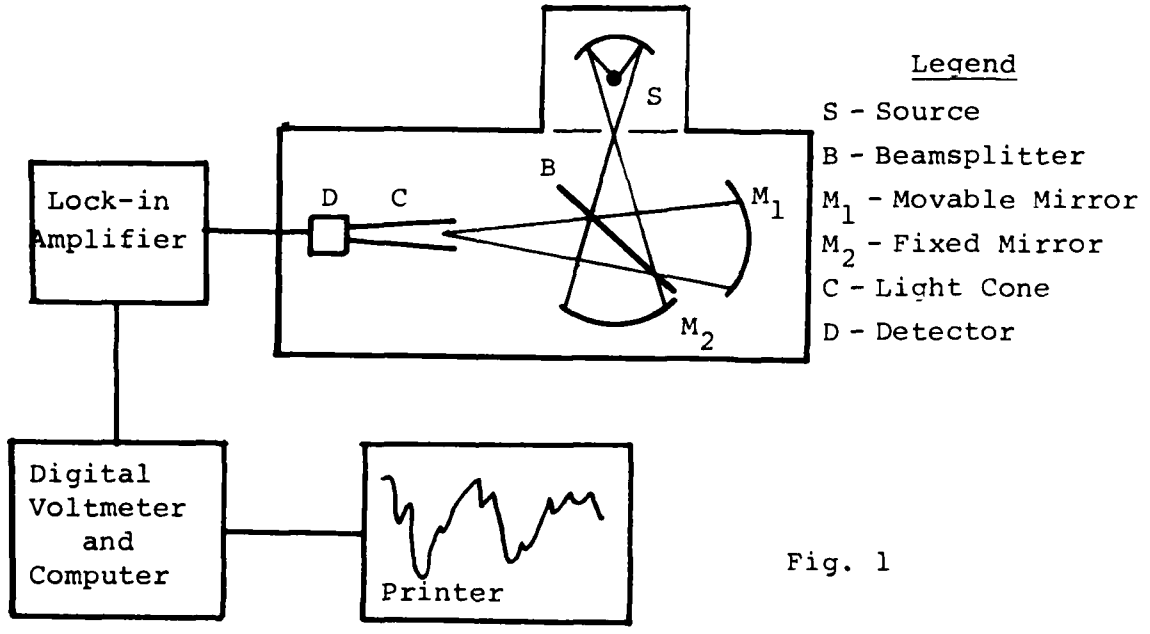

Fig. 1

different recording system. It has functioned satisfactorily on preliminary test measurements.

FUTURE STUDIES

In addition to the comparison of the noise tube and mercury lamp as sources, we have planned to study the absorption spectra of intercalated graphites in this spectral region. Some of the intercalated graphite compounds we acquired contain molecular groups of the type $AlCl_3$ and $AlBr_3$. The low frequency modes of these molecular groups, if observable, will be found in the far infrared region. Preliminary near infrared studies of some of the intercalated compounds have shown strong overall absorption similar to that of graphite. Since graphite is a conductor in the plane of the molecules, we are interested in a comparison of the far infrared absorption of pure graphite and its intercalated compounds to that of metal powders. In aluminum powders, for example, it has been observed that the absorption coefficient is proportional to the square of the frequency, in wavenumbers, that is $\alpha = C\nu^2$. Theoretical calculations for the constant C have been made by considering the influence of (a) the aluminum oxide layer on the surface of the aluminum particles, and (b) the shape of the particles. Both theories give the correct order of magnitude.

We will measure the absorption coefficient of graphite and the intercalated graphite compounds, which have high conductivities, but not layers of a different material on particle surface. Of interest here is to see if the ν^2-law is valid for these compounds.

COMPLEX REFRACTIVE INDICES OF SELECTED MATERIALS IN THE INFRARED

Marvin R. Querry
Department of Physics
University of Missouri-Kansas City

PUBLICATIONS

M. R. Querry and I. L. Tyler, "Reflectance and complex refractive indices in the infrared for aqueous solutions of nitric acid," J. Chem. Phys. 72, (in press).

J. B. Ross, I. L. Tyler, and M. R. Querry, "A microcomputer-based interface to expand the capabilities of a desktop programmable calculator," J. Phys. E: Sci. Instrum. 12, 266-267 (1979).

M. R. Querry, P. G. Cary, R. C. Waring, "Split-pulse laser method for measuring attenuation coefficients of transparent liquids: application to deionized filtered water in the visible region," Appl. Opt. 17, 3587-3592 (1978).

M. R. Querry, G. Osborne, K. Lies, R. Jordon, and R. M. Coveney, "Complex refractive index of limestone in the visible and infrared," Appl. Opt. 17, 353-356 (1978).

I. L. Tyler, G. Taylor, and M. R. Querry, "Thin-Wedge-shaped cell for highly absorbent liquids," Appl. Opt. 17, 960-963 (1978).

I. L. Tyler and M. R. Querry, "Complex refractive indices in the infrared for $ZnCl_2$ in water," J. Chem. Phys. 68, 1230-1236 (1977).

M. R. Querry, W. E. Holland, R. C. Waring, L. M. Earls and M. D. Querry, "Relative reflectance and complex refractive index in the infrared for saline environmental waters," J. Geophys. Res. 82, 1425-1433 (1977).

PRESENTATIONS

G. M. Hale, I. L. Tyler, and M. R. Querry, "Complex refractive indices in the infrared for selected oils and alcohols," J. Opt. Soc. Am. 68, 1403 (1978).

M. R. Querry and I. L. Tyler, "Complex refractive indices in the infrared for H_3PO_4 in water," J. Opt. Soc. Am. 68, 1404 (1978).

G. M. Hale, K. Biagi, and W. Holland, "Classical dispersion theory applied to the infrared reflectance of calcite, dolomite, and limestone," J. Opt. Soc. Am. 68, 1403 (1978).

I. L. Tyler and M. R. Querry, "Complex refractive index in the infrared for $ZnCl_2$ in water," Bull. Am. Phys. Soc. 22, 641 (1977).

M. R. Querry, I. L. Tyler, and W. E. Holland, "Complex refractive index in the infrared for phosphoric acid (H_3PO_4) in water," Bull. Am. Phys. Soc. 22, 641 (1977).

THESIS

Roy D. Holt, "The Optical properties of crystalline graphite," M.S. Thesis, Department of Physics, University of Missouri-Kansas City (1979).

REPORTS

M. R. Querry, Molecular and crystalline electromagnetic properties of selected condensed materials in the infrared, Final Report ARO Grant DAAG-29-76-GS-0185, 30 August 1979. (50 copies submitted to ARO)

INTRODUCTION

Research conducted during the three year term of ARO Grant DAAG-29-76-GS-0185 was: (1) measurement of infrared reflectance spectra $R(\nu)$ for all the materials, except graphite, listed in Table 1, (2) Kramers-Kronig analyses of the $R(\nu)$ spectra to obtain spectral values of the complex refractive index $N(\nu) = n(\nu) + ik(\nu)$ of each material, and (3) further analysis of the spectra in terms of fundamental intra- and inter-molecular vibrational modes.

Current knowledge of the propagation of electromagnetic radiation through aerosols/obscurants is based primarily on Mie-scattering computations. Such computations are meaningful only if there is prior knowledge of $N(\nu)$ for the aerosol/obscurant. The spectral values of $N(\nu)$ obtained during the term of this Grant are now routinely used in Mie-scattering computations conducted at many U.S. Army Laboratories and by many DOD contractors. Tabulated values of $N(\nu)$ were sent to, and may be obtained from, Aerosol/Obscuration Science Office, DRDAR-CLB-PS (M. Milham), Aberdeen Proving Ground, Md. 21010; or by consulting publications associated with this project.

EXPERIMENTAL METHODS

A block diagram of the reflectometer and data acquisition system is shown in Fig. 1. Radiant flux from a glower G was chopped at C and was then focussed by an f/5 optical system, consisting of plane mirror M_1 and spherical mirror M_2, on the surface of the sample S. The angle of incidence θ was 6.2 degrees for the central ray from M_2 incident on the surface of S. Radiant flux reflected from S was imaged by an identical optical system (M_3 and M_4) on the entrance slit of a Perkin-Elmer Ebert double-pass grating monochromator. The entrance slits were manually adjusted to assure spectral resolution $\nu/\Delta\nu$ of 100 or better. After passage through the monochromator, the radiant flux was optically filtered to remove higher diffraction orders, and was then focussed on a thermopile detector equipped with a CsI window. The signal from the detector was

TABLE 1. Bulk materials investigated during the term of Grant DAAG29-76-G-0185.

Material	Sample Concentration	Spectral Range	Obtained n + ik
H_3PO_4	5,10,20,40,50,65,75,85%, Cold 85% sample.	2-33 μm	Yes
$ZnCl_2$	20,30,40,50,65,75%	2-33 μm	Yes
Fog Oil	100%	2-33 μm	Yes
Diesel Fuel	100%	2-33 μm	Yes
DC-704 Silicon Oil	100%	2-33 μm	Yes
Plexiglas	100%	2-33 μm	Yes
HNO_3	0.5,1,2,4,8,15.7 M	2-33 μm	Yes
1-hexadecanol	100%	2-33 μm	Yes
1-octadecanol	100%	2-33 μm	Yes
1-eicosanol	100%	2-33 μm	Yes
Rutile	Natural sample	2-33 μm	Yes
Limestone*	Natural sample	.2-33 μm	Yes
Water*	purified & deionized	.42-.64 μm	Yes
Natural Waters*	six samples	2-20 μm	Yes
Graphite*	crystalline (E_1C)	1.24×10^{-6}-1240 μm	Yes

*Denotes materials investigated for which only partial support was provided by DAAG29-76-G-0185.

synchronously processed by a Princeton Applied Research (PAR) Model 124 lock-in amplifier. The analog output signal from the Model 124 was applied to the input of a PAR Model 260 analog-to-digital converter (ADC) which both digitized the signal and inserted an index corresponding to the spectral position of the monochromator.

In order to facilitate data acquisition and analysis the system described above was interfaced to a Hewlett-Packard (HP) Model 9820A programmable calculator equipped with an HP 9862A plotter and an HP11223A magnetic cassette tape unit. This entire system was then interfaced through a decwriter L-36 TSO terminal to an IBM 370/168 computer which was used for the subsequent Kramers-Kronig analysis of the data.

During this investigation we measured relative specular reflectance $R(\nu) = R(\nu)_S/R(\nu)_W$, where s denotes the sample and w denotes the water standard. Prior to use the water standard w was purified, deionized, and filtered through a 0.2 μm Millipore filter. Aqueous solutions were prepared using purified water and reagent grade chemicals. The aqueous solutions and purified water were placed in separate petri dishes which served as sample holders. Each dish was filled to precisely the same level as determined by use of a cathetometer. The levels of all samples were monitored routinely during data collection and purified water was added to the samples as needed to compensate for evaporation. Each sample was also stirred thoroughly at the beginning of a spectral scan to assure isotropic homogeneity. Data were acquired at 200 equally spaced wavelength positions in each of the wavelength regions 2-3, 3-4, 4-6, 6-8, 8-10, 10-15, 15-20, 20-30, and 30-40 μm. For some samples, individual relative reflectance measurements were made at 30.15, 32.3, 34.0, and 37.1 μm where atmospheric absorption was a minimum, rather than throughout the 30-40 μm region.

Procedures were slightly different for handling the solid samples. The solid samples were placed one-at-a-time on a small three-legged stand within the reflectometer. The top surface of the water standard and the polished surface of the solid sample were placed at the same height by adjusting the legs of the stand while viewing the surface edge through a cathetometer. Additionally, the beam from a He-Ne laser was reflected from the level surface of the water standard to a fiducial mark on the ceiling of the laboratory. The legs of the stand were further adjusted to bring the laser beam to the same fiducial mark when the water was replaced by a solid sample. The latter leveling adjustments were made so that the height of the solid surface was also at the proper position. Reflectance spectra were then acquired for the solids at the same wavelength positions as for the liquids.

All spectra were obtained with the samples at about 27°C, except for one cold sample of 85% phosphoric acid which was at about -10°C. The reflectance spectra $R(\nu)$ were converted from wavelength to wave number. The standard deviations, based on three independent measurements, were generally $\pm$ 0.005 $R(\nu)$ but increased to about $\pm$ 0.01 $R(\nu)$ in relatively narrow spectral regions where atmospheric water vapor and carbon dioxide were strongly absorbing.

The $R(\nu)$ spectra for the natural waters were obtained by use of a similar procedure, but were obtained at a 70° angle of incidence and the incident radiant flux linear polarized with the electric field vector perpendicular to the plane of incidence.

R(ν) AND N(ν) SPECTRA

The R(ν) spectra were analyzed by use of Kramers-Kronig techniques to obtain spectral values of N(ν) for each material. As an example, the R(ν) and N(ν) spectra for three aqueous solutions of zinc chloride are presented in Figs. 2-7. The reader is referred to the Final Report, GRANT DAAG-29-76-GS-0185 for discussions of the intra- and inter-molecular vibrational modes of these materials.

OPTICAL PROPERTIES OF CRYSTALLINE GRAPHITE

A search of the scientific literature on the optical properties of carbon in any spectral region provided experimental data from which the imaginary part of $N(\xi) = n(\xi) + ik(\xi)$ could be determined in the 10^{-3} ev $\leq \xi \leq 10^{6}$ ev spectral region. By use of high and low energy approximations the $k(\xi)$ epectrum thus obtained was defined piecewise analytically over the entire electromagnetic spectrum. Compton scattering and pair production were ignored in the high energy approximations. Kramers-Kronig analysis of the $k(\xi)$ spectrum provided values for $n(\xi)$, which along with knowledge of $k(\xi)$ were used to compute the reflectance spectrum, the relative dielectric function, and the energy loss function. The evaluation of five different sum rules showed the data to be of high quality.

Graphite is an optically uniaxial material. In the infrared spectral region, therefore, two $k(\xi)$ spectra are required to completely specify the optical constants. The search of the scientific literature, however, provided a $k(\xi)$ spectrum only for the electric vector of the electromagnetic wave linearly polarized perpendicular to the c-axis of the graphite crystal. The results here are only for the case $E_{\perp}C$. In the energy region above $\xi = 1$ ev this constraint of $E_{\perp}C$ is not pertinent.

These investigations of graphite are based on a M.S. Thesis (UMKC, 1979) by Mr. Roy Holt.

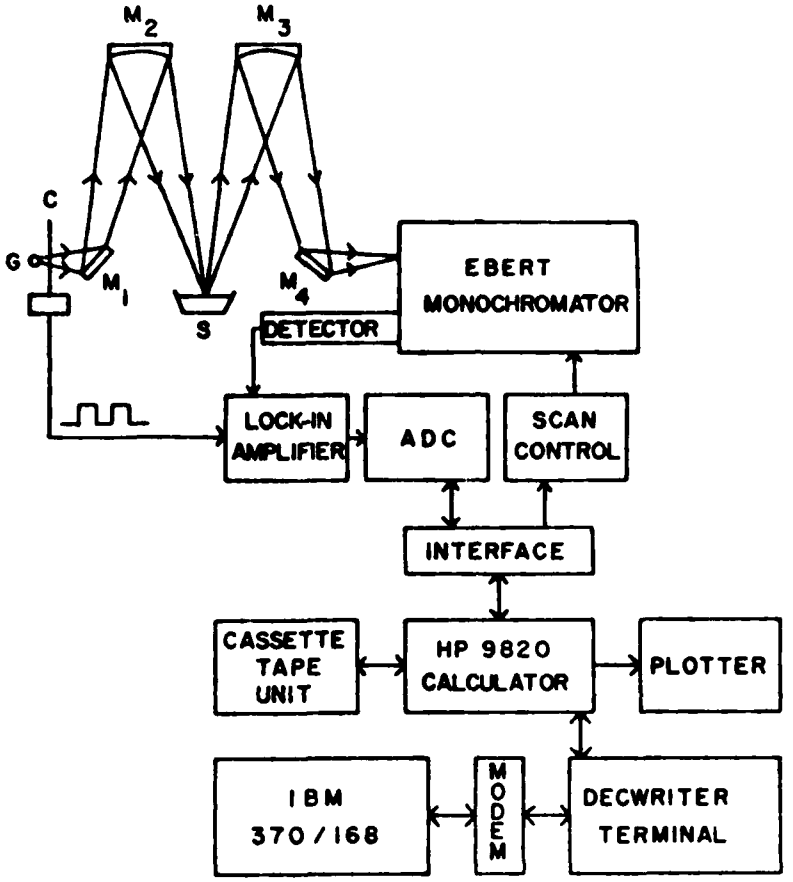

Figure 1. A block diagram of the reflectometer-spectrophotometer and data acquisition system.

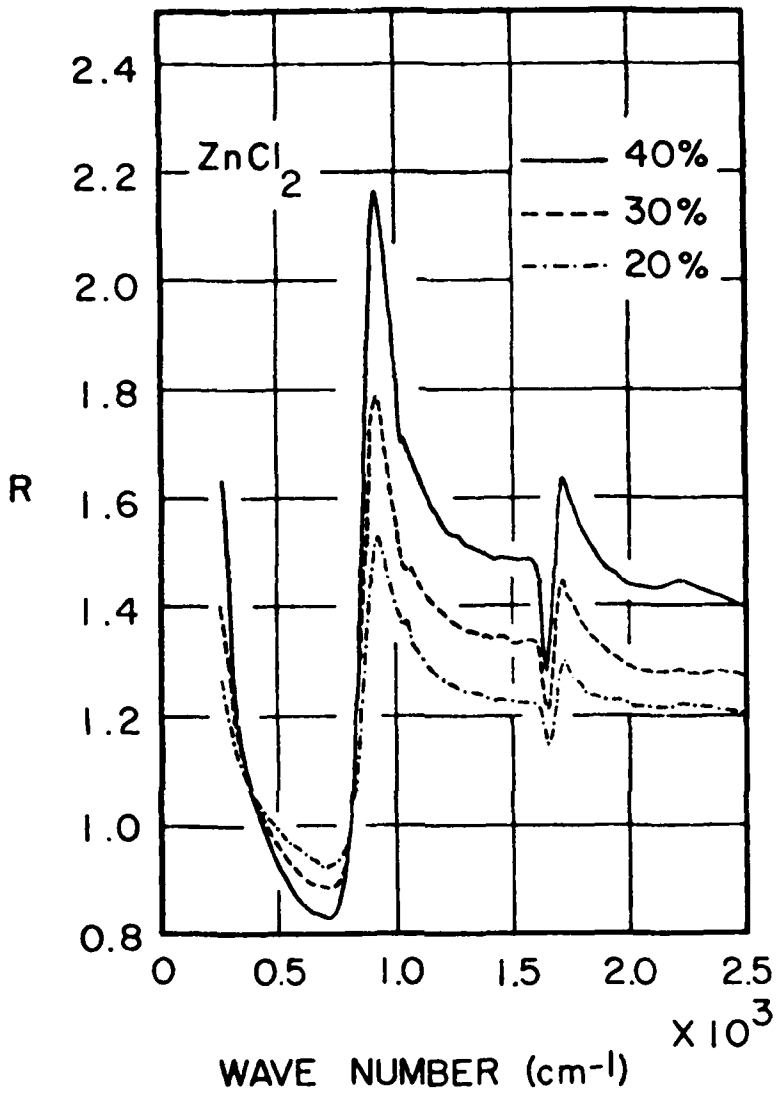

Figure 2. Near-normal incidence relative specular reflectance $R(\nu) = R(\nu)_s/R(\nu)_w$ in the spectral region from 270 to 2500 cm^{-1} for 20.3, 29.4, and 40.2 percent aqueous solutions containing $ZnCl_2$. Nominal values of 20, 30, and 40 percent are listed in the key for the various spectra.

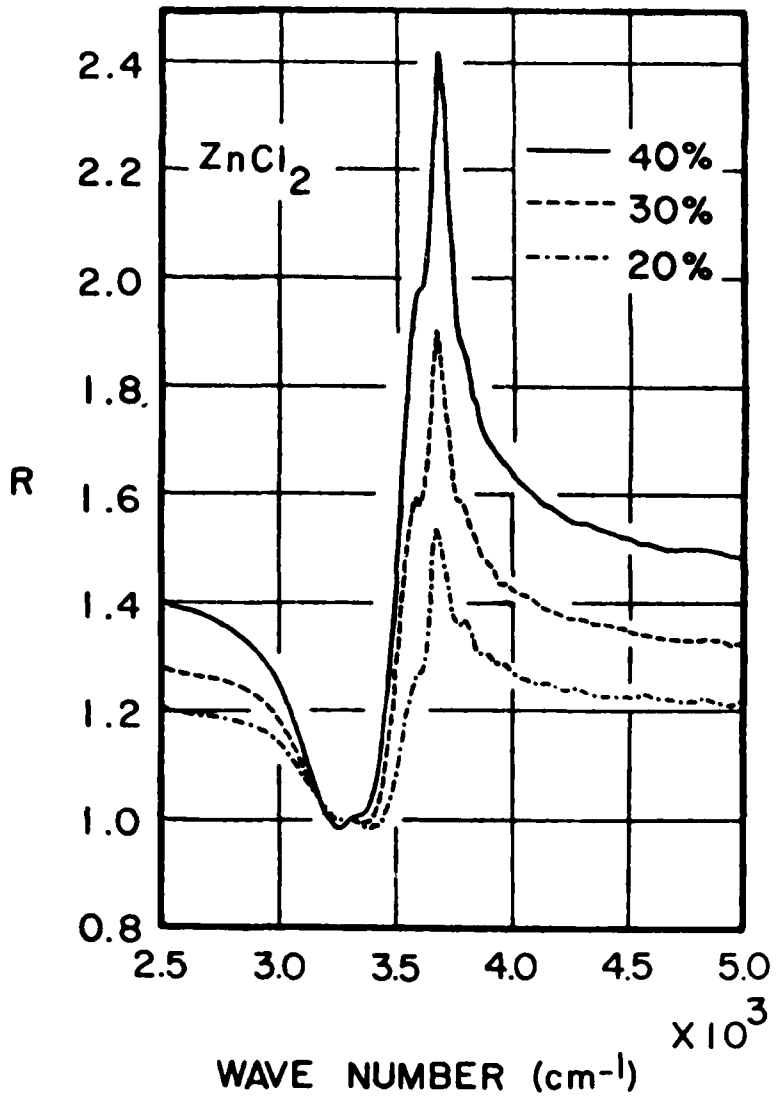

Figure 3. Near-normal incidence relative specular reflectance $R(\nu) = R(\nu)_s/R(\nu)_w$ in the spectral region from 2500 to 5000 cm^{-1} for 20.3, 29.4, and 40.2 percent aqueous solutions containing $ZlCl_2$. Nominal values of 20, 30, and 40 percent are listed in the key for the various spectra.

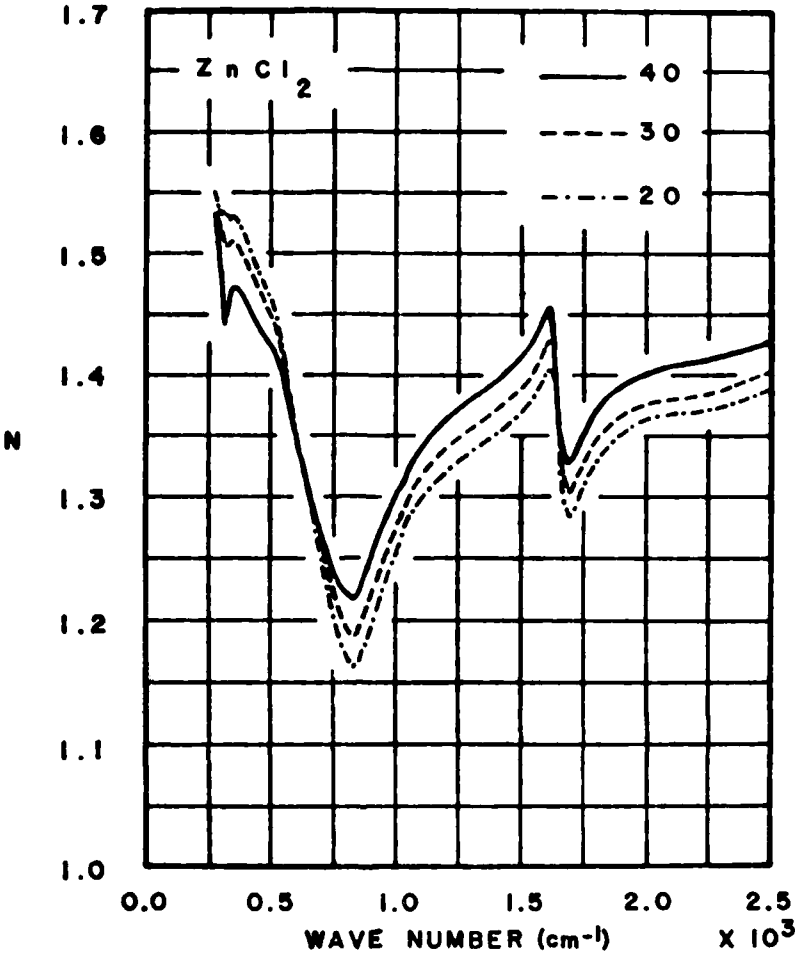

Figure 4. Index of refraction $n(\nu)_s$ in the spectral region from 270 to 2500 cm^{-1} for 20.3, 29.4, and 40.2 percent aqueous solutions containing $ZnCl_2$.

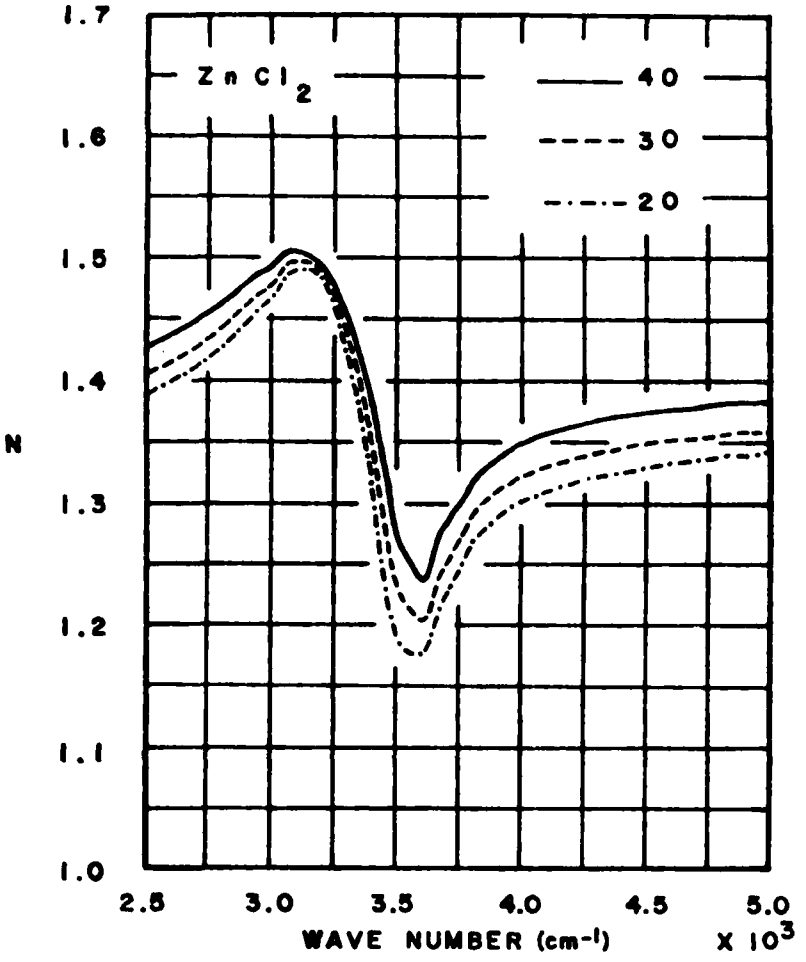

Figure 5. Index of refraction $n(\nu)_s$ in the spectral region from 2500 to 5000 cm^{-1} for 20.3, 29.4, and 40.2 percent aqueous solutions containing $ZnCl_2$.

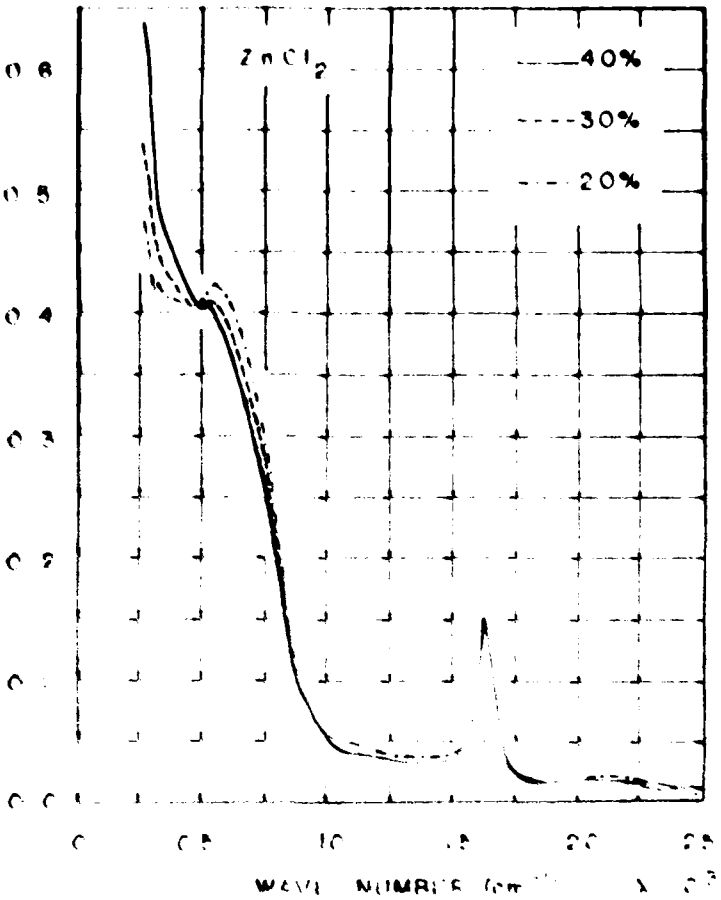
$ZnCl_2$
40%
30%
20%

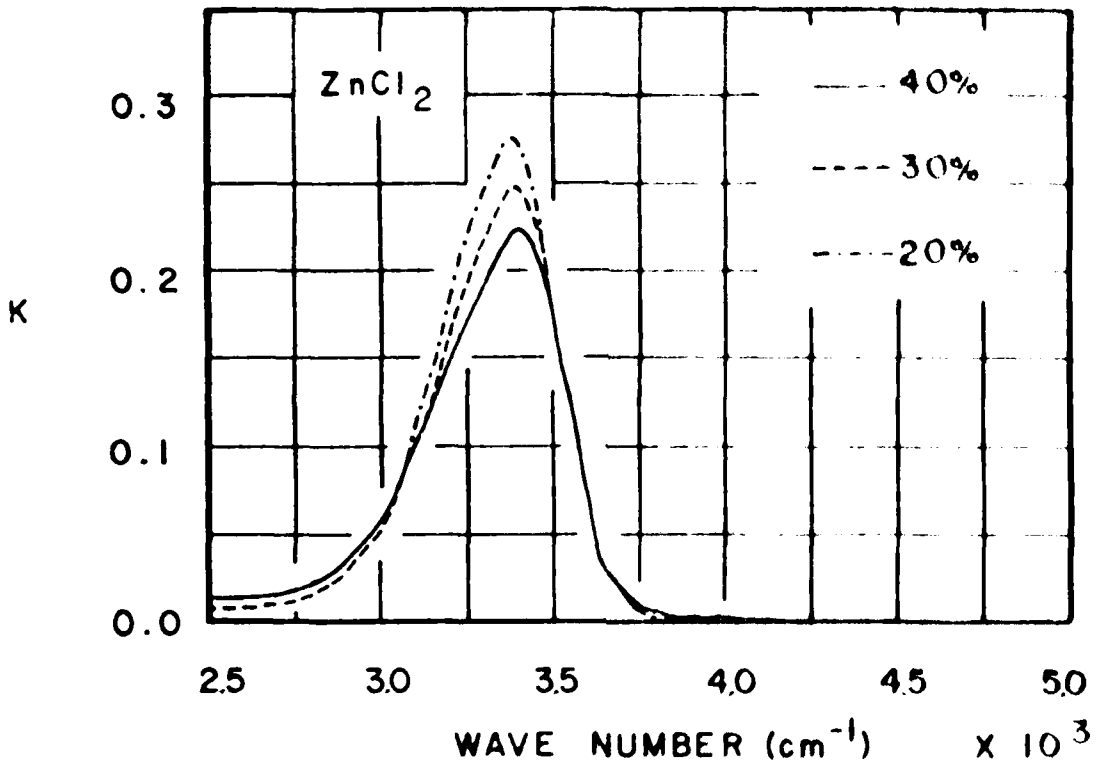

Figure 7. Extinction coefficient $k(\nu)_s$ in the spectral region from 2500 to 5000 cm^{-1} for 20.1, 30.4, and 40.2 percent aqueous solutions containing $ZnCl_2$.

EXPERIMENTAL STUDIES OF THE OPTICAL EXTINCTION OF VARIOUS FORMS OF CARBON

J. Pinto and D. Wiegand
Energetic Materials Division
Large Caliber Weapon Systems Laboratory
US Army Armament Research and Development Command

INTRODUCTION

Recently the Army has been focusing some interest on using various forms of carbon as obscuring agents because of their broad band extinction properties. The optical properties of crystalline carbon or graphite and highly disordered carbon[1], which we shall refer to as carbon black, are quite different. We have made measurements of the transmission of these materials dispersed in pressed pellets of potassium bromide (KBr) in the UV, visible and IR, and of the diffuse reflectance in the UV and visible. We have compared these results with data found in the literature on single crystals of graphite in the UV and visible and on powdered samples of graphite and carbon black in the IR. The objective is to determine the relative importance of particle size and optical constants in the observed differences between the two forms of carbon when used as obscuring agents.

EXPERIMENTAL PROCEDURE

Transmission through KBr pellets - Potassium bromide, which had been ground very fine and dried overnight at 100°C, was mixed with various concentrations of graphite and carbon black, and pellets of these mixtures were pressed at about 27,000 psi. Infra-red spectra were recorded on a Perkin Elmer 611 spectrometer between 2.5μ and 30μ, and UV, visible and near IR spectra were recorded on a Cary 14R spectrophotometer between 0.35μ and 2.5μ.

Data from the Perkin Elmer 611 is in percent transmission (%T) while the Cary 14R data is in units of optical density (O.D.). Percent transmission and optical densities were converted to extinction coefficients in units of m^2/gm by the relation

$$\alpha = \frac{O.D.}{2.303\ \ell c}$$

where

$$O.D. = -\log_{10}(\%T/100)$$

and where the constant 2.303 is the conversion factor between base 10 and natural logarithms, ℓ is the path length through the sample, and c is the concentration of the sample in the host matrix, in this case KBr, and is in units of gms of carbon or graphite per m^3 of KBr.

Pressed KBr pellets scatter very strongly at wavelengths shorter than about 0.35μ due to the presence of sub-micron sized particles of KBr in the pellet. Thus, the lower limit for transmission data presented here is 0.35μ. These spectra were recorded with air in the reference path. Spectra of potassium bromide pellets were recorded and this baseline was subtracted from the spectra of the graphite and carbon black in KBr.

Diffuse Reflectance - Diffuse reflectance spectra were recorded using a Cary 14R Spectrophotometer with a Model 1411 Diffuse Reflectance attachment. This attachment uses an integrating sphere coated with MgO and diffuse reflectance is measured relative to $MgCO_3$ blocks. The phototube detector on this attachment limits the wavelength range to 0.24 to 0.70μ. Samples are simply poured into a quartz sample holder, the sample being sufficiently thick so that transmission is not significant. Specular reflectance was eliminated in these measurements.

Optical Microscopy - Samples of carbon and graphite were dispersed in immersion oil between microscope slides. Photographs of the samples were taken at magnifications of 400X and 640X.[2]

RESULTS AND DISCUSSION

Transmission through KBr pellets - The extinction coefficient versus wavelength for graphite and carbon black are shown in figure 1. To understand these curves, it is necessary to have some knowledge of the average particle size or the particle size distribution of the sample. Figure 2 shows graphite particles magnified 400 and 640 times, and figure 3 shows carbon black also magnified 400 and 640 times. Figure 2 indicates that the graphite particles are irregularly shaped. While it is not possible to specify a diameter for such particles, one can approximate some sort of average size parameter. This parameter in the case of graphite is on the order of 10μ. On the other hand, figure 3 shows the carbon black particles to be much more regular and spherical in shape, making it easier to assign a particle diameter. In the case of carbon black, most of the particles seem to be 2-3μ or less in diameter.

Figure 1 shows that the extinction coefficient of graphite is flat through the wavelength range studied. Data from 1 to 10μ can be compared with the optical constants, n and k for polycrystalline graphite from Foster and Howarth[3], shown in figure 4. The real component, n, ranges from about 1.8 at 1.0μ to 4.0 at 10.0μ while k ranges from 0.85 to 1.60. According to Mie scattering theory, these optical constants

would result in a plot of extinction efficiency, Q_{ext}, versus particle size parameter, x, similar to the solid curve shown in figure 5, where Q_{ext} is given by,

$$Q_{ext} = \frac{\alpha c}{\pi r^2 n}$$

where α is the extinction coefficient in m^2/gm, c is the concentration in gms/m^3, n is the number density in m^{-3}, and πr^2 is the geometrical cross section of the scattering particles. This curve is schematic, not calculated. On the basis of figure 5, one would expect constant α for x greater than 6.0 or for the wavelength shorter than about half the particle diameter. For graphite particles on the order of 5μ 30μ in diameter, α will be constant for wavelengths shorter than 1μ. Figure 1 shows that this is the case, at least for wavelengths longer than 0.4μ.

For x less than 6.0 or for wavelengths longer than 1μ the extinction coefficient should start decreasing. This is not readily apparent from figure 1 since the initial decrease in Q_{ext} might be slight due to a distribution of the particle sizes. Other workers making measurements at longer wavelengths have found a sharp decrease in the extinction coefficient above 40μ.[4]

There is a small increase in extinction on the short wavelength side of 0.4μ that might be due to changes in the optical constants (see figure 1). These changes have been detected by specular reflectance measurements on single crystals[5] and diffuse reflectance measurements on powders, made in the UV and visible. This will be explained further in the discussion of the diffuse reflectance data.

A similar argument can be used to explain the extinction behavior of carbon black which has also been referred to as soot[3]. Optical constants for this material are shown in figure 6 in the 1 to 30μ range. The theory would predict a Q_{ext} for these optical constants that would look similar to the dashed curve shown in figure 5. Again this curve is merely schematic. Since most of the carbon black particles are less than 1μ in diameter, Q_{ext} as shown in figure 1 would be expected to remain constant for wavelengths longer than this. This is shown to be the case [illegible] for wavelengths longer than 35μ.[3]

[illegible]

neutron scattering data indicate that there are many carbon particles on the order of 10^{-3} and 10^{-2} microns.[1] Also, if figure 3 is studied closely enough, one can note diffraction rings around some of the particles, indicating that the size is on the order of the wavelength of the visible light. (This may not be visible on copies.)

Diffuse Reflectance - Diffuse reflectance spectroscopy was performed on graphite and carbon in order to obtain an estimate of the optical constants of these materials in the visible and UV. Diffuse reflectance is a complicated function of the real and imaginary components of the refractive index and particle size and shape. Many different models have been proposed to treat diffuse reflectance, and each has its advantages and shortcomings. Johnson[6] has proposed a layered plane model which should work well for graphite because of its layered structure. However, Johnson's model has fared poorly in describing substances that are strong absorbers, such as graphite because of an inadequate account of internal reflections. Melamed[7] has proposed a model that works well for strong absorbers, but assumes spherical particles. Because of the limitations of the models available, one can, at best, only make qualitative deductions about the optical constants from the diffuse reflectance of these materials.

The diffuse reflectance of graphite and carbon black are plotted in figure 7. It is interesting to note that the diffuse reflectance of graphite is constant through the visible and then turns sharply upward at about 0.35μ and continues rising to 0.24μ, the low wavelength limit of the instrument. Other workers[5] have found that the specular reflectance of single crystals of graphite also increases at wavelengths between 0.35μ and 0.24μ. Optical constants n and k have been calculated from this specular reflectance data, and results show that parallel to the planes n decreases and k increases, and perpendicular to the planes both n and k remain constant. This data has been explained in terms of the band structure of graphite. While there is no simple connection between single crystal and polycrystalline optical constants, diffuse reflectance data indicate that n and k do change between 0.35μ and 0.24μ, in agreement with what is to be expected from single crystal data.

The diffuse reflectance of carbon black in the visible and UV is about 5.0% which indicates that this material absorbs very strongly. This agrees with the strong extinction observed in the transmission measurements. There is also very little structure in the spectrum outside of a slight increase below 0.35μ. Since carbon black is highly disordered, one does not expect to find the same structure found in the spectrum of graphite. However, the slight increase in the diffuse reflectance observed at shorter wavelengths could be due to small areas of crystallinity similar to graphite and is also indicative of some change in the optical constants.

SUMMARY AND CONCLUSIONS

Qualitative explanations have been provided in terms of particle sizes and optical constants to explain the different extinction characteristics of dispersed carbon and graphite. It is still necessary to perform similar experiments on monodisperse powders and to compare these results with computer calculations in order to obtain a quantitative verification of the proposed results over a wider wavelength range.

REFERENCES

1. Prask, H. J., and Choi, C. S., these Proceedings.

2. Morrow, S. - private communication

3. Foster, P. J. and Howarth, C. R., Carbon 6, 719 (1968)

4. Moeller, K. D. - private communication

5. Greenaway, D. L., Harbeke, G., Bassani, F. and Tosatti, E., Phys Rev. 178, 1340 (1969)

6. Johnson, P. D., J. Opt. Soc. Am. 42, 978 (1952)

7. Melamed, N. T., J. Appl. Phys. 34, 560 (1963)

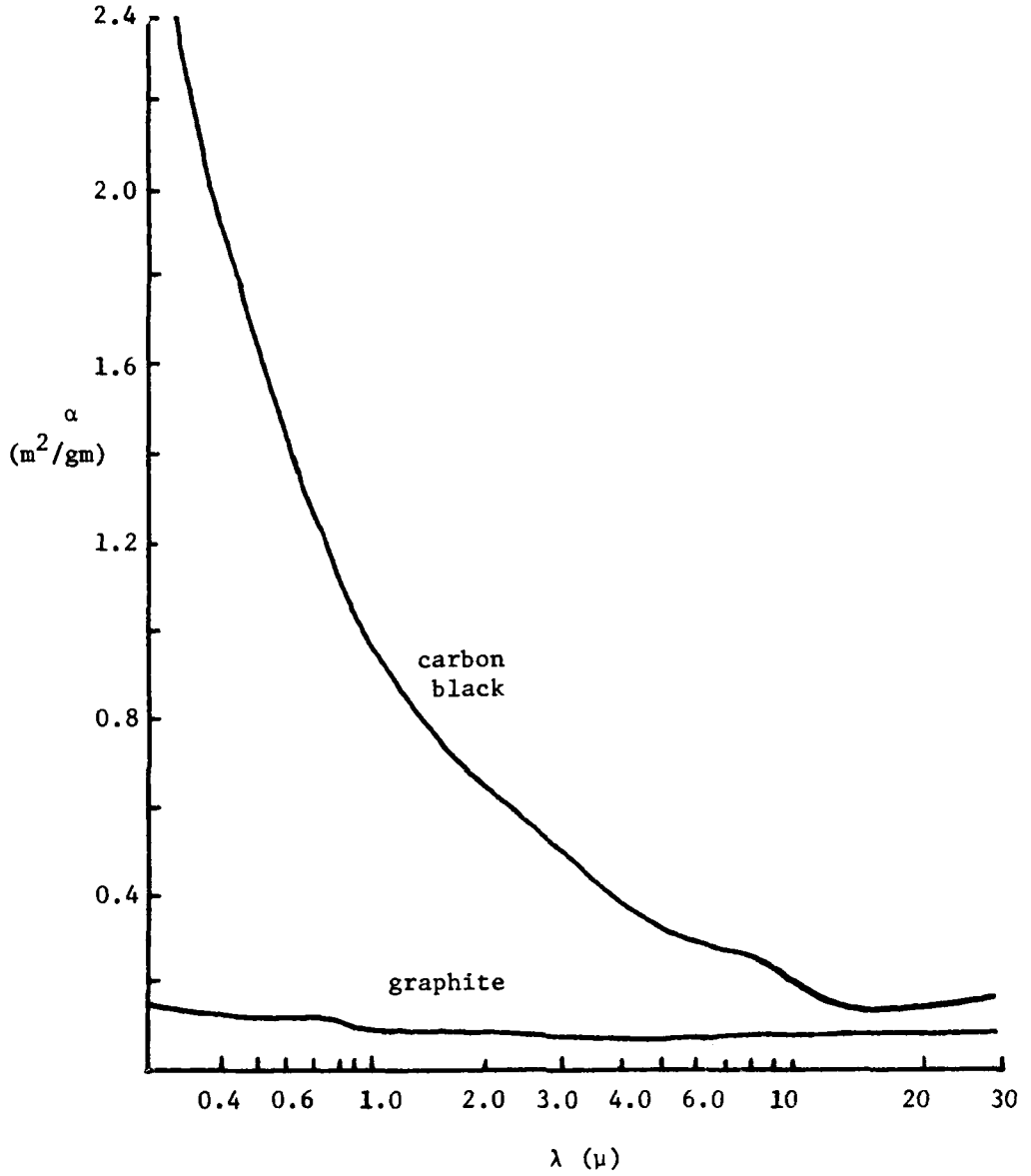

Figure 1. Extinction coefficient, α, vs. wavelength, λ, for carbon black and graphite. Data was recorded in transmission through KBr pellets. The extinction of the KBr was subtracted to give data plotted.

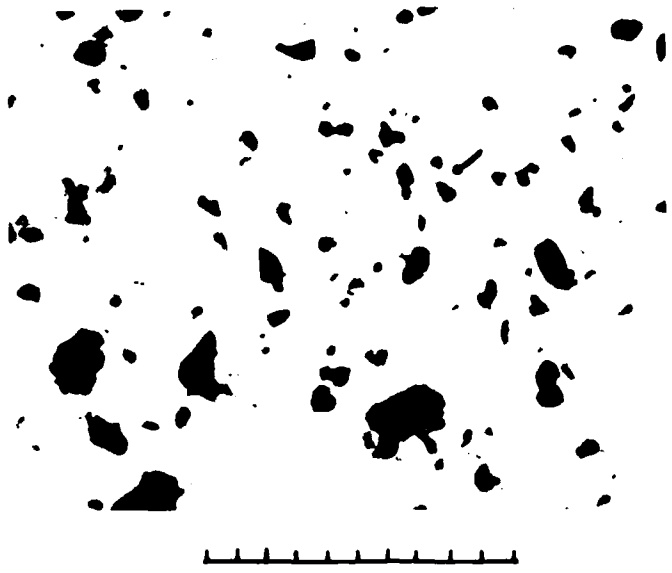

10μ/div

∿ 400X

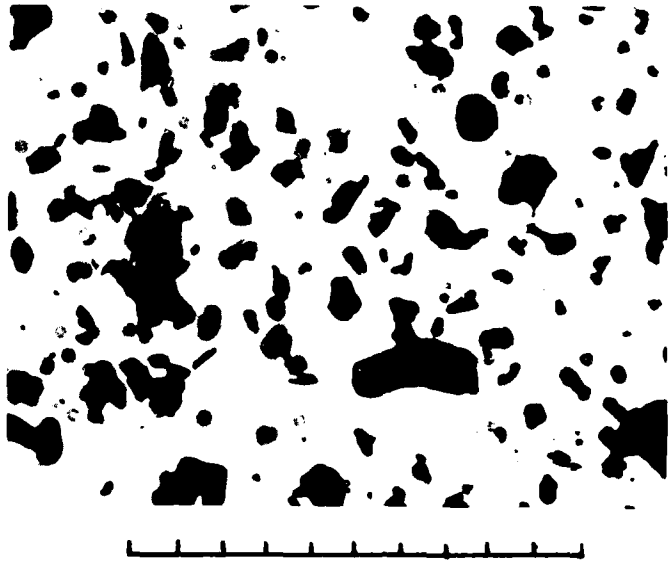

10μ/div

∿ 640X

Figure 2. Graphite particles magnified 400 and 640 times.

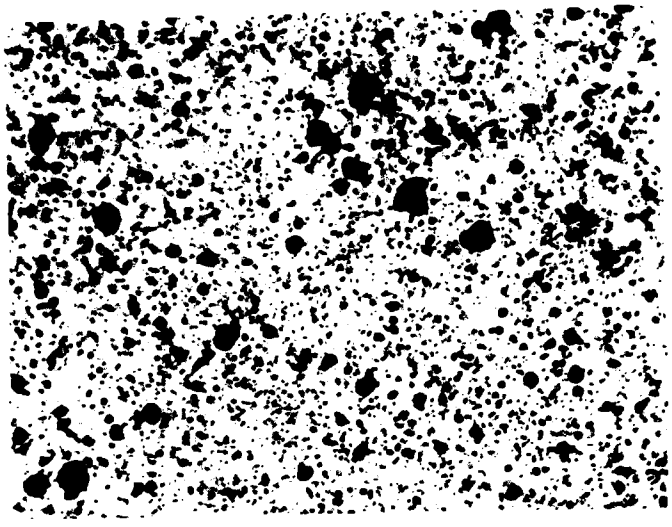

10μ/div

∿ 400X

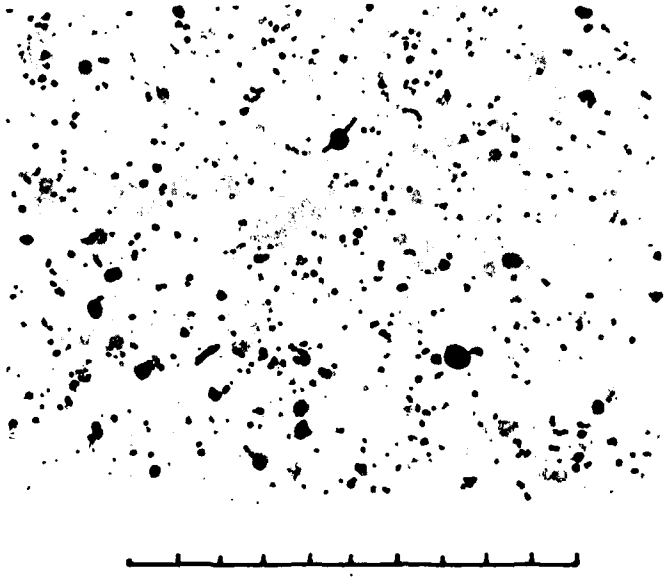

10μ/div

∿ 640X

Figure 3. Carbon black particles magnified 400 and 640 times.

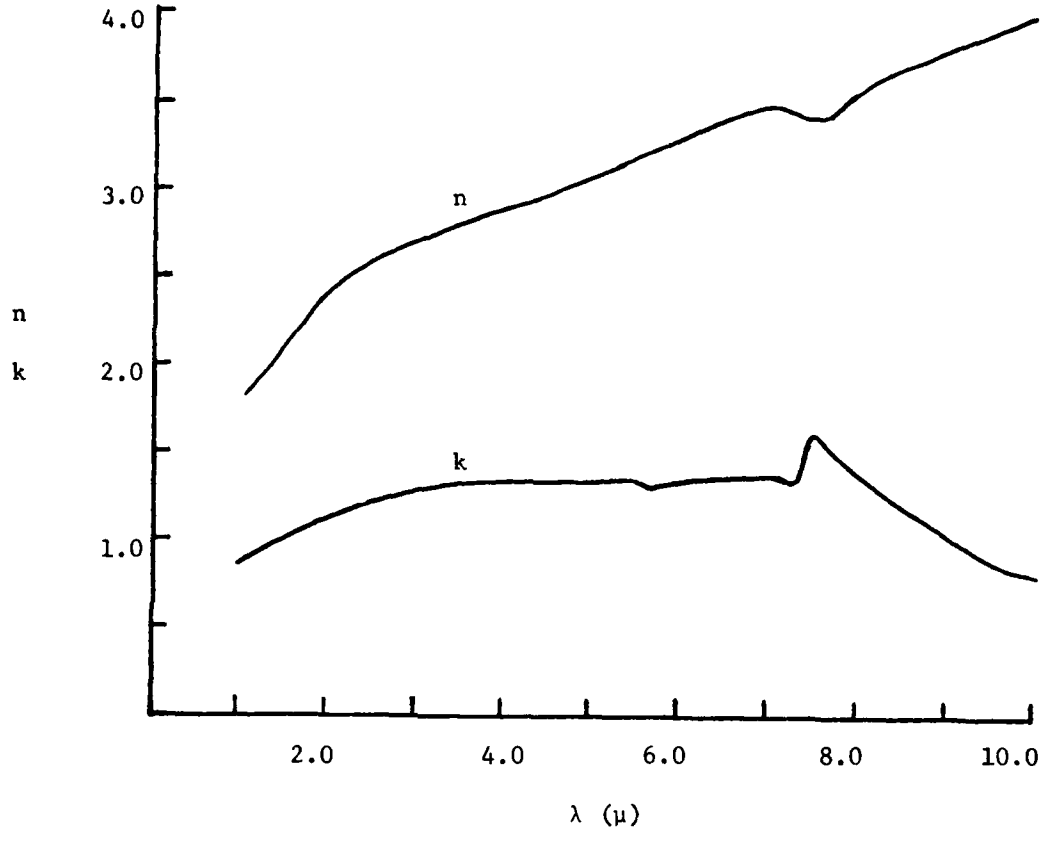

Figure 4. Real (n) and imaginary (k) components of the refractive index vs. wavelength, λ, in the infrared for graphite, from Foster and Howarth (ref. 3). Data was derived from specular reflectance measurements on polycrystalline samples and using the Fresnel equations.

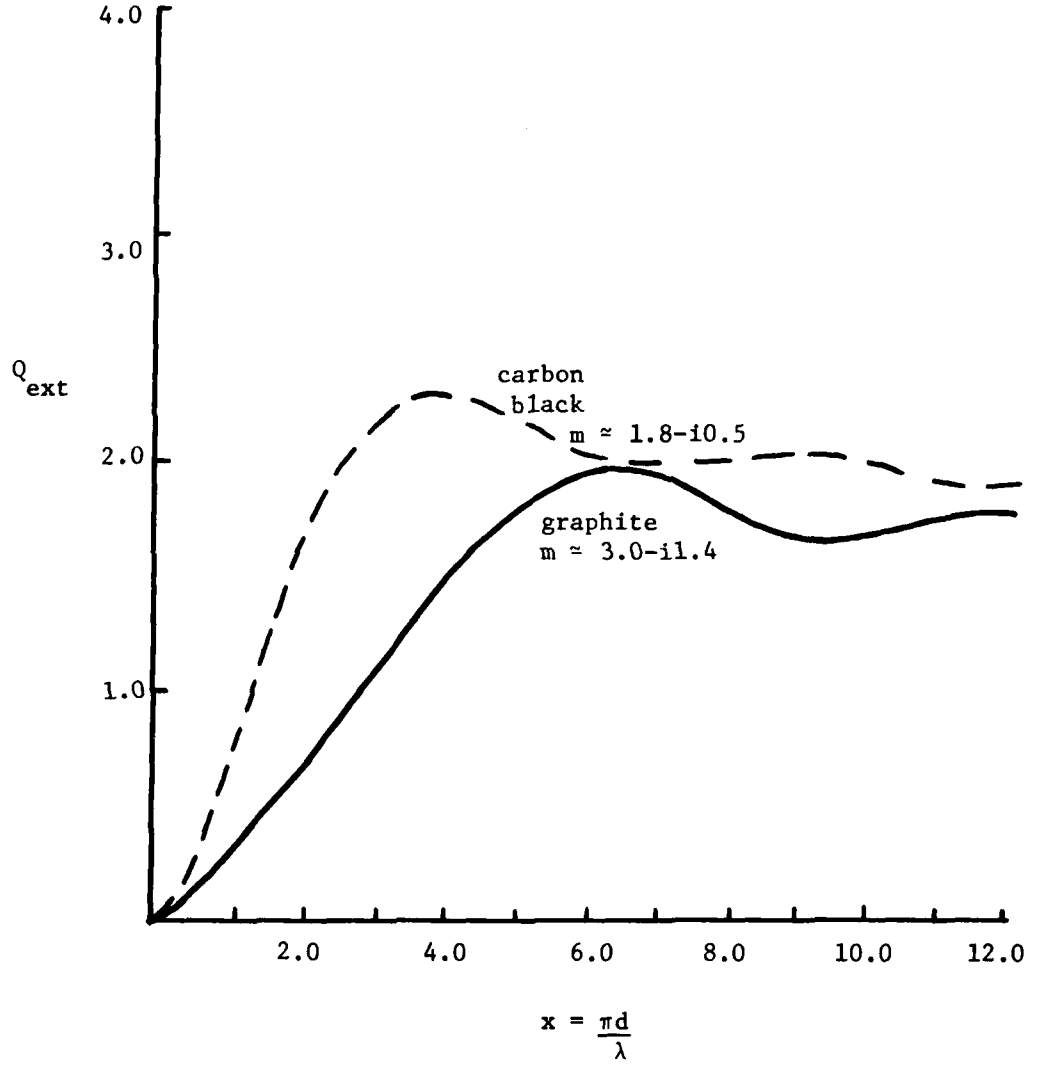

Figure 5. Schematic representation of the extinction efficiency (Q_{ext}) vs. the particle size parameter (x), for complex refractive indices (m) that approximate those of graphite and carbon black in the infrared. m = n-ik.

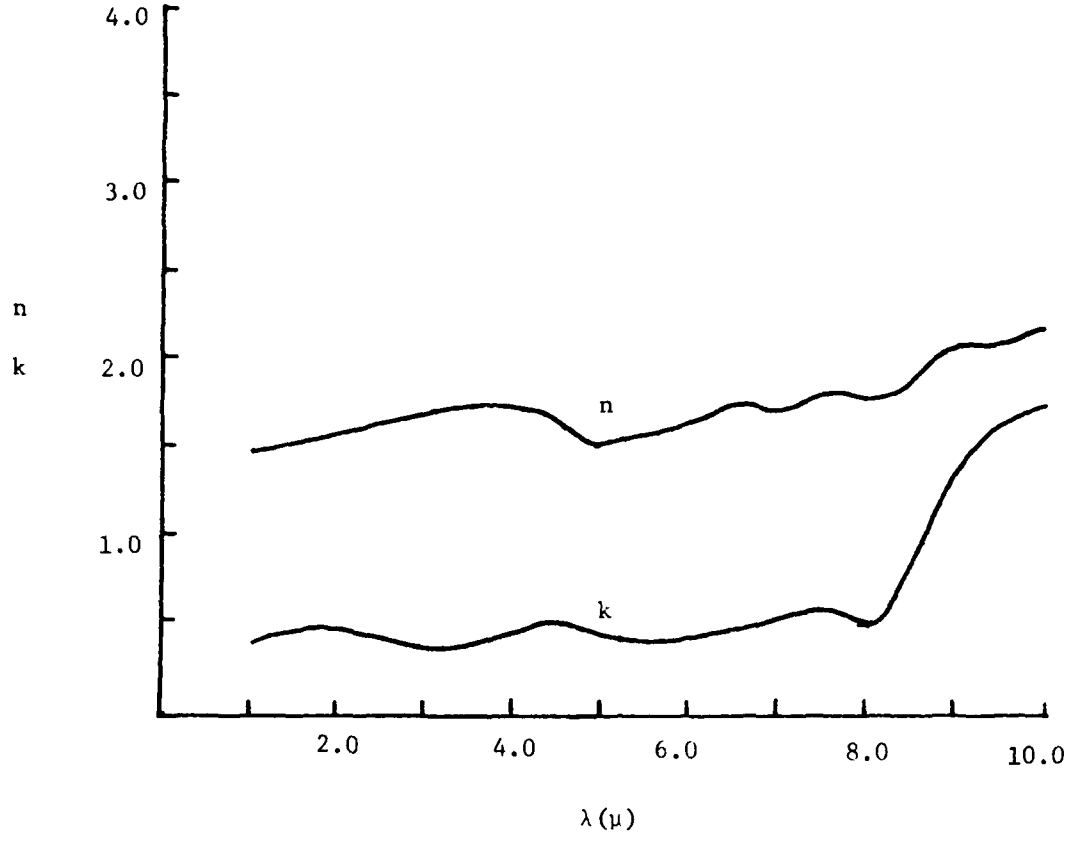

Figure 6. Real (n) and imaginary (k) components of the refractive index vs. the wavelength (λ) in the infrared for carbon black, from Foster and Howarth (ref. 3). Data was derived from specular reflectance measurements on powdered samples and using the Fresnel equations. Note that Foster and Howarth refer to carbon black as Mogul Plus.

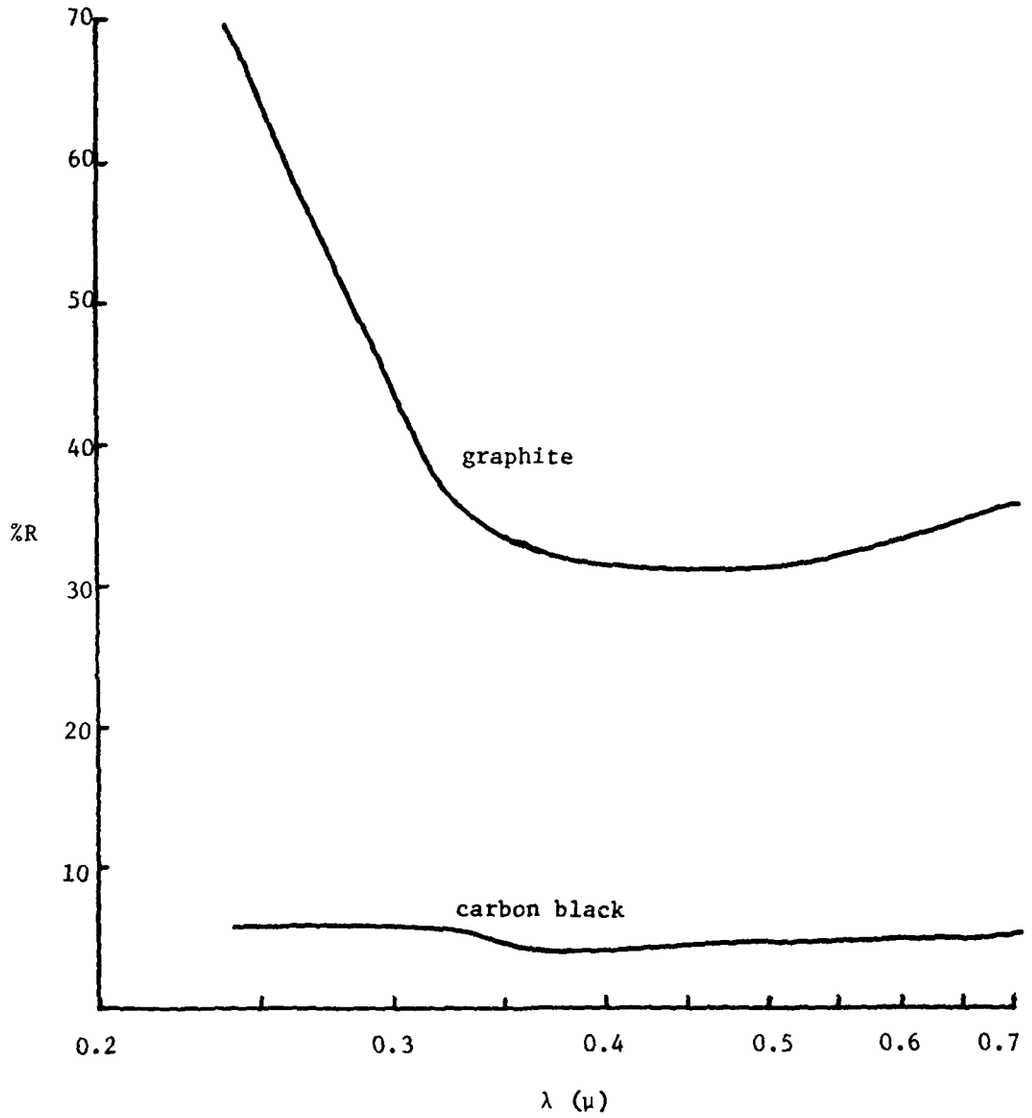

Figure 7. Diffuse reflectance (%R) vs. wavelength (λ) for polydispersed powders of graphite and carbon black.

LOW DIMENSIONAL MATERIALS AS POTENTIAL OBSCURANTS

J. Sharma
Energetic Materials Division
Large Caliber Weapon Systems Laboratory
US Army Armament Research and Development Command

In recent years much progress has been made to intercalate low dimensional solids such as graphite, polyacetylenes, and poly (para) phenylenes.[1,2,3,4,5]. Some of these materials exhibit super-conductivity at low temperatures. At room temperature, electrical conduction comparable with highly purified copper and silver is observed. Therefore, these conducting materials exhibit large reflectivity of the visible and infrared radiation up to 16μ. High reflectivity of microwave radiation is possible. In addition, intercalation has produced graphite with apparent density of 0.003 gm/cc, four times heavier than air. This graphite, if dispersed in the air, will remain suspended for a very long period of time (20μ x 20μ particles require sixty hours to fall through 20 ft. of still air). The obscurant potential of these new low dimensional materials should be investigated.

Graphite is a two-dimenisonal solid. The atoms of carbon are arranged hexagonally in planes with a bond distance of 1.418A compared to 1.39A in the benzene ring. The bonding is essentially sp^2 type. The bond distance between the planes is 3.35A which is about twice that of a Van Der Waal bond. The out of plane bonding is π type. The difference in bonding results in a large anisotropy in all the properties of graphite. For example, the electrical conduction along the planes is 2.3×10^3 times the electrical conductivity in the perpendicular direction. This anisotropic behavior can be further accentuated by inserting or intercalating some other atoms or molecules between the hexagonal planes. The spacing between these planes can be increased from 3.35A to as much as 8A. The physical properties can simultaneously be changed over many orders of magnitude. For example, alkali atoms, can be introduced between the planes causing enhanced n-type conduction to make the graphite a super conductor. Halogens act as acceptor atoms and cause p-type conduction. The number of molecules that can be used to intercalate is large and various types of new properties are developed.[1,3]. In Table 1, the conductivity in typically intercalated graphite is compared with that of Cu and Ag. A detailed general discussion on intercalated graphite can be found in several review articles.[1,3].

In this laboratory, samples of graphite oxide prepared by Dr. U. Sandus were studied. This intercalated graphite was produced by the action of potassium permanganate and sulfuric acid on graphite. If this graphite is dropped on a hot plate kept at 300°C, the graphite shows violent burning and puffs off as extremely fine particles of low density carbon. The carbon appears to be very light, although its

density has not yet been measured. X-ray diffraction of graphite, graphitic oxide and the carbon produced from graphitic oxide by burning, has been studied by J. Pinto. He finds that intercalation increases the interplaner spacing form 3.35A to 7.76A. The carbon which is produced on the hot plate has small particle size, almost becoming colloidal and yet some semblance of graphitic nature is still retained. Broadened and weak diffraction lines corresponding to 4.05A and 3.44A spacing indicate that all the graphite layers have not separated. Some of the graphitic oxide still exists in an intercalated form. The graphitic oxide should be further studied to determine if it can be dispersed over a desired area with the aid of an explosive. The reflectivity, particle size, and other physical properties of the carbon produced should also be measured. The behavior of other intercalated graphites containing alkali atoms, halogen, and AsF_5 requires investigation to determine if low density material is produced at elevated temperatures.

Table 1. a-axis and c-axis electrical conductivity of graphite and some graphite intercalation compounds compared with Cu and Ag metals.

Material	$\sigma_a\ (\Omega cm)^{-1}$	$\sigma_c(\Omega cm)^{-1}$	Anisotropy
Graphite	2.7×10^4	11.4	2.3×10^3
$C_{12}HNO_3$	2.7×10^5	1.96	1.4×10^5
$C_{16}AsF_5$	2.2×10^5	0.23	2.7×10^5
C_8Rb	1.0×10^5	-	-
C_8K	9.5×10^4	4.8×10^4	2.1
Cu (room temp)	0.6×10^6		
Cu (liquid N_2 temp)	6×10^6		
Ag (room temp)	0.7×10^6		
Af (liquid N_2 temp)	3×10^6		

One commercially available graphite, produced by Le Carbonne Lorraine, Rue Jean Jaures, 9223, Gennevillier, France, requires special attention. By intercalating with bisulfate, and by separating the layers of graphite, Le Carbonne Lorraine, has succeeded in producing graphite of apparent density 0.003 gm/cc (density of air = 0.00129 gm/cc). This low density graphite exhibits enhanced electrical conductivity and therefore, should show large reflectivity in the visible and infrared region of the spectrum. Of course this light and fluffy powder (20μ-120μ size) cannot be used as

such in a battlefield. A logistic problem would arise from the fact that one Kgm of the material will occupy a volume of 1 cubic meter. However, if the intercalated material with a density of $\sim$ 1 gm/cc can be blown up by heat into flaky graphite of apparent density 0.003 gm/cc, with the help of an explosive, (as graphitic oxide does on a hot plate) the material will have interesting possibilities. Twenty micron particles of Lorraine graphite will remain suspended in the air for hours.

In view of the outline given above, efforts will be continued to study the optical and physical properties of intercalated graphite using diagnostic techniques like ESCA and x-ray diffraction.

In the above, a sketchy description of some aspects of intercalated graphite has been given. In addition, there are other materials which are low dimensional and yield accentuated properties due to intercalation. Examples are:

(a) Tetracyano-p-quinodimethane, (TCNQ)

(b) Tetra-thiafulvalene (TTF)

(c) N-Methyl phenazinium (NMP)

(d) $(SN)_x$

(e) Tetracynoplatinate (TCP)

(f) Ti and Ta Dichalcogenides

(g) Polyacetylenes

(h) Polyphenylenes

References [4,5] give detailed review of these materials. The development of poly para phenylene doped with AsF_5 (Allied Chemcial Corporation)[4,7] merits special mention. Between the doped and undoped poly para phenylene the electrical conductivity changes over fourteen order of magnitude. The conductivity of undoped polymer is of the order of 10^{-10} MHO cm^{-1}, while that of the doped polymer is 5×10^4 MHOS cm^{-1} (between a semiconductor and a metal). The optical abosorbance of AsF_5 poly (p) phenylene in the infrared is large from visible to 16μ. Polyacetylene intercalated with bromine conducts almost like a metal. The films of polyacetylene can be made in various thicknesses and the electrical conduction can be controlled. Obviously, intercalated low dimensional solids are exciting materials for study. The novel properties which they exhibit include the following:

(a) High electrical conductivity

(b) Metallic state

(c) Metal insulator transition

(d) Charge density waves

(e) Superconductivity

(f) Homogeneous nonstoichiometry

(g) Mixed valency

(h) Cooperative magnetic interaction

(i) Large anisotropic ratios of intensive properties

The reader is referred to Reference 5 for a review article on low dimensional solids.

ACKNOWLEDGMENT

The author is indebted to Dr. O. Sandus, of this laboratory, for kindly providing a sample of graphitic oxide prepared by him.

REFERENCES

1. Physics Today, 31, July 1978, J. E. Fischer, T. E. Thompson.

2. Synthesis and Properties of Low Dimensional Materials, Annals of N.Y. Academy of Sciences, 313 1-828 (1978).

3. Material Science Engineering, 31 (1977).

4. Physics Today, Sept 1979.

5. Scientific American, A. J. Epstein & J. S. Miller, Vol. 241, No. 4, 52 (Oct 1979).

6. Electrical and Optical Properties of Highly Conducting Charge-Transfer Complexes of poly(p-phenylenes), L. W. Shacklette, R. R. Chance, D. M. Ivory, G. G. Miller, and R. H. Baughman, J. of Synthetic Metals (in print).

DIFFRACTION STUDIES OF VARIOUS FORMS OF CARBON

H. J. Prask and C. S. Choi
EMD, LCWSL, ARRADCOM
Dover, NJ 07801

INTRODUCTION

Carbon is a material which has been the subject of an enormous amount of study over the last several decades. Within the context of the Army obscuration and aerosal research program it is, perhaps, not a material of primary interest, per se. However, because of very interesting possibilities for intercalated graphites as obscurants (and future needs for characterizing them), and because of known efforts by other countries to employ carbonaceous materials in "smokes", some effort toward understanding the optical properties of different carbons has been sought. In the present paper we describe neutron diffraction and small-angle scattering measurements on four carbon samples. The techniques employed are of general utility and equally applicable to other materials where similar information is needed.

In the past, the type of measurements we describe for carbons have been performed primarily by x-ray techniques. We have used neutrons because of availability and convenience for data processing and to test high resolution capabilities of our existing instruments.*

In general, the scattered intensity for neutrons (or x-rays) in the $\sim$1A wavelength regime is comprised of two distinct contributions: 1) one which depends on local density fluctuations at the atomic level; and 2) a contribution which depends only on the size and shape of the particles or domains which make up the sample. It is from the "atomic level" term that Bragg scattering arises in the case of crystalline materials. More importantly for the present study, crystallite size ($\lesssim$2000A) and strain effects can manifest themselves by broadening the Bragg peaks in the diffraction pattern. An enormous amount of research[2] has been devoted to this phenomenon and very sophisticated methods of analysis are available when size and strain effects are both present. Similarly, the "domain" contribution ($\lesssim$1000A), which manifests itself through small-angle scattering, has been the subject of considerable research.[1,3] It should be emphasized that the two techniques are complementary in that Bragg peak broadening provides size information on individual crystallites ("single" crystals) of the sample; in addition, these crystallites can singly or in aggregate form domains of the size for which small-angle scattering can provide information.

---

*Work performed at the National Bureau of Standards Reactor.

RESULTS AND DISCUSSION

In the present work we have studied diffraction line broadening for four representative carbon samples: two graphites, a lampblack and a carbon black. We have also performed small-angle neutron scattering measurements (SANS) on the lampblack and carbon black in a water suspension. The differences these samples exhibit in optical properties are illustrated in Figure 1. In order to begin to correlate optical properties with "micro-structural" properties, reference to the well-established crystal structure of graphite is most useful.

The crystal structure of graphite (Figure 2) consists of covalently bonded layers, comprised of trigonally coordinated carbons, with layers arranged in ABAB... sequence (hexagonal structure) or ABCABC... sequence (rhombohedral structure). That is, the projection on the basal plane of either every second or every third layer coincides. The weak bonding between layers is Van der Waals in nature giving rise to interplanar distances of 3.348A whereas the intraplanar C-C distances are 1.418A and the width of a hexagon in a plane is 2.836A.

Because of the highly anisotropic bonding, it is possible that within the layered structure random rotations of layers can occur which destroy the perfect crystal arrangement but preserve the parallel layer structure.[4] With regard to Bragg-peak broadening, this has the consequence that (00.ℓ) planes (i.e. those planes with normals parallel to Z in Figure 2) exhibit broadenings characteristic of distances in which parallel, but not necessarily perfect, structure is preserved; (hk.0) planes (i.e. those planes with normals parallel to the X-Y plane of Figure 2) exhibit broadenings characteristic of the largest dimension of the perfect crystallites; and (hk.ℓ) planes exhibit broadenings which can be related to the perfect crystallite dimension in other directions, including the Z-axis in Figure 2. It should be mentioned that systematic studies have shown that in highly disordered structures (e.g. carbonblack), general (hk.ℓ) reflections vanish and only (00.ℓ) and (hk.0) reflections remain.[3]

In Figure 3 diffraction patterns of a graphite and carbon black are shown. Several points should be noted: 1) the diffraction patterns of the two graphites are nearly identical, similarly for the two "blacks"; 2) the graphite samples contain both hexagonal and rhombohedral forms; and 3) the "blacks" exhibit a very intense small-angle component which indicates that microscopic "domains" are present. As mentioned earlier, rather sophisticated techniques are available for analyzing diffraction peak broadenings in terms of particle size and strain effects. For the present work we make use only of the relatively simple approach of Scherrer[2], and assume all broadening is due only to particle size effects.

In Table 1, the Bragg-peak line-broadenings for all four samples are summarized. We have assumed Cauchy forms[2] for the intrinsic line shapes and "folded" these with measured Gaussian instrumental resolution functions in the least-squares fits to the data. The results show the expected types of differences but should be viewed with the following limitations in mind: 1) in the graphite samples, strains may well be present since the (00.2) and (00.4) line broadenings should be the same if crystallite size broadening alone were present (however, it should be noted that the (00.2) values are less reliable since the line-widths are closer to the resolution-limit than the (00.4) widths); and 2) even within a Scherrer approach to line broadening the multiplicative factor (0.89 in this case) is in fact crystallite shape and plane dependent and has been shown for simpler structures to vary over a range of some 20% or more.[2] On the other had, the weight fractions of hexagonal and rhombohedral forms of graphite, also shown in Table 1, do not depend on the above factors and therefore, should be quite reliable.

Finally, some preliminary SANS results for the lampblack and carbon-black should be described. As mentioned above, SANS is sensitive to the size (≤1000A) and shape of crystallites or aggregates of crystallites. The scattered intensity depends, however, in an integral relationship on size and shape so that a model is required to perform a detailed analysis of SANS data.[1] Guinier has proposed an approximation which has proven extremely useful in small-angle studies. In the Guinier regime the logarithm of intensity depends linearly on the square of momentum-transfer. The intercept and slope are related to density of scatterers and size (actually radius of gyration) of the scatterers.

In Figure 4 are shown Guinier plots of 2 wt% (with 0.7% of sodium dodecyl sulphate to maintain dispersion) of carbon and lampblack suspended in H_2O. Although the data show considerable scatter, two distinct regions are seen for each sample which yield the results shown in Table 2. The radii of gyration, $R_G(1)$ and $R_G(2)$, come directly from least squares fits to the "straight line" portions of Figure 4. If one takes the results of the Bragg-peak line broadenings (Table 1) and assumes an ellipsoid-of-revolution particle shape, the $R'_G(2)$ values of Table 2 are obtained. Agreement is sufficiently good to give us some confidence in the analysis.

Some further-very tentative-results can be extracted under certain assumptions. In a dilute system of identical particles the Q=0 intercept of the intensity vs. Q^2 plot is proportional to $N_D(\rho V)^2$ where N_D is the number of domains, ρ is the density and V is the domain volume. Assuming that the larger domains ($R_G(1)$) and smaller domains have identical densities and that the domains are all spherical ($R=R_G(5/3)^{1/2}$), the relative weight fractions shown in Table 2 are obtained. It is most surprising that this approach suggests that from one to two orders of magnitude more carbon atoms are concentrated in isolated crystallites

than in aggregates of crystallites. Before real confidence can be placed in this tentative result better data, more realistic shape-analysis, and differentiation between particle and void scattering are required.

The present results can be summarized as follows:

1) Crystallite sizes of the "blacks" are grossly different from crystallite sizes of the graphites;

2) Significant amounts of rhombohedral phase graphite are present in the two graphite samples studied;

3) Crystallite sizes and shapes (cf L(10.2)) of the graphites are measurably different;

4) Some indication of a preponderance of carbons in isolated crystallites rather than in aggregates is suggested for the "blacks".

REFERENCES

1. See, for example, "X-ray Diffraction" by A. Guinier (W. H. Freeman and Co., San Francisco and London, 1963).

2. Reviewed in "X-ray Diffraction Procedures for Polycrystalline and Amorphous Materials (2d Edition)" by H. P. Klug and L. E. Alexander. (Wiley-Interscience, New York, 1974), Chapter 9.

3. See, for example, "X-ray Studies of Carbon" by S. Ergun in "Chemistry and Physics of Carbon", edited by P. W. Walker, Jr. (Dekker, NY, 1968). Vol. 3, pp. 211-88.

4. G. E. Bacon in Proc. 3rd. Conf. on Carbon, (Pergamon Press, NY 1959) p. 475.

Table 1. Particle Dimensions From Diffraction

HEX	RHOMB[A)]	DIXON[B)]	ASBURY[B)]	MOGUL-L	LAMP BLACK
(00.2)	(111)	1050 ± 20A	1440 ± 50A	12 ± 0.4A[B)]	15.3 ± 0.3A[B)]
(10.0)		820 ± 140	780 ± 130	36 ± 0.9[C)]	34.5 ± 1.4[C)]
	(100)	145 ± 15	200 ± 20		
(10.1)		280 ± 10	210 ± 10		
	(110)	95 ± 11	95 ± 11		
(10.2)		280 ± 10	130 ± 15		
(00.4)	(222)	600 ± 20	940 ± 70		
WT(H)/WT(R)[D)]		1.03 ± 0.23	1.3 ± 0.27		

A) Some Rhombohedral-Structure plane spacings identical to hexagonal

B) $L(HKL) = 0.89\ \lambda/(FWHM)\cos\theta$

C) $L(HK) = 1.84\ \lambda/(FWHM)\cos\theta$

D) Hexagonal to rhombohedral weight ratio

Table 2. SANS Summary

	MOGUL-L	LAMP BLACK
REL. WT(1)	1.0A)	0.35 ± 0.11
R_G(1)	142 ± 3A	149 ± 7A
REL. WT(2)	36 ± 9	53 ± 19
R_G(2)	9.8 ± 0.8A	8.2 ± 1.2A
R^1_G(2)B)	11.7A	11.4A

A) See text.

B) From diffraction data.

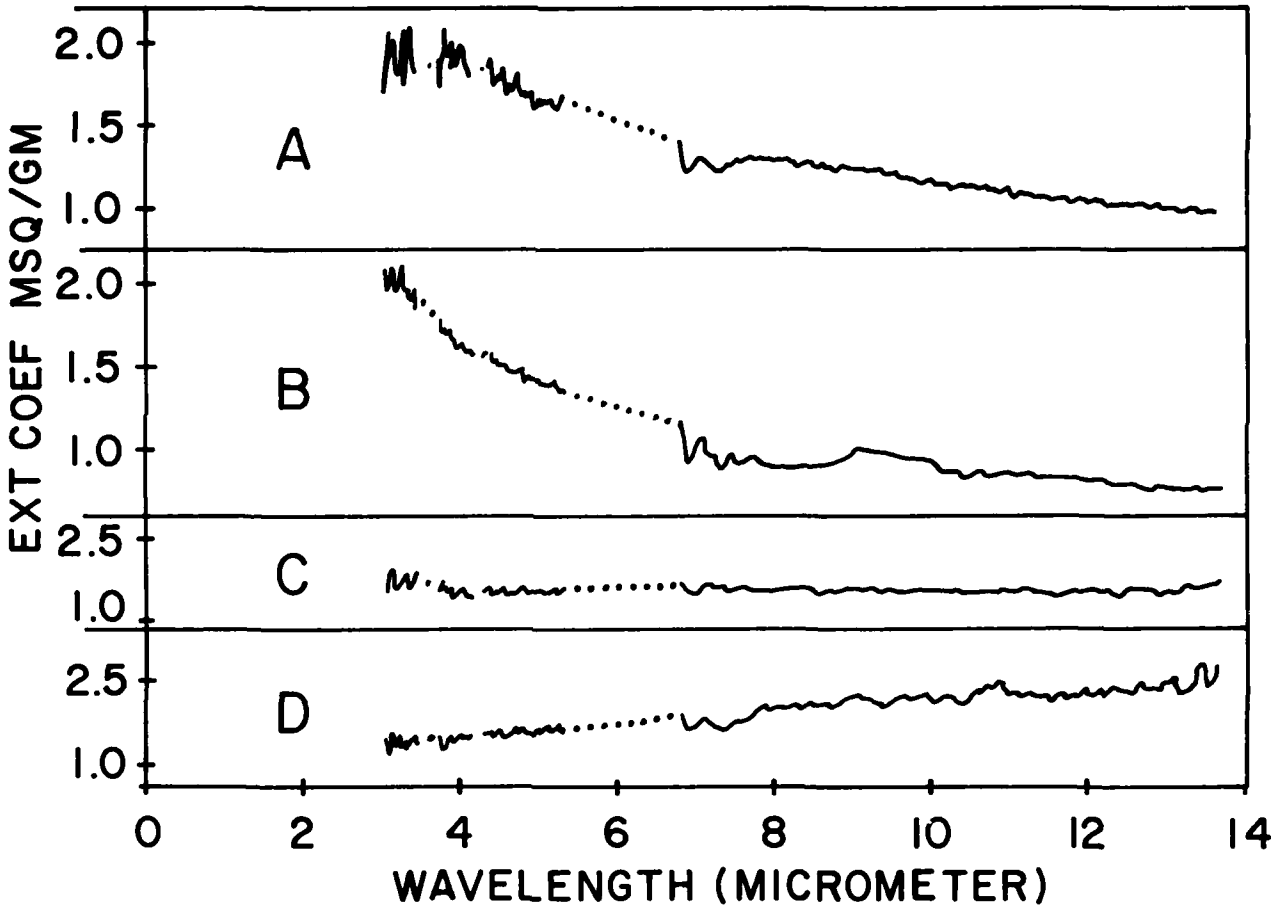

Figure 1. Extinction spectra for aerosols of the four carbon samples studied (from R. W. Doherty, CSL): A = Fisher C-198 lampblack, B = MOGUL-L carbonblack, C = Dixon Microfyne graphite, D = Asbury 6353 graphite.

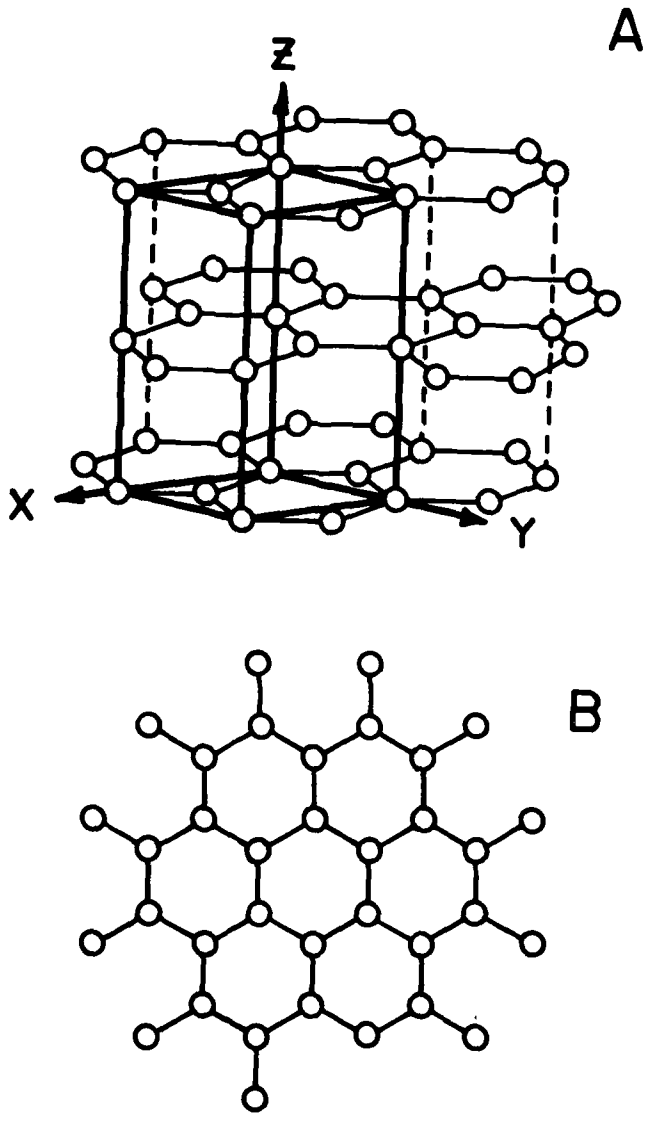

Figure 2. Crystal structure of hexagonal graphite. A, three-dimensional arrangement of layers. B, trigonally bonded array of carbons in a layer.

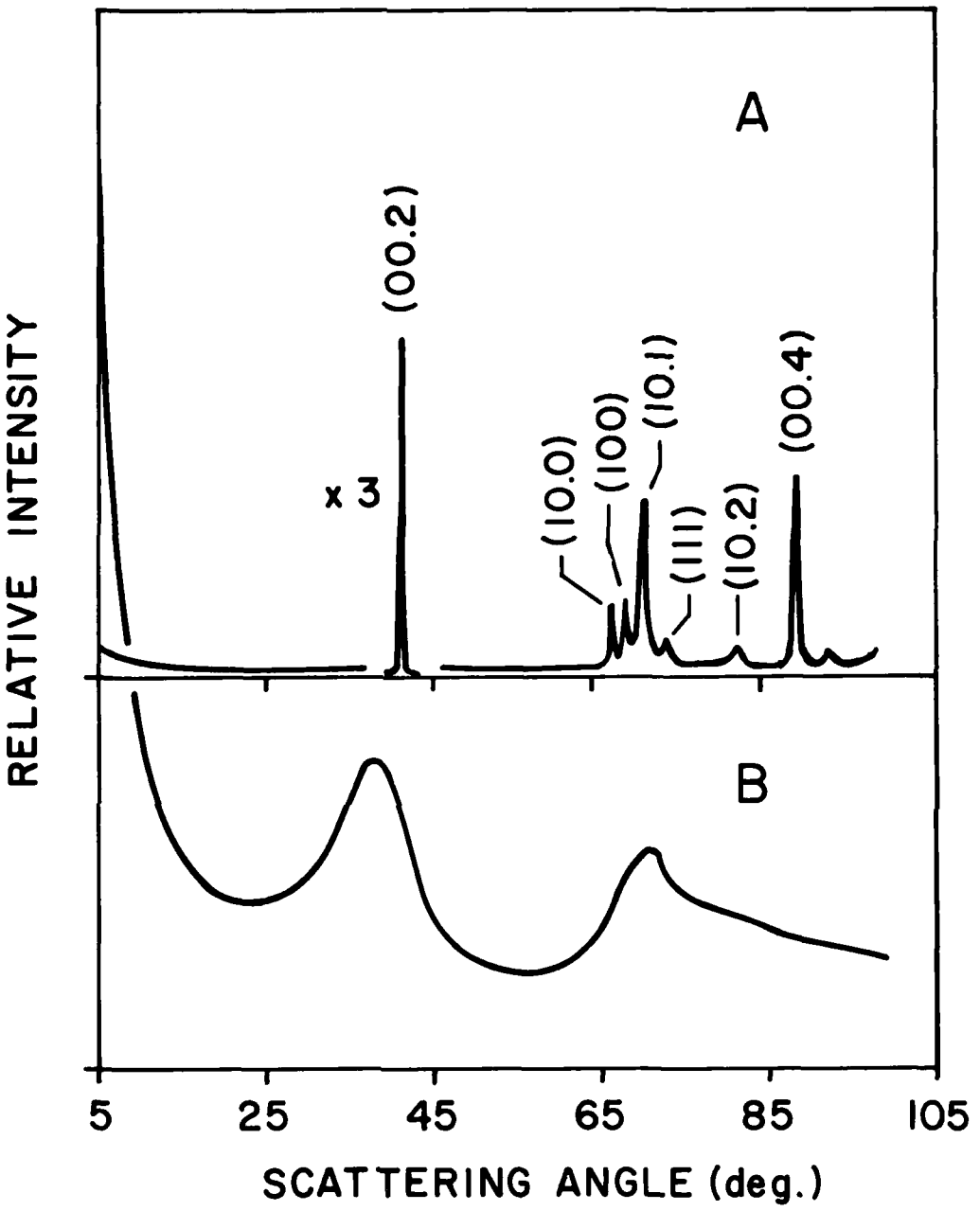

Figure 3. Neutron diffraction patterns ("large" angle) for Asbury 6353 graphite (A) and MOGUL-L carbonblack (B). Resolution and wavelength (2.36 A) were the same for both samples. In Figure 3A hexagonal (hk.l) and rhombohedral (hkl) planes are indicated but see Table 1.

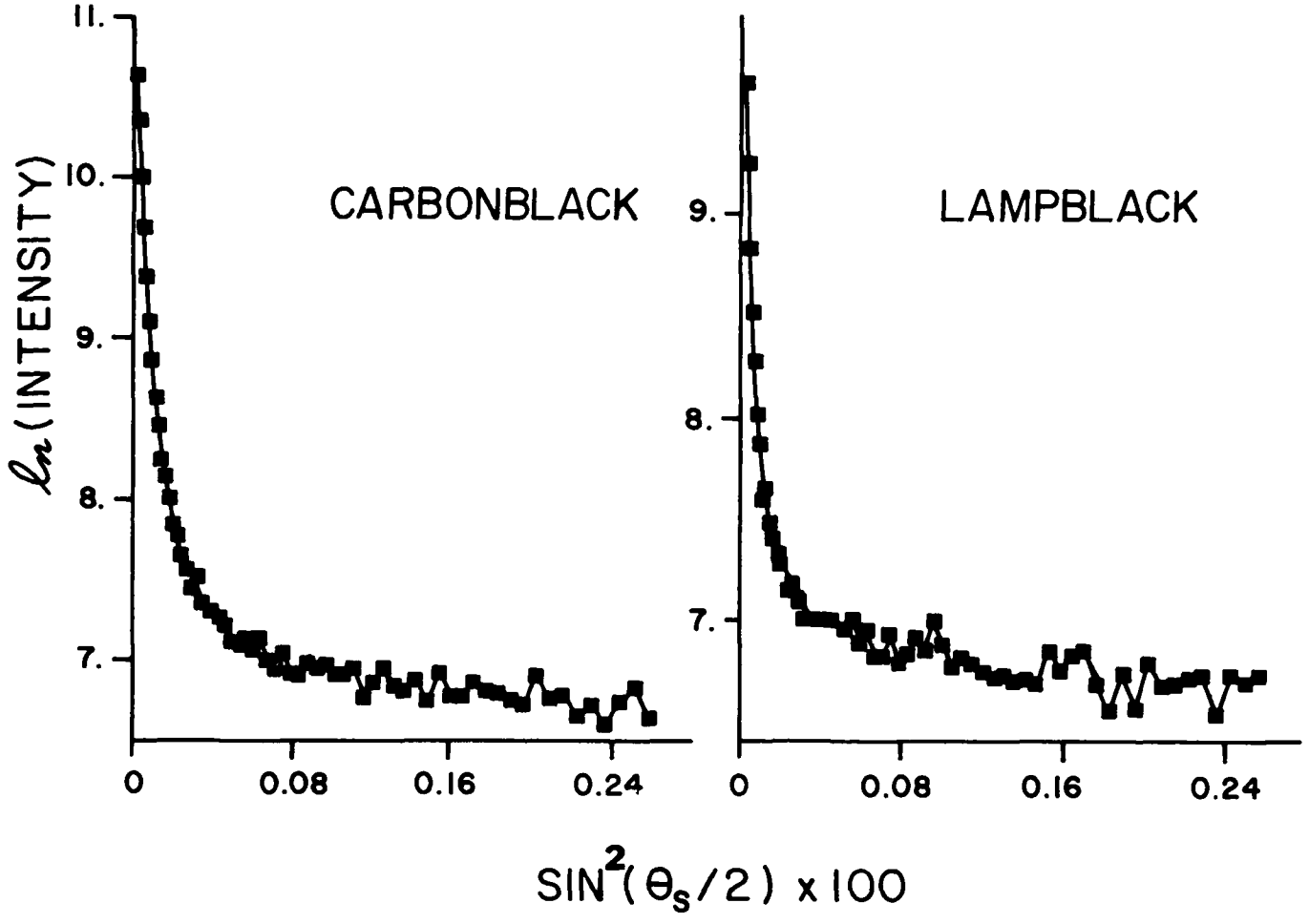

Figure 4. Guinier plots of small-angle neutron scattering data for 2 wt% MOGUL-L carbonblack and Fisher C-198 lampblack suspended in H_2O.

INFRARED EXTINCTION IN ORGANIC COMPOUNDS AND POLYMERS

T. O. Poehler
Applied Physics Laboratory, The Johns Hopkins University

INTRODUCTION

Organic compounds and polymers constitute a large class of solids with electronic properties ranging from metals to insulators. The largest group is composed of molecular crystals that are constructed from molecules that interact by van der Waal's forces, and are primarily insulators from an electronic viewpoint. The optical absorption spectra in molecular crystals arise from either Frenkel excitons or direct band to band transitions[1] so the optical absorption spectra are primarily in the visible and ultraviolet regions of the spectrum.

Complexes between molecules acting as electron donors and molecules acting as electron acceptors have been studied extensively in recent years.[2] These charge-transfer complexes exhibit closer packing than do molecular crystals, particularly in complexes resulting in the formation of a columnar arrangement of stacked donor and acceptor molecules. These charge-transfer complexes exhibit lower activation energies for electronic conductance, and generally significant anisotropy in their electrical and optical properties due to their anisotropic structure. Their optical spectra often exhibits strong intramolecular absorption bands arising from the free radical cations and anions formed in the ionic complexes. In strongly ionic complexes the ion absorption bands appear in addition to charge-transfer bands while in non-ionic complexes only the charge-transfer bands will appear.[3] The infrared spectrum of a non-ionic complex will be the sum of the spectra of the neutral donor and acceptors although the spectrum of the ionic complex is broadened, with little fine structure and having an absorption edge shifted toward longer wavelengths. Those materials in this class for which optical data exists exhibit strong absorption in the near infrared ($\lambda < 5$ μm).

Another important class of organic materials is the rapidly expanding group of ion radical organic crystals such as salts of 7,7,8,8-tetracyanoquinodimethane (TCNQ).[4] The salts have the general stoichiometric formula $D^+A_n^-$ where n is a fraction of ≥ 1. If n = 1 the salt is a simple salt while n > 1 the salt is termed complex. The strongest donors (D) and the strongest acceptors (A) form salts based on D^+ or A^- ion radicals while some compounds have non-integral electron occupancy or fractional charge. Characteristically, most organic compounds are insulators or semiconductors with room temperature conductivities less than 10^{-8} $(\Omega cm)^{-1}$ and with conductivities that decrease exponentially as the temperature is lowered. In the 1960's Melby and co-workers at DuPont discovered that some salts of 7,7,8,8-tetracyanoquinodimethane (TCNQ) (Figure 1) had electrical conductivities as high as 100 $(\Omega cm)^{-1}$. This was a remarkable value of conductivity for an organic compound although low compared to a metal such as copper where the room temperature conductivity is $5\times10^5(\Omega cm)^{-1}$ The great majority of these compounds such as the TCNQ salts are semiconductors with the electrical conductivities varying over a wide range as is also observed in the charge-transfer complexes.

AD-A113 733 KOHL (RONALD H) AND ASSOCIATES TULLAHOMA TN F/G 4/1
PROCEEDINGS OF THE 1979 CHEMICAL SYSTEM LABORATORY SCIENTIFIC C--ETC(U)
DEC 80 R H KOHL DAAK11-80-M-0021

UNCLASSIFIED ARCSL-CR-81023 NL

5 OF 5
AD
A113 733

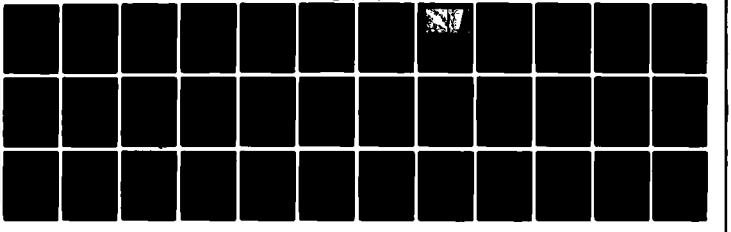

END
DATE FILMED
5-82
DTIC

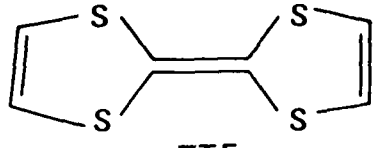

TTF
(TETRA THIOFULVALENE)

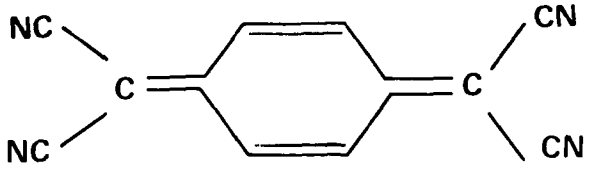

TCNQ
(TETRACYANO-P-QUINODIMETHANE)

Figure 1. Molecular structure of TTF and TCNQ.

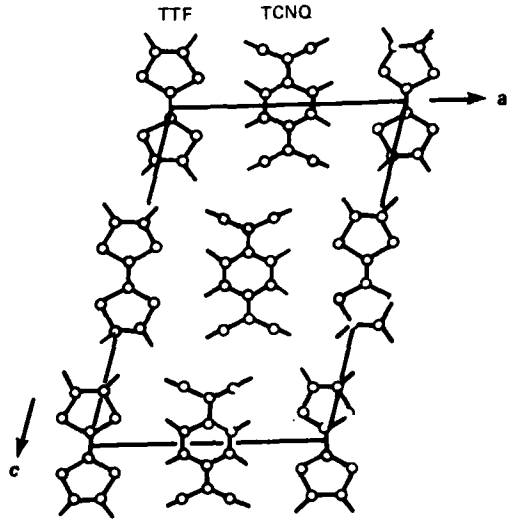

Figure 2. Crystal structure of TTF-TCNQ.

ION RADICAL SALTS

A number of these salts are observed to be semimetals rather than semiconductors.[5] The first of these was discovered by Cowan and co-workers at Johns Hopkins in 1972 when they synthesized tetrathiofulvalenium-7,7,8,8-tetracyanoquinodimethanide (TTF-TCNQ).[6] (Figure 1) This material had a room temperature conductivity of 500 $(\Omega cm)^{-1}$, and the conductivity increased as the temperature was lowered to a maximum of greater than 10^4 $(\Omega cm)^{-1}$ at about 59K. This magnitude of conductivity is sufficiently large to suggest that true metallic conduction is the conduction mechanism. Further, the increase in conductivity as the temperature is lowered is characteristic of metallic conduction where the increased conductivity is associated with decreased scattering from the crystal.

Both the optical and electrical properties of the organic compounds are determined largely by their crystal structure. When a crystal of the compound TTF-TCNQ is grown, it forms a lattice consisting of parallel conducting chains of TTF and TCNQ molecular ions separately stacked along the crystallographic b-axis.[7] The crystal structure of TTF-TCNQ projected along the conducting b-axis, shown in Figure 2, is highly anisotropic and all of the observable physical properties are likewise anisotropic. The highest occupied molecular orbital wave functions of the individual molecules are Π orbitals perpendicular to the plane of the molecules. The intermolecular spacing along each stack of molecules in the b-direction is such that the Π orbitals overlap in this direction, allowing electrons to move freely from molecule to molecule along the stack. Hence, electronic conduction along parallel conducting chains of TTF and TCNQ molecules occurs primarily along the b-axis. The weaker interaction between chains of unlike molecules along the a-axis is important in establishing position of the Fermi level so that the highest energy band is partially filled which is the criterion for metallic behavior. The highly anisotropic crystal structure of compounds such as TTF-TCNQ and the high electrical conductivity in one crystallographic direction has caused these materials to be characterized as "one-dimensional metals".

Where they have been measured, these compounds show electronic transitions in the visible or infrared along with impurity transitions usually in the infrared portion of the spectrum. The absorption coefficient for the anisotropic conducting compound TTF-TCNQ is shown in Figure 3. The absorption where the electric field is aligned parallel to the conducting b-axis is on the order of 1×10^5 cm^{-1} throughout the region 3 to 10 μm. In the same regime, the absorption coefficient for one of the perpendicular directions is smaller by at least an order of magnitude. The absorption coefficient for an unoriented thin film specimen, also shown in Figure 3 as a dashed curve, has similar features to the single crystal although the overall strength is decreased in the 1000 to 1×10^4 cm^{-1} region due to the averaging over the crystallographic directions yielding a maximum absorption coefficient of 5×10^4 cm^{-1}. The single crystal spectrum also shows strong absorption for energies above 1×10^4 cm^{-1} associated with interband transitions.

Analysis of the absorption spectrum and the reflection spectrum, which shows Drude-like behavior in the region 2000 to 8000 cm^{-1}, leads to a dielectric

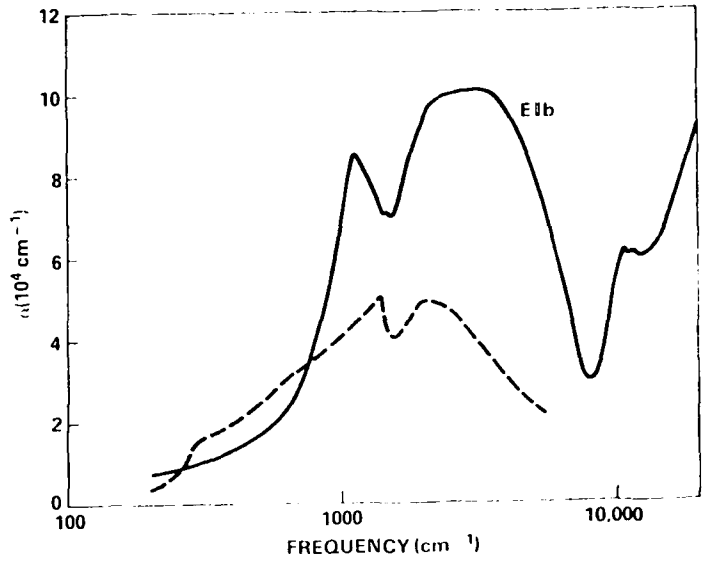

Figure 3. Infrared absorption coefficient of TTF-TCNQ.

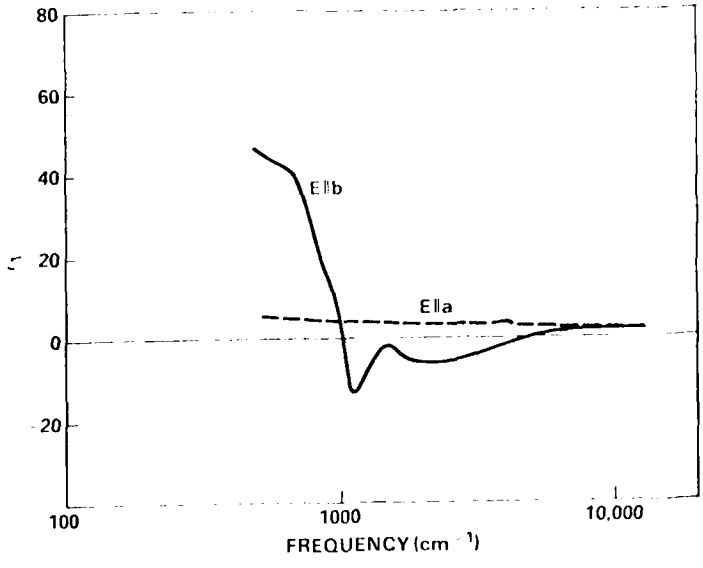

Figure 4. Dielectric constant (ε_1) of TTF-TCNQ.

function with strong frequency dependence that attains large values of the real part of the dielectric constant in some spectral regions. The real part of the dielectric constant, ε_1, is shown in Figure 4 for TTF-TCNQ in both the a- and b-crystallographic directions. In the b-direction, ε, is negative over the range 3 to 10 μm and then increases sharply to over 40 at 20 μm. The strong interactions with radiation are, of course, characterized in bulk materials by resonances in the dielectric constant, $\varepsilon(\omega)$.

$$\varepsilon(\omega) = 1 + \frac{4\pi N e^2}{m} \sum_j f_j \left\{ \frac{\omega_j^2 - \omega^2}{(\omega_j^2-\omega^2)^2 + \omega^2\Gamma_j^2} + \frac{i\Gamma_j\omega}{(\omega_j^2-\omega^2)^2 + \omega^2\Gamma_j^2} \right\}$$

In the neighborhood of each singularity in $\varepsilon(\omega)$ at $\omega = \omega_j$, $\varepsilon(\omega)$ becomes large and changes sign. These resonances are associated with various excitations such as intraband and interband electronic transitions, phonons (lattice vibration), excitons, and polarons. Collective excitation such as plasma excitations at a frequency $\omega_p = 4\pi N e^2/m$ are also responsible for strong features in the spectrum such as the reflection edge associated with $\omega_p \approx 1.2$ eV in TTF-TCNQ. It has been observed, however, that in small particles the absorptions associated with the strong resonances are shifted and broadened. In samples with dimensions much smaller than the infrared wavelength, the bulk mode contribution to the absorption diminishes and long wavelength surface modes become important.[8] Conversely, absorption associated with non-collective resonances will follow bulk spectral behavior.

It is possible to realize major modifications to organic systems by molecular substitutions which gradually alter the interchain coupling or dimensionality of the compounds. The compound TTF-TCNQ is a particularly useful prototype in this process because of the amenability of the TTF donor molecule to chemical modification. Some of the variations are illustrated in Figure 5. Some or all of the sulfur heteroatoms can be replaced by selenium while the terminal protons can be replaced with a variety of substituent groups. Likewise, new acceptor molecules such as TNAP can be substituted in place of TCNQ. In studying the role of interchain coupling, it is desirable to maintain the molecular electronic structure and intrachain stacking patterns as constant as possible while introducing steric factors chosen so as to induce changes in crystal structure.

Two methods of modifying the donor molecule (TTF) of the salt have been employed. First, the terminal protons on TTF can be replaced by electronically inert, but physically bulky substituent groups. For example, adding methyl groups gives the tetramethyl derivative TMTTF-TCNQ.[9] This molecule is too large to be accommodated by the crystal structure of TTF-TCNQ, and so forces a rotation of each molecular stack about its axis (Figure 6). The rotation weakens the interchain coupling along the a-axis and makes TMTTF-TCNQ more "one-dimensional" than its parent compound. A second modification to the donor module consists of replacing the sulfur heteroatoms by selenium to form TSF, TMTSF, or HMTSF.[10] The arrangement of interchain contacts in TCNQ salts of these molecules are qualitatively unchanged, but because of the greater spatial extent of Se and the shorter Se-N interchain separations the interchain coupling

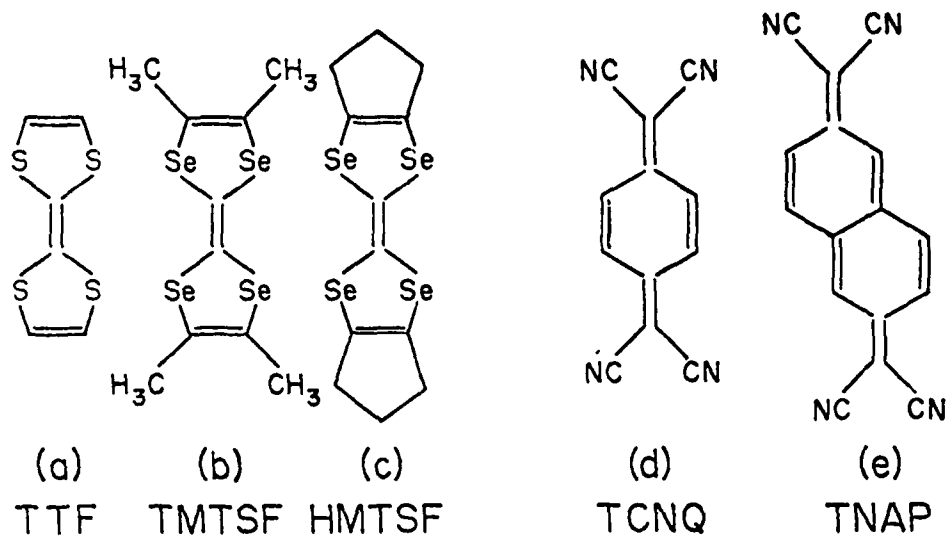

Figure 5. Modified organic molecules.

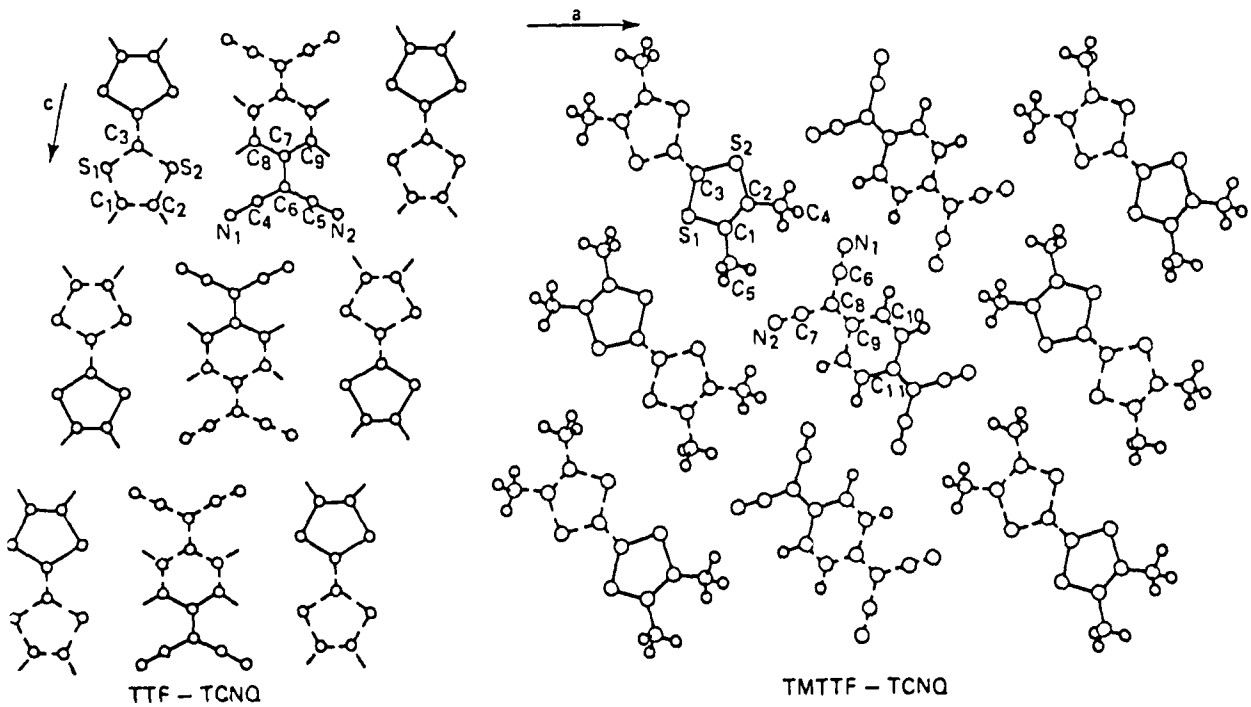

Figure 6. Crystal structure of TMTTF-TCNQ compared to TTF-TCNQ structure.

is considerably larger. From crystallographic structural studies HMTSF-TCNQ, which is the largest of these molecules, is found to adopt a lattice structure which is the most two dimensional of all the materials in the series.

These compounds are interesting prototypes for organic infrared extinction materials although not necessarily strong candidates for practical applications because of the difficulty of the synthesis procedures, but other simple salts may be expected to exhibit similar interesting features. Thus, while only a few of the charge-transfer and ion-radical organic salts have been studied for detailed optical properties, it appears that these are an important class to be evaluated based on the properties of those materials which have been investigated. A number of the simple ion-radical salts are listed in Table 1. They are generally semiconductors with activation energies for electrical conductivity ranging

Table 1. Electrical properties of compactions of some ion-radical salts.

Compound	Electrical Conductivity	
	Value at 23°C (Ω^{-1} cm^{-1})	Activation energy (eV)
Cu(TCNQ)	1×10^{-2}	0.16
Cs(TCNQ)	3×10^{-4}	0.18
K(TCNQ)	1×10^{-4}	0.35
Li(TCNQ)	5×10^{-5}	0.32
$Fe(TCNQ)_2\cdot3H_2O$	2×10^{5}	0.24
Ag(TCNQ)	2×10^{5}	0.37
Na(TCNQ)	1×10^{5}	0.33
$Mn(TCNQ)_2\cdot3H_2O$	1×10^{5}	0.16
quinolinium $(TCNQ)_2$	4.0	0.03
N-methylquinolinium $(TCNQ)_2$	0.5	0.07
diaminodurene $(TCNQ)_2$	0.5	0.08
5,8-dihydroxyquinolinium $(TCNQ)_2$	0.1	0.07
2,4,6-triphenylperylium $(TCNQ)_2$	0.1	0.04

from 0.03 to 0.4 eV. Preliminary examination of some of the simple salts for their optical properties shows them to be strong absorbers in the visible and near infrared.

As is illustrated in Table 1, many of the simple salts are obtained if a molecule such as TCNQ undergoes a one-electron reduction when combined with a number of common metals.[1] For example, the TCNQ will oxidize an iodide ion to free iodine and takes up the electron to form $TCNQ^{\cdot}$ as in

$$CuI + TCNQ \longrightarrow Cu^{+}TCNQ^{\cdot} + \frac{1}{2} I_2.$$

Alternatively, molecules like TCNQ dissolved in a solvent such as acetonitrile (CH_3CN) will undergo an oxidation-reduction reaction with some metals to form an insoluble metal salt of the anion-radical $TCNQ^{\cdot}$.

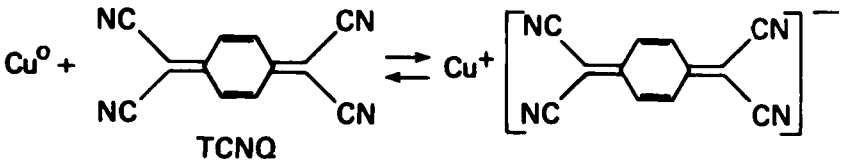

This technique can be used to prepare films of charge-transfer complexes on metallic substrates or to grow small dimension particles of these salts.[11] The scanning electron microscope pictures shown in Figure 7 show the small tightly-packed crystallites grown on a copper substrate for copper-TCNQ (Figure 7a) and copper-$TCNQF_4$ (Figure 7b). In each picture the sample is magnified 1000× and the polycrystalline layer is separated from the copper base to expose both surface and bulk properties. The size and morphology of the crystallites vary considerably as the donor metal and/or acceptor is changed in different complexes. These parameters are also different in the bulk and surface of any one material. The nonuniformity in crystals seen in any single charge-transfer complex grown from the same solution is probably the result of different rates of crystallization.

The transmission spectrum of a typical simple metal-organic salt of Li(TCNQ) is shown in Figure 8. The measurement was made using a very dilute polycrystalline powder in a KBr pellet approximately 1 mm thick. A number of strong spectral features are observed at 2200, 1575, 1500, 1325, and 1180 cm^{-1} due to vibrational absorption bands such as the $-C\equiv N$ stretch at 2200 cm^{-1}. In addition to the vibrational absorption bands, there is a broader absorption near 3400 cm^{-1} due to electronic absorption presumably related to a band-to-band transition observable in the electrical conductivity. This rich spectrum is typical of many simple metal organic salts.

POLYMERS

A significant group of materials to be considered for infrared extinction are the long chain conjugated molecules. Most polymers are characterized by

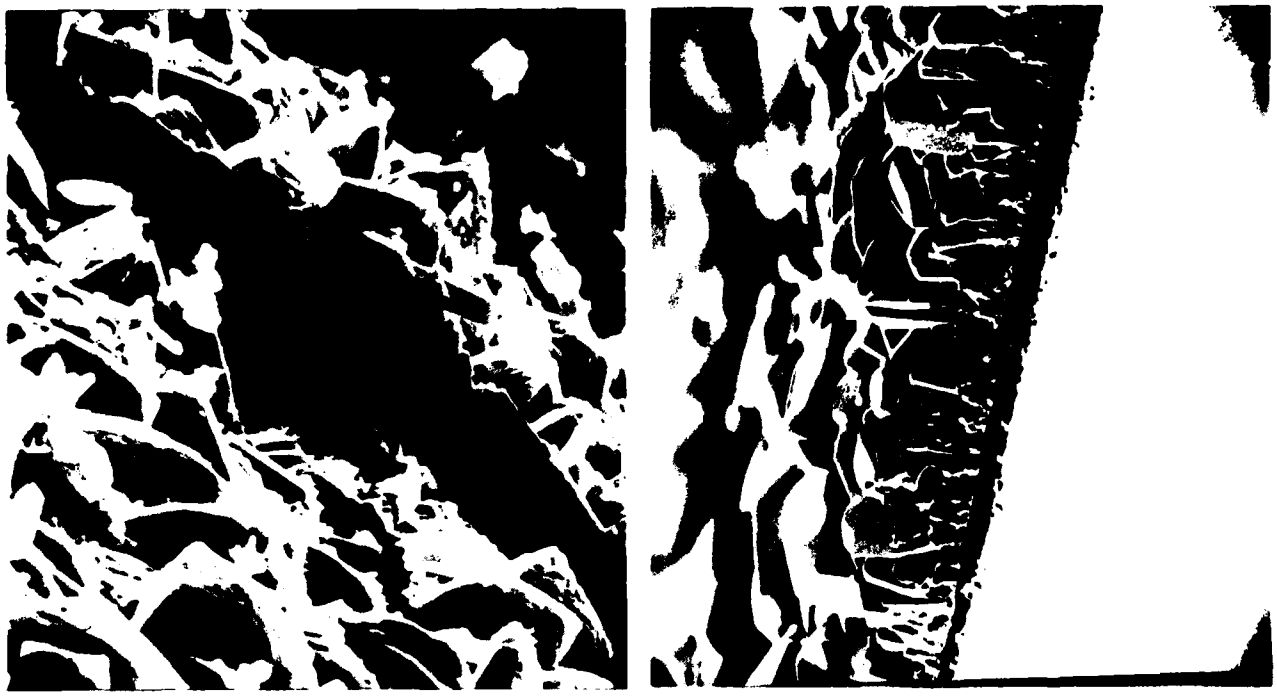

(a) (1000×) (b)

Figure 7. Scanning electron microscope pictures of (a) Cu TCNQ and (b) Cu-TNAP

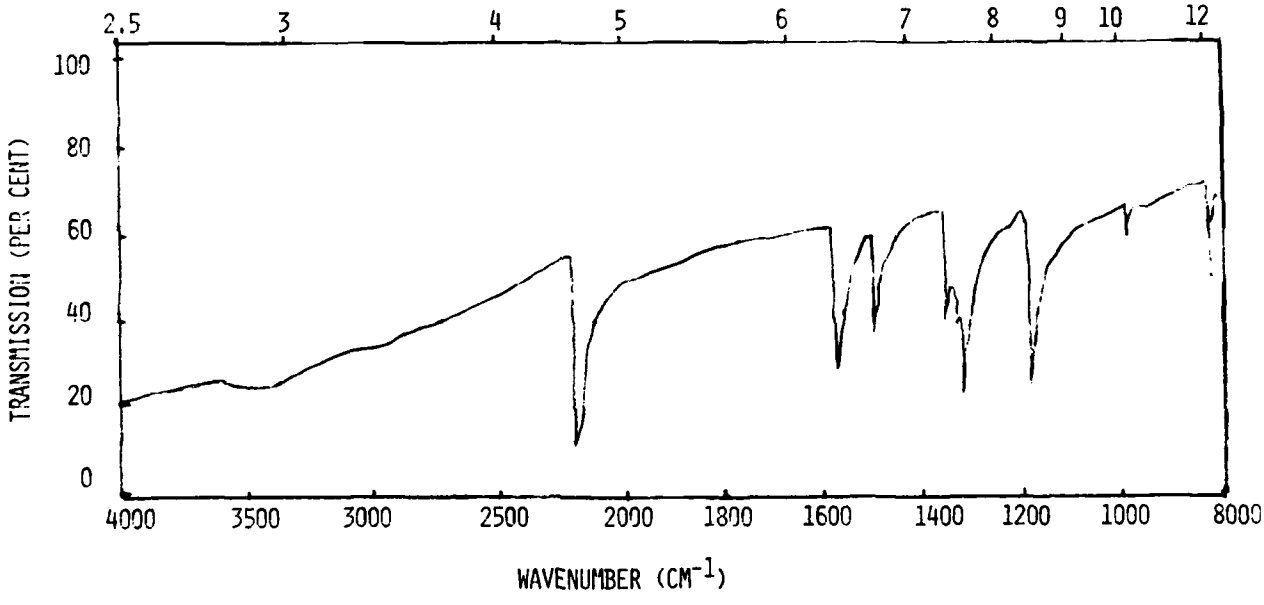

Figure 8. Infrared spectrum of Li(TCNQ) in KBR pellet.

their fundamental electronic transport properties as insulating low-mobility materials. Electromagnetic radiation is absorbed in these materials through intrinsic, impurity, dye-sensitization, or charge-transfer absorption. Considerable detailed studies have been performed on poly-N-vinyl carbazole (PVK)[12] and on charge-transfer complexes with PVK with 2,4,7-trinitro-9-fluoronone (TNF). The predominant absorption spectra of PVK and PVK:TNF are in ultraviolet and visible regions of the spectrum as a result of exciton and charge-transfer absorption, respectively. While the strong spectral features of these and other widely studied systems such as the simple linear conjugated polyacetylene[13] are in the visible region of the spectrum, introduction of impurities can produce semiconductors with high optical density in the infrared portion of the spectrum.

An overwhelming amount of chemical and physical literature has been devoted to discussions of the polymerization of systems such as acetylenes and diacetylenes.[14] Basically, these compounds can be polymerized by using either free radical or anionic initiators. The reactions require thermal catalysts, organo-metallic complex catalysts, special catalytic systems, radiochemical or photochemical techniques depending on the monomer of interest. In all cases the product of the polymerization reaction is dependent upon the type of catalyst used.

Many of the polymers which show high electrical conduction have been synthesized using organo-metallic catalysts (Ziegler-Natta type) or contain defects such as solvent molecules interstitially placed in the macromolecular structure.[15] It has been suggested that the high electrical conduction in these systems is due in part to traces of the catalyst which may form charge-transfer complexes in the polymeric material. In this way impurity levels are increased which results in an increase in intermolecular electron exchange. This tends to reduce a major barrier to electrical conduction. However, these defects which tend to increase the dark conductivity can also produce recombination centers and increase trap densities thereby lowering the lifetime, mobility and diffusion length of photogenerated carriers.[16] Large quantities of potential absorbing polymers can be produced by one of these reactions based on special catalyst systems.

Linear polyacetylene, $(CH)_x$, is the simplest conjugated organic polymer forming either *cis* or *trans* isomers as is shown in Figure 9. Measurements of optical absorption in the visible part of the spectrum show a direct band-gap semiconductor with a maximum absorption coefficient of approximately 3×10^5 cm^{-1} at 1.9 eV in *trans* $(CH)_x$ while the *cis* isomer has a 0.3 eV larger gap. Large changes in the electrical conductivity and infrared absorption can be obtained by deliberately introducing impurities in relatively low concentrations.

A simple model of localized donor or acceptor states in $(CH)_x$ uses the traditional semiconductor approach for impurity states. However, the impurity is thought to be located interstitially near the polymer chains or between chains rather than in a substitutional position. The photo-ionization of the bound impurity takes place at energy given by a typical hydrogenic model in a medium with a dielectric constant of approximately 10, leading to an impurity ionization energy of about 0.1 eV.

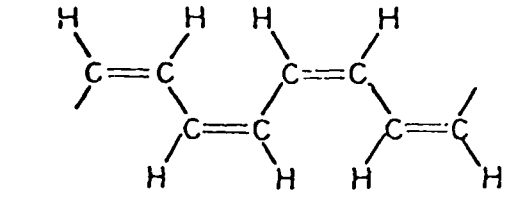

CIS

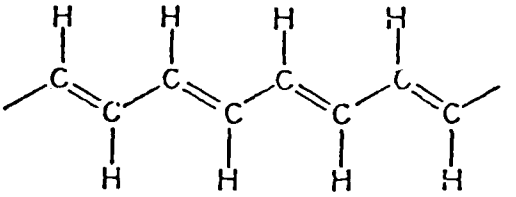

TRANS

Figure 9. Polyacetylene *cis* and *trans* structures.

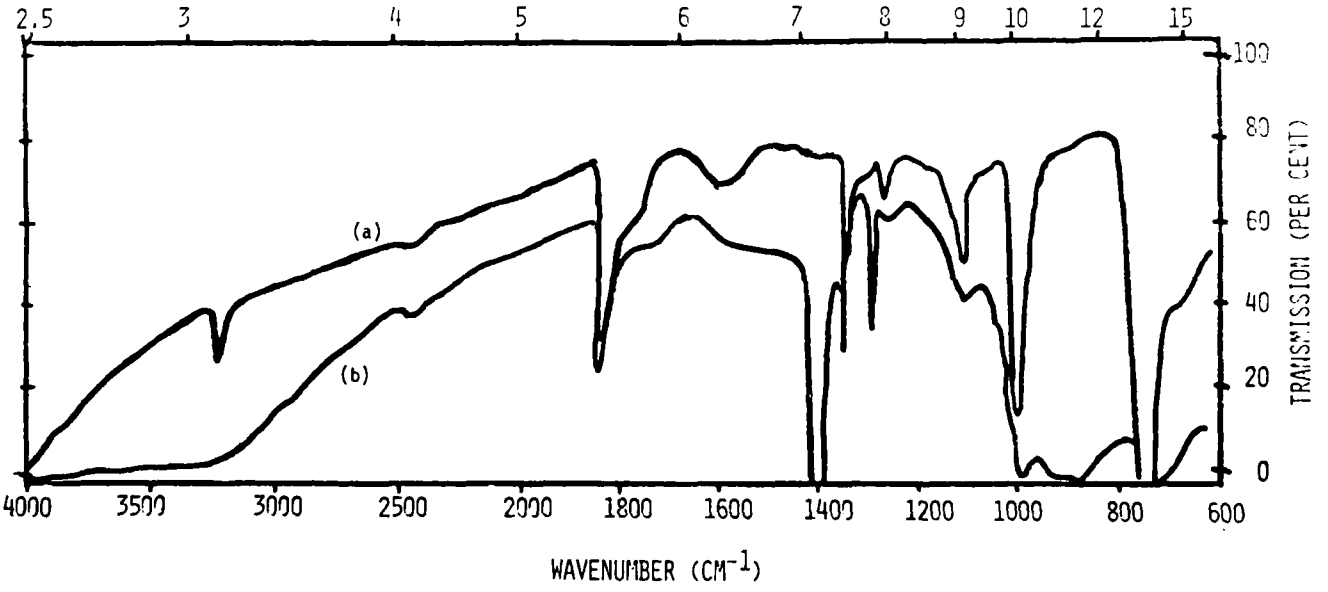

Figure 10. Infrared transmission of $(CH)_x$ films (a) undoped; (b) doped 0.1% I_2.

The infrared absorption spectrum for a thin (0.05 mm) polyacetylene film is shown in Figure 10. This upper trace shows an undoped film with strong CH vibrational transitions at 1800, 1000, and 740 cm^{-1}. Doping of approximately 0.1% iodine (lower trace) leads to a strong, broad impurity absorption in the region from 9 to 15 μm. Another, intense molecular-like absorption band at 1400 cm^{-1} also appears but cannot be explained in terms of a simple impurity transition. For concentrations of dopants greater than 3%, the infrared properties of $(CH)_x$ become those of a metal. The sensitized or impurity polymers form an important class for evaluation on their known optical properties and the relative ease of synthesis.

REFERENCES

[1] D. P. Craig and S. H. Walmsley, *Physics and Chemistry of the Organic Solid State,* D. Fox, M. M. Labes, and A. Weissberger, ed., Interscience, N.Y. (1963).

[2] J. Kommandeur, *ibid.,* Vol. II (1965).

[3] Y. Matsuaaga, J. Chem. Phys. 42, 2248 (1965).

[4] C. R. Melby, R. J. Harder, W. R. Hertler, W. Mahler, R. E. Benson, and W. E. Mochel, J. Am. Chem. Soc. 84, 3374 (1962).

[5] A. N. Bloch, T. F. Carruthers, T. O. Poehler, and D. O. Cowan, *Chemistry and Physics of One-Dimensional Metals,* H. J. Keller, ed., Plenum, N.Y. (1977).

[6] J. Ferraris, D. O. Cowan, V. Walatka, and J. H. Perlstein, J. Am. Chem. Soc. 95, 498 (1973).

[7] T. J. Kistenmacher, T. E. Phillips, and D. O. Cowan, Acta Cryst. B30, 763 (1974).

[8] D. R. Huffman, Adv. Phys. 26, 129 (1977).

[9] J. P. Ferraris, T. O. Poehler, A. N. Bloch, and D. O. Cowan, Tetrahedron Ltrs. 27, 2553 (1973).

[10] A. N. Bloch, D. O. Cowan, K. Bechgaard, R. E. Pyle, and T. O. Poehler, Phys. Rev. Ltrs. 34, 1561 (1975).

[11] R. S. Potember, T. O. Poehler, and D. O. Cowan, Appl. Phys. Ltrs. 34, 405 (1979).

[12] H. Hoegl, J. Phys. Chem. 69, 755 (1965).

[13] H. Shirakawa and S. Ikeda, Polym. J. 2, 231 (1971).

[14] M. F. Shostakovskii and A. V. Bogdanova, *The Chemistry of Diacetylenes,* Wiley, N.Y. (1974).

[15] E. Hädicke, et al, Angew Chem. 83, 253 (1971).

[16] V. Y. Merritt and H. J. Hovel, Appl. Phys. Lett. 29, 414 (1976).

INDEXES FOR PAPERS IN THESE PROCEEDINGS

INDEX A

INDEX OF AUTHORS
OF PAPERS IN THESE PROCEEDINGS

INDEX B

INDEX OF AUTHORS' ORGANIZATIONS
FOR PAPERS IN THESE PROCEEDINGS

APPENDIXES

APPENDIX A

LIST OF CONFERENCE ATTENDEES

ACADEMIC AND INDUSTRIAL ATTENDEES

ACQUISTA, PROF. CHARLES
Department of Physics
Drexel University
Philadelphia, PA 19104
(215) 895-2730

ANDREO, DR. ROBERT H.
Johns Hopkins University
Applied Physics Laboratory
Johns Hopkins Road
Laurel, MD 20810
(301) 953-7100, ext. 568

ARONSON, DR. JAMES
Arthur D. Little, Inc.
Acorn Park
Cambridge, MA 02140
(617) 864-5770

BACHMAN, DR. PAUL
Aerodyne Research, Inc.
Bedford Research Park
Crosby Drive
Bedford, MA 01730
(617) 275-9400

BAEK, DR. S. H.
Department of Chemical Engineering
University of Texas
Austin, TX 78712
(512) 471-3348

BARBER, PROF. PETER
Becton Center
Yale University
P. O. Box 2157
New Haven, CT 06520
(203) 432-4892

BICKEL, DR. WILLIAM
Department of Physics
University of Arizona
Tucson, AZ 85721
(602) 626-2534

BOTTIGER, MR. JERROLD
Department of Physics
Texas A&M University
College Station, TX 77843
(713) 845-5125

BROCK, PROF. JAMES R.
Department of Chemical Engineering
University of Texas
Austin, TX 78712
(512) 471-3348

CHANG, PROF. RICHARD K.
Becton Center
Yale University
Dept. of Engineering &
Applied Science
15 Prospect Street
New Haven, CT 06520
(203) 432-4470

CHENG, DR. WAI
Aerodyne Research, Inc.
Bedford Research Park
Crosby Drive
Bedford, MA 01730
(617) 275-9400

CHYLEK, DR. PETER
Department of Meteorology
MIT
Cambridge, MA 02139
(617) 253-2419

DAVIDSON, DR. ROBERT
R&D Associates
1401 Wilson Boulevard
Arlington, VA 22209
(703) 522-5400

DEEPAK, DR. ADARSH
Institute for Atmospheric Optics
and Remote Sensing
P. O. Box P
Hampton, VA 23666
(804) 275-9400

EBERSOLE, DR. JOHN F.
Aerodyne Research, Inc.
Bedford Research Park
Crosby Drive
Bedford, MA 01730
(617) 275-9400

FARMER, DR. MICHAEL
University of Tennessee
Space Institute
Tullahoma, TN 37388
(615) 455-0631, ext. 324

FARRELL, DR. RICHARD
Johns Hopkins University
Applied Physics Laboratory
Johns Hopkins Road
Laurel, MD 20810
(301) 953-7100, ext. 571

FEINSTEIN, DR. MATTHEW
Johns Hopkins University
Applied Physics Laboratory
Johns Hopkins Road
Laurel, MD 20810
(301) 953-7100, ext. 568

GENTRY, PROF. JAMES
Department of Chemical &
Nuclear Engineering
University of Maryland
College Park, MD 20742
(301) 454-5098/2431

GRAMS, PROF. GERALD W.
School of Geophysical Sciences
Georgia Tech
Atlanta, GA 30332
(404) 894-3897

GUINN, DR. JOHN
Radiation Research Associates
3550 Hulen Street
Ft. Worth, TX 76107
(817) 731-2711

HESS, DR. GEORGE
The Boeing Company
P. O. Box 3999
M/S 8C-23
Seattle, WA 98124
(206) 773-9678

HUFFMAN, PROF. DONALD R.
Department of Physics
University of Physics
Tucson, AZ 85721
(602) 626-4804

ISHIMARU, PROF. AKIRA
Department of Electrical Engineering
University of Washington
Seattle, WA 98195
(206) 543-2169

KENLEY, DR. RICHARD
SRI
Bldg 320
333 Ravenswood Avenue
Menlo Park, CA 94025
(415) 326-6200, ext. 5127

KERKER, PROF. MILTON
Clarkson College of Technology
Potsdam, NY 13676
(315) 268-2390

KOHL, DR. RONALD
University of Tennessee
Space Institute
Tullahoma, TN 37388
(615) 455-0631, ext. 234

KRILL, DR. JERRY A.
Johns Hopkins University
Applied Physics Laboratory
Johns Hopkins Road
Laurel, MD 20810
(301) 953-7100, ext. 568

MACK, MR. EUGENE
Calspan Corporation
Buffalo, NY 14225
(716) 632-7500, ext. 382

MACKAY, PROF. RAYMOND
Department of Chemistry
Drexel University
32nd and Market Street
Philadelphia, PA 19104
(215) 895-2642

MOELLER, PROF. K. D.
Department of Physics
Fairleigh Dickinson University
Teaneck, NJ 07666
(201) 836-6300, ext. 441

MURRAY, DR. EDWARD
SRI
Bldg 320
333 Ravenswood Avenue
Menlo Park, CA 94025
(415) 326-6200, ext. 4518

PARKER, DR. LEE W.
Lee W. Parker, Inc.
252 Lexington Road
Concord, MA 01742
(617) 369-1490

PEDERSEN, DR. NORMAN
Panametrics
221 Crescent Street
Waltham, MA 02140
(617) 899-2719

PEDERSEN, DR. JEANNE
Panametrics
221 Crescent Street
Waltham, MA 02140
(617) 899-2719

PODZIMEK, PROF. JOSEF
Graduate Center for Cloud
Physics Research
109 Norwood Hall
University of Missouri
Rolla, MO 65401
(314) 341-0338

POEHLER, DR. T. O.
Johns Hopkins University
Applied Physics Laboratory
Johns Hopkins Road
Laurel, MD 20810
(301) 792-7800, ext. 2043

QUERRY, PROF. MARVIN
Department of Physics
University of Missouri
Kansas City, MO 64110
(816) 276-1604

REED, DR. X. B.
Cloud Physics Center
University of Missouri/Rolla
Rolla, MO 65401
(314) 341-4423

SNELSON, DR. ALAN
Illinois Institute of Technology
Research Institute
10 W. 35th Street
Chicago, IL 60616
(312) 567-4260

TURNER, DR. ROBERT
Science Applications, Inc.
15 Research Drive
Ann Arbor, MI 48107
(313) 662-3261

WAGGONER, PROF. ALAN P.
Department of Civil Engineering
University of Washington
Seattle, WA 98195
(206) 543-2044

WATERMAN, DR. PETER
8 Baron Park Lane
Burlington, MA 01803
(617) 272-4494

WEINMAN, PROF. JAMES
Department of Meteorology
University of Wisconsin
1225 West Dayton Street
Madison, WI 53706
(608) 263-4052

WEIL, PROF. HERSCHEL
Department of Electronic &
Computer Engineering
University of Michigan
Ann Arbor, MI 48109
(313) 764-4329

WITHAM, MR. CLYDE
SRI
Bldg 320
333 Ravensworth Avenue
Menlo Park, CA 94025
(415) 326-6200

YUE, DR. GLENN
Institute for Atmospheric Optics
& Remote Sensing
P. O. Box P
Hampton, VA 23666
(804) 275-9400

U.S. GOVERNMENT ATTENDEES

Non-CSL Attendees

DAUM, MR. GALEN
Director
US Army Ballistics Research Laboratory
ATTN: DRDAR-BLB/Gaelen Daum
Aberdeen Proving Ground,
MD 21005
AUTOVON 283-4482
(301) 278-4482

DOLCE, MR. THOMAS
Commander
US Army Materiel Systems Analysis Activity
ATTN: DRXSY/Mr. Thomas Dolce
Bldg 392
Aberdeen Proving Ground, MD 21005
AUTOVON 283-3254
(301) 278-3254

FLOOD, DR. W. A.
Army Research Office
P. O. Box 12211
Research Triangle Park
North Carolina 27709
AUTOVON 935-3331, ext. 247
(919) 549-0641

GHIRARDELLI, DR. ROBERT G.
Army Research Office
P. O. Box 12211
Research Triangle Park
North Carolina 27709
AUTOVON 935-3331, ext. 209
(919) 549-0641

HOLLAND, MR. ALFRED
DAS/E 106
NASA Wallops Flight Center
Wallops Island, VA 23337
(804) 824-3411, ext. 328

MORRISON, DR. CLYDE
Commander
Harry Diamond Laboratories
ATTN: DRXDO-RCB
Dr. Clyde Morrison
Branch 320
2800 Powder Mill Road
Adelphi, MD 20783
AUTOVON 282-2042
(202) 394-2042

NILES, DR. FRANK
Commander/Director
Atmospheric Sciences Laboratory
ATTN: DELAS-EO-ME
Dr. Frank Niles
White Sands Missile Range,
NM 88002
AUTOVON 258-3721
(915) 678-5634

PINNICK, DR. RONALD
Commander/Director
Atmospheric Sciences Laboratory
ATTN: DELAS-EO-ME
Dr. Ronald Pinnick
White Sands Missile Range,
NM 88002
AUTOVON 258-5634
(915) 678-5634

PINTO, MR. JIM
Commander/Director
LCWSL
ATTN: DRDAR-LCE/Mr. Jim Pinto
Bldg 407
Dover, NJ 07801
AUTOVON 880-2736
(201) 328-2736

PRASK, DR. HENRY
National Bureau of Standards
Bldg 235, Room A-106
Washington, DC 20234
(301) 921-3634

ROSENWASSER, DR. H.
Commander
Naval Air Systems
ATTN: Code AIR-310C
Dr. H. Rosenwasser
Washington, DC 20361
AUTOVON 222-0372
(202) 692-0372/2516

RUHNKE, DR. LOTHAR
Naval Research Laboratory
Code 8320/Dr. Lothar Ruhnke
Washington, DC 20375
AUTOVON 297-2951
(202) 767-2951

SHARMA, DR. JAGADESH
Commander/Director
LCESL
ATTN: DRDAR-LCE/Dr. J. Sharma
Bldg 407
Dover, NJ 07801
AUTOVON 880-5490
(201) 328-5490

VAN de WAL, DR. ANTHONY
Project Manager
Smoke/Obscurants
ATTN: DRCPM-SMK
Dr. A. Van de Wal
Bldg 324
Aberdeen Proving Ground,
MD 21005
AUTOVON 283-4716
(301) 278-4716

CSL Attendees

Commander/Director
Chemical Systems Laboratory
ATTN: _____
Aberdeen Proving Ground, MD 21010

BAER, MR. LEROY
DRDAR-CLY

CARLON, MR. HUGH
DRDAR-CLB-PO

CRUMB, MR. EDGAR A.
DRDAR-CLB

DAVIS, MR. PAUL
DRDAR-CLB-A

DOHERTY, MR. ROBERT
DRDAR-CLB-PS

DOMANICO, MR. JOSEPH
DRDAR-CLN-S

EMBURY, DR. JANON
DRDAR-CLB-PS

FLANIGAN, MR. DENNIS
DRDAR-CLY

FRICKEL, MR. ROBERT
DRDAR-CLB-PS

FRY, MR. RAYMOND
DRDAR-CLN

GORDON, MR. MALCOM
DRDAR-CLN

GRAF, DR. LLOYD
DRDAR-CLC

HARRIS, DR. B. L.
DRDAR-CLD

HEYL, MS. MONICA
DRDAR-CLB-PS

HOLST, DR. GERALD C.
DRDAR-CLB-PS

KERN, MR. HARRY
DRDAR-CLN

KIMBALL, MR. DAVID
DRDAR-CLB-PO

LISAK,MR. KEITH
DRDAR-CLN

MILHAM, MR. MERRILL
DRDAR-CLB-PS

PENNSYLE, MR. RON
DRDAR-CLY

POZIOMEK, DR. EDWARD J.
DRDAR-CLB

RUBEL, MR. GLENN O.
DRDAR-CLB-PS

SARVER, DR. WILLIAM
DRDAR-CLB-A

SINDONI, DR. ORAZIO I.
DRDAR-CLB-PS

SIM, DR. VAN
DRDAR-CLB

SOMMER, MR. HAROLD
DRDAR-CLB-A

SPENCE, COL. JOHN D.
DRDAR-CLD

STUEBING, DR. EDWARD W.
DRDAR-CLB-PS

TARNOVE, MR. TED
DRDAR-CLN

TURETSKY, MR. ABRAHAM
DRDAR-CLB-PS

VERVIER, MR. JOSEPH J.
DRDAR-CLB-PS

WASEL, MR. W. DAVID
DRDAR-CLB-PO

WRIGHT, MR. ROBERT J.
DRDAR-CLB-PO

APPENDIX B

AGENDA

1979 CSL SCIENTIFIC CONFERENCE ON OBSCURATION AND AEROSOL RESEARCH

17-21 September, Bldg E4140

DETAILS OF EACH SESSION ARE GIVEN IN THE FOLLOWING LIST OF SESSION CONTENTS

MONDAY 17 September

9:30	Registration Opens
10:00	Opening of Conference Welcome - Dr. B. Harris, Deputy Director, CSL
10:15	Administrative Remarks
10:35	Smoke Research Program - Dr. E. Stuebing
11:45	Lunch
1:00	Session II A: Physical and Chemical Properties of Aerosols/Drop Growth and Composition
2:45	Coffee Break
3:15	Session II A (continued)
4:15	Adjournment
6:00	Cocktails at The Red Fox, Bel Air, MD
7:00	Dinner at The Red Fox

TUESDAY 18 September

8:30	Session III A: Aerosol Characterization Methods/Optical Particle Sizing
9:45	Coffee Break
10:15	Session III A (continued)
11:00	Session I C: Infrared Emission from Aerosols
11:30	Lunch
1:00	Session II C: Physical and Chemical Properties of Aerosols/Aerosol Elimination
1:45	Session II B: Physical and Chemical Properties of Aerosols/Particle and Plume Mechanics
2:45	Coffee Break
3:15	Session II B (continued)
4:30	Adjournment
6:00	Cocktails and dinner at Haussner's Restaurant, Baltimore, MD

WEDNESDAY 19 September

8:30	Session I A: Optical Properties of Aerosols/Light Scattering from Spherical (Including Layered) Particles Talks 1-3
9:40	Session I B: Optical Properties of Aerosols/Light Scattering from Nonspherical Particles
10:20	Coffee Break
10:45	Session I B (continued)
12:10	Lunch
1:15	Session III D: Aerosol Characterization Methods/Workshop Discussion: Selection of Phase Matrix Elements for Nonspherical Particle Distribution Signatures
2:15	Session I B: Optical Properties of Aerosols/Light Scattering from Nonspherical Particles
3:00	Coffee Break
3:30	Session I B (continued)
5:00	Adjournment
5:00-6:30	Happy Hour at Officers' Club
6:30	Beef and Burgundy Dinner at Officers' Club

THURSDAY 20 September

8:30	Session I A: Optical Properties of Aerosols/Light Scattering from Spherical (Including Layered) Particles Talks 4-7
9:50	Coffee Break
10:15	Session I D: Optical Properties of Aerosols/Cooperative Scatter, Multiple Scatter, and Radiative Transfer
11:55	Lunch
1:55	Session III B: Aerosol Characterization Methods/In-Situ Optical Constants Measurements on Aerosols
2:55	Coffee Break
3:20	Session III C: Aerosol Characterization Methods/Inversion Methods
4:00	Session IV A: Obscurant Materials/Optical Constants of Liquids and Powders
5:00	Adjournment
6:00	Crab Feast at Jackie's Bar Harbor Inn, Abingdon, MD

FRIDAY 21 September

8:30	Session IV B: Obscurant Materials/Selection of Optically Interesting Materials
10:20	Coffee Break
10:45	Concluding Discussion: Directions for Future Research
12:00	Closing of Conference

APPENDIX C

SESSION CONTENTS

1979 CSL SCIENTIFIC CONFERENCE ON OBSCURATION AND AEROSOL RESEARCH

17-21 September

I. Optical Properties of Aerosols

A. Light Scattering from Spherical (Including Layered) Particles (Wed & Thurs am)

1. Milton Kerker, Light Scattering by Active Particles

2. Richard Chang, Intensity and Angular Pattern of the Inelastic Radiation from Monodispersed Spherical Hydrosols

3. Richard Chang, Intensity Enhancement and Angular Pattern of Inelastic Radiation

4. Peter Chylek, Resonances in Light Scattering

5. Ronald Pinnick, Extinction and Mass Concentration of Carbon, FS, HC, Phosphoric Acid and Fog Oil Smokes

6. Richard Farrell, Jerry Krill, and Robert Andreo, Variational Methods for Electromagnetic Wave Scattering from Stochastic Systems

7. M. Feinstein, R. Hart, R. Farrell, Variational Calculation of Scattering from a Sphere

8. Adarsh Deepak, The Effects and Remote Sensing of Aerosol Microphysical Processes on the Extinction of Infrared/Visible Laser Beams

B. Light Scattering from Nonspherical Particles (Wed am & pm)

1. Milton Kerker, Inelastic Scattering by Nonspherical Particles

2. Milton Kerker, Light Scattering by Inhomogeneous Particles

3. Peter Barber, Extinction Properties of Inhomogeneous Particles

4. Janon Embury, Extinction by Nonspherical Particles

5. Bill Bickel, Information Content in Off Diagonal Matrix Elements for Nonspherical Particles

6. Jerry Bottiger, Phase Matrix Measurements for Cubic Particles of NaCl

7. George Hess, A Comparison between Scattering by Spherical and Nonspherical Particles

8. Herschel Weil, EM Scattering by Discs and Hollow, Noncircular Cylinders

9. Charles Acquista, (title not available at present time)

10. Norm Pedersen, Results and Limitations of Present Electro-Magnetic Theory for Lossy Cylinders

11. Jean Pedersen, EM Scattering by Lossy Cylinders

12. Galen Daum, EM Absorption and Scattering from Thin Cylinders

13. Donald Schuerman, Summary of the Workshop on Light Scattering by Irregularly Shaped Particles

14. R. T. Wang, Extinction Signatures of Non-Spherical/Non-Isotropic Particles

C. Infrared Emission from Aerosols (Tues am)

1. Raymond McKay, Infrared Emission from Gas Aerosol Reactions

D. Cooperative Scatter, Multiple Scatter, and Radiative Transfer (Thurs am)

1. Akira Ishimaru, Multiple Scattering Effects on Short Pulses in a Dense Medium

2. A. C. Holland, Radiative Transfer Turbid Media

3. Peter Waterman, Radiative Transfer Analysis

4. James Weinman, Theoretically Derived Radiances from Scattering and Absorbing Media

5. Ronald Kohl, An Approach to Multiple Scattering Calculations

II. Physical and Chemical Properties of Aerosols

A. Drop Growth and Composition (Mon pm)

1. S. H. Baek, Experimental System for Study of Growth of Fog Oil Droplets

2. J. R. Brock, Modeling Oil Droplet Growth in Dense Plumes: Assymptotic Limitsize Distributions, Brownian Coagulation, and Particle Growth and Evaporation.

3. Alan Snelson, Chemical Composition of Droplets of HC and Fog Oil Smokes

4. Paul Davis and William Sarver, Gas Liquid Chromatography Studies of Oil Smoke Materials

5. G. Rubel, Particle Growth in Phosphorus Smokes

B. Particle and Plume Mechanics (Tues pm)

1. J. R. Brock, Nongauusian Plume Modeling: K-Theory of Dispersion in the Surface Boundary Layer, Probabalistic Model of Internal Structure, and Cell Models of Effects of Charged Particles and Thermal Activity of Particles

2. Lee Parker, Aerosol Charging and Cloud Electrification

3. Robert Turner, Vaporization of Fog Oil and Phosphorus Smoke Particles in a Laser Beam

4. X. B. Reed, Effect of Turbulence on Aerosol Mechanics-Turbulent Structure

C. Aerosol Elimination (Tues pm)

1. Josef Podzimek, Free Fall of Non-Spherical Collectors of Aerosol Particles

2. X. B. Reed, Coalescence Mechanisms

III. Aerosol Characterization Methods

A. Optical Particle Sizing (Tues am)

1. W. Michael Farmer, Particle Sizing Interferometer Measurements of Hygroscopic Smokes in Laboratory and Field Environments

2. James Gentry, Optical and Gravimetric Measurement for Characterizing Distributions of Fibers

3. Clyde Morrison, Extended Rayleigh Theory of the Oscillation of Liquid Droplets

4. W. Michael Farmer, Measurement of Fiber Size Characteristics in Static Settling Chambers and Under Expanded Jets

5. J. R. Brock, New Fast Response Instrument for Measurement of Aerosol Particle Size Distribution

B. In-Situ Optical Constants Measurements on Aerosols (Thurs pm)

1. Allan Waggoner, Measurement of Aerosol Absorption, Scattering and Extinction Coefficients

2. W. Chang, J. Ebersole, M. Camac, Laboratory Measurement of the Optical Properties of Smoke

3. Gerald Grams, In-Situ Aerosol Measurements with Polar Nephelometers

C. Inversion Methods (Thurs pm)

1. James Gentry, Inversion of Diffusion Battery Data for Particle Size Distribution

D. Workshop Discussion: Selection of Phase Matrix Elements for Nonspherical Particle Distribution Signatures

IV. Obscurant Materials

A. Optical Constants of Liquids and Powders (Thurs pm)

1. Karl Moeller, Reflection Spectroscopy in the Near IR

2. Karl Moeller, Optical Instrumentation for the Millimeter Region

3. Marvin Querry, Optical Constants of Selected Liquids, Solids and Powders in the IR

B. Selection of Optically Interesting Materials (Fri am)

1. Don Huffman, Enhanced IR Absorption Due to Quantum Size Effects?

2. Donald Weigand, Experimental Studies of the Optical Extinction of Various Forms of Carbon

3. Jag Sharma, Intercallation Compounds of Graphite for Obscurant Material

4. Hank Prask, Diffraction Studies of Various Forms of Carbon

5. T. O. Poehler, Infrared Extinction in Polymers and Mixed Alloys

DISTRIBUTION LIST FOR SMOKE RESEARCH CONFERENCES

Names	Copies
CHEMICAL SYSTEMS LABORATORY	
ATTN: DRDAR-CLB	1
ATTN: DRDAR-CLB (Mr. Joseph J. Vervier)	1
ATTN: DRDAR-CLB (Dr. Edward Poziomek)	1
ATTN: DRDAR-CLB (Richard L. Dimmick)	1
ATTN: DRDAR-CLB-A (Mr. Paul Davis)	1
ATTN: DRDAR-CLB-A (Dr. William Sarver)	1
ATTN: DRDAR-CLB-A (Mr. Harold Sommer)	1
ATTN: DRDAR-CLB-B	1
ATTN: DRDAR-CLB-P (Mr. Bernard V. Gerber)	1
ATTN: DRDAR-CLB-PO (Mr. Robert V. Jolliffe)	1
ATTN: DRDAR-CLB-PO (Mr. Arthur K. Stuempfle)	1
ATTN: DRDAR-CLB-PO (Mr. Hugh Carlon)	1
ATTN: DRDAR-CLB-PO (Mr. David Kimball)	1
ATTN: DRDAR-CLB-PO (Mr. Roy E. Shaffer)	1
ATTN: DRDAR-CLB-PO (Mr. W. David Wasel)	1
ATTN: DRDAR-CLB-PO (Mr. Robert J. Wright)	1
ATTN: DRDAR-CLB-PS (Mr. David Anderson)	1
ATTN: DRDAR-CLB-PS (Dr. J. Bottiger)	1
ATTN: DRDAR-CLB-PS (Mr. Robert Doherty)	1
ATTN: DRDAR-CLB-PS (Dr. Janon Embury)	1
ATTN: DRDAR-CLB-PS (Mr. Robert Frickel)	1
ATTN: DRDAR-CLB-PS (Ms. Monica Heyl)	1
ATTN: DRDAR-CLB-PS (Dr. Gerald C. Holst)	1
ATTN: DRDAR-CLB-PS (Mr. Merrill Milham)	1
ATTN: DRDAR-CLB-PS (Mr. Glenn Rubel)	1
ATTN: DRDAR-CLB-PS (Dr. James Savage)	1
ATTN: DRDAR-CLB-PS (Dr. Orazio I. Sindoni)	1
ATTN: DRDAR-CLB-PS (Dr. Edward W. Stuebing)	10
ATTN: DRDAR-CLB-PS (Mr. Abraham Turetsky)	1
ATTN: DRDAR-CLB-T	1
ATTN: DRDAR-CLC	1
ATTN: DRDAR-CLC (Mr. Stan Mumford)	1
ATTN: DRDAR-CLC-BA (Mr. Edward Boyce)	1
ATTN: DRDAR-CLC-BD (Mr. Patrick Berry)	1
ATTN: DRDAR-CLC-CR (Mr. Dennis Flanigan)	1
ATTN: DRDAR-CLC-PO (Mr. William A. Cooper)	1
ATTN: DRDAR-CLD	1
ATTN: DRDAR-CLG	1
ATTN: DRDAR-CLJ-R	3
ATTN: DRDAR-CLJ-L	3
ATTN: DRDAR-CLJ-M	1
ATTN: DRDAR-CLN	
ATTN: DRDAR-CLN (Mr. Edward Fry)	1
ATTN: DRDAR-CLN (Mr. Harry Kern)	1
ATTN: DRDAR-CLN (Mr. Keith Lisak)	2
ATTN: DRDAR-CLN (Mr. Ted Tarnove)	1
ATTN: DRDAR-CLN-S	1
ATTN: DRDAR-CLN-S (Mr. Robert Dow)	1
ATTN: DRDAR-CLN-S (Mr. Joseph Domanico)	1
ATTN: DRDAR-CLN-ST	1
ATTN: DRDAR-CLP	1
ATTN: DRDAR-CLW-P	1
ATTN: DRDAR-CLY	4
ATTN: DRDAR-CLY (Mr. Leroy Baer)	1
ATTN: DRDAR-CLY (Mr. Ron Pennsyle)	1
ATTN: DRDAR-CLY-R	1
DEPARTMENT OF DEFENSE	
Defense Technical Information Center	
ATTN: DTIC-DDA-2	2
Cameron Station, Building 5	
Alexandria, VA 22314	
Under Secretary of Defense Research and Engineering	
ATTN: DUSDRE (Mr. Thomas Dashiell)	1
Room 3D129, The Pentagon	
Washington, DC 20301	
Office of the Director	
Defense Research and Engineering	
ATTN: Dr. T.C. Walsh, Rm 3D-1079	1
Washington, DC 20310	
Institute for Defense Analysis	
400 Army-Navy Drive	
ATTN: L. Biberman	1
ATTN: R. E. Roberts	1
Arlington, VA 22202	
Advanced Research Projects Agency	1
1400 Wilson Boulevard	
Arlington, VA 22209	

DEPARTMENT OF THE ARMY

HQDA (DAMO-NCC) 1
HQDA (DAMA-ARZ, Dr. Verderame) 1
HQDA (DAMA-CSS-C) 1
HQDA (DAMI-FIT) 1
WASH, DC 20310

HQDA, OCE (DAEN-RDM, Dr. Gomez) 1
Massachusetts Ave, NW
WASH, DC 20314

US ARMY MATERIEL DEVELOPMENT AND
READINESS COMMAND

Commander
US Army Materiel Development and
Readiness Command
ATTN: DRCDE-DM 1
ATTN: DRCLDC 1
ATTN: DRCMT 1
ATTN: DRCSF-S 1
ATTN: DRCSF-P 1
ATTN: DRCDL (Mr. N. Klein) 1
ATTN: DRCBI (COL Gearin) 1
ATTN: DRCLD (Mr. T. Shirata) 1
5001 Eisenhower Ave
Alexandria, VA 22333

Army Research Office
ATTN: DRXRO-GS 1
ATTN: Dr. Robert G. Ghirardelli 1
ATTN: Dr. W.A. Flood 1
P.O. Box 12211
Research Triangle Park, NC 27709

Commander
Harry Diamond Laboratories
ATTN: DRXDO-RCB (Dr. Donald Wortman) 1
ATTN: DRXDO-RCB (Dr. Clyde Morrison) 1
ATTN: DRXDO-RDC (Mr. D. Giglio) 1
2800 Powder Mill Road
Adelphi, MD 20783

Chief, Office of Missile Electronic Warfare
US Army Electronic Warfare Laboratory
ATTN: DRSEL-WLM-SE (Mr. K. Larson) 1
White Sands Missile Range, NM 88002

Commander/Director
Atmospheric Sciences Laboratory
ATTN: DELAS-AS (Dr. Charles Bruce) 1
ATTN: DELAS-EO (Dr. Frank Niles) 1
ATTN: DELAS-EO-ME 1
ATTN: DELAS-EO-EN (Dr. Donald Snider) 1
ATTN: DELAS-EO-EN (Mr. James Gillespie) 1
ATTN: DELAS-EO-EN (Dr. Ronald Pinnick) 1
ATTN: DELAS=EO-MO (Dr. Melvin Heaps) 1
ATTN: DELAS-EO-MO (Dr. Robert Sutherland) 1
ATTN: DELAS-EO-S (Dr. Louis Duncan) 1
White Sands Missile Range, NM 88002

Director
NVEOL
ATTN: DRSEL-NV-VI (Dr. R. G. Buser) 1
ATTN: DRSEL-NV-VI (Mr. R. Bergemann) 1
Fort Belvoir, VA 23651

US Army Mobility Equipment Research and
Development Center
ATTN: Code/DROME-RT (Mr. O.F. Kezer) 1
Fort Belvoir, VA 22060

Commander
US Army Electronics Command
ATTN: DRSEL-WL-S (Mr. J. Charlton) 1
Ft. Monmouth, NJ 07703

Director
Human Engineering Laboratory
ATTN: DRXHE-SP (CB Defense Team) 1
Aberdeen Proving Ground, MD 21005

Commander
US Army Foreign Science & Technology
Center
ATTN: DRXST-CD (Mr. V. Rague) 1
ATTN: DRXST-MT3 1
220 Seventh St., NE
Charlottesville, VA 22901

Director
US Army Materiel Systems Analysis Activity
ATTN: DRXSY (Mr. Thomas Dolce) 1
ATTN: DRXSY-MP 1
ATTN: DRXSY-D (Dr. Fallin) 1
ATTN: DRXSY-GS (Mr. Chernick) 1
ATTN: DRXSY-LA (Dr. Liu) 1
ATTN: DRXSY-TN (Mr. Metz) 2
Aberdeen Proving Ground, MD 21005

Commander
US Army Missile Command
Redstone Scientific Information Center
ATTN: DRSMI-RPR (Documents) 1
ATTN: DRSMI-RGT (Mr. Matt Maddix) 1
ATTN: DRDMI-CGA (Dr. B. Fowler) 1
ATTN: DRDMI-KL (Dr. W. Wharton) 1
ATTN: DRDMI-TE (Mr. H. Anderson) 1
Redstone Arsenal, AL 35809

Commander
USA Materials & Mechanics Research Center
ATTN: DRXMR-KA (Dr. Saul Isserow) 1
Watertown, MA 02172

US ARMY ARMAMENT RESEARCH AND DEVELOPMENT COMMAND

Commander
US Army Armament Research and Development Command
ATTN: DRDAR-LCE (Mr. Jim Pinto) 1
ATTN: DRDAR-LCE (Dr. D. A. Weigand) 1
ATTN: DRDAR-TSS 5
Dover, NJ 07801

Commander
US Army Armament Research and Development Command
ATTN: DRDAR-QAC-D (Mr. Francis) 1
Aberdeen Proving Ground, MD 21010

Project Manager Smoke/Obscurants
ATTN: DRCPM-SMK 3
ATTN: DRCPM-SMK (Dr. A. Van de Wal) 1
ATTN: DRCPM-SMK-T (Mr. Gary Nelson) 1
Aberdeen Proving Ground, MD 21005

Director
Ballistic Research Laboratory, ARRADCOM
ATTN: DRXBR-CL (Mr. T. Finnerty) 1
ATTN: DRXBR-P (Mr. N. Gerri) 1
ATTN: DRDAR-BLB (Mr. P. Reitz) 1
ATTN: DRDAR-BLB (Mr. A LaGrange) 1
ATTN: DRDAR-BLB (Dr. Gaelen Daum) 1
ATTN: DRDAR-TSB-S 1
Aberdeen Proving Ground, MD 21005

US ARMY ARMAMENT MATERIEL READINESS COMMAND

Commander
US Army Armament Materiel Readiness Command
ATTN: DRSAR-ASN 1
ATTN: DRSAR-PE 1
Rock Island, IL 61299

Commander
USA ARRCOM
ATTN: DRSAR-MAS-C 1
ATTN: DRSAR-MAD-E 1
ATTN: SARTE 1
Aberdeen Proving Ground, MD 21010

US ARMY TRAINING & DOCTRINE COMMAND

Commandant
US Army Infantry School
ATTN: NBC Division 1
Fort Benning, GA 31905

Commandant
US Army Missile & Munitions Center and School
ATTN: ATSK-CD-MD 1
ATTN: ATSK-DT-MU-EOD 1
Restone Arsenal, AL 35809

Commander
US Army Logistics Center
ATTN: ATCL-MG 1
Fort Lee, VA 23801

Commandant
USAMP&CS/TC&FM
ATTN: ATZN-CM-CDM 1
Fort McClellan, AL 36205

Commander
USA Training and Doctrine Command
ATTN: ATCD-TEC (Dr. M. Pastel) 1
ATTN: ATCD-Z 1
Fort Monroe, VA 23651

Commander
US Army TRADOC System Analysis Activity
ATTN: ATAA-SL 1
White Sands Missile Range, NM 88002

US ARMY TEST & EVALUATION COMMAND

Commander
US Army Test & Evaluation Command
ATTN: DRSTE-CM-F 1
ATTN: DRSTE-CT-T 1
Aberdeen Proving Ground, MD 21005

Commander
US Army Dugway Proving Ground
ATTN: Technical Library, Docu Sect 1
ATTN: STEDP-PO 1
ATTN: STEDP-MT (Dr. L. Salamon) 1
ATTN: STEDP-MT-DA-E 1
ATTN: STEDP-MT-DA-T 1
Dugway, UT 84022

DEPARTMENT OF THE NAVY

Chief of Naval Research
ATTN: Code 443 1
800 N. Quincy Street
Arlington, VA 22217

Commander
Naval Explosive Ordnance Disposal Facility
ATTN: USA Technical Detachment 1
ATTN: Army Chemical Officer (Code AC-3) 1
Indian Head, MD 20640

Commander
Naval Surface Weapons Center
White Oak Site
ATTN: Library I-321 1
Silver Spring, MD 20910

Chief, Bureau of Medicine & Surgery
Department of the Navy
ATTN: MED 3C33 1
Washington, DC 20372

Commander
Naval Weapons Center
ATTN: Code 3542 (Dr. J. Carroz) 1
ATTN: Code 382 (Dr. P. St. Amand) 1
ATTN: Technical Library (Code 343) 1
China Lake, CA 93555

Commanding Officer
Naval Weapons Support Center
ATTN: Code 5042 (Dr. B.E. Douda) 1
ATTN: Code 5041 1
Crane, IN 47522

Commander
Naval Intelligence Suport Center 1
4301 Suitland Road
Washington, DC 20390

Commander
Naval Surface Weapons Center
Dahlgren Laboratory
ATTN: DX-21 1
ATTN: Mr. R.L. Hudson 1
ATTN: F-56 (Mr. Douglas Marker) 1
Dahlgren, VA 22448

Commander
Naval Research Laboratory
ATTN: Code 5709 (Mr. W. E. Howell) 1
ATTN: Code 8326 (Dr. James Fitzgerald) 1
ATTN: Code 43202 (Dr. Hermann Gerber) 1
ATTN: Code 8320 (Dr. Lothar Ruhnke) 1
4555 Overlook Avenue, SW
Washington, DC 20375

Commander
Naval Air Systems Command
ATTN: Code AIR-301C (Dr. H. Rosenwasser) 1
Washington, DC 20361

US MARINE CORPS

Commandant
HQ, US Marine Corps
ATTN: Code LMW 1
Washington, DC 20380

Director, Development Center
Marine Corps Development and
Education Command
ATTN: Fire Power Division 1
Quantico, VA 22134

DEPARTMENT OF THE AIR FORCE

HQ Foreign Technology Division (AFSC)
ATTN: TQTR 1
Wright-Patterson AFB, OH 45433

Commander
Armament Development & Test Center
ATTN: DLOSL (Technical Library) 1
Eglin AFB, FL 32542

Commander
Aeronautical Systems Division
ATTN: ASD/AESD 1
Wright-Patterson AFB, OH 45433

HQ AFLC/LOWMM 1
Wright-Patterson AFB, OH 45433

HQ, AFSC/SDNE 1
Andrews AFB, MD 20334

HQ AMD/RD
ATTN: Chemical Defense OPR 1
Brooks AFB, TX 78235

HQ AFISC/SEV 1
Norton AFB, CA 92409

NORAD Combat Operations Center/DOUN 1
Cheyenne Mtn Complex, CO 80914

Air Force Aerospace Medical Research Laboratory
ATTN: AFAMRL/HE (Dr. C.R. Replogle) 1
Wright-Patterson AFB, OH 45433

USAF SAM/RZW 1
Brooks AFB, TX 78235

HQ AFTEC/SGB 1
Kirtland AFB, NM 87117

Commander, AFGL
Hanscom Air Force Base
ATTN: AFGL-POA (Dr. Frederick Volz) 1
Bedford, MA 01731

Dr. Robert N. Buchal
Air Force Office of Scientific Research
ATTN: AFOSR-NM 1
Bolling AFB, DC 20332

OUTSIDE AGENCIES

Battelle, Columbus Laboratories
ATTN: TACTEC 1
505 King Avenue
Columbus, OH 43201

Toxicology Information Center, WG 1008
National Research Council 1
2101 Constitution Ave., NW
Washington, DC 20418

US Public Health Service
Center for Disease Control
ATTN: Lewis Webb, Jr. 1
Building 4, Room 232
Atlanta, GA 30333

Director
Central Intelligence Agency
ATTN: ORD/DD/S&T 1
Washington, DC 20505

NASA Wallops Flight Center
ATTN: Mr. Alfred Holland 1
DAS/E 106
Wallops Island, VA 23337

Los Alamos Scientific Laboratory
Mail Stop 896
ATTN: Dr. Gary Salzman 1
Los Alamos, NM 87545

ADDITIONAL ADDRESSEES

National Bureau of Standards
ATTN: Dr. Henry Prask 1
Bldg. 235, Room A-106
Washington, DC 20234

Prof Charles Acquista 1
Department of Physics
Drexel University
Philadelphia, PA 19104

Dr. James Aronson 1
Arthur D. Little, Inc.
Acorn Park
Cambridge, MA 02140

Dr. Paul Bachman 1
Aerodyne Research, Inc.
Bedford Research Park
Crosby Drive
Bedford, MA 01730

Mr. Ray Baker 1
Lockheed Missile & Space Co.
4800 Bradford Blvd.
Huntsville, AL 35807

Dr. Peter Barber 1
Dept of Electrical Engineering
University of Utah
Salt Lake City, UT 84112

Dr. William Bickel 1
Department of Physics
University of Arizona
Tucson, AZ 85721

Dr. Richard Bird 1
Solar Energy Research Institute
1536 Cole Boulevard
Golden, CO 80401

Mr. Wolfram Blattner 1
Radiation Research Assocs., Inc.
3550 Helen Street
Fort Worth, TX 76107

Prof V.N. Bringi 1
Dept of Engineering Mechanics and
Atmospheric Sciences Program
Ohio State University
Columbus, OH 43210

Prof. James R. Brock 1
Department of Chemical Engineering
University of Texas
Austin, TX 78712

Dr. Albert Brunsting 1
Coulter Electronics, Inc.
440 W. 20th St.
Hialeah, FL 33010

Dr. Chris W. Busch 1
Spectrum Development Laboratories, Inc.
3303 Harbor Blvd.
Suite G-3
Costa Mesa, CA 92626

Prof. John Carstens 1
Graduate Center for Cloud Physics Research
University of Missouri
109 Norwood Hall
Rolla, MO 65401

Prof. A. W. Castleman 1
Department of Chemistry
University of Colorado
Campus Box #215
Boulder, CO 80309

Prof. J. Cermak 1
Department of Civil Engineering
Colorado State University
Fluid Mechanics & Wind Engineering Program
Ft. Collins, CO 80523

Prof. Richard K. Chang 1
Becton Center
Yale University
15 Prospect Street
New Haven, CT 06520

Dr. Wai Cheng 1
Aerodyne Research, Inc.
Bedford Research Park
Crosby Drive
Bedford, MA 01730

Dr. Peter Chylek 1
Center for Earth and Plantary Science
Harvard University
Pierce Hall
Cambridge, MA 02138

Prof. Ariel Cohen 1
Department of Atmospheric Sciences
Hebrew University of Jerusalem
Jerusalem,
ISRAEL

Mr. William Curry 1
PWT/ATD CALSPAN, Inc.
MS-640
Arnold Air Force Station, TN 37389

Dr. Robert Davidson 1
R&D Associates
1401 Wilson Boulevard
Arlington, VA 22209

Dr. Adarsh Deepak 1
Institute for Atmosphereic Optics and
Remote Sensing
P.O. Box P
Hampton, VA 23666

Mr. Dale Divis 1
Lockheed Missile & Space Co.
4800 Bradford Blvd
Huntsville, AL 35807

Dr. John F. Ebersole 1
OPTIMETRIES, INC.
2000 Hogback Rd, Suite 2
Ann Arbor, MI 48104

Dr. Michael Farmer 1
University of Tennessee
Space Institute
Tullahoma, TN 37388

Dr. Richard Farrell 1
Johns Hopkins University
Applied Physics Laboratory
Johns Hopkins Road
Laurel, MD 20810

Dr. Edward Fry 1
Department of Physics
Texas A&M University
College Station, TX 77843

Prof. I. Galilly 1
Dept of Atmospheric Sciences
Hebrew University of Jerusalem
Jerusalem,
ISRAEL

Prof. James Gentry 1
Dept of Chemical & Nuclear Engineering
University of Maryland
College Park, MD 20742

Prof. Gerald W. Grams 1
School of Geophysical Sciences
Georgia Tech
Atlanta, GA 30332

Dr. John Guinn 1
Radiation Research Associates
3550 Helen Street
Ft. Worth, TX 76107

Prof. Benjamin M. Herman 1
Institute of Atmosphere Physics
Building No. 81
University of Arizona
Tucson, AZ 85721

Dr. George Hess 1
The Boeing Company
P.O. Box 3999
M/S 8C-23
Seattle, WA 98124

Prof. Donald R. Huffman 1
Department of Physics
University of Arizona
Tucson, AZ 85721

Prof. Akira Ishimaru 1
Department of Electrical Engineering
University of Washington
Seattle, WA 98195

Dr. S.G. Jennings 1
Department of Pure and Applied Physics
U.M.I.S.T
P.O. Box 88
Manchester M60 1QD
ENGLAND

Prof. George Kattawar 1
Department of Physics
Texas A&M University
College Station, TX 77843

Dr. Sidney Katz 1
ITT Research Institute
10 West 35th Street
Chicago, IL 60616

Dr. Richard Kenley 1
SRI
Bldg. 320
333 Ravenswood Avenue
Menlo Park, CA 94025

Prof. Milton Kerker 1
Clarkson College of Technology
Potsdam, NY 13676

Dr. Ralph E. Kleinman 1
Dept of Mathematics
University of Delaware
Newark, DE 19711

Dr. Robert Knoellenberg 1
Particle Measuring Systems, Inc.
1855 South 57th Court
Boulder, CO 80301

Dr. Ronald Kohl 1
University of Tennessee
Space Institute
Tullahoma, TN 37388

Prof. J. Latham 1
U.N.I.S.T.
P.O. Box 88
Manchester MGO 1QD
ENGLAND

Mr. Paul Latimer
Department of Physics
Auburn University
Auburn, AL 36849
1

Prof. Kuo-nan Liou
Department of Physics
University of Utah
Salt Lake City, UT 84112
1

Prof. Y.H. Benjamin Liu
Dept. of Mechanical Engineering
University of Minnesota
Minneapolis, MN 55455
1

Prof. Dwight Look
Dept. of Mechanical and Aerospace Engineering
University of Missouri-Rolla
Rolla, MO 65401
1

Dr. Hendricis G. Loos
Laguna Research Laboratory
21421 Stans Lane
Laguna Beach, CA 92651
1

Mr. Eugene Mack
Calspan Corporation
Buffalo, NY 14225
1

Prof. Raymond Mackay
Department of Chemistry
Drexel University
32nd and Market Street
Philadelphia, PA 19104
1

Dr. William Marlow
Brookhaven Nat'l Lab
Upton, NY 11973
1

Mr. John Martin
University of Missouri
Cloud Physics
Rolla, MO 65401
1

Prof. August Miller
Department of Physics
New Mexico State University
P.O. Box 3D
Las Cruces, NM 88003
1

Prof. K.D. Moeller
Department of Physics
Fairleigh Dickinson University
Teaneck, NJ 07666
1

Dr. Edward Murray
SRI
Bldg. 320
333 Ravenswood Avenue
Menlo Park, CA 94025
1

Dr. Lee W. Parker
Lee W. Parker, Inc.
252 Lexington Road
Concord, MA 01742
1

Dr. William A. Pearce
E.G.G Washington Analytical Service Center
P.O. Box 398
Riverdale, MD 20890
1

Dr. Norman Pedersen
Panametrics
221 Crescent Street
Waltham, MA 02140
1

Dr. Richard L. Pitter
University of Maryland
Dept of Meteorology
College Park, MD 20742
1

Mr. Antonino Piuchino
The Aerospace Corporation
Bldg. A6-1647
P.O. Box 92957
Los Angles, CA 90009
1

Prof. Joseph Podzimek
Graduate Center for Cloud Physics Research
109 Norwood Hall
University of Missouri
Rolla, MO 65401
1

Dr. T.O. Poehler
Johns Hopkins University
Applied Physics Laboratory
Johns Hopkins Road
Laurel, MD 20810
1

Prof. Marvin Querry
Department of Physics
University of Missouri
Kansas City, MO 64110
1

Dr. X.B. Reed
Cloud Physics Center
University of Missouri-Rolla
Rolla, MO 65401
1

Dr. David M. Roessler
Physics Department
General Motors
Research Laboratories
Warren, MI 48090
1

Dr. Stuart A. Schleusener
Department of Electrical and Computer Engineering
New Mexico State University
Las Cruces, NM 88003
1

Dr. Donald Schuerman
Space Astronomy Laboratory
University of Florida
1810 N.W. 6th St.
Gainesville, FL 32601
1

Prof. David T. Shaw
Laboratory for Power and Environmental Studies
State University of New York at Buffalo
4232 Ridge Lea Road
Buffalo, NY 14226
1

Dr. Alan Snelson
Illinois Institute of Technology
Research Institute
10 W. 35th Street
Chicago, IL 60616
1

Dr. Wolfgang H Steinicke
Buck gmbH & Co.
823 Bad Reichenhall
Germany
1

Mr. Igantius Tang
Bldg. 815
Brookhaven National Laboratory
Upton, NY 11973
1

Prof. Vincent Tomaselli
Department of Physics
Fairleigh Dickinson University
Teaneck, NJ 07666
1

Dr. Robert Turner
Science Applications, Inc.
15 Research Drive
P.O. Box 7329
Ann Arbor, MI 48107
1

Dr. Edward E. Uthe
SREI, International
Menlo Park, CA 94025
1

Prof. V. Varadan
Wave Propgation Group
Dept of Engineering Mechanics and Atmospheric Sciences Program
Ohio State University
Columbus, OH 43210
1

Prof. Alan P. Waggoner
Department of Civil Engineering
University of Washington
Seattle, WA 98195
1

Dr. Peter Waterman
8 Baron Park Lane
Burlington, MA 01803
1

Prof. Herschel Weil
Department of Electrical and Computer Engineering
University of Michigan
Ann Arbor, MI 48109
1

Prof. James Weinman
Department of Meteorology
University of Wisconsin
1225 West Dayton Street
Madison, WI 53706
1

Mr. Clyde Witham
SRI
Bldg. 320
333 Ravensworth Ave.
Menlo Park, CA 94025
1

Dr. Arvel B. Witte
ATTN: R1/1032
Engineering Sciences Laboratory
TRW, INC.
One Space Park
Redondo Beach, CA 90278

1

Dr. Phillip J. Wyatt
Science Spectrum
P.O. Box 3003
Santa Barbara, CA 93105

1

Prof. Cavour Yeh
Dept. of Engineering
UCLA
405 Highland Ave.
Los Angeles, CA 90024

1

Dr. Paul C. Yue
Graduate Center for Cloud
Physics Research
108 Norwood Hall
University of Missouri
Rolla, MO 65401

1

*U.S. GOVERNMENT PRINTING OFFICE : 1982 0-522-000/3026

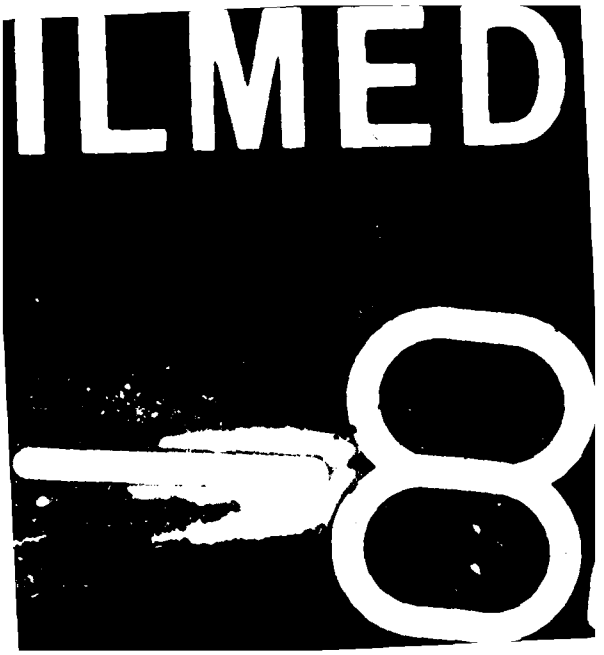
ILMED